THE UNIVERSITY OF QUEENSLAND

AUSTRALIA

Properties of Materials for Organic Light Emitting Diodes

Arthur Robert Gordon Smith

A thesis submitted for the degree of Doctor of Philosophy at

The University of Queensland in November 2011

School of Chemistry and Molecular Biosciences

Declaration by author

This thesis is composed of my original work, and contains no material previously published or written by another person except where due reference has been made in the text. I have clearly stated the contribution by others to jointly-authored works that I have included in my thesis.

I have clearly stated the contribution of others to my thesis as a whole, including statistical assistance, survey design, data analysis, significant technical procedures, professional editorial advice, and any other original research work used or reported in my thesis. The content of my thesis is the result of work I have carried out since the commencement of my research higher degree candidature and does not include a substantial part of work that has been submitted to qualify for the award of any other degree or diploma in any university or other tertiary institution. I have clearly stated which parts of my thesis, if any, have been submitted to qualify for another award.

I acknowledge that an electronic copy of my thesis must be lodged with the University Library and, subject to the General Award Rules of The University of Queensland, immediately made available for research and study in accordance with the *Copyright Act 1968*.

I acknowledge that copyright of all material contained in my thesis resides with the copyright holder(s) of that material.

Statement of Contributions to Jointly Authored Works Contained in the Thesis

Smith, A. R. G.; Riley, M. J.; Lo, S.-C.; Burn, P. L.; Gentle, I. R.; Powell, B. J. *Phys. Rev. B* **2011**, *83*, 041105(R). – ARGS was responsible for 90% of data collection, 50% of data interpretation and analysis, 50% of drafting and writing and 10% of conception and design; MJR was responsible for 10% of data collection and 10% of data interpretation and analysis; PLB was responsible for 10% of data interpretation and analysis, 10% of drafting and writing and 50% of conception and design; BJP was responsible for 40% of data interpretation and analysis, 40% of drafting and writing and 40% of conception and design. SCL and IRG helped with drafting and writing.

Smith, A. R. G.; Burn, P. L.; Powell, B. J. *ChemPhysChem* **2011**, *12*, 2429. – ARGS was responsible for 100% of data collection, 45% of data interpretation and analysis and 50% of drafting and writing; PLB was responsible for 10% of data interpretation and analysis, 10% of drafting and writing and 40% of conception and design; BJP was responsible for 45% of data interpretation and analysis, 40% of drafting and writing and 60% of conception and design.

Smith, A. R. G.; Riley, M. J.; Burn, P. L.; Gentle, I. R.; Lo, S.-C.; Powell, B. J. *Inorg. Chem.* **2012**, *51*, 2821. – ARGS was responsible for 95% of data collection, 50% of data interpretation and

analysis, 50% of drafting and writing and 10% of conception and design; MJR was responsible for 5% of data collection and 5% of data interpretation and analysis; PLB was responsible for 5% of data interpretation and analysis, 10% of drafting and writing and 50% of conception and design; BJP was responsible for 40% of data interpretation and analysis, 40% of drafting and writing and 40% of conception and design. SCL and IRG helped with drafting and writing.

Smith, A. R. G.; Ruggles, J. L.; Cavaye, H.; Shaw, P. E.; Darwish, T. A.; James, M.; Gentle, I. R.; Burn, P. L. *Adv. Funct. Mater.* **2011**, *21*, 2225. – ARGS was responsible for 100% of sample preparation, 50% of chemical synthesis, 60% of data collection, 80% of data interpretation and analysis, 50% of drafting and writing and 20% of conception and design; JLR was responsible for 20% of data collection; HC was responsible for 10% of data collection; PES was responsible for 10% of data collection; TAD was responsible for 40% of chemical synthesis; MJ was responsible for 10% of chemical synthesis and 5% of drafting and writing; IRG was responsible for 10% of data interpretation and analysis, 15% of drafting and writing and 40% of conception and design; PLB was responsible for 10% of data interpretation and analysis, 30% of drafting and writing and 40% of conception and design.

Smith, A. R. G.; Lee, K. H.; Nelson, A.; James, M.; Burn, P. L.; Gentle, I. R. *Adv. Mater.* **2012**, *24*, 822. – ARGS was responsible for 95% of sample preparation, 60% of data collection, 70% of data interpretation and analysis, 60% of drafting and writing and 40% of conception and design; KHL was responsible for 5% of sample preparation and 20% of data collection; AN was responsible for 10% of data interpretation and analysis; MJ was responsible for 20% of data collection; PLB was responsible for 10% of data interpretation and analysis, 20% of drafting and writing and 30% of conception and design; IRG was responsible for 10% of data interpretation and analysis, 20% of drafting and writing and 30% of conception and design.

Statement of Contributions by Others to the Thesis as a Whole

Prof. P.L. Burn, Prof. I.R. Gentle and Assoc. Prof. B.J. Powell had significant and substantial input into the concept and design of the project, as well as critical revision of this thesis so as to contribute to the interpretation.

Statement of Parts of the Thesis Submitted to Qualify for the Award of Another Degree

None.

Published Works by the Author Incorporated into the Thesis

Smith, A. R. G.; Riley, M. J.; Lo, S.-C.; Burn, P. L.; Gentle, I. R.; Powell, B. J. *Phys. Rev. B* **2011**, *83*, 041105(R). – Incorporated as Chapter 2

Smith, A. R. G.; Burn, P. L.; Powell, B. J. *ChemPhysChem* **2011**, *12*, 2429. – Incorporated as Chapter 3

Smith, A. R. G.; Riley, M. J.; Burn, P. L.; Gentle, I. R.; Lo, S.-C.; Powell, B. J. *Inorg. Chem.* **2012**, *51*, 2821. – Incorporated as Chapter 4.

Smith, A. R. G.; Ruggles, J. L.; Cavaye, H.; Shaw, P. E.; Darwish, T. A.; James, M.; Gentle, I. R.; Burn, P. L. *Adv. Funct. Mater.* **2011**, *21*, 2225. – Incorporated as Chapter 5

Smith, A. R. G.; Lee, K. H.; Nelson, A.; James, M.; Burn, P. L.; Gentle, I. R. *Adv. Mater.* **2012**, *24*, 822. – Incorporated as Chapter 6.

Additional Published Works by the Author Relevant to the Thesis but not Forming Part of it

Lee, K. H.; Schwenn, P. E.; Smith, A. R. G.; Cavaye, H.; Shaw, P. E.; James, M.; Krueger, K. B.; Gentle, I. R.; Meredith, P.; Burn, P. L. *Adv. Mater.* **2011**, *23*, 766.

Darwish, T. A.; Smith, A. R. G.; Gentle, I. R.; Burn, P. L.; Luks, E.; Moraes, G.; Gillon, M.; Holden, P. J.; James, M. *Tetrahedron Lett.* **2012**, *53*, 931.

Acknowledgements

I don't think anyone really knows what they are getting themselves in for when starting a PhD. I must admit I didn't. I have only made it this far because of the support I have received from numerous friends and colleagues in their academic, professional and personal roles.

I am indebted to Prof. Paul Burn and Prof. Ian Gentle for taking me on over the past four years. Together they have guided my research through *many* twists and turns; this final product is nothing like what was envisioned. Firstly, to Ian, who encouraged me to undertake a PhD after completing my Honours degree, thank you for all the time you have devoted to my education and development as a member of the scientific community. You have always been approachable and willing to listen to my (sometimes) wild imaginings. Secondly, to Paul, thank you for all the time you have spent guiding my work. While I was very 'green' to the organic electronics field, you accepted me as a member of the fledgling Centre for Organic Photonics and Electronics (COPE). Although my forays into organic synthesis weren't particularly productive (ha!), I am nonetheless happy to have had the chance to try my hand at it. I am grateful for all the opportunities and experiences that COPE has offered me.

Financial support was primarily provided by The University of Queensland in the form of a UQ Mid-Year Scholarship, which later morphed into an Australian Postgraduate Award (I don't know how or why this happened!). In addition, the Australian Institute of Nuclear Science and Engineering (AINSE) were kind enough to grant me a Postgraduate Research Award which not only acted as a top-up to my primary scholarship, but enabled my access to the neutron facilities that have been so fundamental to my research.

Prof. Michael James and Dr Andrew Nelson have been central to the neutron experiments, providing guidance and support through numerous beam times and late (seemingly unending) nights. Platypus has been a fantastic machine, and we always seem to push it that much further with every experiment. I really don't know where I would have been without Motofit to model the neutron data, it is truly brilliant. Mike, you have been a good mate and source of confidence to me, thank you for all your hard work and advice.

Under the tutelage of Assoc. Prof. Ben Powell my knowledge and understanding of electronic structure theory and quantum chemistry have expanded immeasurably. Much of this work would not have been possible if Ben had not adopted me as one of his *de facto* students. Writing cogent and precise scientific discussions has been one area where I have learnt a great deal from Ben. I have truly enjoyed the experience of working together throughout the course of my PhD.

The MCD and low temperature spectroscopic experiments were performed in collaboration with Assoc. Prof. Mark Riley, who helped me understand what the measurements actually meant. His knowledge of spectroscopy, electronic structure and group theory was most helpful. He also played a key role in the discussion, preparation and drafting stages of the papers arising from this thesis.

The initial stages of my foray into quantum chemistry were guided by Dr Seth Olsen. Some of my first calculations were performed on his supercomputer time, and I learnt a lot about how calculations are *actually* performed. Descriptions in papers often sound easy, but the application of those ideas to tangible working code is not always straightforward. Access to the National Computational Infrastructure National Facility (NCI-NF) was supported over the years by numerous help desk requests, but I would like to particularly thank Dr David Singleton who endured my seemingly never-ending calculations. I think the longest job ran for over a month continuously, and there were a number of others that exceed several thousand CPU hours. On this point I would like to say that ADF needs to add checkpoints to TDDFT calculations!

Through my association at COPE I have been able to make use of the Australian National Fabrication Facility Queensland Node facilities. Without the help and enthusiasm of Dr Muhsen Aljada I would surely have been lost to the cleanroom. The fluorescence microscope images found in this thesis, which made the cover of Advanced Functional Materials, would not have been possible if not for the access to the instruments afford by Dr Bronwyn Battersby. I also wish to acknowledge the Australian National Deuteration Facility for providing deuterated TCTA and BCP, in particular Dr Tamim Darwish for his tireless work. The design, construction and modification of the neutron cell were in large part due to the skill and expertise of Graham Rose, who far too often goes unacknowledged.

To all my fellow and long-suffering PhD students at COPE it has been a pleasure to work with you. The lively (and sometimes deeply disturbing) lunch time banter will stay with me as one of my fondest memories from my PhD. To the soon to be doctors Ben Langley and Hamish Cavaye, thank you for your advice and help in the lab, but more importantly your friendship over the last four years.

My family, who have supported me throughout my life, you have been an endless source of care, humour and concern throughout these turbulent few years. Mum, I have always looked forward to your weekly dinners, and although now they are more difficult, your eternal optimism and grace have been a constant source of reassurance to me. Dad, your support and interest in my work has always made me strive for better things, but it has been your down to earth knowledge that has

aided me the most. To Beatrice, Charles and Owen thank you for putting up with an overbearing, bossy older brother. Although we have our disagreements, I can't imagine growing up without any of you.

Finally, to my darling Dr Badrick! Alison, you have cared for me, worried over me, and most importantly loved me. You have been patient while I dither, and supported me (emotionally and financially) while I finish this PhD. This thesis really belongs to you, for without you none of this would have been possible. With all my love, thank you.

Arthur R G Smith

Brisbane, November 2011

Abstract

Organic light emitting diodes (OLED) promise new and exciting possibilities for display and lighting technologies. High performance phosphorescent materials can achieve 100% internal quantum efficiencies. This is highly attractive, but to achieve this phosphorescent complexes used in OLEDs must have a high photoluminescence quantum yield (PLQY), but also a suitable emission wavelength. Furthermore, the overall stability of the multilayer organic films that form the active component of OLEDs must also be highly durable against thermal degradation.

In the first part of the thesis a study of the factors that affect the luminosity of phosphorescent iridium(III) complexes is reported. Blue phosphors, which typically have low performance or unsuitable colour characteristics, are particularly important for efficient OLEDs with a balanced emission spectrum. To learn more about the challenges associated with producing deep blue phosphors, a family of blue emitting iridium(III) complexes was investigated with magnetic circular dichroism spectroscopy and then described by relativistic quantum chemistry calculations. Heavy metals like iridium need relativistic corrections to properly describe their electronic properties. Density functional theory (DFT) calculations on the complex *fac*-tris(1-methyl-5-phenyl-3-*n*-propyl-[1,2,4]triazolyl)iridium(III) [$Ir(ptz)_3$] showed that so-called scalar relativistic effects lead to an indirect destabilisation of the 5*d* orbitals. The core orbitals of the iridium are relativistically contracted, which electrostatically shields the nucleus and contributes a ~0.28 eV lowering of the energy of the frontier molecular orbitals. As a result the energies of the singlet and triplet excitations calculated by time-dependent density functional theory (TDDFT) are lowered by ~0.2 eV, compared to the non-relativistic calculations.

Phosphorescence from heavy metal complexes is a direct result of spin-orbit coupling; spin-orbit coupling allows the formally forbidden singlet-triplet crossing to occur. In terms of emission efficiency, the radiative rate of emission should be maximised, while minimising non-radiative contributions. A perturbative TDDFT method was used to describe spin-orbit coupling in a family of fluorinated iridium(III) complexes based on the parent complex $Ir(ptz)_3$. Fluorination drives the emission wavelength to deeper blue, but the PLQY decreases by an order of magnitude. The perturbative TDDFT treatment was found to give excellent agreement with more computationally expensive two-component fully relativistic methods. It was found that the radiative rate across the family of $Ir(ptz)_3$ complexes is critically dependent on the $S_3(E)$-$T_1(A)$ energy gap. These excitations arise predominantly from the highest occupied molecular orbital (HOMO), HOMO-1 and the lowest unoccupied molecular orbital (LUMO). Therefore the primary electronic feature for determining the radiative rate of emission is the energy of splitting between HOMO and HOMO-1.

The second part of the thesis describes a study of film morphology where the films are comprised of small molecules typically found in phosphorescent OLEDs. For durable devices there is a need to better understand the morphology of small molecule based organic multilayer films that are used in phosphorescent OLEDs. In particular the active emissive layer often comprises phosphorescent molecules blended into a host material, which helps to reduce self-quenching and enhances charge transport. Using a combination of 6 wt% *fac*-tris(2-phenylpyridyl)iridium(III) [$Ir(ppy)_3$] blended in 4,4′-bis(*N*-carbazolyl)biphenyl (CBP), it was found that lateral phase separation between the two components occurred after annealing at 80 °C. This phase separation was suppressed when the blend ratio between $Ir(ppy)_3$ and CBP was increased to 12 wt%. Since low blend ratios tend to give higher device efficiency, there therefore exists a trade-off between device durability and performance.

Interactions between layers in a multilayer film are difficult to investigate. Using neutron reflectometry (NR) a multilayer film of tris[4-(carbazoyl-9-yl)phenyl]amine (TCTA)/[$Ir(ppy)_3$:CBP]/bathocuproine (BCP) was subjected to thermal annealing, and the photoluminescence of the film measured *in situ*. The film structure remained stable to 90 °C, but after heating to 100 °C the BCP and $Ir(ppy)_3$:CBP layers rapidly interdiffused. This was accompanied by a significant decrease in the photoluminescence. Using time-dependent NR, the interdiffusion was characterised by a moving interfacial region which propagated according to the time dependence $x \propto t^n$ with $n = 0.34$. This is indicative of anomalous Fickian interdiffusion.

The electronic structure and film morphology of organic semiconductors has broad application in areas beyond OLEDs. Related fields such as dye sensitised solar cells; photocatalytic water splitting; polymer and small molecule photovoltaics; and organic field effect transistors all have similar challenges in understanding and optimising the fundamental electronic and morphological characteristics of their specific organic components.

Keywords

organic light emitting diode, neutron reflectometry, morphology, phase separation, thin film, density functional theory, quantum chemistry, spin-orbit coupling, relativity, magnetic circular dichroism

Australian and New Zealand Standard Research Classifications (ANZSRC)

030701 Quantum Chemistry 50%, 030603 Colloid and Surface Chemistry 30%, 030304 Physical Chemistry of Materials 20%

Table of Contents

List of Figures

List of Tables

Abbreviations

°C	degrees Celsius
2-MeTHF	2-methyltetrahydrofuran
Å	Ångstrom
ADF	Amsterdam Density Functional
AFM	atomic force microscopy
Al	aluminium
AO	atomic orbital
B3LYP	Becke, three-parameter, Lee-Yang-Parr functional
BCP	bathocuproine
C	carbon
CBP	4,4′-bis(*N*-carbazolyl)biphenyl
CIE	1931 Commission Internationale de l'Eclairage
cm	centimetre
DDP	discrete density profile
DFT	density functional theory
DZP	double zeta polarised
eV	electron volt
FWHM	full width half maximum
GAMESS	General Atomic and Molecular Electronic Structure System
h	hour
HOMO	highest occupied molecular orbital
Hz	hertz
IQE	internal quantum efficiency
Ir	iridium
$Ir(ppy)_3$	*fac*-tris(2-phenylpyridyl)iridium(III)
$Ir(ptz)_3$	*fac*-tris(1-methyl-5-phenyl-3-*n*-propyl-[1,2,4]triazolyl)iridium(III)
ITO	indium tin oxide
K	kelvin
k_{nr}	non-radiative rate
k_r	radiative rate
λ	wavelength
LANL2DZ	Los Alamos National Laboratory 2-Double Zeta
LED	light emitting diode
LMCT	ligand-to-metal charge transfer
LT	low temperature
LUMO	lowest unoccupied molecular orbital
M	molar
MALDI	matrix assisted laser desorption ionisation
MCD	magnetic circular dichroism
min	minute
MLCT	metal-to-ligand charge transfer
MO	molecular orbital
N	nitrogen
nm	nanometre
NMR	nuclear magnetic resonance
NonR	non-relativistic
NR	neutron reflectivity
NTSC	National Television System Committee

OLED	organic light emitting diode
PL	photoluminescence
PLQY	photoluminescence quantum yield
RT	room temperature
SLD	scattering length density
SOC	spin-orbit coupling
SOP	spin-orbit perturbation
SR	scalar relativistic
T	tesla
τ	lifetime
TCTA	tris[4-(carbazoyl-9-yl)phenyl]amine
TDDFT	time-dependent density functional theory
T_g	glass transition temperature
TZP	triple zeta polarised
UV	ultraviolet
vis	visible
wt%	weight percent
XRR	x-ray reflectivity
ZFS	zero-field splitting
ZORA	zeroth-order regular approximation

Chapter 1. Introduction

1.1 Organic Light Emitting Diodes

Organic light emitting diodes (OLEDs) represent a new paradigm in display and lighting technology. High contrast ratio, colour vibrancy, excellent power efficiency and a range of fabrication conditions make OLEDs suitable for ultrathin displays, flexible substrates and unique lighting solutions.[1]

Figure 1.1 The Sony XEL-1 11" OLED display. The panel is only 3 mm thick.

Organic electroluminescence has been known for well over five decades,[2] but the first high performance OLED devices were only demonstrated in the late 1980's. Tang and Van Slyke published the seminal paper on thin film OLEDs in 1987,[3] establishing many of the fundamental OLED attributes and catalysing extensive academic and industrial development over the next two decades.[4] In 2007 Sony introduced the 11" XEL-1 OLED display (Figure 1.1) which confirmed the potential of OLEDs as a revolutionary display technology.[5,6] The XEL-1 established the superiority of OLEDs over every existing display technology. OLED penetration in the marketplace continues to grow. Over the past couple of years OLED displays have gained a substantial foothold in the rapidly expanding smartphone market. By the end of 2010 Samsung had sold over 10 million OLED display equipped smartphones.[7]

However, beyond their use in displays, OLEDs are also attracting attention for their application in unique lighting solutions. The efficiency and performance of white light emitting OLEDs is now comparable to or better than that of fluorescent tubes and inorganic LEDs,[8,9] and the processability of the organic materials allows new product designs and lighting opportunities.[10] White OLED

products from lighting companies like Philips and OSRAM are becoming commercially available, which promises a bright future for OLED technology.

Yet a number of fundamental issues remain unresolved. The successful application of functional organic materials in OLEDs demands control over their molecular and electronic structure, and also their morphological and physical behaviour. Controlling the electronic and emissive properties of OLED materials remains a key research area from both an experimental and theoretical perspective.[11-19] Equally important are the morphology, interfacial interactions and thermal stability of organic thin films, which together play a vital role in device performance, longevity and durability.[20-27] In this thesis both the electronic and morphological properties will be explored with a particular emphasis on *phosphorescent* OLED designs.

1.2 OLED Device Structure

The basic OLED design devised by Tang and Van Slyke[3,24] is fundamentally the same as those found in modern OLEDs.[4,26] A typical device consists of organic layers sequentially deposited onto a conducting and transparent substrate (usually indium tin oxide (ITO) on glass). The electrical circuit is completed by a metal cathode deposited atop the organic film (Figure 1.2). Electroluminescence is observed after applying an electric field across the organic heterostructure. This is the basic principle according to which all OLEDs are designed and operated.

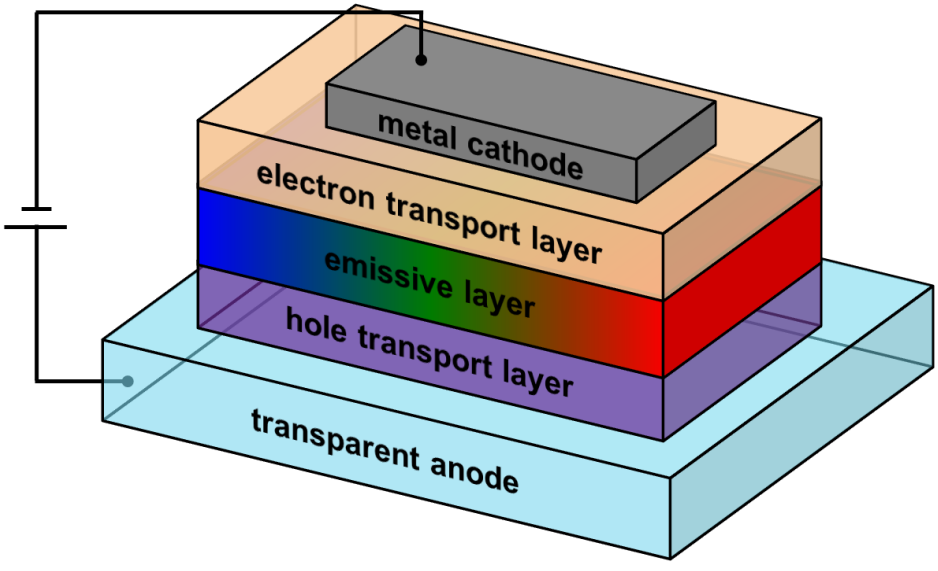

Figure 1.2 Schematic design of a basic OLED heterostructure. Electrons and holes are transported into the emissive layer where they recombine to give electroluminescence via excitonic decay on the emitting material (which can be either fluorescent or phosphorescent). A transparent electrode (in this case the anode) allows the emitted light to be transmitted outside the device.

Both holes and electrons are needed for the device to work.[25,28] Electrons and holes are generated, respectively, at the cathode and anode interfaces. If there is charge imbalance (where either holes or electrons dominate as the free charge carriers) then electroluminescence will be absent, or have very poor efficiency. When electrons and hole unite they form a coulombically bound electron-hole pair, known as an exciton. Excitons can decay radiatively via the emissive material, generating the observed light, or non-radiatively, in which case no emission is observed.

To aid in charge transport and injection to the emissive layer, OLED designs usually employ additional hole and electron transport layers (Figure 1.3). Hole and electron transport layers carry the charges across their highest occupied molecular orbitals (HOMO) and lowest unoccupied molecular orbitals (LUMO), respectively. To achieve balanced charge injection, transport and recombination, more complicated designs will also use hole and electron blocking layers to confine charges within the emissive layer.[29-31] Therefore, it is critical to optimise the performance of the emitting material, but it is also vital that charge transport within the device is efficient, so that excitons are generated only in the emissive layer.[25,32] The charge transport (electronic) and morphological (physical) properties of the organic layers are central to realizing high performance OLEDs.

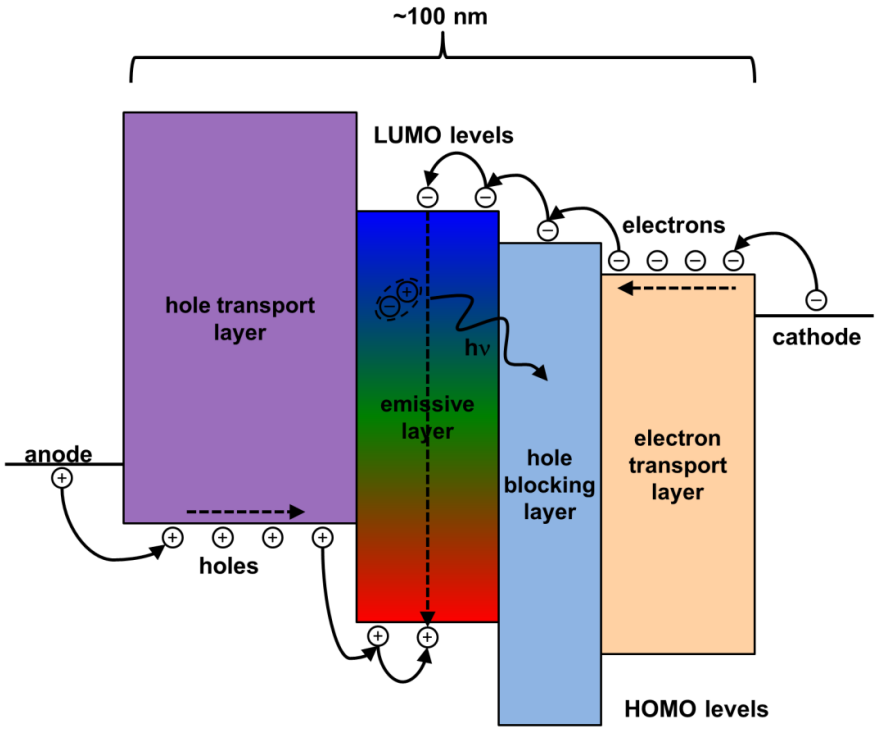

Figure 1.3 Approximate energy level diagram of an OLED, showing the injection of charges from the electrodes into the hole and electron transport layers. When present, hole (and electron) blocking layers confine charges to the emissive layer promoting exciton formation and electroluminescence. Holes are transported across the HOMO levels, while electrons are propagated via the LUMO levels.

1.3 Fluorescence and Phosphorescence

The OLEDs of Tang and Van Slyke used the fluorescent small molecule tris(8-hydroxyquinolinato)aluminium (Alq_3), and much of the early work into OLEDs has focussed on fluorescent small molecules and polymers.[3,8,24,33,34] Fluorescence is a spin-allowed radiative decay process from a singlet excited state back to the (singlet) ground state, S_0. Since there is no change in the molecular spin state, electronic relaxation proceeds unhindered and so fluorescence is characterised by very short emission lifetimes, often on the order of nanoseconds. However, the spin statistics of electron-hole charge injection within an OLED dictate that both singlet *and* triplet excitons are generated, occurring in the ratio of 1:3.[35,36] Thus a large number of injected charges (holes and electrons) are wasted in fluorescent OLEDs, since the fluorescent materials cannot make use of triplet excitons radiatively. The theoretical maximum electroluminescent internal quantum efficiency (IQE) that can be achieved with fluorescent OLEDs is limited by these spin statistics to 25%,[37] although extra singlets can be formed due to triplet-triplet annihilation, raising the IQE of fluorescent OLEDs above 25%.[38,39]

Fortunately, the 25% limit imposed by spin statistics can be overcome by using phosphorescent materials comprised of heavy metals such as iridium. Compared to fluorescence, phosphorescence of heavy metal complexes is characterised by longer emission lifetimes usually lasting several microseconds. The mixing of singlet and triplet states[12,32] allows phosphorescence to occur. The traditionally forbidden crossing between singlet and triplet spin states becomes allowed via the interaction known as spin-orbit coupling (SOC). Therefore when considering phosphorescence it is the total angular momentum (J) of the system that is important [J is defined by the sum of spin (S) and orbital angular momentum (L), where $J = L + S$]. From a device efficiency perspective, radiatively harvesting triplet *and* singlet excitons potentially pushes the internal quantum efficiency to 100%.[32,40,41]

The magnitude of the SOC interaction scales with atomic number. It is not until heavy elements are introduced that the magnitude of the SOC interaction is sufficient for singlet-triplet crossing to gain significant 'allowedness'. Indeed SOC is often referred to as the 'heavy atom effect', and the variation of the effect with atomic number can be observed in a series of metal complexes with different metals, such as the Group 8 transition metals iron, ruthenium and osmium.[42] Of course, general interest in the phosphorescent and excited state properties of transition metal complexes dates back several decades. One of the most studied metal complexes is tris(2,2′-bipyridine)ruthenium(II), or $[Ru(bpy)_3]^{2+}$.[42-46] The electronic structure of $[Ru(bpy)_3]^{2+}$ and similar complexes (notably the ruthenium dye N3, used in dye-sensitised solar cells) is still debated.[14,47-50]

With respect to OLEDs, the sixth row transition metal elements iridium,[21,51] osmium[52,53] and platinum[37] have been particularly fruitful. Complexes based on these metals are characterised by metal-to-ligand charge transfer (MLCT) transitions and higher energy ligand-based π-π^* transitions. The most noteworthy are the cyclometallated organometallic iridium(III) d^6 complexes, because of their relatively short phosphorescent lifetime (and therefore less triplet-triplet annihilation), colour tunability by way of ligand modification and chemical stability.[54,55] Experimental and theoretical work over the past decade has focused heavily on controlling and understanding the absorption and emission processes of these particular complexes in an effort to identify the arrangement of excited state energy levels, and the mechanism through which high efficiency phosphorescence is achieved.[4,51,56]

When discussing phosphorescent (and fluorescent) materials one particularly important concept is the photoluminescence quantum yield (PLQY). Together with emission colour, obtaining a high PLQY (>80%) is vital for high performance OLEDs. PLQY is the ratio between 'photons out' *versus* 'photons in', and indeed photon counting methods are sometimes employed to determine absolute quantum yields.[57] PLQY therefore defines how efficiently a photoexcited state decays radiatively.

Photoexcited states can decay either radiatively via the emission of a photon or non-radiatively, in which case the excited state energy is dissipated and lost, usually via vibrational relaxation to the ground state. The PLQY can be defined by the combination of radiative rate, k_r, non-radiative rate, k_{nr}, the total decay rate and emission lifetime, τ, as described in Equation 1.1.

$$PLQY = \Phi_{PL} = k_r\tau = \frac{k_r}{k_r + k_{nr}} \qquad \textbf{1.1}$$

For high efficiency photoluminescence (and by extension electroluminescence) it is important to maximise the rate at which photons are emitted, k_r, and minimise any process that may lead to quenching of the photo or electrically excited state, such that $k_r \gg k_{nr}$. Minimising non-radiative processes is particularly important for electroluminescence. Non-radiative processes can be inherent to the molecule or can arise from solid-state interactions between organic materials.[58-61]

1.4 Phosphorescence of Iridium(III) Complexes

The development of phosphorescent iridium complexes started with investigations of iridium(III) and rhodium(III) dimer complexes.[62] Such materials were of interest because of their photoreductant behaviour, but were largely overshadowed by the $[Ru(bpy)_3]^{2+}$ class of materials,

alluded to earlier. Cyclometallated iridium(III) complexes consisting of one central metal and three ligands, such as *fac*-tris(2-phenylpyridyl)iridium(III) [$Ir(ppy)_3$], was a major turning point.[63,64]

The drive to develop new iridium(III) phosphors stemmed from the use of $Ir(ppy)_3$ in phosphorescent OLEDs. Baldo *et al.* demonstrated that $Ir(ppy)_3$ could be very successfully used as an electrophosphor by doping it at low concentrations (typically <8 wt%) within a host matrix that facilitated charge transport and reduced intermolecular self-quenching between $Ir(ppy)_3$ molecules.[21] This was followed by Adachi *et al.* who showed that the IQE of a bis(2-phenylpyridyl)iridium(III)acetylacetonate [$(ppy)_2Ir(acac)$] based green phosphorescent OLED was 87±7%, nearly the 100% maximum predicted by spin-statistics.[41]

OLED displays require three basic colours – red, green and blue. Phosphorescent red[17,65-67] and green[21,68,69] iridium(III) complexes are well documented, but it has been the development of high efficiency deep blue phosphorescent materials which has remained elusive.[4,19,70] As a result phosphorescent deep blue iridium(III) complexes have gained substantial attention recently.[19,51,70-74]

1.4.1 Development and Discovery – The Green Emitter $Ir(ppy)_3$

Fac-tris(2-phenylpyridyl)iridium(III) [$Ir(ppy)_3$] is a triply cyclometallated homoleptic complex which was a side product from the preparation of iridium dimer complexes,[64,75] but subsequent work significantly improved the yield and synthetic preparation methods.[76] Only the *facial* isomer of $Ir(ppy)_3$ is of technological interest because the *meridional* form has a very poor PLQY (Figure 1.4).[77] Generally this behaviour is true for all *meridional* iridium(III) complexes,[77,78] and while there are some exceptions,[79] only *facial* isomers will be discussed.

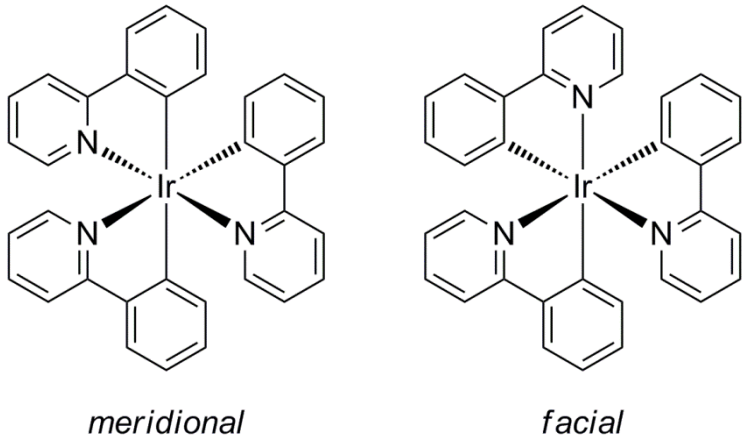

Figure 1.4 *Facial* and *meridional* isomers of $Ir(ppy)_3$. In the *meridional* isomer the iridium coordinating nitrogens rest in the same plane, whereas in the *facial* form all the nitrogens are bonded opposite to the iridium-carbon bonds. Generally *facial* iridium(III) isomers show better performance than their *meridional* analogues.

Both $Ir(ppy)_3$ and the related rhodium(III) complex $Rh(ppy)_3$ have been assigned ^{1}MLCT (i.e. singlet-singlet) transitions with absorption maximas at ~370 nm and absorption extinction coefficients of ~8000 M^{-1} cm^{-1}.[76] However, the absorption onset of $Ir(ppy)_3$ occurs at 500 nm, whereas $Rh(ppy)_3$ only starts absorbing below ~430 nm.[76] Similar behaviour is also seen with other ligand arrangements when iridium(III) is substituted for rhodium.[80] In $Ir(ppy)_3$ these low energy features arise from ^{3}MLCT transitions (the ^{3} denotes at singlet-triplet transition). These transitions are formally forbidden, and hence have very weak absorption <1000 $M^{-1}cm^{-1}$. The appearance of these ^{3}MLCT features is due to the stronger SOC of iridium, which can, unlike rhodium, mix the low energy triplet states with higher lying singlets, thereby gaining significant 'allowedness'. The weak SOC of rhodium is also manifested in the long emission lifetime of $Rh(ppy)_3$, which at 77 K is 46 μs *versus* 5 μs for $Ir(ppy)_3$ under similar conditions.[76] Since the emitting triplet state of $Rh(ppy)_3$ has very little singlet character mixed by SOC, radiative transitions from this state are strongly forbidden, hence the longer emission lifetime.

$Ir(ppy)_3$ exhibits strong green phosphorescence (λ_{max} ~510 nm, just beyond the absorption onset) with an emission lifetime of ~2 μs at room temperature.[77] For a long time the PLQY of $Ir(ppy)_3$ was believed to be 40%[64,77] although in recent years this value has been continually revised up,[81,82] so much so $Ir(ppy)_3$ is now believed to exhibit a room temperature solution PLQY of 100%.[83,84] $Ir(ppy)_3$ also has 1931 Commission Internationale de l'Eclairage (CIE) coordinates of (0.27, 0.63),[21] which correspond closely to the National Television System Committee (NTSC) standard green coordinates of (0.21, 0.71).[4] The CIE colour space is used to gauge the appearance of luminescence, as seen by a human observer.

The calculated molecular orbital distribution of $Ir(ppy)_3$ consists of a HOMO that is delocalised across all three phenyl rings and the coordinated iridium.[19,85,86] The LUMO on the other hand is predominantly found on the pyridine moieties of the ligands. Therefore modification of the phenyl ring will adjust the energy of the HOMO while changing the pyridine moiety affects the energy of the LUMO. A more detailed analysis and appraisal of molecular calculations related to iridium(III) complexes will follow in later chapters.

1.4.2 The Challenge of Tuning Emission to the Blue

There are a number of challenges associated with obtaining high efficiency deep blue phosphorescent materials. Saturated blue emitting iridium(III) complex phosphors (λ_{em} < 450 nm) with high efficiency and CIE coordinates of (0.14, 0.08) have been elusive.[4] These CIE coordinates represent the standard blue colour used in the NTSC colour space, and therefore phosphors with

these coordinates are required for any OLED display. Not only is a short wavelength required for blue emission, but the emission spectrum must not have an extended tail to longer wavelengths, which might dilute the observable colour away from deep blue. The human eye is more sensitive to the green part of the visible spectrum,[87] so achieving a narrow and short wavelength emission spectrum that does not tail into the green is vital for blue OLED pixels. Phosphorescent blue OLEDs are also needed for white OLEDs.[26] Irrespective of the device architecture (whether red-green-blue or yellow-blue), blue emitters are required for a balanced spectrum of white light.[55]

There are several, seemingly simple, strategies for tuning emission colour. The first is to lower, or *stabilise*, the energy of the HOMO. By increasing the energy gap between the HOMO and the LUMO, the absorption and emission spectra should be shifted to higher energy, and therefore shorter wavelengths. Similarly the energy of the LUMO can be raised, or *destabilised*, to also increase the HOMO-LUMO energy gap. Finally, both of these strategies can be combined by simultaneously lowering the HOMO energy while raising the LUMO energy.

In the following discussion orbital energies will be compared relative to those of $Ir(ppy)_3$, since $Ir(ppy)_3$ constitutes the original prototype for all phosphorescent iridium(III) complexes. Substituting fluorine for hydrogen on ligands of $Ir(ppy)_3$ was one of the first techniques for tuning emission colour to the blue. The difluorinated ligand 2-(4,6-difluorophenyl)pyridine (F2ppy), the complex $Ir(F2ppy)_3$ has a blue shift of ~40 nm in the emission spectrum to that of $Ir(ppy)_3$. This is significant, but only achieves an emission peak at room temperature of 468 nm,[77] still far from deep blue. Measured under the same conditions, both $Ir(ppy)_3$ and $Ir(F2ppy)_3$ have essentially the same PLQY (97% and 98% respectively),[83] so fluorination appears to work in driving emission to the blue without affecting the quantum efficiency.

However increasing the amount of fluorination does not facilitate a similar shift in the emission spectrum. *Fac*-tris[2-(3′,4′,5′,6′-tetrafluorophenyl)pyridyl]iridium(III) [$Ir(F4ppy)_3$] was prepared by Ragni *et al.*, yet despite the extra electron withdrawing groups (four fluorines per ligand) the shortest emission wavelength was still 468 nm,[78] the same as the difluorinated $Ir(F2ppy)_3$. Interestingly however, the trifluorinated complex *fac*-tris[2-(3′,4′,6′-trifluorophenyl)pyridyl]iridium(III) [$Ir(F3ppy)_3$] exhibits an emission peak at 459 nm, although it has a PLQY lower than $Ir(F4ppy)_3$ under the same conditions.[78] Clearly the interplay between different degrees and positions of fluorine substitution is complicated.

Lamansky *et al.* investigated a series of heteroleptic bis-cyclometallated complexes and studied the effect of varying the ancillary ligand. The emission wavelength (λ_{max} 516 nm) of the green emitting

$(ppy)_2Ir(acac)$ could also be shifted 40 nm towards the blue by using the difluorinated ligand F2ppy.[67,88] The blue shift was further enhanced by exchanging the acac ligand for the more electron accepting picolinate ligand (producing the complex bis[2-(4′,6′-difluorophenyl)pyridyl]-picolinate iridium(III) known as FIrpic), however even then the shortest emission wavelength was only 470 nm.[88]

More drastic modification of the ppy ligand can produce much stronger blue shifts. *Fac*-tris(1-phenylpyrazolyl)iridium(III) [$Ir(ppz)_3$] has a peak emission at 414 nm when cooled to 77 K. This is a significant improvement when compared to $Ir(ppy)_3$, which under the same conditions emits at 492 nm.[77] However, room temperature emission from $Ir(ppz)_3$ is almost non-existent, with a PLQY <1%.[77,83] Prepared in an OLED, $Ir(ppz)_3$ gave CIE coordinates of (0.16, 0.14).[89] The difluorinated ligand 1-(4,6-difluorophenyl)pyrazolyl (F2ppz) has also been synthesised, and although the emission of the resultant $Ir(F2ppz)_3$ complex was shifted to an impressively low 390 nm,[77] it still has a low PLQY of <1%.[83] Clearly, although emission colour can be tuned to the blue, producing an *efficient* deep blue emitter is not trivial.

An interesting strategy employed by Dedeian *et al.* was to prepare a series of mixed tris-cyclometalled iridium complexes, comprised of the ppy, F2ppy, ppz and F2ppz ligands.[81] The complex, $Ir(F2ppy)(F2ppz)_2$, has an emission peak at 460 nm, with a room temperature solution PLQY of 38% in toluene,[81] which was later revised up to 60% in 2-methyltetrahydrofuran (2-MeTHF).[83] Irrespective of solvent interactions and measurement conditions, the quantum yield is massively increased compared to the $Ir(F2ppz)_3$ complex. However, none of these complexes realise an emission maximum less than 450 nm, necessary for a deep blue emitter.

Lee *et al.* synthesised a fluorinated bipyridine ligand, which coordinates through the usual nitrogen and carbon bonds like ppy.[90] Essentially the phenyl ring was replaced with pyridine. The cyclometallated iridium complex *fac*-tris(2′,6′-difluoro-2,3′-bipyridinato-N,$C^{4'}$)iridium(III) [$Ir(dfpypy)_3$] showed emission with a peak at 438 nm, CIE coordinates of (0.14, 0.12) and a high solution PLQY of 71%.[90] To date this is the best deep blue phosphorescent iridium(III) complex.[4]

1.4.3 $Ir(ptz)_3$ – A Family of Blue Phosphorescent Iridium Complexes

Lo *et al.* prepared a family of phenyltriazolyl ligand based iridium(III) complexes.[19] The basic premise, as with the ppz based complexes, was to modify the pyridine moiety of $Ir(ppy)_3$ and then fluorinate to drive the emission to deep blue.

The parent complex *fac*-tris(1-methyl-5-phenyl-3-*n*-propyl-[1,2,4]triazolyl)iridium(III) [$Ir(ptz)_3$] (Figure 1.5) has a room temperature solution PLQY of 66%, and pale blue emission having a λ_{max}

at 449 nm and CIE coordinates of (0.16, 0.20). By adding a single fluorine group to the phenyl ring of the ligand, as in the previous examples of the ppy and ppz ligands, the emission maximum was shifted to 428 nm, which gave CIE coordinates of (0.16, 0.13), although the solution PLQY was more than halved, decreasing to 27%. The difluorinated complex is even further blue shifted, however its PLQY is a very poor 3%.

This represents something of a quandary. As discussed earlier, similar fluorine substitutions on $Ir(ppy)_3$ do not have a significant effect on the PLQY, but do result in a blue shifting of the emission spectrum.[83] Compared to $Ir(ppy)_3$ the calculated LUMO energy level of $Ir(ptz)_3$ is raised from -1.47 to -1.14 eV, whereas the HOMOs have almost the same energy (-4.95 *versus* -4.94 eV respectively).[19] This suggests that the HOMO is strongly linked to the character of the phenyl moiety.

Encapsulating the mono-fluorinated $Ir(ptz)_3$ complex by way of dendronisation can lead to a dramatic improvement in the quantum yield. Using an especially rigid set of dendrons a solution quantum yield of 94% was obtained, which is substantially higher than that of the isolated complex (27%).[70] The enhanced quantum yield was attributed to a reduction in the non-radiative rate by steric crowding and reduced intermolecular interactions.[70,91]

1.4.4 Spectroscopic Investigations of Iridium(III) Complexes

In an effort to understand the electron and spectroscopic properties of phosphorescent iridium(III) complexes, a variety of model complexes with different structures and emission wavelengths have been used to characterise the excited state dynamics. Yersin *et al.* have investigated the excited state properties of many common iridium(III) complexes.[72,84,92-96] The lowest triplet state (T_1) of the green emitter $Ir(ppy)_3$ was found to consist of three substates **I**, **II** and **III** with an energy separation of $\Delta E_{II,I}$ = 1.7 meV and $\Delta E_{III,I}$ = 10.3 meV. Triplet substate **III** was determined to be the primary emitting state at room temperature, with states **II** and **I** only becoming observable below 30 and 1.5 K respectively. The lifetime of states **I**, **II** and **III** were found to be 145 μs, 11 μs and 750 ns.[96] The so-called zero-field splitting (ZFS) of the triplet is a result of SOC between the triplet state and higher lying singlet states,[32,84,96] and the lifetimes of the substates gives an indication as to the singlet character of each substate (shorter lifetime – more singlet character).

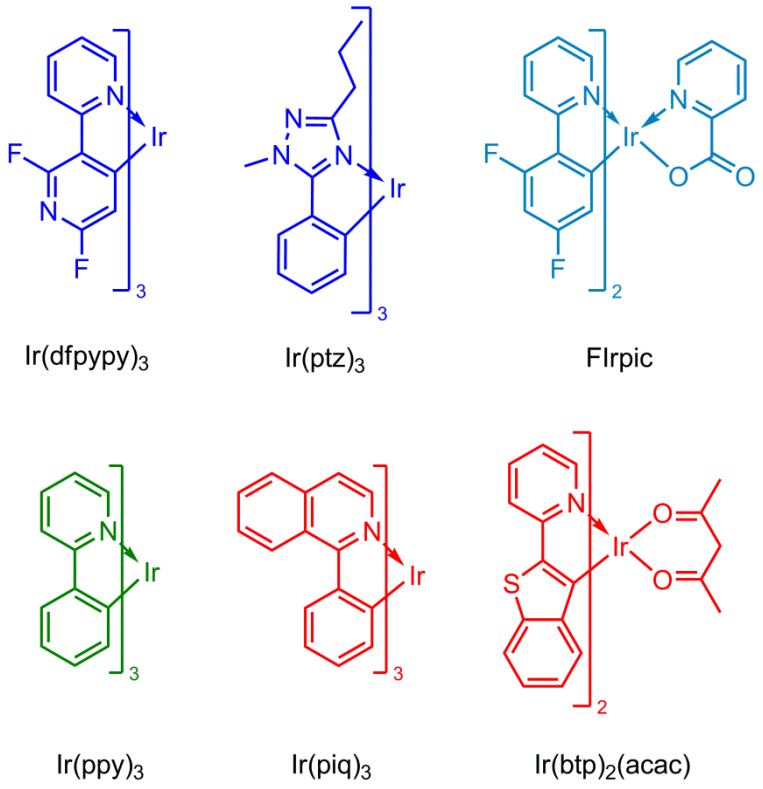

Figure 1.5 A selection of iridium(III) complexes with different emission wavelengths, ranging from blue to red.

Similarly for bis[2-(2′-benzothienyl)-pyridinato-N,$C^{3'}$]iridium(III)(acetylacetonate) [$Ir(btp)_2(acac)$] the emitting triplet comprises three substates, with similar energy separations and lifetimes to those observed for $Ir(ppy)_3$.[93,94] Site selective spectroscopy in a frozen solvent indicated a number of different molecular orientations were present, and the total ZFS of the lowest triplet varied from 1.8 to 3.3 meV.[94] The lifetimes of the triplet substates can vary quite substantially.[93] Finkenzeller *et al.* concludes that complexes with ZFS greater than ~1.2 meV are good candidates for OLEDs,[94] so it is therefore important to understand and characterise the properties of phosphorescent heavy metal complexes with particular regard for SOC.

In the work by Hedley *et al.* the 'intersystem' crossing dynamics of the red emitting tris(1-phenylisoquinoline)iridium(III) [$Ir(piq)_3$] were studied by means of ultrafast photoluminescence (PL) and transient absorption spectroscopy.[97] PL with a time constant of 70 fs was observed prior to the onset of phosphorescence. This is much faster than the transient emission observed for $Ir(ppy)_3$ which has a time constant of 230 fs.[98] Hedley *et al.* rationalised this by explaining that the larger 1-phenylisoquinoline ligand promotes faster vibrational relaxation of the excited state into the ^{3}MLCT manifold than the smaller 2-phenylpyridine ligands of $Ir(ppy)_3$.[97]

The sky-blue emitting FIrpic has also been carefully investigated since it is one of the few successful blue emitting iridium complexes with high quantum yield in both solution and solid

matrices.[72,82,92] Rausch *et al.* observes the same three level splitting of the lowest triplet state as observed in $Ir(ppy)_3$ and $Ir(btp)_2(acac)$. In frozen dichloromethane the total ZFS of the three emitting states varies from 4.8 to 9.3 meV.[92] It is therefore extremely interesting that this recurring ZFS structure occurs across both homo- and heteroleptic complexes, which exhibit different molecular symmetries and emission energies.

1.4.5 Quantum Chemistry Calculations

Amongst the most successful techniques employed to study the electronic and molecular structure of organometallic complexes have been quantum chemistry calculations. Foremost amongst the various methods available is density functional theory (DFT), for which Walter Kohn was awarded the 1998 Nobel Prize in Chemistry. Rather than solving the complete many-electron Schrödinger equation (and the huge computational effort entailed therein) Hohenberg, Kohn and Sham showed that the ground state electron density is equivalent to the Hamiltonian of the system. In a molecular system with *N*-electrons, and therefore 3*N* space dimensions, the utility of DFT becomes obvious since the total electron density need only be calculated in three spatial dimensions. DFT is therefore ideal for studying large systems of atoms, such as complicated inorganic complexes.

Due to the success of DFT in accurately calculating molecular properties it is now common to encounter DFT calculations whenever a new iridium (or any metal) complex is reported.[77,99-101] The ease with which DFT calculations can now be performed has been a major driving force in this uptake. Molecular geometries, orbitals and energy levels as well as electronic transitions are often calculated and compared with experimental results. The intricate details of DFT will not be described here, however there are several excellent reviews on the topic. Perdew *et al.* outlined the fundamentals of DFT without the aid of equations,[102] and a recent review article by Neese sets out the essentials of DFT and the relationships between theory and spectroscopy,[103] while Vlček and Záliš have reviewed DFT calculations with respect to d^6 metal complexes, like iridium(III).[104]

One important aspect which needs some introduction are the relativistic corrections needed to fully describe heavy metal complexes. In special relativity as a particle approaches the speed of light, so its mass approaches infinity, a process which is governed by the Lorentz transformation of mass

$$m = \frac{m_0}{\sqrt{1 - \frac{v^2}{c^2}}} \qquad \textbf{1.2}$$

where m is the particle's relativistic mass, m_0 is its rest mass, v is the particle's velocity and c is the speed of light. In the case of heavy elements the 'velocity' of the inner electrons (*s* and *p*

orbitals in particular) can approach a significant fraction of c, leading to relativistic effects that cannot be ignored. The Dirac equation is preferable over the Schrödinger equation for describing the relativistic conditions, since the Dirac equation is naturally Lorentz invariant. As a four-component vector wavefunction the Dirac equation can be written as

$$\Psi = \begin{pmatrix} \psi_1 \\ \psi_2 \\ \psi_3 \\ \psi_4 \end{pmatrix} \quad \textbf{1.3}$$

where components 1 and 3 are spin ½, and 2 and 4 are spin -½ projections. The top and bottom two components are grouped together for simplicity, forming the so-called large and small component two-spinors; these are the matter and anti-matter solutions respectively. Simplified, the Dirac equation then reads

$$\Psi = \begin{pmatrix} \psi^L \\ \psi^S \end{pmatrix}. \quad \textbf{1.4}$$

Since quantum chemistry is only concerned with the matter solutions, it is convenient to work with the ψ^L two-spinor. In atomic units ($m_0 = 1, \hbar = 1$), the four-component Dirac equation in terms of the large and small components is

$$\begin{pmatrix} V & c\vec{\sigma}.\vec{p} \\ c\vec{\sigma}.\vec{p} & V - 2c^2 \end{pmatrix} \begin{pmatrix} \psi^L \\ \psi^S \end{pmatrix} = E \begin{pmatrix} \psi^L \\ \psi^S \end{pmatrix} \quad \textbf{1.5}$$

or as a pair of equations

$$V\psi^L + c\vec{\sigma}.\vec{p}\psi^S = E\psi^L \quad \textbf{1.6}$$

$$c\vec{\sigma}.\vec{p}\psi^L + (V - 2c^2)\psi^S = E\psi^S \quad \textbf{1.7}$$

where $\vec{\sigma} = (\sigma_x, \sigma_y, \sigma_z)$ is the vector of the Pauli spin matrices, $\vec{p}$ is the momentum and $V = V_{nuc} + V_{elec} + V_{xc}$ is the sum of the self-consistent potentials (V_{nuc} is the nuclear potential, V_{elec} is the electron Coulomb potential and V_{xc} is the exchange-correlation). Rearranging for the small component gives

$$\psi^S = (2c^2 + E - V)^{-1} c\vec{\sigma}.\vec{p}\psi^L \quad \textbf{1.8}$$

which can be substituted into Equation 1.6

$$V\psi^L + c^2\vec{\sigma}.\vec{p}(2c^2 + E - V)^{-1}\vec{\sigma}.\vec{p}\psi^L = E\psi^L. \quad \textbf{1.9}$$

From here the typical procedure is to extract a factor of $2c^2$ and expand $\left(1 + \frac{E-V}{2c^2}\right)^{-1}$. However this can pose problems since this expansion only applies when $|E - V| < 2c^2$, which is never true close to the nucleus (for a point charge the Coulomb potential $V_{elec} \sim -\frac{1}{r}$ becomes infinite as $r \to 0$), and is also where relativistic effects are expected to be most important.[105,106] An alternative method is to isolate $2c^2 - V$, producing

$$V\psi^L + \vec{\sigma}.\vec{p}\frac{c^2}{2c^2 - V}\left(1 + \frac{E}{2c^2 - V}\right)^{-1}\vec{\sigma}.\vec{p}\psi^L = E\psi^L. \quad \textbf{1.10}$$

Expanding $\left(1 + \frac{E}{2c^2 - V}\right)^{-1}$ gives

$$\begin{aligned} V\psi^L + \vec{\sigma}.\vec{p}\frac{c^2}{2c^2 - V}\vec{\sigma}.\vec{p}\psi^L - \vec{\sigma}.\vec{p}\frac{c^2}{2c^2 - V}\frac{E}{2c^2 - V}\vec{\sigma}.\vec{p}\psi^L \\ + \vec{\sigma}.\vec{p}\frac{c^2}{2c^2 - V}\frac{E^2}{(2c^2 - V)^2}\vec{\sigma}.\vec{p}\psi^L + \cdots = E\psi^L \end{aligned} \quad \textbf{1.11}$$

which is regularised (V in the denominator) and can be simplified in zeroth order

$$V\psi^L + \vec{\sigma}.\vec{p}\frac{c^2}{2c^2 - V}\vec{\sigma}.\vec{p}\psi^L = E\psi^L. \quad \textbf{1.12}$$

This is the zeroth order regular approximation (ZORA) developed by van Lenthe *et al.*[106,107] and is equivalent to the Chang-Pélissier-Durand approximation.[108] The ZORA two-component Hamiltonian[106,109,110]

$$H_{ZORA} = V + (\vec{\sigma}.\vec{p})\frac{c^2}{2c^2 - V}(\vec{\sigma}.\vec{p}) \quad \textbf{1.13}$$

can be expanded by the Pauli spin matrix relationship $(\vec{\sigma}.\vec{u})(\vec{\sigma}.\vec{v}) = \vec{u}.\vec{v} + i\vec{\sigma}.\vec{u} \times \vec{v}$ to give

$$H_{ZORA} = V + \vec{p}.\frac{c^2}{2c^2 - V}\vec{p} + \frac{c^2}{(2c^2 - V)^2}\vec{\sigma}.\nabla V \times \vec{p} \quad \textbf{1.14}$$

since the momentum can be expressed as $\vec{p} = -i\nabla$, in atomic units.

Even a zeroth-order approximation to the Dirac equation leads to scalar relativistic (a function of the momentum operators) and spin-orbit effects (where the spin and momentum are coupled)

respectively. These terms themselves are first and second order corrections in $\frac{1}{2c^2-V}$. Therefore the SOC is a small perturbation to the overall electronic picture, and can be explicitly treated as such,[111] but is vital for an accurate description of phosphorescence.

1.4.5.1 Calculations of Phosphorescent Complexes

From even a cursory inspection of the literature on phosphorescent iridium(III) complexes, it is clear that relativistic corrections, such as spin-orbit coupling, are often neglected despite being well known and understood.[105,112] Recently a significant amount of work by a number of researchers has been directed to understanding how to properly include relativistic effects within DFT and the consequences this has for understanding the properties of phosphorescent OLED materials. By including relativistic corrections, it is hoped that DFT calculations may be used to predict the properties of heavy metal complexes, enabling better design rules to aid the selection of synthetic target molecules. Such a lofty goal remains as yet, unfulfilled.

As a model complex, $Ir(ppy)_3$ in particular has been extensively studied.[13,85,113] In his pioneering work on the topic, Hay focussed on the ground and excited state properties of $Ir(ppy)_3$ using DFT and time-dependent density functional theory (TDDFT) respectively.[85] The optimised ground state structure of $Ir(ppy)_3$ showed generally good agreement with the measured crystal structure; the calculated Ir-N and Ir-C bond lengths were longer than the experimentally measured bond lengths by 0.03 Å and 0.01 Å respectively. Although symmetry constraints on the molecular structure were not used during the geometry optimisation procedure, the optimised structure was still very close to the molecular C_3 geometry observed in crystal and gas-phase structures.[114]

Using the optimised structure, electronic excitation energies could be closely matched to the measured absorption spectrum, although only spin-allowed transitions to singlet and triplet states were considered since SOC was not included in the calculations. The distribution of the HOMO was split almost evenly between the iridium 5*d* orbitals and ligand based π orbitals, whereas the LUMO resided almost exclusively on ligand based π^* orbitals. Similar partitioning of orbital density was seen for several complexes, although no finer analysis of the orbital localisation was performed. Hay's results demonstrated that DFT was a reasonable technique for studying the molecular properties of iridium(III) complexes.[85] It was this work that set the ground rules for DFT analysis of phosphorescent metal complexes.

Although not explicitly studying relativistic effects arising from the presence of iridium, Hay nevertheless used a relativistically adapted basis set, which includes many of the simple energy level effects arising due to the relativistic mass increase of the core electrons.[115] Such relativistic

corrections are often included in quantum chemistry calculations via the corrections present in the basis sets, although it is unclear if many authors appreciate the corrections present and their effects on molecular properties.

Since the work by Hay a number of significant advances have been made towards the inclusion of all relativistic corrections, particularly SOC. Nozaki developed a method to include SOC via perturbation theory, which showed that the singlet and triplet states were strongly mixed.[13] Nozaki found in $Ir(ppy)_3$ that 70 electronic transitions with a strong MLCT character exist in the lowest 1 eV of the absorption spectrum. Clearly this significantly complicates the interpretation of the absorption and emission processes. By calculating both the ground state singlet (S_0) and triplet (T_1) geometries Nozaki concluded that the molecular symmetry of $Ir(ppy)_3$ is lowered from C_3 to C_1 due to the Jahn-Teller effect. However, despite correctly predicting the three state model observed by Yersin *et al.*, the excitation spectrum calculated in the T_1 geometry significantly underestimates the emission energy.

Using quadratic response TDDFT Jansson *et al.* calculated the radiative lifetime of the lowest triplet substates in both optimised S_0 and T_1 geometries.[113] Like Nozaki, the excitation energies calculated at the T_1 geometry are significantly lower than expected by experiment, although Jansson *et al.* do note that an intermediate geometry between S_0 and T_1 would be more favourable based on analysis of the vibrational wavefunction.[113]

DFT calculations seem to provide remarkable accuracy and insight, however in systems involving heavy metals the effects of spin-orbit coupling need to be rigorously accounted for.

1.5 Intrinsic Degradation of Organic Thin Films in OLEDs

Aziz and Popovic have defined three types of degradation processes within OLEDs.[116] These are dark spot degradation, catastrophic failure and intrinsic degradation. As its name suggests, intrinsic degradation is primarily associated with the fundamental chemical and morphological character of the organic materials. Dark spot degradation and catastrophic failure arise from inadequate care during device fabrication and encapsulation.

Commercial reality dictates that OLEDs should have operational half-lives of tens of thousands of hours.[116] Early devices often suffered degradation which would evolve quickly over hours to minutes, and was characterised by the appearance of ‘dark spots’ across the emissive surface.[117,118] These dark spots would propagate until the entire device was rendered useless. Such fast and

catastrophic degradation led many to believe that OLEDs could never transition from lab bench to consumer item.[27]

However, much of this degradation was due to poor encapsulation of the device during construction. Oxygen and moisture would penetrate the device and initiate the formation of dark spots. It was determined that dark spots were primarily due to degradation and delamination of the cathode layer,[119] but with proper handling during fabrication and thorough encapsulation techniques, penetration of oxygen and water can be significantly reduced.[116,120] Dark spot formation and growth is now considered to be a largely solved problem.[27]

Vapour deposition has been used extensively to prepare small molecule OLEDs. Vapour deposition usually requires very high vacuum (~10^{-6} mbar), so the equipment and processing conditions essential for film deposition can be quite complicated. The thickness of individual layers can be reliably controlled, and it is reasonably straightforward to prepare blended guest:host layers by co-deposition (which is vital for phosphorescent devices).

Although solution processable polymers[33,36,121] and dendrimers[17,68,122] have been promoted as the future of organic electronics, vapour deposited small molecules are still widely used because they give the best film structures and device performance.[10,25] This is in no small part due to the reliable and precise control afforded by vapour deposition.

1.5.1 Guest:Host Blended Films for Phosphorescent OLEDs

A particular feature of phosphorescent OLEDs is the almost ubiquitous use of guest:host films for the emissive layer,[37,41,55,69,123] although recently host-free phosphorescent materials have begun to appear.[70,124-126] Generally though, a small amount of the phosphorescent dye is doped into a host matrix, the purpose of which is to provide (i) charge transport and (ii) prevent intermolecular interactions between emitting phosphors. So as to make the back transfer of energy from guest to host unfavourable, the LUMO and triplet energy levels of the host should have a higher higher energy than the guest.

Many of the best host materials are comprised of the carbazole moiety,[25] exemplified by molecules such as 4,4′-bis(*N*-carbazolyl)biphenyl (CBP) and tris[4-(carbazoyl-9-yl)phenyl]amine (TCTA). Carbazole is generally considered a hole transport material,[25] and indeed TCTA was used as such before its application as a phosphorescent host material,[127] although CBP can transport both holes and electrons.[128,129] Many more examples of carbazole based materials exist in the literature.[128,130,131] While electron transport materials can also be used as phosphorescent hosts,[132]

compared to hole and bipolar hosts development has been limited.[25] This is due in part to the lower mobility of electrons than holes in organic materials.[30,133]

The first green phosphorescent OLED used $Ir(ppy)_3$ in a matrix of CBP,[21] an optimum device performance was achieved with a concentration of 6 wt% $Ir(ppy)_3$.[21,134] Lower concentrations cannot harvest all the injected charges and therefore suffer poor efficiency, while higher doping concentrations lead to emission quenching due to phosphor aggregation and triplet-triplet annihilation.[58-60] Reineke *et al.* used scanning tunnelling electron microscopy to study the molecular aggregation of $Ir(ppy)_3$ molecules distributed in a TCTA host.[58] Aggregates of $Ir(ppy)_3$ ranged from 3-30 nm in diameter, and the presence of these aggregates could be directly correlated with an increase in the rate of triplet-triplet annihilation. Therefore it is vital that blended guest:host films are homogeneous to ensure aggregation between emitting molecules does not occur. Homogeneous blending and distribution of guest and host should also persist, and not be subject to degradation due to phase separation between the two blended materials.

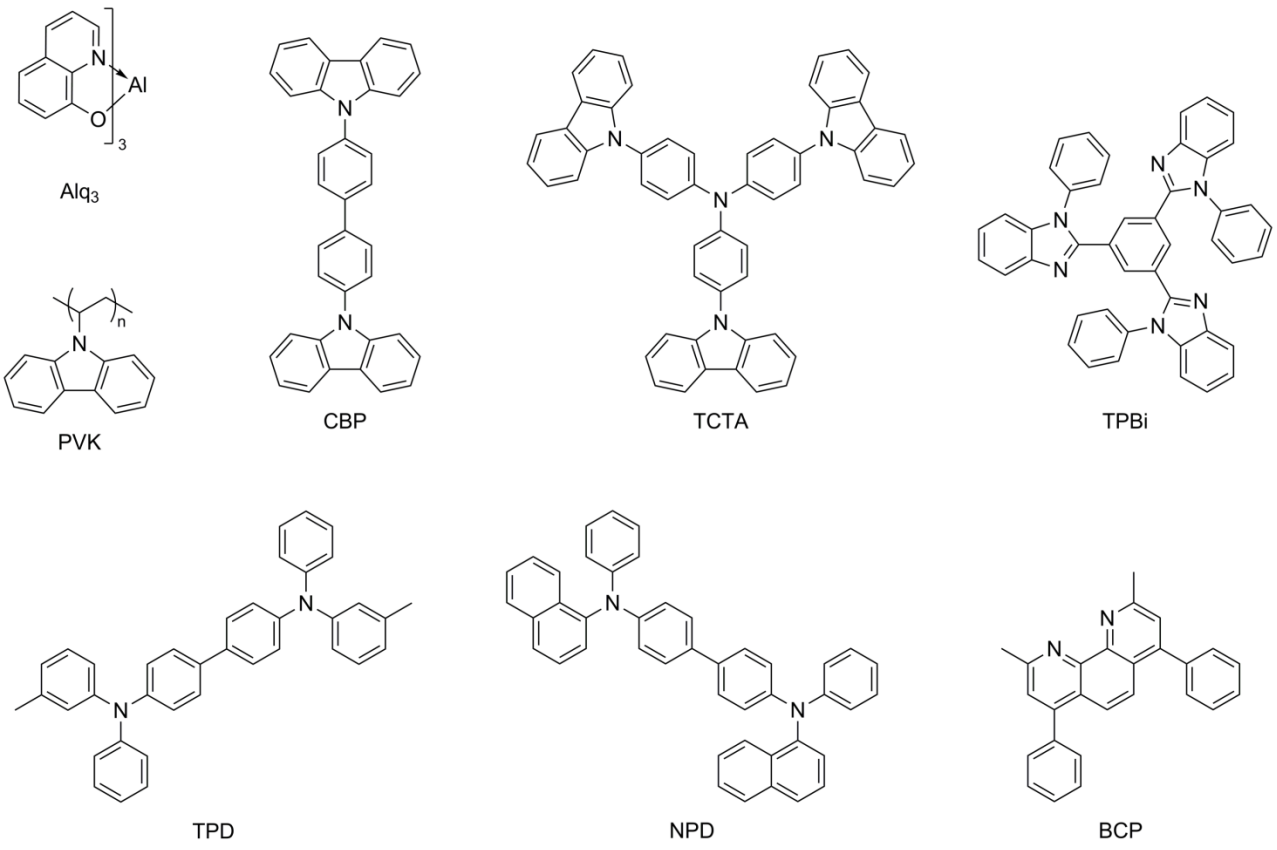

Figure 1.6 Common host (PVK, CBP, TCTA), hole (TCTA, TPD, NPD) and electron (Alq_3, TPBi, BCP) transport materials used in small molecule and polymer OLEDs. These represent only a few of the many hundreds of organic electronic materials prepared for OLED use.

1.5.2 What is Thermal Stability?

The long term thermal stability of OLEDs, especially the organic multilayer film, is a complex problem. OLEDs can be heated from either external (ambient operating and storage conditions) or internal sources. Internal heating arises from Joule heating due to the electrical current applied during device operation.[135,136] Operating devices at elevated temperatures results in a significant reduction of luminescence lifetime.[137-139] Studying how and when thermal degradation of organic thin films occurs is therefore of vital importance towards developing strategies to maximise the working lifetime of OLEDs.

It is important to clarify what is meant by thermal degradation in relation to thin film morphology. Thermal degradation is not chemical breakdown of the component film molecules. Although chemical breakdown can occur[27,140,141] it is generally not a result of a molecule's thermal instability, since the temperatures required for molecular degradation are well beyond those an OLED would ever be expected to experience. Thermal degradation occurs whenever there is a change in the morphology of the film, which causes a reduction in electrical performance (such as high operating voltages) or the purity of the emission colour. Thermally driven degradation can result in crystallisation, phase separation (of considerable concern in blended guest:host systems), interfacial broadening or molecular diffusion.

There are few reports of the operating temperatures of OLEDs. Devices should be stable between temperatures of -40 to 85 °C to meet manufacturing standards.[117] Zhou *et al.* have investigated the internal temperatures that can be generated within an OLED by driving the device at different voltages.[142] Peak temperatures of 86 °C were observed by thermal imaging of the device surface, although the internal temperature was probably higher.[142] The device failure was attributed to the crystallisation of the *N*,*N*′-diphenyl-*N*,*N*′-bis(3-methylphenyl)-1,1′-biphenyl-4,4′-diamine (TPD) layer in the multilayer stack. Scanning electron microscopy (SEM) of the aluminium electrode also showed severe degradation had occurred.

Meanwhile, Chung *et al.* observed a maximum operating temperature of 64.5 °C from an OLED prepared on a glass substrate.[143] This heating occurred within 180 s of the start of operation, which shows that temperatures inside OLEDs can rise rapidly. Using a silicon or metal substrate greatly improved the heat dissipation, however for most conventional OLEDs, electrically conducting glass substrates are necessary for light transmission.

It is perhaps important to put these temperatures into context, since temperatures above 40 °C are very rarely encountered nor experienced in day-to-day life, and so one may ask the question – why

develop materials and devices with high temperature stability? Take for example a car parked in the sun, a common experience for many people. Maximum cabin temperatures can easily approach 90 °C,[144] with average summer time temperatures around 70 °C.[145] Even ambient temperatures of only 20 °C can drive the internal temperature of a car to nearly 60 °C. These temperatures correspond very closely to those observed during device failure.

The most prevalent material property of OLEDs and organic electronics is the glass transition temperature (T_g). Since the early days of OLED research much work has been focussed on developing materials with high (>100 °C) bulk glass transition temperatures.[130] However, Adachi *et al.* found no correlation between the glass transition temperature and the durability of device performance[146] and many low T_g materials are still routinely used in the best performing devices.[21,25,147-152]

1.5.3 Phase Separation in Organic Materials

In a thin film geometry there are two possible ways in which phase separation can occur – laterally or vertically. Lateral phase separation should be easy to observe if the film surface is exposed, while vertical phase separation will require probing the internal film structure, making this significantly more difficult to investigate. In the wider context of organic electronics, the nanoscale phase separation of poly(3-*n*-hexylthiophene) (P3HT) and [6,6]-phenyl C_{61}-butyric acid methyl ester (PCBM) is vital to the photovoltaic performance.[153] Thermal annealing creates an interpenetrated network of donor (hole transport, P3HT) and acceptor (electron transport, PCBM) molecules, which allows charge separation and transport to occur efficiently. If thermal annealing is not performed the P3HT:PCBM layer does not phase separate, and the device efficiency is considerably lower.[153,154]

Lateral phase separation has been observed in blends of $Ir(ppy)_3$ in polymers. When $Ir(ppy)_3$ was blended in poly[9,9′-di-*n*-hexyl-2,7-fluorene-alt-1,4-(2,5-di-*n*-hexyloxy)phenylene] (PFHP) very poor energy transfer between the polymer host and the phosphorescent dye gave blue emission predominantly from the PFHP.[155] Using transmission electron microscopy (TEM) aggregates of $Ir(ppy)_3$ could be detected with domain sizes ranging from 50-200 nm. At low (8 wt%) doping concentrations of $Ir(ppy)_3$ the aggregates were disordered round clusters, while at higher (15 wt%) concentrations the aggregates appeared to form needle-like crystallites. However, by changing the host polymer to poly(*N*-vinylcarbazol) (PVK) phase separation and aggregation of $Ir(ppy)_3$ was suppressed at all doping concentrations, and emission from the blend was only observed from $Ir(ppy)_3$ indicating efficient energy transfer from host to guest. In a device the $Ir(ppy)_3$:PVK blend exhibited a maximum external quantum efficiency of 6%, significantly better than the 0.4%

obtained for an $Ir(ppy)_3$:PFHP based OLED. The tendency for $Ir(ppy)_3$ and PFHP to phase separate and aggregate are therefore directly related to device performance.

To overcome this aggregation You *et al.* prepared a series of carbazole based co-polymers with pendant FIrpic groups.[156] The rationale was to directly tether the iridium(III) complex to the carbazole host so as to prevent phase separation. Spin-coating a blend of FIrpic and the pure carbazole polymer host resulted in aggregation of FIrpic as observed by confocal laser scanning microscopy. A co-polymer of carbazole and FIrpic groups prepared at the same doping concentration showed no signs of aggregation or phase separation, and significantly improved device performance.[156]

In another example, a 2 wt% blend of 1,4-bis(benzothiazole-vinyl)benzene (BT) in 2,2′,2″-(1,3,5-phenylene)tris-[1-phenyl-1*H*-benzimidazole] (TPBi) phase separation with thermal annealing could be observed by scanning tunnelling microscopy, which can directly image a surface with molecular resolution.[136] In the as-cast film of 2 wt% BT in TPBi, a homogeneously blended film surface was observed. The PL showed that emission came only from BT, indicating efficient energy transfer between TPBi and BT, and confirming that the film was well mixed. Annealing the film at 80 °C caused the PL intensity to decrease, which was accompanied by the formation of ordered domains as observed by STM. These domains were attributed to phase separation and crystallisation of BT molecules from the as-cast blend.[136] Increasing the annealing temperature to 100 °C accelerated the formation of BT domains and further decreased the PL intensity. A final annealing step at 180 °C significantly reduced and red-shifted the PL, while large 100 nm domains of BT were observed by STM. The decrease in PL intensity can be directly attributed to the phase separation and aggregation of BT from TPBi, indicating that phase separation in guest:host systems can have a negative impact on PL.

Kang *et al.* used neutron reflectometry (NR) to investigate the vertical structure and organic phases in a blended film of 6,13-bis(triisopropylsilylethynyl)pentacene (TIPS-pentacene) and poly(α-methylstyrene) (PαMS), which were used in an organic thin film transistor.[157] NR is useful for studying buried interfaces in organic films, and can provide information as to the layer thickness, density and interfacial roughness. In an as-cast film of 1:1 TIPS-pentacene and low molecular weight PαMS the two components were homogeneously blended throughout the depth of the film. The films were prepared on silicon wafers, and slightly higher concentrations of TIPS-pentacene could be found at the air and silicon interfaces of the film. When the film was annealed at 100 °C for 20 min (above the bulk glass transition of PαMS of 74 °C) significant vertical phase separation

occurred and the film separated into three distinct layers. The TIPS-pentacene formed layers at both the silicon and air interfaces, while the PαMS made up the intervening middle layer.

Surface modification of the electrode interface often improves device performance.[20] Using NR Mitchell *et al.* investigated the layering behaviour of several conjugated light emitting polymers deposited on a conducting substrate of ITO.[158,159] It was found that a so-called 'low contact layer', approximately 2 nm thick, was formed at the interface of the ITO and polymer film. This layer prevented a good contact between the polymer film and the ITO substrate, potentially impeding charge injection into the polymer film and reducing device performance.

1.5.4 Diffusion Between Organic Layers

Very little literature exists on the phenomenon of molecular diffusion between organic layers like those found in organic electronics, and OLEDs in particular. Diffusion should be viewed as a major problem for the extended operational lifetime and thermal stability of organic multilayers. The greatest impediment to the study of diffusion between organic layers is that the interface between layers is naturally 'buried', that is, there is no easily accessible way of probing the interface. Certainly optical and atomic force microscopy are useless here, since these techniques only probe surface features. In many respects, diffusion is the opposite phenomenon to phase separation, where rather than some morphological incompatibility, different organic layers would rather mix together than remain separate.

Han *et al.* were among the first to attempt to understand diffusion between organic layers in OLEDs by using PL quenching to characterise the rate of diffusion between layers of Alq_3 and TPD.[160,161] The layers were prepared by vapour deposition onto a glass substrate. The PL from both the Alq_3 and TPD layers could be observed from an as-deposited film, but after the film was thermally annealed the ratio between the PL peaks of Alq_3 and TPD changed with time. As the film was annealed the signal from the Alq_3 increased, at the same time as the TPD PL decreased. This behaviour was justified on the basis that if the Alq_3 and TPD layers diffused and mixed into one another, the energy of the photoexcited TPD will be transferred to the Alq_3, thereby quenching the emission from TPD and enhancing the Alq_3 emission; the TPD would act a host for the Alq_3. PL quenching is an indirect technique so whether the two organic layers were fully blended is unclear.

The behaviour of several Alq_3/TPD bilayer films was investigated by this technique at different annealing temperatures. At 60 °C the PL ratio changes quickly over the course of ~1 h reaching a constant ratio by ~6 h. Increasing the annealing temperature to 80 °C greatly accelerated the PL change, but also the ratio of Alq_3 to TPD signal intensity was significantly larger. There was

approximately an order of magnitude difference in the PL ratio between the films annealed at 60 °C and 80 °C. In all cases this behaviour occurs at or above the reported glass transition temperature of TPD (60 °C),[130] however since lower annealing temperatures were not reported the stability of the bilayer at temperatures <60 °C cannot be assessed. Later Fujihira *et al.* showed that the formation of dark spots in an OLED was due to interdiffusion of Alq_3 and TPD, which was attributed to very high Joule heating in the device.[118]

Fenter *et al.* used X-ray reflectometry to study a similar Alq_3/TPD bilayer system.[162] X-ray reflectometry can be used to probe the internal structure of thin films normal to a surface, and can give information as to the thickness, density and interfacial roughness of thin layers. The thickness of the Alq_3 and TPD layers could be precisely determined, and during stepwise annealing it was found that the thickness of the TPD layer increased. The bilayer film was stable through to ~83 °C, at which point structural rearrangement occurred. This was accelerated further by heating to 90 °C. Diffusion between the Alq_3 and TPD layers was not observed, nor considered, which is in stark contrast to the results obtained by PL quenching.[161] Fenter *et al.* concluded that the failure mechanism in these bilayer films is due to stresses induced by the thermal expansion of the TPD layer, well above the glass transition temperature.

An interesting application of this diffusion between organic multilayers has come from the group of Wu *et al.*[163-165] In a multilayer configuration with an active bilayer of Alq_3 and *N*,*N*′-diphenyl-*N*,*N*′-bis(1-naphthyl)-1,1′-biphenyl-4,4′-diamine (NPD) a thin layer of bis-4,4′-[(diphenylmethylsilyl)viny1]biphenyl (DPSVB) was inserted to separate the layers.[165] The as-deposited structure showed blue emission originating from the NPD layer. By thermally or electrically annealing the device above the T_g of DPSVB (30 °C), the DPSVB layer is bypassed and the Alq_3 and NPD layers can mix. This changes the emission colour from blue to green, making this a ‘reconfigurable’ or ‘programmable’ device. No detail is given as to the level of interdiffusion between the two layers, so whether the Alq_3 and NPD layers are fully mixed, or are just joined at the interface is not obvious.

Although the T_g of DPSVB is quite low, the same principle can be applied to higher T_g materials. A three-colour reconfigurable OLED was prepared by using three emitting layers separated by two different electron transport/hole blocking layers, 3-(4′-*tert*-butylphenyl)-4-phenyl-5-(4″-biphenyl)-1,2,4-triazole (TAZ) and bathocuproine (BCP).[163] BCP in particular is used extensively as an electron transport or hole blocking layer.[29,147,166] Wu *et al.* indicated that the T_g of BCP was ~85 °C and TAZ ~70 °C.[163] By choosing two materials with different thermal properties the colour of the OLED emission could be manipulated by annealing the device at different temperatures. The as-

deposited device showed blue emission, and annealing at 95 °C disrupted the TAZ layer so that the emission colour changed to green, and finally heating at 125 °C disrupted the BCP layer so that the emission appeared red. Notice that the temperatures at which diffusion is said to occur are much higher than the stated bulk thermal transitions.

To elucidate the internal structure of OLED multilayers Lin *et al.* used ion sputtering and X-ray photoelectron spectroscopy to etch through an OLED device and determine the elemental composition as a function of sputtering time.[167] Ion sputtering is a highly destructive technique since it relies on ablating material from the surface of the film, destroying the device in the process. The active organic layers consisted of CBP doped with an iridium(III) phosphor at 14 wt%, and an electron transport layer of TPBi. Using the intensity of the nitrogen signal both the CBP and TPBi layers could be observed (TPBi is nitrogen rich compared to CBP), and in an as-deposited film these two layers appeared to form well defined layers separated by a sharp interface. By operating several devices for 0.25, 1, 3 and 6 h it was observed that the CBP and TPBi layers mixed together.

The migration of TPBi was attributed to instantaneous charging of the TPBi during device operation, creating a TPBi anion. Under an electric field the charged TPBi feels a force driving it towards the anode, causing molecular migration and diffusion.[168] Since TPBi has a high T_g of 124 °C, it would seem unlikely that the molecular motion was promoted by Joule heating.[25]

1.6 Thesis Outline

This thesis is comprised of two distinct but equally important aspects critical to the performance and durability of phosphorescent OLEDs.

- The spectroscopic and electronic properties of several blue emitting iridium(III) complexes were investigated and described. Specialised spectroscopic measurements have been used to assign the low energy features of the absorption spectrum. Paying close attention to relativistic corrections, a complete model of the electronic structure was developed and compared to the measured spectroscopic properties.
- The susceptibility of blended organic layers to undergo lateral or out-of-plane phase separation during thermal annealing, and the interfacial stability of multilayer organic films under thermal load were investigated. Both the blend layer morphology and multilayer interfacial structure of representative organic films used in OLEDs were studied with NR. NR non-destructively probes buried interfaces and therefore played an important role in the determination of the film structure. A simultaneous *in situ* measurement of the film PL allowed the morphological and spectroscopic changes to be matched together.

1.6.1 Spectroscopy and Relativistic Theory of Iridium(III) Complexes

The weak low energy electronic features of the $Ir(ptz)_3$ family of blue phosphorescent complexes were studied with low temperature (<10 K) absorption spectroscopy. Cooling and freezing the complexes at low temperature provide better spectral resolution compared to room temperature solution measurements and therefore allows a more precise assignment of the low energy electronic states. However, to aid in this assignment the magnetic circular dichroism (MCD) spectra of the complexes were also measured. Under high magnetic fields electronic states are rearranged leading to small differences in the absorption of circularly polarised light. The MCD of phosphorescent iridium(III) complexes has not been systematically investigated in such a way before.

A series of quantum chemistry calculations were subsequently performed to understand this important low energy electronic regime in these iridium(III) complexes. A complete description of the absorption features necessitates a proper description of all the relativistic effects. A step-by-step approach was taken to see how different levels of relativistic effects can change the theoretical electronic structure. Calculations were performed without any relativistic effects, and then at different stages within the ZORA formalism, which was used extensively to evaluate the contributions that scalar relativistic and spin-orbit coupling effects have on the properties of phosphorescent iridium(III) complexes. By combining spectroscopy with relativistic quantum chemistry the key attributes that explain the effects of fluorination on the photophysics of iridium(III) complexes have been described.

1.6.2 Thin Film Morphology of Phosphorescent OLEDs

The performance of OLEDs is critically dependent on the morphological behaviour of the organic layers. Since blended films are often used in OLEDs it is important to understand how such films degrade. The propensity for blended two component films to phase separate was studied with NR using the $Ir(ppy)_3$:CBP guest:host combination as a model platform. By using deuteration to enhance the contrast between the two organic components it was possible to determine whether vertical phase separation occurred after the film was thermally annealed. The changes induced by thermal annealing were also studied with an *in situ* photoluminescence measurement, which can be directly correlated with the results obtained from NR.

However, very rarely are OLEDs comprised of a single organic layer. Therefore the interactions between layers play an important role in determining device performance. Whether different organic layers form stable interfaces, especially at elevated temperatures, is unknown. To achieve high performance and durable OLEDs, the deposited multilayer organic films must form thermodynamically stable interfaces. To investigate this a number of multilayer films with high

contrast between layers were prepared and measured with NR. Using materials commonly found in small molecule phosphorescent OLEDs, the multilayer films were annealed at different temperatures to determine how and where thermal degradation occurs in multilayer films. Again, *in situ* PL measurements allow the morphological changes to be correlated back to changes in the emission characteristics of the multilayer film stack.

Chapter 2. Relativistic Effects in a Phosphorescent Iridium(III) Complex

Published in Physical Review B, 2011, 83, 041105(R)

2.1 Abstract

High field magnetic circular dichroism, absorption, and photoluminescence spectra for $Ir(ptz)_3$ are compared with time-dependent density functional theory. By gradually turning on the relativistic effects several distinct relativistic effects can be identified in the spectra of this complex. Relativistic effects must be included to accurately predict the low-temperature spectra. This leads to new insights into the low-lying excitations responsible for the observed phosphorescence, and suggests new avenues to improve the performance of organic light emitting diodes.

2.2 Introduction

Relativistic effects lead to many important phenomena in heavy metals such as gold's yellow colour[169] and lead's face-centred cubic crystal structure, which causes it to be a metal rather than an insulator.[170] However, to date, little is known about relativistic effects in organometallic complexes. Relativistic effects are expected to play an important role on the metal, but to be negligible on the organic ligand. Therefore, relativistic effects need to be properly included to give a thorough description of metal-to-ligand charge transfer (MLCT) excitations, which are often important in organometallic complexes. The phosphorescent decay and fast intersystem crossing[171] observed in organometallic complexes are mediated by spin-orbit coupling (SOC). For closed-shell molecules SOC only appears at second order (in, say, $1/c^2$).[105] Therefore first-order corrections also need to be considered.

Understanding these effects is important because organometallic complexes hold enormous promise as the active components in optoelectronic devices such as organic light emitting diodes (OLEDs) and dye-sensitized solar cells. Since the seminal report[21] of an OLED comprised of a phosphorescent iridium(III) complex there has been a plethora of papers describing new complexes and their use in devices.[55] However, while some general design principles are now known[51] less is understood about why small variations can cause large changes in, for example, the photoluminescence quantum yield (PLQY).[19,40,72,172,173] Understanding the photophysical and electronic properties of these complexes remains a major challenge and the major impediment to the rational design of new, highly emissive materials and complexes used in photovoltaic devices.

2.3 Methods

2.3.1 Relativistic Density Functional Calculations

Time-dependent density functional theory (TDDFT) has been routinely applied to describe the optical properties of new iridium(III) complexes since Hay[85] first showed that TDDFT could reproduce excitation energies of iridium(III) complexes reasonably accurately.

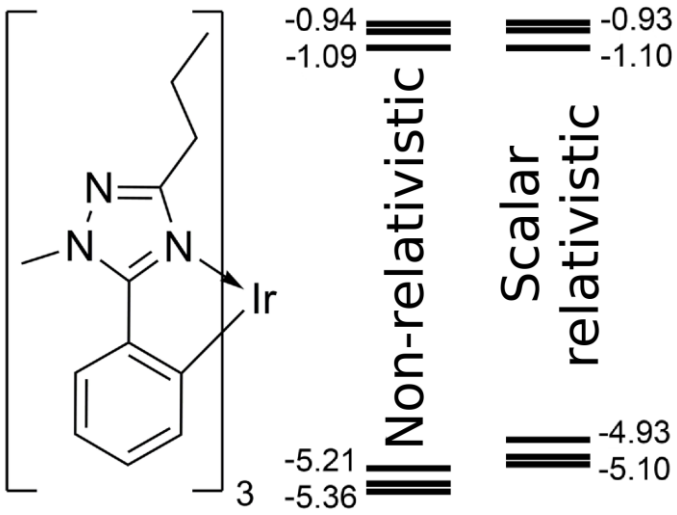

Figure 2.1 *Fac*-tris(1-methyl-5-phenyl-3-*n*-propyl-[1,2,4]triazolyl)iridium(III), Ir(ptz)$_3$, (left) and a schematic molecular orbital energy level diagram for the non-relativistic and scalar relativistic DFT calculations.

However, these TDDFT calculations do not, typically, include relativistic effects, such as SOC.[11,13] They are therefore incapable of describing the fine structure of iridium(III) complexes that low-temperature (LT) spectroscopic measurements reveal.[72,84,96,172,174] This is a major problem as these measurements suggest that the fine structure of the excitations plays an important role in determining optoelectronic properties and hence the performance of OLED's based on these materials. The LT absorption, photoluminescence (PL), and magnetic circular dichroism (MCD) spectra of the blue emissive phosphorescent *fac*-tris(1-methyl-5-phenyl-3-*n*-propyl-[1,2,4]triazolyl)iridium(III) [Ir(ptz)$_3$, Figure 2.1] complex are shown in Figure 2.2.

The spectra are calculated via three flavours of TDDFT: *non-relativistic* (NonR) calculations based on the Schrödinger equation; *scalar relativistic* (SR)[105] calculations based on the zeroth-order regular approximation (ZORA)[108,111] to the Dirac equation; and second-order perturbation theory in the SOC[111] about the SR results. All-electron TDDFT calculations were performed in ADF 2009.01[175-177] using the Becke, three-parameter, Lee-Yang-Parr (B3LYP) functional with a triple-ζ polarized (TZP) basis of Slater orbitals.[178,179]

These calculations demonstrate that relativistic effects must be taken into account before one can accurately predict the spectra of iridium(III) complexes. Once both the SR and SOC corrections are included the observed LT MCD, absorption and PL spectra can be explained. This combination of LT spectroscopy and relativistic theory allows a number of fundamental issues about the nature of the excited states in general, and the emissive state in particular, to be resolved. $Ir(ptz)_3$ has a solution PLQY of 66% and 1931 Commission Internationale de l'Eclairage (CIE) coordinates of (0.16, 0.20).[19] The addition of electron withdrawing groups to the ligand causes the PL to blue shift, but this comes at the cost of a dramatic decrease in the PLQY.[19] Hence, it is important to understand the excitation spectra of this complex as a starting point for developing deeper blue compounds that might form the basis of highly efficient OLED's as well as providing a platform for the design of highly luminescent complexes that emit across the visible spectrum.

The measured crystal structure[19] of $Ir(ptz)_3$ was used as the initial input for the geometry optimization. The *n*-propyl group was removed since it is unlikely to affect the electronic structure and significantly complicates the potential energy surface. The structure was then relaxed via DFT using the B3LYP hybrid functional[180,181] in the GAMESS suite of programs.[182,183] These calculations used a LANL2DZ basis for the iridium[115] and 6-31G basis for hydrogen, carbon and nitrogen.[184,185] Care was taken to conserve the C_3 symmetry of this *facial* complex throughout the geometry optimisation procedure. The converged molecular structure (Appendix A) changed little from the crystal geometry.

Note that the TDDFT calculations performed in ADF did not make use of symmetry. This led to small splittings in between the degenerate E excitations. These splittings are artefacts of the calculation and have no physical significance. Symmetry labels were determined manually by examining the full range of properties of the excitations.

Extensive benchmarking calculations have shown that the choice of basis set has a large effect on the calculated energies and that the TZP basis is the minimum required to get good agreement with experiment (for further details see Chapter 3). However, treating the inner core electrons on the iridium atom in the frozen core approximation has little effect on the excitation spectrum.

The molecule was divided into three fragments comprising iridium, phenyl and triazloyl groups and a Mulliken population analysis[186] was performed according to these divisions for each molecular orbital. The molecular orbitals were characterised by their ligand character. For each singlet and triplet excitation the ligand character difference (excited – ground) was taken and weighted by the contribution of that orbital transition to the excitation, and the sum of the weighted differences

obtained. This number describes the 'MLCT' character. A purely metal orbital would have 0 ligand population, while a ligand orbital would have a population of 1. A transition between these two orbitals would be a pure MLCT transition, +1. Using this nomenclature a difference of -1 would describe a pure LMCT transition.

2.3.2 Magnetic Circular Dichroism Measurement

Magnetic circular dichroism (MCD) spectroscopy experiments were performed at 10 K under a magnetic field of 5 T. Total and differential circularly polarized light intensity were measured simultaneously using a single beam instrument consisting of a xenon arc lamp dispersed by a Jobin/Yvon 750 S monochromator. The beam was linearly polarized by a calcite crystal (extinction $<10^{-6}$), mechanically chopped at 500 Hz (New Focus 3501), circularly polarized by a photoelastic modulator at a frequency of 42 kHz (Hinds PEM II/IS42), and passed through the sample held in an Oxford Instruments Spectromag 7 T superconducting magnet. Light was detected either with an S-5 photomultiplier (Hamamatsu R7459) or a Si avalanche photodiode detector. All instrument control and data collection was achieved with GPIB protocols and LABVIEW software.

LT (10 K), high field (5 T) MCD spectrum of $Ir(ptz)_3$ was collected in 2-methyltetrahydrofuran due to its capacity to form high quality glasses suitable for low temperature measurements (Figure 2.2). The LT absorption spectrum, measured simultaneously, is significantly sharper than that at room temperature[19] and shows extra features throughout the absorption band. A clear MCD A-term, indicating a transition to a degenerate excited state,[187] is found around the lowest-energy band at ~2.8 eV. There appears to be at least one shoulder in this peak, suggesting that there is more than one degenerate state in this energy range. The oscillations present at higher energies could be several overlapping A-terms, or a combination of A and B-terms. A detailed mapping of the low-energy excitations of $Ir(ptz)_3$ is therefore not possible from this experimental data alone. Nonetheless, the MCD clearly demonstrates that there are several states with small oscillator strengths at low energies.

2.4 Time-Dependent Density Functional Calculations

In an effort to understand the photophysical properties of $Ir(ptz)_3$ NonR-TDDFT was used to calculate its excitation spectrum. Figure 2.2a shows a level of agreement with the measured absorption spectrum that is typical of the accuracy of this method for this type of complex. Specifically, there is a large density of states coincident with the strongest peak in the absorption with a smaller number of weaker transitions at longer wavelengths. If the comparison to the experiment were limited to room temperature absorption this may appear to be reasonable

agreement. However, the LT spectroscopic data make it clear that there are a large number of states at lower energies not reproduced by NonR-TDDFT. Further, NonR-TDDFT does not predict sufficient numbers of low-energy states to describe the MCD spectrum even qualitatively. Finally, the lowest-energy triplet state is 0.25 eV above the first peak in the PL spectrum.

Therefore SR-TDDFT was employed (Figure 2.2b). Comparing the SR-TDDFT results to the NonR-TDDFT (Figure 2.2a), one immediately notices dramatic improvements in the correlation between the calculated transitions and measured absorption spectrum. There are singlet states with large oscillator strengths at energies close to each of the three largest peaks in the absorption. Further, the SR calculation also predicts three low energy triplets with energies comparable to the lowest-energy features in the absorption and, importantly, the highest-energy features in the PL. However, these calculations do not provide sufficient accuracy to explain the MCD. It will be demonstrated in the following that SOC is vital for understanding the MCD.

Understanding of the physical origin of the differences in the NonR and SR excitation spectra is aided by considering the Kohn-Sham molecular orbitals (MO's) of the underlying DFT calculations. Both calculations predict that the highest occupied MO (HOMO) and lowest unoccupied MO (LUMO) are non-degenerate A states, whereas the HOMO−1 and LUMO+1 are two-fold degenerate E manifolds (cf., Figure 2.1). Plots of the electron densities of these MO's (Figure 2.3) show that the occupied orbitals have a significant contribution from the iridium atom whereas the virtual orbitals do not. A Mulliken population analysis (Appendix A) shows that the iridium 5*d* orbitals contribute ~50% of the electron density in both the HOMO and HOMO−1.

To connect the DFT orbitals to the TDDFT spectra the MO weights of the transitions were calculated (Appendix A). The two strongest singlets, S_3(E) and S_5(E), belong to the E irreducible representation of C_3. These excitations are dominated (>92%) by the HOMO−1→LUMO and HOMO→LUMO+1 transitions, respectively. Thus these transitions have a significant MLCT character (~50%, Appendix A).

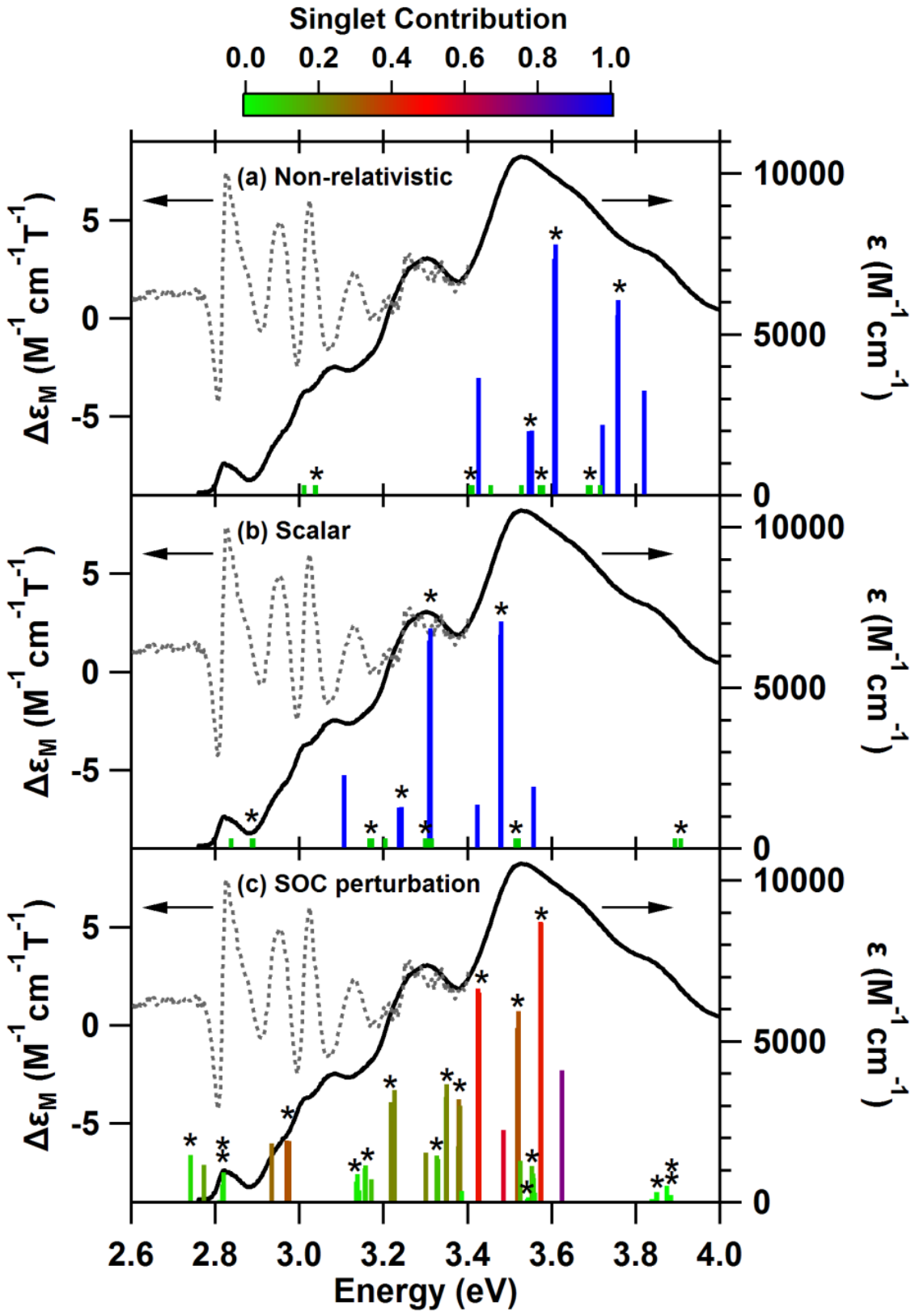

Figure 2.2 Absorption (solid line) and MCD (dashed line) spectra of $Ir(ptz)_3$ collected at 10 K under an applied field of 5 T compared to the "stick" absorption spectra calculated by (a) NonR-TDDFT, (b) SR-TDDFT, and (c) perturbative SOC correction to the SR calculation. Degenerate (E) states are denoted with a * (marks two nearby E states). In the NonR and SR calculations the (formally forbidden) triplet excitations are given small arbitrary oscillator strengths for clarity.**

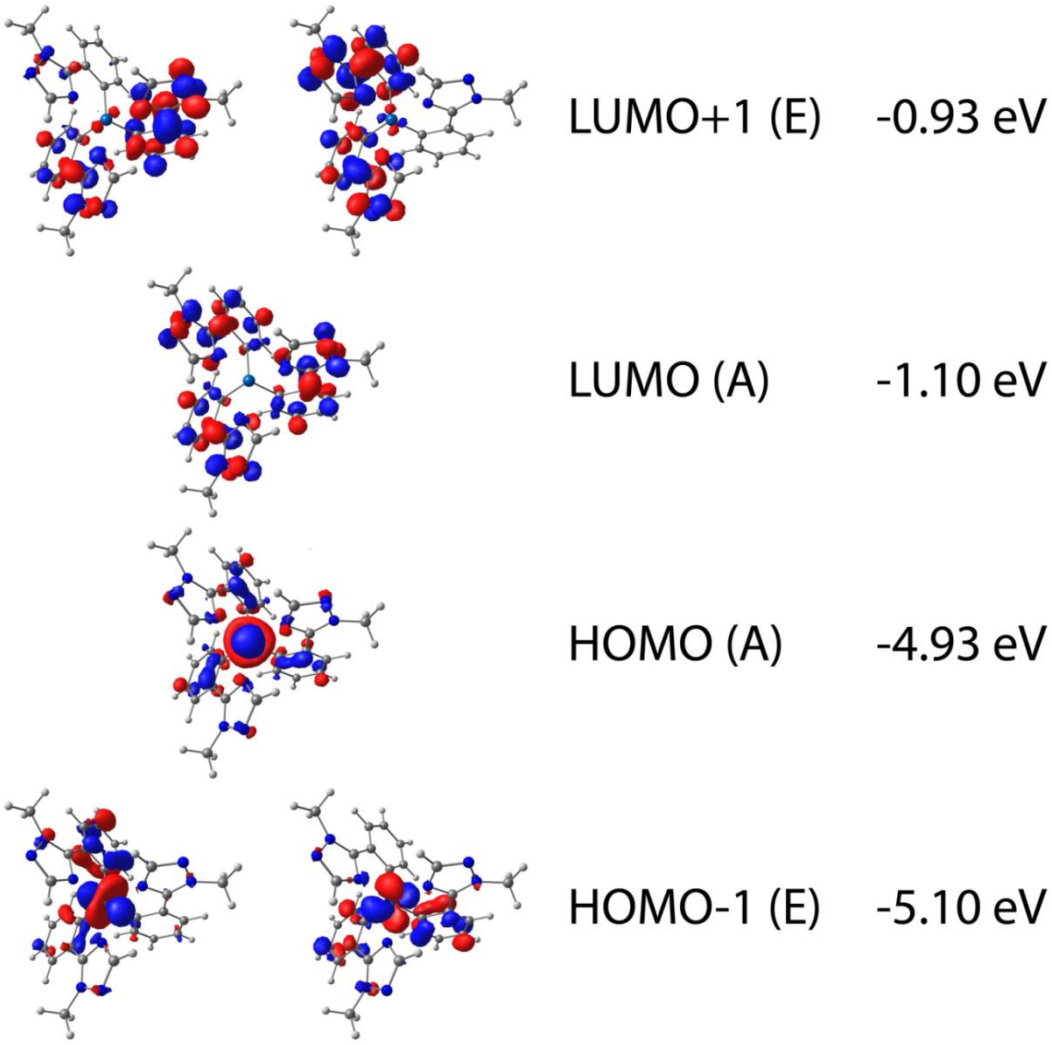

Figure 2.3 Electron densities in the frontier orbitals of $Ir(ptz)_3$ calculated from SR-DFT, all-electron TZP basis set.

It is well known from atomic physics[188,189] that there are two important relativistic effects on atomic orbitals (AOs). The *direct* relativistic effect arises from the increase in the mass of the electron due to its relativistic velocity, which leads to a decrease in the Bohr radius of the electron and hence a stabilization of the AOs. An *indirect* effect is also observed because the core electrons are closer to the nucleus due to the direct effect. Thus the core electrons screen the valence electrons more effectively, which destabilizes the valence electrons. The direct effect dominates for *s* electrons; for *p* electrons the two effects nearly cancel; but for *d* electrons the indirect effect is larger. SR-DFT calculations for the isolated iridium atom nicely reproduce these trends (Table 2.1). In particular, there is a ~0.28 eV destabilization of the iridium 5*d* AOs at the level of theory used for $Ir(ptz)_3$.

Table 2.1 Isolated iridium atomic orbital energies calculated from NonR and SR-DFT, all-electron TZP basis set.

atomic orbital	occupation	non-relativistic (eV)	scalar relativistic (eV)
1*s*	2	-69361.2373	-76024.4432
2*s*	2	-11512.8713	-13326.7666
2*p*	6	-11068.0705	-11581.4228
3*s*	2	-2657.8964	-3127.0854
3*p*	6	-2467.3286	-2615.0101
3*d*	10	-2065.2894	-2048.9580
4*s*	2	-546.8233	-669.9624
4*p*	6	-466.2059	-501.6919
4*d*	10	-297.2044	-293.5522
5*s*	2	-73.8820	-96.4965
4*f*	14	-72.5287	-61.5605
5*p*	6	-47.5421	-52.7315
5*d*	9	-4.8237	-4.5431
6*s*	0	-2.2155	-3.8675
6*p*	0	2.5174	1.8442
7*s*	0	3.9067	2.7527
6*d*	0	8.2581	8.2463
8*s*	0	25.9173	20.6968

The above discussion leads to a simple explanation of the observed differences between the NonR and SR excitation spectra. The indirect relativistic effect destabilizes the iridium 5*d* AOs. This destabilizes the HOMO and HOMO−1 levels, which have a large contribution from the iridium 5*d* orbitals, by 0.27–0.28 eV. However, the LUMO and LUMO+1 do not contain any significant contribution from the iridium AOs. Thus, there are only small SR corrections (<10 meV) to the LUMO and LUMO+1 energies (cf., Figure 2.1). This shift in MO energies is the single largest effect responsible for the changes between the NonR and SR-TDDFT excitation spectra. Therefore, the relativistic effects in the absorption of $Ir(ptz)_3$ are closely related to the relativistic effects responsible for the yellow colour of gold[169] and the metallicity of lead.[170]

The relativistic effects on the low-lying triplet excitations are slightly more complicated. In the NonR calculation the HOMO → LUMO transition contributes 53% of the weight of T_1(A). In the SR calculation this increases to 69%. This lowers the T_1(A) excitation even more than would be expected from the relativistic destabilization of the iridium 5*d* AOs alone. Similar changes occur in T_2(E), which arises predominately from the HOMO→LUMO+1 and HOMO−1→LUMO transitions (Appendix A).

2.4.1 Spin-Orbit Coupling

SOC mixes singlets and triplets. Nevertheless, many excitations retain a strong triplet character after the SOC perturbation is included, in particular, the lowest-energy excitations remain predominately triplet. Thus, the description of the emission as phosphorescence remains substantially valid even after SOC is included. An important consequence of the reduced symmetry, once SOC is included, is the zero-field splitting (ZFS) of the triplets, which are degenerate in the scalar calculation. This is responsible for the increased number of lines in Figure 2.2c.

A significant number of low-lying states are important for understanding the MCD spectrum. The lowest two excitations (which are henceforth referred to as 1A and 2E as the first excitation has A symmetry and the second has E symmetry) result primarily from the ZFS of T_1(A). 1A is predicted to have a very weak oscillator strength because it remains almost a pure triplet even when SOC is included. Indeed the "stick" corresponding to this state is too small to be visible in Figure 2.2c. Hence, it is doubtful that 1A plays a significant role in any of our measurements.

Higher-lying excited states play an important role in the photophysics, particularly at room temperature.[84,96,174] Therefore it is important to understand and control these states if one wants to tailor the properties of organometallic complexes for optoelectronic applications. The excitations 3A, 4E, 5A, and 6E arise predominately from the ZFS of T_2(E). Excitations 7A and 8E are rather more complex and have significantly more singlet character than the lower-energy excitations. However, the singlet character of 7A and 8E arises predominately from S_1(A) and S_2(E), whereas most of the singlet character of 2E–6E comes from S_3(E). S_3(E) has significantly more oscillator strength than S_1(A) and S_2(E) (Figure 2.2b). This explains why 7A and 8E are not significantly brighter than 2E–6E despite their greater singlet character.

Thus the inclusion of SOC allows for a natural interpretation of the MCD spectrum. Before giving a detailed assignment, it is important to recall that the states belonging to the E representation of C_3 are only two-fold degenerate under the assumption of time-reversal symmetry. As the application of a magnetic field breaks time reversal symmetry it will always lift this degeneracy, leading to A-terms in the MCD spectrum. The A-term at low energies is assigned to the manifold of triplet states around 2.8 eV, which can be traced back through T_1(A) and T_2(E) to HOMO→LUMO, HOMO→LUMO+1, and HOMO−1→LUMO transitions. Significant contributions to this feature arise from both 2E and 6E and a B-term from 3A may also be implicated in the apparent shoulder(s) in this term. There is then a B-term arising from excitation 7A and a second A-term arising from excitation 8E. Although the natures of these excitations can also be traced back to the MO's, this

yields little insight as these higher energy excitations are complex combinations of many MO transitions (Appendix A). This assignment has been tested by comparison to similar predictions for a series of related compounds, which will be discussed later (Chapter 4).

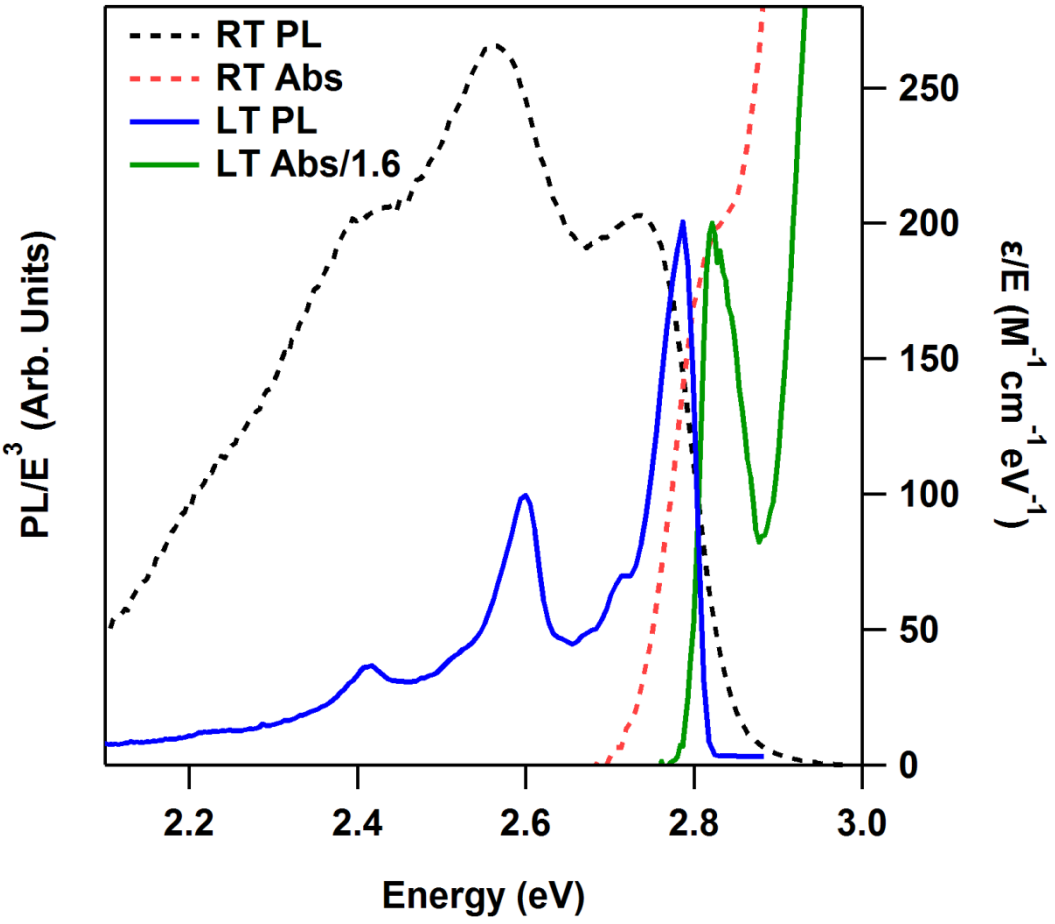

Figure 2.4 Scaled absorption and PL spectra of $Ir(ptz)_3$ at room temperature (RT) and low temperature (LT). A clear mirror image rule is observed in the LT data. The Stokes shift is significantly reduced at LT due to the freezing of the solvent.

The energy of the lowest excitations, 1A and 2E, correspond, to within the inherent accuracy of the calculation, to the first peak. This suggests that, neglecting ZFS for the moment, $T_1(A)$ is the phosphorescent state at LT, as one would expect from Kasha's rule.[190] If this is correct one should expect the mirror image rule to be obeyed. It can be seen from Figure 2.4 that this is indeed the case. As best as can be determined, this is the first demonstration of the applicability of the mirror image rule to this type of complex. However, SOC produces very different oscillator strengths in the ZFS states. Excitation 2E will have a much shorter radiative lifetime than 1A. This should be manifest as a strongly temperature dependent lifetime. One should also expect that the coupling of these two states to vibrational excitations is very different because of their different symmetry.

Understanding how these effects are modified by chemical substitutions may allow one to increase the efficiency of OLED's based on iridium(III) complexes.

2.5 Conclusions

It is clear that both spin-free (scalar) relativistic effects and SOC are vital for understanding the spectra of phosphorescent iridium(III) complexes. SR corrections destabilize the iridium 5*d* orbitals and, as the low-lying excitations in phosphorescent iridium(III) complexes involve considerable MLCT character, this significantly alters the spectra. SOC is also important, not only for the phosphorescence and fast intersystem crossing, but also to understand the ZFS and subtle redistribution of spectral weight observed via the MCD.

Chapter 3. Spin-Orbit Coupling in Phosphorescent Iridium(III) Complexes

Published in ChemPhysChem, 2011, 12, 2429

3.1 Abstract

The excited states of two iridium(III) complexes with potential applications in organic light-emitting diodes are examined: *fac*-tris(2-phenylpyridyl)iridium(III) [$Ir(ppy)_3$] and *fac*-tris(1-methyl-5-phenyl-3-*n*-propyl-[1,2,4]triazolyl)iridium(III) [$Ir(ptz)_3$]. The excited states of these complexes were calculated from time dependent density functional theory (TDDFT) with the zeroth order regular approximation (ZORA). The results from the one-component formulation of ZORA, with spin-orbit coupling included perturbatively, accurately reproduce both the results of the two-component calculations and the experimental absorption spectra of the complexes. The effects of both scalar relativistic correction and spin-orbit coupling are traced through the low energy excitations and radiative lifetimes of these complexes. In particular, it is demonstrated that there is an indirect relativistic stabilisation of the metal-to-ligand charge transfer (MLCT) states. This is important because it means that indirect relativistic effects increase the degree to which SOC can hybridise singlet and triplet states and hence plays an important role in determining the optical properties of these complexes. The two compounds are remarkably similar in these respects, despite $Ir(ppy)_3$ and $Ir(ptz)_3$ emitting green and blue light respectively. However, it is predicted that these two complexes will show marked differences in their magnetic circular dichroism (MCD) spectra.

3.2 Introduction

Phosphorescent iridium(III) complexes show significant promise as active materials in organic light diodes (OLEDs). Phosphorescent materials are particularly desirable over fluorescent emitters due to their potential to harvest both singlet and triplet excitations generated in a device.[37,173] However, the development of efficient deep-blue phosphorescent emitters, which are required for full colour OLED displays,[19,51,73,191] has remained a persistent problem since the field was established with the discovery of the green phosphorescent complex *fac*-tris(2-phenylpyridine)iridium(III) [$Ir(ppy)_3$; Figure 3.1 and Table 3.1].[21] *Fac*-tris(1-methyl-5-phenyl-3-*n*-propyl-[1,2,4]triazolyl)iridium(III) [$Ir(ptz)_3$; Figure 3.1] emits blue light at room temperature,[19] *cf*. Table 3.1. Thus a study of both complexes is needed to develop a clear understanding of the differences between the optoelectronic properties of these materials. A complete understanding of all the processes responsible for highly efficient organometallic phosphorescent complexes has remained elusive. This significantly hampers the goal of designing new complexes for OLED applications.

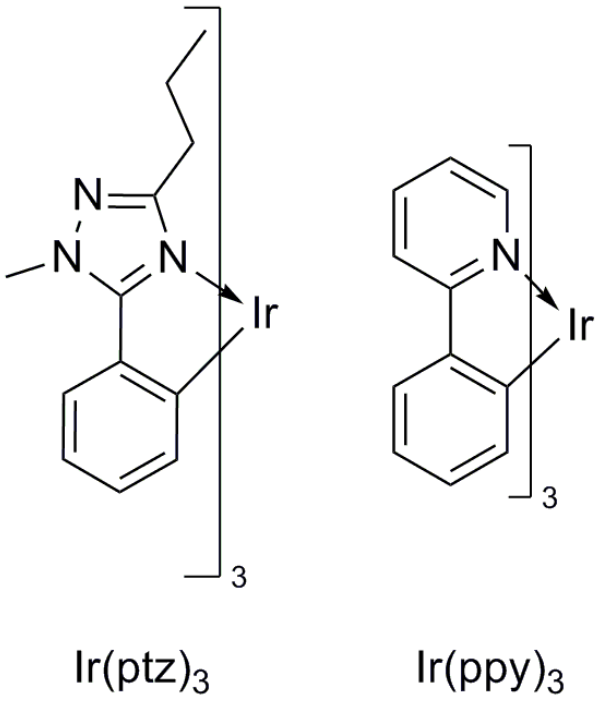

Figure 3.1 Complexes studied in this work: *fac*-tris(1-methyl-5-phenyl-3-*n*-propyl-[1,2,4]triazolyl)iridium(III) [$Ir(ptz)_3$; left] and *fac*-tris(2-phenylpyridyl)iridium(III) [$Ir(ppy)_3$; right].

Table 3.1 Selected properties of $Ir(ptz)_3$ and $Ir(ppy)_3$ at 300 K; from Lo *et al.*[19] and Hofbeck and Yersin[84] respectively.

Complex	PLQY (%)	Lifetime (μs)	PL CIE (x, y)
$Ir(ptz)_3$	66 ± 7	1.08	(0.16, 0.20)
$Ir(ppy)_3$	90 ± 5	1.6	(0.33, 0.61)

There are a number of clear indications that relativistic effects are important for understanding the optical and optoelectronic properties of iridium(III) complexes. Firstly, these materials display signatures of strong spin-orbit coupling (SOC): most notably phosphorescent decay and fast intersystem crossing,[171] which are both mediated by SOC. This has motivated several groups to include SOC in their calculations. Both Matsushita *et al.*[11] and Jansson *et al.*[113] studied $Ir(ppy)_3$ with SOC included via the semi-empirical effective nuclear charge method,[192,193] which includes SOC on top of non-relativistic calculations. Matsushita *et al.*[11] studied the mixing of singlet and triplet states and the implications of this for phosphorescence and Jansson *et al.*[113] investigated the nature of the T_1 excitation in some depth. Minaev *et al.*[194] used quadratic response TDDFT to calculate the radiative rates of several phosphorescent complexes, while De Angelis *et al.* have presented a qualitative analysis of the SOC matrix elements in iridium(III) complexes[12] and discussed the effects of solvation on these matrix elements.[195] Nozaki *et al.*[13,14] have also investigated organometallic complexes with the SOC included perturbatively about non-relativistic

TDDFT calculations. Nozaki[13] showed that this method provides a reasonable description of the zero-field splittings and oscillator strengths of $Ir(ppy)_3$, and in a further study Nozaki and collaborators investigated the differences in the optical properties in a range of tris(2,2′-bipyridine) transition metal complexes using the same method.[14]

However, as shown in Chapter 2 scalar relativistic corrections are also important.[196] In particular, scalar relativistic TDDFT calculations with spin-orbit coupling included perturbatively accurately predict the low temperature, high field magnetic circular dichroism and absorption spectra of $Ir(ptz)_3$. The low-lying excited states are believed to have a strong metal-to-ligand charge transfer (MLCT) character. Although DFT has some well-known issues in describing charge transfer transitions,[197,198] the use of hybrid functionals, which include exact exchange can alleviate this problem.[104] As one expects relativistic effects to be important on the metal, but negligible on the ligand, this suggests that a correct description of the relativistic corrections is necessary for the accurate description of these excitations. Therefore, relativistic effects need to be included to correctly describe the excitations that need to be controlled in order to design new active materials for OLED applications.

The field of relativistic quantum chemistry is well established, but outside the experience of many practicing chemists. Readers interested in more details would be well served by the works of Dyall and Fægri[105] or Dreizler.[199] A short description follows which introduces many of the fundamental features of relativistic quantum chemistry, especially within the zeroth order regular approximation (ZORA).

The Dirac equation[200,201] provides a Lorentz invariant formulation of quantum mechanics for spin ½ particles, such as electrons, and therefore represents the unification of quantum mechanics with special relativity. This is one of the greatest achievements of theoretical physics and leads directly to a natural explanation of spin, the prediction of the positron and development of quantum electrodynamics (QED). However, whereas in non-relativistic quantum theory the wavefunction is a complex scalar field, in the relativistic theory the wavefunction for spin ½ particles is a complex four-vector field, *i.e.*, a four-spinor. For each solution of the Schrödinger equation the Dirac equation has four eigenvalues. These have a simple physical interpretation: two eigenvalues have positive energy and represent matter with spin-α and spin-β; the two negative energy solutions represent antimatter with spin-α and spin-β. This significantly increases the difficulty, and hence the computational cost, of relativistic calculations.

A significant difficulty with relativistic theory is that the Coulomb interaction is retarded, that is, the Coulomb interaction is mediated by photons, which travel at the, finite, speed of light. The correct treatment of this retarded interaction requires a Lorentz invariant interaction, the quantisation of the field and the full machinery of QED. This would render quantum chemical calculations intractable. Therefore, approximations need to be introduced. An important simplification is to work in the Born-Oppenheimer frame. This means that the theory is no longer Lorentz invariant, but allows the most important relativistic corrections to be kept.

The full relativistic machinery is not necessary for most chemical problems. Therefore, it is natural to consider only the leading relativistic correlations in a perturbation theory in $\frac{1}{mc^2}$, where m is the mass of the electron and c is the speed of light. This leads to the Breit-Pauli Hamiltonian. However, the Breit-Pauli Hamiltonian is not ideal for quantum chemistry because the expansion is only valid for $|V-E| < 2mc^2$, where V is the potential and E is the orbital energy. Neither V nor E are bounded from above; in particular, $|V-E|$ is always greater than $2mc^2$ sufficiently close to the nucleus. Therefore it is preferable to perform the expansion in $\frac{1}{2mc^2-V}$ which leads to an analytic expansion, even arbitrarily close to the nucleus. This is known as the regular or Chang-Pélissier-Durand approximation.[108] The regular approximation contains corrections to all orders in $\frac{1}{mc^2}$, even at zeroth order. This can be seen immediately from the Hamiltonian for zeroth order regular approximation (ZORA), which is

$$H_{ZORA} = V + (\vec{\sigma}.\vec{p})\frac{c^2}{2mc^2 - V}(\vec{\sigma}.\vec{p}) \quad \textbf{3.1}$$

$$= V + \frac{1}{2m}(\vec{\sigma}.\vec{p})\left[1 + \frac{V}{2mc^2} + \frac{V^2}{4m^2c^4} + \cdots\right](\vec{\sigma}.\vec{p}) \quad \textbf{3.2}$$

where $\vec{\sigma}$ is the vector of Pauli matrices, and $\vec{p}$ is the momentum three-vector.

The relativistic Hohenberg-Kohn theorem[202-204] proves that the ground state energy of a covariant system is a unique functional of the ground state four-current. However, analogously to non-relativistic theory, practical implementations require the solution of the Dirac-Kohn-Sham equations,[105,199]

$$\begin{pmatrix} V & c\vec{\sigma}.\vec{p} \\ c\vec{\sigma}.\vec{p} & V - 2mc^2 \end{pmatrix}\begin{pmatrix} \psi^L \\ \psi^S \end{pmatrix} = E\begin{pmatrix} \psi^L \\ \psi^S \end{pmatrix} \quad \textbf{3.3}$$

where $V = V_{nuc} + V_{Hartree} + V_{xc}$, $V_{Hartree}$ is the Hartree potential, V_{xc} is the exchange-correlation potential and ψ^L and ψ^S are two-spinors, known as the large and small components respectively.

These names arise because for the matter solutions the large component is larger than the small component (somewhat confusingly the reverse is true for the antimatter solutions). Since only matter solutions are required, the Kohn-Sham equations can be simplified by eliminating the small component, which yields

$$\left[(T+V-E)+\frac{V-E}{2mc^2+E-V}T-\frac{c^2}{(2mc^2+E-V)^2}[(\vec{p}V).\vec{p}+i\vec{\sigma}.(\vec{p}V)\times\vec{p}]\right]\psi^L=0 \qquad \textbf{3.4}$$

where T is the non-relativistic kinetic energy operator. This two-component relativistic theory is a dramatic simplification as now one need only deal with a two-spinor. The loss of information about the antimatter solutions is not a significant drawback for chemical applications.

Note that only the last term in Equation 3.4, the SOC, is spin dependent and that this term only appears at second order; whereas, there are spin-free (scalar) relativistic corrections even at first order. This motivates the scalar relativistic approximation, where one neglects the SOC. In this approximation the two components of ψ^L decouple and the problem reduces to a one-component theory. This one-component theory is as computationally tractable as the non-relativistic Schrödinger equation. SOC can then be included perturbatively around the results of the scalar calculation.[111]

3.3 Methods

Closed shell geometry optimisation of both complexes was performed using GAMESS[182,183] with the B3LYP hybrid functional.[180,181] The LANL2DZ basis[115] set was employed for iridium, while the 6-31G basis set[184,185] was used for nitrogen, carbon and hydrogen. C_3 symmetry was enforced during the optimisation routine. The geometry of $Ir(ptz)_3$ was optimised without the *n*-propyl solubilising groups (substituted by a single hydrogen) as these additional degrees of freedom significantly increase the computational cost of both the geometry optimisation procedure and the higher level calculations to follow, whereas the *n*-propyl groups only have a weak inductive effect and hence will not alter the optical properties of $Ir(ptz)_3$ significantly.

TDDFT calculations were carried out with the Amsterdam Density Functional (ADF) 2009.01 program.[175-177] As with the geometry optimisation, the B3LYP functional was used throughout. Self-consistent two-component spin-orbit TDDFT calculations within the ZORA[106,107,109] were performed for the 50 lowest spin-polarized excitations. One-component ZORA TDDFT calculations,[111] which included SOC perturbatively, were performed on the 50 lowest scalar relativistic singlet and triplet excitations. This results in a total of 200 spin-mixed excitations.

All calculations use a triple-ζ with polarization function (TZP) basis set on the iridium, and henceforth the basis set of a particular calculation refers to that applied to the light elements.[178,179] Due to their computational cost, the two-component calculations were limited to a double-ζ with polarization function (DZP) basis set on the light elements and a frozen core approximation encompassing the iridium 1*s* 2*s* 2*p* 3*s* 3*p* 3*d* 4*s* 4*p* 4*d* 4*f* orbitals, the nitrogen 1*s* orbital and carbon 1*s* orbital. Both DZP and TZP basis sets were investigated in the single component theory. Further, the lower computational cost of the single component calculations allowed a comparison of the all-electron calculations and the frozen core approximation.

The B3LYP functional and the basis sets described above were chosen because of their widespread use. However, further improvement of these calculations may be possible by judicious choice of functional and basis set.[103]

All calculations were performed on the VAYU cluster at the Australian National Computing Infrastructure National Facility (NCI-NF). The cluster is comprised of Infiniband connected nodes of Sun X6275 blade servers each containing two quad-core 2.93 GHz Intel CPUs and 24 Gbytes of accessible memory.

3.4 Results and Discussion

3.4.1 Optimised Geometries

The optimised geometries of $Ir(ppy)_3$ and $Ir(ptz)_3$ are summarised in Table 3.2, and full structures can be found in Appendix B. The optimised geometry of $Ir(ppy)_3$ is in very good agreement to the optimised geometry reported by Hay,[85] who used a similar methodology to determine the geometry, and also good agreement to recent solid state and gas phase structural studies.[114] The optimised geometry of $Ir(ptz)_3$ is also a good match to the reported crystal structure.[19]

Table 3.2 Selected bond lengths (in Å) of the optimised molecular geometries of $Ir(ppy)_3$ and $Ir(ptz)_3$.

Bond	$Ir(ptz)_3$ this work	$Ir(ptz)_3$ x-ray diffraction[19]	$Ir(ppy)_3$ this work	$Ir(ppy)_3$ gas-phase electron diffraction[114]	$Ir(ppy)_3$ x-ray diffraction[114]
Ir-N	2.151	2.166	2.168	2.158	2.130
Ir-N	2.151	2.151	2.168	2.158	2.130
Ir-N	2.151	2.135	2.168	2.158	2.130
Ir-C	2.046	2.042	2.036	2.033	2.016
Ir-C	2.046	2.022	2.036	2.033	2.016
Ir-C	2.046	2.002	2.036	2.033	2.016

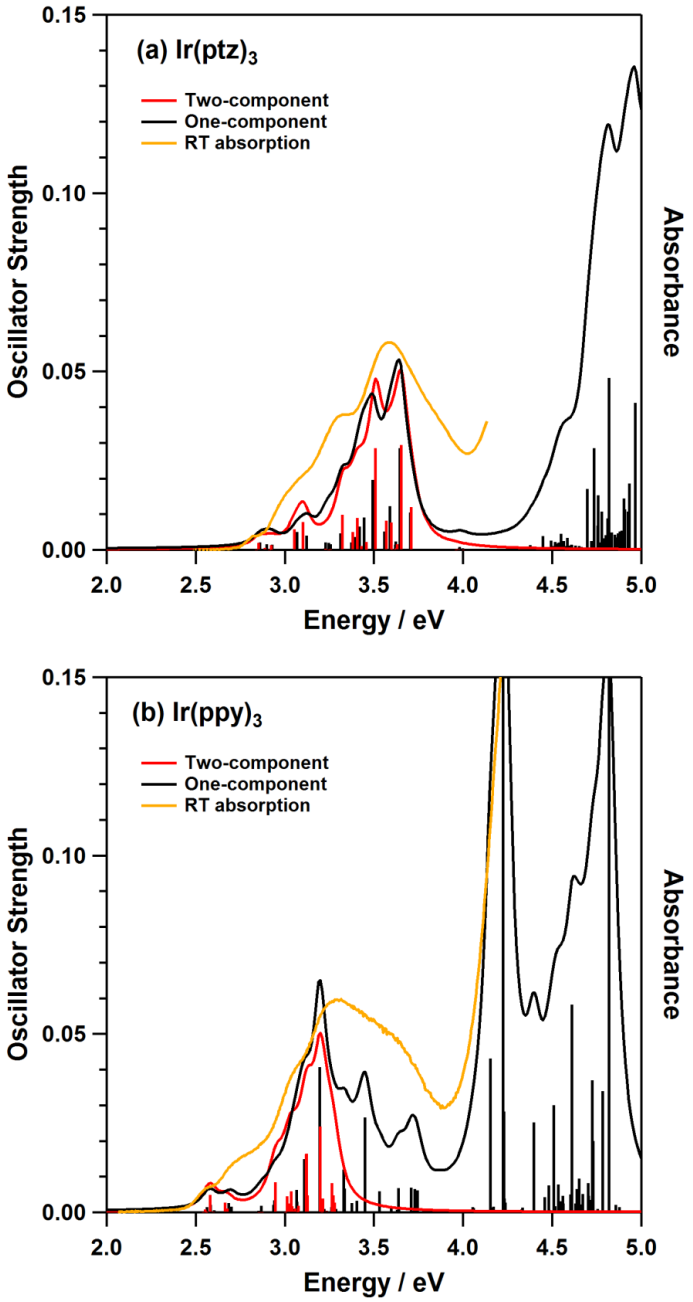

Figure 3.2 Comparison of the excitation spectra calculated from one- and two-component ZORA-TDDFT with the absorption spectra previously measured by Smith et al.[196] and Hofbeck and Yersin[84] of (a) $Ir(ptz)_3$ and (b) $Ir(ppy)_3$. Bars indicate transitions with the height indicating the calculated oscillator strengths. Curves represent the calculated excitation spectra broadened by Lorentzians of full width half maximum 0.1 eV; this is intended as a guide to the eye, rather than as a serious simulation of the broadening. Both calculations use the DZP basis with a frozen core electron approximation.

3.4.2 Two-Component Calculations

The 50 lowest energy electronic excitations of $Ir(ptz)_3$ and $Ir(ppy)_3$ were calculated with the self-consistent two-component ZORA method. The excitation energies and oscillator strengths of these transitions are tabulated in Appendix B and plotted in Figure 3.2. In order to facilitate comparison

with experiment the 'spectra' is shown where each transition is broadened by a Lorentzian of width 0.1 eV. This is not intended as a realistic estimate of the broadening, but rather as a guide to the eye. Indeed comparison with previously published experimental data, reproduced in Figure 3.2, shows that this somewhat underestimates the broadening at room temperature.

The low energy excitations in both complexes have previously been assigned as metal-to-ligand charge transfer (MLCT) bands. This nomenclature will be followed; however, a detailed discussion of the degree of MLCT will be given towards the end of this section. For $Ir(ptz)_3$ the calculated spectrum is in excellent agreement with the measured spectrum of the MLCT band. However, higher energy excitations are not included in the calculation and so are not reproduced. This results from the major limitation of the two-component methodology for complexes of this size, *viz.* the large computational cost, which will be discussed further below. Interestingly, the density of states is much higher in $Ir(ppy)_3$. This means that only the lowest energy part of the MLCT band is described by the 50 lowest energy excitations. Nevertheless, this part of the spectrum is reproduced quite accurately by the two-component theory.

3.4.3 One-Component Calculations

A wider range of the spectrum can be calculated using the one-component theory, with SOC included perturbatively. The lowest 200 excitations are calculated at this level of theory. In order to make a fair comparison of these calculations with the two-component theory the one-component calculations were performed in the same (DZP) basis set and with the same frozen core as used for the two-component calculations. The calculated excitation energies and oscillator strengths are tabulated in Appendix B and plotted in Figure 3.2. The calculated spectrum, broadened by Lorentzians with 0.1 eV full width half maxima is also plotted in Figure 3.2.

The lowest 50 excitations of both theories are in excellent agreement with one another. This is clearly evident for $Ir(ptz)_3$ where, since the MLCT band is completely described within 50 excitations, the energies, oscillator strengths and symmetry designations of the two-component results are almost perfectly replicated by the one-component perturbation calculation. In the case of $Ir(ppy)_3$ the comparison is a little more difficult because only part of the MLCT band is described by the lowest 50 excitations. From the one-component perturbation calculation 90 excitations were required to describe the MLCT band. Nonetheless there is still good agreement between the low energy excitations. Figure 3.3 shows a comparison of the lowest energy excitations in the two complexes, where the excellent agreement is particularly clear despite the small ranges on both axes.

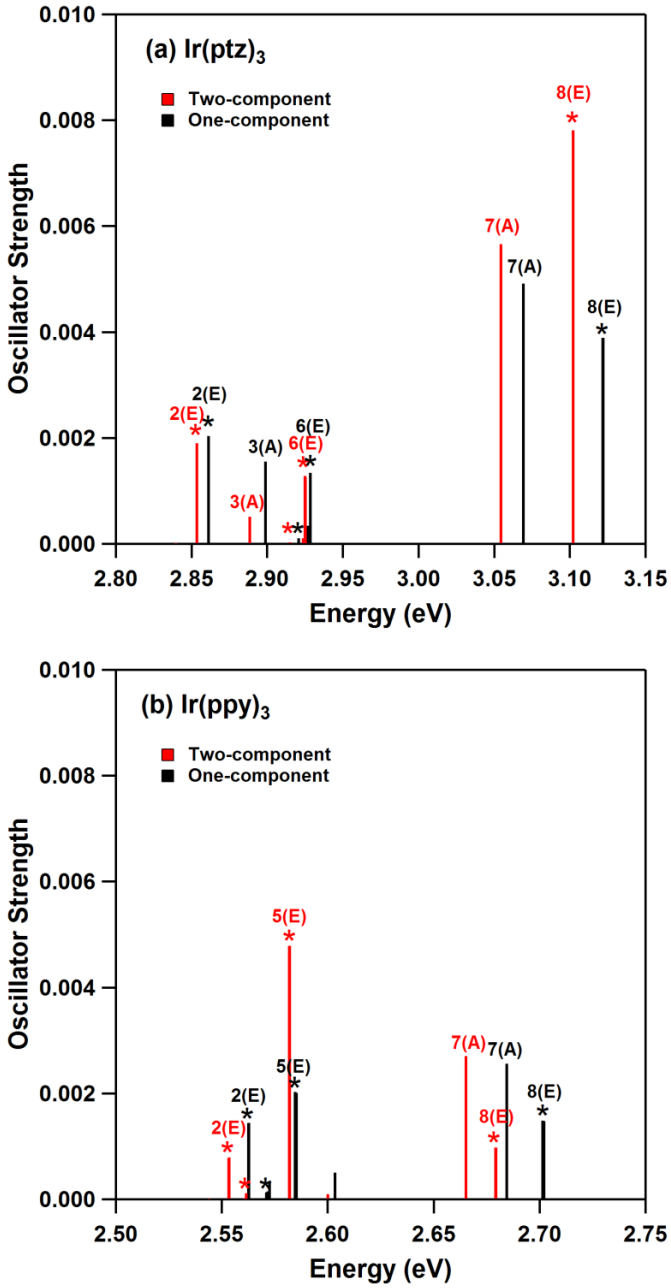

Figure 3.3 Excitations 1-8 calculated from one- and two-component methods with DZP and frozen core (note the different energy scales for the different complexes). Asterisks mark two-fold degenerate E states and states with significant oscillator strengths are labelled. Very good agreement between the two methods is found for both complexes. These low-lying excitations dominate the optical properties, and hence the technological applications, of these complexes. The excitation spectra of the two complexes are quite similar in this energy range. However, note that the 7A and 8E excitations have significantly more oscillator strength in $Ir(ptz)_3$ than the equivalent excitations in $Ir(ppy)_3$. These excitations are responsible for strong features in the MCD of $Ir(ptz)_3$ therefore it is predicted that the MCD signal in $Ir(ppy)_3$ will not show such pronounced features in MCD spectra.

The most significant deviations between the one- and two-component calculations is that the one-component calculation assigns a small oscillator strength to states that, in the two-component calculation, are essentially dark. Thus, on a casual inspection of Figure 3.2 there appears to be a

lower density of states in the two-component calculation. This is not the case, but is due to the presence of a large number of states with very little oscillator strength. For example, for $Ir(ptz)_3$ the transitions around 3.25 eV are almost completely forbidden in the two-component calculation, whereas in the one-component calculation they are given a small oscillator strength (*cf*. Figure 3.2). A closer examination of these states reveals that they are of predominately triplet character. This can be understood because SOC is only included via second order perturbation theory in the one-component theory. Pure triplet excitations are forbidden and therefore have zero oscillator strength. However, SOC mixes singlet and triplets states.[†] States with small oscillator strengths typically correspond to predominately triplet states with only small singlet admixtures. Thus, for weakly allowed transitions, extremely small changes in the *fraction* of singlet character will lead to large changes in the *relative* oscillator strength. Hence, one expects these oscillator strengths to show the largest discrepancy between the one- and two-component calculations, as observed numerically. In perturbation theory the singlet contribution to the wavefunctions of states that are triplet at zeroth order depends sensitively on $\left(E_i^{(0)} - E_j^{(0)}\right)^{-1}$, where $E_i^{(0)}$ is the energy of the triplet state at zeroth order and $E_j^{(0)}$ is the energy of singlet state at zeroth order.[40] Thus, any finite order of perturbation theory will have larger errors when states are nearly degenerate. Generically, one expects that such accidental near degeneracies will be most important in regions with high densities of states.[205] This is indeed borne out by the calculations reported above where these issues are slightly more prominent in the MLCT band of $Ir(ppy)_3$ than they are in the MLCT band of $Ir(ptz)_3$.

Nevertheless, it should be stressed that the issues above only appear for the transitions that are *least* important spectroscopically. Therefore, the one-component calculations do an excellent job of reproducing spectra predicted by the two-component calculations and hence the experimental absorption spectra. However, it is interesting and surprising that these problems *do not* lead to widespread or significant errors in the calculated spectrum of excitations.

In terms of computational cost, the one-component calculations are, unsurprisingly, significantly faster. On a single node of the Australian National Computational Infrastructure National Facility (NCI-NF) VAYU cluster the one-component calculation is an order of magnitude faster per self-consistent TDDFT iteration than the two-component calculation (~2 vs. ~16 hours/self-consistent field iteration). This is in spite of the fact that 200 excitations are calculated in the one-component theory, but only 50 excitations in the two-component calculations. Practical limitations, such as the available computational time available, prevent improvement on the DZP basis with a frozen core

[†]Formally, once SOC is included the energy eigenstates are required to be eigenstates of the total angular momentum, J=L+S, rather than of the spin, S, and orbital angular momentum, L, separately.

approximation for the two-component calculations on the current cluster. However, one-component all-electron calculations in a TZP basis, which will be discussed below, still have a significantly lower cost than two-component calculations presented above.

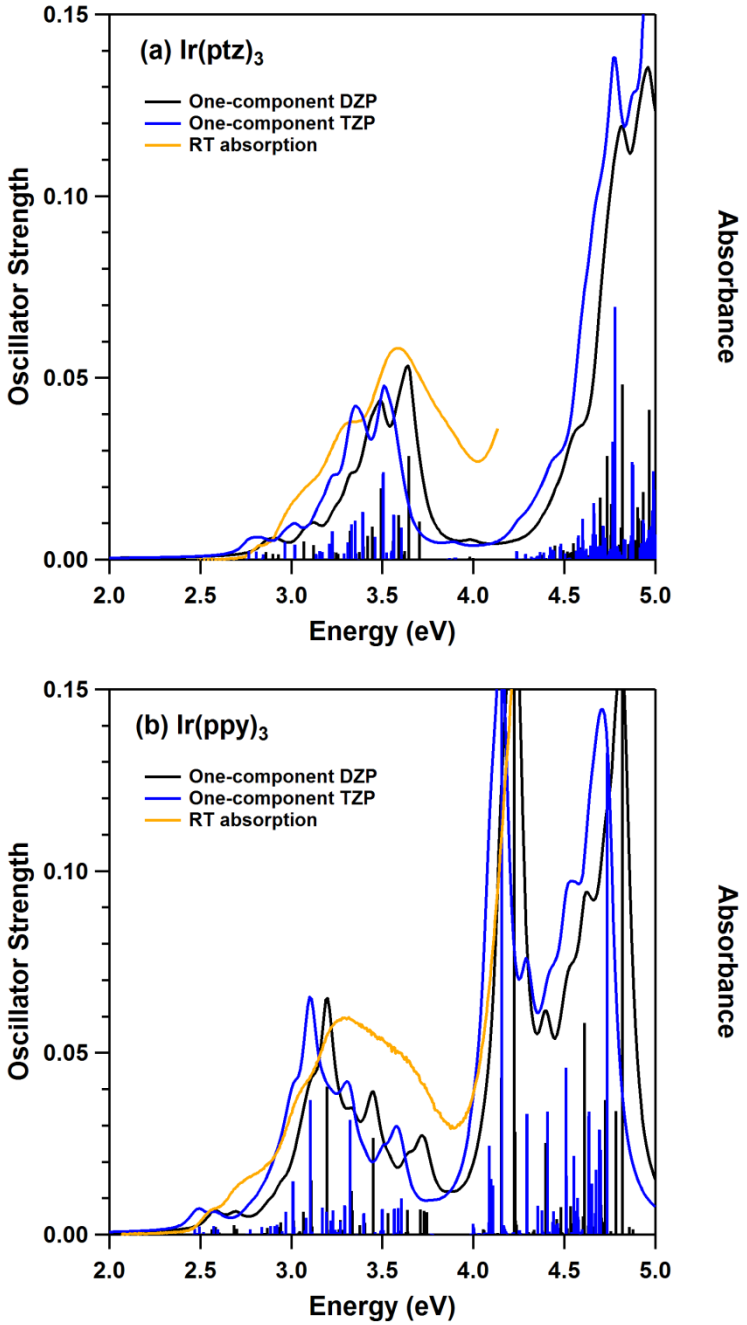

Figure 3.4 Comparison of one-component calculations in different basis sets. Both calculations were performed with the same frozen core. Curves represent the sum over all transitions broadened by Lorentzians with full width half maxima of 0.1 eV. The experimental spectra are from Smith *et al.*[196] and Hofbeck and Yersin.[84] Note that the changes are more significant than the differences from the two-component calculations (*cf.* Figure 3.2).

3.4.3.1 Basis Sets and Cores

Here the effects of increasing the quality of the basis set and the differences between frozen core and all-electron calculations are compared. This is limited to the one-component calculations because of the computational expense associated with the two-component formalism. It is interesting to note that the changes from increasing the size of the basis sets are more significant than the differences between the one- and two-component theories. This suggests that, given the current limitations on computer power, all-electron one-component calculations performed in a high quality basis set will give more reliable answers than frozen core two-component calculations in a small basis set for iridium(III) complexes.

In Figure 3.4 the frozen core, single component calculations in the DZP basis, are compared with calculations that are identical except for the use of a TZP basis (the energies and oscillator strengths of these excitations are tabulated in Appendix B, Tables B5-8). The reorganisation of the spectrum is not insignificant. Most notably, the additional degrees of freedom provided by the TZP basis allow many of the excitations to relax to lower energies. There is also some redistribution of spectral weight between the excitations. These changes are significantly larger and more important than the differences between the one- and two-component calculations described above.

In Figure 3.5 two single component calculations in the TZP basis are compared, one with a frozen core and the other including all electrons fully (the energies and oscillator strengths of these excitations are tabulated below in Appendix B, Tables B7-10). The changes in excitation energies are very small in both $Ir(ppy)_3$ and $Ir(ptz)_3$, however the changes in oscillator strength are somewhat more significant.

3.4.4 Analysis of Spin Mixing, Metal-to-Ligand Charge Transfer, Degeneracy, Radiative Lifetime and Magnetic Circular Dichroism

Now that the reliability of the one component ZORA with spin-orbit coupling included perturbatively has been established, both in relation to the higher level two-component formalism and in reproducing previously measured spectra, issues of real chemical and technological interest will be discussed. The one-component calculations lend themselves naturally to analyses that allow one to extract important information for understanding the nature of the low-lying excitations in these complexes. In the following section an analysis for the all-electron calculations in a TZP basis is presented.

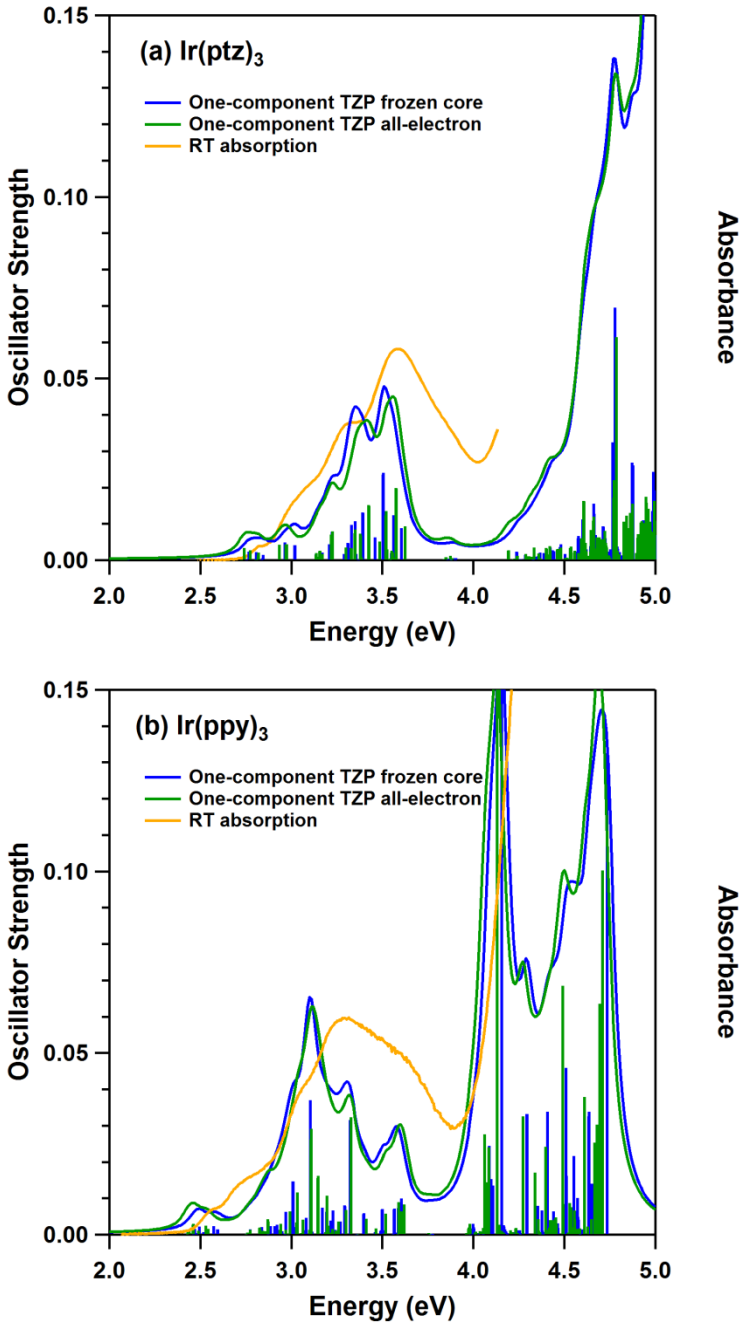

Figure 3.5 Comparison of frozen core and all electron one-component calculations. Both calculations were performed in the same TZP basis set. Curves represent the sum over all transitions broadened by Lorentzians with full width half maxima of 0.1 eV. The experimental data are from Smith *et al.*[196] and Hofbeck and Yersin.[84]

The degree of singlet character for the calculated excitations in both complexes is reported in Figure 3.6 and Appendix B. As one might expect, there is a strong correlation between the strength of the transition and degree of singlet character. In $Ir(ptz)_3$ there are very few transitions in the MLCT band with more than 50% singlet character, but there are several transitions with a very large singlet weight in $Ir(ppy)_3$. This is clearly correlated with the much larger oscillator strengths predicted in $Ir(ppy)_3$, particularly for these predominately singlet transitions. An interesting question for future

work will be to understand how these differences relate to the very different colours of the two complexes, and how it affects each of the energy transfer processes that occur on photo- or electrical excitation.

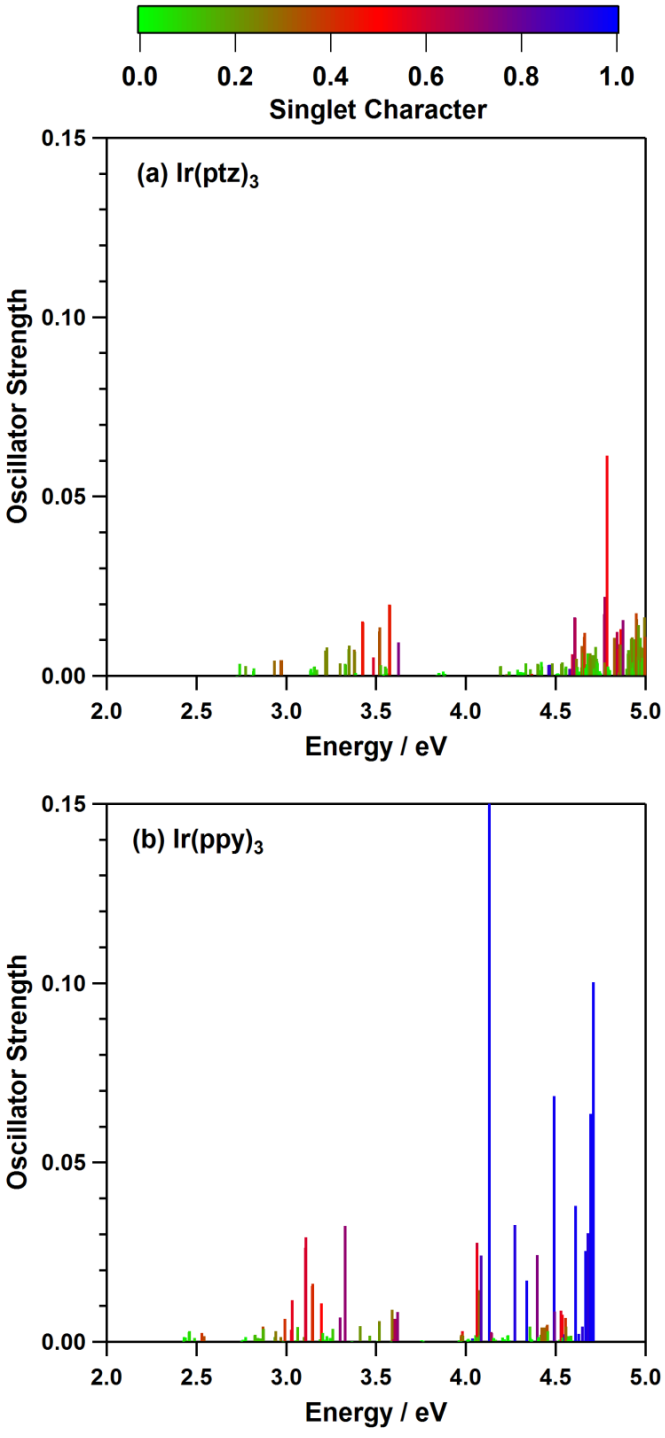

Figure 3.6 Singlet character of the low lying excitations in (a) $Ir(ptz)_3$ and (b) $Ir(ppy)_3$. Both sets of data are from all-electron, one component ZORA-TDDFT calculations in a TZP basis set. There is a clear correspondence between the oscillator strengths and the degree of singlet character, as one would expect. In particular the several states that are nearly pure singlets give rise to the stronger oscillator strengths observed in $Ir(ppy)_3$, while such transitions are absent in $Ir(ptz)_3$.

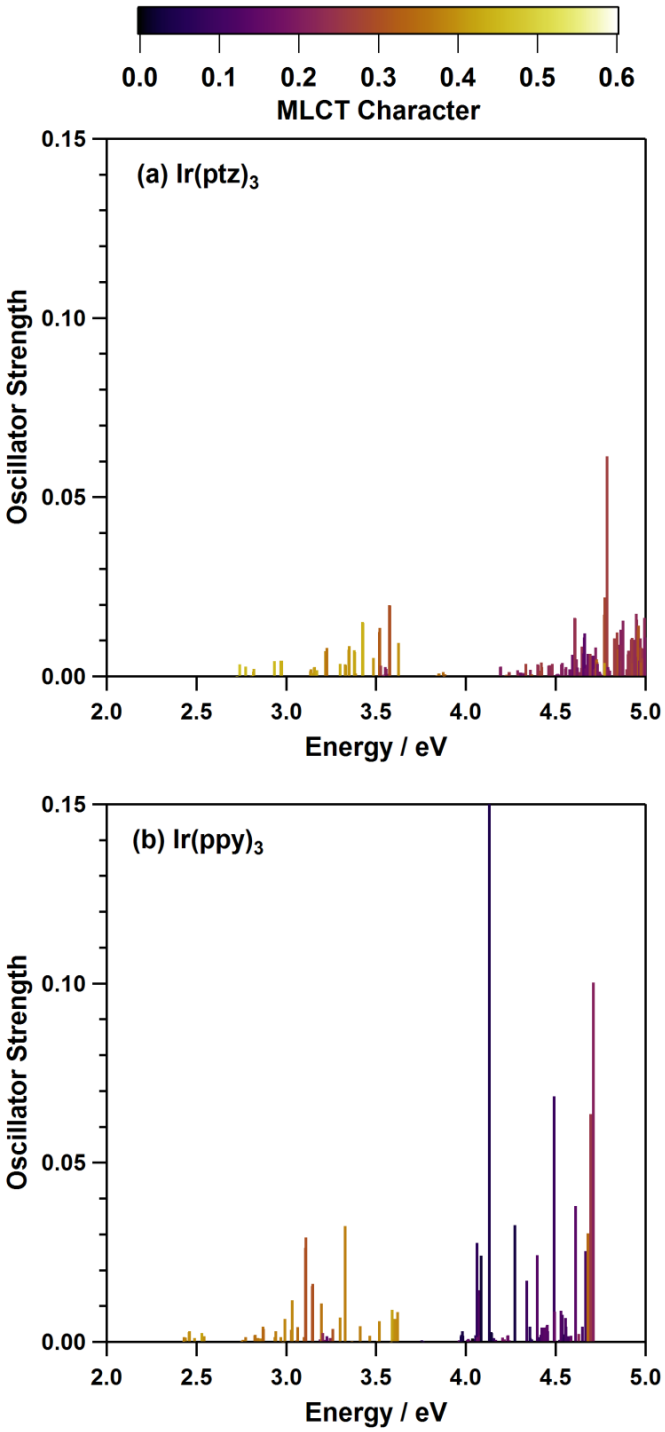

Figure 3.7 Metal-to-ligand charge transfer character of the low lying excitations in (a) $Ir(ptz)_3$ and (b) $Ir(ppy)_3$. Both sets of data are from all-electron, one-component ZORA-TDDFT calculations in a TZP basis set. In neither complex does one observe states with more than ~50% MLCT character. However, given this restriction the characterisation of the lowest bands in both complexes as 'MLCT' bands is largely borne out by the observation that these bands do have substantially more MLCT character than the higher lying excited states.

An important question, which has strongly influenced design strategies for iridium(III) complexes is the degree of MLCT in the low lying excited states. To investigate this question a Mulliken population analysis was performed and MLCT character for the low-energy excitations was

calculated, details of which are given in Appendix B. In Figure 3.7 and Appendix B the MLCT character of the low-lying excitations of both complexes are reported. It should be noted that even in the lowest lying band, which is usually assigned as the 'MLCT band', none of the excitations have more than ~50% MLCT character. This can be understood by relating the TDDFT excitations to the Kohn-Sham orbitals in the single component ZORA (time independent) DFT calculation underlying the TDDFT. Details of the Kohn-Sham molecular orbitals, including a Mulliken population analysis of the contribution from the iridium 5*d* orbital to each MO is given in Appendix B. Both complexes have similar structures in their frontier orbitals, shown in Figure 3.8 and Figure 3.9. Recall that both complexes are C_3 symmetric; and under the assumption of time reversal symmetry C_3 has a one-dimensional irreducible representation (A) and a two-dimensional irreducible representation (E). In both complexes the HOMO and LUMO are non-degenerate (A) and the HOMO-1 and LUMO+1 are two-fold degenerate (E). Further, in both complexes the HOMO is rather similar to the HOMO-1 and the LUMO is similar to the LUMO+1. In particular the HOMO and HOMO-1 have a significant (~50%) contribution weight on the iridium atom, whereas the LUMO and LUMO+1 do not.

Both complexes have approximate O_h symmetries. If they were truly O_h symmetric the frontier orbitals would have t_{2g} symmetry and form a three-fold degenerate manifold. The true C_3 symmetry splits the t_{2g} manifold into the, observed, A and E motif. Nevertheless the approximate O_h symmetry is still manifest in the similarities between the HOMO and the HOMO-1 and the similarities between the LUMO and the LUMO+1.

If one writes the scalar TDDFT excitations in terms of transitions between the Kohn-Sham orbitals (see Appendix B) one finds that the low-energy excitations are dominated by transitions between the frontier orbitals (Table 3.3). For $Ir(ppy)_3$ S_1 is dominated (97%) by the HOMO→LUMO transition and (the two-fold degenerate) S_2 is predominately (97%) a HOMO→LUMO+1 transition. The situation is slightly more complicated for the triplets, but T_1 is still 70% HOMO→LUMO (and 19% HOMO-1→LUMO+1) and (the two-fold degenerate) T_2 has 63% HOMO→LUMO+1 (plus 14% HOMO-1→LUMO and 11% HOMO-1→LUMO+1) character. The picture for $Ir(ptz)_3$ is eerily similar: S_1 is 98% HOMO→LUMO; S_2 is 98% HOMO→LUMO+1; T_1 has 69% HOMO→LUMO character and 21% HOMO-1→LUMO+1 character; and T_2 has 48% HOMO→LUMO+1 character, 25% HOMO-1→LUMO and 5% HOMO-1→LUMO+1 (see Tables B11 and B12 in Appendix B for details of other excitations).

Table 3.3 Make up of selected excitations in terms of transitions between Kohn-Sham orbital transitions. Details for all studied excitations are given in Appendix B (Tables B11 and B12).

Excitation	$Ir(ptz)_3$	$Ir(ppy)_3$
$S_1(A)$	HOMO→LUMO (98 %)	HOMO→LUMO (97 %)
$S_2(E)$	HOMO→LUMO+1 (98 %)	HOMO→LUMO+1 (97 %)
$T_1(A)$	HOMO→LUMO (69 %) HOMO-1→LUMO+1 (21 %)	HOMO→LUMO (70 %) HOMO-1→LUMO+1 (19 %)
$T_2(E)$	HOMO→LUMO+1 (48 %) HOMO-1→LUMO (25 %) HOMO-1→LUMO+1 (5 %)	HOMO→LUMO+1 (63 %) HOMO-1→LUMO (14 %) HOMO-1→LUMO+1 (11 %)

Thus the approximately 50% limit on the MLCT character in the 'MLCT band' observed in both complexes arises from transitions from the HOMO, HOMO-1 to the LUMO, LUMO+1. The high lying occupied Kohn-Sham orbitals below the HOMO-1 have smaller contributions from the iridium 5*d* orbitals. The low-lying unoccupied Kohn-Sham orbitals above the LUMO+1 also have negligible contributions from the iridium 5*d* orbitals. Thus, no excitations can have more than ~50% MLCT character.

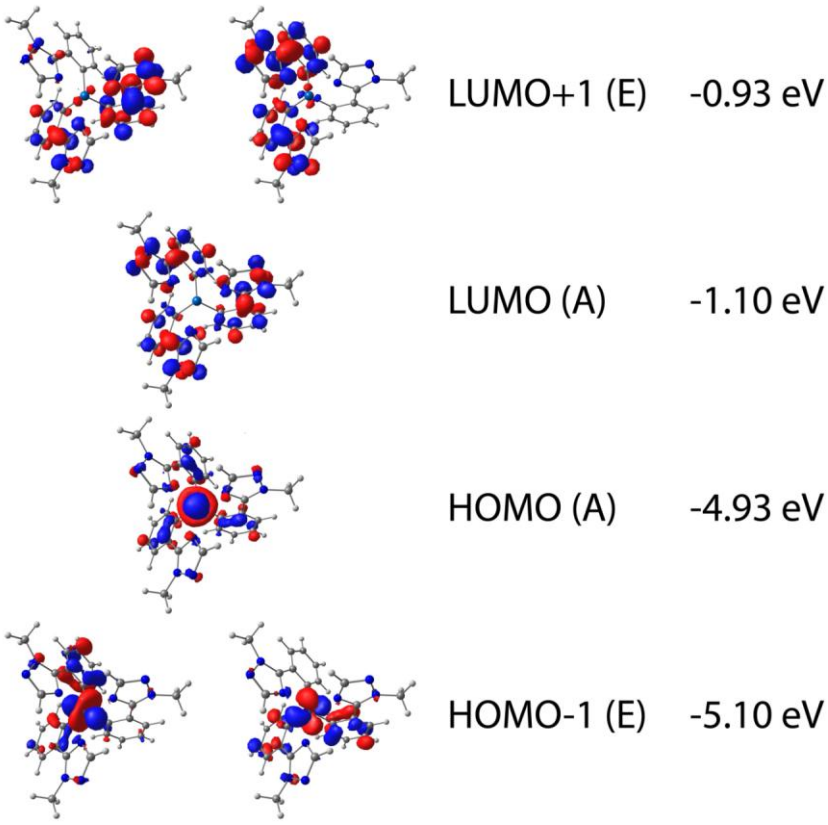

Figure 3.8 Frontier Kohn-Sham molecular orbitals and their energies in $Ir(ptz)_3$ and the corresponding molecular orbital energies. Calculated from all-electron ZORA-DFT in the TZP basis set.

The low energy excitations of these complexes can be further understood by examining how the scalar relativistic TDDFT results, obtained prior to the perturbation due to SOC, hybridise to give

the excitations found in the SOC perturbation theory (Tables B9 and B10 in Appendix B report the largest contributions to each of the excitations in the SOC). In both complexes T_1 is a non-degenerate state (A symmetry) and T_2 is two-fold degenerate (E). SOC coupling induces a zero-field splitting in these states. In both complexes T_1 is split into a non-degenerate state, labelled 1A, and a two-fold level, 2E, at slightly higher energy. It is interesting to note that in both complexes 1A has a very small oscillator strength. This has previously been found experimentally.[84,196] However, the zero-field splitting of T_2 shows some subtle differences between the two complexes. In $Ir(ptz)_3$ the T_2 manifold has symmetry A, E, A, E (in order of increasing excitation energy) whereas in $Ir(ppy)_3$ the same triplet manifold has symmetry E, A, E, A. Thus the zero-field splitting has different signs in the two T_2 manifolds.

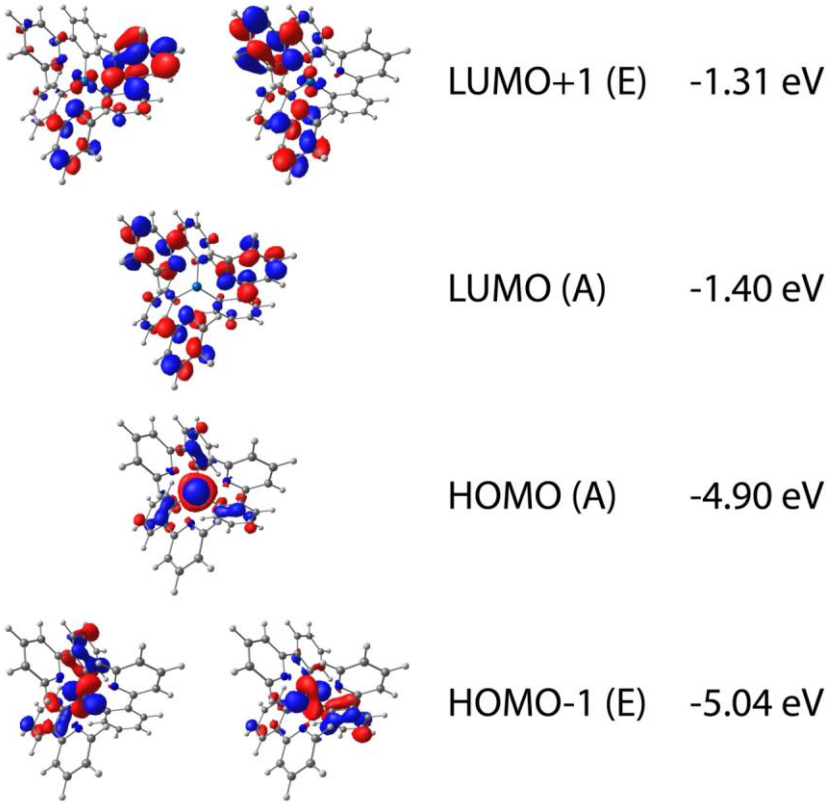

Figure 3.9 Frontier Kohn-Sham molecular orbitals and their energies in $Ir(ppy)_3$ and the corresponding molecular orbital energies. Calculated from all-electron ZORA-DFT in the TZP basis set.

This redistribution of the states has some important experimental consequences. In Figure 3.10 the radiative lifetimes for both complexes are plotted at different levels of theory, assuming that excitations are populated according to the Boltzmann distribution, i.e.,

$$\frac{1}{\tau_R(T)} = \frac{\sum_i \left(\frac{e^{-E_i/k_B T}}{\tau_R^{(i)}} \right)}{\sum_i e^{-E_i/k_B T}} \qquad \textbf{3.5}$$

where $\tau_R(T)$ is the radiative lifetime of the complex at temperature T, $\tau_R^{(i)}$ is the radiative lifetime of the i^{th} excited state, and E_i is the energy of the i^{th} excitation. It is important to note that the E excitations appear twice in the sums in Equation 3.5, once for each of the degenerate states. The radiative lifetime (and hence the radiative rate) for each excitation is calculated from the Strickler-Berg relation.[206,207]

A number of interesting effects can be observed from Figure 3.10. The calculation that includes spin-orbit coupling is most directly relevant to experiment. A dramatic variation in τ_R in both complexes is observed. This can be understood as follows. At low temperatures only the lowest state (1A) is occupied, and as noted above, this state has a very long radiative lifetime. Hence, so does the complex. As the temperature is raised, higher lying excitations are (thermally) populated. These excitations have lower radiative lifetimes and therefore as the temperature is raised the total radiative lifetime of the complex decreases. At room temperature six excitations (three A and three E) have a significant thermal population. These states arise from the zero-field split T_1(A) and T_2(E) states, which are basically t_{2g} states. Hofbeck and Yersin[84] have observed a similar temperature dependence in the *total* lifetime of $Ir(ppy)_3$ experimentally. Herzberg-Teller coupling is an important complication that is *not* included in our calculation. Given the long radiative lifetime of the lowest energy excitation it may be expected that the Herzberg-Teller effect will somewhat decrease the radiative lifetime of this excitation. Therefore, although it might be expected that the overall trend predicted in this calculation is correct, the prediction for the radiative lifetime at low temperatures may not be quantitatively accurate. Indeed the radiative lifetime can be strongly dependent on small changes in the perturbation calculation (see Figure 3.11).

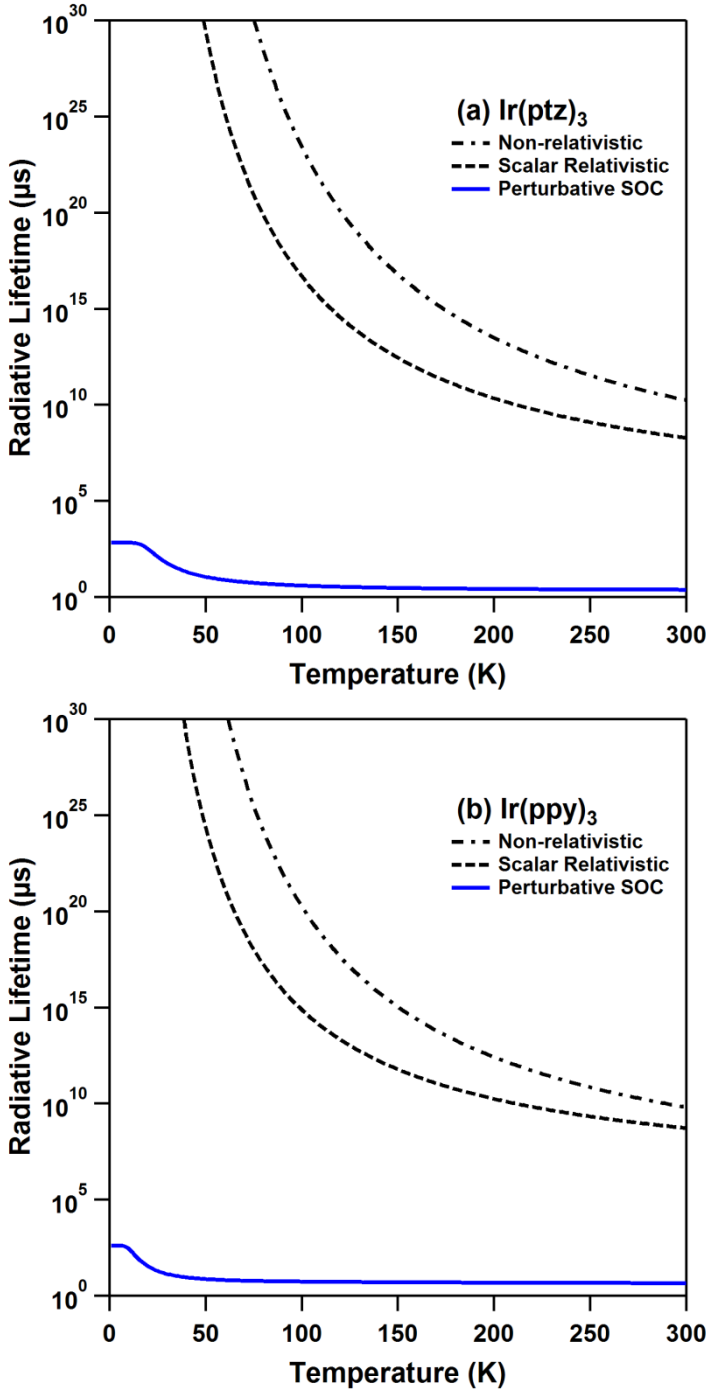

Figure 3.10 The radiative lifetime of (a) $Ir(ptz)_3$ and (b) $Ir(ppy)_3$ predicted at various levels of theory in an all-electron TZP basis. The predictions are remarkably similar for both complexes. The calculation including spin-orbit coupling (SOC) perturbatively is directly relevant to experiment and predicts that the radiative lifetime is strongly temperature dependent. This is similar to what is observed experimentally for the total lifetime.[84] However, the differences between the scalar relativistic and non-relativistic calculations also provide important insights to the relativistic effects in these complexes. In particular the difference of several orders of magnitude between these complexes is due to the indirect relativistic stabilisation of metal-to-ligand charge transfer states.

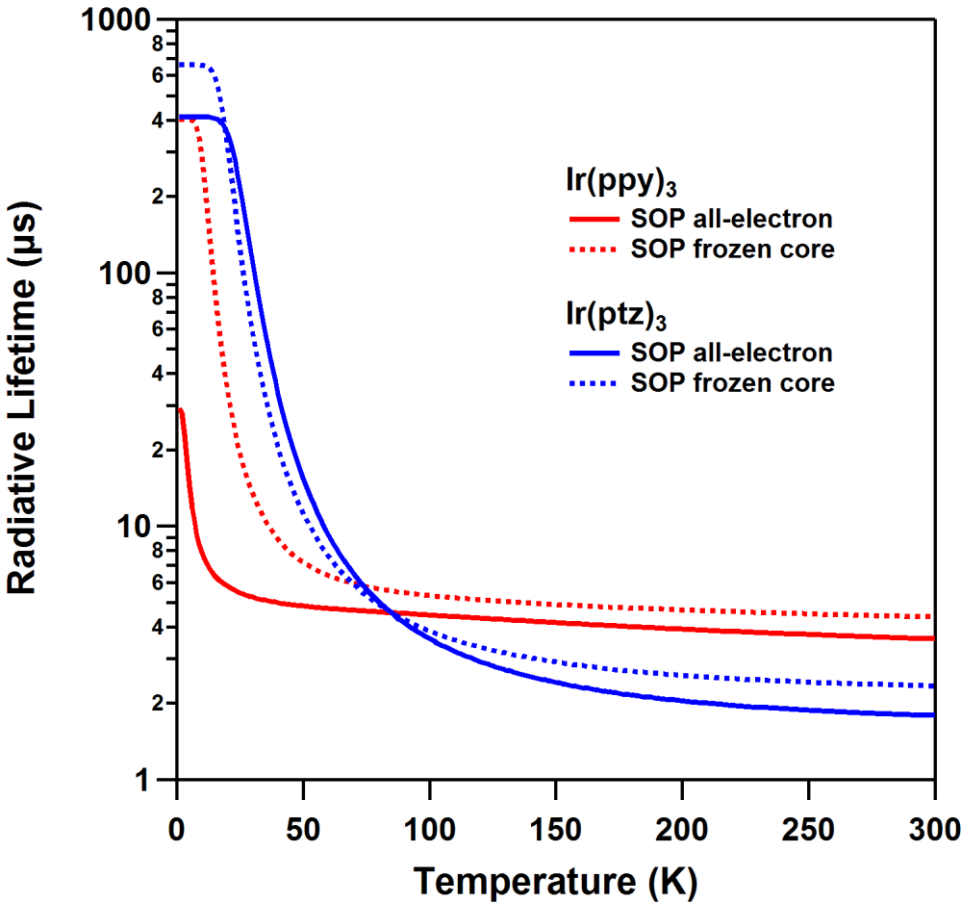

Figure 3.11 Comparison between the radiative lifetimes calculated with either the frozen core approximation or an all-electron basis, using TZP basis in the one-component spin-orbit perturbation TDDFT. The instability of the perturbation calculation is clear in the $Ir(ppy)_3$ calculations. This arises for two reasons. Firstly the lowest excitation 1A has a much stronger oscillator strength in the all-electron calculation (1.3×10^{-4}) than in the frozen core calculation (9.5×10^{-6}). Secondly, in the all-electron calculation the difference in energy between the 1A and the 2E excitations is a tiny 0.9 meV, whereas in the frozen core calculation the energy difference is much larger, 5.6 meV.

Some further insights can be gained from looking at the radiative rates at different levels of calculation. Unsurprisingly the scalar relativistic and non-relativistic calculations predict that the complexes have very much longer radiative lifetimes than the above calculation. This is a result of the neglect of spin-orbit coupling in the scalar relativistic and non-relativistic calculations. In the absence of spin-orbit coupling phosphorescence is strictly forbidden and all radiative decay results from singlet states. As these are at significantly higher energies than the triplets the radiative lifetime of the complex is exponentially enhanced (cf. Equation 3.5). What is more interesting is that the radiative lifetime is predicted to be several orders of magnitude smaller by the scalar relativistic calculation than by the non-relativistic calculation. Remarkably, this has a simple explanation in terms of atomic physics and important consequences for the high PLQYs observed in these two complexes at room temperature. It has long been understood that there are two important

scalar relativistic effects in atomic physics: the "direct effect" – the relativistic mass enhancement of the electron reduces the Bohr radius and means that electrons are more tightly bound to the nucleus – and the "indirect effect" whereby electrons far from the nucleus are more effectively screened because of the direct effect on the electrons closer to the nucleus – this means that electrons are more weakly bound.[188,189] The direct effect dominates for *s* electrons, the two effects roughly cancel for *p* electrons, but the indirect effect dominates for *d* electrons. The two lowest energy singlet states, S_1 and S_2, have ~50% MLCT character in both complexes, as discussed above. Therefore the indirect relativistic effect lowers the energies of S_1 and S_2 because it destabilises the iridium 5*d* orbital, so less energy is required to cause an MLCT transition. This effect is important because the closer the singlet is in energy to a triplet the more strongly spin-orbit coupling can hybridise the two states.[205] Thus the indirect relativistic effect increases the phosphorescent decay rate and hence increases the PLQY of these complexes.

Low temperature, high field magnetic circular dichroism (MCD) experiments have been reported for $Ir(ptz)_3$ (Chapter 2).[196] These show an interesting structure that can be understood on the basis of the type of calculations reported here. Briefly, one observes an MCD A-term at low energies arising from the manifold of triplet states around 2.8 eV, which can be traced back through T_1 and T_2 to HOMO→LUMO, HOMO→LUMO+1 and HOMO-1→LUMO transitions. There is then a B-term arising from excitation 7A and a second A-term arising from excitation 8E. Although the natures of these excitations can also be traced back to the MOs, this yields less insight as these higher energy excitations are complex combinations of many molecular orbital transitions, the largest contributions come from the T_3 and S_1 (7A) and S_2 (8E) excitations. Neither the non-relativistic nor the scalar relativistic calculation predict any excitations at energies comparable to those of 7A and 8E, consistent with the finding that these excitations are of highly mixed character due to the SOC. Thus, neither the non-relativistic nor the scalar relativistic calculations accurately predict the MCD data for $Ir(ptz)_3$.[196]

Excitations 7A and 8E, which give rise to the exceptional MCD signal observed in $Ir(ptz)_3$, have significantly lower oscillator strength in $Ir(ppy)_3$ and are closer spaced in energy. These relativistic calculations therefore lead to the prediction that the MCD signal from $Ir(ppy)_3$ will be greatly reduced compared to that of $Ir(ptz)_3$. The only reported MCD experiments on $Ir(ppy)_3$ were carried out on a thin film of $Ir(ppy)_3$ at 15 K under an applied field of 0.84 T.[208] Low temperature, high field solution MCD measurements for $Ir(ppy)_3$ would therefore be an interesting test of these predictions. However, the poor solubility of $Ir(ppy)_3$ makes performing these measurements difficult.

3.4.5 Correlation and Solvent Effects

It is worthwhile to ask how reasonable the excellent agreement with experiment found above is. In particular electronic correlations have only been included at the B3LYP level and solvent effects have been entirely neglected. Transition metals are well known to lead to strong electronic correlations, so the success of B3LYP, particularly of excited state energies is surprising. Further, solvent and solid state environments are known to have significant effects on the optoelectronic properties of organic electronic materials.[209] It has recently been shown that for a simple (and exactly soluble) model of organometallic complexes, such as those discussed in this paper, the configuration interaction singles (CIS) approximation gives accurate results.[205] The CIS approximation is closely related to TDDFT, particularly when the time-dependent Kohn-Sham equations are solved by a linear response approximation (the Tamm-Dankoff approximation to the Hartree-Fock equations is precisely equivalent to CIS[210]). This accuracy arises because the low-lying excitations in the simple model are predominately singles (or a linear superposition of singles) and therefore relatively weakly correlated. As one expects TDDFT to outperform CIS for this problem this suggests that TDDFT will be reliable, consistent with the excellent agreement found between these calculations and experiment. The TDDFT results above show that the excitations are predominately singles or mixtures of singles – which is consistent with the above argument. Therefore it appears that correlations are correctly described even at the B3LYP level of theory.

The absence of a significant solvatochromic effect is more difficult to understand,[209] but does seem broadly consistent with what is observed experimentally in these complexes.[84] In materials such as these iridium complexes which exhibit weak MLCT transitions, changing the dipole strength of the surrounding environment does not greatly perturb the system.[74] In cases where strong MLCT transitions occur (e.g. the ruthenium dye N3) significant solvatochromism is observed.[50,211,212] Nevertheless, explicit calculation of the solvent effects would be an interesting subject to pursue in the future. There are a number of mature methods by which this could be undertaken.[213,214] This could provide useful insights beyond those of De Angelis *et al.*[195]

3.5 Conclusions

Here it has been shown it is possible to trace the genealogy of the excited states of $Ir(ppy)_3$ and $Ir(tpz)_3$ back to atomic physics by considering a series of calculations at different levels of theory. Firstly, it was shown that one-component ZORA calculations, with spin-orbit coupling included perturbatively, accurately reproduce the results of two-component calculations. As well as being significantly lower cost, the one-component calculations allow one to systematically "turn off" relativistic effects and thus to understand them better. This showed that both scalar relativistic and

spin-orbit effects lead to important consequences for the photophysics of these complexes. In particular, there is an indirect relativistic stabilisation of the MLCT states. This means that indirect relativistic effects increase the degree to which SOC can hybridise singlet and triplet states[205] and hence plays an important role in determining the optical properties of these complexes. The low energy spectra of these two complexes share very similar structures and can be qualitatively understood in the same terms. Nevertheless there are important differences between these two complexes beyond their colour, which should be particularly apparent in MCD experiments.

Chapter 4. Effects of Fluorination on Iridium(III) Complex Phosphorescence

Published in Inorganic Chemistry, 2012, 51, 2821

4.1 Abstract

A combination of low temperature, high field magnetic circular dichroism, absorption and emission spectroscopy with relativistic time-dependent density functional calculations are used to reveal a subtle interplay between the effects of chemical substitution and spin-orbit coupling in a family of iridium(III) complexes. Fluorination at the *ortho* and *para* positions of the phenyl group of *fac*-tris(1-methyl-5-phenyl-3-*n*-propyl-[1,2,4]triazolyl)iridium(III) cause changes that are independent of whether the other position is fluorinated or protonated. This is demonstrated by a simple linear relationship found for a range of measured and calculated properties of these complexes. Further, it is shown that the phosphorescent radiative rate, k_r, is determined by the degree to which spin-orbit coupling is able to hybridise T_1 to S_3 and that k_r is proportional to the inverse fourth power of the energy gap between these excitations. Fluorination in the *para* position leads to a much larger increase of the energy gap than fluorination at the *ortho* position. Theory is used to trace this back to the fact that fluorination at the *para* position increases the difference in electron density between the phenyl and triazolyl groups, which distorts the complex further from octahedral symmetry, and increases the energy separation between the highest occupied molecular orbital (HOMO) and the HOMO-1 orbital. This provides a new design criterion for phosphorescent iridium(III) complexes for organic optoelectronic applications. In contrast, the non-radiative rate is greatly enhanced by fluorination at the *ortho* position. This may be connected to a significant redistribution of spectral weight. It is revealed that the lowest energy excitation, 1A, has almost no oscillator strength, therefore the second lowest excitation, 2E, is the dominant emissive state at room temperature. Nevertheless the apparent mirror image between absorption and emission is obeyed, as 2E is responsible for both absorption and emission at all but very low (<10 K) temperatures.

4.2 Introduction

Organic light emitting diodes (OLEDs) based on phosphorescent emitters can efficiently harvest both singlet and triplet excitons.[4,21,53] From a device point of view this is advantageous, since the internal quantum efficiency can approach 100%,[41] making phosphorescent materials prime candidates for full-colour displays[4,54] and solid-state lighting.[9,10,26]

To date, the best phosphorescent materials for OLEDs are based on iridium(III) complexes.[19,53,70,215] Ligand modification has been used to tune the emission colour,[51] but it is not possible to predict the photoluminescence quantum yields (PLQYs) of the resultant metal complexes.[19,99] The subtle effect played by spin-orbit coupling (SOC) in enabling phosphorescence, has been inadequately studied in

this respect, which makes it difficult to understand the relationship between ligand substitution and the radiative rate of phosphorescence.

For display and lighting applications, the development of highly efficient deep blue OLEDs remains an outstanding problem.[4] Here the focus is on *fac*-tris(1-methyl-5-phenyl-3-*n*-propyl-[1,2,4]triazolyl)iridium(III) [Ir(ptz)$_3$; **1**; Figure 4.1], which displays light sky blue phosphorescence with a high PLQY of 66%.[19] Fluorination at the X and/or Y positions (*ortho* and *para* to the triazolyl ring) successfully drives the phosphorescence to a deeper blue (shorter λ), however this also results in a dramatic drop in the PLQY (see Table 4.1).[19]

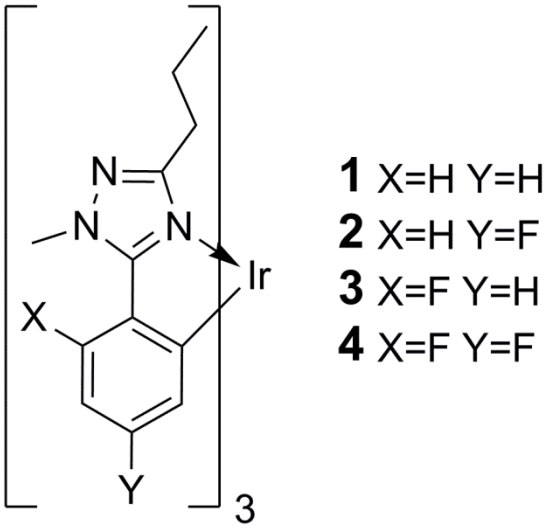

Figure 4.1 The structures of complexes 1-4 investigated in this study based on the parent *fac*-tris(1-methyl-5-phenyl-3-*n*-propyl-[1,2,4]triazolyl)iridium(III). Fluorination on the ligand phenyl ring blue shifts the emission, but results in a decrease in the PLQY.[19]

Both the absolute values and the trend in the calculated radiative rates are similar to those determined experimentally. Like the experimental data[19] complexes 1 and 3 have higher calculated radiative rates than 2 and 4. Errors have not been reported for complex 3. Nevertheless it is important to note that the radiative rates of complexes 2 and 4 are the same within experimental error and if there is a difference between the radiative rates of complexes 1 and 3 it has not yet been seen in these experiments. The calculated ZFS of the lowest triplet T_1(A) is also given.

Understanding the changes in PLQY caused by ligand substitution in complexes **1-4** is a daunting task. In particular it is important to note that there are two competing contributions to the PLQY: radiative decay and non-radiative decay. Here particular attention will be paid to understanding the differences in the radiative decay of these four iridium(III) complexes. It will be demonstrated that

these can be understood in terms of the interplay between spin-orbit coupling and the changes in electronic structure caused by chemical substitutions.

Table 4.1 Selected room temperature spectroscopic properties of iridium(III) complexes 1-4. Fluorine substitution shifts the emission from sky to deep blue [as evidenced by the Commission Internationale de l'Eclairage (CIE) coordinates], however the PLQY (Φ_{PL}) falls off precipitously.

	Experimental					Calculated	
Complex	**CIE (x, y)**	**Φ_{PL}**	**τ (μs)**	**k_r ($\times 10^5$ s^{-1})**	**k_{nr} ($\times 10^5$ s^{-1})**	**k_r ($\times 10^5$ s^{-1})**	**ZFS T_1(A) $\Delta E_{1A\text{-}2E}$ (meV)**
1	0.158, 0.202	0.66±0.07	1.08±0.03	6.1±0.8	3.2±1.0	4.3	11.6
2	0.157, 0.127	0.27±0.05	1.25±0.30	2.2±0.9	5.8±2.8	3.8	8.7
3	0.155, 0.161	0.06	0.15	4.0	63	4.4	11.3
4	0.159, 0.117	0.03±0.01	0.15±0.07	2.0±1.6	65±33	3.7	7.3

There have been few reported attempts to understand the role of SOC in phosphorescent iridium(III) complexes and in particular to blue emissive materials. Previous work has focused on the green phosphorescent complex *fac*-tris(2-phenylpyridyl)iridium(III), [Ir(ppy)$_3$]. Hofbeck and Yersin[84] identified three close lying excited states from low temperature spectroscopic measurements as the zero field split sublevels of the lowest triplet excitation, T_1. Ir(ppy)$_3$ has C_3 symmetry, and one expects SOC to split a non-orbitally-degenerate triplet state into a non-degenerate (A) state and a two-fold degenerate (E), with the A state having slightly lower energy.[216] It is therefore interesting that Hofbeck and Yersin found three distinct states – none of which were split by a magnetic field, suggesting that they are all non-degenerate. Thus, Hofbeck and Yersin argued that the C_3 symmetry is lifted by solvent effects. Interestingly, a number of *in vacuo* density functional calculations[13,113] suggest that the symmetry of the iridium(III) complex is lower in the T_1 state than in the ground state, S_0. Since the symmetry lowering can occur in equivalent ways due to the 3-fold symmetry of the S_0 state, this results in the existence of equivalent minima on the T_1 potential energy surface.

The three level substructure of the emitting "triplet" manifold has similarities to the related d^6 systems Ru(bpy)$_3^{2+}$ and Os(bpy)$_3^{2+}$.[45,217,218] The existence of three non-degenerate states implies lower than the ground state D_3 symmetry in these cases. With isotropic substitution in suitable host lattices, the direct study of these origins using high resolution spectroscopy, it is possible to show that the excited emitting states correspond to a localisation of the MLCT state onto one ligand.[219] The driving force for this low symmetry distortion (vibronic coupling) and the interaction with the environment is beyond the scope of this work. A major difference between the Ru and Os systems and the iridium(III) complexes of the present study is the dominate influence of the spin-orbit coupling in mixing singlet character into the lowest T_1 state.

A number of groups have studied relativistic effects theoretically.[11,13,15,86,113,194-196,220] Most approaches taken have included SOC perturbatively. In Chapter 3 it was shown that this approximation accurately reproduces the results of calculations in the two-component formalism, which includes SOC to all orders, in these complexes.[86] Furthermore, it was seen in Chapter 2 that scalar relativistic effects are also sizeable in these iridium(III) complexes, and play a key role in determining the degree of metal-to-ligand charge transfer (MLCT) character and hence their optical properties.[196] Both Matsushita *et al.*[11] and Jansson *et al.*[113] studied $Ir(ppy)_3$ with SOC included via the semi-empirical effective nuclear charge method, which includes SOC on top of non-relativistic calculations. Matsushita *et al.*[11] studied the mixing of singlet and triplet states and the implications of this for phosphorescence and Jansson *et al.*[113] investigated the nature of the T_1 excitation in some depth. Nozaki *et al.*[13,14] have also investigated organometallic complexes with the SOC included perturbatively about non-relativistic TDDFT calculations. It was shown[13] that this method provides a reasonable description of the zero-field splittings and oscillator strengths of $Ir(ppy)_3$, and in a further study Nozaki and collaborators investigated the differences in the optical properties in a range of tris(2,2′-bipyridine) transition metal complexes using the same method.[14]

Trends across related molecules can also provide important insights into the role of SOC in iridium(III) complexes. Li *et al.*[101] pointed out that, to leading order in perturbation theory, the radiative rate from T_1 is proportional to the inverse square of energy gap between T_1 and S_1. Haneder *et al.*[191] also discussed this effect, but found poor agreement with experiment. However, Jacko *et al.*[40,173,205] have recently found that an additional dependence on the energy gap between T_1 and S_1, which is also inverse square to leading order, arises from the details of the hybridisation between ligand centred and MLCT excitations required to form T_1. Thus Jacko *et al.*'s[205] work predicts that the radiative rate of T_1 varies as the fourth power of the inverse of the energy gap between T_1 and S_1.

4.3 Experimental

4.3.1 Synthesis and Characterisation

The synthesis and characterisation of complexes **1**, **2** and **4** has been previously reported by Lo *et al.*[19] **3** was prepared by Dr Shih-Chun (Lawrence) Lo using a similar synthetic method, details of which can be found elsewhere.[221] Oxidation potentials were determined by cyclic voltammetry in dichloromethane and referenced against the ferricenium/ferrocene couple.[19,221]

4.3.2 Experimental Method

Magnetic circular dichroism (MCD) experiments were performed at 10 K, and an applied 5 T magnetic field. The iridium(III) complexes were dissolved in 2-methyltetrahydrofuran, which was chosen for its capacity to form high quality glasses suitable for low temperature MCD measurements. The total and differential circularly polarized light intensities were measured simultaneously using a single beam instrument consisting of a xenon arc lamp dispersed by a Jobin/Yvon 750 S monochromator. The beam was linearly polarized by a calcite crystal (extinction $<10^{-6}$), mechanically chopped at 500 Hz (New Focus 3501), circularly polarized by a photoelastic modulator at a frequency of 42 kHz (Hinds PEM II/IS42), and passed through the sample held in an Oxford Instruments Spectromag 7 T superconducting magnet. Light was detected either with an S-5 photomultiplier (Hamamatsu R7459) or a Si avalanche photodiode detector. All instrument control and data collection was achieved with GPIB protocols and LABVIEW software. Emission spectra were collected using the 350.7 nm line of a Kr^+ laser and a SPEX1704 monochromator.

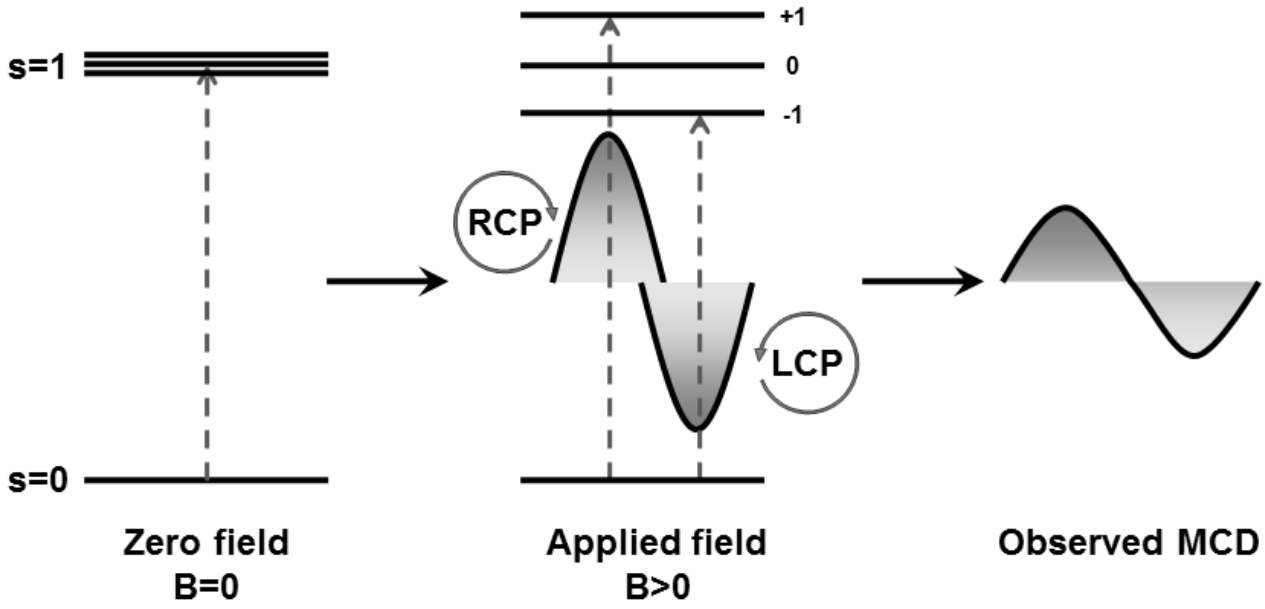

Figure 4.2 Schematic representation of an MCD A-term resulting from a transition into a degenerate excited state. In this example, a triplet spin state is split by an applied magnetic field. Selection rules dictate that right and left-hand polarised light are absorbed by different substates. For simplicity spin-orbit coupling is neglected in this diagram.

MCD is the differential absorption of left and right circularly polarised light in the presence of a magnetic field.[187] MCD spectra can be analysed in terms of the so-called A, B and C-terms. A and C-terms arise from degeneracy in the excited or ground states respectively (C-terms are therefore strongly temperature dependent), while B-terms are from mixing between electronic states or changes in the total angular momentum. MCD A-terms appear as a derivative line shape in the

spectra, owing to spectral overlap between degeneracies lifted by the magnetic field (see for example Figure 4.2). C-terms appear as a single band, but due to their ground state degeneracy C-terms are temperature sensitive. B-terms also appear as single bands, but show no temperature dependence; the line shape is not determined by degenerate states.

4.3.3 Computational Method

The crystal structure of **1**[19] was used as the initial input for the geometry optimization. The *n*-propyl groups were removed from the ligands since they have only a weak inductive effect and are unlikely to affect the electronic structure significantly and will complicate the potential energy surface. The structures of **1-4** were relaxed via DFT using the B3LYP hybrid functional[180,181,222] in the GAMESS suite of programs.[182,183] These calculations used a LANL2DZ[115] basis for the iridium and 6-31G basis for hydrogen, carbon, nitrogen and fluorine.[184,185] Care was taken to conserve the C_3 symmetry of these *facial* complexes throughout the geometry optimisation procedure. The converged molecular structures changed little from the experimental crystal geometries (see Appendix C).

Time-dependent DFT (TDDFT) property calculations were carried out with the ADF2009.01 program.[175-177] As with the geometry optimisation, the B3LYP hybrid functional was used. Based on the one-component zeroth order regular approximation (ZORA),[106,107] the 50 lowest scalar relativistic singlet and triplet excitations were calculated. Spin-orbit coupling was included perturbatively around the one-component TDDFT calculations,[111] leading to a total of 200 spin-mixed excitations. The calculations were performed with a TZP basis set[178,179] and a frozen core approximating the iridium 1*s* 2*s* 2*p* 3*s* 3*p* 3*d* 4*s* 4*p* 4*d* 4*f*, fluorine 1*s*, nitrogen 1*s* and carbon 1*s* shells. Non-relativistic calculations were also carried out for comparison.

Extensive benchmarking calculations (Chapter 3; Appendix B) have shown that the choice of basis set has a large effect on the calculated energies and that the TZP basis is the minimum required to get good agreement with experiment.[86] Treating the core electrons on the iridium atom within the frozen core approximation has little effect on the calculated excitations. Including SOC as a perturbation to the scalar ZORA TDDFT gives essentially the same results as those obtained from more expensive two-component methods, and is more easily related to the underlying spin restricted excitations.[86]

C_3 molecular symmetry could not be utilised in the ADF TDDFT calculations because the C_3 point group contains a complex irreducible representation. As a result small splittings between formally degenerate excitations can occur (Appendix C), despite the C_3 symmetry of the input geometry.

These small splittings are artefacts of the calculation and have no physical significance. Symmetry labels were determined manually by examining the full range of properties of the excitations.

To estimate the 'MLCT' character of individual transitions, the molecule was divided into three fragments comprising the iridium, phenyl and triazolyl moieties. A Mulliken population analysis[186] was performed according to these divisions for each molecular orbital. However, to investigate the redistribution of charge within the molecule after successive fluorination, the total charge density is better approximated by the Hirshfeld method,[223] which does not suffer the overestimation of charge separation that the Mulliken method often produces.[224]

The molecular orbitals were characterised according to their ligand character, and for each excitation the ensemble of orbital transitions was analysed by the ligand character difference between ground and excited state. The sum of the weighted differences of all orbital transitions per excitation was then obtained. This number defines the 'MLCT character' of that excitation. In this scheme, a purely metal orbital would have 0 ligand character, while a purely ligand orbital would have a character of +1. Thus, a transition between these two orbitals would describe a pure MLCT transition, with a character of +1. Using this nomenclature a difference of -1 would describe a pure ligand-to-metal charge transfer (LMCT) transition.

4.4 Results and Discussion

4.4.1 Degeneracy and Symmetry

The absorption and MCD of complexes **1**-**4** share many similarities (Figure 4.3). Only low temperature measurements will be discussed below, however many of the features are still present at room temperature but are, as might be expected, considerably broadened and therefore poorly resolved.

In the MCD spectra between 2.7 – 3.2 eV a number of features can be clearly identified. The MCD spectra continue above 3.2 eV but due to the strong optical absorption the spectra become noisy and unreliable. In addition, it is clear that the higher energy absorptions beyond 3.2 eV are the result of a complex ensemble of excitations, so it is not clear that MCD data in this region provides significant insight into the electronic structure. Further, these higher lying states (>0.5 eV above the absorption onset) are of little significance to the emission mechanism at room temperature.

The first feature to note in the MCD is the strong A-term localised just after the absorption onset. The peak energy of the corresponding absorption band is reported in Table 4.2. In all the complexes the A-term feature has similar intensity.

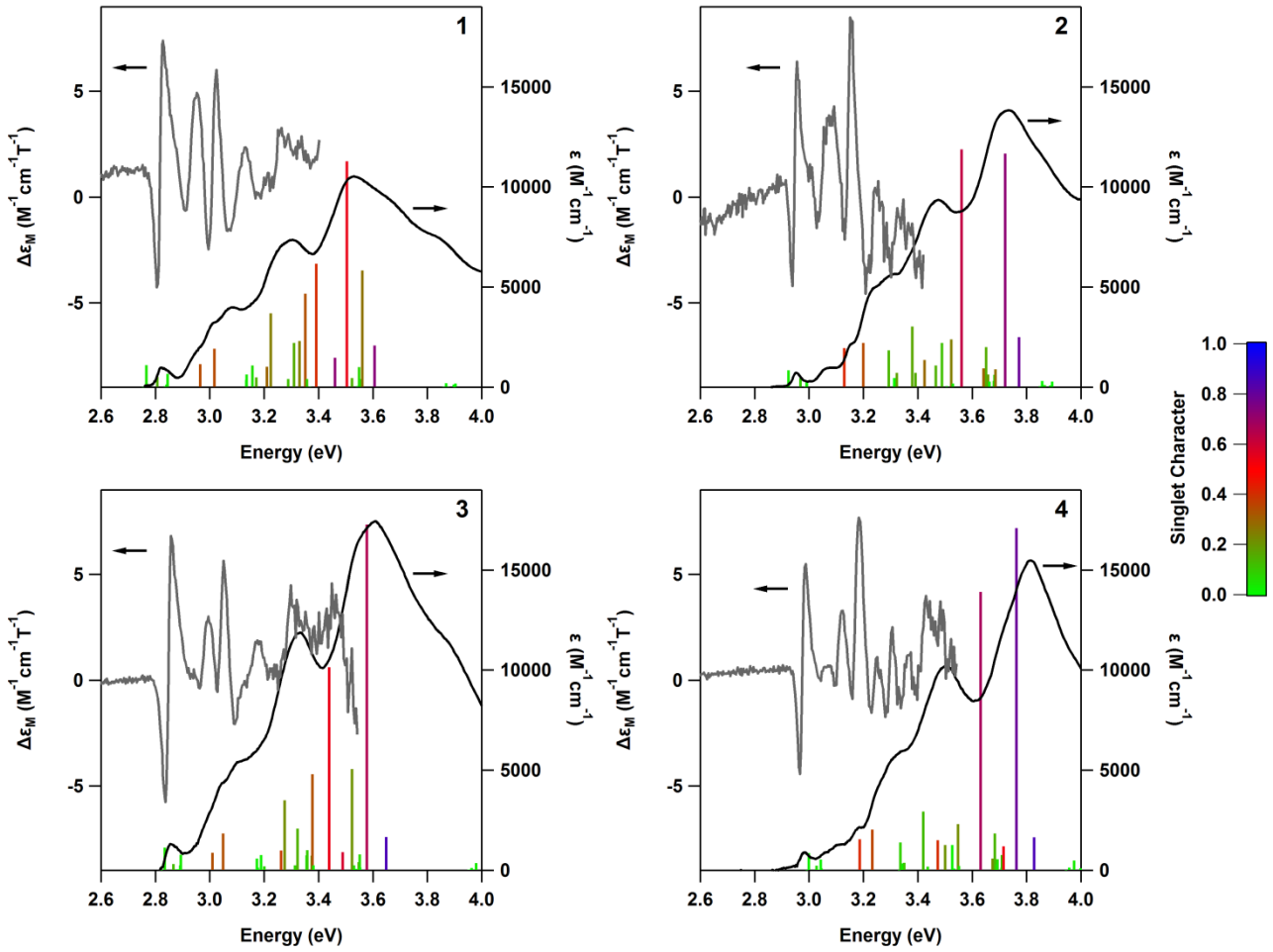

Figure 4.3 Low temperature absorption, MCD and calculated relativistic TDDFT excitations for iridium(III) complexes 1-4. ε is the usual molar extinction coefficient while $\Delta\varepsilon_M$ is the MCD extinction coefficient scaled to the magnetic field strength. The calculated excitations are colour-coded according to the degree of singlet character. In all the complexes, a strong MCD A-term occurs around the first absorption band.

It is interesting to compare this result with Hofbeck and Yersin's spectroscopic studies of $Ir(ppy)_3$, which shares many similarities with complexes **1-4**.[86] On the basis of these measurements Hofbeck and Yersin argued that in $Ir(ppy)_3$ the lowest triplet excitation, T_1, is split into three substates. This led them to argue that the symmetry of $Ir(ppy)_3$ is lowered from C_3 by distortions induced from a host material, whether a solvent or a solid matrix.[84,96] Indeed this group has argued that spectroscopic measurements reveal three distinct substates of T_1 in many iridium(III) complexes.[92-94,96]

Therefore, the clear resolution of MCD A-terms in all four complexes is an interesting result. While an A-term is due to an excited state degeneracy, the degree of degeneracy is only established within the linewidth of the feature. These linewidths are comparable with the observed splitting in $Ir(ppy)_3$,[84] but the clear equal and opposite signed peaks observed in Fig. 2 indicates that the "pseudo A-term" must arise from the 2E state at C_3 symmetry. That is, the symmetry lowering that

results in the three close-lying levels of the lowest T_1 manifold does not destroy the derivative shaped $\Delta\varepsilon$ expected for an A-term from a degenerate E state. The symmetric shape of this MCD feature is maintained at all field strengths and so is not a result of (B-term) magnetic field mixing. Therefore, the observed MCD "A-term" must be due to excitation into the (degenerate) E electronic substate of the first triplet state in C_3. This is consistent with the underlying three level structure where the higher two levels are much more allowed than the lowest level. Further, an approximate mirror image symmetry is observed between the lowest energy feature in absorption and the highest energy feature in emission (Figure 4.4). The relatively small Stokes shift (~220 cm^{-1}) is consistent with the observed lowest energy absorption feature also being responsile for the emission. At temperatures $\geq$ 10K most of the emission is coming from the upper state, the same state which carries the absorption intensity. At low temperature (2K) the emission changes dramatically as the upper levels are depopulated. Similar to that described for $Ir(ppy)_3$,[84] a "Herzberg-Teller" vibronically allowed emission is observed and this, together with the MCPL, will be the subject of a future publication.[225]

At energies above the first A-term two positive bands can be identified in the MCD spectra in Figure 4.3. It is not possible to definitively label these features as arising from particular MCD terms using the experimental data alone, although a number of B and A-terms are clearly required to describe the spectrum.

Table 4.2 The measured optical energy gaps from low temperature absorption spectroscopy, oxidation potentials from cyclic voltammetry,[19] and the orbital energies from scalar relativistic DFT calculations. The row labelled (1+4)-(2+3) is a test of the sum rule, Equation 4.6, formally, $(\Pi_1+\Pi_4)-(\Pi_2+\Pi_3)$. Hence, an entry of 0 indicates perfect agreement between experiment/DFT and the predictions of that equation. The observation that entries of this row are all zero to a very high accuracy indicates that the changes to the excitation energies caused by fluorination at the X and Y positions act independently of one another.

Complex	Experimental		Calculated Energy (eV)						
	E_{opt} (eV)	$E_{1/2}$ (ox) (V)	HOMO-1	HOMO	LUMO	LUMO+1	$\Delta E_{HOMO-HOMO-1}$	$\Delta E_{LUMO-HOMO}$	$\Delta E_{LUMO+1-LUMO}$
1	2.82	0.28	-5.154	-4.980	-1.166	-0.989	0.174	3.814	0.177
2	2.95	0.50	-5.583	-5.393	-1.405	-1.229	0.190	3.988	0.176
3	2.85	0.50	-5.544	-5.382	-1.489	-1.335	0.162	3.893	0.154
4	2.98	0.72	-5.969	-5.781	-1.701	-1.557	0.188	4.080	0.144
(**1**+**4**)-(**2**+**3**)	0.00	0.00	0.004	0.014	0.027	0.018	0.010	0.013	-0.009

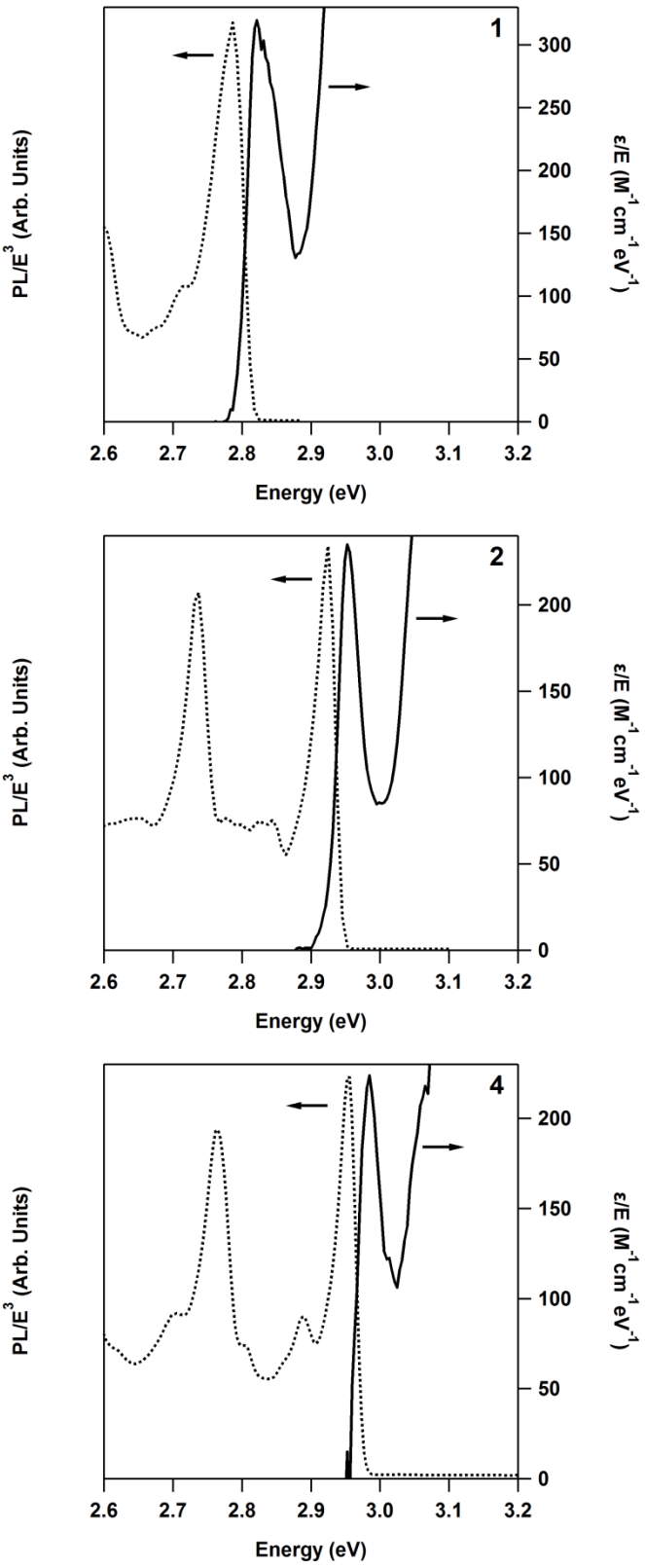

Figure 4.4 Plots of absorption and emission of the iridium(III) complexes 1, 2 and 4 at 10 K. The absorption and emission axes have been rescaled according to the energy and energy cubed, respectively. Similar spectra are obtained at temperatures above 10 K, but are significantly broader and poorly resolved.[19,196]

4.4.2 Relativistic Electronic Structure Calculations: Comparison with Spectroscopy

In order to further understand the MCD spectra relativistic TDDFT calculations were carried out, which were performed with C_3 symmetric geometries. These calculations give information at three levels of theory: (i) scalar relativistic DFT, these are the simplest calculations to understand and interpret as they fit most closely with chemical intuition about molecular orbitals; (ii) scalar relativistic TDDFT, these calculations offer access to what the excited states of the complexes would be in the absence of spin-orbit coupling and can allow us to understand the excitations in terms of transitions between the orbitals in the scalar relativistic DFT calculations; and (iii) perturbation theory with spin-orbit coupling about the scalar relativistic TDDFT. These calculations are the most accurate and are directly comparable to experiment, and also allow an understanding of these transitions in terms of the scalar relativistic DFT. Full results of all three levels of theory listed here are tabulated in Appendix C.

The calculations that include spin-orbit coupling and a comparison of these with experiment will be discussed first. It was previously shown in Chapter 3 that this level of theory gives good agreement with full two-component ZORA calculations for iridium(III) complexes, despite the much lower computational cost of the perturbation calculations, and therefore good agreement with experiment is expected.[86]

The vertical lines in Figure 4.3 show the calculated excitation spectrum - the heights of the lines indicate the calculated oscillator strengths and the colours indicate the degree of singlet character of the excitations (due to the mixing of singlets and triplets by spin-orbit coupling). The calculations accurately reproduce the experimentally measured absorption spectrum. In the Figure 4.5 the calculated spectra have been convoluted with bandshapes of finite width, making the agreement with experiment even more clear. In particular, the absorption onset and peak energies are very closely reproduced. Further, the relativistic TDDFT calculations provide an accurate prediction of the energy at which light is emitted.

SOC splits the first triplet state T_1(A) (the label A is to stress that there is no orbital degeneracy as the orbital part of this state transforms according to the A irrep of C_3) into a non-degenerate A and two-fold degenerate E spin-orbit states (which will henceforth be referred to as 1A and 2E). The calculated zero field splitting (ZFS) of T_1(A) is presented in Table 4.1. The lowest energy state, 1A, is predicted to have a very small calculated oscillator strength ($<10^{-5}$ au) in all four complexes. Four higher energy excitations (two A and two E; numbered 3-6) lie above the T_1(A) manifold due to the ZFS of the second triplet state T_2(E) (Figure 4.6).

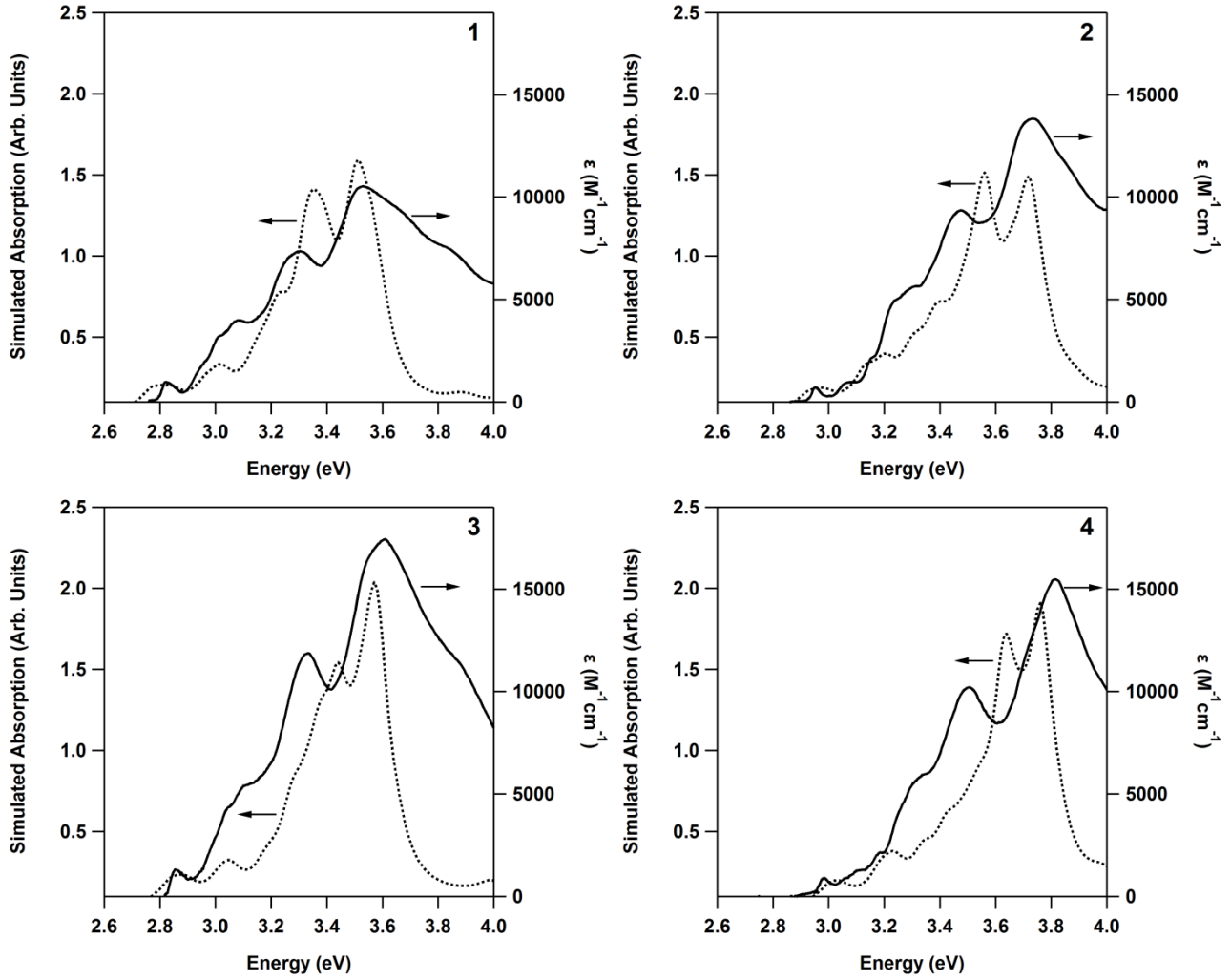

Figure 4.5 Experimental (solid) and calculated (dashed) absorption spectra. ε is the usual spectroscopic extinction coefficient. The calculated absorption spectra are derived from the SOC perturbation TDDFT excitations, broadened with a Lorentzian function (FWHM 0.1 eV). The calculated spectra closely match the experimentally measured spectra. Absorption onset energies are obtained within 0.05 eV, and the absorption peaks follow very closely with experiment.

In light of the calculated excitations the MCD spectrum can be assigned. The lowest energy MCD A-term feature can be assigned as originating from the transitions to the 2E levels which may be split by some small symmetry lowering perturbation as occurs in $Ir(ppy)_3$ and similar systems as discussed above. The calculated oscillator strength of the transition to the 2E state is similar across all four complexes as is the observed MCD signal. It is also the strongest excitation in the entire manifold of T_1(A) and T_2(E) excitations (Figure 4.6). The negligible oscillator strength predicted for 1A in all complexes is consistent with this first A-term being the lowest energy observable feature in the MCD and with the energy of this feature coinciding with the absorption onset.

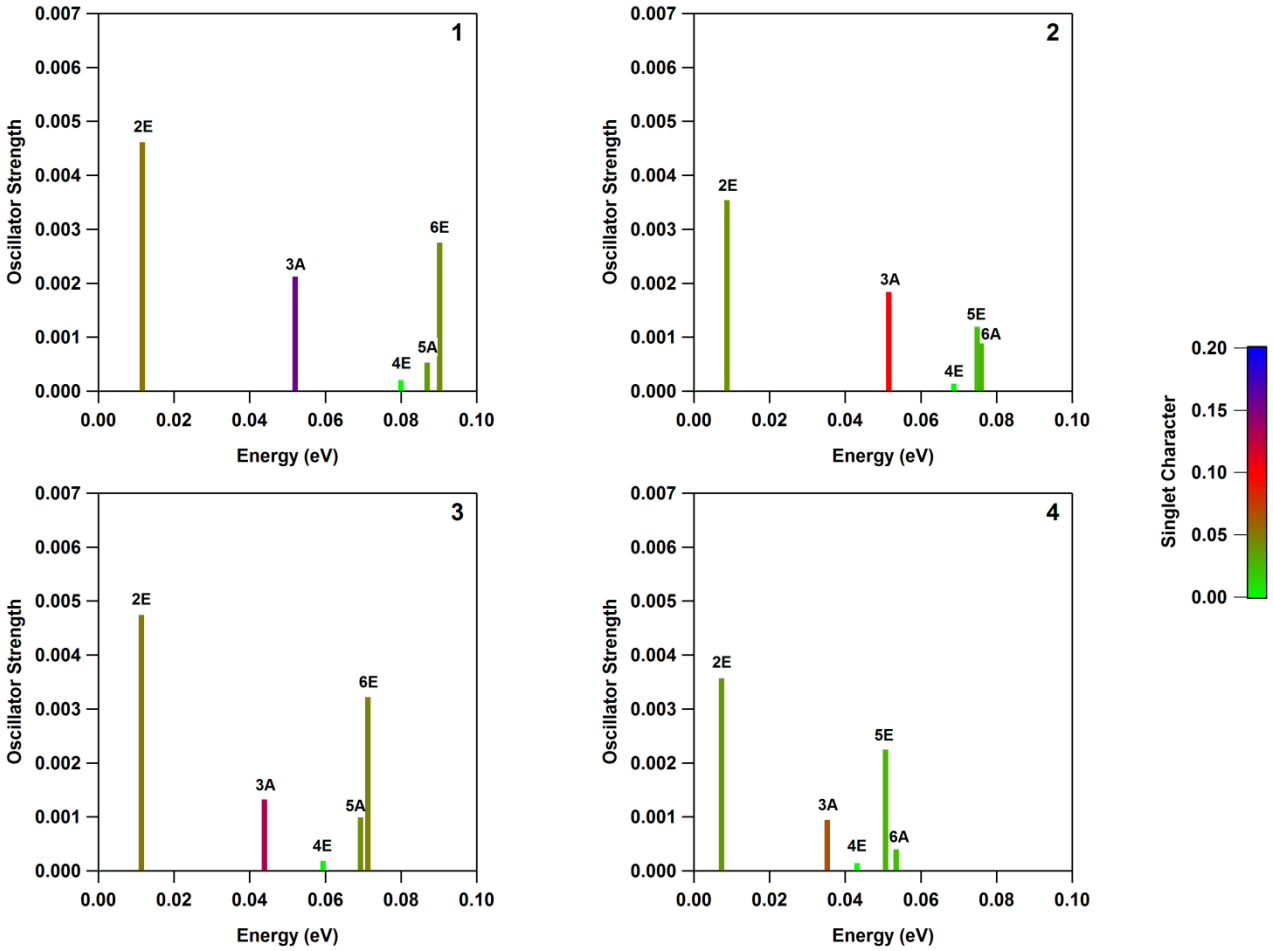

Figure 4.6 Lowest six excitations of iridium(III) complexes 1-4 calculated from SOC perturbation TDDFT with the complexes constrained to C_3 symmetry. Plotted with respect to the energy of the first excitation 1A [which has an extremely small ($f < 10^{-5}$ au) oscillator strength], the energy range between excitations 1 and 6 decreases with fluorine substitution. The ZFS of the T_2 manifold (excitations 3-6) is also reduced by fluorination. Note that the colour coding indicating the singlet character has been rescaled, compared to Figure 4.3, to emphasis the small differences in singlet character. Of particular note is excitation 3A, the singlet character of which is reduced by fluorination in an additive manner depending on the substitution position of the fluorine.

Higher energy excitations 7A and 8E coincide with the strong MCD features between 2.9 and 3.2 eV, which allows their assignment to an MCD B-term followed by an A-term (Figure 4.3). This pair of excitations arise from a complex mix of scalar excitations with no one singlet or triplet excitation dominating. Above ~3.2 eV the density of states becomes much greater and unambiguous identification of MCD features is difficult. However, as noted above, these states are not important for the emissive properties of the complexes at room temperature.

4.4.3 The Temperature Dependence of Radiative Rates

Note that the assignments above predict that 1A does not play a significant role in the absorption of light by these complexes. It is clearly interesting, given the potential optoelectronic applications of

these complexes, to ask what role excitation 2E, and more generally all of the excited states, play in the emission of light. To examine this question assume that the vibration relaxation from the initially excited state achieves thermal equilibrium. The fractional Boltzmann probability, $p_i(T)$, of an excited complex being in the i^{th} excited state at temperature T is given by

$$p_i(T) = \frac{g_i e^{\frac{-(E_i - E_{1A})}{k_B T}}}{\sum_j g_j e^{\frac{-(E_j - E_{1A})}{k_B T}}} \qquad \textbf{4.1}$$

where g_i is the degeneracy, E_i is the energy, k_B is Boltzmann's constant and E_{1A} is the energy of the lowest energy excitation, 1A. Thence, the probability $P_i(T)$ that a detected photon was emitted from excitation i is given by

$$P_i(T) = \frac{p_i(T)k_i}{\sum_i p_i(T)k_i} \qquad \textbf{4.2}$$

where k_i is the radiative rate from excitation i. Radiative rates and lifetimes were calculated from the TDDFT results via the Stickler-Berg relation.[206,207] The predictions of Equation 4.2 for all four complexes at 300 K are reported in Figure 4.7. In particular, at 300 K, ≥80% of the emission comes from 2E in all four complexes. The vanishingly small probability of emission from 1A suggests that the bulk of the emission is not occurring from the lowest excited state level in these complexes at temperatures >10 K.

The calculations predict that the lowest state with significant absorption (2E) is also responsible for the bulk of the emission at 300K. This is responsible for the mirror image symmetry between absorption and emission spectra as neither the absorption or emission processes involve the lowest energy excited state. Therefore, theory predicts that these complexes will display mirror image symmetry at 300 K. The mirror image rule is indeed obeyed experimentally as shown by the results in Figure 4.4. This is strong experimental evidence that the excitation responsible for the MCD A-term and the absorption onset (2E) also dominates the emission process at temperatures great than about 10 K.

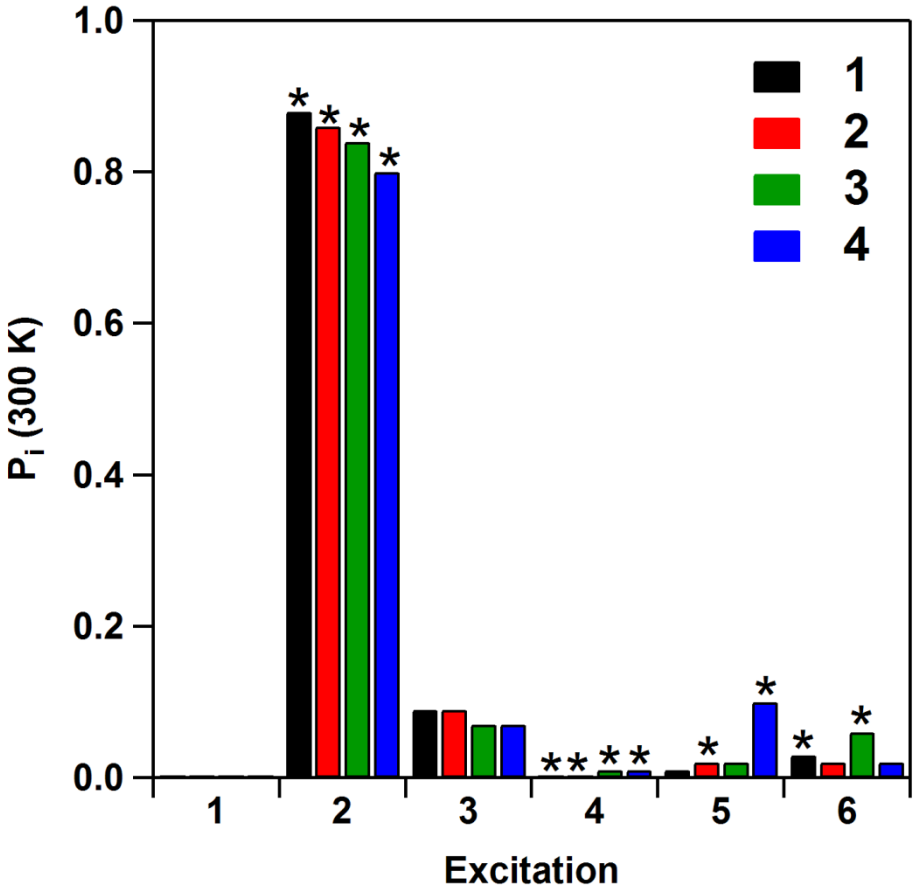

Figure 4.7 The probability P_i(300 K) of observing emission from iridium(III) complexes 1-4 for the lowest six excitations calculated from SOC perturbation TDDFT. At room temperature ≥80% of all emission is calculated to occur from 2E. The probability of observing emission from 1A is close to zero. Degenerate, E, excitations are denoted by an *.

The calculated radiative lifetime of all four complexes reveals very similar temperature dependent profiles (Figure 4.8), which closely resemble the measured total lifetime of many similar iridium(III) complexes.[83,84,92] Below ~10 K the radiative lifetime plateaus, as the lowest energy state, 1A, is essentially fully populated. As the lowest state has such weak oscillator strength even a slight change in the calculated oscillator strength for this state will have a dramatic effect on the final lifetime at low temperature (see for example Figure 3.11).[86] The true radiative rate at low temperature is likely to be enhanced by Herzberg-Teller (HT) coupling, which may well give rise to a radiative rate larger than, or of a similar magnitude to, the calculated direct radiative rate. Nevertheless the qualitative shape of the curves in Figure 4.8 is expected to be correct although the intercepts may be somewhat lower.

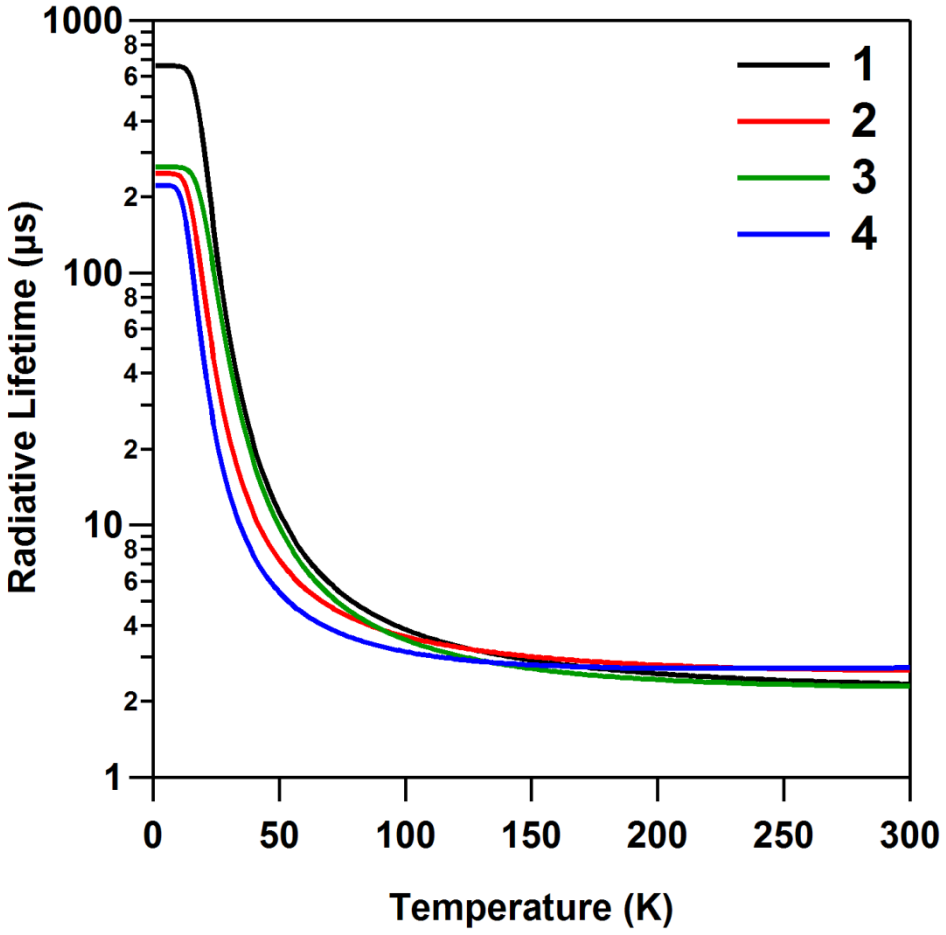

Figure 4.8 Predicted temperature dependent radiative lifetimes of iridium(III) complexes 1-4, calculated from SOC perturbation TDDFT excitations. The radiative lifetime of all four complexes follows a similar temperature dependence. Below 10 K only the lowest state 1A has significant population and so the radiative lifetime is long and plateaus. At 300 K complexes 1 and 3, which have protons at the Y position, have similar lifetimes, as do complexes 2 and 4, which have fluorines at the Y position.

Although most of the light is emitted from 2E, a substate of T_1(A), the occupation of the T_2(E) states may still have important consequences for the optoelectronic properties of these complexes. Figure 4.6 shows that fluorination leads to important changes in properties of the T_2(E) manifold:

Firstly, relative to the energy of the first excitation, 1A, the T_2(E) manifold of excitations (3-6) shift down in energy following fluorine substitution (Figure 4.6). This can be understood by considering the scalar relativistic TDDFT calculations where the energy separation between the T_1(A) and T_2(E) excitations is also reduced with fluorine substitution (see Appendix C). These low energy excitations are formed almost exclusively from transitions between the frontier orbitals. In all complexes T_1(A) is primarily composed of HOMO→LUMO (>62%) and HOMO-1→LUMO+1 (>15%) transitions, whereas T_2(E) is made up of HOMO→LUMO+1 (>47%) and HOMO-1→LUMO (>11%) transitions (see Appendix C). The changes in excitation energy can be

traced back to the effects that fluorination has on these orbital energies. Specifically, the orbital transitions with the greatest contribution in the $T_1(A)$ and $T_2(E)$ excitations (HOMO→LUMO and HOMO→LUMO+1 respectively) have an energy separation between the $T_1(A)$ and $T_2(E)$ excitations that is dependent only on the LUMO–LUMO+1 energy gap. In order of complexes **1**-**4** the LUMO/LUMO+1 energy separation decreases (Table 4.2) consistent with the calculated decrease in the $T_1(A)$-$T_2(E)$ separation.

Secondly, the predicted overall splitting of the $T_2(E)$ excitation manifold (excitations 3-6) decreases with fluorination, from a maximum of 38 meV for **1** to 18 meV for **4** (Figure 4.6).

These two effects have important consequences for the occupation of the T_2 manifold. In the parent complex, **1**, an excitation only has a Boltzmann probability of 12% of being in the T_2 manifold at room temperature (Figure 4.9). This probability rises to 15% in **2**, 20% in **3** and 29% in **4**. Excitations 3-6 all have weaker oscillator strengths (and therefore slow radiative rates) compared to 2E, so this is the first clue to why fluorination lowers the radiative rate of the complexes at room temperature.

Moreover, this redistribution of spectral weight may also be important for the non-radiative rate. The increase in the population of the T_2 manifold is much larger for fluorination at the X position (which takes **1**→**3** and **2**→**4** and increases the occupation of the T_2 states by a factor of two) than for fluorination at the Y position (which takes **1**→**2** and **3**→**4**). Although the non-radiative decay rates for individual excitations has not been calculated or measured it is reasonable to expect that, because they are embedded in the vibrational bands based on the lower T_1 state, the T_2 states may have much higher non-radiative decay rates than the T_1 states. This speculative explanation would then give a natural explanation of why fluorination at the X position increases the non-radiative decay rate much more dramatically than fluorination at the Y position does.

It is interesting to note that the redistribution of spectral weight is not simply an effect of the blue shift. **2** is shifted further to the blue than **3** (Figure 4.3) yet the population of the T_2 manifold is, respectively, only 15% in **2** compared to 20% in **3**.

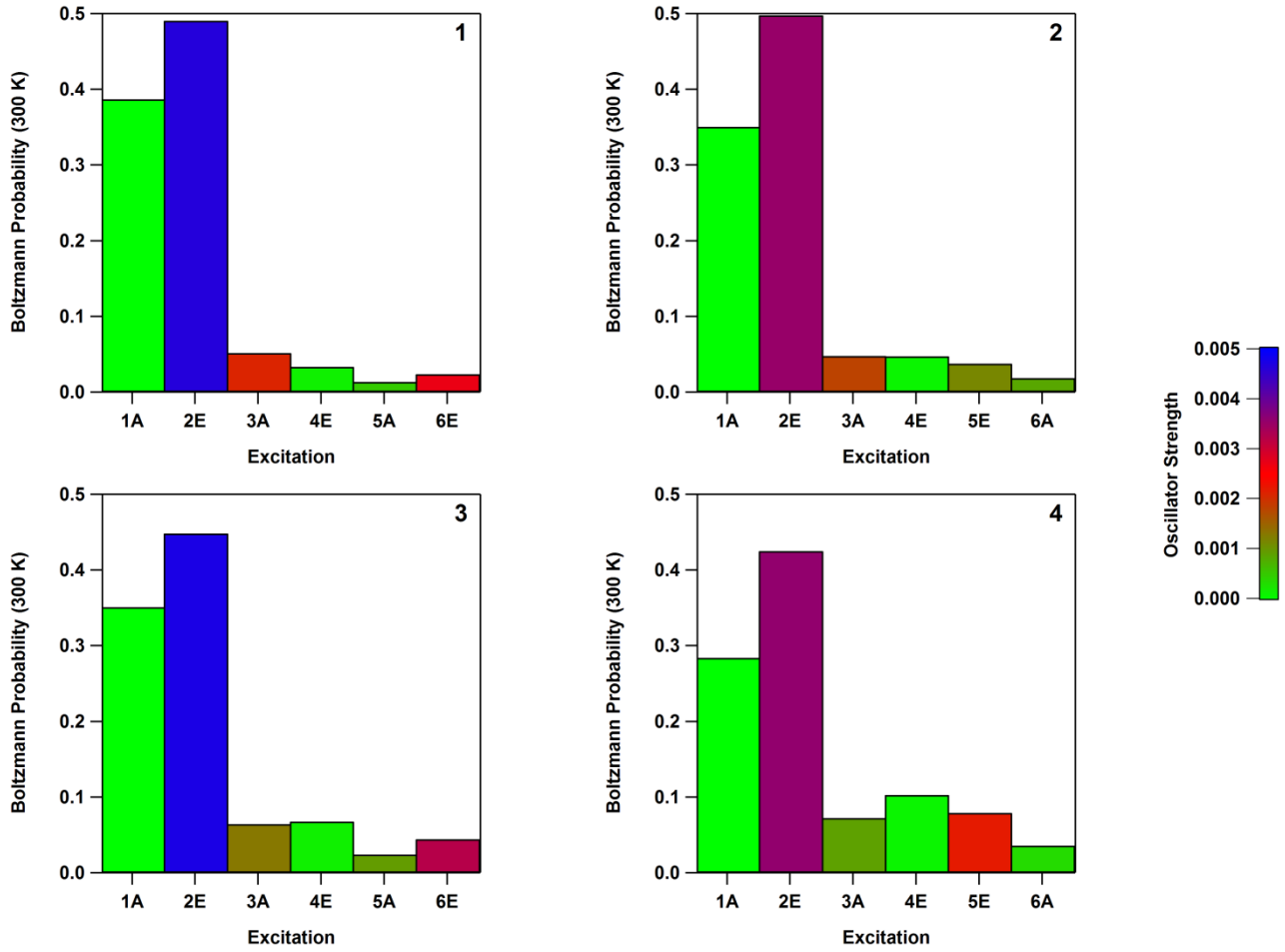

Figure 4.9 With successive fluorine substitution the manifold of T_2 excitations (3-6) become increasingly populated to the detriment of the T_1 manifold, excitations 1A and 2E. For the difluorinated complex 4 the population in excitations 3-6 is 29%, more than double the non-fluorinated parent complex 1, with only 12%.

4.4.4 Linear Response to Fluorination

To demonstrate that fluorination at the X and Y positions act independently a wide range of measured and calculated properties of complexes **1-4** will be compared. Let us assume initially that fluorination causes a *small* shift in some property, Π, of the complex. The assumption of the small shift allows one to develop a linear response theory[226] for chemical substitution. If the change in Π caused by fluorination at the X position is denoted by $\delta\Pi_X$ and the change in Π caused by fluorination at the Y position by $\delta\Pi_Y$, then the assumptions of linearity and independence lead directly to the prediction that

$$\Pi_2 = \Pi_1 + \delta\Pi_Y \qquad \textbf{4.3}$$

$$\Pi_3 = \Pi_1 + \delta\Pi_X \qquad \textbf{4.4}$$

$$\Pi_{\mathbf{4}} = \Pi_{\mathbf{1}} + \delta\Pi_X + \delta\Pi_Y \qquad \textbf{4.5}$$

where Π_n is the value of the property Π for the *n*th complex. Note that **1** is unfluorinated, **2** is fluorinated in only at the Y position, **3** is fluorinated only at the X position and **4** is fluorinated at both the X and Y positions. Thus,

$$\Pi_{\mathbf{1}} + \Pi_{\mathbf{4}} = \Pi_{\mathbf{2}} + \Pi_{\mathbf{3}} \qquad \textbf{4.6}$$

Where the property Π is clear from context, it will be useful to introduce the shorthand (**1**+**4**)-(**2**+**3**) = 0 to summarise Equation 4.6.

The Equation 4.6 is potentially quite general for different families of complexes and where substitutions cause sufficiently subtle effects of the property measured. It will be demonstrated below that a range of important properties in complexes **1-4** display this behaviour. Therefore, it may be possible to use this as a design principle for tailoring the properties of organometallic complexes to specific applications.

In Table 4.2 the experimentally measured optical excitation and oxidation potentials (reversible reduction potentials could not be determined for comparison) of complexes **1-4** are reported. The HOMO-LUMO gap calculated from scalar relativistic DFT calculations (upon which the TDDFT and SOC perturbation calculations are all based) follows the trend observed spectroscopically, although, unsurprisingly, it vastly overestimates the measured optical gap (Table 4.2). Nevertheless, for all three of these properties, Equation 4.6 holds to a very high accuracy.

Reported in Table 4.3 are the results of a Mulliken population analysis of the HOMO-1, HOMO, LUMO and LUMO+1 orbitals of complexes **1-4**. This reveals that, unlike the orbital energies, the effect of fluorination on the electronic distribution in the frontier orbitals is rather subtle. This is curious, since the fluorine should act as an electron withdrawing group to the phenyl ring and will be discussed further below. The rule (**1**+**4**)-(**2**+**3**) = 0 is observed here too, however the weak dependence that the Mulliken populations show to fluorine substitution means that this does not represent a severe test of Equation 4.6.

Table 4.3 Mulliken population analysis of selected orbitals with respect to the molecular fragments from SR-DFT. The populations in these frontier orbitals changes very little with fluorine substitution. The column labelled (1+4)-(2+3) is a test of the sum rule for fluorination, Equation 4.6, where an entry of 0 indicates perfect agreement between TDDFT and the predictions of that equation. However, the overall changes in the Mulliken populations are too small to draw strong conclusions from the finding that the sum rule holds for this property.

Orbital	*Fragment*	1	2	3	4	(1+4)-(2+3)
	iridium	0.50	0.49	0.49	0.49	0.01
HOMO-1 (E)	*triazolyl*	0.10	0.12	0.11	0.12	-0.01
	phenyl	0.40	0.39	0.41	0.39	-0.01
	iridium	0.55	0.53	0.55	0.53	0.00
HOMO (A)	*triazolyl*	0.10	0.12	0.11	0.13	0.00
	phenyl	0.35	0.35	0.35	0.34	-0.01
	iridium	0.00	0.00	0.00	0.00	0.00
LUMO (A)	*triazolyl*	0.47	0.47	0.48	0.49	0.01
	phenyl	0.53	0.53	0.53	0.52	-0.01
	iridium	0.03	0.02	0.03	0.02	0.00
LUMO+1 (E)	*triazolyl*	0.48	0.49	0.47	0.49	0.01
	phenyl	0.50	0.49	0.51	0.49	-0.01

Analysis of the fragment charge distribution (Table 4.4) shows the effect of fluorination more clearly. In both the Mulliken and Hirshfeld methods the successive addition of fluorine promotes the redistribution of charge from the triazolyl ring towards the phenyl ring. Although the Mulliken method overestimates the charge separation and is known to have a strong basis set dependence,[224] the trend of charge redistribution towards the phenyl ring with fluorine substitution is consistent between the two techniques. This shows that the electron withdrawal due to the fluorine substitution happens mostly in the orbitals below the HOMO-1 orbital. Here one sees that the relationship (**1**+**4**)-(**2**+**3**) = 0 with fluorination very clearly. This indicates that the redistributions of charge caused by fluorination at the X and Y positions are uncorrelated.

The charge transfer character of the excitations also changes upon fluorination, with **1** having the strongest MLCT character in the low energy triplet states (Table 4.5, Figure 4.10), and like the singlet character discussed earlier, the MLCT character decreases as more fluorines are substituted onto the ligands. Once again, fluorine substitution is additive, as observed by the relationship (**1**+**4**)-(**2**+**3**) = 0 in the MLCT character of the first two triplet excitations (Table 4.5).

Table 4.4 Partial charge per fragment based on Mulliken and Hirshfeld population analysis from SR-DFT. The total charge distribution changes with fluorination, as electron density is redistributed from the triazolyl to the phenyl ring. The Mulliken method overestimates the charge separation, but is consistent with the Hirshfeld analysis. The column labelled (1+4)-(2+3) is a test of the sum rule for fluorination, Equation 4.6, where an entry of 0 indicates perfect agreement between the Mulliken/Hirshfeld population analysis and the predictions of that equation. The observation that entries of this row are all zero to a very high accuracy indicates that redistributions of charge caused by fluorination at the X and Y positions are independent of one another.

Method	*Fragment*	1	2	3	4	(1+4)-(2+3)
Mulliken	*iridium*	0.97	0.99	0.98	1.00	0.00
	triazolyl	-0.32	-0.29	-0.19	-0.15	0.01
	phenyl	-0.65	-0.71	-0.80	-0.86	0.00
Hirshfeld	*iridium*	0.4383	0.4417	0.4086	0.4130	0.0010
	triazolyl	0.0368	0.0360	0.1391	0.1392	0.0009
	phenyl	-0.4705	-0.4731	-0.5461	-0.5482	0.0005

Table 4.5 MLCT character of the low energy triplet states/manifolds from SR and SOC perturbation TDDFT. In the SOC perturbation case, the MLCT character is an average over all the excitations in that manifold. Fluorination reduces the MLCT character of the excitations, indicating that fluorination makes the excitations more ligand oriented. The column labelled (1+4)-(2+3) is a test of the sum rule for fluorination, Equation 4.6, where an entry of 0 indicates perfect agreement between TDDFT and the predictions of that equation. The observation that entries of this row are all small indicates that the changes in the MLCT character caused by fluorination at the X and Y positions are independent of one another.

Excitation	Method	1	2	3	4	(1+4)-(2+3)
T_1(A)	**SR**	0.49	0.45	0.47	0.42	-0.01
	SOC	0.48	0.44	0.46	0.41	-0.01
T_2(E)	**SR**	0.46	0.41	0.44	0.38	-0.01
	SOC	0.45	0.41	0.43	0.38	-0.01

One can also observe the sum rule in relativistic effects. In all complexes, states arising from the T_2(E) manifold remain predominantly triplet in character (>95%), apart from the 3A state, which has a significant component of singlet character due to the S_1(A) manifold. In complex **1** the singlet character of 3A reaches 16%, but fluorination reduces the singlet component to 10% and 13% for **2** and **3**, respectively (see Appendix C). The difluorinated complex **4** has the lowest singlet component in 3A with only a 7% contribution. Again the same linear response to fluorination is observed.

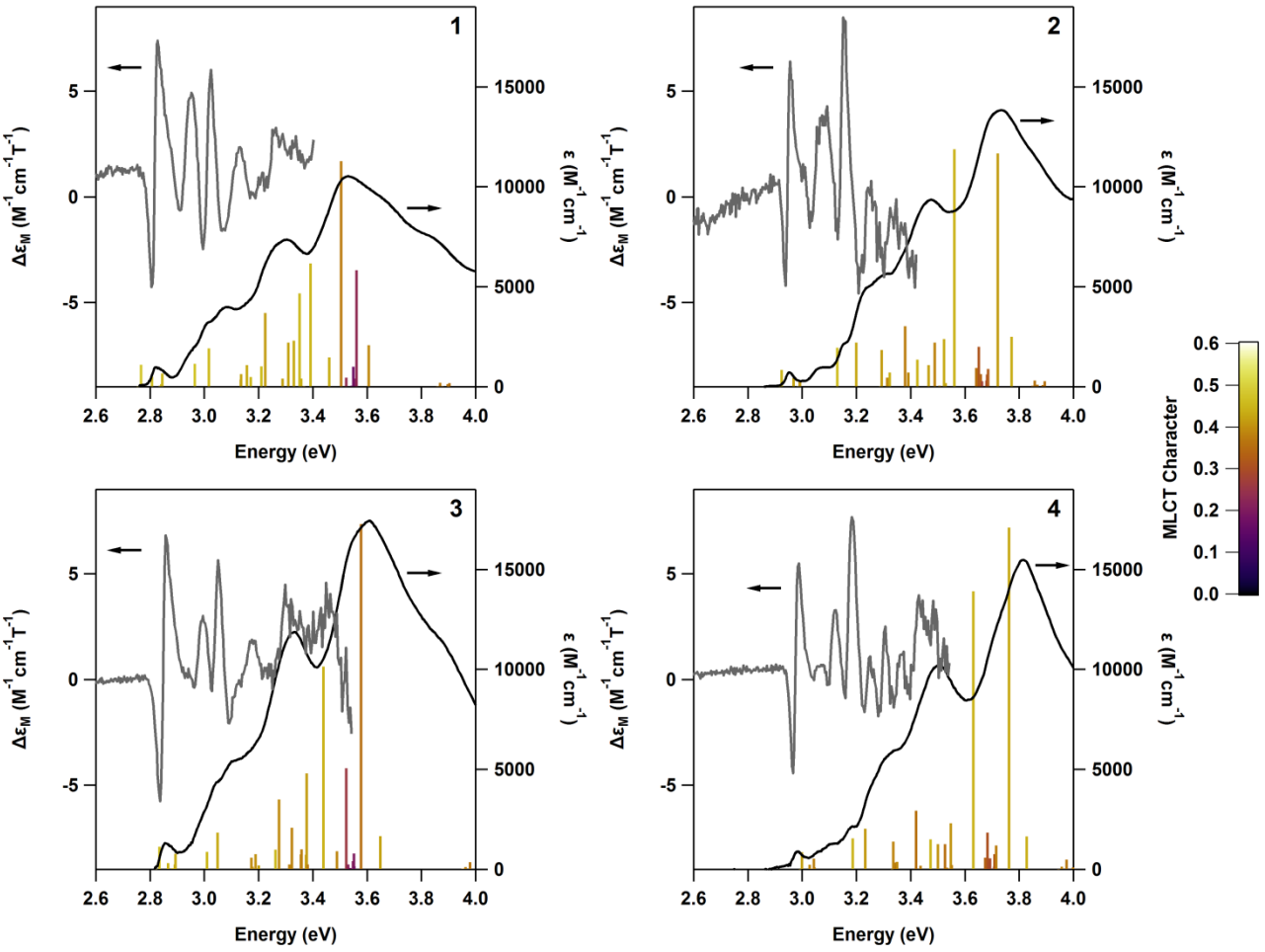

Figure 4.10 Low temperature absorption, MCD and calculated SOC perturbation TDDFT excitations. ε is the usual spectroscopic extinction coefficient while $\Delta\varepsilon_M$ is the MCD extinction coefficient scaled to the magnetic field strength. The calculated excitations are colour-coded according to the degree of MLCT character. In all the complexes, a strong MCD A-term is localised around the first absorption band. The calculated excitations reproduce the experimental energies and density of states expected due to SOC.

At 300 K the radiative rate of complexes **1-4** are calculated to be 4.3×10^5, 3.8×10^5, 4.4×10^5, and 3.7×10^5 s^{-1} respectively, which is the same order of magnitude as measured experimentally (Table 4.1).[19] Complexes **1** and **3** have similar radiative rates as do complexes **2** and **4**. This suggests that the important difference, in terms of radiative rates, is whether the Y position is protonated (as in complexes **1** and **3**) or fluorinated (as in complexes **2** and **4**). The same trend is observed in the experimentally measured radiative rates (Table 4.1). Conversely, the experimental data shows that fluorination at the X position increases the non-radiative rate by more than an order of magnitude, whereas fluorination at the Y position has a much smaller effect on the k_{nr}.

4.4.5 Mechanism of Changes in the Radiative Rate due to Fluorination

Phosphorescence occurs because SOC mixes singlets and triplets. This mixing is reduced as the energy gap between the relevant singlets and triplets is increased. In a related series of complexes one expects the radiative rate to depend on the energy gap between a triplet and the singlet that it mixes with.[40,92,101] Li *et al.*[101] pointed out that the rate depends on the inverse square of this gap at the lowest order in perturbation theory. However, recently Jacko *et al.*[40,92,205] have shown that a second inverse square relationship arises because of the hybridisation between metal and ligand orbitals. Thus overall the radiative rate should exhibit a quadratic dependence on the inverse of the energy gap between a triplet and the singlet that it mixes with.[205]

As discussed earlier, the complexes studied here predominately emit from the 2E level at room temperature. If the TDDFT results are compared with and without the effects of spin-orbit perturbation (see Appendix C for full tabulation) in all of the complexes the 2E state is basically a substate of T_1(A) with small but significant contribution from S_3(E) of 5.2%, 4.1%, 5.1% and 3.7% for complexes **1**-**4**, respectively. It is worth noting that S_3(E) and S_5(E) are the strongest singlet excitations in the MLCT manifold, so it is interesting that a strong excitation like S_3(E) should couple into the lowest triplet more strongly than the closer lying S_1(A) and S_2(E) excitations. This is clearly important for the large radiative rate and hence the high PLQY of, at least, the parent complex (**1**).

The calculated energy gap S_3(E)-T_1(A) is strongly dependent on fluorination at the Y position: this gap is ~10% larger in complexes **2** and **4** (where Y=F) than in complexes **1** and **3** (where Y=H). However, fluorination at the X position has little effect on the S_3(E)-T_1(A) gap. In Figure 4.11 the calculated S_3(E)-T_1(A) gap is compared with the calculated radiative rates. This shows that the radiative rate decreases as the fourth power of the S_3(E)-T_1(A) energy gap (Figure 4.11), as predicted by Jacko and Powell.[205]

Therefore, the question becomes why does fluorination increase the S_3(E)-T_1(A) gap? To understand this it is helpful to compare the scalar relativistic DFT and TDDFT calculations. In Appendix C the largest contributions to each TDDFT excitation are tabulated in terms of transitions between DFT molecular orbitals. In all four complexes, T_1(A) is predominately a HOMO→LUMO transition (with weights of 72%, 66%, 69% and 62% in complexes **1**-**4**, respectively) and S_3(E) is dominated by the HOMO-1→LUMO transition (with weights of 94%, 96%, 94% and 97% in complexes **1**-**4**, respectively). Note that both of these weights obey the (**1**+**4**)-(**2**+**3**) = 0 rule and that in both cases fluorination at the Y position has a greater effect than that at the X position.

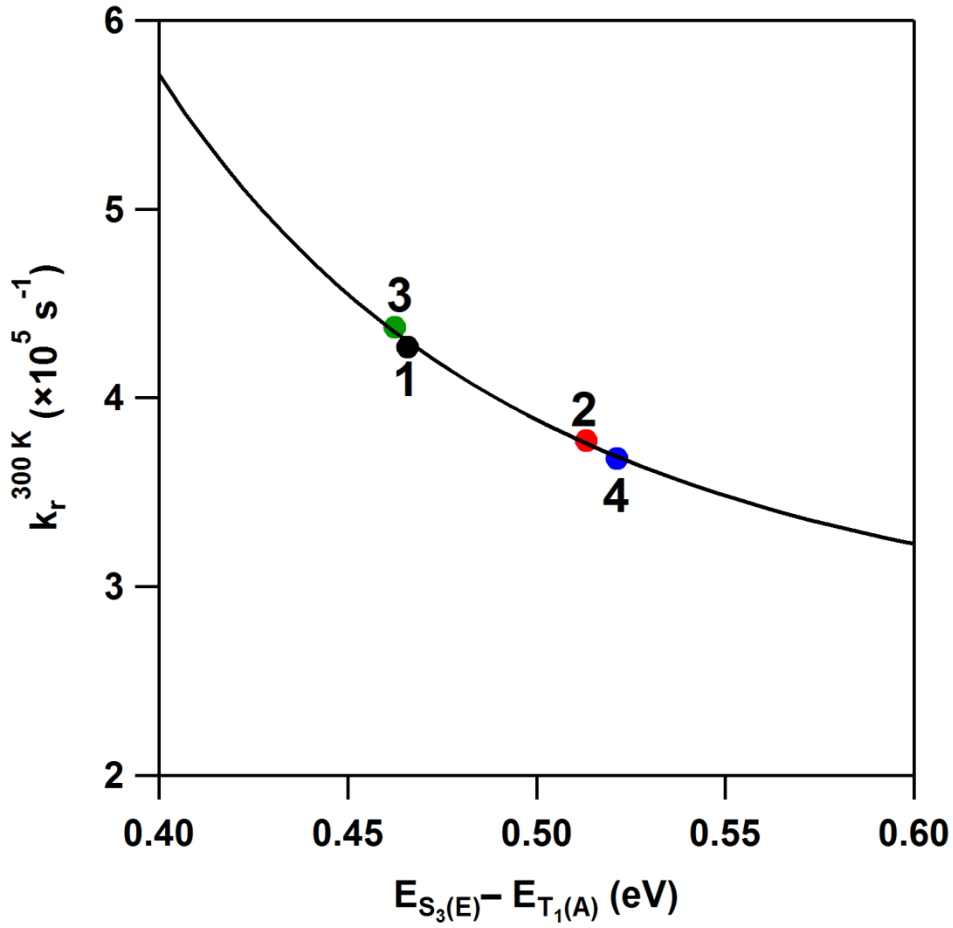

Figure 4.11 Calculated total radiative rate at 300 K for iridium(III) complexes 1-4, plotted against the calculated energy gap between the scalar TDDFT excitations S_3(E) and T_1(A). The S_3(E)-T_1(A) energy gap is found to be strongly dependent on the fluorination at the Y position, whereas fluorination at X does not change the relative energy separation significantly. The line is a best fit for the predicted dependence between the inverse fourth power of the radiative rate and the singlet-triplet energy gap.[205] The calculated radiative rate is the same order of magnitude as the experimentally measured rate.[19]

On the basis of the above analysis one expects that, to leading order, the main effect of fluorination on the S_3(E)-T_1(A) energy gap, and hence on the radiative rate, is therefore to increase the energy gap between the HOMO and HOMO-1. (One might also ask if there is an effect on the strength of the exchange interaction, but this will not be considered here.) In Table 4.2 the energies of the frontier orbitals are listed. The energy gap between the HOMO and HOMO-1 clearly obeys the (**1**+**4**)-(**2**+**3**) = 0 rule. Although these complexes have C_3 symmetry, the iridium(III) atom sits in an approximately octahedral environment formed by the covalent bonds to the carbon atoms and the dative bonds to the nitrogen atoms. If this octahedral symmetry were exact the HOMO (A) and HOMO-1 (E) would form a triply degenerate t_{2g} manifold. This is responsible for the marked similarities between the HOMOs and HOMO-1s of homoleptic iridium(III) complexes.[86,196]

Fluorination at the Y position (**1**→**2**, **3**→**4**) has an important effect on increasing the HOMO−HOMO-1 gap (~0.2 eV) whereas fluorination at the X position (**1**→**3**, **2**→**4**) has a much smaller effect on the HOMO−HOMO-1 gap. Therefore fluorination at the Y position changes the radiative rate by increasing the degree to which octahedral symmetry is broken, whereas fluorination at the X position only weakly effects the radiative rate. This simple molecular orbital analysis overestimates the magnitude of the increase in the S_3(E)-T_1(A) gap because it neglects the other molecular orbital transitions that contribute to S_3(E) and, particularly T_1(A). Nevertheless, this simple molecular orbital picture does correctly reproduce the trend seen in both the relativistic TDDFT calculation with spin orbit coupling and experiment.

Finally, it is worth noting that this analysis does not just apply to excitation 2E. For example, the character of 3A is dominated by the combination of the T_2(E) and S_1(A) states. The singlet character of 3A can be directly related to the energy difference between the T_2(E) and S_1(A) states, which in order of the complexes **1**-**4** is 0.20, 0.24, 0.21 and 0.26 eV, these values again satisfy Equation 4.6. As the energy difference between the two states increases, less of the S_1(A) excitation is coupled into 3A.

4.5 Conclusions

The combination of low temperature, high field MCD, absorption and emission spectroscopy with relativistic time-dependent density functional calculations has allowed a rather complete mapping of the low-energy excited states of a family of iridium(III) complexes. The subtle changes induced by fluorination on the experimental spectra and accurately describe the molecular properties could be closely followed. This has revealed a subtle interplay between the effects of chemical substitutions and spin-orbit coupling and thus photoluminescence efficiency.

The current experiments can be interpreted in terms of C_3 symmetry although symmetry lowering effects are possible in some excited states due to vibronic coupling and interaction with the environment that would result in localisation. The lowest energy excitation 1A has an extremely small oscillator strength, and as a result transitions to and from the second lowest excitation 2E dominate in both the absorption and emission spectra, respectively, at room temperature (Figure 4.7). Therefore, a mirror image between absorption and emission is still observed (Figure 4.4). 2E is a two-fold degenerate excitation and, as such, is responsible for the distinct MCD A-term found in all complexes (Figure 4.3).

The properties of a family of fluorinated phosphorescent iridium(III) complexes are determined by the independent action of each fluorine substitution (Table 4.2, Table 4.3, Table 4.4, Table 4.5).

This independence is encapsulated by the (**1**+**4**)-(**2**+**3**) = 0 rule, Equation 4.6, which one should expect to hold provided the changes due to a substitution are sufficiently small to be additive. Therefore, this may represent a general rule to aid the design of new phosphorescent complexes. In this context it is interesting to note (cf. Table 4.1) that fluorination of the Y position (which takes **1**→**2** and **3**→**4**) reduces the radiative rate by a factor of 2-3; whereas fluorination of the X position (**1**→**3** and **2**→**4**) leads to an order of magnitude increase in the non-radiative rate, but has a much smaller change in the radiative rate.

The calculated radiative lifetime in this family of complexes is found to be dependent on the S_3(E)-T_1(A) energy gap, and is consistent with the predicted quadratic dependence on the inverse of the singlet-triplet energy gap. Fluorination in the Y position lowers this gap (Figure 4.11) and is responsible for suppression of the radiative rate between complexes **1** and **2** and complexes **3** and **4**. On the other hand, fluorination of the X position does not significantly alter the gap (Figure 4.11), which explains the similar radiative rates observed in complexes **1** and **3**, and in complexes **2** and **4**. As non-radiative decay mechanisms have not been considered, a full explanation of why fluorinations at the X and Y positions have such different effects on the non-radiative decay rates cannot be given. However, the fluorination at the X position causes more significant redistribution of the low energy spectral weight: decreasing the T_1-T_2 energy difference by reducing the LUMO+1-LUMO gap and decreasing the ZFS of T_2. This reduces the probability of excitations equilibrating into the main emissive state, 2E, which, it is tempting to speculate, may be related to the dramatic increase in the non-radiative rate.

Chapter 5. Morphology of Evaporated Phosphorescent Organic Films

Published in Advanced Functional Materials, 2011, 21, 2225

5.1 Abstract

Stable film morphology is critical for long-term high performance organic light-emitting diodes (OLEDs). Neutron reflectometry (NR) was used to study the out-of-plane structure of blended thin films and multilayer structures comprised evaporated small molecules. It was found that as-prepared blended films of *fac*-tris(2-phenylpyridyl)iridium(III) [$Ir(ppy)_3$] in 4,4′-bis(*N*-carbazolyl)biphenyl (CBP) were uniformly mixed, but the occurrence of phase separation upon thermal annealing was dependent on the blend ratio. Films comprised of the ratio of 6 wt% of $Ir(ppy)_3$ in CBP typically used in OLEDs were found to phase separate with moderate heating while a higher weight percent mixture (12 wt%) was found to be stable. Furthermore, it was found that thermal annealing a multilayer film comprised of typical layers found in efficient devices {tris[4-(carbazoyl-9-yl)phenyl]amine (TCTA)/$Ir(ppy)_3$:CBP/bathocuproine (BCP)} caused the BCP layer to become mixed with the emissive blend layer, whereas the TCTA/$Ir(ppy)_3$:CBP interface remained unchanged. This significant structural change caused no appreciable difference in the photoluminescence of the stack although such a change would have a dramatic effect on the charge transport through the device leading to changes in performance. These results demonstrate the effect of thermal stress on the delicate interplay between the chemical composition and morphology of OLED films.

5.2 Introduction

Organic light-emitting diode (OLED) materials fall into three main classes; small molecules,[3,24] conjugated polymers,[227] and dendrimers[122,228] with small molecules being generally processed by evaporation under high vacuum while polymers and dendrimers are solution processed. While the early work on OLEDs focused on fluorescent materials the discovery that phosphorescent materials could be used in the light-emitting layer led to a step change in device performance.[3,21,24,41] At the vanguard of this revolution has been the development of iridium(III) complexes with materials that emit from saturated blue through to red being reported.[4] Since the first results much effort has gone into improving the performance in terms of efficiency and lifetime of phosphorescent based OLEDs. The most efficient OLEDs based on small molecule phosphorescent iridium(III) complexes are now reported to have essentially 100% internal quantum efficiencies.[41,229] The reason why such high efficiencies are achievable is that both the singlet and triplet excitons that are formed in the device can be captured for emission. These highly efficient devices tend to have complicated architectures with numerous layers and the emissive layer comprised of a phosphorescent iridium(III) complex blended with a host material which is generally the major component. For example, blends of *fac*-tris(2-phenylpyridyl)iridium(III) [$Ir(ppy)_3$] in 4,4′-bis(*N*-carbazolyl)biphenyl (CBP) (Figure 5.1) typically comprise between 6-8 weight percent (wt%) of the complex in the

most efficient devices.[21] While efficiencies of OLEDs have risen quickly the task of preparing OLEDs with lifetimes suitable for displays and lighting has proved challenging. Intrinsic factors such as photochemical, electrochemical, and thermal degradation of the active layers,[61,140,230,231] and extrinsic factors including encapsulation and layer adhesion all effect the lifetime of OLEDs.[27] However, in addition to the intrinsic and extrinsic factors the morphological stability of the layers in the device can affect device efficiency and lifetime. This latter factor is particularly important for OLEDs based on small molecule phosphorescent iridium(III) complexes due to the differing thermal properties of the materials in the different layers, and the fact that the complex is blended in a host. In fact with blends it is difficult to elucidate whether the guest is evenly distributed throughout the film or whether there are concentration variations in parts of the film.

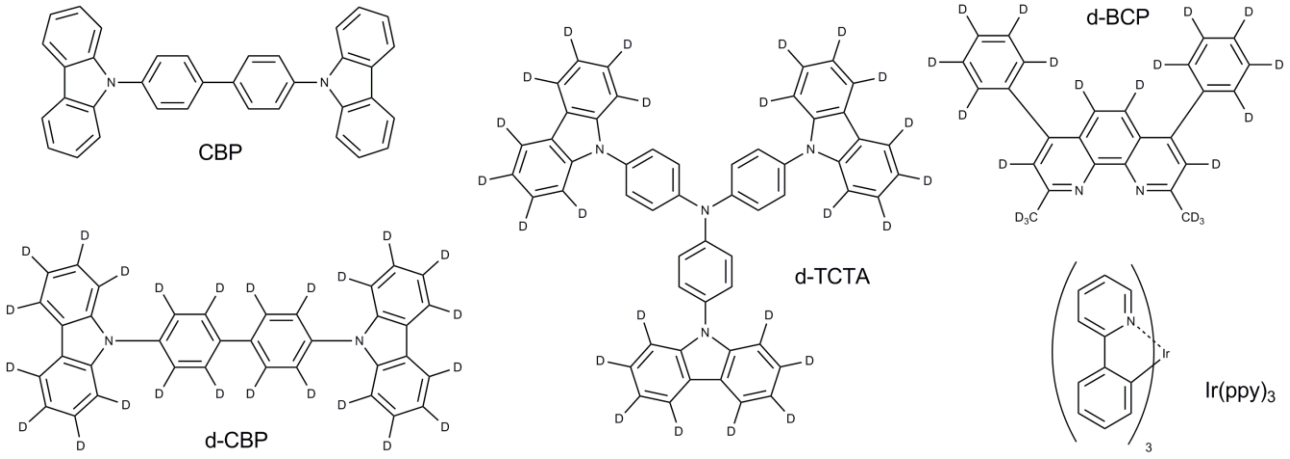

Figure 5.1 Structures of the materials used in this study. D represents deuterium and shows the positions that are at least partially deuterated.

The ability to relate the physical structure with the optoelectronic properties of a film is a challenge. One recently reported method uses a combination of grazing incidence wide angle X-ray scattering and optical reflectance to probe the structure of pentacene films.[232] However, X-ray reflectometry is not the ideal technique for studying the structure of multilayers or blends where the electron density is similar in each of the materials. A more powerful technique for probing such structures is neutron reflectometry (NR). NR is an excellent method for investigating the internal structure of thin (typically <1000 Å) films perpendicular to the substrate. In blended films, where there may be vertical phase separation of the components within the blend, judicious deuteration enables differentiation of the components in the blend and any separation to be observed. In the case of multilayer structures a combination of deuterated and protonated layers can give excellent contrast in the NR experiment. In this context NR has been used to study the physical structure of films of conjugated materials on silicon wafers[233-236] and indium tin oxide.[158,159,237] A combined *in situ* NR/photoluminescence (PL) measurement allows the simultaneous collection of the neutron

reflectivity data and emission spectrum.[158] An additional feature of the experiment is that the sample can be heated *in situ* thus enabling the direct determination of the effect of annealing on the physical and photophysical properties.

The combined NR/PL technique was used to study blends of $Ir(ppy)_3$ in CBP and the effect of thermal annealing. The morphological stability of the film is dependent on the wt% of the $Ir(ppy)_3$ in the CBP. In addition, the effects of thermal annealing a three layer structure typical of those found in multilayer phosphorescent OLEDs, tris[4-(carbazoyl-9-yl)phenyl]amine (TCTA)/$Ir(ppy)_3$:CBP/bathocuproine (BCP), and show that the BCP diffuses into a blended $Ir(ppy)_3$:CBP layer even at modest temperatures. In contrast the TCTA was found to give a well-defined interface with the $Ir(ppy)_3$:CBP layer with no diffusion occurring at elevated temperatures. The thermal annealing temperatures are to those which the devices might encounter during their lifetime.

5.3 Neutron Reflectometry

Neutron reflectometry is a specular scattering technique which probes the structure of films normal (perpendicular) to a surface.[238-240] Many of the principles discussed below apply to the complementary technique of X-ray reflectometry (XRR). Films studied with NR usually range from 10 – 1000 Å in thickness (henceforth Ångströms will be used to describe thickness), a restriction which is dependent on specific sample properties and instrument setup.

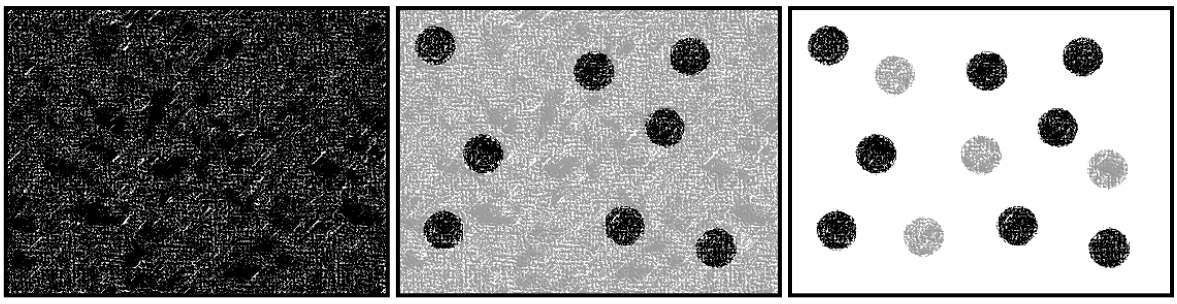

Figure 5.2 In a fully protonated system no structural features can be distinguished by neutron scattering (left). By selective deuteration different features can be revealed in a sample which would otherwise be chemically homogeneous (middle). Further tuning the contrast allows even more information about the structure to be extracted (right). This ability is unique to neutron scattering, and is impossible with X-rays.

The scattering power of neutrons is dependent on the nuclear composition of the scattering atom, whereas X-ray scattering depends only on atomic number (X-rays are scattered by electrons, so scattering power increases linearly with atomic number). Isotopic substitution can have a dramatic effect on the neutron scattering power. In particular hydrogen (^1H) and deuterium (^2H) have vastly different neutron scattering lengths (-3.74 fm *versus* 6.67 fm respectively),[241] which makes selective

deuteration a potent attribute of neutron scattering. By carefully controlling the contrast ratio it becomes easier to examine systems which would otherwise be chemically homogenous (Figure 5.2).

The bulk scattering power of a material is given by its scattering length density (SLD). The SLD of a material is a product of the bound coherent scattering lengths (b), density (ρ), molecular weight (MW) and Avogadro's number (N_A).

$$SLD = \frac{\rho N_A \sum_i b_i}{MW} \quad \textbf{5.1}$$

In a typical NR experiment a collimated beam of neutrons impinges a surface at an incident angle θ_i which is reflected back from the surface at an angle θ_r; specular reflection occurs when $\theta_i = \theta_r$ following the conventional rules of optical reflection (Snell's law; Figure 5.3). Total external reflection of the incident beam occurs *below* a critical angle, θ_c. The ratio between incident (I_i) and reflected (I_r) beam intensity is referred to as the reflectivity and is plotted according to the momentum transfer vector Q, which is related to the angle of reflection and the wavelength of the incident radiation by Equation 5.2.

$$Q = \frac{4\pi sin\theta}{\lambda} \quad \textbf{5.2}$$

Q is dependent on both the scattering angle and the incident radiation wavelength, therefore reflectivity can be measured either at constant θ or λ. Particles with non-zero rest mass (such as neutrons) are governed by the de Broglie relationship, therefore the energy, wavelength and velocity of a particle are all intimately connected. Neutron measurements collected in time-of-flight (ToF) mode make use of this relationship by generating pulses of thermal neutrons with a characteristic spectrum and timing the arrival of the scattered neutrons at the detector. Neutrons with shorter wavelengths will reach the detector before neutrons with longer wavelengths, and by knowing the precise flight distance of the neutrons, their velocity, wavelength and energy can be accurately determined. Reflecting the full beam at a fixed angle provides a simultaneous measurement over a wide range of Q without needing to vary the angle, although in practice multiple reflection angles with overlapping Q ranges are often collected and 'stitched' together afterwards. X-ray measurements, on the other hand, are usually performed with a monochromatic X-ray source and the angle of reflection is varied.

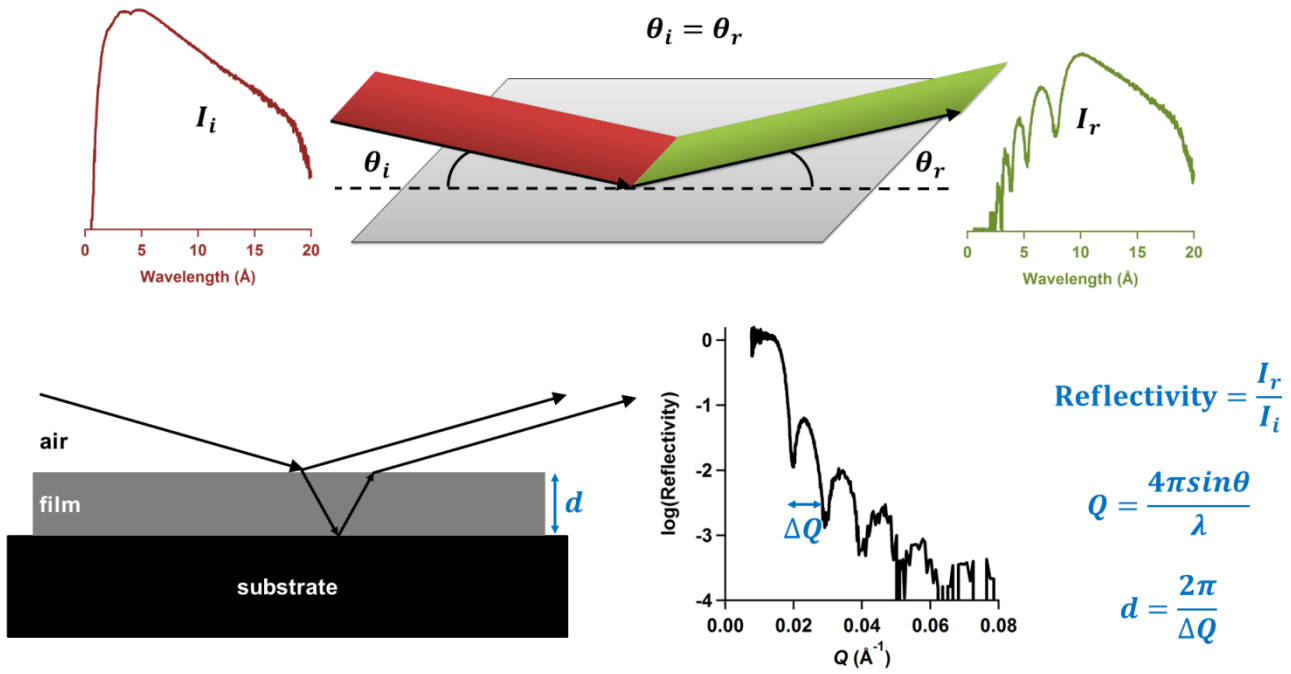

Figure 5.3 Time-of-flight neutron reflectometry uses a pulsed beam of collimated neutrons with a characteristic incident spectrum (I_i) and reflected neutron spectrum (I_r). In this case the angle of incidence is 0.7° and total reflection occurs for neutrons with a wavelength >10 Å. The reflectivity is determined from the ratio of reflected and incident beams and is plotted according to the momentum transfer vector Q. In this example the fringe pattern of the measured reflectivity is typical of a single layer film with characteristic thickness d. The Kiessig fringe spacing (ΔQ) can be used to estimate the film thickness. Bragg peaks (if present) indicate higher order structure, and would be observed in a multilayer film with a constant repeat element.

The reflectivity derived from a surface can be used to determine the underlying structure of the surface. The appearance of Kiessig fringes is due to the interference pattern arising from the constructive and destructive scattering of neutrons and X-rays as they pass through layers with different SLDs. When a single layer film is being studied, the film thickness d can be estimated from the fringe spacing ΔQ by

$$d = \frac{2\pi}{\Delta Q} \qquad \textbf{5.3}$$

More complicated reflectivity patterns arise from multilayer films and the Fourier transform of the Kiessig fringe spacing can be used to estimate the total film thickness, and the thickness of the individual components of the multilayer. Bragg peaks, if present, are due to higher order scattering arising from a repeat unit in the film, and can be observed in, for example, a multilayer film of repeated protonated/deuterated layers.[242] However, reconstructing the film structure from the measured reflectivity is generally determined by modelling methods which can be used to precisely calculate the thickness, density and roughness of multiple layers within a film.[243]

5.4 Experimental

5.4.1 Organic Synthesis

$Ir(ppy)_3$, CBP and d-CBP were all synthesised for this work. $Ir(ppy)_3$ was prepared according to literature procedures.[62,76,244] CBP was deuterated via a platinum catalysed hydrothermal exchange reaction, similar to those described in the literature.[245-247] The complete CBP molecule was deuterated rather than preparing deuterated carbazole and biphenyl precursors. This reduced the number of chemical and deuteration reactions.

d-TCTA and d-BCP were supplied by the Australian National Deuteration Facility. d-TCTA, and d-BCP had deuteration levels of 63% and 70% respectively.

5.4.1.1 General Synthetic Details

Organic solvents were distilled before use. The proportions of solvent mixtures are given by volume. Chemical deuterations were performed using a 100 mL Parr stirred pressure reactor. Mass spectrometry was performed with either a Voyager DE STR MALDI-TOF or a Finnigan MAT 900 XL – Trap. ^1H NMR spectra were recorded on a Bruker AV300 spectrometer (300 MHz), and ^2H NMR on a Bruker AV400 spectrometer (operating in ^2H mode at 60 MHz). Chemical shifts are reported in parts per million (ppm) and are referenced to the residual solvent peak. Peak multiplicities are described as doublet (d), triplet (t) or multiplet (m). Luminescence spectra were recorded on a Horiba Jobin-Yvon Fluorolog-3 Tau or FluoroMax-4. Absorption spectra were measured on a Varian Cary 5000 UV-vis-NIR spectrophotometer.

5.4.1.2 Fac-tris(2-phenylpyridyl)iridium(III) [Ir(ppy)$_3$]

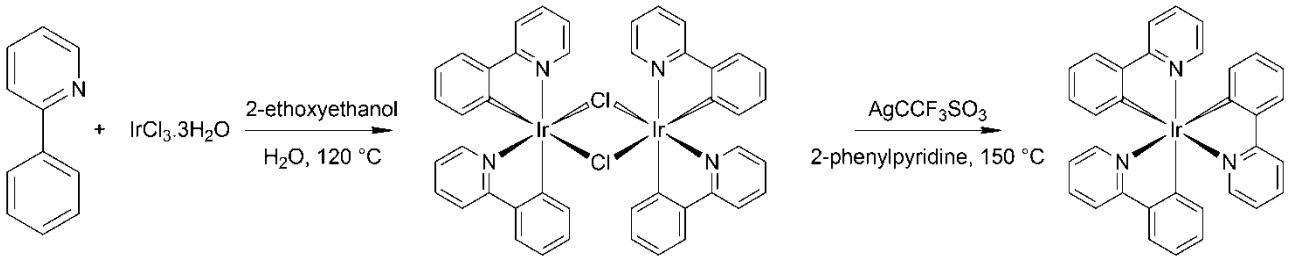

2-Phenylpyridine (4.02 g, 25.9 mmol), iridium(III) chloride hydrate (2.00 g, 5.7 mmol), 2-ethoxyethanol (20 mL) and water (7 mL) were combined in a Schlenk tube. The reaction was sealed under argon and heated to reflux (120 °C). The mixture changed colour from black to bright yellow, indicating formation of the iridium dimer. The reaction proceeded for two days after which the mixture was cooled to room temperature. The solid product was collected on a sintered funnel and washed with ethanol, methanol and acetone. The remaining yellow solid was dried under high

vacuum to afford the chloro-bridged dimer $[Ir(ppy)_2Cl]_2$ (2.57 g). $[Ir(ppy)_2Cl]_2$ (1.00 g, 0.9 mmol), 2-phenylpyridine (5.36 g, 34.5 mmol) and silver triflate (0.49 g, 1.9 mmol) were combined in a round bottom flask. The vessel was degassed, sealed under argon and heated to reflux (130 °C). The reaction proceeded for 1 day, after which the mixture was allowed to cool to room temperature. The mixture was purified by column chromatography over silica using dichloromethane as eluent to afford *fac*-$Ir(ppy)_3$ as a yellow solid (1.11 g, 30% total conversion). δ^1H (300 MHz, DMSO-d_6): 6.62-6.70 (m, 6H), 6.79 (t, J=7.2 Hz, 3H), 7.12 (t, J=6.5 Hz, 3H), 7.47 (d, J=4.6 Hz, 3H), 7.74 (d, J=8.3 Hz, 3H), 7.78 (t, J=8.2 Hz, 3H), 8.12 (d, J=8.3 Hz, 3H). *m/z* [EI] calculated $[C_{33}N_3H_{24}Ir]^+$ 653.2 (57%), 654.2 (21%), 655.2 (100%), 656.2 (36%); found $[M]^+$ 653.4 (61%), 654.4 (41%), 655.4 (100%), 656.4 (32%). The eight integrated ^1H NMR resonances are consistent with the *facial* isomer and literature spectra.[76,77,79]

5.4.1.3 4,4'-bis(N-carbazolyl)biphenyl (CBP)

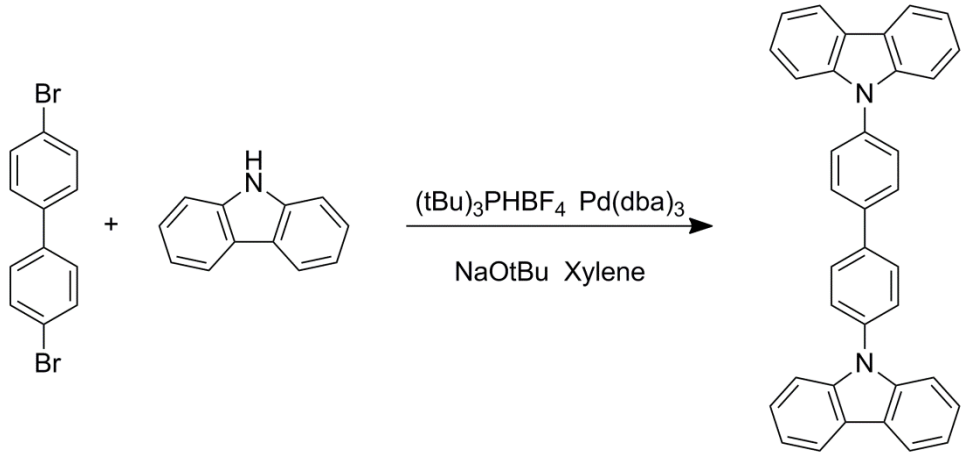

4,4′-Dibromobiphenyl (1.03 g, 3.3 mmol), carbazole (1.28 g, 7.7 mmol), sodium *tert*-butoxide (1.66 g, 17.3 mmol), tri-*tert*-butylphosphonium tetrafluoroborate (186 mg, 0.64 mmol) and tris[dibenzylideneacetonedipalladium(0)] (165 mg, 0.16 mmol) were combined in a Schlenk tube under a constant stream of argon. The vessel was sealed and freshly distilled anhydrous xylene (20 mL) was injected through a rubber septum. The solution was degassed under vacuum five times before being resealed under argon with a glass stopper. The reaction was heated at 130 °C for 3 days. After cooling, diethyl ether (20 mL) and water (20 mL) were added and the layers separated. The organic phase was extracted with water (2 x 50 mL), and the aqueous phase with dichloromethane (2 x 20 mL). The organic fractions were combined and the solvent removed under reduced pressure. The residue was purified by column chromatography over silica using dichloromethane:*n*-hexane (1:4) as eluent to afford CBP as a white solid (1.24 g, 83%). δ^1H (300 MHz, $CDCl_3$): 7.30 (t, J=7.4 Hz, 4H), 7.44 (t, J=7.5 Hz, 4H), 7.47-7.53 (m, 4H), 7.70 (AA′, J=8.7Hz 4H), 7.91 (BB′, J=8.4Hz, 4H), 8.16 (d, J=7.8 Hz, 4H). *m/z* [MALDI] calculated

$[C_{36}N_2H_{24}]^+$ 484.2 (100%), 485.2 (40%), 486.2 (8%); found $[M]^+$ 484.2 (100%), 485.2 (52%), 486.2 (7%). Literature spectra are consistent with the ^{1}H NMR and molecular mass.[130,248,249]

5.4.1.4 Per-deutero-4,4'-bis(N-carbazolyl)biphenyl (d-CBP)

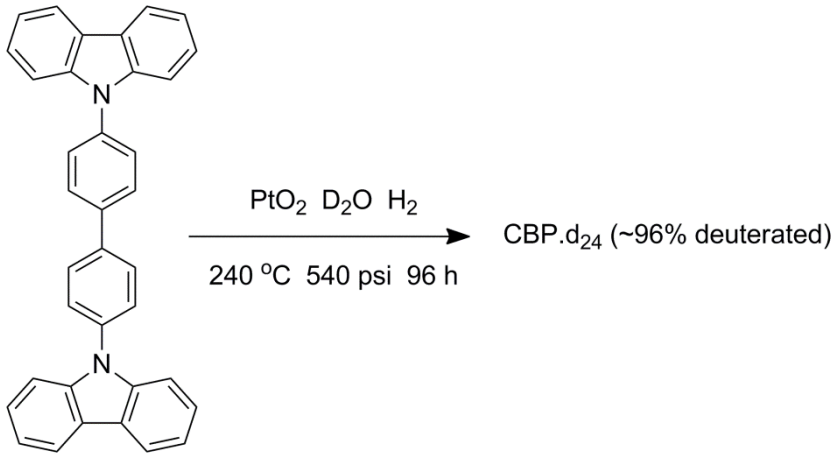

4,4′-Bis(*N*-carbazolyl)biphenyl (CBP) (1.00 g, 2.1 mmol), platinum(IV) oxide (302 mg, 1.3 mmol) and deuterium oxide (40 mL) were combined in the reactor which was then sealed. With constant stirring, the reactor was purged with nitrogen five times, purged with hydrogen five times, and then left under a 60 psi hydrogen atmosphere. The reactor was heated to 240 °C at which point the pressure inside the reactor reached 3.7 MPa. The reaction proceeded under these conditions for four days. After cooling, the reactor was purged with nitrogen to remove the remaining hydrogen. The mixture was extracted with dichloromethane (2 x 100 mL), and the organic and aqueous layers were separated. The organic fraction was dried with magnesium sulfate, filtered and the solvent removed under reduced pressure. The residue was purified by column chromatography over silica using dichloromethane as eluent. This afforded d-CBP as an off-white solid (0.77 g, 73%). δ^1H (300 MHz, $CDCl_3$): very weak singlets at 7.31, 7.44, 7.51, 7.71, 7.91, 8.16. δ^2H (60 MHz, $CHCl_3$): 7.35 (sh), 7.47, 7.73, 7.94, 8.18 (sh). *m/z* [EI] calculated $[C_{36}N_2D_{24}]^+$ 508.3 (100%), 509.3 (40%), 510.4 (8%); found $[M]^+$ 505.3 (4%), 506.5 (15%), 507.6 (48%), 508.5 (100%), 509.6 (30%), 510.6 (5%). An isotopic distribution of $C_{36}N_2D_{24}$, $C_{36}N_2H_1D_{23}$ and $C_{36}N_2H_2D_{22}$ in the ratio 82:17:1 yields a calculated mass spectrum of 506.3 (15%), 507.3 (48%), 508.3 (100%), 509.3 (36%), 510.4 (7%). λ_{abs} (CH_2Cl_2)/nm : 293 (logε/$M^{-1}cm^{-1}$, 4.59), 318 (4.47), 339 (4.35). λ_{em} (CH_2Cl_2)/nm: 378. Optical absorption and emission are consistent with the literature of protonated CBP.[130,248,250]

Comparing the ^{1}H NMR of CBP, and the ^{2}H NMR of d-CBP the features of the two spectra are similar (Figure 5.4). Only aromatic deuterium signals were detected. The ^{2}H NMR is significantly broader than the ^{1}H NMR due to the lower resolution of the measurement (60 *versus* 300 MHz), and the extra spin projections that an s=1 atom can relax through. The average deuteration of d-CBP

was calculated from the integrated signal of the residual ^{1}H NMR which was measured against an internal cyclohexane standard. d-CBP was calculated to be 96% deuterated, which is consistent with the isotopic mass analysis and the high SLD (5.9±0.1 × 10^{-6} Å^{-2}) determined by NR (see below, 5.5.1.1).

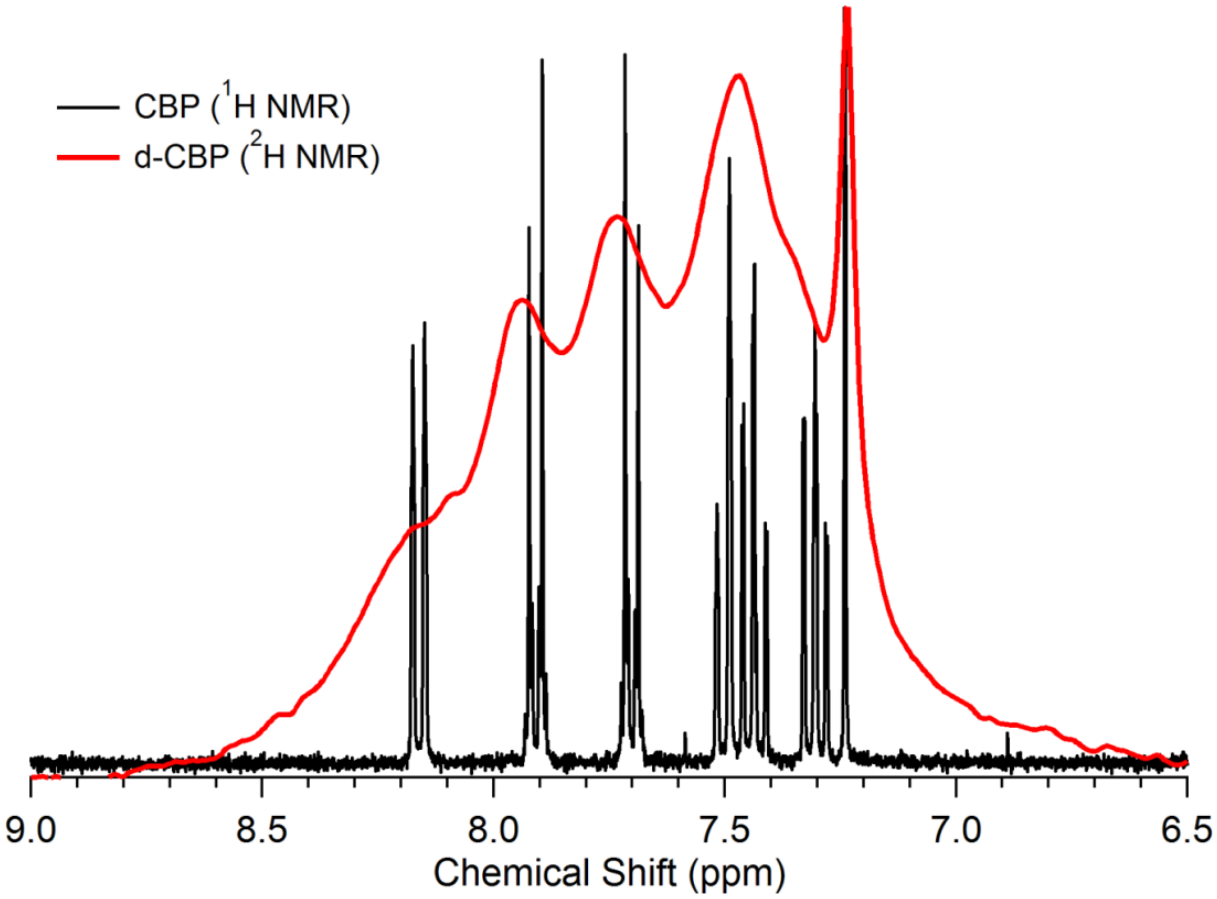

Figure 5.4 Comparison of the proton and deuterium NMR spectra of CBP and d-CBP respectively. The ^{2}H NMR is significantly broader due to lower resolution of the measurement (60 *versus* 300 MHz) and the extra atomic spin levels that exist for s=1. Despite this the deuterium NMR of d-CBP shows similar features to the proton NMR of CBP.

5.4.2 Film Preparation

Films were prepared by thermal evaporation under high vacuum (~10^{-6} mbar) onto silicon wafers and quartz substrates. Silicon wafers (Si-Mat, Germany) of 50 mm diameter and quartz slides (H. A. Groiss & Co., Australia) were cleaned with piranha solution (a 2:1 mixture of sulfuric acid and 30% hydrogen peroxide). The silicon wafers had a native oxide layer, which was not removed. Prior to film deposition the substrates were sonicated in acetone for 5 min, rinsed with 2-propanol and then dried under a stream of clean nitrogen. Film thicknesses were measured with a Veeco Dektak 150 Surface Profilometer. Atomic Force Microscope (AFM) images were obtained using an

Asylum Research MFP-3D Atomic Force Microscope operated in AC mode, placed on a Herzan anti-vibration table within a TCM acoustic isolation enclosure (Herzan, CA, USA). TAP 300 cantilevers (Budget Sensors, Bulgaria) driven close to their resonant frequency, 300 kHz, at scanning rates between 0.4 to 0.6 Hz were used for all the samples. Luminescence spectra were recorded on a Horiba Jobin-Yvon Fluorolog-3 Tau or FluoroMax-4. Absorption spectra were measured on a Varian Cary 5000 UV-vis-NIR spectrophotometer.

5.4.3 Neutron Reflectometry

Neutron reflectivity experiments were made on the 'white beam' reflectometer SURF at the Rutherford-Appleton Laboratory, United Kingdom. The wavelength of the neutrons used ranged from 0.55 Å < λ < 6.8 Å. Blank silicon wafer measurements were performed for substrate characterization. A flat background, determined by extrapolation to high values of momentum transfer Q ($Q = (4\pi \sin \theta)/\lambda$, where θ is the glancing angle of incidence and λ the wavelength) was subtracted. Reflectivity profiles were measured at incident angles 0.25°, 0.5°, and 0.8° or 0.35° and 0.8° taking ~3 hours with the data reduced to yield a single reflectivity profile for fitting. NR measurements were also recorded using the Platypus time-of-flight neutron reflectometer and a cold neutron spectrum (2.8 Å < λ < 18.0 Å) at the OPAL 20 MW research reactor [Australian Nuclear Science and Technology Organisation (ANSTO), Sydney, Australia].[251,252] 20 Hz neutron pulses were generated using a disk chopper system (EADS Astrium GmbH) in the medium resolution mode ($\Delta\lambda/\lambda$ = 4%) and recorded on a 2-dimensional helium-3 neutron detector (Denex GmbH). Reflected beam spectra were collected at 0.5° for 1 h (0.2 mm slits) and 2.0° for 2 h (0.8 mm slits). Direct beam measurements were collected under the same collimation conditions. A custom built experimental cell was used for simultaneous NR and PL measurements, with *in situ* annealing capabilities. The luminescence of the films was monitored with an Ocean Optics USB2000 spectrometer using a Nichia UV-LED 365 nm excitation source. An aluminium block heating stage, isolated from the neutron cell by a ceramic stand, was heated (10 K min^{-1} during ramp) with two cartridge heaters and the temperature controlled by a Watlow series 988 temperature controller. The cell was under vacuum (~1 mbar) during all experiments. Analysis of the reflectivity profiles was performed using the Motofit reflectometry analysis program.[243,253] All the NR fits included a ~12 Å oxide layer on the surface of the substrate.

5.4.4 Microscopy

Luminescence microscopy images were obtained on a Nikon Eclipse TE2000-E microscope with a Cairn 150 W xenon arc lamp and an Olympus IX70 microscope with a mercury lamp UV excitation source.

5.5 Results and Discussion

5.5.1 $Ir(ppy)_3$:CBP Blend Films

An integral part of the study was determining the effect of thermal annealing on the blended and multilayer films. Previous accelerated degradation tests on OLEDs have been done in the temperature range from room temperature to 100 °C[137] and hence thermal annealing was limited to less than or equal to 100 °C. It is important to note that temperatures of this magnitude are realistic for real applications. For example, temperatures in multilayer OLEDs have been measured to be above ambient[143] and as high as 86 °C.[142] In addition, it is not just the temperature of the device that is important but the environment in which the device is being used or stored. For example, the ambient cabin temperature in a car on a hot summer's day can easily exceed 80 °C.[144,145]

In the first part of this study the composition of $Ir(ppy)_3$:d-CBP blended films was investigated. Three film combinations were prepared; neat d-CBP and d-CBP:$Ir(ppy)_3$ blends (where the prefix d- denotes the molecules where a least a portion of the protons are replaced by deuterons) with nominal composition of 6 wt% and 10 wt% of $Ir(ppy)_3$ based on relative evaporation rates. The photoluminescence (PL) spectra of the films on quartz are shown in Figure 5.5. The films were excited at 340 nm thus enabling excitation of both the d-CBP and the $Ir(ppy)_3$. The neat d-CBP film was found to have an emission maximum at 393 nm, consistent with the emission observed from protonated CBP.[130] In contrast the emission (λ_{em} = 516 nm) from both blend concentrations was entirely from the $Ir(ppy)_3$ indicating that the $Ir(ppy)_3$ was distributed such that it was within the diffusion length of an exciton formed on the d-CBP.

5.5.1.1 Neat d-CBP

The NR and PL of the films were measured on the SURF reflectometer. The films were measured under vacuum at 25 °C, 50 °C, and 80 °C before being allowed to cool to room temperature. The films were held at each elevated temperature for around ten minutes before the NR profile was collected. The reflectivity profiles, scattering length density (SLD) *versus* thickness, and PL spectra of the neat d-CBP film after annealing at different temperatures are shown in Figure 5.6.

At 25 °C the NR profile could be modelled with the bulk of the film having a thickness of 638±7 Å and a SLD of 5.9±0.1 × 10^{-6} $Å^{-2}$. In addition, the best fit to the NR profile included a low density layer with a thickness of ~15 Å and a SLD of 2.5±1.1 × 10^{-6} $Å^{-2}$ at the silicon/d-CBP interface, and a thin (typically less than 20 Å) dense layer (SLD of 7.0±0.5 × 10^{-6} $Å^{-2}$) at the d-CBP/air interface (see Figure 5.6b). Low-density layers have previously been observed at conjugated polymer/substrate interfaces.[159] The dense layer at the d-CBP/air interface could be due to the

presence of a highly structured, possibly crystalline layer, which forms at the surface after film preparation.

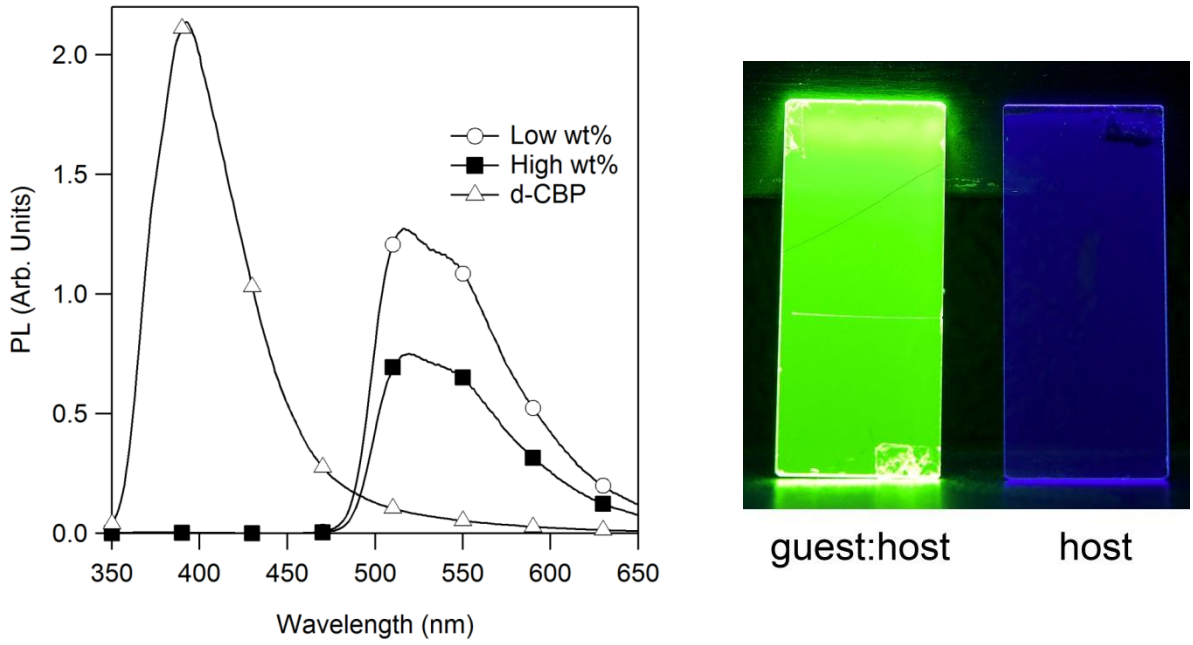

Figure 5.5 PL spectra of films of neat d-CBP and nominally 6 wt% (low) and 10 wt% (high) guest:host blends of $Ir(ppy)_3$ in d-CBP. The films were excited at 340 nm which enables excitation of both the d-CBP and the $Ir(ppy)_3$. No emission from the d-CBP is observed in the blended films, indicating efficient energy transfer from host to guest.

On heating to 50 °C the NR profile only changed a small amount, with the neutron fit being consistent with the film having expanded slightly and becoming a little less dense. However, between 50 °C and 80 °C there was a substantial change to the NR profile with a significant shift of the critical edge from 0.018 to 0.013 $Å^{-1}$ and it was no longer possible to fit the NR profile with a simple model. The *in situ* PL measurements gave important insight to the changes that had occurred in the film (Figure 5.6c). In the experimental set up the UV excitation source is incident on the sample at an angle of 45° with detector placed normal to the substrate. This arrangement is designed to minimize detection of the excitation light, which occurs due to scattering. Nevertheless, in the case where the film is completely smooth (Figure 5.6e) a small level of scattered or reflected excitation light is always detected and hence the PL spectrum has two components; one peak at 365 nm corresponding to reflected excitation light and the second due to the luminescence of the film under interrogation. For the neat film of CBP at 25 °C the ratio of the reflected light to the PL of CBP is relatively small (Figure 5.6c).

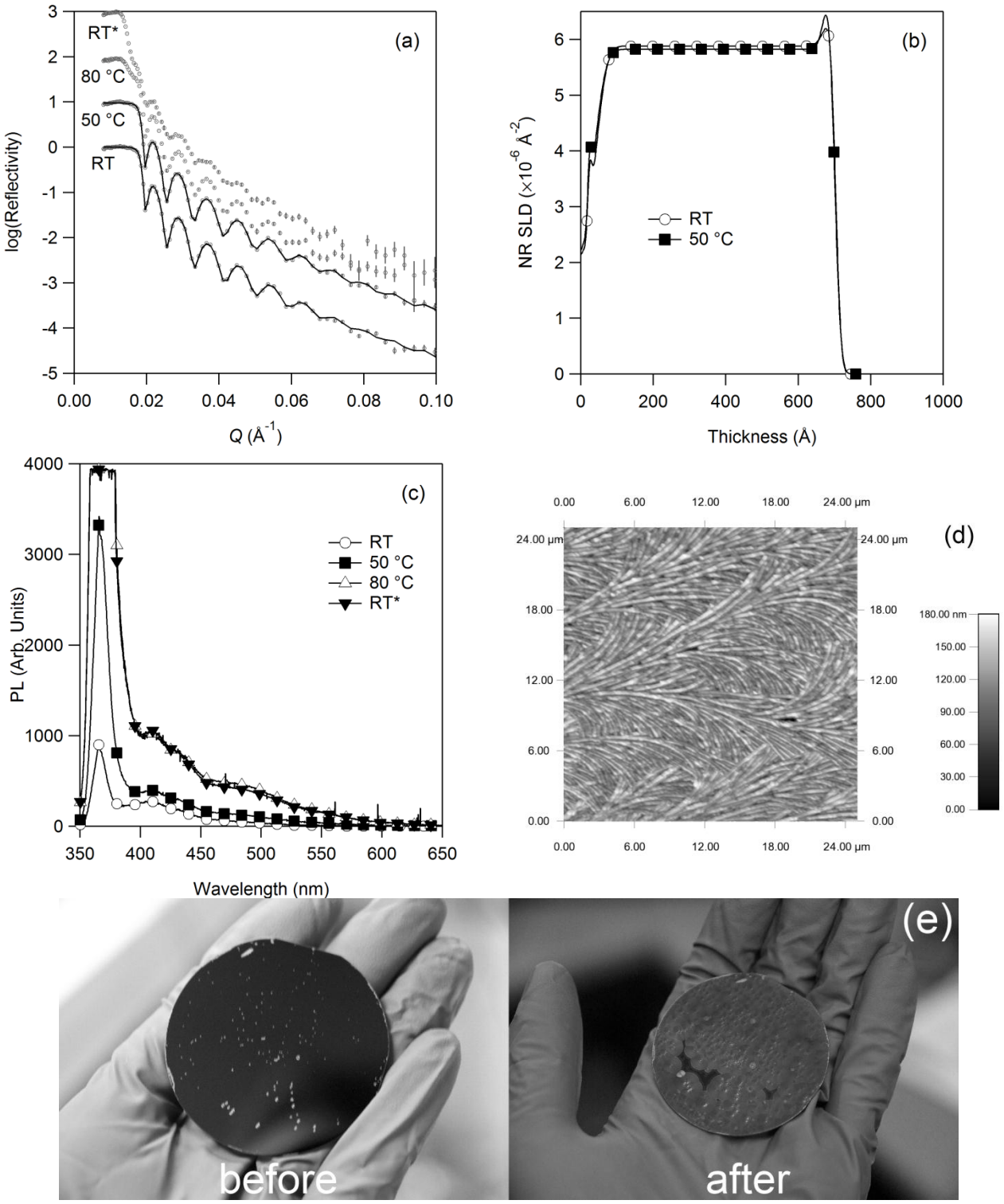

Figure 5.6 (a) NR profiles collected for the d-CBP film. The points are the NR data and the solid lines the fit to the profile. (b) SLD *versus* thickness for the d-CBP film. (c) *In situ* PL measurements for the d-CBP film. (d) AFM image of the neat d-CBP film after annealing and cooling to room temperature. Fibre-like structures spread across the film surface radiating outwards to form disc structures on the macro scale. (e) Neat d-CBP film before and after annealing to 80 °C.

However, on heating to 50 °C and then 80 °C the reflected excitation beam dominates the emission from the CBP, and this is consistent with the surface of the film becoming significantly rougher.

That is, even at these relatively low temperatures there are significant changes in the surface morphology of the film. On cooling to room temperature the amount of reflected excitation beam becomes even larger. Microscopy measurements on the film (Figure 5.6d) reveal that fibre-like structures which propagated radially outward forming circular disc like structures (Figure 5.6e) formed during the thermal anneal, indicating that crystallization has at least occurred on the surface.

5.5.1.2 Low wt% Blend

The blend films were investigated under the same conditions as the neat d-CBP film. Apart from a small low density region at the interface between film and substrate (~25 Å, SLD 2.3±2.4 × 10^{-6} $Å^{-2}$), the profile for the 6 wt% blend (Figure 5.7) could be fitted as a single layer. Figure 5.7b shows the SLD *versus* film thickness at the different temperatures. This is an important result as it provides physical evidence for the first time that homogeneous co-evaporated films can be prepared. That is, there is no localisation of either component within a specific layer in the film. Up to 80 °C there was little change in the NR profile suggesting that the film structure was quite stable. The SLD of the film was measured as 5.6±0.1 × 10^{-6} $Å^{-2}$. Given the SLD of d-CBP is 5.9±0.1 × 10^{-6} $Å^{-2}$ and that of $Ir(ppy)_3$ being 2.0±0.1 × 10^{-6} $Å^{-2}$ (determined from a bilayer Si/$Ir(ppy)_3$/d-CBP film, Figure 5.8) the weight percent of $Ir(ppy)_3$ in CBP is calculated to be 6.4±3.6 wt%, which is essentially the same as that expected from the evaporation rates. The PL spectra of the film under the different conditions gave important insight into changes that had occurred in the film during the annealing process (Figure 5.7c). The scattered excitation beam (365 nm) was found to increase relative to the luminescence of the film with each temperature step. The increase in reflected excitation light indicates that the surface roughness has increased in a similar manner as the neat CBP film. There was also weak emission at 400 nm arising from CBP, which shows that during the annealing process phase separation was occurring. That is, there is no longer complete energy transfer from the CBP to the $Ir(ppy)_3$. After annealing and cooling to room temperature crystalline regions (disks) could be clearly seen (Figure 5.7e) and luminescence microscopy (Figure 5.7d and Figure 5.9) revealed that fibre-like phase separation between CBP and $Ir(ppy)_3$ had occurred.

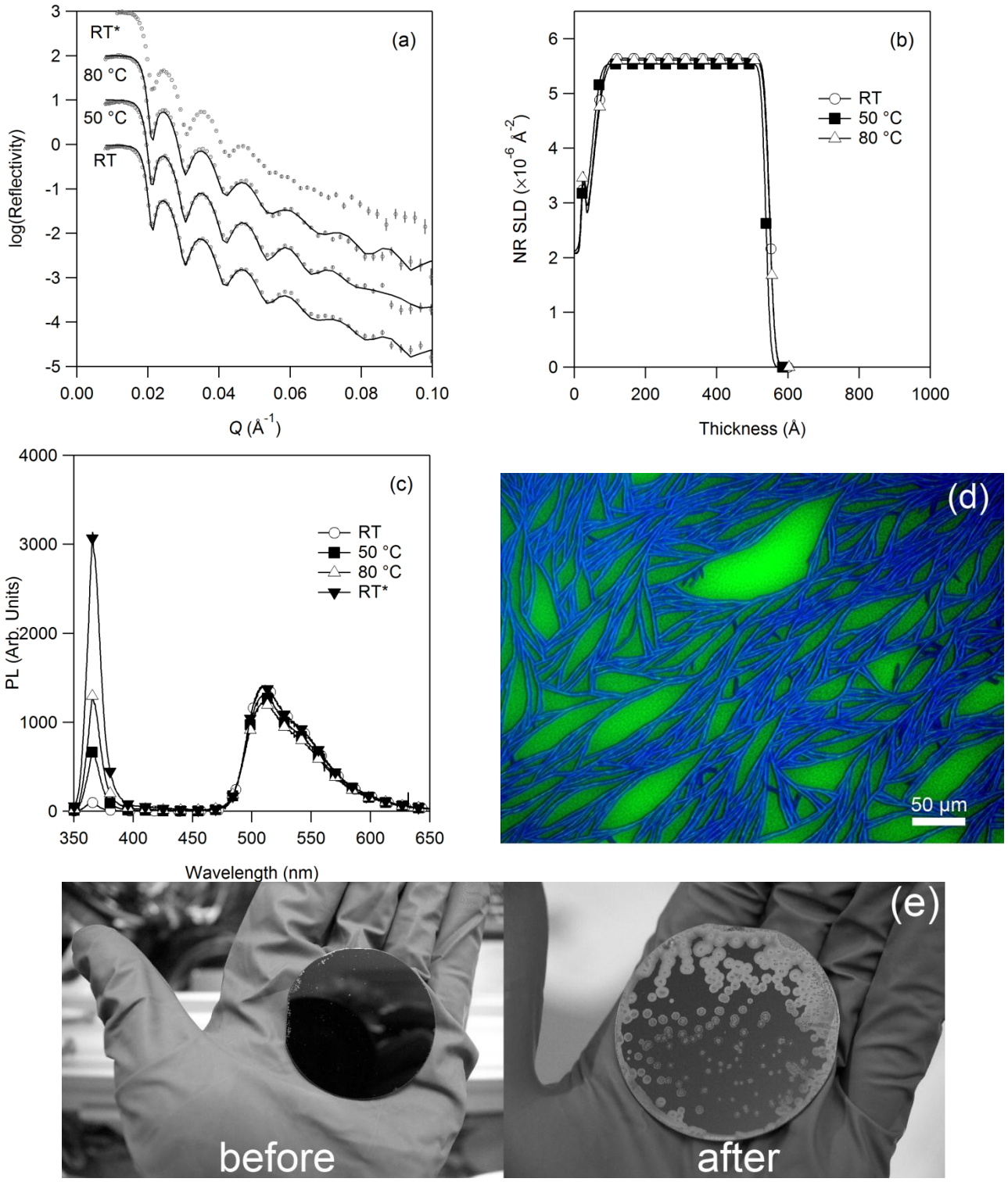

Figure 5.7 (a) NR profiles collected for the 6 wt% blend of Ir(ppy)$_3$ in d-CBP. The points are the NR data and the solid lines the fit to the profile. (b) SLD *versus* film thickness for the 6 wt% blend of Ir(ppy)$_3$ in d-CBP. (c) *In situ* PL measurements for the 6 wt% blend of Ir(ppy)$_3$ in d-CBP. (d) Luminescence microscopy of the 6 wt% blend film, after heating to 80 °C and then cooling. The figure is a composite of two images taken at different excitation and emission wavelengths (blue–340 nm excitation, 370–400 nm capture; green–390 nm excitation, 495–550 nm capture) to discriminate between CBP (blue) and Ir(ppy)$_3$ (green) emission. (e) 6 wt% (low) blend film before and after annealing to 80 °C.

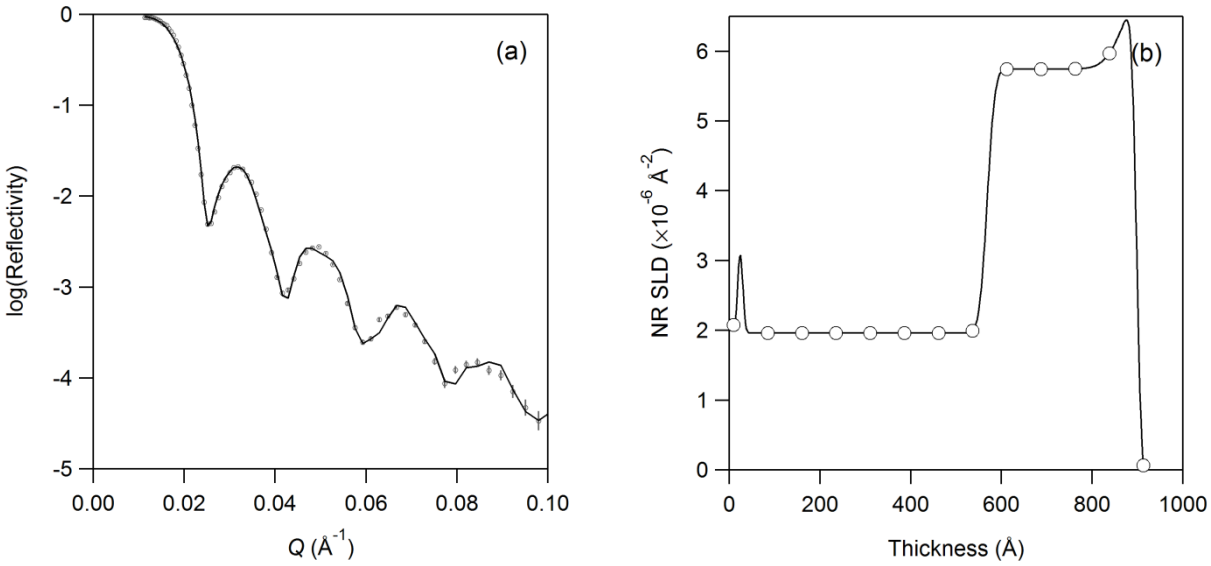

Figure 5.8 (a) NR profiles collected for a bilayer of Ir(ppy)$_3$/d-CBP. The points are the NR data and the solid lines the fit to the profile. (b) The SLD of the Ir(ppy)$_3$ layer was calculated to be 2.0±0.1 × 10^{-6} Å^{-2}.

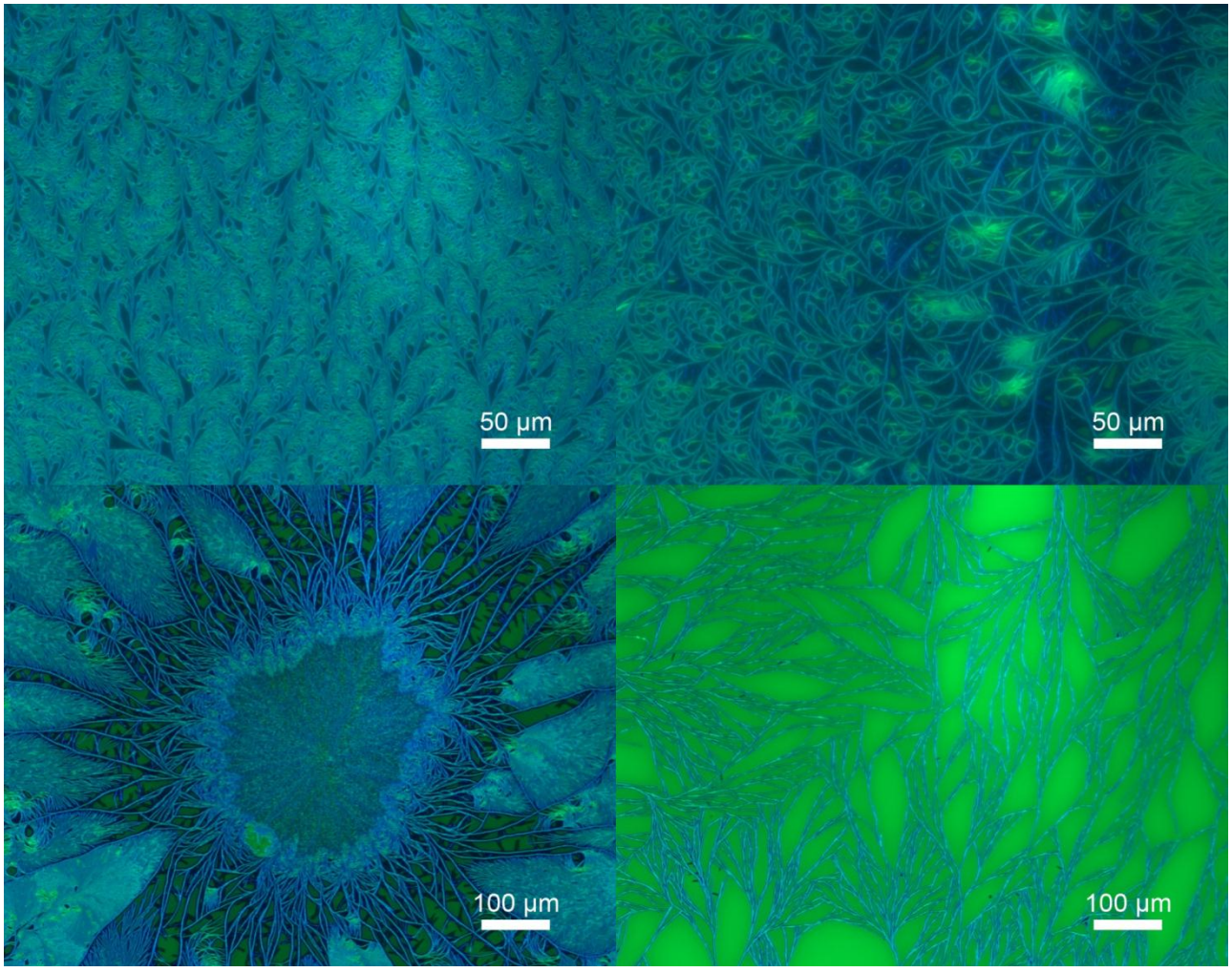

Figure 5.9 Luminescence microscopy images of the 6 wt% (low) Ir(ppy)$_3$:d-CBP blend film heated to 80 °C and then cooled. Films were excited at 365 nm and full colour images captured.

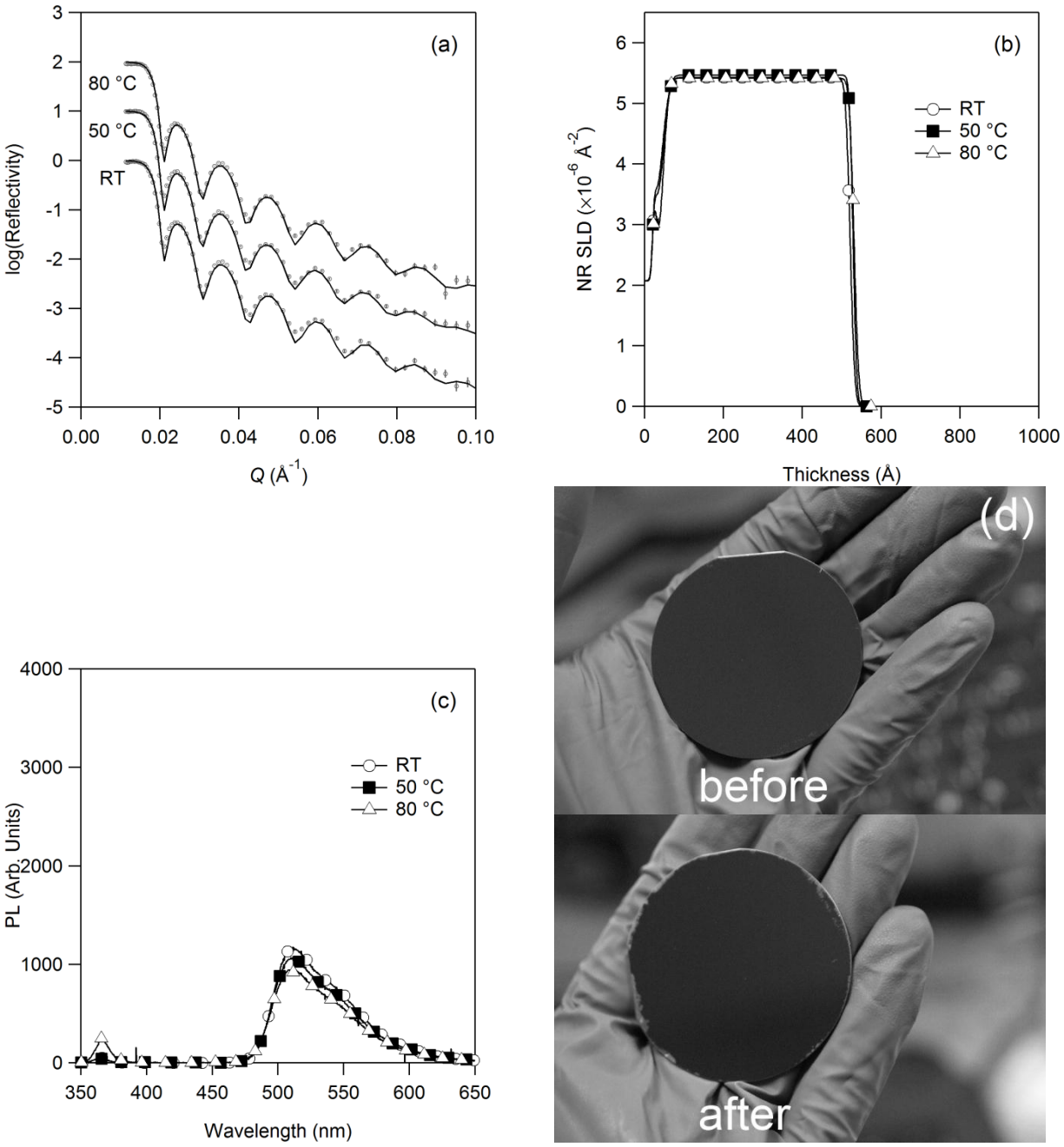

Figure 5.10 (a) NR profiles collected for the 12 wt% blend of Ir(ppy)$_3$ in d-CBP. The points are the NR data and the solid lines the fit to the profile. (b) Scattering length density *versus* film thickness for the 12 wt% blend of Ir(ppy)$_3$ in d-CBP. (c) *In situ* PL measurements for the 12 wt% blend of Ir(ppy)$_3$ in d-CBP. (d) 12 wt% (high) blend film before and after annealing to 80 °C. Note the film has not degraded like that of the 6 wt% blend.

5.5.1.3 High wt% Blend

The higher concentration (nominally 10 wt%) film of Ir(ppy)$_3$ blended with d-CBP was measured while going through the same annealing cycle. At room temperature the NR profile (Figure 5.10a) could be modelled as a single uniform layer showing that even at this higher concentration the Ir(ppy)$_3$ is evenly distributed throughout the film (Figure 5.10b). From the SLD of the film the blend ratio was calculated to be 12.2±3.2 wt%. The lack of change in the NR profile was mirrored

in the PL spectra (Figure 5.10c). At higher temperatures (80 °C) the film remained essentially the same and after cooling there were no obvious crystalline domains (Figure 5.10d). Unlike the low wt% blend the reflected light component of the spectra did not increase dramatically during the thermal annealing process and in addition, no CBP emission was observed. When viewed by luminescence microscopy the entire field of view was saturated green emission, indicating no phase separation between $Ir(ppy)_3$ and CBP.

This is an important result as while films with blend ratios of 6-8 wt% are usually considered the best in terms of device efficiency, higher blend ratios may confer greater operational stability. The effect of the $Ir(ppy)_3$ is straightforward to understand and is similar to the effect of impurities seen in the crystallisation of organic compounds - impurities can hinder the crystal packing. CBP has a strong propensity to crystallise[254] and in the doped film the $Ir(ppy)_3$ is acting as an impurity, which depresses the ability of the CBP to order in the solid state and thus keeping the film amorphous.

5.5.2 Multilayer Film Si/d-TCTA/($Ir(ppy)_3$:CBP)/d-BCP

The final part of the study was to investigate the effect of thermal annealing on a multilayer stack comprised of d-tris(4-carbazoyl-9-ylphenyl)amine (d-TCTA)/($Ir(ppy)_3$:CBP)/d-bathocuproine (d-BCP), with the NR measurements being undertaken using the Platypus reflectometer. Having the TCTA and BCP deuterated and the CBP and $Ir(ppy)_3$ protonated provides substantial scattering contrast and allows each of the layers to be identified as the TCTA and BCP have significantly higher SLDs. The $Ir(ppy)_3$:CBP blend layer was prepared under the same conditions for the low wt% film and hence the concentration was ≈6 wt%. The lack of scattering contrast between the (protonated) CBP and $Ir(ppy)_3$ prevents an accurate determination of the blend ratio by NR.

The observed and fitted NR profiles from this multilayer film before, during and after annealing are shown in Figure 5.11a. It can be clearly seen that the reflectivity profiles are more complicated than for a single uniform film. Figure 5.11b shows the SLD profiles for this multilayer film and it can be seen that at room temperature the as-formed film has sharp interfaces between each of the layers. The film structure is stable to 60 °C, but at 100 °C there is a dramatic change in the profile of the multilayer film. At this modest temperature the model of the NR profile shows that the d-BCP has substantially diffused into the $Ir(ppy)_3$:CBP blend layer. In contrast, the interface between the d-TCTA remains the same showing that it does not diffuse into the 'emissive layer'. Comparison between the 100 °C data and that for the cooled film indicate that during cooling to room temperature the d-BCP continues to migrate into the emissive $Ir(ppy)_3$:CBP layer such that there is only a small amount of pristine $Ir(ppy)_3$:CBP left.

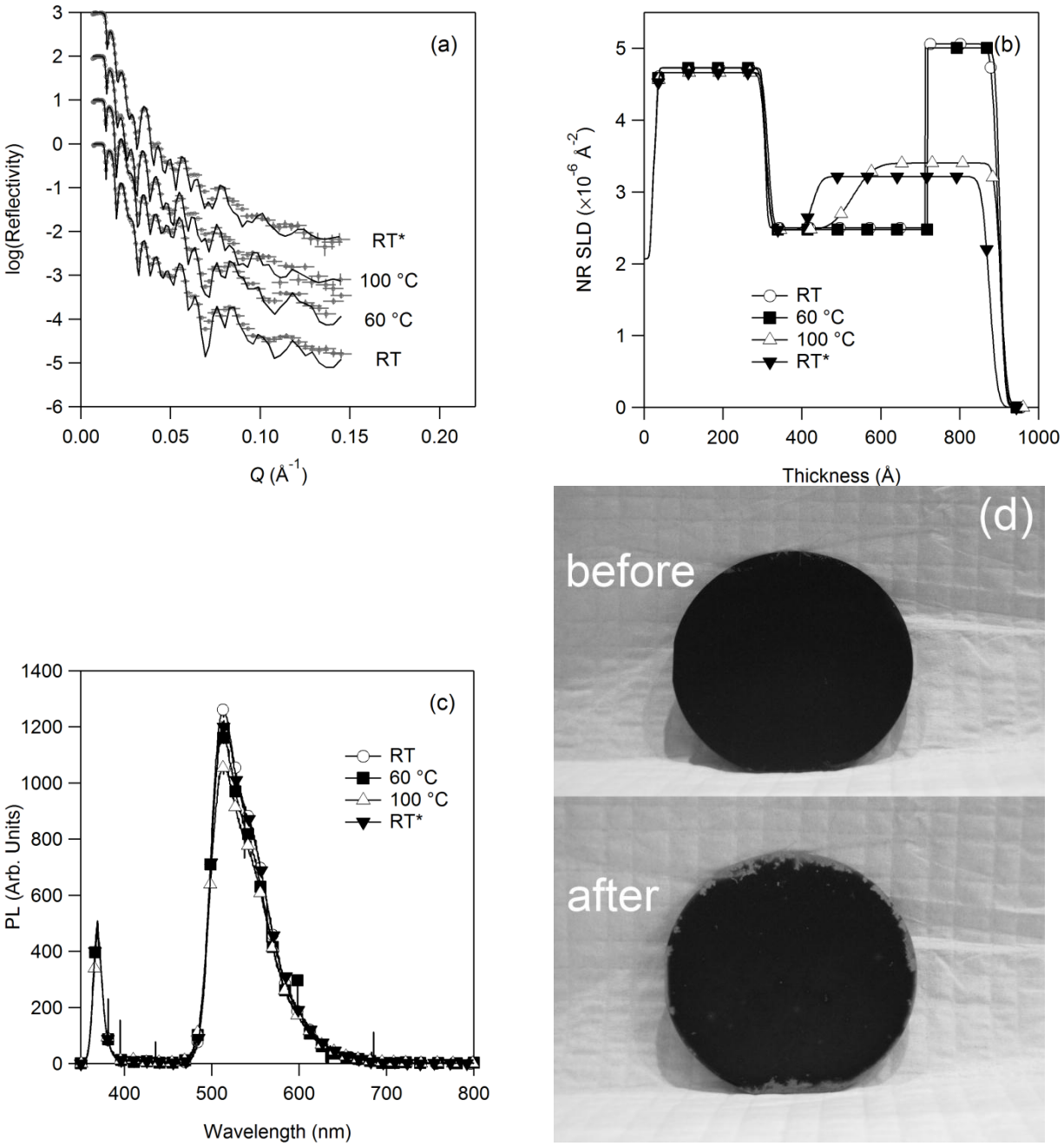

Figure 5.11 (a) NR profiles collected for the d-TCTA/(Ir(ppy)$_3$:CBP)/d-BCP multilayer structure. The points are the NR data and the solid lines the fit to the profile. (b) SLD *versus* film thickness for the d-TCTA/(Ir(ppy)$_3$:CBP)/d-BCP multilayer structure. (c) *In situ* PL measurements for the d-TCTA/(Ir(ppy)$_3$:CBP)/d-BCP multilayer structure. (d) d-TCTA/(Ir(ppy)$_3$:CBP)/d-BCP multilayer film before and after annealing to 100 °C.

The diffusion of the d-BCP into the emissive layer caused little change in either the amount of reflected light or indeed the luminescence from the deposited layer (see Figure 5.11c). After heating to 100 °C the integrated luminescence between 460-800 nm decreased by 11% compared to the as-formed film. However, after cooling back to room temperature the difference was only 1%. The fact that the luminescence does not change is easily understood. In the emissive layer the Ir(ppy)$_3$ is

diluted in the CBP to avoid intermolecular interactions that lead to quenching. The rapid heating (60 °C to 100 °C in ~4 min) and subsequent diffusion of BCP effectively dilutes the $Ir(ppy)_3$ in the layer further and hence there is no change in the photoluminescence spectra. This is an important result because it shows that photophysical measurements on their own may not be an effective probe to changes in these types of films. However, while diffusion of BCP in the $Ir(ppy)_3$:CBP layer does not affect the luminescence spectrum it will affect charge transport in the stack. For example, it could lead to charge trapping or an imbalance of charge injection and transport leading to a change in device performance. Indeed, it is interesting to note that the instability of BCP film morphology has been directly attributed to degradation in device performance.[255]

5.5.3 Bilayer Films Si/d-TCTA/($Ir(ppy)_3$:CBP) and Si/($Ir(ppy)_3$:CBP)/d-BCP

To confirm that the d-BCP was the diffusing species, and not d-TCTA, bilayer films of d-TCTA/($Ir(ppy)_3$:CBP) (B1) and ($Ir(ppy)_3$:CBP)/d-BCP (B2) were prepared. These films were deposited during the same deposition procedure as the multilayer film to ensure that all layer thicknesses and densities were the same. As demonstrated previously (5.5.1), the blend ratio of the $Ir(ppy)_3$:CBP layer significantly affects the morphological stability, therefore it is also important that the $Ir(ppy)_3$:CBP layer used in the bilayer films have an identical composition as that in the multilayer film so that a meaningful comparison can be made.

Films B1 and B2 were subjected to the same annealing cycle as the multilayer film. Reflectivity profiles and modelled film parameters before and after annealing are summarised in Figure 5.12. The reflectivity of B1 did not change over the course of the annealing, however the reflectivity of B2 changes significantly after annealing. Good models of the B1 film are obtained which closely match the thickness and SLD of the corresponding layers in the multilayer film (Figure 5.12b).

Modelling the reflectivity of B2 before annealing was difficult. The SLD of the $Ir(ppy)_3$:CBP layer is very close to that of the silicon substrate, so the $Ir(ppy)_3$:CBP layer almost perfectly contrast matches with the silicon. As a result the measured reflectivity is more characteristic of a single thin layer rather than a bilayer. The fringe spacing corresponds predominantly to the d-BCP layer thickness since the $Ir(ppy)_3$:CBP layer is almost indistinguishable from the silicon subphase. However a single layer would not perfectly define all the reflectivity features, and a reasonable bilayer model is obtained which matches the ($Ir(ppy)_3$:CBP)/d-BCP layers from the multilayer film (5.5.2). The reflectivity and the film structure change dramatically after the full annealing cycle. The reflectivity modelling reveals that diffusion between the $Ir(ppy)_3$:CBP and d-BCP layers has occurred, replicating the result from the multilayer film. The d-BCP diffused throughout the entire bilayer, mixing with the $Ir(ppy)_3$:CBP. Refining the reflectivity of bilayers B1 and B2 confirms that

diffusion between layers only occurs at the ($Ir(ppy)_3$:CBP)/d-BCP interface and not the d-TCTA/($Ir(ppy)_3$:CBP) interface.

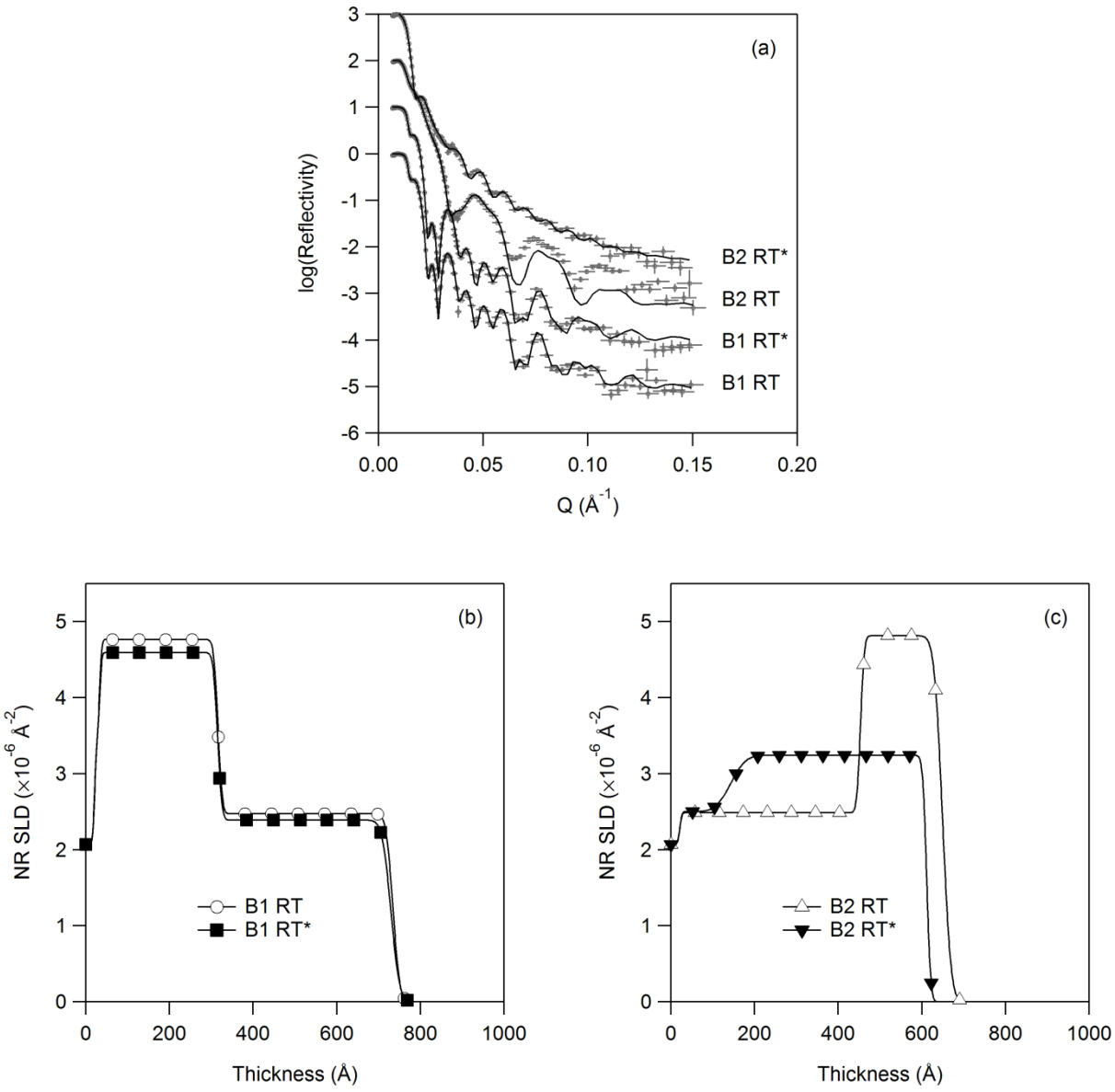

Figure 5.12 (a) NR profiles collected for the d-TCTA/($Ir(ppy)_3$:CBP) bilayer (B1) and ($Ir(ppy)_3$:CBP)/d-BCP bilayer (B2) structures before (RT) and after (RT*) annealing. The points are the NR data and the solid lines the fit to the profile. (b) SLD *versus* film thickness for the d-TCTA/($Ir(ppy)_3$:CBP) bilayer structure. (c) SLD *versus* film thickness for the ($Ir(ppy)_3$:CBP)/d-BCP bilayer structure.

5.6 Conclusions

The combination of NR and *in situ* PL measurements provide a powerful tool to study the relationship between film morphology and photophysical properties. In applying this for the first time to small molecule evaporated layers of materials used in highly efficient OLEDs it has been established that the morphological stability of $Ir(ppy)_3$ blends is dependent on the concentration of

the $Ir(ppy)_3$ in the CBP. The higher weight percent blend did not phase separate suggesting that in terms of long-term device behaviour there could be a trade-off between efficiency and durability. It was also found that the structure of multilayer stacks could change significantly under relatively mild annealing conditions. In this work BCP was found to diffuse readily into an emissive $Ir(ppy)_3$:CBP blend in contrast to TCTA, which was found to form a stable layer. These results have important implications for materials and device design not only for OLEDs but also for stacked organic photovoltaic devices.

Chapter 6. Interdiffusion in Multilayer Light Emitting Organic Films

Published in Advanced Materials, 2012, 24, 822

6.1 Abstract

Interdiffusion in multilayer organic films representative of those found in organic light emitting diodes (OLEDs) is shown to occur rapidly after annealing beyond a critical temperature. In multilayer films of bathocuproine (BCP), *fac*-tris(2-phenylpyridyl)iridium(III) [$Ir(ppy)_3$] blended in 4,4′-bis(*N*-carbazolyl)biphenyl (CBP), and tris[4-(carbazoyl-9-yl)phenyl]amine (TCTA), the BCP and $Ir(ppy)_3$:CBP layers readily interdiffuse over several minutes when heated to 100 °C. At equilibrium the BCP and $Ir(ppy)_3$:CBP layers are almost fully blended. Diffusion leads to a decrease of up to 33% in the integrated solid state emission. These results demonstrate that organic multilayers readily interdiffuse with serious consequences for their operational properties.

6.2 Introduction

Multilayer organic films are found in many cutting-edge organic semiconductor technologies such as organic light emitting diodes (OLEDs). OLEDs consist of a light emitting layer sandwiched between hole and electron transport layers, supported on a transparent electrode, although more complicated designs are sometimes employed.[3,8,9,21,229,256,257] A top contact, such as a metallic layer, completes the device. Careful selection of hole and electron transport materials allows excitons to be generated and confined within the light emitting layer. Internal efficiencies approaching 100% have been common for several years,[41] yet the degradation processes that occur over time, particularly at elevated temperatures, are not entirely understood.[142,258]

OLEDs based on phosphorescent small molecules are assembled by high-vacuum vapour deposition, and the interfaces between layers are believed to be well defined with negligible mixing between layers. The interface between organic layers plays a crucial role in determining the charge transport properties, so a careful study of interface dynamics is of vital importance. Device performance degrades over time as a result of extended operation or external stresses,[27,116,120] but whether this occurs due to material degradation or changes at the layer interfaces is not always clear. The morphological stability of organic films is therefore a serious issue for prolonged device operation and performance.

Buried interfaces in multilayer films are difficult to study. Changes in morphology of organic films are often inferred from electrical or photophysical properties,[146,152,259,260] or scattering techniques such as X-ray reflectometry[157,162,258,261] and grazing incidence X-ray diffraction.[157,232] A better technique for investigating organic multilayer structures is neutron reflectometry (NR). By enhancing the scattering contrast with selective deuteration, NR can reveal the precise structure and morphological features of multilayer organic films.

Using NR, layer diffusion was examined in a series of organic multilayer films composed of *fac*-tris(2-phenylpyridyl)iridium(III) ($Ir(ppy)_3$) blended in 4,4'-bis(*N*-carbazolyl)biphenyl (CBP), deuterated bathocuproine (d-BCP) and deuterated tris[4-(carbazoyl-9-yl)phenyl]amine (d-TCTA) (Figure 6.1). Inverted structures were prepared to explore whether deposition order and layer confinement play any role in layer diffusion. In addition, a thin layer of aluminium (simulating an electrode) was evaporated onto the organic multilayer to determine what effect metal deposition has on the structure and properties of the multilayer film.

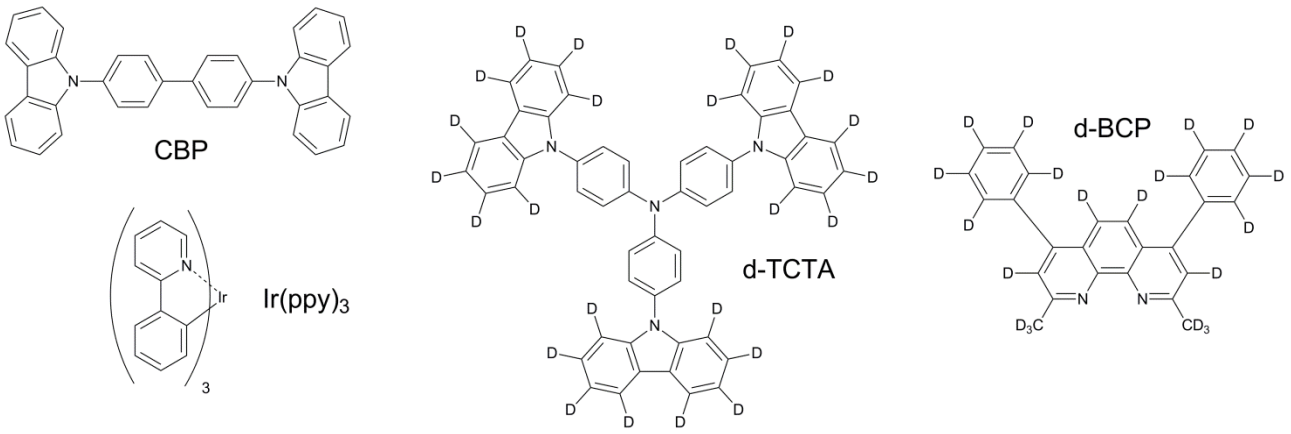

Figure 6.1 Compounds used in this study. The locations of at least partial deuteration are indicated by D for d-TCTA and d-BCP.

6.3 Experimental

6.3.1 Film Preparation

Films were prepared by thermal evaporation under high vacuum (10^{-6} mbar) onto silicon substrates. Silicon wafers (Si-Mat, Germany) of 50 mm diameter were cleaned with piranha solution (a 2:1 mixture of sulfuric acid and 30% hydrogen peroxide). The native oxide layer was not removed. Prior to film deposition the substrates were sonicated in acetone for 5 min, rinsed with 2-propanol and then dried under a stream of clean nitrogen.

6.3.2 X-ray Reflectometry

X-ray reflectivity profiles were measured using a Panalytical Ltd X'Pert Pro Reflectometer using Cu Kα X-ray radiation. The X-ray beam was collimated using a Göbel mirror, a 0.1 mm slit and a post-sample parallel collimator. Reflectivity data were collected over the angular range $0.05° \leq \theta \leq 4.00°$, with a step size of 0.005° and counting times of 1 s per step. Least squares analysis of the reflectivity profiles were performed using the Motofit reflectometry analysis program,[243] with error estimates on fitted parameters reported as ±1 standard deviation.

6.3.3 Neutron Reflectometry

NR measurements were recorded using the Platypus time-of-flight neutron reflectometer and a cold neutron spectrum (2.8 Å < λ < 18.0 Å) at the OPAL 20 MW research reactor [Australian Nuclear Science and Technology Organisation (ANSTO), Sydney, Australia].[251,252] 20 Hz Neutron pulses were generated using a disk chopper system (EADS Astrium GmbH) in the medium resolution mode ($\Delta\lambda/\lambda$ = 4%) and recorded on a 2-dimensional helium-3 neutron detector (Denex GmbH). Reflected beam spectra were collected at 0.7° for 20 min (0.27 mm slits) and 2.5° for 110 min (0.95 mm slits). Direct beam measurements were collected under the same collimation conditions. Time dependent NR measurements were acquired in event mode (Time of flight, x and y position and frame number time are recorded for each neutron), and rebinned to 5 min time intervals for analysis.

A custom built experimental cell was used for simultaneous NR and PL measurements, with *in situ* annealing capabilities. The luminescence of the films was monitored with an Ocean Optics USB2000 spectrometer using a Nichia UV-LED 365 nm excitation source. An aluminium block heating stage, isolated from the neutron cell by a ceramic stand, was heated (10 °C min^{-1} during ramp) with two cartridge heaters and the temperature controlled by a Watlow series 988 temperature controller. Measurements were taken at room temperature (RT, 22 °C) and at 10 °C steps from 60 to 100 °C. The film was then cooled (RT*, <30 °C) under a stream of clean nitrogen when a final measurement was taken. The cell was under vacuum (~1 mbar) during all experiments. NR measurements were performed at each temperature until such a time as the film had reached thermal equilibrium. Least squares analysis of the reflectivity profiles were performed using the Motofit reflectometry analysis program,[243,253] with error estimates on fitted parameters reported as ±1 standard deviation.

6.4 Results and Discussion

A series of films was prepared as shown in Figure 6.2. The thicknesses of the layers in each film are representative of those used in actual OLED devices. The emissive guest:host layer $Ir(ppy)_3$:CBP was deposited simultaneously across all four films, which ensured that the thickness, and more importantly, the blend ratio were identical. The blend ratio of guest:host layers can affect the morphological stability,[262] and so for a proper comparison of the diffusion processes in these films it is important that the composition of each layer is the same. The nominal blend ratio for all the films listed was 6 wt%. A lack of scattering contrast between the CBP and $Ir(ppy)_3$ prevents a precise determination of the blend ratio from the neutron measurements. The bulk thermal properties of CBP, BCP and TCTA are relatively well known. The glass transition temperature (T_g) of CBP is difficult to determine[130] although it has been reported to be as low as 62 °C[131] but up to

78 °C.[263] BCP, and the related 4,7-diphenyl-1,10-phenanthroline (BPhen), also have glass transition temperatures around 62 °C[255,264] although one report puts the T_g of BCP at 83 °C.[265] The T_g of TCTA is ~150 °C.[266,267]

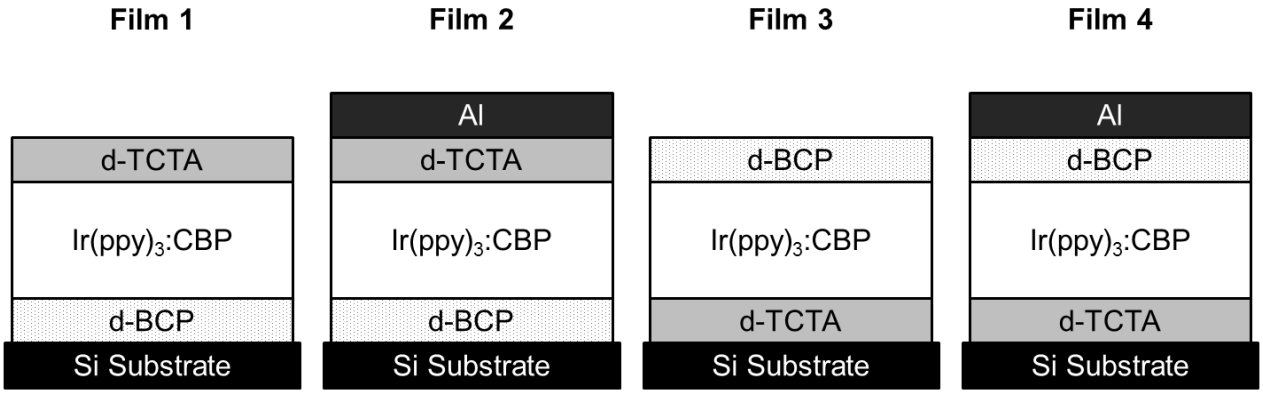

Figure 6.2 Schematic layout of the various films structures. The Ir(ppy)$_3$:CBP guest:host emissive layer was deposited simultaneously across all the films to ensure a consistent blend ratio.

6.4.1 Film 1 Si/d-BCP/(Ir(ppy)$_3$:CBP)/d-TCTA

The NR of the Si/d-BCP/(Ir(ppy)$_3$:CBP)/d-TCTA film measured at room temperature (RT, 22 °C) can be described by a three layer model, consistent with the deposition order and the relative neutron scattering length density (SLD) contrast of the layers. SLD is a measure of how strongly a material scatters radiation, depending on the chemical composition and is proportional to mass density. The layer thicknesses were d-BCP/(Ir(ppy)$_3$:CBP)/d-TCTA 150.3±0.3 Å, 346.7±0.3 Å and 267.2±0.2 Å respectively, with very low roughness (<10 Å) at all interfaces. A strong PL signal was observed primarily due to emission from Ir(ppy)$_3$ (λ_{max} = 510 nm). A small amount of the reflected excitation beam was also observed at 365 nm. The NR profile remained essentially unchanged as the film was heated in 10 °C steps to 80 °C. At 90 °C, the interface between d-BCP and Ir(ppy)$_3$:CBP layers was slightly perturbed as the interfacial roughness doubled to 20.6±0.7 Å (Figure 6.3). The *in situ* PL was unchanged by the thermal annealing at this temperature. Scattered light from the excitation source can be used to gauge the relative surface roughness of the film,[262] and indicates that the surface roughness of this film does not change.

On heating to 100 °C the NR profile showed distinct changes and the fitted model indicates that the d-BCP and Ir(ppy)$_3$:CBP layers are almost completely blended together. A small section of the Ir(ppy)$_3$:CBP layer remains (87.0±1.2 Å), but the d-BCP rich layer is perfectly uniform in SLD. There is a high interfacial roughness of 32.0±1.3 Å between the d-BCP rich layer and the remaining Ir(ppy)$_3$:CBP layer. The uniform SLD of the d-BCP rich layer and the constancy of the overall

multilayer film thickness indicates that diffusion between the d-BCP and the $Ir(ppy)_3$:CBP occurred in both directions; that is the layers interdiffused.

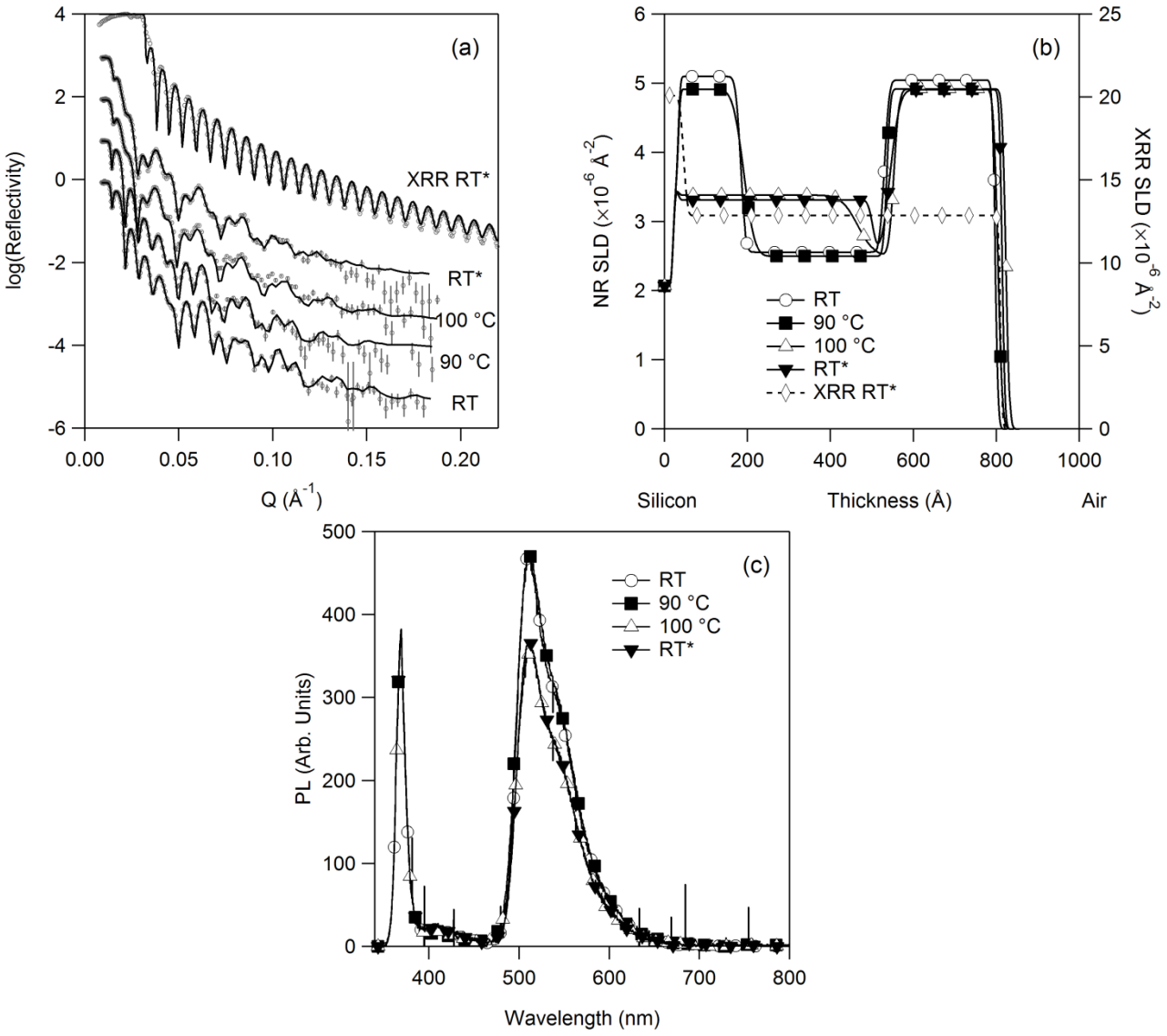

Figure 6.3 Si/d-BCP/($Ir(ppy)_3$:CBP)/d-TCTA Film 1. (a) Neutron and X-ray reflectivity data (points) and refined models (lines) at different stages of the annealing cycle. (b) The corresponding NR and XRR SLD profiles to the reflectivity models. The film thickness after annealing determined by XRR is essentially the same as that found by NR. (c) PL spectra collected *in situ* with the neutron experiments reveal a decrease in the PL intensity of the $Ir(ppy)_3$ after annealing at 100 °C. The scattered excitation intensity does not change indicating a constant surface roughness. RT* indicates measurements taken after the annealing process, and once the film had cooled below 30 °C.

It is interesting that the NR profile obtained after annealing should fit a simple slab model so well. The question arises – is it possible to describe the d-BCP diffusion by a SLD gradient? To describe such a film structure the discrete density profile (DDP) model was employed.[268,269] The DDP model uses an ensemble of thin slices with a characteristic thickness (l) and roughness (σ), but a

variable SLD parameter. The minimum roughness is determined by $\sigma \approx 1/Q_{max}$, where Q_{max} is the maximum momentum transfer at which coherent reflectivity is still observable. The minimum slice thickness is therefore $l \approx 3\sigma \approx \pi / Q_{max}$.

From the data collected at 100 °C, coherent scattering is observable to $Q_{max} \approx 0.1$ Å^{-1} which places the lower limit on the slice roughness at 10 Å, and therefore a minimum slice thickness of 30 Å. In the actual model, the d-BCP and Ir(ppy)$_3$:CBP layers were described by 12 slices each 37 Å thick, with a corresponding roughness of 12.5 Å. The d-TCTA layer parameters were fixed. Before model refinement each DDP slice had a SLD of 4×10^{-6} Å^{-2}. The only constraint on the SLD was that it could not drop below 2.5×10^{-6} Å^{-2} (the SLD of the Ir(ppy)$_3$:CBP layer).

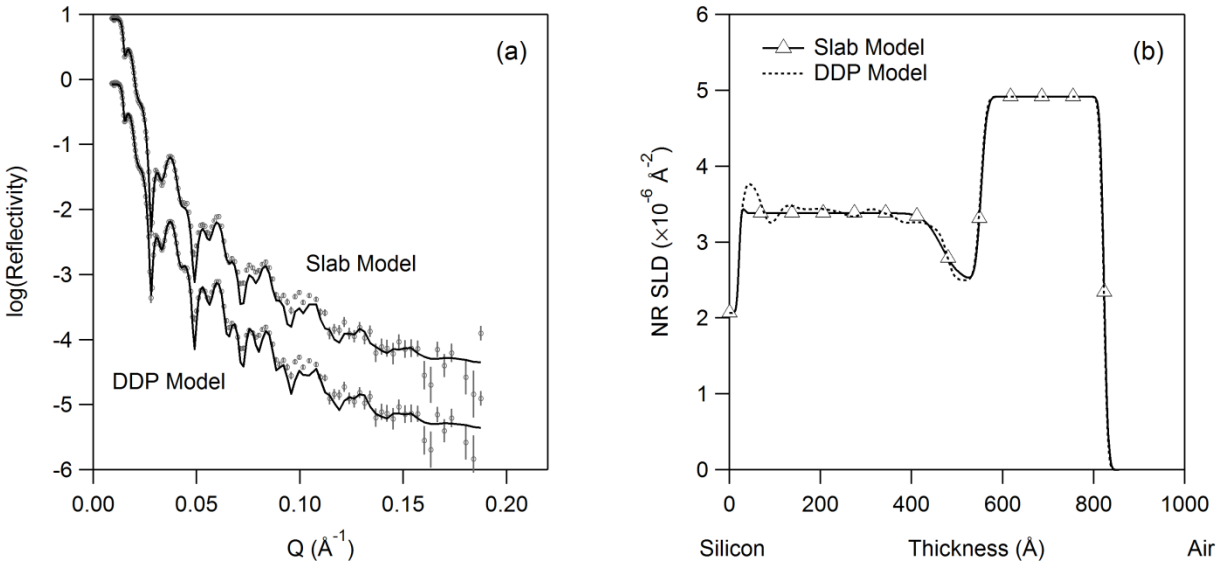

Figure 6.4 Comparison of the slab and discrete density profile (DDP) models for Film 1 collected at 100 °C. The modelled reflectivity (a) shows that after ~0.05 Å^{-1} the DDP model follows the data more closely than the slab model, however the DDP SLD profile (b) does not show any significant differences to the slab model. The DDP model consists of 12 slices 37 Å thick with a fixed slab of d-TCTA. The roughness of the DDP slices was 12.5 Å.

After refinement of the DDP model the SLD profile closely matched that obtained via the slab model (Figure 6.4). The slab model utilises far fewer parameters but gives essentially the same result as the more complex DDP model. The DDP and slab models both indicate that the equilibrium structure of the fully interdiffused d-BCP and Ir(ppy)$_3$:CBP layers is such that there is no concentration or SLD gradient.

In conjunction with the interdiffusion between the d-BCP and Ir(ppy)$_3$:CBP layers, the integrated PL intensity of Ir(ppy)$_3$ (460-800 nm) and therefore the relative quantum efficiency of the guest:host layer decreased by 20% (Figure 6.3c). CBP[21] and BCP[132] are both used as efficient hosts for Ir(ppy)$_3$ therefore it is not likely that the interaction of d-BCP quenches Ir(ppy)$_3$. Rather since

$Ir(ppy)_3$:CBP films formed by vapour deposition are not thermally stable and phase separate (as demonstrated in Chapter 5),[262] it is conceivable that the decrease in the PL signal observed here is due to phase separation and aggregation of $Ir(ppy)_3$ which leads to excited state quenching via triplet-triplet annihilation.[58]

After cooling, the NR showed little change, indicating that the film morphology obtained at 100 °C was essentially 'frozen'. The PL intensity was the same as that measured at 100 °C, 20% less than the PL of the as-formed film. XRR of the film at the completion of the neutron experiments independently confirmed the thickness of the multilayer film (764.0±0.2 Å), closely matching the multilayer film thickness of 780.6±1.2 Å obtained from NR (Figure 6.3b). Comparison of the NR and XRR results is a clear demonstration of the difference between X-ray and neutron scattering contrast. While the NR profile is a complicated series of interference fringes modelled by a multilayer film structure, the XRR profile has a single repeating fringe spacing which can be well modelled by a single layer. The electron densities of the organic layers, which determine the interactions with X-rays, are very similar, whereas the neutron SLDs vary significantly between layers, due to enhanced contrast from selective deuteration. The small amount of iridium present from the $Ir(ppy)_3$ did not alter the electron density of the guest:host layer sufficiently so that a layered structure in the XRR could be observed.

In the previous experiments in which similar samples were heated rapidly from 60 to 100 °C it was observed that no change occurred to the PL of the multilayer stack after a full heat and cool cycle (Chapter 5).[262] The reason for the different behaviour observed in this experiment is not certain, however it is possible that the very different heating rates to reach 100 °C (several hours for **Film 1** in this experiment as opposed to four minutes in the earlier work) may be responsible. It is also possible that the blend ratio of the $Ir(ppy)_3$:CBP layer in the film was different between the two experiments and that may have an impact on the emission intensity and morphological properties.

6.4.1.1 Time Dependent Measurements

It is clear that interdiffusion between layers is occurring, but the question remains as to what is the mechanism of the diffusion process. During the course of thermal annealing at 100 °C the structural evolution of the film was followed by time dependent NR. After heating from 90 to 100 °C at 10 °C/min, data at a fixed angle (0.7°) were collected in event mode and rebinned to 5 min intervals for analysis. A selection of the measured NR and calculated models is presented in Figure 6.5. There is a significant difference between the measured structure at 90 °C and the first measurement taken at 100 °C (which encompasses a time window of 15-20 min after first heating to 100 °C). Reflectivity features which change over time are difficult to discern from Figure 6.5a, but an

animation of all the rebinned profiles shows the time dependent NR changes more clearly (see Appendix D).

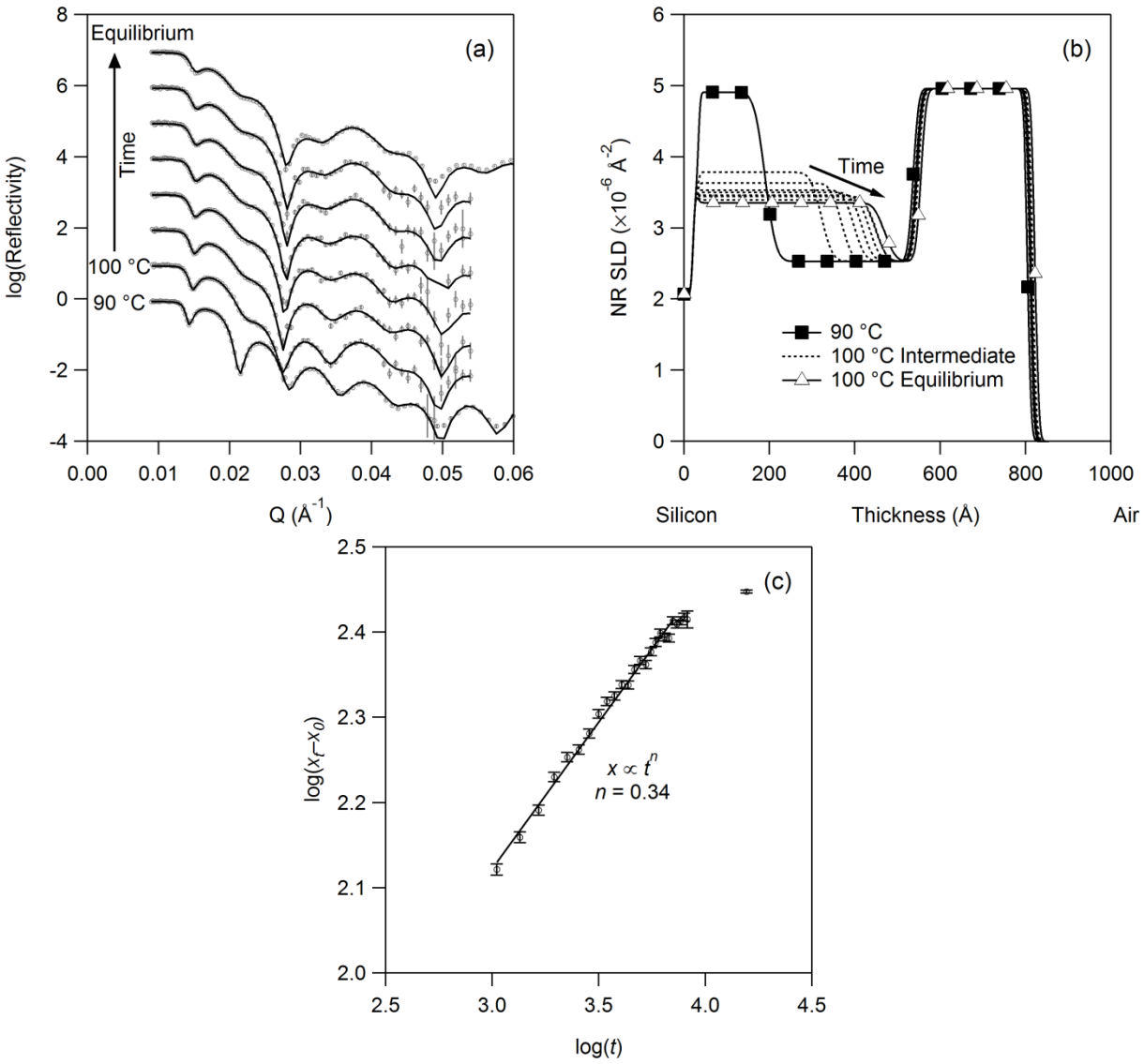

Figure 6.5 Monitoring the diffusion of d-BCP into the Ir(ppy)$_3$:CBP guest:host layer. (a) NR profiles collected in 5 min time bins for the first angle until equilibrium was reached (only a selection of the NR profiles is shown for clarity). Sequential modelling (b) of the intermediate and equilibrium measurements was performed with only three free parameters – d-BCP layer thickness, Ir(ppy)$_3$:CBP layer thickness and d-BCP layer SLD. (c) The position of the interface between the d-BCP rich and Ir(ppy)$_3$:CBP layers is described by $x \propto t^n$ with n = 0.34. The absolute interface position, x_t, with respect to the initial thickness of the d-BCP layer, x_0, is plotted according to the midpoint of each time window.

Assuming that the slab model reasonably describes the film structure, the reflectivity profiles were modelled sequentially with the model obtained at 90 °C used as a starting point. All roughness parameters were fixed as were the SLD and thickness of the d-TCTA layer. The thickness and SLD of the d-BCP layer were allowed to vary, and while the Ir(ppy)$_3$:CBP layer thickness could vary, its

SLD was partly restrained ($\geq 2.5 \times 10^{-6}$ Å^{-2}). Thus only three parameters were allowed to vary during the course of the sequential fitting routine of the time dependent diffusion. Low χ^2 values were obtained for all the NR measurements.

The total film thickness did not change to any great degree during the 100 °C annealing process, as was expected (and independently confirmed by XRR after cooling back to RT). The thickness and SLD of the d-BCP-rich layer did change with time, reaching an equilibrium structure ~2.5 hours after the film was first heated from 90 to 100 °C (Figure 6.5b). While the slab models are almost certainly too simple to describe all the changes that occur to the multilayer structure, it is nonetheless interesting that they reproduce the measured reflectivity so well.

The propagation of interfaces in diffusion couples (in this case the d-BCP/ $Ir(ppy)_3$:CBP couple) occurs when the two diffusing species have different intrinsic diffusion coefficients. Diffusion is described as Fickian when the time dependence of the position of the interface follows $x \propto t^n$ with $n = 0.5$, while so-called Case II diffusion occurs for $n = 1$.[270-272] However, in the case of the d-BCP/ $Ir(ppy)_3$:CBP couple the moving interface displays time dependence with an exponent of $n = 0.34$, and this situation is defined as anomalous Fickian interdiffusion.[273-275] Such behaviour indicates diffusion asymmetry and that the diffusion coefficients are strongly dependent on layer composition. Behaviour like this has been observed and modelled in the diffusion of Si/Ge multilayers.[273,275] Si diffuses rapidly through Ge, while diffusion of Ge into Si is poor, and the interface propagates into the Si. Therefore, by analogy the $Ir(ppy)_3$:CBP diffuses very quickly in d-BCP, whereas diffusion of d-BCP in $Ir(ppy)_3$:CBP is limited.[272,273,275] The uniform SLD of the d-BCP-rich layer also indicates that this layer is highly mobile, and rapidly mixes any material incorporated by the moving interface.

6.4.2 Film 2 Si/d-BCP/($Ir(ppy)_3$:CBP)/d-TCTA/Al

This film has the same organic layer structure as **Film 1**, but is supplemented with aluminium deposited as the topmost layer to simulate a cathode. At room temperature the layer thicknesses d-BCP/($Ir(ppy)_3$:CBP)/d-TCTA/Al are 150.7±0.2 Å, 330.0±0.3 Å, 263.3±0.5 Å and 103.7±0.4 Å. The thicknesses of the organic layers compare very well to those found in **Film 1**. The roughness values at all layer interfaces were low (~10 Å), except at the d-TCTA/Al interface, which was 32.2±0.7 Å. The surface roughness of the Al/air interface was very low, 8.7±0.7 Å.

The changes to the film morphology which accompany thermal annealing are similar to those observed in **Film 1**. From RT to 80 °C there was no significant change to the NR or the PL spectra (Figure 6.6), except that, compared to **Film 1**, the absolute PL intensity is much lower. The

aluminium layer may either block the excitation source from penetrating through to the organic layers and/or prevent the emitted light from leaving the film through the top interface.

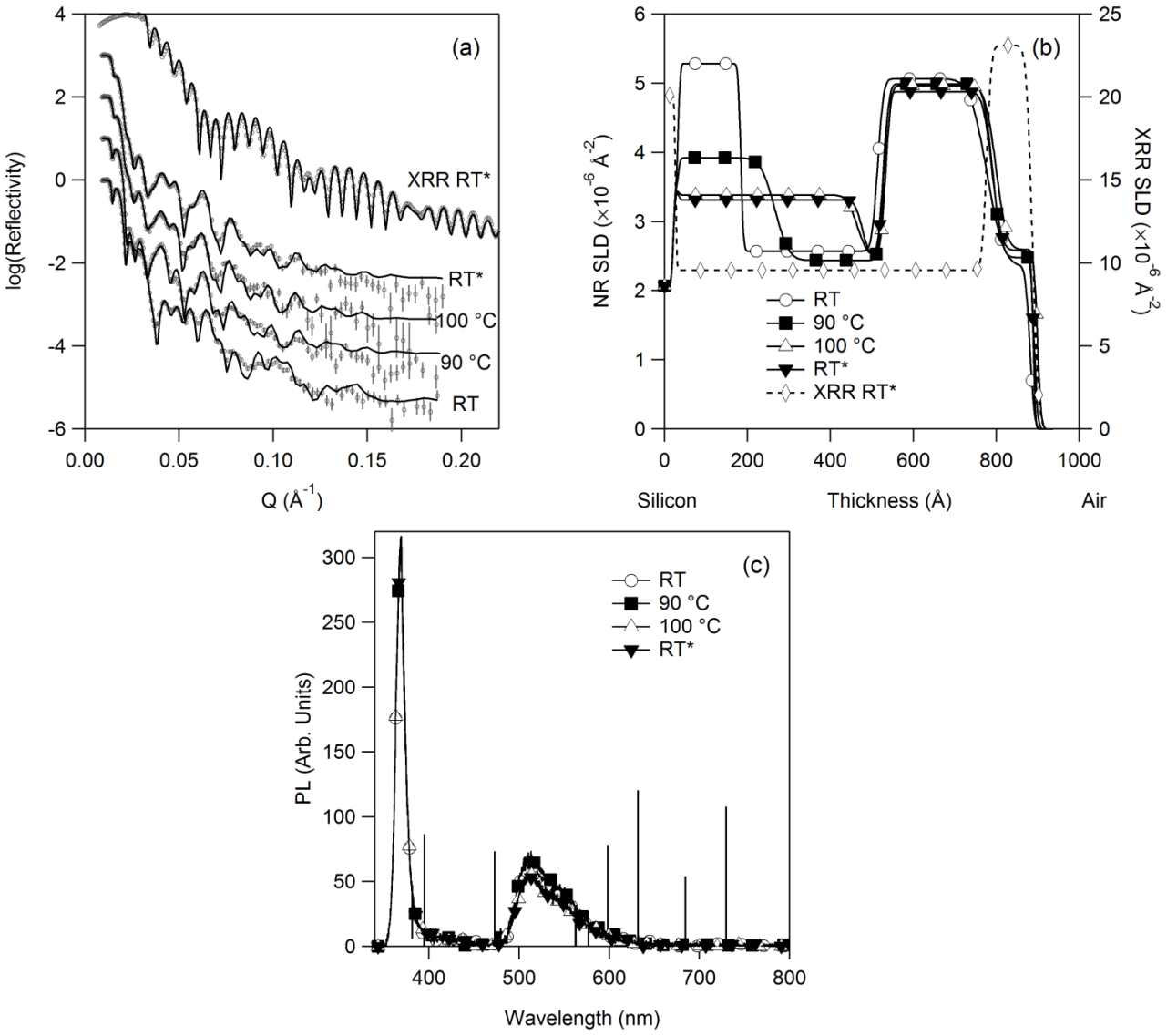

Figure 6.6 Si/d-BCP/(Ir(ppy)$_3$:CBP)/d-TCTA/Al Film 2. (a) Neutron and X-ray reflectivity data (points) and refined models (lines) at different stages of the annealing cycle. (b) The corresponding NR and XRR SLD profiles to the reflectivity models. The film thickness after annealing determined by XRR is essentially the same as that found by NR. (c) PL spectra collected *in situ* with the neutron experiments reveal a slight decrease in the PL intensity of the Ir(ppy)$_3$ after annealing at 100 °C. The scattered excitation intensity does not change indicating a constant surface roughness. RT* indicates measurements taken after the annealing process, and once the film had cooled below 30 °C.

At 90 °C, the NR indicates that some diffusion between the d-BCP and guest:host layer has taken place, although the amount of diffusion appears to have no impact on the PL spectra. As seen in **Film 1**, heating to 100 °C induces a much greater degree mixing between the d-BCP and the guest:host emissive layers. The d-BCP and Ir(ppy)$_3$:CBP layers are almost completely blended

together at this temperature. This mixing once again coincides with a decrease (14%) in the integrated PL from the $Ir(ppy)_3$ in the guest:host layer. Upon cooling the new structure persists. The total film thickness independently determined by NR and XRR was essentially the same, 857.5±1.2 Å and 860.1±0.3 Å respectively.

XRR is particularly useful for studying this film, because the scattering contrast between the organic (low electron density) and aluminium (high electron density) layers is so large. In the NR measurements there was no indication of significant disruption between the d-TCTA and aluminium layers. The thickness of the aluminium layer determined by NR and XRR was 100.8±0.3 Å and 109.9±0.2 Å respectively. The interface between the organic and metal layers is quite distinct (Figure 6.6b) and the interfacial roughness determined by XRR was 9.2±0.2 Å. Thus there does not appear to be any diffusion between the Al and d-TCTA layer after annealing to 100 °C.

6.4.3 Film 3 Si/d-TCTA/(Ir(ppy)$_3$:CBP)/d-BCP

Film 3 was composed of the same layers as **Film 1** however the deposition order was reversed. This is the same film geometry previously investigated (5.5.2).[262] However, due to the different annealing conditions a number of interesting observations were made (Figure 6.7). At room temperature the layer thicknesses d-TCTA/($Ir(ppy)_3$:CBP)/d-BCP were 294.7±0.3 Å, 322.9±0.3 Å and 166.9±0.2 Å which compare well with those of **Film 1** and **Film2**. The interfacial roughness values were all very low, ~10 Å.

As with **Film 1** and **Film 2**, **Film 3** was thermally stable at temperatures up to 80 °C, with no appreciable changes in the NR or PL. At 90 °C changes in the reflectivity occur. A stable reflectivity profile was not obtained until ~2.5 hours after the annealing at 90 °C was started. The best model of the NR at 90 °C would suggest that some diffusion of the d-BCP into the guest:host layer has occurred, but a large amount of d-BCP appears to have been lost from the film surface. It was difficult to obtain a satisfactory model. It is not clear that diffusion has actually occurred, and the NR suggests that the film had considerable disorder which would interfere with obtaining an accurate model of the film structure.

At 100 °C the NR profile is more suggestive of a bilayer rather than a trilayer structure. This is borne out by the modelling, which is significantly better than that at 90 °C, and indicates that the entire d-BCP layer has disappeared. The NR changed little after cooling, confirming the bilayer d-TCTA/($Ir(ppy)_3$:CBP) structure.

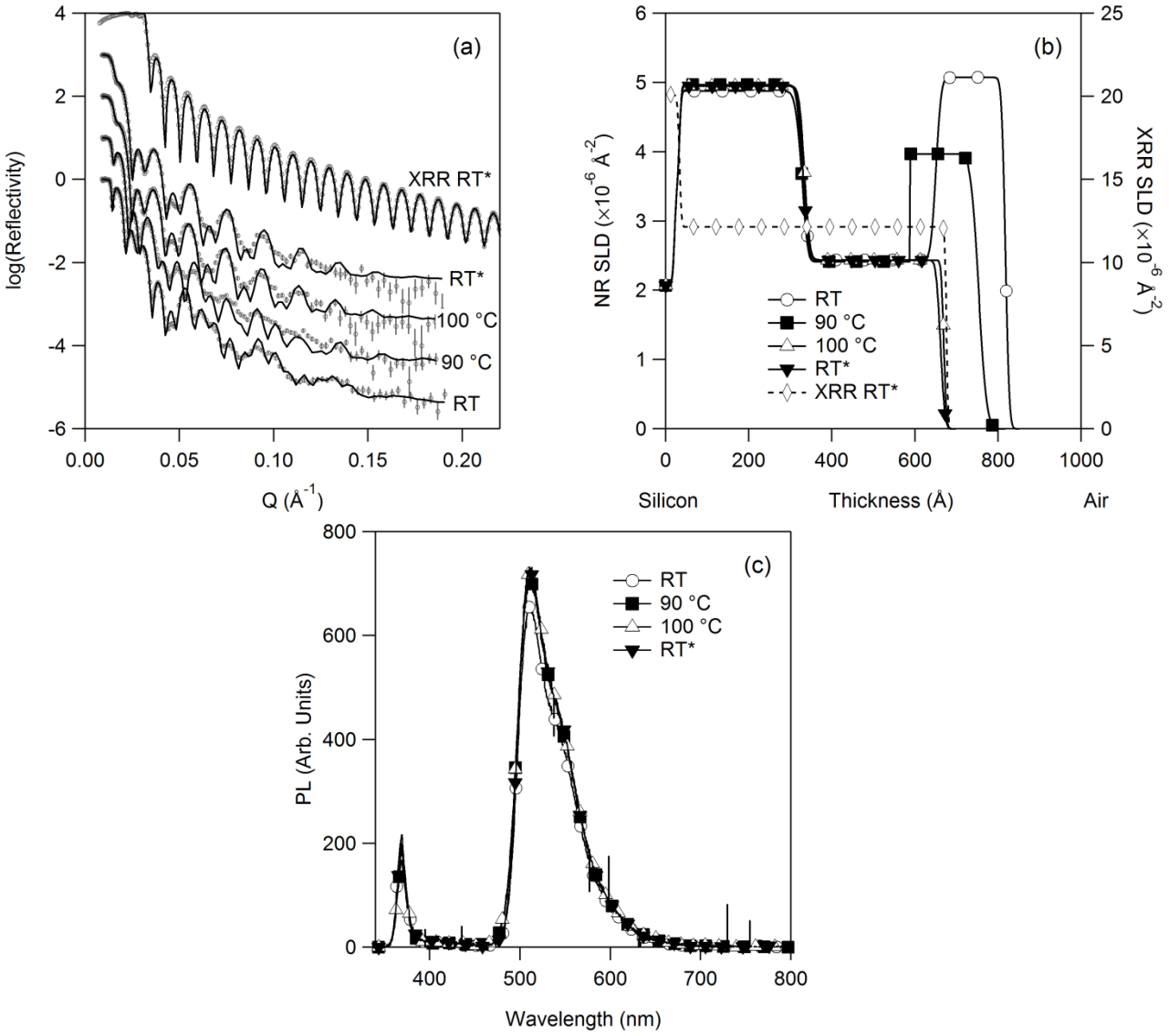

Figure 6.7 Si/d-TCTA/(Ir(ppy)$_3$:CBP)/d-BCP Film 3. (a) Neutron and X-ray reflectivity data (points) and refined models (lines) at different stages of the annealing cycle. (b) The corresponding NR and XRR SLD profiles to the reflectivity models. The film thickness after annealing determined by XRR is essentially the same as that found by NR, and indicates that the top most layer, d-BCP, has disappeared. (c) PL spectra collected *in situ* with the neutron experiments show no significant change in the PL intensity of the Ir(ppy)$_3$ after annealing at 100 °C. The scattered excitation intensity does not change indicating a constant surface roughness. RT* indicates measurements taken after the annealing process, and once the film had cooled below 30 °C.

Confirmation of the disappearance of the d-BCP layer was provided independently by XRR. Before annealing the total film thickness was 784.5±0.5 Å by NR, and after annealing, the thickness decreased to around 630 Å [XRR (642.7±0.1 Å) and NR (628.3±0.4 Å)], with the difference corresponding to the thickness of the original d-BCP layer (166.9±0.2 Å). Since interdiffusion of the d-BCP and Ir(ppy)$_3$:CBP layers did not occur, the integrated PL of the film did not decrease, but actually increased slightly (by 13%). This provides further evidence that the diffusion and mixing of d-BCP has a negative impact on the PL of the film.

Again, comparison with previous measurements on the same film structure (Chapter 5) reveal the importance of the annealing conditions to the film behaviour.[262] When slow annealing is performed, as was the case in this work, the d-BCP began subliming from the surface at 90°C and above. If the film is held at 90°C for sufficient time almost all the d-BCP is removed from the surface. If, on the other hand, the sample is heated rapidly beyond 90° to 100°C as was the case in the earlier work (5.5.2),[262] the interdiffusion process becomes more rapid than sublimation with the result that the d-BCP mixes with the $Ir(ppy)_3$:CBP layer before the majority can sublime. With the removal of the d-BCP layer it is possible to observe the $Ir(ppy)_3$:CBP layer directly. No apparent phase separation of the $Ir(ppy)_3$:CBP layer was observed. Since single layer films of 6 wt% $Ir(ppy)_3$:CBP readily phase separate (Chapter 5) this suggests that either the d-TCTA layer stabilises the morphology of the $Ir(ppy)_3$:CBP layer, or the blend ratio was higher than the nominal 6 wt%.

6.4.4 Film 4 Si/d-TCTA/($Ir(ppy)_3$:CBP)/d-BCP/Al

Film 4 was composed of the same organic layers as **Film 3** but with the addition of an aluminium electrode (Figure 6.8). Prior to annealing the layer thicknesses were measured as d-TCTA/($Ir(ppy)_3$:CBP/d-BCP/Al 277.5±0.2 Å, 335.0±0.2 Å, 156.2±0.3 Å, and 94.4±0.3 Å. All interface roughness values were low (<10 Å), except the d-BCP/Al interface where the roughness was 20.8±0.3 Å.

As with all the other films, no changes were observed in the NR or the PL between room temperature and 80 °C. The NR began to change at 90 °C, with some evidence that the d-BCP layer had started diffusing into the emissive guest:host layer (Figure 6.8). After heating to 100 °C the d-BCP diffused throughout the $Ir(ppy)_3$:CBP layer. While a layer that can be attributed to the aluminium coating is present in the NR models it is almost indiscernible due to the high film/air interfacial roughness and reduced contrast to the d-BCP rich layer. The thickness of the Al layer decreased to 66.2±1.2 Å after cooling indicating that some of the aluminium layer had been incorporated into the mixed d-BCP/$Ir(ppy)_3$/CBP layer (*cf.* original Al layer thickness 94.4±0.3 Å).

XRR on the film after cooling shows a profile reminiscent of **Film 2**, although the reflectivity decays away rather more quickly with increasing *Q*, indicative of high roughness at one or more interfaces in the film. The surface roughness after the full annealing cycle (Al/air interface) as determined by NR was 16.5±1.6 Å and modelling of the XRR is consistent with this value (21.1±1.9 Å). The total film thicknesses obtained from NR and XRR are approximately the same (838.8±5.5 Å and 858.1±1.5 Å).

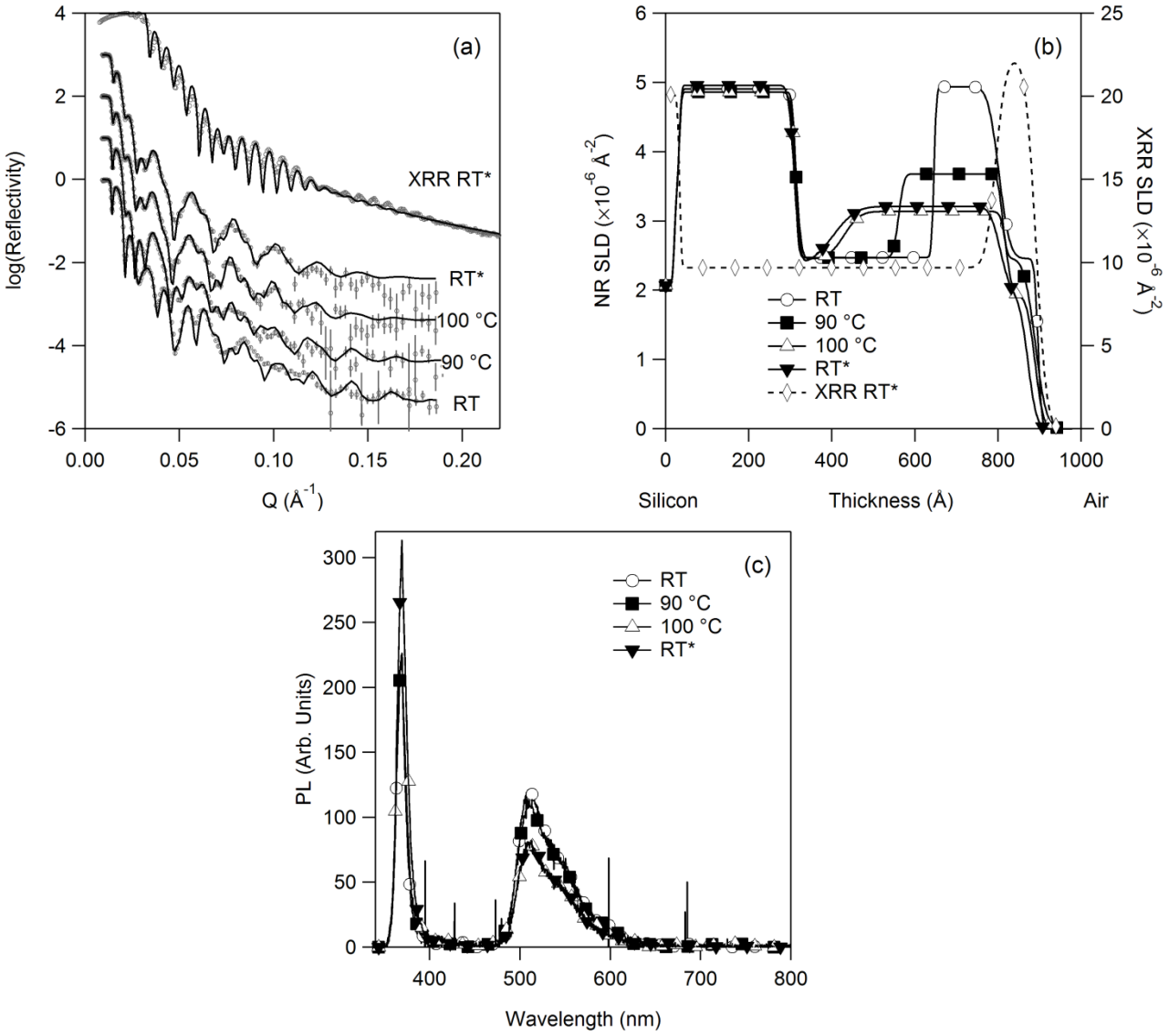

Figure 6.8 Si/d-TCTA/(Ir(ppy)$_3$:CBP)/d-BCP/Al Film 4. (a) Neutron and X-ray reflectivity data (points) and refined models (lines) at different stages of the annealing cycle. (b) The corresponding NR and XRR SLD profiles to the reflectivity models. The film thickness after annealing determined by XRR is essentially the same as that found by NR. (c) PL spectra collected *in situ* with the neutron experiments reveal a decrease in the PL intensity of the Ir(ppy)$_3$ after annealing at 100 °C. The scattered excitation intensity increases after annealing at 100 °C indicating a higher surface roughness than before annealing. RT* indicates measurements taken after the annealing process, and once the film had cooled below 30 °C.

The annealed interface between the organic and aluminium layers is significantly more diffuse than in **Film 2**, with the roughness determined by XRR to be 19.6±0.7 Å. The presence of the aluminium layer prevented the d-BCP from subliming (*cf.* **Film 3**), so the mobile d-BCP diffused into the lower layer. The XRR model indicates that the aluminium layer is 97.4±1.0 Å thick, which matches the layer thickness from NR before annealing, but is significantly thicker than the ~66 Å layer determined by NR after the full annealing cycle. This demonstrates that the aluminium and d-

BCP containing layer have partially mixed, in contrast to **Film 2** where a very sharp interface between the d-TCTA/Al remained even after annealing.

The PL changed in the same manner as was observed in **Films 1** and **2** with the integrated PL decreased by 33%. The reflected excitation beam at 365 nm, which is related to diffuse scatter from the film caused by surface roughness, increased after heating to 100 °C. This is consistent with both the NR and XRR results, and confirms a high degree of surface roughness or disorder, which is not observed in any of the other films, brought on by the disruption of the highly reflective aluminium layer.

6.5 Conclusions

Multilayer films formed by evaporation of small molecule materials can form sharp interfaces. However, the extent to which multilayer organic films can be perturbed by thermal stress has been clearly demonstrated. Interdiffusion between layers is a thermally activated process, which follows rapidly after a critical temperature is reached with the diffusion occurring over several hours before reaching an equilibrium film structure. d-BCP was found to be very mobile and providing that the layer was capped diffused into the $Ir(ppy)_3$:CBP layer, irrespective of the layering order. Diffusion of d-BCP into $Ir(ppy)_3$:CBP greatly disrupted the aluminium deposited on the d-BCP layer, however, a thermally stable layer of d-TCTA was resistant to diffusion from both organic and metal layers. These results clearly show that the choice of materials is critical for the provision of stable layers and interfaces.

The photoluminescence of the films can be directly correlated to the interdiffusion of the d-BCP and $Ir(ppy)_3$:CBP layers, and the annealing duration. This has significant consequences for the operational stability of OLEDs. When the films were slowly heated to the critical temperature (100 °C) interdiffusion of d-BCP caused the photoluminescence to decrease by allowing aggregation of $Ir(ppy)_3$ leading to triplet-triplet annihilation. This is in contrast to Chapter 5 where it was found that rapid heating to the critical temperature still initiates diffusion, but does not result in a decrease in the photoluminescence since phase separation of $Ir(ppy)_3$ is prevented. However, device performance can still be expected to suffer as a result of both the reduction in the emission efficiency and change in charge transport properties by the mixing of the host (CBP) and electron (BCP) transport layers.

Chapter 7. Conclusions

7.1 Conclusions

7.1.1 Electronic Properties of Iridium(III) Complexes

Relativistic DFT, TDDFT, low temperature and high field MCD, absorption and emission spectroscopy are a powerful combination for understanding the electronic structure of iridium(III) complexes. The low energy excited states in a family of blue phosphorescent iridium(III) complexes have been thoroughly charted.

By selectively turning on relativistic effects, it was seen that the energy of the iridium 5*d* orbitals are destabilised by the addition of scalar (spin-free) relativistic corrections. Since the low energy excitations in phosphorescent iridium(III) complexes have strong MLCT character, scalar relativistic effects lead to important changes in the absorption spectra. Most dramatically, scalar relativistic effects are responsible for lowering the singlet and triplet excitation energies by ~0.2 eV.

SOC is an essential relativistic effect for understanding the fine details of the MCD and absorption spectra, and is vital for the phosphorescence and fast intersystem crossing. Based on the one-component ZORA, SOC perturbation calculations reproduce the essential features of more computationally difficult and expensive two-component calculations. This is significant because it is easier to relate the underlying scalar relativistic excitations of the one-component methodology to molecular orbital theory. By tracing the orbital heritage of individual excitations it was found that indirect relativistic effects on the valence 5*d* electrons (due to charge screening by the core electrons) stabilise the MLCT states by increasing the degree to which singlet and triplet excitations can mix by SOC.

Building upon this foundation for describing relativistic effects, the changes wrought by fluorination on the molecular properties of phosphorescent iridium(III) complexes have been investigated. Within the family of $Ir(ptz)_3$ complexes the substitution of hydrogen for fluorine can have a significant effect on both the colour and photoluminescence efficiency.[19] Using relativistic TDDFT a subtle interplay between chemical substitution and SOC appears. The lowest energy excitation 1A has a vanishingly small oscillator strength, so at temperatures >10 K the degenerate second lowest excitation 2E dominates both the absorption and emission processes. In all the complexes studied the characteristic MCD A-term is due to the magnetic splitting of 2E.

Fluorine substitutions act independently to affect the properties of phosphorescent iridium(III) complexes. A simple linear and additive relationship was observed across a range of molecular properties, both experimental and calculated, including optical energy gaps, oxidation potentials,

orbital energies and charge distribution. This additive relationship may therefore be a useful method for designing and predicting the properties of new phosphorescent iridium(III) complexes.

For phosphorescent OLEDs it is important to maximise the radiative rate. Therefore an understanding of the underlying features of the electronic structure that lead to high radiative rates is invaluable. If this can be accomplished without performing expensive and complicated calculations which include SOC, then much greater versatility is afforded in the study of this class of complexes. It was found that the radiative rate across the family of $Ir(ptz)_3$ complexes is critically dependent on the $S_3(E)$-$T_1(A)$ energy gap. Since these particular excitations arise predominantly from HOMO-1→LUMO and HOMO→LUMO transitions respectively, the primary electronic feature for determining the radiative rate is the energy of splitting between HOMO and HOMO-1. In a perfectly octahedral environment the HOMO (A) and HOMO-1 (E) would form a triply degenerate t_{2g} orbital manifold, therefore the decrease in radiative rate which occurs as the HOMO/HOMO-1 energy gap increases is determined by the distortion of the orbital symmetry from octahedral.

7.1.2 Morphology of Phosphorescent Organic Films

Studying buried interfaces in organic films is challenging because such interfaces are inherently difficult to probe without damaging or disrupting the delicate film structure. However, NR and *in situ* PL have proved to be a successful combination for correlating morphological changes with the emissive properties of the film, while conserving the integrity of the organic film.

In blend films of $Ir(ppy)_3$ in CBP it was found that phase separation between the two components occurred laterally across the film surface after thermal annealing at 80 °C. There was no evidence of vertical (perpendicular to the substrate surface) phase separation. The propensity for this combination of organic materials to phase separate was dependent on the blend ratio, and by employing selective deuteration it was possible to precisely determine the blending ratio non-destructively. High blend ratios suppress phase separation, but generally afford lower device efficiencies, so a compromise exists between device efficiency and film durability.

In a multilayer film system comprising BCP, TCTA and $Ir(ppy)_3$:CBP layers, diffusion between BCP and $Ir(ppy)_3$:CBP layers occurred rapidly after the film was heated to a critical temperature (90-100 °C). Diffusion between BCP and $Ir(ppy)_3$:CBP layers was directly correlated to a decrease in the photoluminescence performance of the multilayer stack. However, the TCTA/$Ir(ppy)_3$:CBP interface was stable under all annealing conditions and film geometries. These results show that it

is important to carefully choose suitable materials that form stable layers and interfaces so as to maximise the performance and durability of OLEDs.

7.2 Future Prospects

The development of better and more efficient phosphorescent OLEDs will depend critically on a deeper understanding of the molecular design principles of phosphorescent complexes and the specific interfacial interactions between organic charge transport layers.

As one of the heaviest stable elements in the periodic table (and therefore with the strongest SOC), iridium(III) complexes look fated to remain the preferred metal centre for phosphorescent OLEDs. Intelligent ligand design will therefore play a vital role in creating new high performance phosphors. While great strides have been made in the synthesis and rapid expansion of known complexes, a better understanding and application of quantum chemical theory will ultimately lead to clearer design rationales. This will only happen if synthetic and theoretical chemists work more closely together. The key to fostering this association will be more reliable and computationally efficient techniques for evaluating molecular targets before synthesis is attempted. While it is tempting to prepare only high performance targets, any predictive scheme must be continually refined so molecules anticipated to have poor performance should also be prepared and characterised.

However, several difficult problems must be tackled before a complete model of phosphorescent molecules is achieved. Firstly, molecular vibrations are a key contributor to the non-radiative rate. Only when both the radiative and non-radiative processes are understood will accurate predictions of PLQY be possible. Like the calculations presented in this thesis for electronic transitions, benchmarking calculations will be needed to characterise the vibrational landscape of a number of phosphorescent complexes. The vibrational landscape then needs to be mapped on the electronic transitions, to understand the specific interactions through which vibrational modes couple to electronic excited states.

Second, and perhaps most challenging, will be the determination of the excited state molecular structure. It is from this transient geometry that phosphorescence ultimately occurs, not the ground state geometry used for this thesis and throughout the literature. However, unlike ground state crystal structures, excited state geometries are far more difficult to probe experimentally. While structural techniques do exist for examining excited state geometries[47,48,276] they are not routine techniques, requiring complicated experimental set-ups and detailed interpretation. Certainly, a clear picture like that offered by a crystal structure will not be possible. TDDFT calculations are

now available that allow geometry optimisations to be performed with respect to individual excited states, although a cautious approach should be taken when tackling the calculation of excited state geometries due to the lack of experimental data.

In the realm of thin film morphology it has been shown in this thesis that, to temperatures of 100 °C, small molecule organic films are not morphologically stable. It would be interesting to correlate these morphological changes with the electrical performance of a working device. While the PL measurements suggest that the emission performance of the multilayer stack is degraded, how does the charge transport change within the film? A highly ambitious and technical challenge would be the *in situ* NR measurement of an operational OLED.

A comprehensive study of diffusion between bilayer couples composed of common OLED materials, beyond the small sample of materials studied in this thesis, would help to answer a few key questions related to the interfacial interaction of organic multilayers. Does diffusion occur when there is just one highly mobile species, or do both layers of a diffusion couple have to be compatible? How does doping concentration affect diffusion? At lower temperatures does diffusion or phase separation still occur, and on what time scale? Does the thermal stability of a multilayer film depend on deposition conditions, or is it an intrinsic property of the materials it is composed of? The structural data provided by NR of thin organic films is difficult to obtain from any other technique, so NR will surely have an extensive role to play in understanding the interfacial interactions between organic multilayers.

Appendix A

Supplement to Chapter 2

Molecular Geometry

Table A1. Optimised molecular geometry of $Ir(ptz)_3$.

Atom	X	Y	Z
Ir	0.000000000	0.000000000	0.012999633
N	-1.770209685	0.500451732	1.128722922
N	0.451700929	-1.783272423	1.128722922
N	1.318508756	1.282820691	1.128722922
C	-2.170144347	1.235038888	2.212995842
C	0.015497122	-2.496919578	2.212995842
C	2.154647225	1.261880690	2.212995842
N	-3.488770329	1.190783019	2.417800708
N	0.713136819	-3.616755242	2.417800708
N	2.775633509	2.425972223	2.417800708
N	-3.945340993	0.367580989	1.379115489
N	1.654336022	-3.600556021	1.379115489
N	2.291004971	3.232975032	1.379115489
C	-2.901588729	-0.044443416	0.604043746
C	1.489283492	-2.490627842	0.604043746
C	1.412305237	2.535071258	0.604043746
C	0.629737473	2.853210414	-0.572182841
C	-2.785821437	-0.881236558	-0.572182841
C	2.156083964	-1.971973856	-0.572182841
C	0.605879817	4.112311686	-1.205211381
C	-3.864306297	-1.531448530	-1.205211381
C	3.258426480	-2.580863156	-1.205211381
C	-0.182418397	4.305534414	-2.337688610
C	-3.637492981	-2.310746174	-2.337688610
C	3.819911379	-1.994788241	-2.337688610
C	-0.944761954	3.236568171	-2.834133282
C	-2.330569280	-2.436471938	-2.834133282
C	3.275331234	-0.800096233	-2.834133282
C	-0.924353516	1.987014972	-2.205068530
C	-1.258628685	-1.794021113	-2.205068530
C	2.182982202	-0.192993859	-2.205068530
C	-0.144462410	1.740039154	-1.053442369
C	-1.434686906	-0.995127694	-1.053442369
C	1.579149316	-0.744911460	-1.053442369
C	-5.372924205	0.104141948	1.270546792
C	2.596272530	-4.705159828	1.270546792
C	2.776651675	4.601017880	1.270546792
H	1.193618076	4.939925664	-0.821827699
H	-4.874910156	-1.436259256	-0.821827699

H	3.681292080	-3.503666409	-0.821827699
H	-0.205189173	5.273465222	-2.828574694
H	-4.464360262	-2.814431648	-2.828574694
H	4.669549435	-2.459033575	-2.828574694
H	-1.558722296	3.381498721	-3.719702336
H	-2.149102647	-3.040642467	-3.719702336
H	3.707824943	-0.340856255	-3.719702336
H	-1.522010736	1.181746940	-2.618595203
H	-0.262417503	-1.908973432	-2.618595203
H	1.784428239	0.727226492	-2.618595203
H	-5.856684371	0.662554661	2.071334791
H	2.354553018	-5.403314777	2.071334791
H	3.502131353	4.740760117	2.071334791
H	-5.584110283	-0.962650743	1.390797439
H	3.625735140	-4.354655991	1.390797439
H	1.958375143	5.317306734	1.390797439
H	-5.756188433	0.444972412	0.304528391
H	2.492736804	-5.207491618	0.304528391
H	3.263451629	4.762519206	0.304528391
H	-1.500379133	1.796288274	2.839677927
H	-0.805441711	-2.197510581	2.839677927
H	2.305820844	0.401222308	2.839677927

Orbital Energies

Table A2. Selected Molecular Orbital Energies and C_3 Symmetry Assignment

	Non-relativistic		*Scalar relativistic*	
Orbital	*Energy (eV)*	*Ligand contribution*	*Energy (eV)*	*Ligand contribution*
HOMO-9 (A)	-7.842	0.99	-7.845	1.00
HOMO-8 (E)	-7.755	1.00	-7.762	1.00
HOMO-8 (E)	-7.746	1.00	-7.754	1.00
HOMO-7 (E)	-7.219	0.79	-7.283	0.80
HOMO-7 (E)	-7.216	0.77	-7.279	0.79
HOMO-6 (A)	-6.778	0.67	-6.877	0.91
HOMO-5 (E)	-6.735	0.76	-6.626	0.80
HOMO-5 (E)	-6.732	0.76	-6.624	0.80
HOMO-4 (A)	-6.420	0.92	-6.611	0.76
HOMO-3 (A)	-6.212	0.97	-6.230	0.96
HOMO-2 (E)	-6.084	0.94	-6.056	0.95
HOMO-2 (E)	-6.080	0.94	-6.052	0.95
HOMO-1 (E)	-5.366	0.62	-5.100	0.51
HOMO-1 (E)	-5.364	0.63	-5.098	0.50
HOMO (A)	-5.213	0.58	-4.932	0.46

LUMO (A)	-1.093	1.00	-1.098	1.00
LUMO+1 (E)	-0.936	0.98	-0.926	0.97
LUMO+1 (E)	-0.929	0.98	-0.920	0.97
LUMO+2 (A)	0.191	0.99	0.193	0.99
LUMO+3 (E)	0.311	0.96	0.349	0.95
LUMO+3 (E)	0.313	0.96	0.350	0.96
LUMO+4 (A)	0.374	0.99	0.360	0.99
LUMO+5 (A)	0.427	1.00	0.422	1.01
LUMO+6 (E)	0.493	1.00	0.492	1.00
LUMO+6 (E)	0.497	1.00	0.496	1.00
LUMO+7 (E)	0.606	0.99	0.590	0.99
LUMO+7 (E)	0.612	0.99	0.595	0.99

Excitation Energies

*Only transitions with >=5% contribution are reported. H-*n *indicates the HOMO-*n *level and L-*n *indicates the LUMO-*n *level. The symmetry of the MOs are given in parentheses after their name.*

Table A3. Symmetries, energies, oscillator strengths, MLCT weights, and largest MO transition components to the lowest 50 excitations of $Ir(ptz)_3$ calculated by non-relativistic TDDFT in the TZP basis with all electrons included.

Non-relativistic				
Excitation (symmetry assignment)	*E/eV*	*f*	*MLCT*	*Transitions*
S_1 (A)	3.4273	2.32E-02	0.4152	H (A)→L (A) (98%)
S_2 (E)	3.5471	1.26E-02	0.3949	H (A)→L+1 (E) (97%)
	3.5535	1.27E-02	0.3949	H (A)→L+1 (E) (97%)
S_3 (E)	3.6073	4.67E-02	0.3680	H-1 (E)→L (A) (97%)
	3.6096	4.96E-02	0.3731	H-1 (E)→L (A) (97%)
S_4 (A)	3.7217	1.39E-02	0.3502	H-1 (E)→L+1 (E) (98%)
S_5 (E)	3.7580	3.56E-02	0.3506	H-1 (E)→L+1 (E) (96%)
	3.7592	3.86E-02	0.3500	H-1 (E)→L+1 (E) (96%)
S_6 (A)	3.8210	2.07E-02	0.3481	H-1 (E)→L+1 (E) (97%)
S_7 (A)	4.4293	3.29E-03	0.0551	H-3 (A)→L (A) (56%), H-4 (A)→L (A) (39%)
S_8 (E)	4.4831	9.10E-04	0.0633	H-2 (E)→L (A) (85%)
	4.4900	1.51E-03	0.0626	H-2 (E)→L (A) (83%), H-3 (A)→L+1 (E) (5%)
S_9 (E)	4.5549	3.46E-03	0.0400	H-3 (A)→L+1 (E) (49%), H-4 (A)→L+1 (E) (34%)
	4.5605	3.76E-03	0.0396	H-3 (A)→L+1 (E) (51%), H-4 (A)→L+1 (E)

				(35%), H-2 (E)→L+1 (E) (5%)
S_{10} (A)	4.5867	5.27E-03	0.0911	H-2 (E)→L+1 (E) (73%), H (A)→L+2 (A) (12%)
S_{11} (A)	4.6237	5.19E-02	0.1625	H-2 (E)→L+1 (E) (57%), H (A)→L+2 (A) (30%)
S_{12} (E)	4.6305	3.05E-02	0.0991	H-2 (E)→L+1 (E) (64%), H (A)→L+3 (E) (13%)
	4.6339	3.22E-02	0.1014	H-2 (E)→L+1 (E) (68%), H (A)→L+3 (E) (13%)
S_{13} (A)	4.6783	7.50E-05	0.1244	H-4 (A)→L (A) (44%), H-3 (A)→L (A) (23%), H (A)→L+2 (A) (18%), H-2 (E)→L+1 (E) (11%)
S_{14} (E)	4.7572	1.63E-02	0.2408	H (A)→L+3 (E) (53%), H-4 (A)→L+1 (E) (20%), H-3 (A)→L+1 (E) (6%)
	4.7612	1.74E-02	0.2427	H (A)→L+3 (E) (54%), H-4 (A)→L+1 (E) (19%), H-3 (A)→L+1 (E) (6%)
S_{15} (A)	4.7949	0.149	0.2293	H-1 (E)→L+3 (E) (30%), H (A)→L+2 (A) (24%), H-2 (E)→L+1 (E) (20%), H-3 (A)→L (A) (11%), H-4 (A)→L (A) (8%)
S_{16} (E)	4.8075	2.90E-02	0.2778	H-1 (E)→L+2 (A) (56%), H-4 (A)→L+1 (E) (14%), H (A)→L+3 (E) (10%), H-3 (A)→L+1 (E) (7%)
	4.8086	2.59E-02	0.2767	H-1 (E)→L+2 (A) (58%), H-4 (A)→L+1 (E) (14%), H (A)→L+3 (E) (9%), H-3 (A)→L+1 (E) (7%)
S_{17} (E)	4.9017	9.38E-03	0.2110	H-1 (E)→L+2 (A) (22%), H-1 (E)→L+3 (E) (21%), H-3 (A)→L+1 (E) (14%), H-4 (A)→L+1 (E) (12%), H-5 (E)→L (A) (5%)
	4.9033	7.97E-03	0.2240	H-1 (E)→L+3 (E) (20%), H-1 (E)→L+2 (A) (17%), H-3 (A)→L+1 (E) (13%), H-4 (A)→L+1 (E) (11%), H (A)→L+4 (A) (8%)
S_{18} (A)	4.9051	6.17E-03	0.3587	H (A)→L+4 (A) (66%), H (A)→L+5 (A) (6%)
S_{19} (A)	4.9347	6.75E-02	0.2894	H-1 (E)→L+3 (E) (64%), H (A)→L+4 (A) (7%)
S_{20} (E)	4.9514	1.19E-02	0.2498	H-5 (E)→L (A) (39%), H-1 (E)→L+3 (E) (26%)
	4.9537	1.22E-02	0.2473	H-5 (E)→L (A) (39%), H-1 (E)→L+3 (E) (25%)
S_{21} (A)	5.0195	1.91E-02	0.2845	H-6 (A)→L (A) (52%), H-1 (E)→L+3 (E) (17%), H-5 (E)→L+1 (E) (14%)
S_{22} (E)	5.0456	1.01E-02	0.3338	H-1 (E)→L+4 (A) (36%), H (A)→L+7 (E) (13%), H (A)→L+6 (E) (12%), H-1 (E)→L+3 (E) (11%)
	5.0488	9.28E-03	0.3319	H-1 (E)→L+4 (A) (42%), H (A)→L+7 (E) (11%), H (A)→L+6 (E) (5%), H-1 (E)→L+3 (E) (5%)
S_{23} (E)	5.0868	2.05E-03	0.3723	H-1 (E)→L+4 (A) (35%), H (A)→L+6 (E) (29%), H (A)→L+7 (E) (19%)
	5.0886	3.19E-03	0.3734	H-1 (E)→L+4 (A) (34%), H (A)→L+6 (E) (30%), H (A)→L+7 (E) (20%)
S_{24} (A)	5.0982	2.95E-03	0.3883	H (A)→L+5 (A) (66%), H (A)→L+4 (A) (9%)
S_{25} (E)	5.1041	9.63E-02	0.2444	H-5 (E)→L (A) (30%), H-5 (E)→L+1 (E) (25%), H-1 (E)→L+4 (A) (10%)
	5.1084	9.27E-02	0.2441	H-5 (E)→L (A) (28%), H-5 (E)→L+1 (E) (25%), H-1 (E)→L+4 (A) (8%), H-6 (A)→L+1 (E) (5%)

S_{26} (A)	5.1129	1.12E-02	0.2618	H-5 (E)→L+1 (E) (40%), H-6 (A)→L (A) (21%), H (A)→L+5 (A) (9%)
S_{27} (E)	5.1625	3.78E-02	0.3022	H-6 (A)→L+1 (E) (42%), H (A)→L+6 (E) (12%)
	5.1646	3.35E-02	0.2999	H-6 (A)→L+1 (E) (33%), H (A)→L+6 (E) (14%), H-1 (E)→L+5 (A) (5%)
S_{28} (A)	5.1731	1.03E-02	0.2191	H-5 (E)→L+1 (E) (92%)
S_{29} (E)	5.1879	4.45E-02	0.3258	H (A)→L+7 (E) (27%), H-1 (E)→L+5 (A) (16%), H-6 (A)→L+1 (E) (14%), H (A)→L+6 (E) (9%), H-5 (E)→L+1 (E) (5%)
	5.1888	3.94E-02	0.3477	H (A)→L+7 (E) (35%), H-1 (E)→L+5 (A) (16%), H-6 (A)→L+1 (E) (12%), H (A)→L+6 (E) (8%)
S_{30} (E)	5.1960	1.60E-02	0.2761	H-5 (E)→L+1 (E) (31%), H-6 (A)→L+1 (E) (19%), H (A)→L+7 (E) (13%), H-1 (E)→L+5 (A) (8%)
	5.1991	2.29E-02	0.2637	H-5 (E)→L+1 (E) (31%), H-6 (A)→L+1 (E) (30%), H (A)→L+7 (E) (7%), H-1 (E)→L+5 (A) (5%)
S_{31} (A)	5.2099	4.82E-02	0.3054	H-1 (E)→L+7 (E) (31%), H-1 (E)→L+6 (E) (16%), H-1 (E)→L+3 (E) (14%)
S_{32} (A)	5.2583	4.16E-02	0.3439	H-1 (E)→L+6 (E) (48%), H-1 (E)→L+7 (E) (35%)
S_{33} (E)	5.2804	9.80E-03	0.3317	H-1 (E)→L+7 (E) (40%), H-1 (E)→L+6 (E) (17%), H-1 (E)→L+5 (A) (16%)
	5.2811	1.38E-02	0.3333	H-1 (E)→L+7 (E) (41%), H-1 (E)→L+5 (A) (18%), H-1 (E)→L+6 (E) (14%)
T_1 (A)	3.0120	0	0.3370	H (A)→L (A) (53%), H-1 (E)→L+1 (E) (28%), H-2 (E)→L+1 (E) (11%)
T_2 (E)	3.0379	0	0.3158	H (A)→L+1 (E) (39%), H-1 (E)→L (A) (24%), H-1 (E)→L+1 (E) (14%), H-2 (E)→L (A) (8%)
	3.0395	0	0.3139	H (A)→L+1 (E) (39%), H-1 (E)→L (A) (22%), H-1 (E)→L+1 (E) (14%), H-2 (E)→L (A) (7%)
T_3 (E)	3.4073	0	0.2376	H-1 (E)→L (A) (41%), H-1 (E)→L+1 (E) (16%), H-2 (E)→L (A) (13%), H-3 (A)→L+1 (E) (7%)
	3.4118	0	0.2365	H-1 (E)→L (A) (38%), H-1 (E)→L+1 (E) (17%), H-2 (E)→L (A) (12%), H-3 (A)→L+1 (E) (6%)
T_4 (A)	3.4563	0	0.1962	H-1 (E)→L+1 (E) (46%), H-2 (E)→L+1 (E) (26%), H-3 (A)→L (A) (13%)
T_5 (A)	3.5292	0	0.3472	H (A)→L (A) (43%), H-1 (E)→L+1 (E) (40%)
T_6 (E)	3.5730	0	0.3414	H (A)→L+1 (E) (53%), H-1 (E)→L+1 (E) (17%), H-1 (E)→L (A) (14%)
	3.5793	0	0.3386	H (A)→L+1 (E) (52%), H-1 (E)→L+1 (E) (18%), H-1 (E)→L (A) (14%)
T_7 (E)	3.6870	0	0.2641	H-1 (E)→L+1 (E) (39%), H-1 (E)→L (A) (17%), H-2 (E)→L (A) (8%)
	3.6921	0	0.2659	H-1 (E)→L+1 (E) (44%), H-1 (E)→L (A) (16%), H-2 (E)→L (A) (8%)
T_8 (A)	3.7160	0	0.2932	H-1 (E)→L+1 (E) (66%)
T_9 (A)	4.0191	0	0.2805	H (A)→L+2 (A) (32%), H-1 (E)→L+3 (E)

				(31%), H-3 (A)→L (A) (5%)
T_{10} (E)	4.0200	0	0.2714	H (A)→L+3 (E) (24%), H-1 (E)→L+2 (A) (20%), H-1 (E)→L+3 (E) (15%)
	4.0200	0	0.2722	H-1 (E)→L+2 (A) (26%), H (A)→L+3 (E) (24%), H-1 (E)→L+3 (E) (16%)
T_{11} (A)	4.3397	0	0.0661	H-4 (A)→L (A) (49%), H-3 (A)→L (A) (36%)
T_{12} (E)	4.4150	0	0.0885	H-2 (E)→L (A) (22%), H-3 (A)→L+1 (E) (14%), H-2 (E)→L+1 (E) (11%), H-5 (E)→L (A) (8%)
	4.4215	0	0.0891	H-2 (E)→L (A) (20%), H-3 (A)→L+1 (E) (14%), H-5 (E)→L (A) (8%), H-2 (E)→L+1 (E) (6%)
T_{13} (E)	4.4454	0	0.0702	H-4 (A)→L+1 (E) (34%), H-3 (A)→L+1 (E) (21%)
T_{14} (A)	4.4481	0	0.1322	H-5 (E)→L+1 (E) (20%), H-4 (A)→L (A) (8%), H-2 (E)→L+1 (E) (6%), H-6 (A)→L (A) (5%)
T_{13}' (E)	4.4498	0	0.0716	H-4 (A)→L+1 (E) (37%), H-3 (A)→L+1 (E) (22%)
T_{15} (A)	4.4833	0	0.1663	H (A)→L+4 (A) (26%)
T_{16} (E)	4.5116	0	0.1097	H-2 (E)→L (A) (14%), H (A)→L+7 (E) (9%), H-4 (A)→L+1 (E) (8%), H-1 (E)→L+4 (A) (5%)
	4.5147	0	0.1077	H-2 (E)→L (A) (14%), H (A)→L+7 (E) (9%), H-4 (A)→L+1 (E) (7%)
T_{17} (E)	4.5562	0	0.1096	H-2 (E)→L+1 (E) (28%), H-5 (E)→L (A) (12%), H-5 (E)→L+1 (E) (7%), H-2 (E)→L (A) (7%)
	4.5634	0	0.1135	H-2 (E)→L+1 (E) (27%), H-5 (E)→L+1 (E) (13%), H-5 (E)→L (A) (13%), H-2 (E)→L (A) (8%)
T_{18} (A)	4.5695	0	0.0750	H-2 (E)→L+1 (E) (62%)
T_{19} (E)	4.6861	0	0.3035	H (A)→L+3 (E) (47%), H-1 (E)→L+2 (A) (12%), H (A)→L+7 (E) (6%)
	4.6894	0	0.3037	H (A)→L+3 (E) (47%), H-1 (E)→L+2 (A) (12%), H (A)→L+7 (E) (6%)
T_{20} (A)	4.6959	0	0.2349	H (A)→L+2 (A) (33%), H-3 (A)→L (A) (14%), H-1 (E)→L+3 (E) (14%), H-4 (A)→L (A) (10%), H-2 (E)→L+1 (E) (5%)
T_{21} (A)	4.7605	0	0.2557	H-6 (A)→L (A) (23%), H-1 (E)→L+3 (E) (18%), H (A)→L+2 (A) (14%), H-5 (E)→L+1 (E) (11%), H-4 (A)→L (A) (6%)
T_{22} (E)	4.7767	0	0.1494	H-4 (A)→L+1 (E) (21%), H-3 (A)→L+1 (E) (16%), H-1 (E)→L+3 (E) (14%), H-1 (E)→L+2 (A) (10%), H-6 (A)→L+1 (E) (6%)
	4.7815	0	0.1594	H-4 (A)→L+1 (E) (20%), H-1 (E)→L+3 (E) (16%), H-3 (A)→L+1 (E) (15%), H-1 (E)→L+2 (A) (11%), H-6 (A)→L+1 (E) (6%)
T_{23} (E)	4.8160	0	0.2285	H-1 (E)→L+3 (E) (18%), H-5 (E)→L (A) (15%), H-1 (E)→L+2 (A) (14%), H-3 (A)→L+1 (E) (9%)
	4.8198	0	0.2186	H-1 (E)→L+3 (E) (23%), H-5 (E)→L (A) (16%), H-1 (E)→L+2 (A) (12%), H-3 (A)→L+1 (E) (10%), H-4 (A)→L+1 (E) (5%)

T_{24} (A)	4.8343	0	0.2719	H-1 (E)→L+3 (E) (49%), H-6 (A)→L (A) (17%)
T_{25} (A)	4.8669	0	0.2180	H-5 (E)→L+1 (E) (41%), H-6 (A)→L (A) (23%)
T_{26} (E)	4.8982	0	0.1956	H-6 (A)→L+1 (E) (27%), H-5 (E)→L+1 (E) (17%), H-5 (E)→L (A) (13%)
	4.9010	0	0.1937	H-6 (A)→L+1 (E) (27%), H-5 (E)→L+1 (E) (14%), H-5 (E)→L (A) (12%)
T_{27} (A)	4.9429	0	0.2460	H (A)→L+4 (A) (43%), H-9 (A)→L (A) (5%)
T_{28} (E)	4.9806	0	0.2348	H (A)→L+6 (E) (16%), H (A)→L+7 (E) (13%), H-1 (E)→L+4 (A) (11%), H-6 (A)→L+1 (E) (10%)
	4.9824	0	0.2299	H (A)→L+6 (E) (16%), H (A)→L+7 (E) (14%), H-6 (A)→L+1 (E) (9%), H-1 (E)→L+4 (A) (5%)
T_{29} (A)	5.0081	0	0.1246	H-3 (A)→L+2 (A) (12%), H-2 (E)→L+3 (E) (5%)
T_{30} (E)	5.0206	0	0.2314	H-1 (E)→L+4 (A) (29%), H (A)→L+7 (E) (16%)
	5.0237	0	0.2278	H-1 (E)→L+4 (A) (28%), H (A)→L+7 (E) (15%)
T_{31} (E)	5.0617	0	0.1317	H-2 (E)→L+2 (A) (12%), H-1 (E)→L+4 (A) (10%), H-3 (A)→L+3 (E) (6%)
	5.0637	0	0.1291	H-2 (E)→L+2 (A) (13%), H-1 (E)→L+4 (A) (10%), H-3 (A)→L+3 (E) (7%), H (A)→L+7 (E) (5%)
T_{32} (A)	5.0918	0	0.3963	H (A)→L+5 (A) (76%), H (A)→L+4 (A) (8%)
T_{33} (E)	5.1068	0	0.2241	H-5 (E)→L+1 (E) (31%), H-5 (E)→L (A) (19%), H-6 (A)→L+1 (E) (15%), H-7 (E)→L (A) (6%)
	5.1142	0	0.2314	H-5 (E)→L+1 (E) (27%), H-5 (E)→L (A) (18%), H-6 (A)→L+1 (E) (18%), H-7 (E)→L (A) (5%)

Table A4. Symmetries, energies, oscillator strengths, MLCT weights, and largest MO transition components to the lowest 50 excitations of $Ir(ptz)_3$ calculated by scalar relativistic TDDFT in the TZP basis with all electrons included.

Scalar Relativistic				
Excitations	*E/eV*	*f*	*MLCT*	*Transitions*
S_1 (A)	3.1068	1.45E-02	0.5348	H (A)→L (A) (98%)
S_2 (E)	3.2378	8.04E-03	0.5045	H (A)→L+1 (E) (98%)
	3.2436	8.11E-03	0.5045	H (A)→L+1 (E) (98%)
S_3 (E)	3.3099	4.12E-02	0.4891	H-1 (E)→L (A) (96%)
	3.3119	4.36E-02	0.4889	H-1 (E)→L (A) (96%)
S_4 (A)	3.4234	8.65E-03	0.4597	H-1 (E)→L+1 (E) (98%)
S_5 (E)	3.4793	4.23E-02	0.4599	H-1 (E)→L+1 (E) (93%)
	3.4809	4.49E-02	0.4600	H-1 (E)→L+1 (E) (92%)
S_6 (A)	3.5579	1.22E-02	0.4574	H-1 (E)→L+1 (E) (97%)

S_7 (A)	4.3646	7.15E-05	0.4835	H (A)→L+2 (A) (89%)
S_8 (E)	4.4389	3.83E-03	0.1756	H-2 (E)→L (A) (65%), H (A)→L+3 (E) (25%)
	4.4422	4.31E-03	0.1979	H-2 (E)→L (A) (60%), H (A)→L+3 (E) (30%)
S_9 (E)	4.4942	8.69E-04	0.3182	H (A)→L+3 (E) (55%), H-2 (E)→L (A) (20%)
	4.4966	8.06E-04	0.2991	H (A)→L+3 (E) (52%), H-2 (E)→L (A) (24%), H-2 (E)→L+1 (E) (5%)
S_{10} (E)	4.5377	2.48E-02	0.4183	H-1 (E)→L+2 (A) (82%)
	4.5392	2.45E-02	0.4144	H-1 (E)→L+2 (A) (81%)
S_{11} (A)	4.5752	1.40E-04	0.1056	H-2 (E)→L+1 (E) (73%), H (A)→L+4 (A) (10%)
S_{12} (A)	4.5828	1.23E-03	0.4361	H (A)→L+4 (A) (64%), H-1 (E)→L+3 (E) (14%)
S_{13} (A)	4.5998	1.80E-03	0.0648	H-3 (A)→L (A) (58%), H-2 (E)→L+1 (E) (28%)
S_{14} (E)	4.6376	2.74E-02	0.1028	H-2 (E)→L+1 (E) (62%), H-3 (A)→L+1 (E) (11%)
	4.6414	2.72E-02	0.1160	H-2 (E)→L+1 (E) (60%), H-3 (A)→L+1 (E) (11%), H-1 (E)→L+3 (E) (5%)
S_{15} (A)	4.6504	4.04E-02	0.2890	H-1 (E)→L+3 (E) (51%), H-2 (E)→L+1 (E) (31%), H (A)→L+4 (A) (6%)
S_{16} (E)	4.7234	2.54E-02	0.3363	H-1 (E)→L+3 (E) (68%), H-3 (A)→L+1 (E) (19%)
	4.7250	2.77E-02	0.3320	H-1 (E)→L+3 (E) (65%), H-3 (A)→L+1 (E) (20%)
S_{17} (A)	4.7312	1.19E-01	0.2966	H-1 (E)→L+3 (E) (52%), H-3 (A)→L (A) (16%), H-2 (E)→L+1 (E) (16%)
S_{18} (E)	4.7545	1.03E-03	0.4589	H-1 (E)→L+4 (A) (56%), H (A)→L+7 (E) (14%), H (A)→L+6 (E) (6%), H-3 (A)→L+1 (E) (5%)
	4.7572	2.98E-03	0.4554	H-1 (E)→L+4 (A) (66%), H (A)→L+7 (E) (10%)
S_{19} (E)	4.7741	2.22E-02	0.4806	H (A)→L+6 (E) (33%), H (A)→L+7 (E) (32%), H-1 (E)→L+4 (A) (22%)
	4.7783	2.24E-02	0.4862	H (A)→L+7 (E) (37%), H (A)→L+6 (E) (35%), H-1 (E)→L+4 (A) (17%)
S_{20} (A)	4.8251	3.08E-04	0.5289	H (A)→L+5 (A) (85%)
S_{21} (E)	4.8420	3.12E-02	0.1523	H-3 (A)→L+1 (E) (38%), H-5 (E)→L (A) (29%)
	4.8432	2.90E-02	0.1490	H-3 (A)→L+1 (E) (39%), H-5 (E)→L (A) (27%)
S_{22} (A)	4.8491	2.01E-02	0.2248	H-4 (A)→L (A) (70%), H-6 (A)→L (A) (6%)
S_{23} (A)	4.9086	2.34E-02	0.4171	H-1 (E)→L+7 (E) (33%), H-1 (E)→L+3 (E) (23%), H-1 (E)→L+6 (E) (20%)
S_{24} (E)	4.9247	1.34E-02	0.4471	H (A)→L+6 (E) (21%), H-1 (E)→L+6 (E) (18%), H-1 (E)→L+5 (A) (17%), H (A)→L+7 (E) (14%), H-5 (E)→L (A) (7%)
	4.9265	2.31E-02	0.4199	H-1 (E)→L+6 (E) (20%), H (A)→L+6 (E) (18%), H-1 (E)→L+5 (A) (13%), H-5 (E)→L (A) (9%), H (A)→L+7 (E) (7%)
S_{25} (E)	4.9419	8.28E-02	0.3388	H-5 (E)→L (A) (21%), H (A)→L+7 (E) (19%), H-1 (E)→L+5 (A) (8%), H-4 (A)→L+1 (E) (7%)

	4.9429	7.57E-02	0.3440	H (A)→L+7 (E) (20%), H-5 (E)→L (A) (18%), H-1 (E)→L+5 (A) (10%), H-4 (A)→L+1 (E) (7%)
S_{26} (A)	4.9627	1.05E-02	0.2279	H-6 (A)→L (A) (46%), H-1 (E)→L+7 (E) (16%), H-1 (E)→L+6 (E) (10%)
S_{27} (E)	4.9754	6.12E-02	0.2859	H-4 (A)→L+1 (E) (28%), H-1 (E)→L+7 (E) (19%), H-1 (E)→L+6 (E) (7%), H-6 (A)→L+1 (E) (6%), H-5 (E)→L (A) (5%)
	4.9785	7.07E-02	0.2860	H-4 (A)→L+1 (E) (31%), H-1 (E)→L+7 (E) (18%), H-5 (E)→L (A) (7%), H-6 (A)→L+1 (E) (5%)
S_{28} (A)	4.9867	6.47E-02	0.3442	H-1 (E)→L+6 (E) (35%), H-5 (E)→L+1 (E) (15%), H-1 (E)→L+7 (E) (12%), H-6 (A)→L (A) (8%)
S_{29} (E)	5.0162	2.66E-02	0.2195	H-4 (A)→L+1 (E) (28%), H-5 (E)→L (A) (12%), H-6 (A)→L+1 (E) (6%), H-1 (E)→L+5 (A) (6%)
	5.0186	2.19E-02	0.2478	H-4 (A)→L+1 (E) (22%), H-1 (E)→L+5 (A) (15%), H-5 (E)→L (A) (11%), H-5 (E)→L+1 (E) (7%), H-6 (A)→L+1 (E) (5%)
S_{30} (E)	5.0262	1.99E-03	0.4799	H-1 (E)→L+5 (A) (52%), H (A)→L+6 (E) (18%), H (A)→L+7 (E) (9%)
	5.0285	5.83E-03	0.4210	H-1 (E)→L+5 (A) (41%), H (A)→L+6 (E) (16%), H (A)→L+7 (E) (8%)
S_{31} (A)	5.0400	4.95E-05	0.1920	H-5 (E)→L+1 (E) (37%), H-6 (A)→L (A) (26%), H-4 (A)→L (A) (13%)
S_{32} (E)	5.0887	2.85E-02	0.1483	H-5 (E)→L+1 (E) (47%), H-6 (A)→L+1 (E) (9%)
	5.0891	2.99E-02	0.1519	H-5 (E)→L+1 (E) (48%), H-6 (A)→L+1 (E) (10%)
S_{33} (A)	5.1025	2.87E-03	0.2767	H-5 (E)→L+1 (E) (52%), H-1 (E)→L+6 (E) (17%), H-1 (E)→L+7 (E) (12%)
T_1 (A)	2.8386	0	0.4767	H (A)→L (A) (69%), H-1 (E)→L+1 (E) (21%)
T_2 (E)	2.8882	0	0.4459	H (A)→L+1 (E) (48%), H-1 (E)→L (A) (26%), H-1 (E)→L+1 (E) (5%)
	2.8908	0	0.4451	H (A)→L+1 (E) (48%), H-1 (E)→L (A) (25%), H-1 (E)→L+1 (E) (5%)
T_3 (E)	3.1681	0	0.4395	H-1 (E)→L (A) (53%), H (A)→L+1 (E) (17%), H-1 (E)→L+1 (E) (16%)
	3.1732	0	0.4392	H-1 (E)→L (A) (53%), H (A)→L+1 (E) (18%), H-1 (E)→L+1 (E) (17%)
T_4 (A)	3.2055	0	0.4508	H-1 (E)→L+1 (E) (80%), H (A)→L (A) (13%)
T_5 (E)	3.3004	0	0.4394	H-1 (E)→L+1 (E) (52%), H (A)→L+1 (E) (22%), H-1 (E)→L (A) (12%)
	3.3061	0	0.4402	H-1 (E)→L+1 (E) (52%), H (A)→L+1 (E) (22%), H-1 (E)→L (A) (12%)
T_6 (A)	3.3151	0	0.3879	H-1 (E)→L+1 (E) (62%), H (A)→L (A) (12%), H-3 (A)→L (A) (6%), H-2 (E)→L+1 (E) (6%)
T_7 (E)	3.5147	0	0.1617	H-2 (E)→L (A) (20%), H-3 (A)→L+1 (E) (14%), H-2 (E)→L+1 (E) (13%), H-1 (E)→L+1 (E) (6%), H (A)→L+1 (E) (5%)

	3.5179	0	0.1591	H-2 (E)→L (A) (19%), H-2 (E)→L+1 (E) (16%), H-3 (A)→L+1 (E) (14%), H (A)→L+1 (E) (6%)
T_8 (A)	3.5217	0	0.1896	H-2 (E)→L+1 (E) (28%), H-1 (E)→L+1 (E) (21%), H-3 (A)→L (A) (17%)
T_9 (A)	3.8943	0	0.3724	H (A)→L+2 (A) (39%), H-1 (E)→L+3 (E) (25%), H-2 (E)→L+1 (E) (10%), H-3 (A)→L (A) (5%)
T_{10} (E)	3.9076	0	0.3521	H-1 (E)→L+2 (A) (25%), H (A)→L+3 (E) (24%), H-1 (E)→L+3 (E) (16%), H-2 (E)→L (A) (6%)
	3.9079	0	0.3545	H (A)→L+3 (E) (24%), H-1 (E)→L+2 (A) (24%), H-1 (E)→L+3 (E) (15%), H-2 (E)→L (A) (6%)
T_{11} (A)	4.2812	0	0.2356	H (A)→L+2 (A) (18%), H-5 (E)→L+1 (E) (17%), H-4 (A)→L (A) (12%), H-2 (E)→L+1 (E) (5%)
T_{12} (E)	4.3061	0	0.1406	H-5 (E)→L (A) (28%), H-5 (E)→L+1 (E) (14%), H-2 (E)→L (A) (10%), H-4 (A)→L+1 (E) (10%), H-2 (E)→L+1 (E) (5%)
	4.3104	0	0.1415	H-5 (E)→L (A) (27%), H-5 (E)→L+1 (E) (16%), H-2 (E)→L (A) (9%), H-4 (A)→L+1 (E) (9%)
T_{13} (A)	4.3402	0	0.3440	H (A)→L+4 (A) (50%)
T_{14} (E)	4.3844	0	0.3375	H (A)→L+3 (E) (23%), H (A)→L+7 (E) (17%), H-1 (E)→L+4 (A) (8%)
	4.3868	0	0.3377	H (A)→L+3 (E) (22%), H (A)→L+7 (E) (17%), H-1 (E)→L+4 (A) (6%), H-2 (E)→L (A) (5%), H-1 (E)→L+2 (A) (5%)
T_{15} (E)	4.4500	0	0.3243	H (A)→L+3 (E) (15%), H (A)→L+2 (A) (12%), H-1 (E)→L+2 (A) (11%), H-1 (E)→L+3 (E) (9%)
T_{16} (A)	4.4529	0	0.3333	H (A)→L+3 (E) (24%), H-1 (E)→L+2 (A) (22%), H-1 (E)→L+4 (A) (6%)
T_{15}' (E)	4.4533	0	0.3275	H (A)→L+2 (A) (16%), H (A)→L+3 (E) (10%), H-1 (E)→L+3 (E) (9%), H-2 (E)→L+1 (E) (5%), H-1 (E)→L+2 (A) (5%)
T_{17} (E)	4.4954	0	0.1583	H-2 (E)→L (A) (26%), H-2 (E)→L+1 (E) (25%), H-5 (E)→L (A) (6%), H-1 (E)→L+3 (E) (5%)
	4.5016	0	0.1645	H-2 (E)→L+1 (E) (26%), H-2 (E)→L (A) (24%), H-5 (E)→L (A) (5%), H-1 (E)→L+3 (E) (5%)
T_{18} (A)	4.5473	0	0.1714	H-2 (E)→L+1 (E) (46%), H-1 (E)→L+3 (E) (19%), H-3 (A)→L (A) (7%)
T_{19} (E)	4.5584	0	0.3121	H-1 (E)→L+3 (E) (30%), H-1 (E)→L+2 (A) (17%), H-2 (E)→L+1 (E) (8%), H-2 (E)→L (A) (5%)
	4.5621	0	0.3076	H-1 (E)→L+3 (E) (26%), H-1 (E)→L+2 (A) (17%), H-2 (E)→L+1 (E) (13%), H-2 (E)→L (A) (6%), H-1 (E)→L+4 (A) (6%)
T_{20} (A)	4.5896	0	0.2615	H-1 (E)→L+3 (E) (42%), H-3 (A)→L (A) (18%), H-2 (E)→L+1 (E) (11%)
T_{21} (A)	4.6592	0	0.1352	H-2 (E)→L+1 (E) (29%), H-3 (A)→L (A) (24%), H-4 (A)→L (A) (13%), H-1 (E)→L+3 (E) (5%)

T_{22} (E)	4.6954	0	0.3203	H-1 (E)→L+4 (A) (36%), H-3 (A)→L+1 (E) (17%), H (A)→L+7 (E) (9%), H (A)→L+6 (E) (7%)
	4.6971	0	0.3210	H-1 (E)→L+4 (A) (35%), H-3 (A)→L+1 (E) (18%), H (A)→L+7 (E) (10%), H (A)→L+6 (E) (7%)
T_{23} (A)	4.7102	0	0.2675	H (A)→L+4 (A) (20%), H-1 (E)→L+7 (E) (15%), H-4 (A)→L (A) (14%)
T_{24} (A)	4.7196	0	0.1961	H-4 (A)→L (A) (27%), H-6 (A)→L (A) (22%), H-5 (E)→L+1 (E) (17%)
T_{25} (E)	4.7317	0	0.1964	H-3 (A)→L+1 (E) (35%), H-1 (E)→L+4 (A) (10%), H (A)→L+7 (E) (9%), H-5 (E)→L (A) (6%), H (A)→L+6 (E) (5%), H-4 (A)→L+1 (E) (5%)
	4.7368	0	0.1570	H-3 (A)→L+1 (E) (41%), H (A)→L+7 (E) (7%), H-1 (E)→L+4 (A) (7%), H-5 (E)→L (A) (6%)
T_{26} (E)	4.7711	0	0.1844	H-4 (A)→L+1 (E) (22%), H (A)→L+6 (E) (8%), H-5 (E)→L+1 (E) (5%)
	4.7734	0	0.1975	H-4 (A)→L+1 (E) (26%), H (A)→L+6 (E) (8%)
T_{27} (A)	4.8193	0	0.5338	H (A)→L+5 (A) (87%)
T_{28} (E)	4.8293	0	0.3049	H-4 (A)→L+1 (E) (15%), H (A)→L+6 (E) (14%), H-1 (E)→L+7 (E) (13%), H-1 (E)→L+4 (A) (8%)
	4.8324	0	0.3089	H-1 (E)→L+7 (E) (14%), H (A)→L+6 (E) (13%), H-4 (A)→L+1 (E) (10%), H-1 (E)→L+4 (A) (8%), H-1 (E)→L+6 (E) (5%)
T_{29} (A)	4.8567	0	0.3258	H-1 (E)→L+7 (E) (31%), H-1 (E)→L+6 (E) (19%)
T_{30} (E)	4.8859	0	0.3206	H-1 (E)→L+7 (E) (14%), H (A)→L+6 (E) (8%), H (A)→L+7 (E) (8%), H-4 (A)→L+1 (E) (6%), H-1 (E)→L+6 (E) (5%)
	4.8887	0	0.3221	H-1 (E)→L+7 (E) (14%), H (A)→L+7 (E) (8%), H (A)→L+6 (E) (7%), H-4 (A)→L+1 (E) (6%), H-1 (E)→L+6 (E) (5%)
T_{31} (A)	4.9028	0	0.1944	H-6 (A)→L (A) (28%), H-5 (E)→L+1 (E) (14%), H-1 (E)→L+6 (E) (6%)
T_{32} (E)	4.9197	0	0.3641	H-1 (E)→L+5 (A) (19%), H (A)→L+7 (E) (16%), H (A)→L+6 (E) (15%), H-1 (E)→L+6 (E) (13%)
	4.9215	0	0.3703	H-1 (E)→L+5 (A) (18%), H (A)→L+7 (E) (17%), H-1 (E)→L+6 (E) (14%), H (A)→L+6 (E) (14%)
T_{33} (A)	4.9295	0	0.2045	H-1 (E)→L+6 (E) (16%), H-6 (A)→L (A) (16%), H-5 (E)→L+1 (E) (7%)
T_{34} (E)	4.9524	0	0.1353	H-6 (A)→L+1 (E) (29%), H-5 (E)→L+1 (E) (15%), H-5 (E)→L (A) (13%), H-7 (E)→L (A) (9%)

Table A5. Symmetries, energies, oscillator strengths, MLCT weights, and largest MO transition components to the lowest 200 excitations of $Ir(ptz)_3$ calculated by spin-orbit perturbation scalar relativistic TDDFT in the TZP basis with all electrons included.

Spin-orbit Perturbation					
Excitation (symmetry assignment)	*E/eV*	*f*	*Singlet*	*MLCT*	*Transitions*
1 (A)	2.72693	7.59E-06	0.0000	0.4575	T1 (64%)
2 (E)	2.74126	3.15E-03	0.0785	0.4635	T1 (72%), T3 (8%), S3 (7%), T2 (6%)
	2.74237	3.30E-03	0.0771	0.4645	T1 (72%), T3 (8%), S3 (7%), T2 (6%)
3 (A)	2.77378	2.63E-03	0.1852	0.4509	T2 (70%), S1 (17%)
4 (E)	2.80647	8.38E-05	0.0000	0.4300	T2 (65%)
	2.81016	1.16E-04	0.0000	0.4277	T2 (65%)
5 (A)	2.81709	1.22E-03	0.0641	0.4390	T2 (68%), T1 (8%)
6 (E)	2.81983	2.08E-03	0.0693	0.4284	T2 (77%)
	2.82097	1.51E-03	0.0581	0.4302	T2 (68%), T1 (5%)
7 (A)	2.93431	4.14E-03	0.2912	0.4511	T3 (40%), S1 (24%)
8 (E)	2.97087	4.33E-03	0.3408	0.4382	S2 (30%), T5 (22%), T4 (16%)
	2.97660	4.32E-03	0.3397	0.4353	S2 (30%), T4 (20%), T6 (12%)
9 (E)	3.13639	1.42E-03	0.0480	0.4077	T3 (36%), T1 (14%)
	3.13880	1.96E-03	0.0478	0.3918	T3 (35%), T4 (12%), T1 (12%)
10 (A)	3.14243	8.32E-04	0.0440	0.4161	T3 (56%), T1 (15%)
11 (E)	3.15666	2.36E-03	0.0583	0.4036	T3 (36%), T5 (10%), T2 (7%)
	3.15826	2.60E-03	0.0837	0.4138	T3 (30%), T4 (14%), T5 (11%), T2 (8%)
12 (A)	3.17193	1.60E-03	0.1218	0.4312	T4 (44%), T2 (10%), S1 (8%)
13 (E)	3.21922	7.03E-03	0.2329	0.3920	T5 (30%), S1 (6%), T2 (5%)
	3.22536	5.68E-03	0.2525	0.3736	T5 (18%), S1 (13%), T6 (12%)
14 (A)	3.22684	7.89E-03	0.2357	0.3620	T6 (18%), S3 (7%), T2 (6%), S2 (6%), T5 (5%), S5 (5%)
15 (A)	3.30182	3.47E-03	0.2400	0.4316	T3 (36%), S1 (22%), T6 (13%)
16 (E)	3.32787	3.29E-03	0.1240	0.4091	T3 (42%), T5 (10%), S2 (7%)
	3.33084	3.04E-03	0.1207	0.4017	T3 (40%), T5 (14%), S2 (8%)
17 (E)	3.34975	7.42E-03	0.1781	0.4069	T5 (18%), T3 (18%), T6 (16%), S3 (14%)
	3.35137	8.32E-03	0.2313	0.4036	T5 (17%), S3 (16%), T3 (16%)
18 (A)	3.37874	3.94E-03	0.1719	0.4097	T5 (32%), T4 (11%), S2 (7%), S3 (6%), T6 (5%)
19 (E)	3.37942	7.26E-03	0.2981	0.4288	T4 (24%), S2 (15%), S3 (14%), T6 (12%), T5 (11%)

	3.38233	6.79E-03	0.2569	0.4227	T4 (25%), T5 (20%), S3 (12%), S2 (11%)
20 (A)	3.38721	7.65E-04	0.0375	0.3981	T5 (36%), T6 (32%), T4 (9%), T8 (6%)
21 (E)	3.42535	1.51E-02	0.4722	0.4429	S3 (33%), T6 (26%), S2 (14%)
	3.42810	1.48E-02	0.4595	0.4373	T6 (36%), S3 (31%), S2 (14%)
22 (A)	3.48559	5.09E-03	0.5720	0.4038	S4 (55%), T5 (20%)
23 (E)	3.51922	1.23E-02	0.3294	0.3221	T7 (31%), S5 (26%), T5 (21%)
	3.52154	1.35E-02	0.3421	0.3223	T7 (39%), S5 (27%), T5 (9%), S2 (5%)
24 (A)	3.52593	2.91E-03	0.1431	0.2618	T8 (33%), T7 (24%), T5 (10%), S6 (7%)
25 (E)	3.54203	1.87E-04	0.0035	0.1958	T7 (61%), T8 (16%), T5 (7%)
	3.54568	3.27E-04	0.0065	0.2045	T8 (40%), T7 (40%), T5 (8%)
26 (A)	3.55331	2.55E-03	0.1383	0.2084	T7 (60%), S4 (7%)
27 (E)	3.55649	2.02E-03	0.0901	0.2061	T8 (50%), T7 (32%)
	3.55733	1.70E-03	0.0865	0.2053	T8 (52%), T7 (24%)
28 (A)	3.56017	6.49E-04	0.0555	0.1989	T7 (56%), T8 (19%)
29 (E)	3.57373	1.98E-02	0.4609	0.3056	T7 (48%), S5 (46%)
	3.57622	1.97E-02	0.4435	0.2994	S5 (45%), T7 (40%)
30 (A)	3.62530	9.31E-03	0.7573	0.3984	S6 (76%), T8 (12%)
31 (A)	3.83825	2.22E-04	0.0000	0.3515	T9 (67%), T10 (24%)
32 (A)	3.84931	2.97E-04	0.0618	0.3477	T10 (82%)
33 (E)	3.85032	7.14E-04	0.0240	0.3586	T9 (72%), T10 (14%)
	3.85065	7.14E-04	0.0237	0.3589	T9 (72%), T10 (14%)
34 (A)	3.87431	1.15E-03	0.0149	0.3465	T10 (74%), T9 (18%)
35 (E)	3.87853	4.49E-05	0.0000	0.3387	T10 (82%)
	3.87922	4.62E-05	0.0000	0.3393	T10 (82%)
36 (E)	3.88385	4.50E-04	0.0239	0.3416	T10 (83%), T9 (10%)
	3.88413	4.90E-04	0.0241	0.3414	T10 (83%)
37 (E)	4.19300	2.59E-03	0.1725	0.2070	T11 (30%), S8 (5%)
	4.19520	2.67E-03	0.1734	0.1984	T11 (28%)
38 (A)	4.22279	3.14E-04	0.0000	0.2449	T11 (34%), T13 (29%)
39 (A)	4.22694	3.38E-04	0.3380	0.3237	S7 (30%), T15 (12%)
40 (E)	4.24162	1.08E-03	0.0802	0.2542	T13 (36%), T11 (14%), T14 (7%)
	4.24349	1.14E-03	0.0773	0.2526	T13 (36%), T11 (12%), T14 (7%)
41 (A)	4.28747	1.61E-03	0.0561	0.2081	T12 (50%), T14 (30%)
42 (A)	4.28958	6.39E-04	0.0267	0.2414	T13 (32%), T11 (18%), T14 (5%)
43 (E)	4.29058	4.28E-04	0.0000	0.2386	T13 (31%), T14 (12%), T11 (10%)
	4.29241	3.89E-04	0.0000	0.2472	T13 (30%), T11 (16%), T14 (15%), T15 (5%)

44 (E)	4.30519	1.01E-03	0.0263	0.1820	T12 (43%), T14 (5%)
	4.30583	1.00E-03	0.0268	0.1947	T12 (41%), T14 (18%)
45 (A)	4.30808	4.79E-04	0.0226	0.1658	T12 (66%)
46 (E)	4.31944	8.27E-04	0.0142	0.1998	T12 (29%), T14 (12%)
	4.32225	7.55E-04	0.0117	0.1955	T12 (37%), T14 (11%)
47 (A)	4.32375	4.39E-04	0.0201	0.1933	T12 (48%), T11 (10%)
48 (E)	4.32593	3.43E-04	0.0000	0.1688	T12 (69%), T14 (7%)
	4.32781	4.69E-04	0.0160	0.1797	T12 (58%), T14 (7%)
49 (A)	4.33386	3.45E-03	0.1210	0.2691	T14 (46%), S7 (7%)
50 (E)	4.35865	1.74E-03	0.1432	0.2311	T14 (31%), T11 (12%), S8 (6%)
	4.36059	1.75E-03	0.1411	0.2197	T14 (26%), T11 (10%)
51 (A)	4.36807	5.01E-04	0.4281	0.3075	S7 (23%), S12 (17%)
52 (A)	4.40047	2.25E-03	0.0117	0.2734	T15 (49%), T13 (9%), T16 (8%)
53 (E)	4.40128	3.32E-03	0.2030	0.2279	T15 (22%), S10 (8%), T17 (7%), S8 (6%)
	4.40215	3.10E-03	0.1747	0.2416	T16 (28%), T15 (10%), S10 (7%), T17 (6%), S8 (5%)
54 (E)	4.41345	1.58E-03	0.1272	0.2666	T15 (30%), T16 (12%), T14 (8%)
	4.41450	1.25E-03	0.1015	0.2771	T15 (39%), T14 (10%), T16 (6%)
55 (E)	4.42039	3.78E-03	0.0422	0.2654	T16 (29%), T15 (28%)
56 (A)	4.42228	2.52E-03	0.0778	0.2723	T15 (60%)
55' (E)	4.42400	2.42E-03	0.0953	0.2748	T16 (36%), T15 (22%)
57 (E)	4.46122	2.89E-03	0.8886	0.2169	S8 (57%), S9 (29%)
	4.46700	3.03E-03	0.8937	0.2282	S8 (52%), S9 (33%)
58 (A)	4.48169	3.39E-03	0.2094	0.2420	T22 (20%), T15 (12%), S12 (9%), S11 (6%)
59 (E)	4.50431	3.40E-04	0.0063	0.1761	T17 (72%), T19 (7%)
60 (E)	4.50547	3.63E-04	0.0159	0.1833	T17 (65%), T19 (12%)
61 (E)	4.50788	4.69E-04	0.0247	0.1866	T17 (63%), T19 (9%)
	4.51281	5.72E-04	0.0207	0.1875	T17 (65%), T19 (11%)
60' (E)	4.51411	4.97E-04	0.0160	0.1932	T17 (70%), T19 (8%)
59' (E)	4.51672	3.35E-04	0.0078	0.1858	T17 (62%), T19 (14%)
62 (E)	4.53343	3.31E-03	0.2138	0.2099	T18 (14%), T23 (10%), S18 (10%), S19 (8%)
	4.53679	3.63E-03	0.1828	0.2045	T18 (20%), T23 (12%), S19 (9%), S18 (8%)
63 (A)	4.55293	2.19E-04	0.0178	0.1849	T18 (73%), T20 (12%)
64 (E)	4.55606	2.01E-03	0.0980	0.2075	T18 (52%), T20 (16%)
	4.55699	2.49E-03	0.1162	0.2130	T18 (44%), T20 (18%)
65 (A)	4.57774	1.85E-03	0.8428	0.1815	S11 (66%), S12 (12%)

66 (A)	4.59442	5.97E-03	0.6043	0.1773	S13 (32%), S11 (13%), S7 (6%), S15 (6%)
67 (A)	4.60242	5.64E-03	0.6574	0.1583	S13 (48%)
68 (E)	4.60620	1.62E-02	0.7206	0.2256	S10 (31%), S14 (24%), S13 (6%)
	4.60775	1.61E-02	0.6519	0.2429	S10 (35%), S14 (18%)
69 (E)	4.61655	4.75E-03	0.2078	0.2275	T19 (16%), S10 (9%), T15 (6%)
	4.61713	4.69E-03	0.2545	0.2215	T19 (10%), S10 (7%), S14 (7%)
70 (A)	4.62067	2.43E-03	0.1172	0.1882	T19 (12%), T20 (10%), S9 (5%)
71 (A)	4.62133	1.66E-03	0.0483	0.1780	T20 (24%), T21 (9%), T23 (6%)
72 (A)	4.62267	1.48E-03	0.0725	0.1943	T20 (18%), T19 (16%)
73 (A)	4.63711	1.12E-03	0.0123	0.2441	T19 (48%), T16 (5%)
74 (E)	4.64332	2.17E-03	0.0152	0.1798	T21 (18%), T20 (12%), T19 (10%)
	4.64422	2.26E-03	0.0450	0.1833	T21 (16%), T20 (14%), T19 (12%)
75 (A)	4.64697	8.26E-03	0.3337	0.2401	T22 (24%), S15 (13%), S12 (11%)
76 (A)	4.65470	6.32E-03	0.1961	0.1638	T21 (12%), S14 (9%), S19 (6%)
77 (A)	4.65619	4.37E-03	0.0899	0.1407	T21 (16%)
78 (A)	4.65839	1.08E-02	0.3387	0.1460	S14 (20%), T21 (12%), S10 (7%)
79 (A)	4.66135	1.19E-02	0.3864	0.1395	S14 (23%), S10 (7%)
80 (A)	4.66598	2.20E-03	0.0355	0.1700	T21 (23%), T24 (10%), T23 (9%)
81 (E)	4.67377	3.19E-03	0.0825	0.1815	T22 (17%), T19 (5%)
	4.67541	2.88E-03	0.0202	0.1741	T22 (19%), T19 (5%)
82 (A)	4.68077	6.22E-03	0.0756	0.1725	T21 (25%)
83 (E)	4.68677	4.70E-03	0.1611	0.1586	T23 (16%), S19 (6%)
	4.68892	5.26E-03	0.1812	0.1773	T23 (24%), S14 (6%), S19 (6%)
84 (A)	4.69341	6.22E-03	0.2305	0.2534	T19 (32%), S15 (14%), T23 (9%), S12 (6%)
85 (A)	4.70713	5.77E-03	0.0943	0.1777	T24 (22%), T23 (15%), T25 (14%)
86 (E)	4.70786	4.76E-03	0.2054	0.1761	T21 (16%), T24 (12%), S14 (8%), T25 (5%)
	4.71004	5.73E-03	0.1946	0.1609	T21 (14%), T24 (10%), S14 (7%)
87 (E)	4.71482	1.91E-03	0.0479	0.2048	T25 (20%), T22 (19%), T24 (16%)
	4.71775	1.56E-03	0.0477	0.2055	T24 (26%), T25 (21%), T22 (12%)
88 (A)	4.72436	7.99E-03	0.1727	0.2045	T25 (22%), S15 (14%), T22 (10%), T20 (7%), T21 (7%)
80 (A)	4.72572	2.26E-03	0.0536	0.2752	T25 (30%), T27 (18%), T22 (16%)
81 (E)	4.72806	4.68E-03	0.1134	0.2969	T27 (30%), T25 (14%)
82 (A)	4.72881	4.48E-03	0.1786	0.3399	T27 (36%), T25 (12%), S30 (7%)
81' (E)	4.72949	3.94E-03	0.1181	0.3051	T27 (30%), T25 (16%)
83 (A)	4.73410	3.42E-03	0.0803	0.1928	T25 (54%), T22 (16%)
84 (A)	4.74437	1.27E-03	0.0464	0.2092	T24 (40%), T25 (28%)
85 (A)	4.74571	1.19E-03	0.0408	0.1898	T25 (39%), T24 (32%)
86 (A)	4.75084	6.20E-04	0.0080	0.1937	T25 (42%), T24 (37%)
87 (A)	4.77236	1.32E-02	0.5075	0.3739	S20 (21%), S16 (19%), T27 (18%), S17 (6%)
88 (A)	4.77258	1.72E-02	0.6802	0.3037	S16 (51%), S20 (12%)
89 (A)	4.77397	2.20E-02	0.6790	0.2835	S16 (63%), T27 (6%)
90 (A)	4.77440	3.71E-03	0.2767	0.4080	T27 (33%), S20 (21%), T32 (10%)

91 (A)	4.78556	6.13E-02	0.5293	0.2660	S17 (51%), T27 (10%)
92 (E)	4.79233	2.55E-03	0.0483	0.1818	T26 (48%)
93 (A)	4.79351	1.54E-03	0.0267	0.1905	T26 (64%), T28 (10%)
92' (E)	4.79517	1.89E-03	0.0746	0.2080	T26 (48%)
94 (A)	4.79784	1.33E-03	0.1679	0.2237	T26 (56%), S20 (7%), S12 (5%)
95 (E)	4.80016	1.55E-03	0.0415	0.1936	T26 (60%), T28 (8%)
	4.80301	1.57E-03	0.0484	0.2019	T26 (58%), T28 (7%)
96 (A)	4.82693	1.06E-02	0.3178	0.2621	T28 (38%), S22 (15%), S12 (8%), S17 (5%)
97 (A)	4.84309	1.22E-02	0.6412	0.2643	S21 (29%), S18 (25%), T23 (10%), S19 (5%)
98 (A)	4.84705	7.52E-03	0.5885	0.3002	S18 (39%), S21 (13%), T23 (12%), S19 (5%)
99 (A)	4.85637	9.39E-04	0.0216	0.2330	T28 (32%), T30 (8%)
100 (E)	4.85817	8.76E-03	0.3054	0.2152	S21 (25%), T28 (14%), T22 (8%)
	4.86005	7.66E-03	0.2889	0.2083	S21 (19%), T28 (13%), T23 (12%), S18 (7%)
101 (A)	4.86265	1.29E-02	0.4709	0.2070	S21 (34%), S18 (7%), T28 (5%)
102 (A)	4.86544	8.66E-03	0.2393	0.2251	T28 (24%), S21 (16%), T23 (12%), T29 (6%), S20 (6%)
103 (E)	4.86832	4.27E-03	0.2111	0.2481	T28 (24%), S18 (14%)
	4.86939	5.18E-03	0.1918	0.2287	T28 (18%), S18 (10%)
104 (A)	4.87602	1.55E-02	0.7175	0.2148	S22 (70%)
105 (A)	4.89633	1.94E-03	0.1349	0.2497	T31 (37%), T33 (16%), S20 (6%)
106 (E)	4.90248	6.16E-03	0.1662	0.2528	T31 (16%), T29 (12%), S24 (7%), T30 (5%)
	4.90569	7.16E-03	0.1740	0.2423	T31 (18%), T29 (14%), S24 (5%)
107 (A)	4.91273	5.86E-03	0.2386	0.2557	T30 (26%), S23 (10%)
108 (A)	4.92149	1.03E-02	0.1779	0.2437	T31 (16%), T33 (12%), S25 (8%)
109 (A)	4.92452	5.14E-03	0.0962	0.2667	T30 (24%), T32 (14%)
110 (A)	4.92599	1.07E-02	0.2411	0.2616	T30 (12%), T31 (10%), S24 (9%), S25 (6%)
111 (A)	4.92806	3.73E-03	0.1285	0.2721	T32 (24%), T30 (11%), S24 (6%)
112 (A)	4.92821	2.18E-03	0.0562	0.2772	T30 (32%), T32 (22%)
113 (A)	4.93829	1.01E-02	0.1846	0.2358	T29 (16%), T31 (12%), S25 (8%)
114 (A)	4.94054	1.01E-02	0.1443	0.2349	T31 (14%), T29 (14%), S25 (9%), T32 (5%)
115 (A)	4.94292	1.15E-03	0.0241	0.2533	T29 (31%)
116 (E)	4.94939	1.74E-02	0.3756	0.2244	S24 (9%), T30 (8%), T32 (8%), S27 (6%), S19 (6%), S25 (5%)
	4.95203	1.58E-02	0.3362	0.2326	T30 (12%), S24 (10%), S27 (6%), S25 (6%), S19 (5%)
117 (A)	4.95671	1.28E-02	0.3268	0.2794	S24 (16%), T34 (15%), T32 (14%), S25 (6%)
118 (A)	4.95993	5.35E-03	0.1859	0.2197	T34 (24%), T30 (13%), T32 (10%), S26 (9%), T31 (6%)
119 (A)	4.96312	1.41E-02	0.2066	0.3103	T32 (32%), S25 (13%), T29 (10%)
120 (E)	4.96624	4.36E-03	0.1026	0.2098	T34 (38%), S24 (9%), T32 (6%)

	4.97308	1.05E-02	0.1431	0.2286	T34 (39%), T32 (12%), S25 (8%)
121 (A)	4.97547	7.98E-03	0.2463	0.2778	T32 (27%), S24 (12%)
122 (A)	4.97962	3.77E-03	0.1449	0.3336	T32 (38%), T30 (10%), T29 (10%), S23 (9%), T27 (7%)
123 (A)	4.98389	7.70E-03	0.2020	0.2466	T34 (22%), T32 (18%), S24 (10%)
124 (A)	4.98556	4.99E-03	0.0936	0.2799	T32 (22%), T30 (22%)
125 (A)	4.99431	1.62E-02	0.2659	0.2254	T33 (24%), S25 (16%)
126 (A)	4.99777	1.08E-02	0.3717	0.1983	S26 (21%), T34 (14%), T31 (8%), T33 (7%), S28 (5%)
127 (A)	5.00121	9.21E-03	0.1618	0.1909	T33 (32%), T34 (12%), T31 (12%), S25 (7%)
128 (A)	5.00643	4.36E-03	0.2362	0.2037	T33 (28%), S26 (16%), T31 (10%)
129 (A)	5.01029	1.99E-02	0.4179	0.2496	S25 (17%), T33 (14%), S24 (9%), S26 (6%), S19 (6%)
130 (A)	5.01247	1.35E-02	0.3754	0.2622	S23 (24%), T33 (6%)
131 (A)	5.01293	1.74E-02	0.4121	0.2442	S23 (15%), S25 (7%), S29 (6%)
132 (E)	5.01839	4.07E-02	0.8354	0.2539	S27 (50%), S29 (25%)
	5.02085	3.80E-02	0.7713	0.2515	S27 (43%), S29 (24%)
133 (A)	5.04943	4.42E-02	0.7718	0.2878	S28 (61%), T33 (8%)
134 (E)	5.05330	2.73E-02	0.8430	0.2621	S29 (42%), S27 (18%), S30 (8%)
	5.05798	2.43E-02	0.8205	0.2689	S29 (35%), S30 (15%), S27 (13%)
135 (A)	5.06937	2.83E-03	0.8950	0.1962	S31 (81%), S26 (5%)
136 (E)	5.09417	7.37E-03	0.7802	0.4215	S30 (61%), T27 (14%), S29 (9%)
	5.09497	7.29E-03	0.7843	0.4158	S30 (63%), T27 (14%), S29 (13%)
137 (E)	5.11263	0.03	0.9245	0.1561	S32 (88%)
	5.11313	0.03	0.9205	0.1604	S32 (86%)
138 (A)	5.13139	0.00	0.8926	0.2821	S33 (88%)

Appendix B

Supplement to Chapter 3

Molecular geometries

Table B1. Atomic coordinates for $Ir(ppy)_3$

Atom	X	Y	Z
Ir	0.000000000	0.000000000	-0.045054061
N	-0.197524306	-1.851384084	1.064769100
N	1.702107802	0.754630975	1.064769100
N	-1.504583496	1.096753109	1.064769100
C	0.558455687	-2.891500989	0.571179214
C	2.224885468	1.929387307	0.571179214
C	-2.783341155	0.962113683	0.571179214
C	0.488310670	-4.151790552	1.197894272
C	3.351400754	2.498784721	1.197894272
C	-3.839711424	1.653005831	1.197894272
C	-0.337004207	-4.344432178	2.302350756
C	3.930890734	1.880361885	2.302350756
C	-3.593886528	2.464070293	2.302350756
C	-1.102179526	-3.272242217	2.784738549
C	3.384934650	0.681605639	2.784738549
C	-2.282755124	2.590636577	2.784738549
C	-1.005192647	-2.045462453	2.135486835
C	2.274018771	0.152208858	2.135486835
C	-1.268826123	1.893253595	2.135486835
C	-1.681673598	-0.476086806	-1.089642875
C	1.253140067	-1.218328653	-1.089642875
C	0.428533531	1.694415459	-1.089642875
C	1.373083536	-2.556857507	-0.596555814
C	1.527761787	2.467553977	-0.596555814
C	-2.900845323	0.089303530	-0.596555814
C	-4.137915100	-0.176137254	-1.221358010
C	2.221496887	-3.495470968	-1.221358010
C	1.916418214	3.671608222	-1.221358010
C	-4.197962029	-0.996924639	-2.344101584
C	2.962343077	-3.137079442	-2.344101584
C	1.235618951	4.134004081	-2.344101584
C	-3.012844303	-1.557555359	-2.848550549
C	2.855304660	-1.830422025	-2.848550549
C	0.157539643	3.387977384	-2.848550549
C	-1.784790203	-1.301344075	-2.232018347
C	2.019392130	-0.895001618	-2.232018347
C	-0.234601927	2.196345694	-2.232018347
H	1.076436018	-4.974406209	0.810693516
H	3.769744137	3.419424042	0.810693516
H	-4.846180155	1.554982168	0.810693516
H	-0.390414509	-5.317347282	2.780230904

H	4.800165081	2.320564758	2.780230904
H	-4.409750572	2.996782524	2.780230904
H	-1.762084243	-3.384984111	3.636916346
H	3.812524353	0.166482337	3.636916346
H	-2.050440110	3.218501773	3.636916346
H	-1.578209672	-1.184853706	2.455702511
H	1.815218245	-0.774342815	2.455702511
H	-0.237008573	1.959196521	2.455702511
H	2.304688618	-4.507951921	-0.835238388
H	2.751656573	4.249894852	-0.835238388
H	-5.056345192	0.258057069	-0.835238388
H	-5.150886925	-1.199035353	-2.823607590
H	3.613838538	-3.861281253	-2.823607590
H	1.537048387	5.060316606	-2.823607590
H	-3.051089255	-2.196489107	-3.727528597
H	3.427759993	-1.544076251	-3.727528597
H	-0.376670738	3.740565357	-3.727528597
H	-0.883850898	-1.742928799	-2.643658305
H	1.951346066	0.106027069	-2.643658305
H	-1.067495168	1.636901730	-2.643658305

Table B2. Atomic coordinates for $Ir(ptz)_3$

Atom	X	Y	Z
Ir	0.000000000	0.000000000	0.012999633
N	-1.770209685	0.500451732	1.128722922
N	0.451700929	-1.783272423	1.128722922
N	1.318508756	1.282820691	1.128722922
C	-2.170144347	1.235038888	2.212995842
C	0.015497122	-2.496919578	2.212995842
C	2.154647225	1.261880690	2.212995842
N	-3.488770329	1.190783019	2.417800708
N	0.713136819	-3.616755242	2.417800708
N	2.775633509	2.425972223	2.417800708
N	-3.945340993	0.367580989	1.379115489
N	1.654336022	-3.600556021	1.379115489
N	2.291004971	3.232975032	1.379115489
C	-2.901588729	-0.044443416	0.604043746
C	1.489283492	-2.490627842	0.604043746
C	1.412305237	2.535071258	0.604043746
C	0.629737473	2.853210414	-0.572182841
C	-2.785821437	-0.881236558	-0.572182841
C	2.156083964	-1.971973856	-0.572182841
C	0.605879817	4.112311686	-1.205211381
C	-3.864306297	-1.531448530	-1.205211381

C	3.258426480	-2.580863156	-1.205211381
C	-0.182418397	4.305534414	-2.337688610
C	-3.637492981	-2.310746174	-2.337688610
C	3.819911379	-1.994788241	-2.337688610
C	-0.944761954	3.236568171	-2.834133282
C	-2.330569280	-2.436471938	-2.834133282
C	3.275331234	-0.800096233	-2.834133282
C	-0.924353516	1.987014972	-2.205068530
C	-1.258628685	-1.794021113	-2.205068530
C	2.182982202	-0.192993859	-2.205068530
C	-0.144462410	1.740039154	-1.053442369
C	-1.434686906	-0.995127694	-1.053442369
C	1.579149316	-0.744911460	-1.053442369
C	-5.372924205	0.104141948	1.270546792
C	2.596272530	-4.705159828	1.270546792
C	2.776651675	4.601017880	1.270546792
H	1.193618076	4.939925664	-0.821827699
H	-4.874910156	-1.436259256	-0.821827699
H	3.681292080	-3.503666409	-0.821827699
H	-0.205189173	5.273465222	-2.828574694
H	-4.464360262	-2.814431648	-2.828574694
H	4.669549435	-2.459033575	-2.828574694
H	-1.558722296	3.381498721	-3.719702336
H	-2.149102647	-3.040642467	-3.719702336
H	3.707824943	-0.340856255	-3.719702336
H	-1.522010736	1.181746940	-2.618595203
H	-0.262417503	-1.908973432	-2.618595203
H	1.784428239	0.727226492	-2.618595203
H	-5.856684371	0.662554661	2.071334791
H	2.354553018	-5.403314777	2.071334791
H	3.502131353	4.740760117	2.071334791
H	-5.584110283	-0.962650743	1.390797439
H	3.625735140	-4.354655991	1.390797439
H	1.958375143	5.317306734	1.390797439
H	-5.756188433	0.444972412	0.304528391
H	2.492736804	-5.207491618	0.304528391
H	3.263451629	4.762519206	0.304528391
H	-1.500379133	1.796288274	2.839677927
H	-0.805441711	-2.197510581	2.839677927
H	2.305820844	0.401222308	2.839677927

Two-component calculations

Table B3. Symmetries, energies and oscillator strengths of the lowest 50 excitations of $Ir(ppy)_3$ calculated in the DZP basis with a frozen core (described in the methods section) in the two-component ZORA.

Label*	Energy	f
1(A)	2.54429	9.17E-07
2(E)	2.55343	0.00077
	2.55353	0.000785
3(A)	2.56091	1.58E-06
4(E)	2.56150	0.000113
	2.56164	0.000109
5(E)	2.58193	0.004772
	2.58204	0.00478
6(A)	2.60015	9.32E-05
7(A)	2.66543	0.002701
8(E)	2.67925	0.000973
	2.67948	0.000974
9(E)	2.85610	4.26E-05
	2.85623	4.39E-05
10(A)	2.85688	4.73E-05
	2.87152	4.82E-06
	2.87165	5E-06
	2.87430	4.4E-07
	2.94743	0.000611
	2.94850	0.008215
	2.94867	0.008354
	3.00574	4.08E-05
	3.01338	0.004398
	3.01342	0.004398
	3.02742	0.00243
	3.03627	0.005769
	3.03640	0.005826
	3.04166	0.001704
	3.05555	0.000476
	3.05575	0.000475
	3.05851	0.001013
	3.07121	8.1E-05
	3.07776	0.001709
	3.07796	0.00173
	3.12146	0.01628
	3.12163	0.01638
	3.12738	0.0047
	3.19787	0.02402

	3.19797	0.02403
	3.20574	0.002796
	3.20589	0.002691
	3.20952	3.61E-05
	3.21449	0.003737
	3.21453	0.003766
	3.23532	0.000222
	3.26447	0.007224
	3.26468	0.008096
	3.26630	0.002447
	3.27178	0.004747
	3.28116	0.002682

*Note that ADF does not implement C_3 symmetry and this leads to small splittings in the E level, which have been identified manually for the lowest few excitations in this and the following tables.

Table B4. Symmetries, energies and oscillator strengths of the lowest 50 excitations of $Ir(ptz)_3$ calculated in the DZP basis with a frozen core (described in the methods section) in the two-component ZORA.

Label	Energy	f
1(A)	2.83964	1.73E-09
2(E)	2.85361	0.0019
	2.85365	0.0019
3(A)	2.88865	0.000504
4(E)	2.91522	2.29E-05
	2.91532	2.22E-05
5(A)	2.92384	0.000104
6(E)	2.92509	0.00128
	2.92524	0.00125
7(A)	3.05468	0.00566
8(E)	3.10217	0.00781
	3.10236	0.00781
9(E)	3.23041	0.000269
	3.23046	0.00021
10(A)	3.23054	6.79E-05
	3.24766	2.54E-05
	3.24774	2.56E-05
	3.25826	0.000176
	3.32231	0.00216
	3.32344	0.00978
	3.32359	0.00978

	3.38091	0.00491
	3.40678	0.00883
	3.40686	0.0088
	3.42956	0.00104
	3.42962	0.00104
	3.45702	0.000179
	3.45716	0.00212
	3.45718	0.00222
	3.45978	9.59E-05
	3.50859	0.0284
	3.50869	0.0284
	3.56894	0.00818
	3.59831	0.00757
	3.59835	0.00756
	3.60228	0.00013
	3.61664	7.46E-05
	3.61675	7.60E-05
	3.62924	0.000538
	3.63042	0.00154
	3.63051	0.00152
	3.63141	0.000508
	3.65403	0.0292
	3.65406	0.0293
	3.71077	0.0119
	3.96199	4.00E-07
	3.97214	0.000164
	3.97220	0.000168
	3.97622	6.46E-05
	4.00167	2.01E-06

One-component calculations

Table B5. Symmetries, energies, oscillator strengths, MLCT and singlet weights of the lowest 200 excitations of $Ir(ppy)_3$ calculated in the DZP basis with a frozen core (described in the methods section) in the one-component ZORA with spin-orbit coupling included perturbatively.

Label	Energy	f	MLCT	Singlet
1(A)	2.55713	6.79E-06	0.40407	0.001
2(E)	2.56273	0.00143	0.40353	0.0567
	2.56282	0.00144	0.40336	0.057
3(E)	2.57118	0.000131	0.37769	0
	2.57167	1.42E-04	0.37719	0
4(A)	2.57266	3.13E-04	0.38837	0.0782
5(E)	2.58472	0.00202	0.387	0.0496

	2.58538	0.00201	0.3875	0.0495
6(A)	2.60355	0.000499	0.39096	0.0399
7(A)	2.68464	0.00256	0.41972	0.4247
8(E)	2.70158	0.00148	0.39315	0.3636
	2.70221	0.00147	0.39341	0.3633
9(E)	2.85172	0.000194	0.36473	0
	2.85184	0.000195	0.36356	0
10(A)	2.85279	3.49E-04	0.37052	0.0722
	2.86828	1.80E-03	0.3608	0.0697
	2.86837	1.82E-03	0.36092	0.0698
	2.87279	2.06E-05	0.3791	0.0059
	2.93822	0.00198	0.40289	0.3044
	2.94284	0.00334	0.35165	0.2451
	2.94301	0.00335	0.35153	0.2452
	3.01317	0.0038	0.35524	0.2111
	3.01333	0.00383	0.35516	0.212
	3.01558	0.000834	0.37281	0.1199
	3.02820	7.06E-05	0.36672	0.0088
	3.04167	0.000468	0.36865	0.057
	3.04178	0.000479	0.36954	0.0594
	3.04551	0.000881	0.37733	0.177
	3.04804	0.00057	0.38445	0.1072
	3.04824	5.58E-04	0.38317	0.1058
	3.06030	4.65E-05	0.36015	0.0158
	3.06686	0.00626	0.382	0.3637
	3.06694	0.00626	0.38213	0.3638
	3.06913	0.00293	0.34302	0.4377
	3.10932	0.0149	0.38464	0.6051
	3.10942	0.0149	0.3846	0.6053
	3.11595	2.11E-03	0.36542	0.6906
	3.19571	4.06E-02	0.34027	0.748
	3.19579	0.0406	0.34009	0.7465
	3.21495	0.00111	0.31841	0.0187
	3.21515	0.00124	0.31866	0.021
	3.21794	0.000559	0.36458	0.0668
	3.22046	0.000904	0.31216	0.034
	3.22058	0.000864	0.31275	0.0339
	3.23498	0.000324	0.28296	0.1667
	3.26252	5.37E-04	0.15372	0.0294
	3.26322	0.0014	0.14864	0.0281
	3.26330	0.00143	0.14902	0.0287
	3.26947	3.91E-03	0.15837	0.0744
	3.26949	3.95E-03	0.15846	0.0749
	3.28028	1.22E-03	0.15162	0.1507
	3.28787	9.52E-04	0.08741	0.0297
	3.28802	0.000939	0.08736	0.0292

	3.29620	5.98E-05	0.18882	0.2194
	3.33095	0.012	0.39435	0.3821
	3.33658	0.00656	0.38336	0.2998
	3.33679	0.00657	0.38299	0.3
	3.37783	0.00249	0.37484	0.114
	3.38247	0.00021	0.35938	0
	3.38260	0.000214	0.35894	0
	3.40418	0.00322	0.36171	0.1547
	3.40423	0.00322	0.36151	0.1549
	3.44950	0.0265	0.39254	0.6225
	3.44994	0.00845	0.39761	0.7693
	3.45004	0.00846	0.39814	0.7693
	3.48194	3.46E-05	0.37435	0
	3.53200	0.00586	0.38963	0.2715
	3.53205	0.00588	0.38928	0.2718
	3.59654	0.00101	0.39322	0.164
	3.63121	0.000558	0.38929	0.0337
	3.63137	0.000574	0.38923	0.0345
	3.63953	0.00673	0.40478	0.2575
	3.63956	0.00675	0.40489	0.2591
	3.64140	0.000808	0.38885	0.1019
	3.70286	3.35E-05	0.39673	0.073
	3.70837	0.00677	0.41208	0.2201
	3.70849	0.00681	0.41223	0.2199
	3.72602	0.000352	0.40141	0.6521
	3.73022	0.00652	0.39735	0.7288
	3.73030	0.00647	0.3974	0.7276
	3.74417	0.00613	0.39004	0.7802
	3.86381	0.000285	0.06568	0.0122
	3.86396	0.000278	0.06566	0.0118
	3.86542	0.000257	0.06624	0.0159
	3.86552	0.000251	0.06616	0.0157
	3.86573	0.000194	0.06579	0.0213
	3.86676	0.000151	0.06326	0.0118
	3.87141	0.000185	0.07768	0.0061
	3.87153	0.000176	0.07769	0.0054
	3.87226	2.28E-05	0.07481	0.0017
	4.05284	7.87E-05	0.0261	0.0013
	4.05435	5.37E-05	0.00788	0.0043
	4.05517	0.00146	0.02299	0.4448
	4.05536	0.00142	0.02719	0.4279
	4.05919	0.00115	0.05837	0.3514
	4.05929	0.00108	0.05325	0.3176
	4.05973	0.000636	0.03282	0.158
	4.05993	0.000737	0.02474	0.181
	4.06037	8.57E-05	0.06804	0.0129

	4.06229	0.000212	0.00797	0.0373
	4.06237	0.000223	0.0049	0.0434
	4.10534	0.000283	0.10936	0.2564
	4.10845	0.000307	0.15137	0.0087
	4.10854	0.000293	0.15153	0.0079
	4.10861	0.000434	0.15061	0.0132
	4.11056	0.000324	0.15284	0.014
	4.11057	0.000306	0.15345	0.0098
	4.11107	0.000237	0.02508	0.7314
	4.12171	0.000136	0.1398	0.0043
	4.12174	0.000137	0.13998	0.0043
	4.12240	8.87E-05	0.14468	0.0025
	4.13312	0.000264	0.0309	0.0171
	4.13480	0.000353	0.03661	0.0083
	4.13491	0.000346	0.03636	0.0082
	4.15441	0.043	-0.00171	0.9173
	4.15460	0.0425	-0.00173	0.9152
	4.15497	0.00772	0.01856	0.8096
	4.16381	0.000889	0.16326	0.0535
	4.16860	0.00129	0.14897	0.126
	4.17087	0.00158	0.16566	0.0361
	4.17102	0.00156	0.16591	0.0358
	4.17456	0.000457	0.1704	0.0097
	4.17458	0.00046	0.1704	0.0097
	4.22398	0.2189	0.03264	0.8759
	4.22524	0.0106	0.03016	0.6082
	4.22536	0.0104	0.03029	0.6065
	4.22814	6.80E-05	0.10135	0.0043
	4.23052	0.0282	0.09011	0.1166
	4.23253	0.00381	0.07539	0.2165
	4.23270	0.00352	0.07655	0.2029
	4.23707	0.00269	0.08033	0.154
	4.23713	0.00271	0.08026	0.155
	4.25928	0.00042	0.18283	0.0199
	4.25944	0.000401	0.18275	0.0182
	4.25979	0.000132	0.18419	0.0034
	4.29655	0.000489	0.20286	0.015
	4.29791	0.000477	0.20321	0.0148
	4.30278	0.000572	0.20314	0.0019
	4.33053	0.000741	0.17113	0.0194
	4.33095	0.000753	0.17139	0.0199
	4.33538	0.00125	0.17663	0.0188
	4.33897	7.29E-05	0.17565	0
	4.33980	7.21E-05	0.17575	0
	4.34143	0.000204	0.1782	0.0154
	4.39707	0.0251	0.0249	0.9778

	4.39720	0.025	0.02498	0.9779
	4.45897	0.0042	0.11699	0.9383
	4.48088	0.00749	0.05322	0.1985
	4.48367	0.000638	0.04382	0.0353
	4.48383	0.000589	0.04358	0.0332
	4.48743	5.43E-05	0.03941	0.0017
	4.48772	5.34E-05	0.03954	0.0018
	4.48831	0.000541	0.04077	0.0145
	4.51049	0.03	0.09298	0.7299
	4.51637	0.00124	0.10481	0.0665
	4.51666	0.00135	0.10518	0.075
	4.51779	0.0016	0.10113	0.0311
	4.53426	0.00771	0.12079	0.4558
	4.53480	0.00707	0.11659	0.4249
	4.53862	0.000231	0.02501	0.0048
	4.53987	0.00188	0.04542	0.1123
	4.54010	0.00204	0.04858	0.1221
	4.54980	0.00305	0.11703	0.224
	4.55030	0.00303	0.11701	0.2213
	4.55995	0.000358	0.10186	0.0105
	4.56080	0.00366	0.11843	0.2122
	4.56159	0.00457	0.12206	0.266
	4.56371	0.00246	0.10547	0.0705
	4.60447	0.005	0.16517	0.798
	4.60492	0.00495	0.16547	0.8049
	4.61182	0.0582	0.07533	0.9663
	4.63146	0.00241	0.08055	0.0863
	4.63384	0.000379	0.07749	0.0256
	4.63395	0.000273	0.07717	0.0205
	4.63825	0.00654	0.09083	0.2684
	4.64622	0.00291	0.08437	0.2848
	4.64687	0.00271	0.08408	0.2718
	4.64970	0.000684	0.06894	0.0194
	4.65187	0.00938	0.10262	0.4044
	4.65490	0.000122	0.06778	0.0101
	4.65541	0.00159	0.07203	0.0712
	4.66550	0.00203	0.07717	0.1954
	4.66620	0.00211	0.0761	0.2071
	4.66952	0.00219	0.07246	0.1082
	4.67185	0.00504	0.09231	0.4754
	4.67296	0.00161	0.04469	0.8848
	4.67338	0.00486	0.08642	0.6127
	4.70292	0.00808	0.14298	0.2056
	4.70623	0.00452	0.14603	0.1302
	4.71157	0.00343	0.148	0.1334
	4.72641	0.0369	0.11906	0.9034

	4.72988	0.0199	0.15169	0.8704
	4.73024	0.0124	0.16861	0.8948
	4.75540	0.000702	0.09411	0.985
	4.75647	0.00094	0.09418	0.9689
	4.78305	0.0339	0.07776	0.974
	4.78323	0.0338	0.0779	0.9724
	4.82088	0.1864	0.17824	0.9765
	4.85782	0.00197	0.30408	0.9837
	4.87778	0.00139	0.34237	0.9768

Table B6. Symmetries, energies, oscillator strengths, MLCT and singlet weights of the lowest 200 excitations of $Ir(ptz)_3$ calculated in the DZP basis with a frozen core (described in the methods section) in the one-component ZORA with spin-orbit coupling included perturbatively.

Label	Energy	f	MLCT	Singlet
1(A)	2.85085	1.02E-05	0.454725	0.0003
2(E)	2.86145	0.00203	0.460494	0.0471
	2.86148	0.00203	0.460559	0.0471
3(A)	2.89890	0.00155	0.438899	0.118
4(E)	2.92084	9.69E-05	0.422268	0
	2.92093	9.78E-05	0.422299	0
5(A)	2.92692	0.000342	0.436702	0.0315
6(E)	2.92852	0.00134	0.426743	0.0401
	2.92854	0.00134	0.426613	0.0401
7(A)	3.06939	0.00491	0.457298	0.3679
8(E)	3.12197	0.00389	0.431985	0.3301
	3.12217	0.00389	0.431419	0.33
9(A)	3.22781	0.000325	0.42026	0.0334
10(E)	3.22849	0.00209	0.404927	0.071
	3.22857	2.09E-03	0.404333	0.0712
	3.24665	1.96E-03	0.403368	0.0467
	3.24673	1.96E-03	0.403623	0.0467
	3.25856	1.58E-03	0.432226	0.1366
	3.31379	0.00457	0.441875	0.3369
	3.32287	0.00784	0.399988	0.2454
	3.32302	0.00784	0.399101	0.2455
	3.37371	0.00203	0.407488	0.1508
	3.39685	0.00355	0.396826	0.1407
	3.39696	0.00354	0.396348	0.1406
	3.42086	6.38E-03	0.394024	0.1615
	3.42094	0.00643	0.392695	0.1634
	3.44525	0.00898	0.436	0.3779
	3.44531	0.00907	0.43613	0.3808
	3.44737	0.000509	0.413256	0.054

	3.45124	3.18E-04	0.402637	0.0352
	3.49335	1.95E-02	0.434108	0.5218
	3.49347	0.0195	0.433272	0.5215
	3.55854	0.00503	0.403095	0.621
	3.59038	0.0122	0.298859	0.2787
	3.59041	0.0122	0.298561	0.2781
	3.59696	0.00104	0.254887	0.089
	3.61008	9.68E-05	0.207138	0.0013
	3.61016	9.75E-05	0.207129	0.0013
	3.62115	0.00139	0.230756	0.1656
	3.62311	0.00229	0.235216	0.0768
	3.62314	0.00225	0.235071	0.0762
	3.62509	0.000232	0.213423	0.0196
	3.64589	0.0285	0.337518	0.5732
	3.64595	0.0285	0.337602	0.573
	3.70562	0.0104	0.409873	0.8161
	3.96977	1.18E-04	0.35063	0.0013
	3.97810	0.000348	0.353209	0.0129
	3.97811	0.000349	0.353194	0.013
	3.98173	7.97E-04	0.343118	0.0362
	3.99833	3.21E-04	0.342661	0.0068
	4.00160	4.75E-05	0.338939	0
	4.00161	4.79E-05	0.339322	0.0011
	4.00542	0.000235	0.339646	0.013
	4.00544	2.35E-04	0.339719	0.013
	4.37683	0.00121	0.164247	0.0731
	4.37688	0.00121	0.16329	0.0728
	4.38729	0.000324	0.152292	0.0045
	4.39830	0.000321	0.130614	0.0268
	4.40836	0.000288	0.143898	0.0118
	4.40866	0.000291	0.12854	0.0084
	4.40872	0.000289	0.128112	0.0119
	4.41263	0.000127	0.128086	0.0024
	4.41274	0.000125	0.127803	0.0029
	4.44824	0.00378	0.308319	0.3831
	4.44953	0.00193	0.17915	0.1607
	4.44963	1.93E-03	0.179104	0.1604
	4.49471	0.00248	0.225386	0.0557
	4.50266	0.000961	0.205521	0.0093
	4.50270	0.000965	0.205548	0.0093
	4.51734	0.0021	0.2729	0.3044
	4.52226	0.00166	0.228332	0.0576
	4.52237	0.00166	0.227362	0.0574
	4.52463	0.000964	0.252612	0.0312
	4.53537	0.00191	0.102864	0.6979
	4.53553	1.92E-03	0.104248	0.6896

	4.54305	0.00196	0.219657	0.2052
	4.54314	0.00198	0.219049	0.2103
	4.55157	0.0045	0.246057	0.0515
	4.56213	0.00101	0.189111	0.1176
	4.56224	0.00101	0.189433	0.1176
	4.56504	0.00244	0.23247	0.0607
	4.57085	0.00078	0.239669	0.0075
	4.57249	0.00106	0.179127	0.0344
	4.57253	0.00105	0.178076	0.034
	4.58487	0.00324	0.242312	0.255
	4.58493	0.00325	0.24055	0.2695
	4.60033	0.00118	0.217499	0.023
	4.60151	0.000462	0.215091	0.0118
	4.60154	0.000463	0.217027	0.0118
	4.60210	6.92E-04	0.218088	0.0113
	4.61004	1.34E-03	0.229325	0.0981
	4.61010	1.33E-03	0.229993	0.0969
	4.63148	0.00111	0.161733	0.0571
	4.63154	0.00111	0.162293	0.0554
	4.63245	0.000363	0.141991	0.006
	4.65307	0.000993	0.037593	0.9727
	4.66580	0.00071	0.036473	0.9769
	4.69682	0.017	0.269645	0.8524
	4.69697	1.70E-02	0.270681	0.8518
	4.72160	0.00246	0.191325	0.0558
	4.72212	0.00225	0.184689	0.0674
	4.72213	0.00224	0.183098	0.0672
	4.73493	0.0285	0.284816	0.3764
	4.75594	0.00671	0.263151	0.2819
	4.75596	0.00665	0.260711	0.2814
	4.75755	0.0153	0.264958	0.2721
	4.76692	0.00157	0.259242	0.0516
	4.76710	0.00157	0.254748	0.0515
	4.76979	0.002	0.229864	0.0332
	4.77860	0.0107	0.166901	0.331
	4.77868	1.06E-02	0.172528	0.3312
	4.78524	0.00193	0.132797	0.0254
	4.78968	0.0032	0.151129	0.1017
	4.78976	0.00317	0.151403	0.1055
	4.79263	0.00276	0.189981	0.0308
	4.80258	0.00402	0.140586	0.1056
	4.80266	0.00399	0.141326	0.1046
	4.80615	0.00309	0.142394	0.1263
	4.80623	0.00309	0.141459	0.1255
	4.81231	0.00877	0.234987	0.1066
	4.81944	0.0482	0.247237	0.5202

	4.82069	0.00231	0.193202	0.1289
	4.82074	0.00236	0.193905	0.129
	4.83381	0.0036	0.171558	0.0422
	4.83534	0.00482	0.231249	0.1287
	4.83543	0.00484	0.231763	0.1285
	4.85357	4.13E-03	0.188846	0.0549
	4.86156	0.00337	0.187889	0.1428
	4.86162	0.00337	0.187863	0.1426
	4.86788	0.00094	0.1858	0.019
	4.86796	0.000932	0.185949	0.019
	4.87141	0.00455	0.179005	0.0718
	4.87992	0.00507	0.255303	0.0992
	4.89077	0.00533	0.211048	0.1881
	4.89083	0.00532	0.210962	0.188
	4.90014	0.00405	0.265016	0.3316
	4.90016	0.00416	0.265321	0.3377
	4.90307	0.0144	0.295165	0.3647
	4.90721	0.00369	0.261612	0.2455
	4.90728	0.00364	0.2618	0.2407
	4.90821	0.0113	0.292738	0.2932
	4.92655	1.07E-02	0.202599	0.2882
	4.92668	1.07E-02	0.20244	0.2894
	4.93315	0.0185	0.326958	0.3391
	4.96663	0.0411	0.250061	0.7721
	4.96679	0.0277	0.208241	0.7278
	4.96687	0.0232	0.199449	0.7205
	5.00701	0.00112	0.113745	0.0929
	5.01759	0.00189	0.11352	0.0463
	5.01767	0.00189	0.113503	0.0461
	5.04384	2.32E-03	0.130663	0.2114
	5.05171	8.17E-03	0.181765	0.1769
	5.05180	0.00806	0.180895	0.1739
	5.06038	0.000575	0.136536	0.0119
	5.06432	0.00703	0.168295	0.1497
	5.06443	0.00686	0.169014	0.1452
	5.06764	0.00996	0.282415	0.2508
	5.06776	0.00987	0.283338	0.25
	5.06971	0.00356	0.295386	0.0717
	5.07461	0.0178	0.311271	0.3448
	5.07920	0.00851	0.227957	0.1933
	5.07928	0.00858	0.22748	0.1956
	5.08966	0.0115	0.242034	0.1493
	5.08972	0.0115	0.241849	0.1473
	5.09998	0.00196	0.210416	0.2549
	5.10467	0.0304	0.259394	0.4686
	5.10485	0.0306	0.259598	0.4698

	5.11243	0.00384	0.189334	0.4501
	5.11848	0.0466	0.254521	0.5721
	5.11856	0.0469	0.254521	0.5745
	5.13030	0.0199	0.248738	0.2145
	5.13041	0.0199	0.248581	0.2134
	5.13569	0.00268	0.219254	0.3795
	5.14902	0.0295	0.250368	0.3644
	5.14916	0.0295	0.250507	0.3635
	5.16373	0.00334	0.281861	0.0478
	5.16793	0.0139	0.254331	0.2318
	5.16796	0.0137	0.254471	0.2315
	5.16995	0.00703	0.255198	0.3739
	5.17696	0.00536	0.252293	0.2214
	5.17833	0.0107	0.233164	0.1575
	5.17836	0.0105	0.234094	0.1573
	5.18412	0.00898	0.219874	0.226
	5.18430	0.00907	0.219481	0.2294
	5.18726	0.0088	0.255207	0.1991
	5.19545	0.0129	0.249878	0.4389
	5.19571	0.0127	0.248817	0.4326
	5.20221	0.00156	0.29339	0.0415
	5.20714	0.00825	0.234408	0.9392
	5.21294	0.0181	0.227149	0.5531
	5.21306	0.0181	0.226772	0.5528
	5.25213	0.0155	0.272937	0.689
	5.26111	0.00976	0.125618	0.9627
	5.26133	0.00979	0.125597	0.9626
	5.28825	0.0158	0.327813	0.8088
	5.28829	0.0158	0.327388	0.8089
	5.29087	0.0784	0.394413	0.8307
	5.36928	0.3362	0.292903	0.9403
	5.50000	0.0138	0.280838	0.9676
	5.50005	0.0137	0.279858	0.968

Table B7. Symmetries, energies, oscillator strengths, MLCT and singlet weights of the lowest 200 excitations of $Ir(ppy)_3$ calculated in the TZP basis with a frozen core (described in the methods section) in the one-component ZORA with spin-orbit coupling included perturbatively.

Label	Energy	f	MLCT	Singlet
1(A)	2.46359	9.52E-06	0.420254	0.0016
2(E)	2.46917	0.001584	0.419226	0.066
	2.46963	0.00155	0.418821	0.0633
3(E)	2.47820	0.000188	0.389876	0
	2.47892	1.55E-04	0.390086	0

4(A)	2.48047	3.27E-04	0.399784	0.0876
5(E)	2.49441	0.002122	0.399577	0.0537
	2.49491	0.002144	0.399312	0.0534
6(A)	2.51721	0.000698	0.40298	0.0473
7(A)	2.57465	0.002329	0.433052	0.4354
8(E)	2.59456	0.001386	0.396401	0.3723
	2.59586	0.0014	0.396523	0.3717
9(A)	2.75695	0.000233	0.3761	0.0483
10(E)	2.75956	0.000261	0.371848	0.007
	2.76003	2.90E-04	0.370617	0.0079
	2.77473	1.36E-03	0.358487	0.0456
	2.77528	1.34E-03	0.356493	0.044
	2.77570	2.48E-04	0.379382	0.0144
	2.83786	0.002004	0.36385	0.1973
	2.83829	0.001905	0.374497	0.2338
	2.83941	0.001969	0.374341	0.235
	2.87339	4.91E-05	0.400586	0.0081
	2.88664	0.002185	0.394443	0.1274
	2.88682	0.002234	0.392981	0.1298
	2.90826	2.23E-03	0.391885	0.3995
	2.92092	0.001297	0.360644	0.1151
	2.92167	0.002683	0.365936	0.2184
	2.92327	0.002624	0.364387	0.2034
	2.94684	0.000261	0.368622	0.03
	2.94829	2.67E-04	0.368464	0.035
	2.94949	8.63E-04	0.383159	0.2172
	2.96507	8.69E-05	0.370589	0.0031
	2.96971	0.006247	0.390142	0.3625
	2.97137	0.006252	0.390028	0.3669
	3.00910	0.01464	0.396378	0.6007
	3.01064	0.01464	0.396595	0.6107
	3.01551	2.08E-03	0.363044	0.7169
	3.07495	1.01E-03	0.357387	0.0113
	3.07615	0.001091	0.355622	0.0121
	3.07825	0.000912	0.389627	0.0729
	3.08189	0.004609	0.364821	0.109
	3.08229	0.004387	0.362255	0.1086
	3.10470	0.03632	0.34276	0.7102
	3.10549	0.03702	0.340862	0.7117
	3.11486	0.000806	0.357105	0.2835
	3.17074	7.34E-03	0.246176	0.2392
	3.17157	0.007186	0.245478	0.2342
	3.19266	0.000602	0.187703	0.0091
	3.19277	5.61E-04	0.199934	0.0697
	3.19318	5.75E-04	0.188261	0.0088
	3.19509	6.18E-03	0.290462	0.3722

	3.21566	3.80E-03	0.270561	0.1626
	3.21582	0.003808	0.269298	0.162
	3.22947	6.66E-03	0.276192	0.1646
	3.23783	0.001125	0.27693	0.0767
	3.24129	0.001292	0.159407	0.0603
	3.24141	0.001317	0.160064	0.06
	3.24873	0.000366	0.12567	0.0173
	3.25748	0.000645	0.219436	0.0274
	3.25778	0.000648	0.21786	0.0148
	3.27003	0.003494	0.320137	0.1262
	3.27016	0.003598	0.31848	0.1271
	3.29375	0.007963	0.389231	0.7268
	3.29461	0.007781	0.388694	0.7307
	3.32359	0.03145	0.375443	0.6913
	3.36013	4.96E-05	0.359017	0
	3.39789	0.005635	0.378457	0.2117
	3.39841	0.005826	0.379051	0.2147
	3.46158	0.000661	0.38409	0.1601
	3.49130	0.000856	0.37853	0.0451
	3.49242	0.001168	0.37938	0.0606
	3.49945	0.006803	0.396373	0.2317
	3.50038	0.007022	0.397768	0.2371
	3.50543	0.001176	0.395375	0.0924
	3.56004	1.19E-04	0.398261	0.1006
	3.56480	0.006824	0.417324	0.2124
	3.56631	0.007065	0.418805	0.2109
	3.58184	0.000556	0.412586	0.6235
	3.58697	0.007186	0.405298	0.7375
	3.58719	0.00711	0.404924	0.725
	3.60419	0.009929	0.395986	0.8006
	3.76854	0.000182	0.042981	0.0066
	3.76865	0.000228	0.043856	0.009
	3.76934	0.000174	0.042703	0.0096
	3.76981	0.000157	0.041293	0.008
	3.77012	0.00015	0.043125	0.0084
	3.77053	0.000129	0.042711	0.0084
	3.77862	0.000162	0.072219	0.0046
	3.77866	0.000139	0.072027	0.0041
	3.77906	4.58E-05	0.0702	0.0031
	3.98558	6.07E-05	0.157326	0.0012
	3.98617	2.25E-04	0.163156	0.0297
	3.98619	0.000205	0.164204	0.0242
	3.99664	5.13E-05	0.030511	0.0004
	3.99809	0.001026	0.040248	0.1859
	3.99836	0.00209	0.0368	0.3993
	4.00012	0.002914	0.033943	0.5481

	4.00275	0.002086	0.027641	0.3865
	4.00462	1.69E-03	0.028648	0.2928
	4.00691	0.000306	0.030216	0.0309
	4.00703	0.000507	0.030012	0.0697
	4.02865	0.000341	0.159111	0.0153
	4.03084	0.000109	0.156735	0.0012
	4.03337	0.00038	0.153602	0.0147
	4.03398	0.000376	0.154347	0.0153
	4.03824	0.000215	0.15841	0.0058
	4.03829	0.000206	0.158475	0.0057
	4.05586	9.82E-05	0.117838	0.0039
	4.05593	0.000108	0.117997	0.0043
	4.05771	0.000196	0.123505	0.0064
	4.06216	5.06E-04	-0.01353	0.9619
	4.07539	0.000446	0.044912	0.02
	4.07836	0.000331	0.046067	0.0103
	4.07841	0.00029	0.045903	0.0091
	4.08660	0.003331	0.154321	0.0964
	4.08774	0.02428	0.073439	0.5271
	4.08795	0.02438	0.07391	0.523
	4.08931	0.000558	0.166814	0.0309
	4.09828	0.01521	0.110533	0.3298
	4.09858	0.01389	0.117861	0.3027
	4.10125	0.005346	0.154444	0.1146
	4.10131	0.005176	0.155218	0.111
	4.10880	0.0135	0.008703	0.8943
	4.15576	0.2013	0.037551	0.9764
	4.16790	0.002576	0.014713	0.7157
	4.16895	0.002185	0.017754	0.6722
	4.17491	1.34E-03	0.087783	0.0098
	4.17663	0.000517	0.067721	0.1296
	4.17740	0.000495	0.078636	0.1158
	4.17952	0.000835	0.058687	0.0338
	4.18014	0.000323	0.054081	0.0486
	4.18095	0.000481	0.05661	0.0669
	4.18465	0.000301	0.141504	0.0608
	4.18525	0.00037	0.135309	0.086
	4.18602	0.000189	0.138398	0.0051
	4.21794	0.000535	0.161945	0.0301
	4.21814	0.00052	0.161672	0.0299
	4.22338	0.000613	0.16583	0.0038
	4.25063	0.001128	0.138434	0.0355
	4.25079	0.001079	0.138403	0.0354
	4.25594	0.001197	0.144767	0.0216
	4.25805	1.80E-04	0.142906	0.0033
	4.25897	1.86E-04	0.14322	0.0035

	4.26029	0.000335	0.146218	0.015
	4.29408	0.03319	0.023831	0.9634
	4.29526	0.03321	0.024415	0.9642
	4.35376	0.007828	0.116486	0.9542
	4.37685	0.006583	0.059078	0.1565
	4.38000	0.000399	0.050962	0.0215
	4.38051	0.001031	0.052138	0.0369
	4.38239	7.80E-05	0.049299	0.0026
	4.38420	6.57E-04	0.051163	0.0188
	4.38457	7.05E-05	0.049644	0.0026
	4.40888	0.03374	0.10184	0.7792
	4.41703	0.000643	0.121118	0.0393
	4.41708	0.000681	0.121205	0.0419
	4.41788	0.000797	0.120514	0.0132
	4.43661	0.003433	0.07517	0.2242
	4.43727	0.002629	0.068916	0.1744
	4.43793	0.000241	0.043564	0.0064
	4.44161	0.006403	0.106313	0.4249
	4.44215	0.006076	0.101511	0.3992
	4.45394	0.002685	0.116796	0.1986
	4.45449	0.002682	0.117142	0.2034
	4.46314	0.001258	0.110612	0.0738
	4.46388	0.003037	0.116542	0.1952
	4.46409	0.002814	0.115962	0.1816
	4.46679	0.001735	0.110974	0.0514
	4.51087	0.04582	0.096655	0.9587
	4.51228	0.01618	0.139518	0.8754
	4.51296	0.007943	0.152028	0.8661
	4.54037	0.000639	0.106574	0.0502
	4.54048	0.000597	0.10648	0.0461
	4.54069	0.000236	0.105187	0.006
	4.55210	0.02159	0.134887	0.6484
	4.55938	0.006359	0.115732	0.4967
	4.55952	0.006474	0.117409	0.514
	4.56321	0.000881	0.110359	0.0376
	4.57215	0.01001	0.092471	0.6474
	4.57452	0.004818	0.075127	0.6866
	4.57680	0.004051	0.117932	0.3519
	4.57723	0.004102	0.122572	0.3289
	4.58808	0.000522	0.102688	0.0419
	4.58876	0.000491	0.091921	0.0375
	4.58932	0.00016	0.108444	0.0132
	4.58963	0.000267	0.118443	0.0183
	4.59192	0.000768	0.115176	0.024
	4.59798	0.000283	0.156148	0.0055
	4.59913	0.001401	0.136859	0.1082

	4.59937	0.001351	0.136982	0.1055
	4.63514	0.0325	0.118167	0.9779
	4.63692	0.03383	0.120772	0.9788
	4.65299	0.01399	0.279495	0.9545
	4.67044	0.005808	0.124231	0.9618
	4.67151	0.004652	0.106078	0.9623
	4.67566	0.01774	0.272744	0.9258
	4.69283	0.02879	0.11058	0.9769
	4.69391	0.02868	0.106582	0.977
	4.69966	0.02325	0.228246	0.983
	4.73621	0.1325	0.178835	0.9842

Table B8. Symmetries, energies, oscillator strengths, MLCT and singlet weights of the lowest 200 excitations of $Ir(ptz)_3$ calculated in the TZP basis with a frozen core (described in the methods section) in the one-component ZORA with spin-orbit coupling included perturbatively.

Label	Energy	f	MLCT	Singlet
1(A)	2.75536	4.63E-06	0.476068	0
2(E)	2.76693	0.002299	0.481333	0.0559
	2.76735	0.002312	0.481815	0.0555
3(A)	2.80739	0.002118	0.463062	0.1566
4(E)	2.83531	8.91E-05	0.445777	0
	2.83766	1.10E-04	0.443691	0
5(A)	2.84227	0.000525	0.455726	0.0388
6(E)	2.84557	0.001429	0.444618	0.0459
	2.84572	0.00132	0.444263	0.0424
7(A)	2.96568	0.004818	0.475058	0.3532
8(E)	3.01758	0.00403	0.454888	0.3519
	3.02150	0.004017	0.453046	0.3519
9(A)	3.13458	0.001483	0.415612	0.0407
10(E)	3.13591	0.00131	0.418946	0.0486
	3.13702	1.31E-03	0.418397	0.0408
	3.15683	2.24E-03	0.429466	0.0636
	3.15835	2.28E-03	0.431245	0.065
	3.17105	2.02E-03	0.45079	0.1557
	3.21028	0.004274	0.460155	0.3072
	3.22443	0.007713	0.410822	0.2525
	3.22778	0.007769	0.408512	0.253
	3.28922	1.66E-03	0.416634	0.1234
	3.31060	0.004683	0.41912	0.1618
	3.31253	0.004594	0.416178	0.1592
	3.32982	8.35E-03	0.427577	0.2069
	3.33065	0.009708	0.428545	0.2547
	3.35114	0.008951	0.451682	0.3498

	3.35239	0.01068	0.451761	0.3918
	3.35722	0.001671	0.438653	0.0996
	3.36815	6.09E-05	0.410957	0.0028
	3.39220	1.31E-02	0.444817	0.4198
	3.39507	1.29E-02	0.440272	0.4137
	3.46077	0.006171	0.433619	0.7206
	3.50508	0.02351	0.371199	0.5471
	3.50657	0.02398	0.364495	0.5352
	3.52375	0.001918	0.2362	0.1507
	3.54194	7.66E-05	0.160878	0.0009
	3.54396	1.43E-04	0.17263	0.0028
	3.54902	0.001858	0.168697	0.0852
	3.55109	0.002354	0.181941	0.0835
	3.55261	0.001711	0.188112	0.0693
	3.55511	0.000224	0.166879	0.0185
	3.56196	0.01237	0.231274	0.2796
	3.56414	0.01216	0.234526	0.2656
	3.60624	0.008762	0.387861	0.735
	3.85981	7.55E-05	0.366296	0
	3.86912	0.000417	0.370392	0.0188
	3.86929	0.000421	0.369726	0.019
	3.87790	1.67E-04	0.360531	0.0478
	3.89752	5.39E-04	0.359699	0.0094
	3.90057	2.00E-05	0.355613	0
	3.90138	2.07E-05	0.353685	0
	3.90446	0.000461	0.354481	0.0183
	3.90474	3.12E-04	0.355087	0.0182
	4.23895	0.002274	0.24314	0.1253
	4.24018	0.002149	0.237782	0.1236
	4.25548	0.000224	0.271558	0.0203
	4.26062	0.000258	0.373288	0.4499
	4.28658	0.001374	0.247131	0.0838
	4.28777	0.001548	0.249862	0.0842
	4.31157	0.000211	0.234645	0.0076
	4.31822	0.000771	0.227612	0.0291
	4.32199	0.000382	0.232121	0
	4.32326	0.000503	0.233308	0
	4.32917	0.000414	0.157157	0.0143
	4.33021	1.68E-04	0.168172	0.0218
	4.33140	0.000403	0.154296	0.0163
	4.34405	0.000458	0.173838	0.016
	4.34567	0.000426	0.179482	0.0063
	4.35013	0.000928	0.284376	0.0411
	4.35283	0.000837	0.276262	0.0188
	4.35490	0.000982	0.276795	0.0166
	4.36680	0.002038	0.330171	0.1381

	4.38801	0.001956	0.277504	0.1623
	4.38893	1.92E-03	0.277947	0.1613
	4.39594	0.000335	0.358502	0.3738
	4.41919	0.001205	0.310552	0
	4.42230	0.003419	0.257602	0.3024
	4.42332	0.003463	0.250728	0.3074
	4.43263	0.000876	0.286592	0.0617
	4.43365	0.001116	0.284702	0.0592
	4.43521	0.002616	0.292639	0.0307
	4.44271	0.001745	0.304021	0.085
	4.44389	0.002381	0.301534	0.0896
	4.47797	0.00353	0.257485	0.8921
	4.48236	0.004333	0.258313	0.8966
	4.50500	0.001705	0.347444	0.293
	4.52315	0.000269	0.186353	0.0151
	4.52350	0.000335	0.184686	0.009
	4.52614	4.21E-04	0.194554	0.0338
	4.52829	4.23E-04	0.196195	0.0151
	4.53004	4.87E-04	0.20337	0.0287
	4.53133	0.000224	0.195806	0.0154
	4.56444	2.34E-03	0.199921	0.1077
	4.56514	0.002205	0.213047	0.0977
	4.56968	0.000399	0.191878	0.0243
	4.57611	0.006028	0.241804	0.294
	4.57763	0.006602	0.236754	0.3039
	4.58709	2.91E-03	0.203971	0.4228
	4.60042	0.01117	0.278759	0.5049
	4.60094	0.01122	0.267839	0.5255
	4.60413	0.00529	0.158197	0.64
	4.61034	0.001844	0.210219	0.1097
	4.61127	0.002382	0.200198	0.141
	4.61416	0.001437	0.053946	0.9137
	4.62041	0.002954	0.196928	0.2167
	4.62188	0.002566	0.212435	0.1744
	4.63015	3.00E-04	0.237484	0.0221
	4.63211	0.000699	0.213944	0.0275
	4.64392	0.003849	0.175529	0.1218
	4.64480	3.65E-03	0.172052	0.0976
	4.65643	0.007001	0.291102	0.3387
	4.66158	0.01549	0.199848	0.62
	4.66351	0.01266	0.222354	0.5154
	4.66962	0.004425	0.174109	0.1284
	4.67119	0.004957	0.165731	0.175
	4.67343	0.006888	0.176977	0.1677
	4.68377	0.003619	0.224745	0.0875
	4.68546	0.003398	0.220401	0.0623

	4.68850	0.003052	0.238985	0.1489
	4.69425	0.0038	0.149692	0.0308
	4.69572	0.003277	0.174905	0.1306
	4.69721	0.003782	0.177855	0.1327
	4.71218	0.007594	0.189005	0.2133
	4.71333	0.009209	0.162251	0.2281
	4.71507	0.009142	0.178722	0.2108
	4.72521	3.13E-03	0.19274	0.0526
	4.72633	0.002358	0.197541	0.0579
	4.72665	0.006027	0.212923	0.1906
	4.73863	0.001045	0.166387	0.0214
	4.74063	0.000923	0.163556	0.0154
	4.74332	0.0014	0.152754	0.0363
	4.74970	0.002223	0.177765	0.0838
	4.75155	0.002341	0.16636	0.0851
	4.75466	0.002968	0.15337	0.0352
	4.76753	0.03236	0.281173	0.7996
	4.76859	0.01978	0.289575	0.8021
	4.77805	0.06946	0.247109	0.6952
	4.78785	0.003042	0.466131	0.1697
	4.79079	0.003729	0.456733	0.1723
	4.79458	0.003006	0.230541	0.1645
	4.80426	2.12E-03	0.193828	0.0419
	4.80526	1.70E-03	0.19581	0.0263
	4.80814	0.000955	0.198622	0.0292
	4.80959	0.000902	0.195156	0.0342
	4.81211	0.001242	0.197118	0.0412
	4.82381	0.000302	0.452512	0.0149
	4.82707	0.005651	0.337989	0.5923
	4.83391	0.005469	0.36183	0.5998
	4.83551	0.005338	0.344483	0.5294
	4.83609	5.14E-03	0.314288	0.3766
	4.86157	1.95E-03	0.265254	0.0456
	4.86402	4.49E-03	0.257807	0.1096
	4.86549	0.005046	0.257796	0.0872
	4.86746	0.005838	0.255502	0.1566
	4.86906	0.006634	0.25034	0.174
	4.87256	0.02686	0.161794	0.6815
	4.87539	0.007435	0.324177	0.8348
	4.87856	0.02604	0.167853	0.6519
	4.91720	0.003306	0.21208	0.1129
	4.92348	0.004058	0.257696	0.1108
	4.92463	0.004475	0.26161	0.1069
	4.93215	0.001226	0.290275	0.0371
	4.93507	0.01086	0.272037	0.2402
	4.93629	0.009913	0.278525	0.2248

	4.94410	0.003482	0.194384	0.0573
	4.94677	0.003915	0.210736	0.0746
	4.94928	0.004783	0.240533	0.1962
	4.95741	0.005282	0.209943	0.0957
	4.95811	0.005787	0.218956	0.0954
	4.96096	0.001919	0.259678	0.0518
	4.96562	0.008078	0.242777	0.1378
	4.96771	0.008081	0.26211	0.1724
	4.97031	0.004058	0.289783	0.0641
	4.97496	0.005814	0.248358	0.1045
	4.97736	0.009162	0.292712	0.2467
	4.98034	0.008282	0.311168	0.1913
	4.98389	0.01341	0.294036	0.3344
	4.98759	0.01148	0.319037	0.2121
	4.99104	0.02426	0.27869	0.3917
	4.99276	0.01572	0.264355	0.3558
	4.99555	0.01916	0.240498	0.4324
	4.99883	0.006822	0.205403	0.1151
	5.00055	0.02799	0.283956	0.4988
	5.00117	0.01222	0.234267	0.2229
	5.00255	0.01245	0.244221	0.2595
	5.00267	0.008909	0.226834	0.1736
	5.00618	0.01217	0.303505	0.3886
	5.00744	0.009289	0.259603	0.4561
	5.02073	0.0297	0.316997	0.8429
	5.02309	0.03003	0.301181	0.8015
	5.04801	0.062	0.297629	0.7994
	5.05442	0.04364	0.202568	0.8821
	5.05734	0.04272	0.203626	0.8689
	5.08118	0.001741	0.200018	0.9418
	5.11375	0.003502	0.451705	0.8502
	5.11603	0.001926	0.48044	0.8416
	5.12128	0.02447	0.156663	0.9649
	5.12198	0.02234	0.174564	0.9576
	5.13528	0.006207	0.164684	0.9826

Table B9. Symmetries, energies, oscillator strengths, MLCT weights, singlet weights and largest scalar contributions to the lowest 200 excitations of $Ir(ppy)_3$ calculated in the TZP basis with all electrons included explicitly in the one-component ZORA with spin-orbit coupling included perturbatively.

Label	Energy	f	MLCT	Singlet	Component Scalar Transitions
1(A)	2.43012	1.34E-04	0.384757	0.0094	T1 (A) (37%), T2 (E) (24%), T3 (A) (7%)
2(E)	2.43102	0.00132	0.379035	0.0523	T2 (E) (29%), T1 (A) (26%), T3 (A) (12%)

	2.43194	0.00111	0.369483	0.035	T2 (E) (25%), T1 (A) (24%), T3 (A) (10%)
3(E)	2.43809	0.0011	0.376578	0.0359	T2 (E) (52%), T1 (A) (14%), T4 (E) (10%)
	2.43873	1.13E-03	0.380849	0.0366	T2 (E) (50%), T1 (A) (18%), T4 (E) (12%)
4(A)	2.44136	3.85E-04	0.393656	0.0935	T2 (E) (44%), T1 (A) (21%), T3 (A) (10%), S4 (A) (7%)
5(E)	2.46097	0.00272	0.398149	0.075	T2 (E) (48%), T1 (A) (32%), T5 (E) (8%)
	2.46218	0.00297	0.397349	0.0768	T2 (E) (52%), T1 (A) (28%), T5 (E) (8%), S5 (E) (5%)
6(A)	2.48984	0.00106	0.397117	0.071	T2 (E) (72%), T1 (A) (9%), T6 (A) (7%)
7(A)	2.53109	0.00242	0.417701	0.3922	S1 (A) (37%), T4 (E) (34%), T3 (A) (5%)
8(E)	2.54266	0.00153	0.392313	0.3574	S2 (E) (34%), T3 (A) (18%), T4 (E) (12%)
	2.54434	0.00157	0.394187	0.358	S2 (E) (34%), T3 (A) (16%), T4 (E) (10%)
9(A)	2.75165	0.000167	0.373628	0.028	T3 (A) (40%), T2 (E) (22%), T7 (A) (9%)
10(E)	2.75867	0.000501	0.361946	0.0152	T3 (A) (30%), T2 (E) (21%), T5 (E) (6%)
	2.75967	5.13E-04	0.363264	0.022	T3 (A) (26%), T2 (E) (21%), T5 (E) (6%)
	2.77378	1.24E-03	0.351486	0.0376	T4 (E) (40%)
	2.77476	1.20E-03	0.354519	0.0377	T4 (E) (40%)
	2.77568	3.78E-04	0.378263	0.0474	T4 (E) (52%), T1 (A) (18%), T7 (A) (5%)
	2.82612	0.00179	0.34979	0.1367	T7 (A) (28%), T8 (E) (9%), S2 (E) (6%)
	2.82688	0.00186	0.354806	0.1374	T7 (A) (28%), T8 (E) (9%), S2 (E) (5%)
	2.84279	0.00103	0.367156	0.117	T7 (A) (17%), S1 (A) (12%), T3 (A) (7%), T1 (A) (5%)
	2.85609	8.56E-04	0.378252	0.1141	T4 (E) (24%), T7 (A) (23%), S1 (A) (10%), T6 (A) (10%)
	2.87064	0.00422	0.361004	0.3655	T8 (E) (44%), S6 (A) (28%)
	2.87237	0.00335	0.340599	0.1499	T7 (A) (22%), T5 (E) (9%), T8 (E) (5%)
	2.87292	3.58E-03	0.339641	0.1527	T7 (A) (22%), T5 (E) (9%), T8 (E) (5%)
	2.93770	0.00131	0.378096	0.1547	T5 (E) (46%), T4 (E) (14%), S1 (A) (13%), T6 (A) (5%)
	2.94190	0.00258	0.372467	0.2559	S2 (E) (19%), T3 (A) (18%), T4 (E) (16%), T5 (E) (10%)
	2.94322	0.00286	0.373219	0.2686	S2 (E) (20%), T3 (A) (16%), T5 (E) (11%), T6 (A) (10%), S3 (E) (6%), T4 (E) (6%)
	2.96847	0.000192	0.360906	0.0168	T5 (E) (58%), T3 (A) (10%)
	2.97016	2.38E-04	0.358343	0.0416	T5 (E) (51%)
	2.97106	1.24E-03	0.379259	0.2784	T5 (E) (48%), T3 (A) (16%), S4 (A) (16%), S1 (A) (11%)
	2.98405	5.09E-05	0.36746	0.0018	T6 (A) (55%), T4 (E) (12%), T5 (E) (10%)
	2.99258	0.00605	0.383142	0.4007	S3 (E) (23%), S2 (E) (16%), T6 (A) (16%), T4 (E) (15%)
	2.99401	0.00641	0.3825	0.4029	S3 (E) (24%), T6 (A) (18%), S2 (E) (16%), T4 (E) (15%)
	3.02995	0.00333	0.350239	0.5605	S4 (A) (46%), T5 (E) (12%), S3 (E) (6%)
	3.03320	0.0108	0.381764	0.5537	S3 (E) (41%), T6 (A) (32%), S2 (E) (7%)
	3.03430	1.15E-02	0.38493	0.5538	S3 (E) (44%), T6 (A) (34%), S2 (E) (7%)
	3.05611	3.33E-04	0.338488	0	T8 (E) (35%), T11 (E) (10%)
	3.05782	0.000391	0.33403	0	T8 (E) (35%), T11 (E) (9%)

	3.06355	0.00376	0.34275	0.1245	T8 (E) (43%)
	3.06437	0.0041	0.349746	0.1239	T8 (E) (58%)
	3.06509	0.00195	0.345847	0.155	T8 (E) (34%), T7 (A) (11%), T12 (A) (11%), S4 (A) (6%)
	3.10007	0.00128	0.332857	0.1948	T8 (E) (28%), S6 (A) (10%), S10 (A) (8%), T14 (A) (8%)
	3.10799	0.0262	0.304074	0.5877	S5 (E) (48%), T5 (E) (7%)
	3.10913	0.0291	0.303332	0.587	S5 (E) (51%), T5 (E) (7%)
	3.14629	1.55E-02	0.298388	0.4143	S5 (E) (17%), S9 (E) (16%)
	3.14772	0.0161	0.304791	0.4161	S5 (E) (18%), S9 (E) (16%), T12 (A) (12%)
	3.18925	0.000449	0.181761	0.0055	T9 (E) (57%)
	3.19002	6.50E-04	0.170994	0.0318	T9 (E) (70%), T7 (A) (8%)
	3.19017	4.24E-04	0.170981	0	T9 (E) (62%)
	3.19680	1.07E-02	0.358371	0.4962	S6 (A) (26%), S8 (A) (18%)
	3.20415	2.42E-03	0.230742	0.0705	T9 (E) (44%), T8 (E) (13%), T12 (A) (10%)
	3.20439	0.00244	0.223039	0.069	T9 (E) (46%), T8 (E) (12%)
	3.21484	5.57E-04	0.197888	0.0693	T9 (E) (70%)
	3.22643	0.00151	0.216154	0.1068	T10 (A) (29%), T12 (A) (8%), S6 (A) (8%)
	3.22732	0.00127	0.141964	0.0576	T10 (A) (54%), T11 (E) (9%), T9 (E) (6%)
	3.22746	0.00156	0.136229	0.0542	T10 (A) (58%), T11 (E) (9%), T9 (E) (6%)
	3.24486	0.00099	0.205697	0.0484	T10 (A) (52%), T12 (A) (7%), T7 (A) (6%)
	3.24982	0.000561	0.229063	0	T10 (A) (26%), T11 (E) (20%), T8 (E) (6%)
	3.25039	0.000568	0.223499	0.016	T10 (A) (26%), T11 (E) (20%), T8 (E) (5%)
	3.26088	0.00357	0.309062	0.1184	T11 (E) (40%), S9 (E) (6%), T13 (E) (5%)
	3.26101	0.00354	0.305206	0.1198	T11 (E) (38%), S9 (E) (6%), T13 (E) (6%), T9 (E) (5%)
	3.30143	0.0067	0.382796	0.7293	S7 (E) (64%)
	3.30177	0.00667	0.383994	0.7294	S7 (E) (64%)
	3.32923	0.0322	0.374846	0.7105	S8 (A) (65%)
	3.36574	7.92E-05	0.359114	0	T12 (A) (49%), T11 (E) (36%)
	3.41284	0.00429	0.373318	0.211	T12 (A) (46%), T11 (E) (18%), S9 (E) (8%), S7 (E) (5%)
	3.41311	0.00434	0.372617	0.2118	T12 (A) (48%), T11 (E) (18%), S9 (E) (8%), S7 (E) (5%)
	3.46586	0.00169	0.375403	0.1669	T13 (E) (42%), T11 (E) (28%), S10 (A) (12%), T14 (A) (10%)
	3.50916	0.00021	0.370237	0.0095	T13 (E) (57%), T11 (E) (22%)
	3.51050	0.000278	0.36877	0.0153	T13 (E) (57%), T11 (E) (10%)
	3.51784	0.00459	0.382047	0.2073	T13 (E) (48%), T11 (E) (9%), S9 (E) (8%)
	3.51798	0.00569	0.384521	0.2402	T13 (E) (38%), S9 (E) (14%), S11 (E) (8%), T11 (E) (7%)
	3.51928	0.00456	0.382849	0.2119	T13 (E) (48%), S9 (E) (9%), T12 (A) (7%), S11 (E) (6%), T11 (E) (6%)

	3.58521	6.25E-05	0.390067	0.0498	T13 (E) (46%), T14 (A) (39%)
	3.58933	0.0086	0.412972	0.2659	T14 (A) (56%), S9 (E) (23%)
	3.59073	0.00887	0.414145	0.2709	T14 (A) (58%), S9 (E) (24%)
	3.59737	0.000616	0.400682	0.6425	S10 (A) (63%), T14 (A) (29%)
	3.60575	0.00635	0.394484	0.6768	S11 (E) (67%), T13 (E) (11%)
	3.60651	0.00622	0.394077	0.6663	S11 (E) (66%), T13 (E) (11%)
	3.62113	0.00821	0.384945	0.7207	S12 (A) (71%)
	3.75365	0.000232	0.049904	0.0088	T15 (E) (87%)
	3.75372	0.000299	0.052202	0.0139	T15 (E) (88%)
	3.75457	0.000241	0.052953	0.01	T15 (E) (83%)
	3.75464	0.000382	0.053063	0.0213	T15 (E) (83%)
	3.75548	0.000335	0.056496	0.0177	T15 (E) (87%)
	3.75566	0.000297	0.054076	0.0162	T15 (E) (85%)
	3.76202	0.00027	0.066173	0.0086	T16 (A) (92%)
	3.76222	0.000198	0.065058	0.0064	T16 (A) (92%)
	3.76295	3.37E-05	0.06308	0.0021	T16 (A) (87%)
	3.96212	1.27E-04	0.126931	0.0019	T17 (A) (73%), T18 (E) (10%)
	3.96323	3.30E-04	0.140005	0.0387	T17 (A) (88%)
	3.96333	0.000326	0.139306	0.0373	T17 (A) (86%)
	3.97135	2.01E-04	0.036186	0.0026	T18 (E) (96%)
	3.97379	0.000186	0.058571	0.0078	T18 (E) (76%), T17 (A) (20%)
	3.97484	0.0015	0.040145	0.2366	T18 (E) (63%), S13 (E) (20%)
	3.97653	0.00188	0.039011	0.3028	T18 (E) (54%), S13 (E) (30%)
	3.98028	0.0029	0.032078	0.5436	S13 (E) (54%), T18 (E) (34%)
	3.98153	2.30E-03	0.032852	0.3938	T18 (E) (53%), S13 (E) (37%)
	3.98321	0.000857	0.035165	0.1139	T18 (E) (84%), S13 (E) (11%)
	3.98361	0.00171	0.034513	0.2693	T18 (E) (64%), S13 (E) (26%)
	4.00981	0.000516	0.154525	0.026	T19 (E) (90%)
	4.01224	0.000106	0.152922	0.003	T19 (E) (88%), T20 (A) (8%)
	4.01469	0.000749	0.147754	0.0307	T19 (E) (85%)
	4.01532	0.000739	0.147829	0.0303	T19 (E) (83%)
	4.02020	0.000343	0.152384	0.01	T19 (E) (92%)
	4.02027	0.000325	0.152376	0.0083	T19 (E) (90%)
	4.03645	8.53E-04	-0.00295	0.9267	S14 (A) (93%)
	4.03728	0.000201	0.125985	0.0101	T20 (A) (78%), T21 (A) (12%), T19 (E) (6%)
	4.03736	0.000212	0.125971	0.0097	T20 (A) (78%), T21 (A) (12%), T19 (E) (7%)
	4.03952	2.90E-04	0.136669	0.0114	T20 (A) (85%)
	4.05187	0.000816	0.058443	0.0407	T21 (A) (86%)
	4.05621	0.00174	0.062226	0.0412	T21 (A) (78%), T20 (A) (12%)
	4.05628	0.00131	0.062872	0.0309	T21 (A) (80%), T20 (A) (12%)
	4.06143	0.00579	0.161385	0.1243	T22 (E) (74%), S16 (A) (6%), S15 (E) (5%)
	4.06227	0.0276	0.065669	0.5948	S15 (E) (58%), T22 (E) (30%)
	4.06279	0.0258	0.074779	0.5453	S15 (E) (52%), T22 (E) (31%)
	4.06544	0.00126	0.173739	0.0471	T22 (E) (82%)

	4.07567	0.0144	0.125603	0.3097	T22 (E) (53%), S15 (E) (31%)
	4.07626	0.0129	0.131531	0.2812	T22 (E) (56%), S15 (E) (28%)
	4.07965	0.00175	0.182771	0.0384	T22 (E) (88%)
	4.07978	0.00181	0.182539	0.0394	T22 (E) (88%)
	4.08486	0.024	0.020804	0.8534	S16 (A) (85%)
	4.13248	0.1825	0.040833	0.9701	S17 (A) (97%)
	4.14229	0.00271	0.021837	0.7177	S18 (E) (72%), T23 (E) (16%)
	4.14355	0.00236	0.024491	0.6871	S18 (E) (68%), T23 (E) (19%)
	4.15307	1.07E-03	0.081314	0.0097	T23 (E) (78%), T24 (A) (7%), T25 (A) (6%)
	4.15431	0.000555	0.072006	0.1035	T23 (E) (65%), T24 (A) (10%), S18 (E) (6%)
	4.15514	0.000399	0.072933	0.0738	T23 (E) (66%), T24 (A) (12%), S18 (E) (6%)
	4.15681	0.000868	0.069863	0.0177	T23 (E) (86%)
	4.15845	0.000342	0.063908	0.0522	T23 (E) (78%)
	4.15876	0.00044	0.066627	0.0738	T23 (E) (80%)
	4.16615	0.000427	0.147181	0.0167	T24 (A) (69%)
	4.16624	0.000469	0.144013	0.0809	T24 (A) (76%), S18 (E) (7%)
	4.16669	0.000439	0.141023	0.1081	T24 (A) (72%), S18 (E) (9%), T23 (E) (6%)
	4.20528	0.00109	0.179632	0.0414	T25 (A) (74%)
	4.20576	0.00104	0.179336	0.04	T25 (A) (74%)
	4.21457	0.000591	0.185998	0.0027	T25 (A) (81%)
	4.23225	0.00165	0.152806	0.0491	T26 (E) (82%)
	4.23273	0.00156	0.152972	0.0464	T26 (E) (82%)
	4.23641	0.00179	0.164184	0.0332	T26 (E) (90%)
	4.24219	3.16E-04	0.160363	0.0063	T26 (E) (81%)
	4.24229	4.23E-04	0.165212	0.0229	T26 (E) (86%)
	4.24325	0.000347	0.161247	0.0074	T26 (E) (82%)
	4.27277	0.0324	0.030194	0.9382	S19 (E) (94%)
	4.27330	0.0325	0.030631	0.9389	S19 (E) (94%)
	4.34052	0.017	0.094034	0.9646	S20 (A) (96%)
	4.35725	0.00418	0.062084	0.12	T27 (E) (84%), S21 (A) (11%)
	4.35967	0.000504	0.053959	0.0291	T27 (E) (92%)
	4.35999	0.000962	0.055185	0.0422	T27 (E) (90%)
	4.36454	8.56E-05	0.051294	0.002	T27 (E) (95%)
	4.36633	8.59E-05	0.051051	0.0021	T27 (E) (94%)
	4.36684	6.36E-04	0.053213	0.0182	T27 (E) (92%)
	4.39675	0.0241	0.1328	0.7442	S21 (A) (74%)
	4.40351	0.00079	0.089494	0.0526	T28 (A) (86%)
	4.40361	0.000763	0.089369	0.0493	T28 (A) (88%)
	4.40511	0.00122	0.086628	0.0215	T28 (A) (95%)
	4.41693	0.000852	0.075296	0.0203	T29 (A) (86%)
	4.41723	0.00185	0.090782	0.1325	T29 (A) (66%), S22 (E) (11%)
	4.41762	0.00154	0.088513	0.1128	T29 (A) (74%), S22 (E) (10%)
	4.42365	0.004	0.129159	0.3212	T30 (E) (44%), S22 (E) (22%), T29 (A)

					(16%), S23 (E) (8%)
	4.42417	0.00392	0.127449	0.3127	T30 (E) (42%), S22 (E) (23%), T29 (A) (20%), S23 (E) (7%)
	4.43772	0.00365	0.136445	0.2882	T30 (E) (50%), S22 (E) (23%), S23 (E) (6%)
	4.43795	0.0039	0.137164	0.3062	T30 (E) (51%), S22 (E) (24%), S23 (E) (6%)
	4.44926	0.000312	0.123738	0.0122	T30 (E) (90%), T29 (A) (6%)
	4.45205	0.00437	0.140468	0.3184	T30 (E) (62%), S22 (E) (30%)
	4.45278	0.00471	0.142436	0.3515	T30 (E) (58%), S22 (E) (33%)
	4.45521	0.00295	0.129108	0.1028	T30 (E) (88%), S21 (A) (7%)
	4.49101	0.0684	0.0864	0.9605	S24 (A) (91%)
	4.49444	0.00832	0.157515	0.7848	S23 (E) (73%), T30 (E) (11%)
	4.49476	0.00669	0.160883	0.7837	S23 (E) (75%), T30 (E) (6%)
	4.52098	0.000242	0.079353	0.0057	T31 (A) (89%)
	4.52137	0.000551	0.080524	0.0406	T31 (A) (90%)
	4.52149	0.00047	0.080654	0.0338	T31 (A) (92%)
	4.52913	0.00869	0.131345	0.5613	S25 (A) (53%), T32 (E) (28%)
	4.53739	0.0073	0.112372	0.5165	S26 (E) (52%), T32 (E) (17%), T33 (A) (7%)
	4.53795	0.00752	0.114516	0.5244	S26 (E) (53%), T32 (E) (18%)
	4.54091	0.00114	0.095361	0.0601	T32 (E) (54%), T33 (A) (31%), T31 (A) (7%)
	4.54954	0.00198	0.043921	0.9622	S27 (A) (94%)
	4.55427	0.00665	0.123796	0.4044	T32 (E) (48%), S25 (A) (35%), T33 (A) (10%)
	4.55835	0.00425	0.104836	0.2972	T32 (E) (33%), S26 (E) (28%), T33 (A) (26%)
	4.55899	0.00405	0.11126	0.2909	T33 (A) (36%), S26 (E) (27%), T32 (E) (21%)
	4.56945	0.000678	0.094648	0.0565	T32 (E) (58%), T33 (A) (26%)
	4.56999	0.000781	0.093333	0.0564	T32 (E) (76%)
	4.57054	0.000472	0.109861	0.0451	T32 (E) (37%), T33 (A) (31%), T34 (A) (20%)
	4.57179	0.000479	0.115743	0.0436	T32 (E) (37%), T34 (A) (24%), T33 (A) (22%)
	4.57411	0.00153	0.10235	0.0617	T32 (E) (39%), T33 (A) (33%), T34 (A) (6%)
	4.58505	0.0017	0.151963	0.1272	T34 (A) (62%), T32 (E) (17%), S26 (E) (6%)
	4.58524	0.00157	0.154995	0.1237	T34 (A) (60%), T32 (E) (9%), S26 (E) (6%), T33 (A) (6%)
	4.58645	0.000457	0.17284	0.0049	T34 (A) (87%)
	4.61101	0.037	0.138259	0.963	S28 (E) (94%)
	4.61246	0.0378	0.139294	0.9668	S28 (E) (95%)
	4.62884	0.00222	0.221778	0.9565	S29 (A) (94%)
	4.64928	0.00375	0.113069	0.9311	S30 (E) (85%), S31 (E) (6%)
	4.65011	0.00415	0.11035	0.9292	S30 (E) (86%), S31 (E) (6%)

	4.66770	0.025	0.106413	0.9608	S31 (E) (89%), S30 (E) (6%)
	4.66828	0.0253	0.108987	0.9609	S31 (E) (87%), S30 (E) (5%)
	4.68001	0.0302	0.338671	0.9262	S32 (A) (88%)
	4.69552	0.0635	0.250364	0.9736	S33 (A) (96%)
	4.71159	0.1002	0.211672	0.9723	S34 (A) (97%)
					T1 (A) (37%), T2 (E) (24%), T3 (A) (7%)

Table B10. Symmetries, energies, oscillator strengths, MLCT weights, singlet weights and largest scalar contributions to the lowest 200 excitations of $Ir(ptz)_3$ calculated in the TZP basis with all electrons included explicitly in the one-component ZORA with spin-orbit coupling included perturbatively.

Label	Energy	f	MLCT	Singlet	Component Scalar Transitions
1(A)	2.72693	7.59E-06	0.457465	0	T1 (A) (64%)
2(E)	2.74126	0.00315	0.463492	0.0785	T1 (A) (72%), T3 (E) (8%), S3 (E) (7%), T2 (E) (6%)
	2.74237	0.0033	0.464496	0.0771	T1 (A) (72%), T3 (E) (8%), S3 (E) (7%), T2 (E) (6%)
3(A)	2.77378	0.00263	0.450901	0.1852	T2 (E) (70%), S1 (A) (17%)
4(E)	2.80647	8.38E-05	0.429956	0	T2 (E) (65%)
	2.81016	1.16E-04	0.42771	0	T2 (E) (65%)
5(A)	2.81709	0.00122	0.438992	0.0641	T2 (E) (68%), T1 (A) (8%)
6(E)	2.81983	0.00208	0.428441	0.0693	T2 (E) (77%)
	2.82097	0.00151	0.430226	0.0581	T2 (E) (68%), T1 (A) (5%)
7(A)	2.93431	0.00414	0.451078	0.2912	T3 (E) (40%), S1 (A) (24%)
8(E)	2.97087	0.00433	0.438249	0.3408	S2 (E) (30%), T5 (E) (22%), T4 (A) (16%)
	2.97660	0.00432	0.435349	0.3397	S2 (E) (30%), T4 (A) (20%), T6 (A) (12%)
9(E)	3.13639	0.00142	0.407686	0.048	T3 (E) (36%), T1 (A) (14%)
	3.13880	0.00196	0.391792	0.0478	T3 (E) (35%), T4 (A) (12%), T1 (A) (12%)
10(A)	3.14243	8.32E-04	0.416136	0.044	T3 (E) (56%), T1 (A) (15%)
	3.15666	2.36E-03	0.403553	0.0583	T3 (E) (36%), T5 (E) (10%), T2 (E) (7%)
	3.15826	2.60E-03	0.413767	0.0837	T3 (E) (30%), T4 (A) (14%), T5 (E) (11%), T2 (E) (8%)
	3.17193	1.60E-03	0.431232	0.1218	T4 (A) (44%), T2 (E) (10%), S1 (A) (8%)
	3.21922	0.00703	0.392011	0.2329	T5 (E) (30%), S1 (A) (6%), T2 (E) (5%)
	3.22536	0.00568	0.37356	0.2525	T5 (E) (18%), S1 (A) (13%), T6 (A) (12%)
	3.22684	0.00789	0.361999	0.2357	T6 (A) (18%), S3 (E) (7%), T2 (E) (6%), S2 (E) (6%), T5 (E) (5%), S5 (E) (5%)
	3.30182	3.47E-03	0.431621	0.24	T3 (E) (36%), S1 (A) (22%), T6 (A) (13%)
	3.32787	0.00329	0.409077	0.124	T3 (E) (42%), T5 (E) (10%), S2 (E) (7%)
	3.33084	0.00304	0.401664	0.1207	T3 (E) (40%), T5 (E) (14%), S2 (E) (8%)
	3.34975	7.42E-03	0.40691	0.1781	T5 (E) (18%), T3 (E) (18%), T6 (A) (16%), S3 (E) (14%)
	3.35137	0.00832	0.403557	0.2313	T5 (E) (17%), S3 (E) (16%), T3 (E) (16%)
	3.37874	0.00394	0.409708	0.1719	T5 (E) (32%), T4 (A) (11%), S2 (E) (7%),

					S3 (E) (6%), T6 (A) (5%)
	3.37942	0.00726	0.428797	0.2981	T4 (A) (24%), S2 (E) (15%), S3 (E) (14%), T6 (A) (12%), T5 (E) (11%)
	3.38233	0.00679	0.422721	0.2569	T4 (A) (25%), T5 (E) (20%), S3 (E) (12%), S2 (E) (11%)
	3.38721	7.65E-04	0.398101	0.0375	T5 (E) (36%), T6 (A) (32%), T4 (A) (9%), T8 (A) (6%)
	3.42535	1.51E-02	0.442872	0.4722	S3 (E) (33%), T6 (A) (26%), S2 (E) (14%)
	3.42810	1.48E-02	0.437278	0.4595	T6 (A) (36%), S3 (E) (31%), S2 (E) (14%)
	3.48559	0.00509	0.403756	0.572	S4 (A) (55%), T5 (E) (20%)
	3.51922	0.0123	0.3221	0.3294	T7 (E) (31%), S5 (E) (26%), T5 (E) (21%)
	3.52154	0.0135	0.322252	0.3421	T7 (E) (39%), S5 (E) (27%), T5 (E) (9%), S2 (E) (5%)
	3.52593	0.00291	0.261758	0.1431	T8 (A) (33%), T7 (E) (24%), T5 (E) (10%), S6 (A) (7%)
	3.54203	1.87E-04	0.195817	0.0035	T7 (E) (61%), T8 (A) (16%), T5 (E) (7%)
	3.54568	3.27E-04	0.20447	0.0065	T8 (A) (40%), T7 (E) (40%), T5 (E) (8%)
	3.55331	0.00255	0.208391	0.1383	T7 (E) (60%), S4 (A) (7%)
	3.55649	0.00202	0.206146	0.0901	T8 (A) (50%), T7 (E) (32%)
	3.55733	0.0017	0.205293	0.0865	T8 (A) (52%), T7 (E) (24%)
	3.56017	0.000649	0.198916	0.0555	T7 (E) (56%), T8 (A) (19%)
	3.57373	0.0198	0.305634	0.4609	T7 (E) (48%), S5 (E) (46%)
	3.57622	0.0197	0.29945	0.4435	S5 (E) (45%), T7 (E) (40%)
	3.62530	0.00931	0.398369	0.7573	S6 (A) (76%), T8 (A) (12%)
	3.83825	2.22E-04	0.351475	0	T9 (A) (67%), T10 (E) (24%)
	3.84931	0.000297	0.347707	0.0618	T10 (E) (82%)
	3.85032	0.000714	0.358597	0.024	T9 (A) (72%), T10 (E) (14%)
	3.85065	7.14E-04	0.358869	0.0237	T9 (A) (72%), T10 (E) (14%)
	3.87431	1.15E-03	0.346524	0.0149	T10 (E) (74%), T9 (A) (18%)
	3.87853	4.49E-05	0.338671	0	T10 (E) (82%)
	3.87922	4.62E-05	0.339295	0	T10 (E) (82%)
	3.88385	0.00045	0.341628	0.0239	T10 (E) (83%), T9 (A) (10%)
	3.88413	4.90E-04	0.341395	0.0241	T10 (E) (83%)
	4.19300	0.00259	0.207009	0.1725	T11 (A) (30%), S8 (E) (5%)
	4.19520	0.00267	0.198383	0.1734	T11 (A) (28%)
	4.22279	0.000314	0.244861	0	T11 (A) (34%), T13 (A) (29%)
	4.22694	0.000338	0.323679	0.338	S7 (A) (30%), T15 (E) (12%)
	4.24162	0.00108	0.254174	0.0802	T13 (A) (36%), T11 (A) (14%), T14 (E) (7%)
	4.24349	0.00114	0.252626	0.0773	T13 (A) (36%), T11 (A) (12%), T14 (E) (7%)
	4.28747	0.00161	0.208139	0.0561	T12 (E) (50%), T14 (E) (30%)
	4.28958	0.000639	0.241437	0.0267	T13 (A) (32%), T11 (A) (18%), T14 (E) (5%)
	4.29058	0.000428	0.238648	0	T13 (A) (31%), T14 (E) (12%), T11 (A) (10%)
	4.29241	0.000389	0.247168	0	T13 (A) (30%), T11 (A) (16%), T14 (E) (15%), T15 (E) (5%)

	4.30519	0.00101	0.181995	0.0263	T12 (E) (43%), T14 (E) (5%)
	4.30583	1.00E-03	0.19467	0.0268	T12 (E) (41%), T14 (E) (18%)
	4.30808	0.000479	0.165812	0.0226	T12 (E) (66%)
	4.31944	0.000827	0.199761	0.0142	T12 (E) (29%), T14 (E) (12%)
	4.32225	0.000755	0.195504	0.0117	T12 (E) (37%), T14 (E) (11%)
	4.32375	0.000439	0.193331	0.0201	T12 (E) (48%), T11 (A) (10%)
	4.32593	0.000343	0.168822	0	T12 (E) (69%), T14 (E) (7%)
	4.32781	0.000469	0.179721	0.016	T12 (E) (58%), T14 (E) (7%)
	4.33386	0.00345	0.269135	0.121	T14 (E) (46%), S7 (A) (7%)
	4.35865	0.00174	0.231088	0.1432	T14 (E) (31%), T11 (A) (12%), S8 (E) (6%)
	4.36059	1.75E-03	0.219664	0.1411	T14 (E) (26%), T11 (A) (10%)
	4.36807	0.000501	0.307486	0.4281	S7 (A) (23%), S12 (A) (17%)
	4.40047	0.00225	0.2734	0.0117	T15 (E) (49%), T13 (A) (9%), T16 (A) (8%)
	4.40128	0.00332	0.227853	0.203	T15 (E) (22%), S10 (E) (8%), T17 (E) (7%), S8 (E) (6%)
	4.40215	0.0031	0.241609	0.1747	T16 (A) (28%), T15 (E) (10%), S10 (E) (7%), T17 (E) (6%), S8 (E) (5%)
	4.41345	0.00158	0.266552	0.1272	T15 (E) (30%), T16 (A) (12%), T14 (E) (8%)
	4.41450	0.00125	0.277083	0.1015	T15 (E) (39%), T14 (E) (10%), T16 (A) (6%)
	4.42039	0.00378	0.265368	0.0422	T16 (A) (29%), T15 (E) (28%)
	4.42228	0.00252	0.272253	0.0778	T15 (E) (60%)
	4.42400	0.00242	0.274775	0.0953	T16 (A) (36%), T15 (E) (22%)
	4.46122	0.00289	0.216857	0.8886	S8 (E) (57%), S9 (E) (29%)
	4.46700	0.00303	0.228244	0.8937	S8 (E) (52%), S9 (E) (33%)
	4.48169	0.00339	0.241989	0.2094	T22 (E) (20%), T15 (E) (12%), S12 (A) (9%), S11 (A) (6%)
	4.50431	0.00034	0.176094	0.0063	T17 (E) (72%), T19 (E) (7%)
	4.50547	0.000363	0.183291	0.0159	T17 (E) (65%), T19 (E) (12%)
	4.50788	4.69E-04	0.186576	0.0247	T17 (E) (63%), T19 (E) (9%)
	4.51281	5.72E-04	0.187489	0.0207	T17 (E) (65%), T19 (E) (11%)
	4.51411	4.97E-04	0.193163	0.016	T17 (E) (70%), T19 (E) (8%)
	4.51672	0.000335	0.185761	0.0078	T17 (E) (62%), T19 (E) (14%)
	4.53343	3.31E-03	0.20986	0.2138	T18 (A) (14%), T23 (A) (10%), S18 (E) (10%), S19 (E) (8%)
	4.53679	0.00363	0.204495	0.1828	T18 (A) (20%), T23 (A) (12%), S19 (E) (9%), S18 (E) (8%)
	4.55293	0.000219	0.184873	0.0178	T18 (A) (73%), T20 (A) (12%)
	4.55606	0.00201	0.207469	0.098	T18 (A) (52%), T20 (A) (16%)
	4.55699	0.00249	0.21301	0.1162	T18 (A) (44%), T20 (A) (18%)
	4.57774	1.85E-03	0.181535	0.8428	S11 (A) (66%), S12 (A) (12%)
	4.59442	0.00597	0.177281	0.6043	S13 (A) (32%), S11 (A) (13%), S7 (A) (6%), S15 (A) (6%)
	4.60242	0.00564	0.158292	0.6574	S13 (A) (48%)
	4.60620	0.0162	0.225606	0.7206	S10 (E) (31%), S14 (E) (24%), S13 (A)

					(6%)
	4.60775	0.0161	0.242876	0.6519	S10 (E) (35%), S14 (E) (18%)
	4.61655	0.00475	0.22752	0.2078	T19 (E) (16%), S10 (E) (9%), T15 (E) (6%)
	4.61713	0.00469	0.221517	0.2545	T19 (E) (10%), S10 (E) (7%), S14 (E) (7%)
	4.62067	0.00243	0.188171	0.1172	T19 (E) (12%), T20 (A) (10%), S9 (E) (5%)
	4.62133	0.00166	0.177966	0.0483	T20 (A) (24%), T21 (A) (9%), T23 (A) (6%)
	4.62267	1.48E-03	0.194276	0.0725	T20 (A) (18%), T19 (E) (16%)
	4.63711	0.00112	0.244101	0.0123	T19 (E) (48%), T16 (A) (5%)
	4.64332	0.00217	0.179795	0.0152	T21 (A) (18%), T20 (A) (12%), T19 (E) (10%)
	4.64422	2.26E-03	0.183297	0.045	T21 (A) (16%), T20 (A) (14%), T19 (E) (12%)
	4.64697	0.00826	0.24013	0.3337	T22 (E) (24%), S15 (A) (13%), S12 (A) (11%)
	4.65470	0.00632	0.163765	0.1961	T21 (A) (12%), S14 (E) (9%), S19 (E) (6%)
	4.65619	0.00437	0.140679	0.0899	T21 (A) (16%)
	4.65839	0.0108	0.145956	0.3387	S14 (E) (20%), T21 (A) (12%), S10 (E) (7%)
	4.66135	0.0119	0.13955	0.3864	S14 (E) (23%), S10 (E) (7%)
	4.66598	0.0022	0.170028	0.0355	T21 (A) (23%), T24 (A) (10%), T23 (A) (9%)
	4.67377	0.00319	0.181463	0.0825	T22 (E) (17%), T19 (E) (5%)
	4.67541	0.00288	0.174098	0.0202	T22 (E) (19%), T19 (E) (5%)
	4.68077	0.00622	0.172501	0.0756	T21 (A) (25%)
	4.68677	0.0047	0.158594	0.1611	T23 (A) (16%), S19 (E) (6%)
	4.68892	0.00526	0.177348	0.1812	T23 (A) (24%), S14 (E) (6%), S19 (E) (6%)
	4.69341	0.00622	0.253406	0.2305	T19 (E) (32%), S15 (A) (14%), T23 (A) (9%), S12 (A) (6%)
	4.70713	0.00577	0.177737	0.0943	T24 (A) (22%), T23 (A) (15%), T25 (E) (14%)
	4.70786	0.00476	0.176121	0.2054	T21 (A) (16%), T24 (A) (12%), S14 (E) (8%), T25 (E) (5%)
	4.71004	0.00573	0.160898	0.1946	T21 (A) (14%), T24 (A) (10%), S14 (E) (7%)
	4.71482	1.91E-03	0.204756	0.0479	T25 (E) (20%), T22 (E) (19%), T24 (A) (16%)
	4.71775	0.00156	0.205482	0.0477	T24 (A) (26%), T25 (E) (21%), T22 (E) (12%)
	4.72436	0.00799	0.204544	0.1727	T25 (E) (22%), S15 (A) (14%), T22 (E) (10%), T20 (A) (7%), T21 (A) (7%)
	4.72572	0.00226	0.275172	0.0536	T25 (E) (30%), T27 (A) (18%), T22 (E) (16%)
	4.72806	0.00468	0.296937	0.1134	T27 (A) (30%), T25 (E) (14%)
	4.72881	0.00448	0.33987	0.1786	T27 (A) (36%), T25 (E) (12%), S30 (E)

					(7%)
	4.72949	0.00394	0.30507	0.1181	T27 (A) (30%), T25 (E) (16%)
	4.73410	0.00342	0.192824	0.0803	T25 (E) (54%), T22 (E) (16%)
	4.74437	0.00127	0.209246	0.0464	T24 (A) (40%), T25 (E) (28%)
	4.74571	0.00119	0.189817	0.0408	T25 (E) (39%), T24 (A) (32%)
	4.75084	0.00062	0.193716	0.008	T25 (E) (42%), T24 (A) (37%)
	4.77236	0.0132	0.373944	0.5075	S20 (A) (21%), S16 (E) (19%), T27 (A) (18%), S17 (A) (6%)
	4.77258	0.0172	0.303748	0.6802	S16 (E) (51%), S20 (A) (12%)
	4.77397	0.022	0.283466	0.679	S16 (E) (63%), T27 (A) (6%)
	4.77440	0.00371	0.408038	0.2767	T27 (A) (33%), S20 (A) (21%), T32 (E) (10%)
	4.78556	6.13E-02	0.265955	0.5293	S17 (A) (51%), T27 (A) (10%)
	4.79233	2.55E-03	0.181848	0.0483	T26 (E) (48%)
	4.79351	0.00154	0.190542	0.0267	T26 (E) (64%), T28 (E) (10%)
	4.79517	0.00189	0.208015	0.0746	T26 (E) (48%)
	4.79784	0.00133	0.223662	0.1679	T26 (E) (56%), S20 (A) (7%), S12 (A) (5%)
	4.80016	0.00155	0.193627	0.0415	T26 (E) (60%), T28 (E) (8%)
	4.80301	0.00157	0.201866	0.0484	T26 (E) (58%), T28 (E) (7%)
	4.82693	0.0106	0.262139	0.3178	T28 (E) (38%), S22 (A) (15%), S12 (A) (8%), S17 (A) (5%)
	4.84309	0.0122	0.264292	0.6412	S21 (E) (29%), S18 (E) (25%), T23 (A) (10%), S19 (E) (5%)
	4.84705	7.52E-03	0.300223	0.5885	S18 (E) (39%), S21 (E) (13%), T23 (A) (12%), S19 (E) (5%)
	4.85637	9.39E-04	0.232951	0.0216	T28 (E) (32%), T30 (E) (8%)
	4.85817	8.76E-03	0.215248	0.3054	S21 (E) (25%), T28 (E) (14%), T22 (E) (8%)
	4.86005	0.00766	0.208294	0.2889	S21 (E) (19%), T28 (E) (13%), T23 (A) (12%), S18 (E) (7%)
	4.86265	0.0129	0.207025	0.4709	S21 (E) (34%), S18 (E) (7%), T28 (E) (5%)
	4.86544	0.00866	0.225123	0.2393	T28 (E) (24%), S21 (E) (16%), T23 (A) (12%), T29 (A) (6%), S20 (A) (6%)
	4.86832	0.00427	0.248122	0.2111	T28 (E) (24%), S18 (E) (14%)
	4.86939	0.00518	0.228682	0.1918	T28 (E) (18%), S18 (E) (10%)
	4.87602	0.0155	0.214752	0.7175	S22 (A) (70%)
	4.89633	0.00194	0.249731	0.1349	T31 (A) (37%), T33 (A) (16%), S20 (A) (6%)
	4.90248	0.00616	0.25281	0.1662	T31 (A) (16%), T29 (A) (12%), S24 (E) (7%), T30 (E) (5%)
	4.90569	0.00716	0.242258	0.174	T31 (A) (18%), T29 (A) (14%), S24 (E) (5%)
	4.91273	0.00586	0.25573	0.2386	T30 (E) (26%), S23 (A) (10%)
	4.92149	0.0103	0.243712	0.1779	T31 (A) (16%), T33 (A) (12%), S25 (E) (8%)
	4.92452	0.00514	0.266737	0.0962	T30 (E) (24%), T32 (E) (14%)
	4.92599	0.0107	0.261574	0.2411	T30 (E) (12%), T31 (A) (10%), S24 (E)

					(9%), S25 (E) (6%)
	4.92806	0.00373	0.272131	0.1285	T32 (E) (24%), T30 (E) (11%), S24 (E) (6%)
	4.92821	0.00218	0.27724	0.0562	T30 (E) (32%), T32 (E) (22%)
	4.93829	0.0101	0.23576	0.1846	T29 (A) (16%), T31 (A) (12%), S25 (E) (8%)
	4.94054	0.0101	0.23494	0.1443	T31 (A) (14%), T29 (A) (14%), S25 (E) (9%), T32 (E) (5%)
	4.94292	0.00115	0.253257	0.0241	T29 (A) (31%)
	4.94939	0.0174	0.224397	0.3756	S24 (E) (9%), T30 (E) (8%), T32 (E) (8%), S27 (E) (6%), S19 (E) (6%), S25 (E) (5%)
	4.95203	0.0158	0.232627	0.3362	T30 (E) (12%), S24 (E) (10%), S27 (E) (6%), S25 (E) (6%), S19 (E) (5%)
	4.95671	0.0128	0.279364	0.3268	S24 (E) (16%), T34 (E) (15%), T32 (E) (14%), S25 (E) (6%)
	4.95993	0.00535	0.219744	0.1859	T34 (E) (24%), T30 (E) (13%), T32 (E) (10%), S26 (A) (9%), T31 (A) (6%)
	4.96312	0.0141	0.310285	0.2066	T32 (E) (32%), S25 (E) (13%), T29 (A) (10%)
	4.96624	0.00436	0.209772	0.1026	T34 (E) (38%), S24 (E) (9%), T32 (E) (6%)
	4.97308	0.0105	0.22861	0.1431	T34 (E) (39%), T32 (E) (12%), S25 (E) (8%)
	4.97547	0.00798	0.277787	0.2463	T32 (E) (27%), S24 (E) (12%)
	4.97962	0.00377	0.333574	0.1449	T32 (E) (38%), T30 (E) (10%), T29 (A) (10%), S23 (A) (9%), T27 (A) (7%)
	4.98389	0.0077	0.246573	0.202	T34 (E) (22%), T32 (E) (18%), S24 (E) (10%)
	4.98556	0.00499	0.27994	0.0936	T32 (E) (22%), T30 (E) (22%)
	4.99431	0.0162	0.225388	0.2659	T33 (A) (24%), S25 (E) (16%)
	4.99777	0.0108	0.198336	0.3717	S26 (A) (21%), T34 (E) (14%), T31 (A) (8%), T33 (A) (7%), S28 (A) (5%)
	5.00121	0.00921	0.190911	0.1618	T33 (A) (32%), T34 (E) (12%), T31 (A) (12%), S25 (E) (7%)
	5.00643	0.00436	0.203691	0.2362	T33 (A) (28%), S26 (A) (16%), T31 (A) (10%)
	5.01029	0.0199	0.249589	0.4179	S25 (E) (17%), T33 (A) (14%), S24 (E) (9%), S26 (A) (6%), S19 (E) (6%)
	5.01247	0.0135	0.262158	0.3754	S23 (A) (24%), T33 (A) (6%)
	5.01293	0.0174	0.244239	0.4121	S23 (A) (15%), S25 (E) (7%), S29 (E) (6%)
	5.01839	0.0407	0.25394	0.8354	S27 (E) (50%), S29 (E) (25%)
	5.02085	0.038	0.251501	0.7713	S27 (E) (43%), S29 (E) (24%)
	5.04943	0.0442	0.287803	0.7718	S28 (A) (61%), T33 (A) (8%)
	5.05330	0.0273	0.262109	0.843	S29 (E) (42%), S27 (E) (18%), S30 (E) (8%)
	5.05798	0.0243	0.26887	0.8205	S29 (E) (35%), S30 (E) (15%), S27 (E) (13%)
	5.06937	0.00283	0.196196	0.895	S31 (A) (81%), S26 (A) (5%)
	5.09417	0.00737	0.421466	0.7802	S30 (E) (61%), T27 (A) (14%), S29 (E)

					(9%)
	5.09497	0.00729	0.41585	0.7843	S30 (E) (63%), T27 (A) (14%), S29 (E) (13%)
	5.11263	0.03	0.156135	0.9245	S32 (E) (88%)
	5.11313	0.03	0.16038	0.9205	S32 (E) (86%)
	5.13139	0	0.28212	0.8926	S33 (A) (88%)

Scalar relativistic calculations

Table B11. Symmetries, energies, oscillator strengths, MLCT weights, and largest MO transition components to the lowest 50 excitations of $Ir(ppy)_3$ calculated in the TZP basis with all electrons included explicitly in the one-component scalar relativistic ZORA.

Excitation	Energy (eV)	f	MLCT	Transitions
S1 (A)	2.74748	5.60E-03	0.4945	H (A)→L (A) (97%)
S2 (E)	2.7995	2.55E-03	0.4448	H (A)→L+1 (E) (97%)
S2’ (E)	2.80115	2.57E-03	0.4448	H (A)→L+1 (E) (97%)
S3 (E)	2.95761	2.39E-02	0.4078	H-1 (E)→L (A) (85%), H-1 (E)→L+1 (E) (5%)
S3’ (E)	2.95911	2.48E-02	0.4098	H-1 (E)→L (A) (85%), H-1 (E)→L+1 (E) (6%)
S4 (A)	2.97055	2.61E-03	0.3677	H-1 (E)→L+1 (E) (95%)
S5 (E)	3.05966	4.86E-02	0.3757	H-1 (E)→L+1 (E) (82%), H-1 (E)→L (A) (6%)
S5’ (E)	3.06089	5.19E-02	0.3720	H-1 (E)→L+1 (E) (87%), H-1 (E)→L (A) (6%)
S6 (A)	3.06265	3.67E-03	0.4503	H (A)→L+2 (A) (69%), H-1 (E)→L+1 (E) (25%)
S7 (E)	3.24187	6.01E-03	0.4032	H-1 (E)→L+2 (A) (96%)
S7’ (E)	3.2422	5.98E-03	0.4067	H-1 (E)→L+2 (A) (96%)
S8 (A)	3.26449	4.93E-02	0.3887	H-1 (E)→L+1 (E) (68%), H (A)→L+2 (A) (24%)
S9 (E)	3.38257	3.45E-02	0.4784	H (A)→L+3 (E) (95%)
S9’ (E)	3.38491	3.45E-02	0.4783	H (A)→L+3 (E) (95%)
S10 (A)	3.51124	5.90E-04	0.4047	H-1 (E)→L+3 (E) (98%)
S11 (E)	3.52955	9.19E-03	0.4026	H-1 (E)→L+3 (E) (98%)
S11’ (E)	3.52958	9.31E-03	0.4025	H-1 (E)→L+3 (E) (96%)
S12 (A)	3.55665	1.14E-02	0.3956	H-1 (E)→L+3 (E) (93%)
S13 (E)	3.98008	5.01E-03	0.0259	H-2 (E)→L (A) (83%), H-2 (E)→L+1 (E) (6%)
S13’ (E)	3.98181	5.36E-03	0.0257	H-2 (E)→L (A) (83%), H-2 (E)→L+1 (E) (10%)
S14 (A)	4.0369	8.68E-04	-0.0124	H-2 (E)→L+1 (E) (88%), H-3 (A)→L (A) (10%)
S15 (E)	4.0645	4.64E-02	-0.0054	H-2 (E)→L+1 (E) (77%), H-2 (E)→L+2 (A) (9%)
S15’ (E)	4.0652	4.74E-02	-0.0051	H-2 (E)→L+1 (E) (76%), H-2 (E)→L+2 (A) (9%)
S16 (A)	4.08363	2.79E-02	-0.0046	H-2 (E)→L+1 (E) (75%), H-3 (A)→L (A) (20%)

S17 (A)	4.13075	0.1882	0.0381	H-3 (A)→L (A) (59%), H-2 (E)→L+1 (E) (21%), H-3 (A)→L+2 (A) (5%)
S18 (E)	4.14599	3.57E-03	-0.0051	H-3 (A)→L+1 (E) (72%), H-2 (E)→L+2 (A) (18%)
S18’ (E)	4.14757	3.22E-03	-0.0051	H-3 (A)→L+1 (E) (72%), H-2 (E)→L+2 (A) (18%)
S19 (E)	4.26947	3.45E-02	0.0220	H-2 (E)→L+2 (A) (63%), H-3 (A)→L+1 (E) (19%)
S19’ (E)	4.27001	3.46E-02	0.0226	H-2 (E)→L+2 (A) (63%), H-3 (A)→L+1 (E) (19%)
S20 (A)	4.33774	1.76E-02	0.0944	H-3 (A)→L+2 (A) (59%), H-4 (A)→L (A) (25%)
S21 (A)	4.38796	3.21E-02	0.1548	H-4 (A)→L (A) (50%), H-3 (A)→L+2 (A) (27%), H-6 (A)→L (A) (6%)
S22 (E)	4.4243	1.37E-02	0.1809	H-4 (A)→L+1 (E) (74%), H-6 (A)→L+1 (E) (6%)
S22’ (E)	4.42543	1.35E-02	0.1803	H-4 (A)→L+1 (E) (74%), H-6 (A)→L+1 (E) (6%)
S23 (E)	4.47479	7.19E-03	0.1765	H-5 (E)→L (A) (51%), H-2 (E)→L+3 (E) (30%)
S23’ (E)	4.47521	7.23E-03	0.1777	H-5 (E)→L (A) (51%), H-2 (E)→L+3 (E) (25%)
S24 (A)	4.48589	7.42E-02	0.0829	H-2 (E)→L+3 (E) (61%), H-5 (E)→L+1 (E) (15%), H-6 (A)→L (A) (7%)
S25 (A)	4.53079	1.50E-02	0.1662	H-6 (A)→L (A) (53%), H-5 (E)→L+1 (E) (33%)
S26 (E)	4.53767	1.39E-02	0.1347	H-2 (E)→L+3 (E) (32%), H-5 (E)→L (A) (22%), H-6 (A)→L+1 (E) (13%)
S26’ (E)	4.53847	1.43E-02	0.1359	H-2 (E)→L+3 (E) (31%), H-5 (E)→L (A) (23%), H-6 (A)→L+1 (E) (13%)
S27 (A)	4.54611	1.54E-03	0.0392	H-2 (E)→L+3 (E) (84%), H-3 (A)→L+2 (A) (6%)
S28 (E)	4.59979	3.88E-02	0.1411	H-5 (E)→L+1 (E) (32%), H-2 (E)→L+3 (E) (20%), H-3 (A)→L+3 (E) (12%), H-6 (A)→L+1 (E) (11%), H-5 (E)→L (A) (6%)
S28’ (E)	4.60134	3.94E-02	0.1415	H-5 (E)→L+1 (E) (32%), H-2 (E)→L+3 (E) (19%), H-6 (A)→L+1 (E) (12%), H-3 (A)→L+3 (E) (11%), H-5 (E)→L (A) (6%)
S29 (A)	4.61433	1.61E-03	0.2246	H-5 (E)→L+1 (E) (64%), H-6 (A)→L (A) (20%)
S30 (E)	4.63758	1.63E-03	0.1115	H-6 (A)→L+1 (E) (44%), H-3 (A)→L+3 (E) (22%), H-5 (E)→L (A) (8%), H-4 (A)→L+1 (E) (5%), H-5 (E)→L+1 (E) (5%)
S30’ (E)	4.63862	2.61E-03	0.1049	H-6 (A)→L+1 (E) (43%), H-3 (A)→L+3 (E) (25%), H-5 (E)→L (A) (8%)
S31 (E)	4.65636	2.73E-02	0.1059	H-3 (A)→L+3 (E) (48%), H-5 (E)→L+1 (E) (22%), H-6 (A)→L+1 (E) (7%)
S31’ (E)	4.65747	2.78E-02	0.1030	H-3 (A)→L+3 (E) (53%), H-5 (E)→L+1 (E) (13%)
S32 (A)	4.65917	3.26E-02	0.3676	H (A)→L+4 (A) (42%), H (A)→L+5 (A) (19%), H-4 (A)→L+2 (A) (17%)

S33 (A)	4.68496	6.54E-02	0.2542	H-4 (A)→L+2 (A) (67%), H (A)→L+4 (A) (7%), H (A)→L+5 (A) (5%)
S34 (A)	4.69823	0.1032	0.2149	H-5 (E)→L+1 (E) (46%), H-2 (E)→L+3 (E) (14%), H (A)→L+4 (A) (11%), H-4 (A)→L+2 (A) (6%)
T1 (A)	2.54532	0	0.4324	H (A)→L (A) (70%), H-1 (E)→L+1 (E) (19%)
T2 (E)	2.55887	0	0.3962	H (A)→L+1 (E) (63%), H-1 (E)→L (A) (14%), H-1 (E)→L+1 (E) (11%)
T2’ (E)	2.55974	0	0.3960	H (A)→L+1 (E) (63%), H-1 (E)→L (A) (14%), H-1 (E)→L+1 (E) (12%)
T3 (A)	2.75023	0	0.3669	H-1 (E)→L+1 (E) (83%), H (A)→L (A) (9%)
T4 (E)	2.7782	0	0.3909	H-1 (E)→L (A) (44%), H-1 (E)→L+1 (E) (36%), H (A)→L+1 (E) (14%)
T4’ (E)	2.77992	0	0.3898	H-1 (E)→L (A) (43%), H-1 (E)→L+1 (E) (38%), H (A)→L+1 (E) (14%)
T5 (E)	2.89267	0	0.3801	H-1 (E)→L+1 (E) (43%), H-1 (E)→L (A) (31%), H (A)→L+1 (E) (15%)
T5’ (E)	2.89476	0	0.3806	H-1 (E)→L+1 (E) (44%), H-1 (E)→L (A) (30%), H (A)→L+1 (E) (15%)
T6 (A)	2.92127	0	0.3699	H-1 (E)→L+1 (E) (79%), H (A)→L (A) (14%)
T7 (A)	2.97264	0	0.4605	H (A)→L+2 (A) (86%)
T8 (E)	3.07055	0	0.3834	H-1 (E)→L+2 (A) (66%), H (A)→L+3 (E) (14%)
T8’ (E)	3.0712	0	0.3831	H-1 (E)→L+2 (A) (66%), H (A)→L+3 (E) (13%)
T9 (E)	3.17656	0	0.1240	H-2 (E)→L (A) (23%), H-2 (E)→L+1 (E) (14%), H-3 (A)→L+1 (E) (12%), H-1 (E)→L+2 (A) (8%), H (A)→L+3 (E) (6%)
T9’ (E)	3.17743	0	0.1230	H-2 (E)→L (A) (23%), H-2 (E)→L+1 (E) (15%), H-3 (A)→L+1 (E) (12%), H-1 (E)→L+2 (A) (8%), H (A)→L+3 (E) (6%)
T10 (A)	3.2182	0	0.0605	H-2 (E)→L+1 (E) (40%), H-3 (A)→L (A) (23%), H-3 (A)→L+2 (A) (5%)
T11 (E)	3.30222	0	0.3729	H (A)→L+3 (E) (53%), H-1 (E)→L+2 (A) (14%), H-2 (E)→L (A) (7%)
T11’ (E)	3.3032	0	0.3712	H (A)→L+3 (E) (53%), H-1 (E)→L+2 (A) (14%), H-2 (E)→L (A) (7%)
T12 (A)	3.31007	0	0.3621	H-1 (E)→L+3 (E) (79%), H (A)→L+2 (A) (6%)
T13 (E)	3.45303	0	0.3983	H-1 (E)→L+3 (E) (70%), H (A)→L+3 (E) (12%), H-1 (E)→L+2 (A) (7%)
T13’ (E)	3.45441	0	0.3975	H-1 (E)→L+3 (E) (70%), H (A)→L+3 (E) (12%), H-1 (E)→L+2 (A) (7%)
T14 (A)	3.50465	0	0.3989	H-1 (E)→L+3 (E) (94%)
T15 (E)	3.74148	0	0.0412	H-2 (E)→L+2 (A) (32%), H-2 (E)→L+3 (E) (11%), H-3 (A)→L+3 (E) (10%)
T15’ (E)	3.7426	0	0.0450	H-2 (E)→L+2 (A) (31%), H-3 (A)→L+3 (E) (10%), H-2 (E)→L+3 (E) (7%)
T16 (A)	3.75169	0	0.0605	H-3 (A)→L+2 (A) (25%), H-2 (E)→L+3 (E) (23%), H-2 (E)→L+1 (E) (16%)
T17 (A)	3.96338	0	0.1513	H-2 (E)→L+1 (E) (19%), H-5 (E)→L+1 (E)

				(11%), H-3 (A)→L (A) (7%), H (A)→L+5 (A) (6%)
T18 (E)	3.97768	0	0.0325	H-2 (E)→L (A) (40%), H-2 (E)→L+1 (E) (35%)
T18’ (E)	3.97982	0	0.0330	H-2 (E)→L (A) (39%), H-2 (E)→L+1 (E) (36%)
T19 (E)	4.01345	0	0.1585	H-5 (E)→L (A) (9%), H (A)→L+6 (E) (8%), H-2 (E)→L (A) (7%), H-1 (E)→L+5 (A) (5%)
T19’ (E)	4.01416	0	0.1585	H-5 (E)→L (A) (9%), H (A)→L+6 (E) (8%), H-2 (E)→L (A) (7%), H-1 (E)→L+5 (A) (5%)
T20 (A)	4.03729	0	0.1363	H-3 (A)→L (A) (27%), H-2 (E)→L+1 (E) (25%), H (A)→L+5 (A) (10%)
T21 (A)	4.05143	0	0.0508	H-2 (E)→L+1 (E) (50%), H-3 (A)→L (A) (19%), H-5 (E)→L+1 (E) (12%)
T22 (E)	4.07292	0	0.1967	H-3 (A)→L+1 (E) (21%), H-5 (E)→L (A) (12%), H (A)→L+6 (E) (11%), H-5 (E)→L+1 (E) (5%), H-1 (E)→L+5 (A) (5%)
T22’ (E)	4.07382	0	0.1961	H-3 (A)→L+1 (E) (21%), H-5 (E)→L (A) (13%), H (A)→L+6 (E) (11%), H-5 (E)→L+1 (E) (10%), H-1 (E)→L+5 (A) (5%)
T23 (E)	4.15599	0	0.0635	H-3 (A)→L+1 (E) (41%), H-5 (E)→L (A) (13%), H-2 (E)→L (A) (6%), H-2 (E)→L+1 (E) (6%)
T23’ (E)	4.15736	0	0.0603	H-3 (A)→L+1 (E) (42%), H-5 (E)→L (A) (13%), H-2 (E)→L+1 (E) (10%), H-2 (E)→L (A) (6%)
T24 (A)	4.16514	0	0.1689	H-5 (E)→L+1 (E) (32%), H-3 (A)→L (A) (13%), H-6 (A)→L (A) (9%), H (A)→L+5 (A) (7%), H-2 (E)→L+1 (E) (5%)
T25 (A)	4.19581	0	0.2084	H-4 (A)→L (A) (67%)
T26 (E)	4.22734	0	0.1685	H-4 (A)→L+1 (E) (54%), H-2 (E)→L+2 (A) (5%)
T26’ (E)	4.22849	0	0.1689	H-4 (A)→L+1 (E) (54%), H-2 (E)→L+2 (A) (5%)
T27 (E)	4.36014	0	0.0487	H-2 (E)→L+2 (A) (34%), H-2 (E)→L+3 (E) (27%), H-3 (A)→L+3 (E) (8%), H-4 (A)→L+1 (E) (6%)
T27’ (E)	4.36204	0	0.0487	H-2 (E)→L+2 (A) (34%), H-2 (E)→L+3 (E) (22%), H-3 (A)→L+3 (E) (8%), H-4 (A)→L+1 (E) (6%)
T28 (A)	4.40342	0	0.0864	H-6 (A)→L (A) (34%), H-2 (E)→L+3 (E) (29%), H-3 (A)→L+2 (A) (14%)
T29 (A)	4.41729	0	0.0723	H-3 (A)→L+2 (A) (32%), H-6 (A)→L (A) (26%), H-2 (E)→L+3 (E) (22%)
T30 (E)	4.44119	0	0.1279	H-6 (A)→L+1 (E) (39%), H-5 (E)→L+1 (E) (15%), H-5 (E)→L (A) (10%), H-4 (A)→L+1 (E) (6%)
T30’ (E)	4.44226	0	0.1280	H-6 (A)→L+1 (E) (39%), H-5 (E)→L+1 (E) (16%), H-5 (E)→L (A) (10%), H-4 (A)→L+1 (E) (6%)
T31 (A)	4.52008	0	0.0783	H-2 (E)→L+3 (E) (51%), H-4 (A)→L+2 (A)

				(9%), H-3 (A)→L+2 (A) (8%)
T32 (E)	4.55666	0	0.0724	H-3 (A)→L+3 (E) (9%), H-8 (E)→L (A) (6%), H-5 (E)→L (A) (6%), H-2 (E)→L+3 (E) (5%)
T33 (A)	4.55723	0	0.1101	H-2 (E)→L+3 (E) (12%), H-8 (E)→L+1 (E) (8%), H (A)→L+5 (A) (7%)
T32’ (E)	4.55861	0	0.0918	H-3 (A)→L+3 (E) (12%), H-2 (E)→L+3 (E) (10%), H-5 (E)→L (A) (8%), H-8 (E)→L (A) (7%)
T34 (A)	4.57536	0	0.1848	H-4 (A)→L+2 (A) (53%), H-2 (E)→L+3 (E) (16%)

Table B12. Symmetries, energies, oscillator strengths, MLCT weights, and largest MO transition components to the lowest 50 excitations of $Ir(ptz)_3$ calculated in the TZP basis with all electrons included explicitly in the one-component scalar relativistic ZORA.

Excitation	Energy (eV)	f	MLCT	Transitions
S1 (A)	3.1068	1.45E-02	0.5348	H (A)→L (A) (98%)
S2 (E)	3.2378	8.04E-03	0.5045	H (A)→L+1 (E) (98%)
S2’ (E)	3.2436	8.11E-03	0.5045	H (A)→L+1 (E) (98%)
S3 (E)	3.3099	4.12E-02	0.4891	H-1 (E)→L (A) (96%)
S3’ (E)	3.3119	4.36E-02	0.4889	H-1 (E)→L (A) (96%)
S4 (A)	3.4234	8.65E-03	0.4597	H-1 (E)→L+1 (E) (98%)
S5 (E)	3.4793	4.23E-02	0.4599	H-1 (E)→L+1 (E) (93%)
S5’ (E)	3.4809	4.49E-02	0.4600	H-1 (E)→L+1 (E) (92%)
S6 (A)	3.5579	1.22E-02	0.4574	H-1 (E)→L+1 (E) (97%)
S7 (A)	4.3646	7.15E-05	0.4835	H (A)→L+2 (A) (89%)
S8 (E)	4.4389	3.83E-03	0.1756	H-2 (E)→L (A) (65%), H (A)→L+3 (E) (25%)
S8’ (E)	4.4422	4.31E-03	0.1979	H-2 (E)→L (A) (60%), H (A)→L+3 (E) (30%)
S9 (E)	4.4942	8.69E-04	0.3182	H (A)→L+3 (E) (55%), H-2 (E)→L (A) (20%)
S9’ (E)	4.4966	8.06E-04	0.2991	H (A)→L+3 (E) (52%), H-2 (E)→L (A) (24%), H-2 (E)→L+1 (E) (5%)
S10 (E)	4.5377	2.48E-02	0.4183	H-1 (E)→L+2 (A) (82%)
S10’ (E)	4.5392	2.45E-02	0.4144	H-1 (E)→L+2 (A) (81%)
S11 (A)	4.5752	1.40E-04	0.1056	H-2 (E)→L+1 (E) (73%), H (A)→L+4 (A) (10%)
S12 (A)	4.5828	1.23E-03	0.4361	H (A)→L+4 (A) (64%), H-1 (E)→L+3 (E) (14%)
S13 (A)	4.5998	1.80E-03	0.0648	H-3 (A)→L (A) (58%), H-2 (E)→L+1 (E) (28%)
S14 (E)	4.6376	2.74E-02	0.1028	H-2 (E)→L+1 (E) (62%), H-3 (A)→L+1 (E) (11%)
S14’ (E)	4.6414	2.72E-02	0.1160	H-2 (E)→L+1 (E) (60%), H-3 (A)→L+1 (E) (11%), H-1 (E)→L+3 (E) (5%)
S15 (A)	4.6504	4.04E-02	0.2890	H-1 (E)→L+3 (E) (51%), H-2 (E)→L+1 (E) (31%), H (A)→L+4 (A) (6%)
S16 (E)	4.7234	2.54E-02	0.3363	H-1 (E)→L+3 (E) (68%), H-3 (A)→L+1 (E) (19%)
S16’ (E)	4.7250	2.77E-02	0.3320	H-1 (E)→L+3 (E) (65%), H-3 (A)→L+1 (E) (20%)
S17 (A)	4.7312	1.19E-01	0.2966	H-1 (E)→L+3 (E) (52%), H-3 (A)→L (A) (16%), H-2 (E)→L+1 (E) (16%)

S18 (E)	4.7545	1.03E-03	0.4589	H-1 (E)→L+4 (A) (56%), H (A)→L+7 (E) (14%), H (A)→L+6 (E) (6%), H-3 (A)→L+1 (E) (5%)
S18’ (E)	4.7572	2.98E-03	0.4554	H-1 (E)→L+4 (A) (66%), H (A)→L+7 (E) (10%)
S19 (E)	4.7741	2.22E-02	0.4806	H (A)→L+6 (E) (33%), H (A)→L+7 (E) (32%), H-1 (E)→L+4 (A) (22%)
S19’ (E)	4.7783	2.24E-02	0.4862	H (A)→L+7 (E) (37%), H (A)→L+6 (E) (35%), H-1 (E)→L+4 (A) (17%)
S20 (A)	4.8251	3.08E-04	0.5289	H (A)→L+5 (A) (85%)
S21 (E)	4.8420	3.12E-02	0.1523	H-3 (A)→L+1 (E) (38%), H-5 (E)→L (A) (29%)
S21’ (E)	4.8432	2.90E-02	0.1490	H-3 (A)→L+1 (E) (39%), H-5 (E)→L (A) (27%)
S22 (A)	4.8491	2.01E-02	0.2248	H-4 (A)→L (A) (70%), H-6 (A)→L (A) (6%)
S23 (A)	4.9086	2.34E-02	0.4171	H-1 (E)→L+7 (E) (33%), H-1 (E)→L+3 (E) (23%), H-1 (E)→L+6 (E) (20%)
S24 (E)	4.9247	1.34E-02	0.4471	H (A)→L+6 (E) (21%), H-1 (E)→L+6 (E) (18%), H-1 (E)→L+5 (A) (17%), H (A)→L+7 (E) (14%), H-5 (E)→L (A) (7%)
S24’ (E)	4.9265	2.31E-02	0.4199	H-1 (E)→L+6 (E) (20%), H (A)→L+6 (E) (18%), H-1 (E)→L+5 (A) (13%), H-5 (E)→L (A) (9%), H (A)→L+7 (E) (7%)
S25 (E)	4.9419	8.28E-02	0.3388	H-5 (E)→L (A) (21%), H (A)→L+7 (E) (19%), H-1 (E)→L+5 (A) (8%), H-4 (A)→L+1 (E) (7%)
S25’ (E)	4.9429	7.57E-02	0.3440	H (A)→L+7 (E) (20%), H-5 (E)→L (A) (18%), H-1 (E)→L+5 (A) (10%), H-4 (A)→L+1 (E) (7%)
S26 (A)	4.9627	1.05E-02	0.2279	H-6 (A)→L (A) (46%), H-1 (E)→L+7 (E) (16%), H-1 (E)→L+6 (E) (10%)
S27 (E)	4.9754	6.12E-02	0.2859	H-4 (A)→L+1 (E) (28%), H-1 (E)→L+7 (E) (19%), H-1 (E)→L+6 (E) (7%), H-6 (A)→L+1 (E) (6%), H-5 (E)→L (A) (5%)
S27’ (E)	4.9785	7.07E-02	0.2860	H-4 (A)→L+1 (E) (31%), H-1 (E)→L+7 (E) (18%), H-5 (E)→L (A) (7%), H-6 (A)→L+1 (E) (5%)
S28 (A)	4.9867	6.47E-02	0.3442	H-1 (E)→L+6 (E) (35%), H-5 (E)→L+1 (E) (15%), H-1 (E)→L+7 (E) (12%), H-6 (A)→L (A) (8%)
S29 (E)	5.0162	2.66E-02	0.2195	H-4 (A)→L+1 (E) (28%), H-5 (E)→L (A) (12%), H-6 (A)→L+1 (E) (6%), H-1 (E)→L+5 (A) (6%)
S29’ (E)	5.0186	2.19E-02	0.2478	H-4 (A)→L+1 (E) (22%), H-1 (E)→L+5 (A) (15%), H-5 (E)→L (A) (11%), H-5 (E)→L+1 (E) (7%), H-6 (A)→L+1 (E) (5%)
S30 (E)	5.0262	1.99E-03	0.4799	H-1 (E)→L+5 (A) (52%), H (A)→L+6 (E) (18%), H (A)→L+7 (E) (9%)
S30’ (E)	5.0285	5.83E-03	0.4210	H-1 (E)→L+5 (A) (41%), H (A)→L+6 (E) (16%), H (A)→L+7 (E) (8%)
S31 (A)	5.0400	4.95E-05	0.1920	H-5 (E)→L+1 (E) (37%), H-6 (A)→L (A) (26%), H-4 (A)→L (A) (13%)
S32 (E)	5.0887	2.85E-02	0.1483	H-5 (E)→L+1 (E) (47%), H-6 (A)→L+1 (E) (9%)
S32’ (E)	5.0891	2.99E-02	0.1519	H-5 (E)→L+1 (E) (48%), H-6 (A)→L+1 (E) (10%)
S33 (A)	5.1025	2.87E-03	0.2767	H-5 (E)→L+1 (E) (52%), H-1 (E)→L+6 (E) (17%), H-1 (E)→L+7 (E) (12%)
T1 (A)	2.8386	0	0.4767	H (A)→L (A) (69%), H-1 (E)→L+1 (E) (21%)
T2 (E)	2.8882	0	0.4459	H (A)→L+1 (E) (48%), H-1 (E)→L (A) (26%), H-1 (E)→L+1 (E) (5%)

T2’ (E)	2.8908	0	0.4451	H (A)→L+1 (E) (48%), H-1 (E)→L (A) (25%), H-1 (E)→L+1 (E) (5%)
T3 (E)	3.1681	0	0.4395	H-1 (E)→L (A) (53%), H (A)→L+1 (E) (17%), H-1 (E)→L+1 (E) (16%)
T3’ (E)	3.1732	0	0.4392	H-1 (E)→L (A) (53%), H (A)→L+1 (E) (18%), H-1 (E)→L+1 (E) (17%)
T4 (A)	3.2055	0	0.4508	H-1 (E)→L+1 (E) (80%), H (A)→L (A) (13%)
T5 (E)	3.3004	0	0.4394	H-1 (E)→L+1 (E) (52%), H (A)→L+1 (E) (22%), H-1 (E)→L (A) (12%)
T5’ (E)	3.3061	0	0.4402	H-1 (E)→L+1 (E) (52%), H (A)→L+1 (E) (22%), H-1 (E)→L (A) (12%)
T6 (A)	3.3151	0	0.3879	H-1 (E)→L+1 (E) (62%), H (A)→L (A) (12%), H-3 (A)→L (A) (6%), H-2 (E)→L+1 (E) (6%)
T7 (E)	3.5147	0	0.1617	H-2 (E)→L (A) (20%), H-3 (A)→L+1 (E) (14%), H-2 (E)→L+1 (E) (13%), H-1 (E)→L+1 (E) (6%), H (A)→L+1 (E) (5%)
T7’ (E)	3.5179	0	0.1591	H-2 (E)→L (A) (19%), H-2 (E)→L+1 (E) (16%), H-3 (A)→L+1 (E) (14%), H (A)→L+1 (E) (6%)
T8 (A)	3.5217	0	0.1896	H-2 (E)→L+1 (E) (28%), H-1 (E)→L+1 (E) (21%), H-3 (A)→L (A) (17%)
T9 (A)	3.8943	0	0.3724	H (A)→L+2 (A) (39%), H-1 (E)→L+3 (E) (25%), H-2 (E)→L+1 (E) (10%), H-3 (A)→L (A) (5%)
T10 (E)	3.9076	0	0.3521	H-1 (E)→L+2 (A) (25%), H (A)→L+3 (E) (24%), H-1 (E)→L+3 (E) (16%), H-2 (E)→L (A) (6%)
T10’ (E)	3.9079	0	0.3545	H (A)→L+3 (E) (24%), H-1 (E)→L+2 (A) (24%), H-1 (E)→L+3 (E) (15%), H-2 (E)→L (A) (6%)
T11 (A)	4.2812	0	0.2356	H (A)→L+2 (A) (18%), H-5 (E)→L+1 (E) (17%), H-4 (A)→L (A) (12%), H-2 (E)→L+1 (E) (5%)
T12 (E)	4.3061	0	0.1406	H-5 (E)→L (A) (28%), H-5 (E)→L+1 (E) (14%), H-2 (E)→L (A) (10%), H-4 (A)→L+1 (E) (10%), H-2 (E)→L+1 (E) (5%)
T12’ (E)	4.3104	0	0.1415	H-5 (E)→L (A) (27%), H-5 (E)→L+1 (E) (16%), H-2 (E)→L (A) (9%), H-4 (A)→L+1 (E) (9%)
T13 (A)	4.3402	0	0.3440	H (A)→L+4 (A) (50%)
T14 (E)	4.3844	0	0.3375	H (A)→L+3 (E) (23%), H (A)→L+7 (E) (17%), H-1 (E)→L+4 (A) (8%)
T14’ (E)	4.3868	0	0.3377	H (A)→L+3 (E) (22%), H (A)→L+7 (E) (17%), H-1 (E)→L+4 (A) (6%), H-2 (E)→L (A) (5%), H-1 (E)→L+2 (A) (5%)
T15 (E)	4.4500	0	0.3243	H (A)→L+3 (E) (15%), H (A)→L+2 (A) (12%), H-1 (E)→L+2 (A) (11%), H-1 (E)→L+3 (E) (9%)
T15’ (E)	4.4529	0	0.3333	H (A)→L+3 (E) (24%), H-1 (E)→L+2 (A) (22%), H-1 (E)→L+4 (A) (6%)
T16 (A)	4.4533	0	0.3275	H (A)→L+2 (A) (16%), H (A)→L+3 (E) (10%), H-1 (E)→L+3 (E) (9%), H-2 (E)→L+1 (E) (5%), H-1 (E)→L+2 (A) (5%)
T17 (E)	4.4954	0	0.1583	H-2 (E)→L (A) (26%), H-2 (E)→L+1 (E) (25%), H-5 (E)→L (A) (6%), H-1 (E)→L+3 (E) (5%)
T17’ (E)	4.5016	0	0.1645	H-2 (E)→L+1 (E) (26%), H-2 (E)→L (A) (24%), H-5 (E)→L (A) (5%), H-1 (E)→L+3 (E) (5%)
T18 (A)	4.5473	0	0.1714	H-2 (E)→L+1 (E) (46%), H-1 (E)→L+3 (E) (19%), H-3

				(A)→L (A) (7%)
T19 (E)	4.5584	0	0.3121	H-1 (E)→L+3 (E) (30%), H-1 (E)→L+2 (A) (17%), H-2 (E)→L+1 (E) (8%), H-2 (E)→L (A) (5%)
T19’ (E)	4.5621	0	0.3076	H-1 (E)→L+3 (E) (26%), H-1 (E)→L+2 (A) (17%), H-2 (E)→L+1 (E) (13%), H-2 (E)→L (A) (6%), H-1 (E)→L+4 (A) (6%)
T20 (A)	4.5896	0	0.2615	H-1 (E)→L+3 (E) (42%), H-3 (A)→L (A) (18%), H-2 (E)→L+1 (E) (11%)
T21 (A)	4.6592	0	0.1352	H-2 (E)→L+1 (E) (29%), H-3 (A)→L (A) (24%), H-4 (A)→L (A) (13%), H-1 (E)→L+3 (E) (5%)
T22 (E)	4.6954	0	0.3203	H-1 (E)→L+4 (A) (36%), H-3 (A)→L+1 (E) (17%), H (A)→L+7 (E) (9%), H (A)→L+6 (E) (7%)
T22’ (E)	4.6971	0	0.3210	H-1 (E)→L+4 (A) (35%), H-3 (A)→L+1 (E) (18%), H (A)→L+7 (E) (10%), H (A)→L+6 (E) (7%)
T23 (A)	4.7102	0	0.2675	H (A)→L+4 (A) (20%), H-1 (E)→L+7 (E) (15%), H-4 (A)→L (A) (14%)
T24 (A)	4.7196	0	0.1961	H-4 (A)→L (A) (27%), H-6 (A)→L (A) (22%), H-5 (E)→L+1 (E) (17%)
T25 (E)	4.7317	0	0.1964	H-3 (A)→L+1 (E) (35%), H-1 (E)→L+4 (A) (10%), H (A)→L+7 (E) (9%), H-5 (E)→L (A) (6%), H (A)→L+6 (E) (5%), H-4 (A)→L+1 (E) (5%)
T25’ (E)	4.7368	0	0.1570	H-3 (A)→L+1 (E) (41%), H (A)→L+7 (E) (7%), H-1 (E)→L+4 (A) (7%), H-5 (E)→L (A) (6%)
T26 (E)	4.7711	0	0.1844	H-4 (A)→L+1 (E) (22%), H (A)→L+6 (E) (8%), H-5 (E)→L+1 (E) (5%)
T26’ (E)	4.7734	0	0.1975	H-4 (A)→L+1 (E) (26%), H (A)→L+6 (E) (8%)
T27 (A)	4.8193	0	0.5338	H (A)→L+5 (A) (87%)
T28 (E)	4.8293	0	0.3049	H-4 (A)→L+1 (E) (15%), H (A)→L+6 (E) (14%), H-1 (E)→L+7 (E) (13%), H-1 (E)→L+4 (A) (8%)
T28’ (E)	4.8324	0	0.3089	H-1 (E)→L+7 (E) (14%), H (A)→L+6 (E) (13%), H-4 (A)→L+1 (E) (10%), H-1 (E)→L+4 (A) (8%), H-1 (E)→L+6 (E) (5%)
T29 (A)	4.8567	0	0.3258	H-1 (E)→L+7 (E) (31%), H-1 (E)→L+6 (E) (19%)
T30 (E)	4.8859	0	0.3206	H-1 (E)→L+7 (E) (14%), H (A)→L+6 (E) (8%), H (A)→L+7 (E) (8%), H-4 (A)→L+1 (E) (6%), H-1 (E)→L+6 (E) (5%)
T30’ (E)	4.8887	0	0.3221	H-1 (E)→L+7 (E) (14%), H (A)→L+7 (E) (8%), H (A)→L+6 (E) (7%), H-4 (A)→L+1 (E) (6%), H-1 (E)→L+6 (E) (5%)
T31 (A)	4.9028	0	0.1944	H-6 (A)→L (A) (28%), H-5 (E)→L+1 (E) (14%), H-1 (E)→L+6 (E) (6%)
T32 (E)	4.9197	0	0.3641	H-1 (E)→L+5 (A) (19%), H (A)→L+7 (E) (16%), H (A)→L+6 (E) (15%), H-1 (E)→L+6 (E) (13%)
T32’ (E)	4.9215	0	0.3703	H-1 (E)→L+5 (A) (18%), H (A)→L+7 (E) (17%), H-1 (E)→L+6 (E) (14%), H (A)→L+6 (E) (14%)
T33 (A)	4.9295	0	0.2045	H-1 (E)→L+6 (E) (16%), H-6 (A)→L (A) (16%), H-5 (E)→L+1 (E) (7%)
T34 (E)	4.9524	0	0.1353	H-6 (A)→L+1 (E) (29%), H-5 (E)→L+1 (E) (15%), H-5 (E)→L (A) (13%), H-7 (E)→L (A) (9%)

Mulliken population analysis and MLCT character

To estimate the 'MLCT' character of individual transitions, the molecule was divided into three fragments comprising the iridium, phenyl and triazloyl functional groups. A Mulliken population analysis[12] was performed according to these divisions for each molecular orbital. Since the orbital contributions to specific excitations need to be considered, a population analysis per basis function (i.e. Mulliken) is more convenient than approaches that use electron density (e.g. Hirshfeld or Voronoi methods).

Each molecular orbital was characterised according to its ligand character. For each singlet and triplet excitation the ligand character difference of each orbital transition (excited – ground) was taken and weighted by the contribution of that orbital transition to the excitation. The sum of the weighted differences per excitation was then obtained. This number describes the 'MLCT' character of that excitation. In this scheme, a purely metal orbital would have 0 ligand population, while a purely ligand orbital would have a population of +1. Thus, a transition between these two orbitals would describe a pure MLCT transition, with a character of +1. Using this nomenclature a difference of -1 would describe a LMCT transition.

Scalar relativistic Kohn-Sham orbital energies

Table B12. Molecular orbital symmetries, energies, ligand contributions from a Mulliken population analysis for $Ir(ppy)_3$ and $Ir(ptz)_3$ calculated in the TZP basis with all electrons included explicitly in the one-component scalar relativistic ZORA.

	$Ir(ppy)_3$		$Ir(ptz)_3$	
Orbital	Energy (eV)	Ligand contribution	Energy (eV)	Ligand contribution
HOMO-9 (A)	-7.763	1.00	-7.845	1.00
HOMO-8 (E)	-7.633	1.00	-7.762	1.00
HOMO-8 (E')	-7.630	1.00	-7.754	1.00
HOMO-7 (E)	-7.134	0.78	-7.283	0.80
HOMO-7 (E')	-7.132	0.78	-7.279	0.79
HOMO-6 (A)	-6.679	0.88	-6.877	0.91
HOMO-5 (E)	-6.558	0.71	-6.626	0.80
HOMO-5 (E')	-6.557	0.71	-6.624	0.80
HOMO-4 (A)	-6.486	0.74	-6.611	0.76
HOMO-3 (A)	-6.009	0.97	-6.230	0.96
HOMO-2 (E)	-5.893	0.97	-6.056	0.95
HOMO-2 (E')	-5.892	0.97	-6.052	0.95
HOMO-1 (E)	-5.040	0.58	-5.100	0.51

HOMO-1 (E’)	-5.039	0.58	-5.098	0.50
HOMO (A)	-4.903	0.50	-4.932	0.46
LUMO (A)	-1.404	1.00	-1.098	1.00
LUMO+1 (E)	-1.310	0.95	-0.926	0.97
LUMO+1 (E’)	-1.308	0.95	-0.920	0.97
LUMO+2 (A)	-1.136	0.99	0.193	0.99
LUMO+3 (E)	-0.860	0.99	0.349	0.95
LUMO+3 (E’)	-0.858	0.99	0.350	0.96
LUMO+4 (A)	0.379	0.97	0.360	0.99
LUMO+5 (A)	0.508	0.99	0.422	1.01
LUMO+6 (E)	0.654	0.97	0.492	1.00
LUMO+6 (E’)	0.655	0.97	0.496	1.00
LUMO+7 (E)	0.701	1.00	0.590	0.99
LUMO+7 (E’)	0.702	1.00	0.595	0.99

Appendix C

Supplement to Chapter 4

Geometry Optimised Structure Comparison

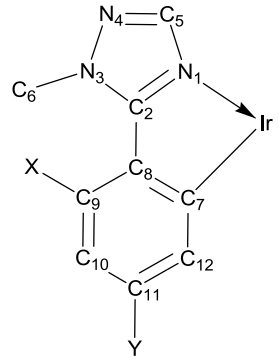

Ir(ptz)$_3$

1 X=H, Y=H
2 X=H, Y=F
3 X=F, Y=H
4 X=F, Y=F

	1		2		3		4
Parameter	**DFT**	**XRD**	**DFT**	**XRD**	**DFT**	**XRD**	**DFT**
Ir-N_1	2.151	2.166, 2.151, 2.135	2.150	2.148, 2.149, 2.148	2.133	2.135, 2.130, 2.155	2.133
Ir-C_7	2.046	2.042, 2.022, 2.002	2.044	2.007, 2.006, 2.005	2.045	2.023, 2.016, 2.023	2.043
N_1-C_2	1.361	1.345, 1.338, 1.357	1.361	1.363, 1.363, 1.363	1.364	1.344, 1.342, 1.348	1.364
C_2-N_3	1.364	1.328, 1.346, 1.335	1.363	1.343, 1.343, 1.343	1.367	1.341, 1.343, 1.351	1.366
N_3-N_4	1.402	1.383, 1.373, 1.383	1.402	1.384, 1.384, 1.384	1.400	1.374, 1.376, 1.365	1.400
N_4-C_5	1.335	1.317, 1.334, 1.314	1.335	1.329, 1.329, 1.329	1.333	1.313, 1.317, 1.319	1.332
C_5-N_1	1.369	1.377, 1.367, 1.370	1.370	1.348, 1.348, 1.348	1.367	1.363, 1.364, 1.357	1.367
N_3-C_6	1.456	1.463, 1.452, 1.457	1.456	1.452, 1.452, 1.452	1.464	1.465, 1.472, 1.480	1.465
C_2-C_8	1.448	1.455, 1.459, 1.455	1.447	1.447, 1.447, 1.447	1.455	1.463, 1.467, 1.452	1.454
C_7-C_8	1.439	1.420, 1.422, 1.432	1.440	1.422, 1.422, 1.422	1.444	1.427, 1.430, 1.422	1.445
C_8-C_9	1.409	1.412, 1.398, 1.394	1.408	1.400, 1.400, 1.400	1.401	1.388, 1.388, 1.397	1.400
C_9-C_{10}	1.393	1.381, 1.390, 1.405	1.393	1.375, 1.375, 1.375	1.383	1.356, 1.374, 1.352	1.384
C_{10}-C_{11}	1.404	1.392, 1.383, 1.371	1.395	1.380, 1.380, 1.380	1.402	1.387, 1.377, 1.381	1.393
C_{11}-C_{12}	1.399	1.397, 1.395, 1.400	1.390	1.381, 1.381, 1.381	1.398	1.373, 1.394, 1.390	1.389
C_{12}-C_7	1.413	1.397, 1.414, 1.402	1.410	1.404, 1.404, 1.404	1.413	1.401, 1.403, 1.405	1.410
C_9-X	1.085	-	1.084	-	1.407	1.372, 1.369, 1.365	1.402
C_{11}-Y	1.087	-	1.394	1.365, 1.365, 1.365	1.086	-	1.390
N_1-Ir-C_7	78.84	78.52, 78.58, 79.54	78.96	79.64, 79.62, 79.68	78.62	78.63, 78.79, 78.90	78.71
N_1-C_2-C_8-C_7	-1.37	-0.64, 0.26, -1.97	-1.29	-4.82, -4.82, -4.82	-1.75	-5.48, -4.24, -6.41	-2.97

Geometry Optimised Structures

Coordinates, in Å, of the optimised geometries as calculated by GAMESS with a mixed LANL2DZ/6-31G basis set using the B3LYP hybrid functional.

Complex 1

Atom	x (Å)	y (Å)	z (Å)
Ir	0.000000000	0.000000000	0.012999633
N	-1.770209685	0.500451732	1.128722922
N	0.451700929	-1.783272423	1.128722922
N	1.318508756	1.282820691	1.128722922
C	-2.170144347	1.235038888	2.212995842
C	0.015497122	-2.496919578	2.212995842
C	2.154647225	1.261880690	2.212995842
N	-3.488770329	1.190783019	2.417800708
N	0.713136819	-3.616755242	2.417800708
N	2.775633509	2.425972223	2.417800708
N	-3.945340993	0.367580989	1.379115489
N	1.654336022	-3.600556021	1.379115489
N	2.291004971	3.232975032	1.379115489
C	-2.901588729	-0.044443416	0.604043746
C	1.489283492	-2.490627842	0.604043746
C	1.412305237	2.535071258	0.604043746
C	0.629737473	2.853210414	-0.572182841
C	-2.785821437	-0.881236558	-0.572182841
C	2.156083964	-1.971973856	-0.572182841
C	0.605879817	4.112311686	-1.205211381
C	-3.864306297	-1.531448530	-1.205211381
C	3.258426480	-2.580863156	-1.205211381
C	-0.182418397	4.305534414	-2.337688610
C	-3.637492981	-2.310746174	-2.337688610
C	3.819911379	-1.994788241	-2.337688610
C	-0.944761954	3.236568171	-2.834133282
C	-2.330569280	-2.436471938	-2.834133282
C	3.275331234	-0.800096233	-2.834133282
C	-0.924353516	1.987014972	-2.205068530
C	-1.258628685	-1.794021113	-2.205068530
C	2.182982202	-0.192993859	-2.205068530
C	-0.144462410	1.740039154	-1.053442369
C	-1.434686906	-0.995127694	-1.053442369
C	1.579149316	-0.744911460	-1.053442369
C	-5.372924205	0.104141948	1.270546792
C	2.596272530	-4.705159828	1.270546792
C	2.776651675	4.601017880	1.270546792

H	1.193618076	4.939925664	-0.821827699
H	-4.874910156	-1.436259256	-0.821827699
H	3.681292080	-3.503666409	-0.821827699
H	-0.205189173	5.273465222	-2.828574694
H	-4.464360262	-2.814431648	-2.828574694
H	4.669549435	-2.459033575	-2.828574694
H	-1.558722296	3.381498721	-3.719702336
H	-2.149102647	-3.040642467	-3.719702336
H	3.707824943	-0.340856255	-3.719702336
H	-1.522010736	1.181746940	-2.618595203
H	-0.262417503	-1.908973432	-2.618595203
H	1.784428239	0.727226492	-2.618595203
H	-5.856684371	0.662554661	2.071334791
H	2.354553018	-5.403314777	2.071334791
H	3.502131353	4.740760117	2.071334791
H	-5.584110283	-0.962650743	1.390797439
H	3.625735140	-4.354655991	1.390797439
H	1.958375143	5.317306734	1.390797439
H	-5.756188433	0.444972412	0.304528391
H	2.492736804	-5.207491618	0.304528391
H	3.263451629	4.762519206	0.304528391
H	-1.500379133	1.796288274	2.839677927
H	-0.805441711	-2.197510581	2.839677927
H	2.305820844	0.401222308	2.839677927

Complex 2

Atom	**x (Å)**	**y (Å)**	**z (Å)**
Ir	0.000000000	0.000000000	0.000705801
N	1.317815105	1.278106646	1.120005414
N	-1.765780376	0.502208036	1.120005414
N	0.447965271	-1.780314681	1.120005414
N	2.770184499	2.421055118	2.414060419
N	-3.481787485	1.188522591	2.414060419
N	0.711602986	-3.609577708	2.414060419
N	2.286246670	3.229687837	1.376461080
N	-3.940115048	0.365103777	1.376461080
N	1.653868378	-3.594791614	1.376461080
C	2.152825728	1.256147056	2.205773658
C	-2.164268126	1.236328242	2.205773658
C	0.011442398	-2.492475299	2.205773658
C	1.487317916	-2.487497559	0.599231887
C	1.410577120	2.531803878	0.599231887
C	-2.897895036	-0.044306319	0.599231887
C	2.154386193	-1.971326059	-0.576604023
C	0.630025349	2.851416202	-0.576604023

C	-2.784411543	-0.880090144	-0.576604023
C	3.257868457	-2.579635512	-1.205743426
C	0.605095657	4.111214602	-1.205743426
C	-3.862964114	-1.531579090	-1.205743426
C	3.828448027	-2.000027260	-2.336616566
C	-0.182149599	4.315546879	-2.336616566
C	-3.646298429	-2.315519619	-2.336616566
C	3.266529363	-0.814192421	-2.809252164
C	-0.928153361	3.235993621	-2.809252164
C	-2.338376002	-2.421801200	-2.809252164
C	2.177697293	-0.189102910	-2.212457734
C	-0.925080722	1.980492633	-2.212457734
C	-1.252616571	-1.791389722	-2.212457734
C	1.578000780	-0.744359700	-1.063335106
C	-0.144365980	1.738768613	-1.063335106
C	-1.433634800	-0.994408913	-1.063335106
C	2.765904924	4.600874086	1.272714366
C	-5.367426300	0.094906885	1.272714366
C	2.601521376	-4.695780971	1.272714366
H	4.677031276	-2.444754154	-2.840785183
H	-0.221296435	5.272804976	-2.840785183
H	-4.455734841	-2.828050822	-2.840785183
H	1.798479330	0.726216557	-2.650099201
H	-1.528161652	1.194420510	-2.650099201
H	-0.270317678	-1.920637066	-2.650099201
H	3.492637226	4.740832068	2.072109901
H	-5.851999619	0.654296530	2.072109901
H	2.359362393	-5.395128598	2.072109901
H	3.628163588	-4.339529687	1.400453188
H	1.944061155	5.311846680	1.400453188
H	-5.572224743	-0.972316993	1.400453188
H	3.249652117	4.768442579	0.306212744
H	-5.754418469	0.430059997	0.306212744
H	2.504766352	-5.198502577	0.306212744
H	2.304812666	0.395057887	2.831675600
H	-1.494536499	1.798497376	2.831675600
H	-0.810276166	-2.193555263	2.831675600
H	3.679363330	-3.502863490	-0.824981563
H	1.193887103	4.937853858	-0.824981563
H	-4.873250433	-1.434990369	-0.824981563
F	3.832274923	-0.228901640	-3.941320669
F	-1.717902826	3.433298258	-3.941320669
F	-2.114372097	-3.204396618	-3.941320669

Complex 3

Atom	x (Å)	y (Å)	z (Å)
Ir	0.000000000	0.000000000	-0.046189897
N	1.302822196	1.272072481	1.064605584
N	-1.753058182	0.492240878	1.064605584
N	0.450235986	-1.764313359	1.064605584
N	2.761274422	2.342980542	2.398208820
N	-3.409717881	1.219843525	2.398208820
N	0.648443459	-3.562824067	2.398208820
N	2.292861670	3.201450781	1.396116336
N	-3.918968541	0.384951063	1.396116336
N	1.626106870	-3.586401844	1.396116336
C	2.132803197	1.194970592	2.147660475
C	-2.101276488	1.249576454	2.147660475
C	-0.031526709	-2.444547046	2.147660475
C	1.501954455	-2.490648885	0.587901541
C	1.405987979	2.546055156	0.587901541
C	-2.907942434	-0.055406271	0.587901541
C	2.176953409	-1.960370522	-0.586820370
C	0.609253969	2.865482216	-0.586820370
C	-2.786207378	-0.905111694	-0.586820370
C	3.296346413	-2.499086342	-1.233788273
C	0.516099052	4.104262904	-1.233788273
C	-3.812445465	-1.605176562	-1.233788273
C	3.870471563	-1.935322067	-2.358745113
C	-0.259197707	4.319587731	-2.358745113
C	-3.611273856	-2.384265664	-2.358745113
C	3.296495896	-0.762553631	-2.868846040
C	-0.987857132	3.236126005	-2.868846040
C	-2.308638764	-2.473572374	-2.868846040
C	2.185154589	-0.183964848	-2.248800878
C	-0.933259063	1.984381809	-2.248800878
C	-1.251895526	-1.800416961	-2.248800878
C	1.589694181	-0.743566145	-1.096451646
C	-0.150899920	1.748498617	-1.096451646
C	-1.438794261	-1.004932473	-1.096451646
C	2.536855892	-4.733188157	1.389945081
C	2.830633239	4.563575726	1.389945081
C	-5.367489131	0.169612431	1.389945081
H	4.736418530	-2.401677391	-2.811581771
H	-0.288295633	5.302697466	-2.811581771
H	-4.448122898	-2.901020075	-2.811581771
H	1.765083451	0.722999651	-2.667867076
H	-1.508677790	1.167107283	-2.667867076
H	-0.256405661	-1.890106934	-2.667867076

H	3.547869492	4.602550858	2.208130821
H	-5.759860711	0.771269681	2.208130821
H	2.211991219	-5.373820538	2.208130821
H	3.566342638	-4.411108671	1.546870441
H	2.036960849	5.294097659	1.546870441
H	-5.603303487	-0.882988988	1.546870441
H	3.325898907	4.775957550	0.442649923
H	-5.799050019	0.492334168	0.442649923
H	2.473151113	-5.268291719	0.442649923
H	2.272835678	0.307369860	2.738036051
H	-1.402607946	1.814648506	2.738036051
H	-0.870227732	-2.122018366	2.738036051
F	3.896662367	-3.670252179	-0.737558890
F	1.230200442	5.209734689	-0.737558890
F	-5.126862809	-1.539482510	-0.737558890
H	3.726781099	-0.301915725	-3.753365143
H	-1.601923862	3.378444969	-3.753365143
H	-2.124857237	-3.076529244	-3.753365143

Complex 4

Atom	**x (Å)**	**y (Å)**	**z (Å)**
Ir	0.000000000	0.000000000	-0.031014508
N	1.301512200	1.277693767	1.074095079
N	-1.757271361	0.488295745	1.074095079
N	0.455759160	-1.765989512	1.074095079
N	2.800692708	2.343646889	2.365534028
N	-3.430004097	1.253647589	2.365534028
N	0.629311389	-3.597294478	2.365534028
N	2.321571798	3.198422242	1.365465352
N	-3.930700813	0.411329032	1.365465352
N	1.609129015	-3.609751275	1.365465352
C	2.154126292	1.200793893	2.140194724
C	-2.116981162	1.265131146	2.140194724
C	-0.037145130	-2.465925038	2.140194724
C	1.501628836	-2.492853595	0.585733771
C	1.408060124	2.546875516	0.585733771
C	-2.909688959	-0.054021921	0.585733771
C	2.184886405	-1.946785248	-0.575604280
C	0.593522278	2.865559755	-0.575604280
C	-2.778408683	-0.918774507	-0.575604280
C	3.318491789	-2.466863074	-1.211197148
C	0.477120195	4.107329729	-1.211197148
C	-3.795611985	-1.640466654	-1.211197148
C	3.903406271	-1.891313120	-2.325484165
C	-0.313777927	4.326105552	-2.325484165

C	-3.589628344	-2.434792432	-2.325484165
C	3.304700482	-0.729375419	-2.808091742
C	-1.020692600	3.226642279	-2.808091742
C	-2.284007883	-2.497266860	-2.808091742
C	2.188055641	-0.148041036	-2.220145703
C	-0.965820522	1.968932288	-2.220145703
C	-1.222235119	-1.820891251	-2.220145703
C	1.594594945	-0.728251921	-1.080530345
C	-0.166612809	1.745085692	-1.080530345
C	-1.427982137	-1.016833771	-1.080530345
C	2.882578604	4.551218722	1.325339567
C	-5.382760333	0.220776939	1.325339567
C	2.500181729	-4.771995660	1.325339567
H	4.779314136	-2.324389072	-2.787042593
H	-0.376677083	5.301201990	-2.787042593
H	-4.402637053	-2.976812918	-2.787042593
H	1.782689537	0.756469179	-2.655006981
H	-1.546466295	1.165619837	-2.655006981
H	-0.236223243	-1.922089016	-2.655006981
H	3.664219354	4.572516150	2.083033656
H	-5.792024822	0.887048970	2.083033656
H	2.127805468	-5.459565120	2.083033656
H	3.526780543	-4.482882506	1.551542221
H	2.118899861	5.295722797	1.551542221
H	-5.645680404	-0.812840291	1.551542221
H	3.304205596	4.761209419	0.342876288
H	-5.775431108	0.480921276	0.342876288
H	2.471225511	-5.242130695	0.342876288
H	2.297393396	0.317120255	2.735665530
H	-1.423330895	1.831040916	2.735665530
H	-0.874062501	-2.148161171	2.735665530
F	3.930547783	-3.626718651	-0.716357721
F	1.175556593	5.217313556	-0.716357721
F	-5.106104376	-1.590594905	-0.716357721
F	3.865488228	-0.127455208	-3.928510555
F	-1.822364666	3.411338607	-3.928510555
F	-2.043123562	-3.283883400	-3.928510555

One-Component (Scalar Relativistic) Excitations

Singlet (S1 (A), S2 (E) etc) and triplet (T1 (A), T2 (E) etc) TDDFT excitation. C_3 symmetry irrep labels A and E are given for all excitations and states. The abbreviations H(A), H-1(E), L+1(E) etc indicate the HOMO(A), HOMO-1(E) and LUMO+1(E) frontier molecular orbitals. The energy and oscillator strength (f) of each excitation are given.

Complex 1

Label	Energy (eV)	f (a.u.)	Orbital Transitions
T1 (A)	2.83228	0	H (A)→L (A) (72%), H-1 (E)→L+1 (E) (19%)
T2 (E)	2.88831	0	H (A)→L+1 (E) (50%), H-1 (E)→L (A) (26%)
T2 (E)	2.89	0	H (A)→L+1 (E) (49%), H-1 (E)→L (A) (26%)
S1 (A)	3.08512	1.39E-02	H (A)→L (A) (99%)
T3 (E)	3.15866	0	H-1 (E)→L (A) (54%), H (A)→L+1 (E) (19%), H-1 (E)→L+1 (E) (16%)
T3 (E)	3.1618	0	H-1 (E)→L (A) (54%), H (A)→L+1 (E) (20%), H-1 (E)→L+1 (E) (16%)
T4 (A)	3.19578	0	H-1 (E)→L+1 (E) (81%), H (A)→L (A) (13%)
S2 (E)	3.22206	7.71E-03	H (A)→L+1 (E) (98%)
S2 (E)	3.22626	7.65E-03	H (A)→L+1 (E) (98%)
T5 (E)	3.29295	0	H-1 (E)→L+1 (E) (55%), H (A)→L+1 (E) (21%), H-1 (E)→L (A) (8%)
T5 (E)	3.29627	0	H-1 (E)→L+1 (E) (55%), H (A)→L+1 (E) (20%), H-1 (E)→L (A) (8%)
S3 (E)	3.29822	4.26E-02	H-1 (E)→L (A) (94%)
S3 (E)	3.30167	4.36E-02	H-1 (E)→L (A) (94%)
T6 (A)	3.3108	0	H-1 (E)→L+1 (E) (63%), H (A)→L (A) (11%), H-3 (A)→L (A) (6%), H-2 (E)→L+1 (E) (5%)
S4 (A)	3.41512	8.50E-03	H-1 (E)→L+1 (E) (97%)
S5 (E)	3.47528	4.40E-02	H-1 (E)→L+1 (E) (95%)
S5 (E)	3.4763	4.60E-02	H-1 (E)→L+1 (E) (96%)
T7 (E)	3.52691	0	H-2 (E)→L (A) (20%), H-3 (A)→L+1 (E) (14%), H-2 (E)→L+1 (E) (9%)
T7 (E)	3.52873	0	H-2 (E)→L (A) (18%), H-2 (E)→L+1 (E) (17%), H-3 (A)→L+1 (E) (13%), H-1 (E)→L+1 (E) (6%)
T8 (A)	3.53258	0	H-2 (E)→L+1 (E) (30%), H-1 (E)→L+1 (E) (20%), H-3 (A)→L (A) (18%)
S6 (A)	3.55398	1.19E-02	H-1 (E)→L+1 (E) (98%)
T9 (A)	3.89937	0	H (A)→L+2 (A) (41%), H-1 (E)→L+3 (E) (29%), H-2 (E)→L+1 (E) (10%), H-3 (A)→L (A) (5%)
T10 (E)	3.91765	0	H (A)→L+3 (E) (26%), H-1 (E)→L+2 (A) (24%), H-1 (E)→L+3 (E) (15%), H-2 (E)→L (A) (7%)
T10 (E)	3.91826	0	H (A)→L+3 (E) (26%), H-1 (E)→L+2 (A) (23%), H-1 (E)→L+3 (E) (16%), H-2 (E)→L (A) (6%)
T11 (A)	4.29399	0	H (A)→L+2 (A) (22%), H-5 (E)→L+1 (E) (22%), H-4 (A)→L

			(A) (11%), H (A)→L+4 (A) (6%), H-2 (E)→L+1 (E) (5%)
T12 (E)	4.32686	0	H-5 (E)→L (A) (28%), H-5 (E)→L+1 (E) (12%), H-2 (E)→L+1 (E) (11%), H-2 (E)→L (A) (9%), H-4 (A)→L+1 (E) (9%)
T12 (E)	4.32935	0	H-5 (E)→L (A) (27%), H-5 (E)→L+1 (E) (13%), H-2 (E)→L+1 (E) (10%), H-4 (A)→L+1 (E) (9%), H-2 (E)→L (A) (8%)
S7 (A)	4.34828	3.51E-04	H (A)→L+2 (A) (90%)
T13 (A)	4.35125	0	H (A)→L+4 (A) (54%)
T14 (E)	4.39918	0	H (A)→L+3 (E) (25%), H (A)→L+6 (E) (11%), H (A)→L+7 (E) (11%), H-1 (E)→L+4 (A) (7%), H-1 (E)→L+2 (A) (7%)
T14 (E)	4.40102	0	H (A)→L+3 (E) (25%), H (A)→L+7 (E) (11%), H (A)→L+6 (E) (10%), H-1 (E)→L+2 (A) (7%), H-1 (E)→L+4 (A) (6%)
S8 (E)	4.44868	4.54E-03	H-2 (E)→L (A) (54%), H (A)→L+3 (E) (39%)
S8 (E)	4.45003	4.75E-03	H-2 (E)→L (A) (51%), H (A)→L+3 (E) (42%)
T15 (A)	4.45301	0	H-1 (E)→L+3 (E) (31%), H (A)→L+2 (A) (25%), H-4 (A)→L (A) (9%)
T16 (E)	4.45827	0	H (A)→L+3 (E) (26%), H-1 (E)→L+2 (A) (26%), H (A)→L+6 (E) (6%), H-1 (E)→L+4 (A) (5%)
T16 (E)	4.45891	0	H (A)→L+3 (E) (25%), H-1 (E)→L+2 (A) (20%), H-1 (E)→L+4 (A) (6%), H (A)→L+6 (E) (6%)
S9 (E)	4.50008	2.29E-03	H (A)→L+3 (E) (45%), H-2 (E)→L (A) (29%), H-1 (E)→L+2 (A) (8%)
S9 (E)	4.50151	3.45E-03	H (A)→L+3 (E) (40%), H-2 (E)→L (A) (33%), H-1 (E)→L+2 (A) (9%)
T17 (E)	4.51196	0	H-2 (E)→L+1 (E) (25%), H-2 (E)→L (A) (24%), H-1 (E)→L+3 (E) (19%)
T17 (E)	4.51613	0	H-2 (E)→L+1 (E) (26%), H-2 (E)→L (A) (23%), H-1 (E)→L+3 (E) (21%), H-1 (E)→L+2 (A) (5%)
S10 (E)	4.53153	2.35E-02	H-1 (E)→L+2 (A) (76%)
S10 (E)	4.53477	2.38E-02	H-1 (E)→L+2 (A) (75%)
T18 (A)	4.56468	0	H-2 (E)→L+1 (E) (45%), H-1 (E)→L+3 (E) (25%), H-3 (A)→L (A) (6%)
T19 (E)	4.56904	0	H-1 (E)→L+3 (E) (32%), H-2 (E)→L+1 (E) (14%), H-1 (E)→L+2 (A) (14%), H-2 (E)→L (A) (7%), H-1 (E)→L+4 (A) (6%)
T19 (E)	4.57183	0	H-1 (E)→L+3 (E) (29%), H-1 (E)→L+2 (A) (15%), H-2 (E)→L+1 (E) (12%), H-2 (E)→L (A) (7%)
S11 (A)	4.57715	3.79E-04	H (A)→L+4 (A) (83%)
S12 (A)	4.59345	2.99E-04	H-2 (E)→L+1 (E) (71%), H-1 (E)→L+3 (E) (11%), H-3 (A)→L (A) (8%)
T20 (A)	4.60369	0	H-1 (E)→L+3 (E) (49%), H-3 (A)→L (A) (20%), H-2 (E)→L+1 (E) (12%)
S13 (A)	4.61335	1.20E-03	H-3 (A)→L (A) (57%), H-2 (E)→L+1 (E) (39%)
S14 (E)	4.65316	2.53E-02	H-2 (E)→L+1 (E) (59%), H-1 (E)→L+3 (E) (10%), H-3 (A)→L+1 (E) (9%)
S14 (E)	4.6557	2.46E-02	H-2 (E)→L+1 (E) (59%), H-3 (A)→L+1 (E) (9%), H-1 (E)→L+3 (E) (6%)
S15 (A)	4.65871	3.37E-02	H-1 (E)→L+3 (E) (43%), H-2 (E)→L+1 (E) (37%)
T21 (A)	4.67374	0	H-2 (E)→L+1 (E) (29%), H-3 (A)→L (A) (24%), H-4 (A)→L (A) (11%), H-1 (E)→L+3 (E) (5%)
T22 (E)	4.69792	0	H-1 (E)→L+4 (A) (44%), H (A)→L+6 (E) (13%), H-3

			(A)→L+1 (E) (8%)
T22 (E)	4.69892	0	H-1 (E)→L+4 (A) (41%), H (A)→L+6 (E) (13%), H-3 (A)→L+1 (E) (9%)
T23 (A)	4.71884	0	H (A)→L+4 (A) (19%), H-1 (E)→L+6 (E) (15%), H-4 (A)→L (A) (13%), H-1 (E)→L+7 (E) (12%)
T24 (A)	4.7238	0	H-4 (A)→L (A) (31%), H-6 (A)→L (A) (25%)
S16 (E)	4.73437	3.61E-02	H-1 (E)→L+3 (E) (61%), H-3 (A)→L+1 (E) (18%)
S16 (E)	4.73605	2.39E-02	H-1 (E)→L+3 (E) (66%), H-3 (A)→L+1 (E) (22%)
S17 (A)	4.73898	0.1041	H-1 (E)→L+3 (E) (50%), H-2 (E)→L+1 (E) (15%), H-3 (A)→L (A) (14%)
T25 (E)	4.74331	0	H-3 (A)→L+1 (E) (46%), H-5 (E)→L (A) (8%), H (A)→L+6 (E) (7%)
T25 (E)	4.748	0	H-3 (A)→L+1 (E) (48%), H-5 (E)→L (A) (9%), H (A)→L+6 (E) (6%)
S18 (E)	4.75674	1.15E-03	H-1 (E)→L+4 (A) (53%), H (A)→L+6 (E) (24%), H (A)→L+7 (E) (10%)
S18 (E)	4.75983	2.86E-03	H-1 (E)→L+4 (A) (58%), H (A)→L+6 (E) (20%), H (A)→L+7 (E) (9%)
S19 (E)	4.77685	3.03E-02	H (A)→L+6 (E) (40%), H-1 (E)→L+4 (A) (30%), H (A)→L+7 (E) (15%)
S19 (E)	4.77996	2.92E-02	H (A)→L+6 (E) (43%), H-1 (E)→L+4 (A) (27%), H (A)→L+7 (E) (18%)
T26 (E)	4.79288	0	H-4 (A)→L+1 (E) (33%), H-5 (E)→L (A) (6%), H (A)→L+6 (E) (6%)
T26 (E)	4.79513	0	H-4 (A)→L+1 (E) (32%), H (A)→L+6 (E) (7%), H-5 (E)→L (A) (6%)
T27 (E)	4.83974	0	H-1 (E)→L+6 (E) (15%), H-1 (E)→L+7 (E) (11%), H-4 (A)→L+1 (E) (10%), H-1 (E)→L+4 (A) (9%), H (A)→L+6 (E) (8%)
T27 (E)	4.84216	0	H-1 (E)→L+6 (E) (15%), H-4 (A)→L+1 (E) (14%), H-1 (E)→L+4 (A) (10%), H (A)→L+6 (E) (8%), H-1 (E)→L+7 (E) (7%)
T28 (A)	4.8535	0	H (A)→L+5 (A) (80%)
S20 (A)	4.85517	4.91E-03	H-4 (A)→L (A) (54%), H (A)→L+5 (A) (26%), H-6 (A)→L (A) (7%)
S21 (E)	4.8613	3.86E-02	H-3 (A)→L+1 (E) (37%), H-5 (E)→L (A) (27%)
S21 (E)	4.86246	3.72E-02	H-3 (A)→L+1 (E) (38%), H-5 (E)→L (A) (27%)
S22 (A)	4.86547	1.18E-02	H (A)→L+5 (A) (66%), H-4 (A)→L (A) (20%)
T29 (A)	4.8696	0	H-1 (E)→L+6 (E) (35%), H-1 (E)→L+7 (E) (23%), H (A)→L+5 (A) (12%)
T30 (A)	4.91944	0	H-6 (A)→L (A) (32%), H-5 (E)→L+1 (E) (16%), H-1 (E)→L+6 (E) (7%)
T31 (E)	4.92184	0	H-1 (E)→L+6 (E) (15%), H-6 (A)→L+1 (E) (7%)
S23 (A)	4.92384	2.29E-02	H-1 (E)→L+6 (E) (39%), H-1 (E)→L+7 (E) (22%), H-1 (E)→L+3 (E) (18%)
T31 (E)	4.92412	0	H-1 (E)→L+6 (E) (14%), H-6 (A)→L+1 (E) (5%)
S24 (E)	4.94828	5.58E-02	H-1 (E)→L+6 (E) (31%), H-5 (E)→L (A) (28%), H-4 (A)→L+1 (E) (7%)
S24 (E)	4.94861	5.52E-02	H-1 (E)→L+6 (E) (31%), H-5 (E)→L (A) (28%), H-4 (A)→L+1 (E) (6%)

T32 (A)	4.95514	0	H-1 (E)→L+6 (E) (18%), H-6 (A)→L (A) (7%), H-5 (E)→L+1 (E) (5%)
T33 (A)	4.95806	0	H-6 (A)→L+1 (E) (19%), H (A)→L+7 (E) (15%), H-5 (E)→L (A) (10%), H-1 (E)→L+5 (A) (10%), H (A)→L+6 (E) (8%), H-5 (E)→L+1 (E) (6%)
T34 (A)	4.96097	0	H (A)→L+7 (E) (27%), H-1 (E)→L+5 (A) (23%), H (A)→L+6 (E) (11%), H-6 (A)→L+1 (E) (6%)
S25 (A)	4.97045	9.27E-03	H-6 (A)→L (A) (49%), H-1 (E)→L+6 (E) (20%), H-5 (E)→L+1 (E) (5%)
T35 (A)	4.97057	0	H (A)→L+7 (E) (17%), H-1 (E)→L+5 (A) (15%), H-6 (A)→L+1 (E) (11%), H-5 (E)→L (A) (6%)
S26 (E)	4.97526	6.27E-02	H (A)→L+7 (E) (22%), H-4 (A)→L+1 (E) (18%), H-1 (E)→L+5 (A) (11%)
S26 (E)	4.97557	6.12E-02	H (A)→L+7 (E) (26%), H-4 (A)→L+1 (E) (15%), H-1 (E)→L+5 (A) (14%)
S27 (E)	4.99119	1.94E-02	H (A)→L+7 (E) (20%), H-1 (E)→L+5 (A) (18%), H-4 (A)→L+1 (E) (15%), H-1 (E)→L+7 (E) (12%), H (A)→L+6 (E) (9%)
S27 (E)	4.99294	2.74E-02	H-4 (A)→L+1 (E) (20%), H (A)→L+7 (E) (14%), H-1 (E)→L+5 (A) (14%), H-1 (E)→L+7 (E) (12%), H (A)→L+6 (E) (8%), H-6 (A)→L+1 (E) (5%)
S28 (A)	5.00277	8.68E-02	H-1 (E)→L+6 (E) (50%), H-6 (A)→L (A) (8%), H-1 (E)→L+7 (E) (7%), H-5 (E)→L+1 (E) (6%)
S29 (E)	5.03346	5.23E-02	H-4 (A)→L+1 (E) (22%), H-5 (E)→L (A) (14%), H-6 (A)→L+1 (E) (8%)
S29 (E)	5.03504	4.93E-02	H-4 (A)→L+1 (E) (23%), H-5 (E)→L (A) (14%), H-6 (A)→L+1 (E) (8%)
S30 (A)	5.0636	9.43E-04	H-5 (E)→L+1 (E) (37%), H-6 (A)→L (A) (19%), H-4 (A)→L (A) (13%)
S31 (E)	5.07024	4.42E-04	H-1 (E)→L+5 (A) (56%), H (A)→L+7 (E) (22%), H (A)→L+6 (E) (10%)
S31 (E)	5.0712	2.08E-04	H-1 (E)→L+5 (A) (59%), H (A)→L+7 (E) (22%), H (A)→L+6 (E) (9%)
S32 (E)	5.1091	2.56E-02	H-5 (E)→L+1 (E) (44%), H-6 (A)→L+1 (E) (15%)
S32 (E)	5.10932	2.46E-02	H-5 (E)→L+1 (E) (46%), H-6 (A)→L+1 (E) (15%)
S33 (A)	5.12873	6.24E-03	H-5 (E)→L+1 (E) (84%)

Complex 2

Label	**Energy (eV)**	**f (a.u.)**	**Orbital Transitions**
T1 (A)	2.97495	0	H (A)→L (A) (66%), H-1 (E)→L+1 (E) (18%), H-2 (E)→L+1 (E) (5%)
T2 (E)	3.02454	0	H (A)→L+1 (E) (47%), H-1 (E)→L (A) (20%), H-2 (E)→L (A) (8%)
T2 (E)	3.0257	0	H (A)→L+1 (E) (47%), H-1 (E)→L (A) (19%), H-2 (E)→L (A) (7%)
S1 (A)	3.26467	1.94E-02	H (A)→L (A) (98%)
T3 (E)	3.33972	0	H-1 (E)→L (A) (58%), H-1 (E)→L+1 (E) (18%), H (A)→L+1 (E) (7%)

T3 (E)	3.34313	0	H-1 (E)→L (A) (58%), H-1 (E)→L+1 (E) (18%), H (A)→L+1 (E) (7%)
T4 (A)	3.39405	0	H-1 (E)→L+1 (E) (84%), H (A)→L (A) (8%)
S2 (E)	3.40014	1.01E-02	H (A)→L+1 (E) (97%)
S2 (E)	3.40409	1.01E-02	H (A)→L+1 (E) (97%)
T5 (A)	3.44512	0	H-1 (E)→L+1 (E) (35%), H (A)→L (A) (23%), H-2 (E)→L+1 (E) (15%), H-3 (A)→L (A) (12%)
T6 (E)	3.46353	0	H-1 (E)→L+1 (E) (40%), H (A)→L+1 (E) (36%)
T6 (E)	3.46724	0	H-1 (E)→L+1 (E) (40%), H (A)→L+1 (E) (36%)
S3 (E)	3.48819	4.21E-02	H-1 (E)→L (A) (95%)
S3 (E)	3.49135	4.31E-02	H-1 (E)→L (A) (95%)
S4 (A)	3.60803	1.24E-02	H-1 (E)→L+1 (E) (96%)
T7 (E)	3.63136	0	H-1 (E)→L+1 (E) (21%), H-2 (E)→L (A) (17%), H-3 (A)→L+1 (E) (11%), H-1 (E)→L (A) (9%)
T7 (E)	3.63347	0	H-1 (E)→L+1 (E) (22%), H-2 (E)→L (A) (16%), H-3 (A)→L+1 (E) (10%), H-1 (E)→L (A) (9%)
T8 (A)	3.64752	0	H-1 (E)→L+1 (E) (43%), H-2 (E)→L+1 (E) (18%), H-3 (A)→L (A) (11%)
S5 (E)	3.65952	3.34E-02	H-1 (E)→L+1 (E) (97%)
S5 (E)	3.6603	3.49E-02	H-1 (E)→L+1 (E) (97%)
S6 (A)	3.72312	1.32E-02	H-1 (E)→L+1 (E) (96%)
T9 (A)	3.88544	0	H (A)→L+2 (A) (44%), H-1 (E)→L+3 (E) (29%), H-2 (E)→L+1 (E) (12%), H-3 (A)→L (A) (6%)
T10 (E)	3.90678	0	H (A)→L+3 (E) (28%), H-1 (E)→L+2 (A) (24%), H-1 (E)→L+3 (E) (17%), H-2 (E)→L (A) (7%)
T10 (E)	3.90745	0	H (A)→L+3 (E) (28%), H-1 (E)→L+2 (A) (24%), H-1 (E)→L+3 (E) (18%), H-2 (E)→L (A) (6%)
S7 (A)	4.33992	6.52E-06	H (A)→L+2 (A) (89%)
T11 (A)	4.3478	0	H (A)→L+2 (A) (35%), H-1 (E)→L+3 (E) (30%)
T12 (A)	4.40576	0	H (A)→L+3 (E) (26%), H (A)→L+4 (A) (13%), H-1 (E)→L+2 (A) (11%)
T13 (E)	4.40698	0	H (A)→L+3 (E) (21%), H (A)→L+4 (A) (21%), H-1 (E)→L+2 (A) (11%)
T13 (E)	4.40778	0	H (A)→L+3 (E) (23%), H (A)→L+4 (A) (18%), H-1 (E)→L+2 (A) (8%)
T14 (E)	4.43239	0	H-2 (E)→L (A) (23%), H-2 (E)→L+1 (E) (12%), H (A)→L+3 (E) (7%), H (A)→L+5 (E) (6%)
T14 (E)	4.43457	0	H-2 (E)→L (A) (20%), H-2 (E)→L+1 (E) (12%), H (A)→L+3 (E) (7%), H (A)→L+5 (E) (6%)
S8 (E)	4.43665	7.01E-03	H-2 (E)→L (A) (48%), H (A)→L+3 (E) (46%)
S8 (E)	4.4378	7.20E-03	H (A)→L+3 (E) (49%), H-2 (E)→L (A) (45%)
T15 (E)	4.47194	0	H (A)→L+5 (E) (12%), H-1 (E)→L+2 (A) (12%), H-2 (E)→L (A) (10%), H-1 (E)→L+4 (A) (7%), H (A)→L+3 (E) (5%)
T15 (E)	4.47364	0	H (A)→L+5 (E) (12%), H-1 (E)→L+2 (A) (11%), H-2 (E)→L (A) (10%), H-1 (E)→L+4 (A) (7%)
S9 (E)	4.48502	1.92E-03	H (A)→L+3 (E) (37%), H-2 (E)→L (A) (36%), H-1 (E)→L+2 (A) (11%)
S9 (E)	4.48711	2.55E-03	H-2 (E)→L (A) (40%), H (A)→L+3 (E) (32%), H-1 (E)→L+2 (A) (12%)

T16 (E)	4.50333	0	H-1 (E)→L+3 (E) (31%), H-1 (E)→L+2 (A) (13%), H-2 (E)→L (A) (9%)
T16 (E)	4.5051	0	H-1 (E)→L+3 (E) (32%), H-1 (E)→L+2 (A) (14%), H-2 (E)→L (A) (10%), H-2 (E)→L+1 (E) (6%)
T17 (A)	4.51664	0	H-2 (E)→L+1 (E) (33%), H-1 (E)→L+3 (E) (13%), H-5 (E)→L+1 (E) (12%), H-4 (A)→L (A) (8%), H (A)→L+2 (A) (8%), H-3 (A)→L (A) (7%)
S10 (E)	4.52206	2.96E-02	H-1 (E)→L+2 (A) (74%), H-2 (E)→L+1 (E) (5%)
S10 (E)	4.5254	2.96E-02	H-1 (E)→L+2 (A) (74%), H-2 (E)→L+1 (E) (6%)
T18 (A)	4.54984	0	H-2 (E)→L+1 (E) (50%), H-1 (E)→L+3 (E) (22%), H-3 (A)→L (A) (8%)
S11 (A)	4.58236	2.15E-04	H-2 (E)→L+1 (E) (85%)
T19 (A)	4.59255	0	H-1 (E)→L+3 (E) (44%), H-3 (A)→L (A) (31%), H-2 (E)→L+1 (E) (8%)
S12 (A)	4.60547	4.38E-03	H-3 (A)→L (A) (56%), H-2 (E)→L+1 (E) (38%)
T20 (E)	4.60871	0	H-3 (A)→L+1 (E) (16%), H-2 (E)→L+1 (E) (15%), H-5 (E)→L (A) (12%), H-1 (E)→L+3 (E) (8%), H-1 (E)→L+2 (A) (7%)
T20 (E)	4.61158	0	H-3 (A)→L+1 (E) (16%), H-2 (E)→L+1 (E) (15%), H-5 (E)→L (A) (12%), H-1 (E)→L+2 (A) (8%), H-1 (E)→L+3 (E) (5%)
S13 (A)	4.64572	3.17E-02	H-1 (E)→L+3 (E) (49%), H-2 (E)→L+1 (E) (28%), H (A)→L+4 (A) (11%)
S14 (E)	4.6506	3.56E-02	H-2 (E)→L+1 (E) (59%), H-1 (E)→L+3 (E) (10%), H-3 (A)→L+1 (E) (9%)
S14 (E)	4.65273	3.59E-02	H-2 (E)→L+1 (E) (60%), H-3 (A)→L+1 (E) (9%), H-1 (E)→L+3 (E) (9%)
S15 (A)	4.69067	1.46E-02	H-1 (E)→L+3 (E) (46%), H (A)→L+4 (A) (34%), H-3 (A)→L (A) (10%)
T21 (A)	4.71823	0	H-5 (E)→L+1 (E) (17%), H-4 (A)→L (A) (17%), H-1 (E)→L+3 (E) (16%), H-3 (A)→L (A) (15%), H-2 (E)→L+1 (E) (6%), H (A)→L+4 (A) (5%)
S16 (E)	4.73162	4.38E-02	H-1 (E)→L+3 (E) (62%), H-3 (A)→L+1 (E) (28%)
S16 (E)	4.73323	4.54E-02	H-1 (E)→L+3 (E) (60%), H-3 (A)→L+1 (E) (29%)
T22 (E)	4.73352	0	H-3 (A)→L+1 (E) (44%), H-1 (E)→L+4 (A) (8%)
T22 (E)	4.73736	0	H-3 (A)→L+1 (E) (44%), H-1 (E)→L+4 (A) (9%)
S17 (A)	4.75829	1.28E-01	H (A)→L+4 (A) (48%), H-2 (E)→L+1 (E) (16%), H-3 (A)→L (A) (12%), H-1 (E)→L+3 (E) (6%)
T23 (A)	4.79597	0	H (A)→L+4 (A) (30%), H-1 (E)→L+5 (E) (20%), H-9 (A)→L (A) (5%)
T24 (E)	4.81592	0	H (A)→L+5 (E) (30%), H-1 (E)→L+4 (A) (25%)
T24 (E)	4.81806	0	H (A)→L+5 (E) (31%), H-1 (E)→L+4 (A) (25%)
S18 (A)	4.88802	1.31E-02	H (A)→L+5 (E) (69%), H-1 (E)→L+4 (A) (11%)
S19 (E)	4.89017	2.06E-02	H (A)→L+5 (E) (36%), H-1 (E)→L+4 (A) (29%), H-3 (A)→L+1 (E) (12%)
T25 (A)	4.89347	0	H-4 (A)→L (A) (39%), H-6 (A)→L (A) (9%), H-3 (A)→L+2 (A) (7%), H-2 (E)→L+3 (E) (6%)
S19 (E)	4.89615	8.32E-02	H (A)→L+5 (E) (34%), H-3 (A)→L+1 (E) (23%), H-1 (E)→L+4 (A) (17%)
S20 (A)	4.89686	6.39E-02	H-1 (E)→L+4 (A) (33%), H-3 (A)→L+1 (E) (21%), H (A)→L+5 (E) (17%)
T26 (E)	4.90069	0	H-1 (E)→L+4 (A) (27%), H (A)→L+5 (E) (8%), H-2 (E)→L+2

			(A) (7%)
T26 (E)	4.90314	0	H-1 (E)→L+4 (A) (27%), H-2 (E)→L+2 (A) (9%), H (A)→L+5 (E) (8%), H-5 (E)→L (A) (5%)
T27 (E)	4.93598	0	H-2 (E)→L+2 (A) (19%), H-3 (A)→L+3 (E) (6%), H-2 (E)→L+3 (E) (5%)
T27 (E)	4.93698	0	H-2 (E)→L+2 (A) (18%), H-3 (A)→L+3 (E) (6%)
S21 (E)	4.93792	7.63E-02	H-1 (E)→L+4 (A) (45%), H-3 (A)→L+1 (E) (21%), H (A)→L+5 (E) (8%)
S21 (E)	4.9389	7.40E-02	H-1 (E)→L+4 (A) (48%), H-3 (A)→L+1 (E) (21%), H (A)→L+5 (E) (7%)
T28 (A)	4.94116	0	H-5 (E)→L+1 (E) (24%), H-2 (E)→L+3 (E) (18%), H-3 (A)→L+2 (A) (11%), H-6 (A)→L (A) (10%), H-4 (A)→L (A) (5%)
T29 (E)	4.98733	0	H-4 (A)→L+1 (E) (27%), H-1 (E)→L+5 (E) (19%), H-5 (E)→L (A) (6%)
T29 (E)	4.98913	0	H-1 (E)→L+5 (E) (29%), H-4 (A)→L+1 (E) (22%)
T30 (A)	4.99299	0	H-1 (E)→L+5 (E) (41%), H-4 (A)→L+1 (E) (6%), H-2 (E)→L+3 (E) (6%)
S22 (A)	4.99791	9.40E-02	H-4 (A)→L (A) (53%), H-5 (E)→L+1 (E) (12%)
T31 (A)	5.04272	0	H-1 (E)→L+5 (E) (44%)
T32 (E)	5.04475	0	H-1 (E)→L+5 (E) (22%), H-4 (A)→L+1 (E) (18%)
T32 (E)	5.04748	0	H-1 (E)→L+5 (E) (24%), H-4 (A)→L+1 (E) (17%)
S23 (A)	5.06447	9.08E-02	H-1 (E)→L+5 (E) (49%), H-1 (E)→L+3 (E) (14%), H-4 (A)→L (A) (11%)
T33 (A)	5.07595	0	H (A)→L+6 (A) (89%)
S24 (A)	5.0826	1.94E-02	H (A)→L+6 (A) (89%)
S25 (E)	5.08457	6.65E-02	H-1 (E)→L+5 (E) (25%), H-5 (E)→L (A) (22%), H-4 (A)→L+1 (E) (13%), H-2 (E)→L+2 (A) (9%)
S25 (E)	5.08518	6.53E-02	H-1 (E)→L+5 (E) (28%), H-5 (E)→L (A) (22%), H-4 (A)→L+1 (E) (12%), H-2 (E)→L+2 (A) (9%)
T34 (A)	5.10058	0	H (A)→L+7 (E) (14%), H (A)→L+10 (E) (9%), H (A)→L+13 (E) (9%), H (A)→L+11 (E) (8%), H (A)→L+16 (E) (5%)
S26 (A)	5.11426	7.95E-02	H-1 (E)→L+5 (E) (43%), H-6 (A)→L (A) (11%), H-4 (A)→L (A) (8%)
S27 (E)	5.11784	2.51E-02	H-1 (E)→L+5 (E) (53%), H-5 (E)→L (A) (9%)
S27 (E)	5.11837	2.71E-02	H-1 (E)→L+5 (E) (52%), H-5 (E)→L (A) (11%)
S28 (A)	5.1372	2.82E-02	H-1 (E)→L+5 (E) (61%), H-6 (A)→L (A) (12%)
S29 (E)	5.19313	7.34E-03	H-4 (A)→L+1 (E) (43%), H-5 (E)→L (A) (19%), H (A)→L+7 (E) (14%), H-6 (A)→L+1 (E) (9%)
S29 (E)	5.19427	5.12E-03	H-4 (A)→L+1 (E) (38%), H (A)→L+7 (E) (20%), H-5 (E)→L (A) (15%), H-6 (A)→L+1 (E) (8%)
S30 (E)	5.20193	5.11E-03	H (A)→L+7 (E) (45%), H-1 (E)→L+6 (A) (13%), H-4 (A)→L+1 (E) (12%), H-5 (E)→L (A) (10%)
S30 (E)	5.20312	3.47E-03	H (A)→L+7 (E) (51%), H-1 (E)→L+6 (A) (15%), H-5 (E)→L (A) (6%), H-4 (A)→L+1 (E) (6%)
S31 (A)	5.23176	1.53E-01	H-6 (A)→L (A) (31%), H-1 (E)→L+3 (E) (16%)
S32 (E)	5.27706	8.49E-03	H-5 (E)→L+1 (E) (52%), H-5 (E)→L (A) (13%), H-6 (A)→L+1 (E) (12%), H-2 (E)→L+2 (A) (6%)
S32 (E)	5.27888	7.60E-03	H-5 (E)→L+1 (E) (51%), H-5 (E)→L (A) (14%), H-6 (A)→L+1 (E) (12%), H-2 (E)→L+2 (A) (6%)

S33 (A)	5.29729	7.27E-02	H-5 (E)→L+1 (E) (57%), H-6 (A)→L (A) (23%), H-4 (A)→L (A) (10%)
S34 (E)	5.30015	1.39E-03	H-1 (E)→L+6 (A) (71%), H (A)→L+7 (E) (18%)
S34 (E)	5.30165	1.57E-03	H-1 (E)→L+6 (A) (72%), H (A)→L+7 (E) (16%)

Complex 3

Label	**Energy (eV)**	**f (a.u.)**	**Orbital Transitions**
T1 (A)	2.89883	0	H (A)→L (A) (69%), H-1 (E)→L+1 (E) (19%)
T2 (E)	2.94306	0	H (A)→L+1 (E) (53%), H-1 (E)→L (A) (21%)
T2 (E)	2.94496	0	H (A)→L+1 (E) (53%), H-1 (E)→L (A) (21%)
S1 (A)	3.15163	1.06E-02	H (A)→L (A) (99%)
T3 (E)	3.18757	0	H-1 (E)→L (A) (51%), H-1 (E)→L+1 (E) (22%), H (A)→L+1 (E) (11%)
T3 (E)	3.19085	0	H-1 (E)→L (A) (50%), H-1 (E)→L+1 (E) (22%), H (A)→L+1 (E) (12%)
T4 (A)	3.21352	0	H-1 (E)→L+1 (E) (80%), H (A)→L (A) (8%)
S2 (E)	3.26159	8.11E-03	H (A)→L+1 (E) (98%)
S2 (E)	3.26581	8.13E-03	H (A)→L+1 (E) (98%)
T5 (E)	3.32863	0	H-1 (E)→L+1 (E) (45%), H (A)→L+1 (E) (25%), H-1 (E)→L (A) (16%)
T5 (E)	3.33196	0	H-1 (E)→L+1 (E) (45%), H (A)→L+1 (E) (24%), H-1 (E)→L (A) (15%)
T6 (A)	3.34249	0	H-1 (E)→L+1 (E) (57%), H (A)→L (A) (17%), H-2 (E)→L+1 (E) (7%), H-3 (A)→L (A) (6%)
S3 (E)	3.36125	4.45E-02	H-1 (E)→L (A) (94%)
S3 (E)	3.36536	4.59E-02	H-1 (E)→L (A) (93%)
S4 (A)	3.4507	6.31E-03	H-1 (E)→L+1 (E) (98%)
T7 (E)	3.51353	0	H-2 (E)→L (A) (22%), H-3 (A)→L+1 (E) (16%), H-1 (E)→L (A) (8%), H-2 (E)→L+1 (E) (6%), H-1 (E)→L+1 (E) (5%)
T7 (E)	3.51566	0	H-2 (E)→L (A) (20%), H-3 (A)→L+1 (E) (14%), H-1 (E)→L+1 (E) (8%), H-1 (E)→L (A) (8%), H-2 (E)→L+1 (E) (7%)
S5 (E)	3.51733	5.48E-02	H-1 (E)→L+1 (E) (95%)
S5 (E)	3.51851	5.75E-02	H-1 (E)→L+1 (E) (96%)
T8 (A)	3.52322	0	H-1 (E)→L+1 (E) (31%), H-2 (E)→L+1 (E) (30%), H-3 (A)→L (A) (19%)
S6 (A)	3.60912	8.16E-03	H-1 (E)→L+1 (E) (97%)
T9 (A)	3.99389	0	H (A)→L+2 (A) (40%), H-1 (E)→L+3 (E) (29%)
T10 (E)	4.01813	0	H-1 (E)→L+2 (A) (26%), H (A)→L+3 (E) (24%), H-1 (E)→L+3 (E) (16%)
T10 (E)	4.01891	0	H-1 (E)→L+2 (A) (26%), H (A)→L+3 (E) (24%), H-1 (E)→L+3 (E) (16%)
T11 (A)	4.29574	0	H-4 (E)→L (A) (23%), H-4 (E)→L+1 (E) (16%), H-5 (A)→L+1 (E) (7%), H-2 (E)→L+1 (E) (7%)
T12 (E)	4.29731	0	H-4 (E)→L+1 (E) (23%), H-4 (E)→L (A) (19%), H-2 (E)→L+1 (E) (13%), H-5 (A)→L (A) (6%), H-2 (E)→L (A) (6%)
T12 (E)	4.30056	0	H-4 (E)→L+1 (E) (27%), H-4 (E)→L (A) (16%), H-2 (E)→L+1

			(E) (9%), H-5 (A)→L (A) (7%), H-5 (A)→L+1 (E) (6%), H-2 (E)→L (A) (5%)
S7 (A)	4.44942	5.98E-03	H (A)→L+2 (A) (75%), H-3 (A)→L (A) (12%)
S8 (E)	4.46416	3.55E-03	H-2 (E)→L (A) (87%)
S8 (E)	4.46929	4.25E-03	H-2 (E)→L (A) (86%)
T13 (A)	4.48188	0	H (A)→L+2 (A) (27%), H (A)→L+4 (A) (25%), H-1 (E)→L+3 (E) (12%)
T14 (E)	4.51345	0	H-2 (E)→L (A) (36%), H-2 (E)→L+1 (E) (8%), H (A)→L+3 (E) (6%)
T14 (E)	4.51777	0	H-2 (E)→L (A) (31%), H (A)→L+3 (E) (9%), H-2 (E)→L+1 (E) (5%)
T15 (E)	4.54578	0	H-2 (E)→L+1 (E) (16%), H (A)→L+3 (E) (13%), H-1 (E)→L+2 (A) (9%), H-2 (E)→L (A) (6%), H (A)→L+5 (E) (5%)
T15 (E)	4.54626	0	H-2 (E)→L+1 (E) (13%), H (A)→L+3 (E) (11%), H-2 (E)→L (A) (8%), H-1 (E)→L+2 (A) (8%), H (A)→L+5 (E) (5%)
S9 (A)	4.55075	2.09E-03	H-3 (A)→L (A) (71%), H-2 (E)→L+1 (E) (22%)
T16 (A)	4.56088	0	H-2 (E)→L+1 (E) (63%), H-3 (A)→L (A) (8%), H (A)→L+4 (A) (6%)
T17 (A)	4.56648	0	H-3 (A)→L (A) (31%), H-2 (E)→L+1 (E) (16%), H (A)→L+2 (A) (14%), H-1 (E)→L+3 (E) (12%), H (A)→L+4 (A) (8%)
S10 (E)	4.5754	1.54E-02	H-2 (E)→L+1 (E) (73%), H (A)→L+3 (E) (11%)
S11 (A)	4.57756	2.78E-02	H-2 (E)→L+1 (E) (53%), H (A)→L+3 (E) (21%), H-1 (E)→L+2 (A) (8%)
S10 (E)	4.58043	1.30E-02	H-2 (E)→L+1 (E) (70%), H (A)→L+3 (E) (10%), H-1 (E)→L+2 (A) (5%)
T18 (E)	4.60439	0	H-1 (E)→L+2 (A) (29%), H (A)→L+3 (E) (28%)
T18 (E)	4.60511	0	H (A)→L+3 (E) (28%), H-1 (E)→L+2 (A) (27%)
S12 (E)	4.63122	6.53E-04	H-3 (A)→L+1 (E) (43%), H-1 (E)→L+2 (A) (23%), H-2 (E)→L+1 (E) (19%), H (A)→L+3 (E) (7%)
S12 (E)	4.63553	3.53E-04	H-3 (A)→L+1 (E) (41%), H-1 (E)→L+2 (A) (29%), H-2 (E)→L+1 (E) (16%), H (A)→L+3 (E) (6%)
T19 (A)	4.63979	0	H-2 (E)→L+1 (E) (19%), H-4 (E)→L+1 (E) (17%), H (A)→L+4 (A) (12%), H-3 (A)→L (A) (11%), H-6 (A)→L (A) (6%)
S13 (E)	4.65023	1.55E-02	H-1 (E)→L+2 (A) (38%), H (A)→L+3 (E) (28%), H-3 (A)→L+1 (E) (15%)
S13 (E)	4.65374	1.60E-02	H-1 (E)→L+2 (A) (35%), H (A)→L+3 (E) (27%), H-3 (A)→L+1 (E) (20%)
T20 (E)	4.6578	0	H-3 (A)→L+1 (E) (47%), H-4 (E)→L (A) (8%)
T20 (E)	4.66254	0	H-3 (A)→L+1 (E) (49%), H-4 (E)→L (A) (8%)
S14 (A)	4.6927	1.67E-01	H-2 (E)→L+1 (E) (49%), H-1 (E)→L+3 (E) (16%), H (A)→L+2 (A) (11%), H-3 (A)→L (A) (5%)
T21 (A)	4.70471	0	H-5 (A)→L (A) (47%), H-4 (E)→L+1 (E) (16%), H-6 (A)→L (A) (12%)
T22 (E)	4.70717	0	H-1 (E)→L+3 (E) (37%), H-1 (E)→L+2 (A) (14%), H-4 (E)→L (A) (6%), H-1 (E)→L+4 (A) (5%)
T22 (E)	4.70917	0	H-1 (E)→L+3 (E) (40%), H-1 (E)→L+2 (A) (14%), H-4 (E)→L (A) (7%)
T23 (E)	4.75851	0	H-5 (A)→L+1 (E) (36%), H-4 (E)→L+1 (E) (15%), H-4 (E)→L (A) (9%)
T23 (E)	4.76108	0	H-5 (A)→L+1 (E) (37%), H-4 (E)→L+1 (E) (15%), H-4 (E)→L

			(A) (9%)
T24 (A)	4.76606	0	H-1 (E)→L+3 (E) (82%)
S15 (E)	4.78267	2.08E-02	H (A)→L+3 (E) (20%), H-1 (E)→L+3 (E) (18%), H-3 (A)→L+1 (E) (16%), H-1 (E)→L+2 (A) (13%)
S15 (E)	4.78324	2.13E-02	H (A)→L+3 (E) (19%), H-1 (E)→L+3 (E) (18%), H-3 (A)→L+1 (E) (17%), H-1 (E)→L+2 (A) (14%)
S16 (A)	4.79283	7.38E-04	H (A)→L+4 (A) (79%), H-5 (A)→L (A) (8%), H-1 (E)→L+3 (E) (6%)
T25 (A)	4.83235	0	H (A)→L+4 (A) (36%), H-1 (E)→L+5 (E) (12%), H-2 (E)→L+3 (E) (11%), 0→L+1 (E) (10%), H-3 (A)→L+2 (A) (6%), 0→L (A) (6%)
S17 (E)	4.84437	4.42E-03	H-4 (E)→L (A) (73%)
S17 (E)	4.84537	4.89E-03	H-4 (E)→L (A) (73%)
S18 (A)	4.85841	6.47E-02	H-1 (E)→L+3 (E) (78%)
T26 (A)	4.88405	0	H-6 (A)→L (A) (64%), H-4 (E)→L+1 (E) (12%)
T27 (E)	4.88586	0	H-1 (E)→L+4 (A) (36%), H (A)→L+5 (E) (31%)
T27 (E)	4.88819	0	H-1 (E)→L+4 (A) (36%), H (A)→L+5 (E) (32%)
S19 (A)	4.92607	3.95E-02	H-5 (A)→L (A) (51%), H-4 (E)→L+1 (E) (19%), H (A)→L+4 (A) (8%)
S20 (E)	4.93316	4.96E-02	H-1 (E)→L+3 (E) (40%), H-1 (E)→L+4 (A) (19%), H (A)→L+5 (E) (7%)
S20 (E)	4.9345	4.83E-02	H-1 (E)→L+3 (E) (40%), H-1 (E)→L+4 (A) (22%), H (A)→L+5 (E) (6%)
T28 (E)	4.94397	0	H-6 (A)→L+1 (E) (42%), H-4 (E)→L (A) (8%), H-5 (A)→L+1 (E) (7%), H-4 (E)→L+1 (E) (6%)
T28 (E)	4.94632	0	H-6 (A)→L+1 (E) (33%), H-1 (E)→L+4 (A) (6%), H-4 (E)→L (A) (6%), H-5 (A)→L+1 (E) (5%), H-4 (E)→L+1 (E) (5%)
T29 (A)	4.9562	0	H-6 (A)→L+1 (E) (18%), H (A)→L+5 (E) (15%), H-1 (E)→L+4 (A) (12%)
T30 (A)	4.95762	0	H (A)→L+5 (E) (16%), H-1 (E)→L+4 (A) (12%), H-6 (A)→L+1 (E) (10%)
S21 (A)	4.96622	2.38E-03	H-6 (A)→L (A) (67%), H-4 (E)→L+1 (E) (22%)
S22 (E)	4.98042	2.38E-03	H-1 (E)→L+4 (A) (36%), H (A)→L+5 (E) (31%), H-4 (E)→L+1 (E) (6%), H-5 (A)→L+1 (E) (5%)
S22 (E)	4.98324	1.40E-03	H-1 (E)→L+4 (A) (37%), H (A)→L+5 (E) (31%), H-5 (A)→L+1 (E) (5%), H-4 (E)→L+1 (E) (5%)
T31 (A)	4.9887	0	H-4 (E)→L+1 (E) (35%), H-5 (A)→L (A) (12%)
S23 (A)	5.00766	1.61E-02	H-4 (E)→L+1 (E) (40%), H-5 (A)→L (A) (28%), H-6 (A)→L (A) (22%)
S24 (E)	5.0185	3.80E-02	H-4 (E)→L+1 (E) (46%), H-1 (E)→L+4 (A) (15%), H-5 (A)→L+1 (E) (11%), H-4 (E)→L (A) (7%)
S24 (E)	5.02145	3.14E-02	H-4 (E)→L+1 (E) (47%), H-1 (E)→L+4 (A) (13%), H-5 (A)→L+1 (E) (9%), H-4 (E)→L (A) (6%)
T32 (E)	5.02145	0	H-5 (A)→L+1 (E) (25%), H-4 (E)→L+1 (E) (25%), H-6 (A)→L+1 (E) (20%), H-4 (E)→L (A) (10%)
T32 (E)	5.02508	0	H-5 (A)→L+1 (E) (25%), H-4 (E)→L+1 (E) (25%), H-6 (A)→L+1 (E) (19%), H-4 (E)→L (A) (9%)
S25 (A)	5.03506	1.68E-02	H-4 (E)→L+1 (E) (85%)
T33 (A)	5.03526	0	H-4 (E)→L+1 (E) (27%), H-1 (E)→L+5 (E) (14%), H-5 (A)→L (A) (8%)

S26 (E)	5.04274	8.76E-02	H (A)→L+5 (E) (40%), H-5 (A)→L+1 (E) (14%), H-1 (E)→L+4 (A) (5%), H-1 (E)→L+3 (E) (5%)
S26 (E)	5.04448	7.19E-02	H (A)→L+5 (E) (42%), H-5 (A)→L+1 (E) (8%)
T34 (E)	5.06292	0	H-1 (E)→L+5 (E) (25%), H (A)→L+5 (E) (12%), H-1 (E)→L+4 (A) (7%)
T34 (E)	5.06554	0	H-1 (E)→L+5 (E) (27%), H (A)→L+5 (E) (12%), H-1 (E)→L+4 (A) (6%)
S27 (E)	5.06599	1.21E-01	H-5 (A)→L+1 (E) (29%), H-6 (A)→L+1 (E) (24%), H-1 (E)→L+4 (A) (9%)
S27 (E)	5.06807	1.22E-01	H-5 (A)→L+1 (E) (30%), H-6 (A)→L+1 (E) (26%), H-1 (E)→L+4 (A) (10%)
S28 (E)	5.11009	3.17E-02	H-6 (A)→L+1 (E) (55%), H-5 (A)→L+1 (E) (26%)
S28 (E)	5.11376	3.16E-02	H-6 (A)→L+1 (E) (55%), H-5 (A)→L+1 (E) (27%)
S29 (A)	5.12147	7.11E-02	H-1 (E)→L+5 (E) (42%), H-1 (E)→L+3 (E) (36%)
S30 (E)	5.20026	8.55E-03	H-1 (E)→L+5 (E) (76%), H (A)→L+6 (A) (6%)
S30 (E)	5.20109	8.72E-03	H-1 (E)→L+5 (E) (70%), H (A)→L+6 (A) (13%)
S31 (A)	5.20225	7.35E-03	H (A)→L+6 (A) (71%), H-1 (E)→L+5 (E) (17%)
S32 (A)	5.2211	9.97E-02	H-1 (E)→L+5 (E) (84%)
S33 (A)	5.30531	2.78E-02	H (A)→L+7 (E) (48%), H-1 (E)→L+6 (A) (11%)
S34 (A)	5.3173	2.60E-01	H-1 (E)→L+5 (E) (33%), H-1 (E)→L+3 (E) (21%)

Complex 4

Label	**Energy (eV)**	**f (a.u.)**	**Orbital Transitions**
T1 (A)	3.04647	0	H (A)→L (A) (62%), H-1 (E)→L+1 (E) (15%), H-2 (E)→L+1 (E) (13%)
T2 (E)	3.07999	0	H (A)→L+1 (E) (49%), H-1 (E)→L (A) (12%), H-2 (E)→L (A) (10%)
T2 (E)	3.0814	0	H (A)→L+1 (E) (49%), H-1 (E)→L (A) (11%), H-2 (E)→L (A) (9%)
S1 (A)	3.34146	1.52E-02	H (A)→L (A) (98%)
T3 (E)	3.38209	0	H-1 (E)→L (A) (54%), H-1 (E)→L+1 (E) (24%)
T3 (E)	3.38583	0	H-1 (E)→L (A) (53%), H-1 (E)→L+1 (E) (26%)
T4 (A)	3.41158	0	H-1 (E)→L+1 (E) (81%)
S2 (E)	3.43752	9.49E-03	H (A)→L+1 (E) (97%)
S2 (E)	3.44161	9.54E-03	H (A)→L+1 (E) (97%)
T5 (A)	3.48806	0	H (A)→L (A) (34%), H-1 (E)→L+1 (E) (30%), H-2 (E)→L+1 (E) (14%), H-3 (A)→L (A) (11%)
T6 (E)	3.49925	0	H (A)→L+1 (E) (41%), H-1 (E)→L+1 (E) (27%), H-1 (E)→L (A) (9%), H-2 (E)→L (A) (6%), H-3 (A)→L+1 (E) (5%)
T6 (E)	3.50242	0	H (A)→L+1 (E) (42%), H-1 (E)→L+1 (E) (27%), H-1 (E)→L (A) (9%), H-2 (E)→L (A) (6%), H-3 (A)→L+1 (E) (5%)
S3 (E)	3.56779	4.52E-02	H-1 (E)→L (A) (93%)
S3 (E)	3.57149	4.64E-02	H-1 (E)→L (A) (93%)
T7 (E)	3.64732	0	H-1 (E)→L+1 (E) (27%), H-2 (E)→L (A) (16%), H-1 (E)→L (A) (15%), H-3 (A)→L+1 (E) (11%)
S4 (A)	3.64847	9.02E-03	H-1 (E)→L+1 (E) (98%)

T7 (E)	3.6502	0	H-1 (E)→L+1 (E) (28%), H-1 (E)→L (A) (15%), H-2 (E)→L (A) (15%), H-3 (A)→L+1 (E) (10%), H-2 (E)→L+1 (E) (5%)
T8 (A)	3.66569	0	H-1 (E)→L+1 (E) (49%), H-2 (E)→L+1 (E) (19%), H-3 (A)→L (A) (11%)
S5 (E)	3.70889	4.38E-02	H-1 (E)→L+1 (E) (94%)
S5 (E)	3.70988	4.63E-02	H-1 (E)→L+1 (E) (94%)
S6 (A)	3.78627	8.11E-03	H-1 (E)→L+1 (E) (97%)
T9 (A)	3.98867	0	H (A)→L+2 (A) (46%), H-1 (E)→L+3 (E) (31%)
T10 (E)	4.01772	0	H-1 (E)→L+2 (A) (28%), H (A)→L+3 (E) (27%), H-1 (E)→L+3 (E) (17%)
T10 (E)	4.01853	0	H-1 (E)→L+2 (A) (28%), H (A)→L+3 (E) (27%), H-1 (E)→L+3 (E) (18%)
T11 (A)	4.41673	0	H-4 (E)→L+1 (E) (23%), H-2 (E)→L+1 (E) (19%), H (A)→L+2 (A) (14%), H-3 (A)→L (A) (10%), H-5 (A)→L (A) (9%)
T12 (E)	4.42297	0	H-2 (E)→L (A) (26%), H-2 (E)→L+1 (E) (23%), H-4 (E)→L (A) (14%), H-5 (A)→L+1 (E) (6%)
T12 (E)	4.42707	0	H-2 (E)→L+1 (E) (23%), H-2 (E)→L (A) (23%), H-4 (E)→L (A) (13%), H-4 (E)→L+1 (E) (6%), H-5 (A)→L+1 (E) (5%)
S7 (A)	4.45914	5.22E-03	H (A)→L+2 (A) (78%), H-2 (E)→L+1 (E) (5%)
S8 (E)	4.46984	2.72E-03	H-2 (E)→L (A) (85%)
S8 (E)	4.4748	3.30E-03	H-2 (E)→L (A) (84%)
T13 (E)	4.51711	0	H-2 (E)→L (A) (19%), H (A)→L+3 (E) (14%), H-1 (E)→L+2 (A) (9%), H-2 (E)→L+1 (E) (9%), H-3 (A)→L+1 (E) (8%), H-4 (E)→L (A) (6%)
T13 (E)	4.52052	0	H-2 (E)→L (A) (18%), H (A)→L+3 (E) (15%), H-1 (E)→L+2 (A) (10%), H-3 (A)→L+1 (E) (7%), H-4 (E)→L (A) (5%), H-2 (E)→L+1 (E) (5%)
T14 (A)	4.53178	0	H-2 (E)→L+1 (E) (28%), H-1 (E)→L+3 (E) (16%), H (A)→L+2 (A) (15%), H (A)→L+4 (A) (10%)
T15 (A)	4.54542	0	H-2 (E)→L+1 (E) (44%), H (A)→L+4 (A) (17%)
T16 (E)	4.5617	0	H (A)→L+3 (E) (10%), H-1 (E)→L+2 (A) (10%), H (A)→L+5 (E) (7%), H-4 (E)→L (A) (6%), H-2 (E)→L (A) (6%)
T16 (E)	4.56325	0	H (A)→L+3 (E) (9%), H-1 (E)→L+2 (A) (9%), H (A)→L+5 (E) (7%), H-2 (E)→L (A) (7%), H-4 (E)→L (A) (6%)
S9 (A)	4.57151	7.52E-03	H-2 (E)→L+1 (E) (85%), H (A)→L+3 (E) (7%)
T17 (A)	4.5727	0	H-3 (A)→L (A) (35%), H-2 (E)→L+1 (E) (22%), H (A)→L+2 (A) (13%), H-1 (E)→L+3 (E) (6%)
S10 (A)	4.57562	2.54E-02	H-2 (E)→L+1 (E) (60%), H (A)→L+3 (E) (28%)
S11 (A)	4.57711	1.42E-02	H-2 (E)→L+1 (E) (48%), H-3 (A)→L (A) (24%), H (A)→L+3 (E) (12%)
S12 (A)	4.57942	7.55E-03	H-3 (A)→L (A) (44%), H-2 (E)→L+1 (E) (39%)
T18 (E)	4.60947	0	H-1 (E)→L+2 (A) (22%), H (A)→L+3 (E) (20%)
T18 (E)	4.6103	0	H (A)→L+3 (E) (25%), H-1 (E)→L+2 (A) (21%)
S13 (E)	4.63434	4.80E-03	H-1 (E)→L+2 (A) (60%), H (A)→L+3 (E) (25%), H-3 (A)→L+1 (E) (5%)
S13 (E)	4.63649	5.98E-03	H-1 (E)→L+2 (A) (59%), H (A)→L+3 (E) (26%)
S14 (E)	4.66403	3.25E-02	H-3 (A)→L+1 (E) (48%), H (A)→L+3 (E) (17%), H-1 (E)→L+2 (A) (14%), H-2 (E)→L+1 (E) (11%)
T19 (E)	4.66558	0	H-3 (A)→L+1 (E) (32%), H-1 (E)→L+3 (E) (17%), H

			(A)→L+3 (E) (6%)
S14 (E)	4.66793	3.26E-02	H-3 (A)→L+1 (E) (48%), H (A)→L+3 (E) (19%), H-2 (E)→L+1 (E) (12%), H-1 (E)→L+2 (A) (11%)
T19 (E)	4.66842	0	H-3 (A)→L+1 (E) (32%), H-1 (E)→L+3 (E) (18%)
T20 (A)	4.68203	0	H-1 (E)→L+3 (E) (19%), H-4 (E)→L+1 (E) (17%), H-3 (A)→L (A) (13%), H-5 (A)→L (A) (9%)
S15 (A)	4.70994	0.1979	H-2 (E)→L+1 (E) (42%), H-1 (E)→L+3 (E) (25%), H-3 (A)→L (A) (14%), H (A)→L+2 (A) (7%)
T21 (E)	4.74244	0	H-1 (E)→L+3 (E) (20%), H-3 (A)→L+1 (E) (17%), H-4 (E)→L (A) (13%), H-1 (E)→L+2 (A) (11%)
T21 (E)	4.74544	0	H-1 (E)→L+3 (E) (22%), H-3 (A)→L+1 (E) (18%), H-4 (E)→L (A) (12%), H-1 (E)→L+2 (A) (11%)
T22 (A)	4.77611	0	H-1 (E)→L+3 (E) (61%), H-4 (E)→L+1 (E) (11%), H (A)→L+4 (A) (7%)
S16 (E)	4.79475	2.74E-02	H-1 (E)→L+3 (E) (30%), H-3 (A)→L+1 (E) (25%), H-1 (E)→L+2 (A) (12%), H (A)→L+3 (E) (10%)
S16 (E)	4.7958	2.78E-02	H-1 (E)→L+3 (E) (31%), H-3 (A)→L+1 (E) (24%), H-1 (E)→L+2 (A) (12%), H (A)→L+3 (E) (9%)
S17 (A)	4.84055	3.82E-02	H-1 (E)→L+3 (E) (85%)
T23 (A)	4.87172	0	H-5 (A)→L (A) (40%), H-4 (E)→L+1 (E) (21%), H-6 (A)→L (A) (8%)
T24 (A)	4.87732	0	H (A)→L+4 (A) (24%), H-2 (E)→L+3 (E) (17%), H-3 (A)→L+2 (A) (11%), H-5 (A)→L (A) (6%)
T25 (E)	4.88493	0	H (A)→L+5 (E) (16%), H-4 (E)→L (A) (12%), H-2 (E)→L+2 (A) (10%), H-5 (A)→L+1 (E) (8%), H (A)→L+9 (E) (6%), H-4 (E)→L+1 (E) (5%), H-3 (A)→L+3 (E) (5%)
T25 (E)	4.88714	0	H (A)→L+5 (E) (15%), H-4 (E)→L (A) (12%), H-2 (E)→L+2 (A) (10%), H-5 (A)→L+1 (E) (8%), H (A)→L+9 (E) (6%), H-3 (A)→L+3 (E) (5%)
S18 (A)	4.92299	4.07E-02	H (A)→L+4 (A) (83%), H-5 (A)→L (A) (5%)
T26 (E)	4.93622	0	H-5 (A)→L+1 (E) (32%), H (A)→L+5 (E) (7%), H-4 (E)→L (A) (6%), H-1 (E)→L+4 (A) (5%)
T26 (E)	4.93841	0	H-5 (A)→L+1 (E) (32%), H (A)→L+5 (E) (6%), H-4 (E)→L (A) (6%)
S19 (E)	4.96649	0.1192	H-1 (E)→L+3 (E) (28%), H-4 (E)→L (A) (23%), H-3 (A)→L+1 (E) (11%)
S19 (E)	4.96753	0.1203	H-1 (E)→L+3 (E) (29%), H-4 (E)→L (A) (22%), H-3 (A)→L+1 (E) (11%)
T27 (A)	4.98583	0	H (A)→L+4 (A) (17%), H-3 (A)→L+2 (A) (11%)
T28 (E)	4.99049	0	H (A)→L+5 (E) (14%), H (A)→L+9 (E) (12%), H (A)→L+7 (E) (8%), H-2 (E)→L+2 (A) (7%)
T28 (E)	4.9917	0	H (A)→L+5 (E) (14%), H (A)→L+9 (E) (12%), H (A)→L+7 (E) (8%), H-2 (E)→L+2 (A) (7%)
S20 (E)	5.03649	5.89E-02	H-4 (E)→L (A) (31%), H-1 (E)→L+3 (E) (18%), H (A)→L+5 (E) (10%), H-5 (A)→L+1 (E) (6%)
S20 (E)	5.03821	6.13E-02	H-4 (E)→L (A) (32%), H-1 (E)→L+3 (E) (18%), H (A)→L+5 (E) (9%), H-5 (A)→L+1 (E) (5%), H-1 (E)→L+4 (A) (5%)
T29 (E)	5.0443	0	H-1 (E)→L+4 (A) (45%)
T29 (E)	5.04699	0	H-1 (E)→L+4 (A) (44%)
S21 (A)	5.05206	4.99E-02	H-5 (A)→L (A) (42%), H-4 (E)→L+1 (E) (29%), H-3 (A)→L+2

			(A) (5%)
T30 (A)	5.10071	0	H-6 (A)→L (A) (40%), H-4 (E)→L+1 (E) (22%)
S22 (E)	5.10299	2.31E-02	H (A)→L+5 (E) (72%), H-4 (E)→L (A) (9%), H-1 (E)→L+4 (A) (9%)
S22 (E)	5.10686	2.20E-02	H (A)→L+5 (E) (73%), H-4 (E)→L (A) (9%), H-1 (E)→L+4 (A) (9%)
T31 (E)	5.12762	0	H-1 (E)→L+4 (A) (8%), H (A)→L+5 (E) (6%), H (A)→L+7 (E) (6%), H-6 (A)→L+1 (E) (5%), H (A)→L+9 (E) (5%)
T31 (E)	5.12846	0	H-1 (E)→L+4 (A) (16%), H (A)→L+5 (E) (9%), H (A)→L+7 (E) (8%), H (A)→L+9 (E) (6%)
S23 (E)	5.13698	8.19E-02	H-1 (E)→L+4 (A) (76%), H (A)→L+5 (E) (5%)
S23 (E)	5.14027	7.89E-02	H-1 (E)→L+4 (A) (76%)
T32 (A)	5.14364	0	H-1 (E)→L+5 (E) (36%), H-6 (A)→L (A) (9%)
T33 (E)	5.14691	0	H-6 (A)→L+1 (E) (26%), H-4 (E)→L (A) (13%), H-4 (E)→L+1 (E) (11%), H-5 (A)→L+1 (E) (9%)
T33 (E)	5.14976	0	H-6 (A)→L+1 (E) (30%), H-4 (E)→L (A) (15%), H-4 (E)→L+1 (E) (13%), H-5 (A)→L+1 (E) (11%)
S24 (A)	5.15794	3.19E-03	H-4 (E)→L+1 (E) (35%), H-5 (A)→L (A) (30%), H-6 (A)→L (A) (26%)
S25 (E)	5.18606	2.98E-02	H-5 (A)→L+1 (E) (29%), H-4 (E)→L+1 (E) (28%), H-4 (E)→L (A) (18%)
S25 (E)	5.18743	3.10E-02	H-5 (A)→L+1 (E) (32%), H-4 (E)→L+1 (E) (21%), H-4 (E)→L (A) (19%)
S26 (A)	5.21813	0.2326	H-1 (E)→L+3 (E) (35%), H-4 (E)→L+1 (E) (22%), H-1 (E)→L+5 (E) (10%)
S27 (E)	5.23012	1.33E-02	H-4 (E)→L+1 (E) (38%), H-5 (A)→L+1 (E) (33%), H-6 (A)→L+1 (E) (10%)
S27 (E)	5.23232	1.47E-02	H-4 (E)→L+1 (E) (36%), H-5 (A)→L+1 (E) (33%), H-6 (A)→L+1 (E) (9%)
S28 (A)	5.2368	4.70E-03	H-4 (E)→L+1 (E) (48%), H-6 (A)→L (A) (23%)
S29 (A)	5.26882	1.97E-02	H-6 (A)→L (A) (41%), H-4 (E)→L+1 (E) (39%), H-5 (A)→L (A) (9%)
S30 (E)	5.29904	2.16E-03	H-1 (E)→L+5 (E) (57%)
S30 (E)	5.2992	2.24E-03	H-1 (E)→L+5 (E) (60%)
S31 (A)	5.3223	5.51E-02	H-1 (E)→L+5 (E) (82%)
S32 (A)	5.3312	8.79E-02	H-1 (E)→L+5 (E) (56%), H (A)→L+6 (A) (10%)
S33 (E)	5.35135	1.46E-03	H-6 (A)→L+1 (E) (66%), H-5 (A)→L+1 (E) (8%)
S33 (E)	5.35538	5.15E-04	H-6 (A)→L+1 (E) (70%), H-5 (A)→L+1 (E) (8%)
S34 (A)	5.36876	2.09E-02	H (A)→L+7 (E) (29%), H-1 (E)→L+5 (E) (19%), H (A)→L+9 (E) (13%), H-6 (A)→L+1 (E) (6%)
S35 (A)	5.37848	1.59E-03	H (A)→L+6 (A) (83%)

Spin-Orbit Perturbation Excitations

Electronic excitations arising from spin-orbit coupling. The contribution, as a percentage, of the scalar relativistic transitions is given per excitation.

Complex 1

Label	Energy (eV)	f (a.u.)	Singlet Amount	MLCT Amount	Transitions
1A	2.75536	4.63E-06	0.0000	0.4761	T1 (A) (71%)
2E	2.76693	2.30E-03	0.0559	0.4813	T1 (A) (78%), T3 (E) (6%)
2E’	2.76735	2.31E-03	0.0555	0.4818	T1 (A) (80%), T3 (E) (5%)
3A	2.80739	2.12E-03	0.1566	0.4631	T2 (E) (76%), S1 (A) (14%)
4E	2.83531	8.91E-05	0.0000	0.4458	T2 (E) (73%)
4E’	2.83766	1.10E-04	0.0000	0.4437	T2 (E) (73%)
5A	2.84227	5.25E-04	0.0388	0.4557	T2 (E) (74%), T1 (A) (11%), T4 (A) (5%)
6E	2.84557	1.43E-03	0.0459	0.4446	T2 (E) (82%)
6E’	2.84572	1.32E-03	0.0424	0.4443	T2 (E) (80%)
7A	2.96568	4.82E-03	0.3532	0.4751	T3 (E) (38%), S1 (A) (32%)
8E	3.01758	4.03E-03	0.3519	0.4549	S2 (E) (32%), T4 (A) (18%), T5 (E) (10%)
8E’	3.02150	4.02E-03	0.3519	0.4530	S2 (E) (32%), T4 (A) (20%), T6 (A) (10%)
	3.13458	1.48E-03	0.0407	0.4156	T3 (E) (41%)
	3.13591	1.31E-03	0.0486	0.4189	T3 (E) (63%), T1 (A) (8%)
	3.13702	1.31E-03	0.0408	0.4184	T3 (E) (47%)
	3.15683	2.24E-03	0.0636	0.4295	T3 (E) (44%), T5 (E) (10%), T4 (A) (10%), T2 (E) (6%)
	3.15835	2.28E-03	0.0650	0.4312	T3 (E) (42%), T4 (A) (16%), T5 (E) (10%), T2 (E) (6%)
	3.17105	2.02E-03	0.1557	0.4508	T4 (A) (50%), S1 (A) (12%)
	3.21028	4.27E-03	0.3072	0.4602	T3 (E) (32%), S1 (A) (28%), T6 (A) (10%), T4 (A) (10%)
	3.22443	7.71E-03	0.2525	0.4108	T5 (E) (34%), T4 (A) (12%), S2 (E) (10%), S3 (E) (6%)
	3.22778	7.77E-03	0.2530	0.4085	T5 (E) (18%), T4 (A) (14%), S3 (E) (11%), T6 (A) (10%), S2 (E) (10%)
	3.28922	1.66E-03	0.1234	0.4166	T5 (E) (30%), T6 (A) (29%), T3 (E) (10%), S1 (A) (9%)
	3.31060	4.68E-03	0.1618	0.4191	T3 (E) (31%), T5 (E) (14%), S2 (E) (7%), S3 (E) (7%)
	3.31253	4.59E-03	0.1592	0.4162	T3 (E) (32%), T5 (E) (18%), T6 (A) (12%), S3 (E) (7%), S2 (E) (7%)
	3.32982	8.35E-03	0.2069	0.4276	T5 (E) (24%), T6 (A) (18%), S3 (E) (14%), T3 (E) (11%)
	3.33065	9.71E-03	0.2547	0.4285	T5 (E) (24%), S3 (E) (17%), T3 (E) (11%), T6 (A) (10%)
	3.35114	8.95E-03	0.3498	0.4517	T4 (A) (24%), S2 (E) (15%), S3 (E) (15%), T5 (E) (11%)
	3.35239	1.07E-02	0.3918	0.4518	T5 (E) (23%), T4 (A) (20%), S3 (E) (18%), S2

					(E) (17%)
	3.35722	1.67E-03	0.0996	0.4387	T5 (E) (62%), T4 (A) (18%), S4 (A) (6%)
	3.36815	6.09E-05	0.0028	0.4110	T5 (E) (44%), T6 (A) (39%)
	3.39220	1.31E-02	0.4198	0.4448	T6 (A) (36%), S3 (E) (24%), S2 (E) (14%)
	3.39507	1.29E-02	0.4137	0.4403	T6 (A) (46%), S3 (E) (23%), S2 (E) (14%)
	3.46077	6.17E-03	0.7206	0.4336	S4 (A) (71%)
	3.50508	2.35E-02	0.5471	0.3712	S5 (E) (53%), T5 (E) (9%), T7 (E) (8%)
	3.50657	2.40E-02	0.5352	0.3645	S5 (E) (52%), T5 (E) (9%), T7 (E) (7%)
	3.52375	1.92E-03	0.1507	0.2362	T8 (A) (38%), T7 (E) (28%), S6 (A) (14%)
	3.54194	7.66E-05	0.0009	0.1609	T7 (E) (76%), T8 (A) (18%)
	3.54396	1.43E-04	0.0028	0.1726	T7 (E) (45%), T8 (A) (40%)
	3.54902	1.86E-03	0.0852	0.1687	T7 (E) (68%)
	3.55109	2.35E-03	0.0835	0.1819	T7 (E) (47%), T8 (A) (36%)
	3.55261	1.71E-03	0.0693	0.1881	T8 (A) (66%), T7 (E) (18%)
	3.55511	2.24E-04	0.0185	0.1669	T7 (E) (58%), T8 (A) (26%)
	3.56196	1.24E-02	0.2796	0.2313	T7 (E) (67%), S5 (E) (24%)
	3.56414	1.22E-02	0.2656	0.2345	T7 (E) (47%), S5 (E) (23%), T8 (A) (14%)
	3.60624	8.76E-03	0.7350	0.3879	S6 (A) (74%), T8 (A) (14%)
	3.85981	7.55E-05	0.0000	0.3663	T9 (A) (71%), T10 (E) (20%)
	3.86912	4.17E-04	0.0188	0.3704	T9 (A) (80%), T10 (E) (14%)
	3.86929	4.21E-04	0.0190	0.3697	T9 (A) (80%), T10 (E) (14%)
	3.87790	1.67E-04	0.0478	0.3605	T10 (E) (92%)
	3.89752	5.39E-04	0.0094	0.3597	T10 (E) (76%), T9 (A) (20%)
	3.90057	2.00E-05	0.0000	0.3556	T10 (E) (72%), T9 (A) (10%)
	3.90138	2.07E-05	0.0000	0.3537	T10 (E) (71%), T9 (A) (10%)
	3.90446	4.61E-04	0.0183	0.3545	T10 (E) (90%)
	3.90474	3.12E-04	0.0182	0.3551	T10 (E) (92%)
	4.23895	2.27E-03	0.1253	0.2431	T11 (A) (54%)
	4.24018	2.15E-03	0.1236	0.2378	T11 (A) (54%)
	4.25548	2.24E-04	0.0203	0.2716	T11 (A) (48%), T13 (A) (19%)
	4.26062	2.58E-04	0.4499	0.3733	S7 (A) (42%), T16 (E) (24%), T11 (A) (5%)
	4.28658	1.37E-03	0.0838	0.2471	T13 (A) (40%), T14 (E) (6%)
	4.28777	1.55E-03	0.0842	0.2499	T13 (A) (42%), T14 (E) (6%)
	4.31157	2.11E-04	0.0076	0.2346	T12 (E) (42%), T13 (A) (35%), T11 (A) (12%)
	4.31822	7.71E-04	0.0291	0.2276	T12 (E) (38%), T13 (A) (20%), T11 (A) (12%)
	4.32199	3.82E-04	0.0000	0.2321	T13 (A) (32%), T12 (E) (22%), T11 (A) (12%), T14 (E) (6%)
	4.32326	5.03E-04	0.0000	0.2333	T13 (A) (32%), T12 (E) (18%), T11 (A) (12%), T14 (E) (5%)
	4.32917	4.14E-04	0.0143	0.1572	T12 (E) (68%)
	4.33021	1.68E-04	0.0218	0.1682	T12 (E) (74%), T11 (A) (6%)
	4.33140	4.03E-04	0.0163	0.1543	T12 (E) (73%)
	4.34405	4.58E-04	0.0160	0.1738	T12 (E) (64%)
	4.34567	4.26E-04	0.0063	0.1795	T12 (E) (60%), T14 (E) (6%)
	4.35013	9.28E-04	0.0411	0.2844	T14 (E) (56%), T12 (E) (16%), T11 (A) (5%)
	4.35283	8.37E-04	0.0188	0.2763	T14 (E) (53%)

	4.35490	9.82E-04	0.0166	0.2768	T14 (E) (45%)
	4.36680	2.04E-03	0.1381	0.3302	T14 (E) (62%), S7 (A) (11%)
	4.38801	1.96E-03	0.1623	0.2775	T14 (E) (34%), T15 (A) (18%), S8 (E) (11%)
	4.38893	1.92E-03	0.1613	0.2779	T14 (E) (34%), T15 (A) (18%), S8 (E) (10%)
	4.39594	3.35E-04	0.3738	0.3585	T16 (E) (34%), S11 (A) (20%), S7 (A) (16%)
	4.41919	1.21E-03	0.0000	0.3106	T16 (E) (44%), T15 (A) (26%), T13 (A) (5%)
	4.42230	3.42E-03	0.3024	0.2576	T15 (A) (24%), S8 (E) (14%), T16 (E) (11%), S10 (E) (8%), T17 (E) (6%)
	4.42332	3.46E-03	0.3074	0.2507	T15 (A) (22%), S8 (E) (15%), T16 (E) (9%), S10 (E) (8%), T17 (E) (5%), S9 (E) (5%)
	4.43263	8.76E-04	0.0617	0.2866	T16 (E) (51%), T14 (E) (7%)
	4.43365	1.12E-03	0.0592	0.2847	T16 (E) (44%), T15 (A) (8%), T14 (E) (7%)
	4.43521	2.62E-03	0.0307	0.2926	T15 (A) (38%), T16 (E) (26%)
	4.44271	1.75E-03	0.0850	0.3040	T16 (E) (56%), T15 (A) (14%)
	4.44389	2.38E-03	0.0896	0.3015	T16 (E) (64%)
	4.47797	3.53E-03	0.8921	0.2575	S9 (E) (46%), S8 (E) (37%)
	4.48236	4.33E-03	0.8966	0.2583	S9 (E) (49%), S8 (E) (33%)
	4.50500	1.71E-03	0.2930	0.3474	S11 (A) (24%), T22 (E) (24%), T16 (E) (24%)
	4.52315	2.69E-04	0.0151	0.1864	T17 (E) (69%)
	4.52350	3.35E-04	0.0090	0.1847	T17 (E) (69%)
	4.52614	4.21E-04	0.0338	0.1946	T17 (E) (65%), T19 (E) (9%)
	4.52829	4.23E-04	0.0151	0.1962	T17 (E) (72%), T19 (E) (12%)
	4.53004	4.87E-04	0.0287	0.2034	T17 (E) (64%), T19 (E) (17%)
	4.53133	2.24E-04	0.0154	0.1958	T17 (E) (66%), T19 (E) (16%)
	4.56444	2.34E-03	0.1077	0.1999	T18 (A) (54%)
	4.56514	2.21E-03	0.0977	0.2130	T18 (A) (48%), T19 (E) (10%)
	4.56968	3.99E-04	0.0243	0.1919	T18 (A) (72%), T20 (A) (7%), T19 (E) (6%)
	4.57611	6.03E-03	0.2940	0.2418	S10 (E) (14%), S19 (E) (6%), S18 (E) (5%)
	4.57763	6.60E-03	0.3039	0.2368	S10 (E) (14%), S19 (E) (7%)
	4.58709	2.91E-03	0.4228	0.2040	S12 (A) (32%), T19 (E) (28%), T20 (A) (13%), S7 (A) (7%)
	4.60042	1.12E-02	0.5049	0.2788	S10 (E) (39%)
	4.60094	1.12E-02	0.5255	0.2678	S10 (E) (36%), S12 (A) (7%)
	4.60413	5.29E-03	0.6400	0.1582	S12 (A) (46%), S10 (E) (8%), S15 (A) (6%)
	4.61034	1.84E-03	0.1097	0.2102	T19 (E) (26%)
	4.61127	2.38E-03	0.1410	0.2002	T19 (E) (22%)
	4.61416	1.44E-03	0.9137	0.0539	S13 (A) (89%)
	4.62041	2.95E-03	0.2167	0.1969	T19 (E) (23%), T20 (A) (10%), S9 (E) (6%), S14 (E) (5%)
	4.62188	2.57E-03	0.1744	0.2124	T19 (E) (23%), T20 (A) (12%), S9 (E) (6%)
	4.63015	3.00E-04	0.0221	0.2375	T20 (A) (32%), T19 (E) (30%), T21 (A) (8%)
	4.63211	6.99E-04	0.0275	0.2139	T19 (E) (36%), T20 (A) (15%), T23 (A) (5%)
	4.64392	3.85E-03	0.1218	0.1755	T20 (A) (28%)
	4.64480	3.65E-03	0.0976	0.1721	T20 (A) (28%)
	4.65643	7.00E-03	0.3387	0.2911	T22 (E) (36%), S15 (A) (12%), S11 (A) (10%)
	4.66158	1.55E-02	0.6200	0.1998	S14 (E) (43%), T22 (E) (5%), S18 (E) (5%)
	4.66351	1.27E-02	0.5154	0.2224	S14 (E) (30%), T22 (E) (9%), S19 (E) (6%), S15

					(A) (6%)
	4.66962	4.43E-03	0.1284	0.1741	T21 (A) (24%), T22 (E) (17%)
	4.67119	4.96E-03	0.1750	0.1657	T21 (A) (24%), T22 (E) (12%), S14 (E) (12%)
	4.67343	6.89E-03	0.1677	0.1770	T21 (A) (20%), T24 (A) (8%), S15 (A) (8%)
	4.68377	3.62E-03	0.0875	0.2247	T22 (E) (36%), T21 (A) (16%)
	4.68546	3.40E-03	0.0623	0.2204	T22 (E) (34%), T21 (A) (16%)
	4.68850	3.05E-03	0.1489	0.2390	T23 (A) (21%), T21 (A) (17%), S11 (A) (9%)
	4.69425	3.80E-03	0.0308	0.1497	T21 (A) (29%), T24 (A) (8%), T23 (A) (7%)
	4.69572	3.28E-03	0.1306	0.1749	T21 (A) (18%), T23 (A) (10%)
	4.69721	3.78E-03	0.1327	0.1779	T21 (A) (16%), T23 (A) (12%)
	4.71218	7.59E-03	0.2133	0.1890	T21 (A) (16%), T23 (A) (14%), S19 (E) (13%), T24 (A) (12%)
	4.71333	9.21E-03	0.2281	0.1623	T24 (A) (11%), T23 (A) (8%), S14 (E) (6%), S15 (A) (6%)
	4.71507	9.14E-03	0.2108	0.1787	T24 (A) (18%), T23 (A) (17%), S15 (A) (10%), S19 (E) (6%)
	4.72521	3.13E-03	0.0526	0.1927	T24 (A) (32%), T25 (E) (21%), T22 (E) (6%)
	4.72633	2.36E-03	0.0579	0.1975	T24 (A) (42%), T25 (E) (17%), T22 (E) (5%)
	4.72665	6.03E-03	0.1906	0.2129	T24 (A) (23%), S15 (A) (14%), T22 (E) (12%), T23 (A) (9%)
	4.73863	1.05E-03	0.0214	0.1664	T25 (E) (68%), T22 (E) (12%)
	4.74063	9.23E-04	0.0154	0.1636	T25 (E) (68%)
	4.74332	1.40E-03	0.0363	0.1528	T25 (E) (70%)
	4.74970	2.22E-03	0.0838	0.1778	T25 (E) (44%), T24 (A) (28%)
	4.75155	2.34E-03	0.0851	0.1664	T25 (E) (56%), T24 (A) (20%)
	4.75466	2.97E-03	0.0352	0.1534	T25 (E) (62%), T24 (A) (25%)
	4.76753	3.24E-02	0.7996	0.2812	S16 (E) (70%), S17 (A) (5%)
	4.76859	1.98E-02	0.8021	0.2896	S16 (E) (75%)
	4.77805	6.95E-02	0.6952	0.2471	S17 (A) (64%)
	4.78785	3.04E-03	0.1697	0.4661	T28 (A) (64%), S31 (E) (7%)
	4.79079	3.73E-03	0.1723	0.4567	T28 (A) (62%), S31 (E) (6%), T34 (A) (5%)
	4.79458	3.01E-03	0.1645	0.2305	T26 (E) (54%), S11 (A) (11%)
	4.80426	2.12E-03	0.0419	0.1938	T26 (E) (66%)
	4.80526	1.70E-03	0.0263	0.1958	T26 (E) (62%)
	4.80814	9.55E-04	0.0292	0.1986	T26 (E) (68%), T23 (A) (5%)
	4.80959	9.02E-04	0.0342	0.1952	T26 (E) (67%)
	4.81211	1.24E-03	0.0412	0.1971	T26 (E) (68%)
	4.82381	3.02E-04	0.0149	0.4525	T28 (A) (64%), T29 (A) (10%)
	4.82707	5.65E-03	0.5923	0.3380	S20 (A) (31%), S22 (A) (26%)
	4.83391	5.47E-03	0.5998	0.3618	S18 (E) (44%), T23 (A) (20%), S19 (E) (11%)
	4.83551	5.34E-03	0.5294	0.3445	S18 (E) (36%), T23 (A) (16%), S19 (E) (8%), S22 (A) (5%)
	4.83609	5.14E-03	0.3766	0.3143	T27 (E) (28%), S22 (A) (18%), S18 (E) (14%)
	4.86157	1.95E-03	0.0456	0.2653	T27 (E) (40%), T22 (E) (9%)
	4.86402	4.49E-03	0.1096	0.2578	T27 (E) (36%), S21 (E) (8%), T22 (E) (7%)
	4.86549	5.05E-03	0.0872	0.2578	T27 (E) (47%), T23 (A) (11%)
	4.86746	5.84E-03	0.1566	0.2555	T27 (E) (40%)

	4.86906	6.63E-03	0.1740	0.2503	T27 (E) (34%), S21 (E) (8%)
	4.87256	2.69E-02	0.6815	0.1618	S21 (E) (61%)
	4.87539	7.44E-03	0.8348	0.3242	S20 (A) (51%), S22 (A) (30%)
	4.87856	2.60E-02	0.6519	0.1679	S21 (E) (54%)
	4.91720	3.31E-03	0.1129	0.2121	T30 (A) (50%), T29 (A) (12%), T32 (A) (6%)
	4.92348	4.06E-03	0.1108	0.2577	T30 (A) (40%), T29 (A) (24%), S19 (E) (6%)
	4.92463	4.48E-03	0.1069	0.2616	T30 (A) (38%), T29 (A) (26%), S19 (E) (5%), T27 (E) (5%)
	4.93215	1.23E-03	0.0371	0.2903	T29 (A) (32%), T30 (A) (8%)
	4.93507	1.09E-02	0.2402	0.2720	T30 (A) (32%), T29 (A) (22%), S19 (E) (10%), S24 (E) (6%)
	4.93629	9.91E-03	0.2248	0.2785	T30 (A) (26%), T29 (A) (24%), S19 (E) (10%)
	4.94410	3.48E-03	0.0573	0.1944	T31 (E) (38%), T30 (A) (7%)
	4.94677	3.92E-03	0.0746	0.2107	T31 (E) (56%), T27 (E) (6%)
	4.94928	4.78E-03	0.1962	0.2405	T31 (E) (20%), T33 (A) (14%), S25 (A) (6%), S23 (A) (5%)
	4.95741	5.28E-03	0.0957	0.2099	T31 (E) (42%)
	4.95811	5.79E-03	0.0954	0.2190	T31 (E) (42%)
	4.96096	1.92E-03	0.0518	0.2597	T31 (E) (40%), T33 (A) (14%), T29 (A) (7%)
	4.96562	8.08E-03	0.1378	0.2428	T33 (A) (32%), T34 (A) (12%), S24 (E) (5%)
	4.96771	8.08E-03	0.1724	0.2621	T33 (A) (50%), S24 (E) (8%)
	4.97031	4.06E-03	0.0641	0.2898	T34 (A) (36%), T33 (A) (21%)
	4.97496	5.81E-03	0.1045	0.2484	T31 (E) (23%), T35 (A) (18%), T34 (A) (14%)
	4.97736	9.16E-03	0.2467	0.2927	T34 (A) (18%), T35 (A) (18%), T33 (A) (16%), S27 (E) (7%), S24 (E) (5%)
	4.98034	8.28E-03	0.1913	0.3112	T34 (A) (39%), T31 (E) (10%), S23 (A) (7%), S26 (E) (7%)
	4.98389	1.34E-02	0.3344	0.2940	T35 (A) (28%), S23 (A) (15%), S26 (E) (12%)
	4.98759	1.15E-02	0.2121	0.3190	T35 (A) (34%), T34 (A) (22%), S24 (E) (12%)
	4.99104	2.43E-02	0.3917	0.2787	S26 (E) (29%), T34 (A) (14%), S24 (E) (7%)
	4.99276	1.57E-02	0.3558	0.2644	T34 (A) (14%), S26 (E) (13%), S25 (A) (10%), T33 (A) (7%)
	4.99555	1.92E-02	0.4324	0.2405	S24 (E) (16%), S25 (A) (12%), T35 (A) (10%), S27 (E) (6%), S26 (E) (6%)
	4.99883	6.82E-03	0.1151	0.2054	T32 (A) (35%), S23 (A) (5%)
	5.00055	2.80E-02	0.4988	0.2840	S26 (E) (36%), T35 (A) (17%), S24 (E) (7%)
	5.00117	1.22E-02	0.2229	0.2343	T32 (A) (14%), T35 (A) (12%), S24 (E) (9%), S27 (E) (8%)
	5.00255	1.25E-02	0.2595	0.2442	T32 (A) (42%), S27 (E) (6%), S24 (E) (6%), S26 (E) (6%)
	5.00267	8.91E-03	0.1736	0.2268	T32 (A) (56%), S26 (E) (9%)
	5.00618	1.22E-02	0.3886	0.3035	T35 (A) (18%), S23 (A) (18%), T34 (A) (14%), S25 (A) (6%), S27 (E) (6%), S26 (E) (6%)
	5.00744	9.29E-03	0.4561	0.2596	S25 (A) (25%), T35 (A) (24%), S23 (A) (11%)
	5.02073	2.97E-02	0.8429	0.3170	S27 (E) (48%), S29 (E) (18%), S24 (E) (7%), S26 (E) (7%)
	5.02309	3.00E-02	0.8015	0.3012	S27 (E) (50%), S29 (E) (12%), S24 (E) (8%), T35 (A) (5%)

	5.04801	6.20E-02	0.7994	0.2976	S28 (A) (68%), T32 (A) (10%)
	5.05442	4.36E-02	0.8821	0.2026	S29 (E) (74%), S27 (E) (6%)
	5.05734	4.27E-02	0.8689	0.2036	S29 (E) (70%)
	5.08118	1.74E-03	0.9418	0.2000	S30 (A) (92%)
	5.11375	3.50E-03	0.8502	0.4517	S31 (E) (71%), S32 (E) (6%)
	5.11603	1.93E-03	0.8416	0.4804	S31 (E) (75%)
	5.12128	2.45E-02	0.9649	0.1567	S32 (E) (93%)
	5.12198	2.23E-02	0.9576	0.1746	S32 (E) (89%), S31 (E) (6%)
	5.13528	6.21E-03	0.9826	0.1647	S33 (A) (98%)

Complex 2

Label	**Energy (eV)**	**f (a.u.)**	**Singlet Amount**	**MLCT Amount**	**Transitions**
1A	2.91664	1.10E-05	0.0000	0.4392	T1 (A) (77%)
2E	2.92532	1.77E-03	0.0424	0.4444	T1 (A) (84%)
2E’	2.92562	1.77E-03	0.0421	0.4448	T1 (A) (84%)
3A	2.96810	1.84E-03	0.0994	0.4208	T2 (E) (82%), S1 (A) (8%)
4E	2.98535	6.32E-05	0.0000	0.4065	T2 (E) (80%)
4E’	2.98704	7.11E-05	0.0000	0.4061	T2 (E) (80%)
5E	2.99150	5.09E-04	0.0244	0.4114	T2 (E) (80%), T1 (A) (7%)
6A	2.99260	8.81E-04	0.0305	0.4090	T2 (E) (86%)
5E’	2.99301	6.82E-04	0.0249	0.4074	T2 (E) (80%)
7A	3.13041	8.20E-03	0.4258	0.4594	S1 (A) (41%), T3 (E) (38%)
8E	3.19936	4.65E-03	0.3569	0.4240	S2 (E) (34%), T4 (A) (16%), T3 (E) (7%)
8E’	3.20275	4.64E-03	0.3627	0.4306	S2 (E) (34%), T4 (A) (16%), T3 (E) (8%)
	3.28821	1.07E-04	0.0043	0.4075	T3 (E) (70%), T5 (A) (11%), T1 (A) (10%)
	3.29394	4.00E-03	0.1440	0.4112	T3 (E) (50%), T4 (A) (10%), S2 (E) (7%)
	3.29609	3.73E-03	0.1359	0.4178	T3 (E) (48%), T4 (A) (14%), S2 (E) (6%)
	3.31359	1.09E-03	0.0162	0.3874	T3 (E) (36%), T6 (E) (20%), T4 (A) (12%), T2 (E) (6%)
	3.31525	8.03E-04	0.0113	0.3822	T3 (E) (34%), T6 (E) (21%), T4 (A) (16%), T2 (E) (6%)
	3.32299	2.95E-03	0.1813	0.4352	T4 (A) (47%), S1 (A) (9%), S4 (A) (9%)
	3.37980	6.27E-03	0.1725	0.3729	T6 (E) (35%), T5 (A) (22%), T7 (E) (9%), S5 (E) (8%)
	3.38266	6.44E-03	0.1744	0.3811	T6 (E) (42%), T5 (A) (16%), T7 (E) (9%), S5 (E) (8%)
	3.39182	3.01E-03	0.1675	0.3910	T6 (E) (32%), T5 (A) (22%), S1 (A) (10%), S6 (A) (7%), T8 (A) (6%)
	3.42512	5.72E-03	0.2953	0.4430	T3 (E) (48%), S1 (A) (28%), T5 (A) (7%)
	3.46629	2.33E-03	0.1599	0.4140	T3 (E) (46%), S2 (E) (14%), T6 (E) (13%)
	3.46834	2.24E-03	0.1584	0.4155	T3 (E) (46%), T6 (E) (16%), S2 (E) (14%)
	3.48930	4.58E-03	0.1243	0.3819	T5 (A) (26%), T3 (E) (23%), S3 (E) (8%), T6 (E) (7%)
	3.48951	4.70E-03	0.1311	0.3901	T3 (E) (24%), T5 (A) (20%), S3 (E) (9%), T6

					(E) (7%)
	3.50644	2.32E-04	0.0096	0.3791	T5 (A) (43%), T6 (E) (30%)
	3.52316	4.66E-03	0.2519	0.4298	T4 (A) (28%), T6 (E) (20%), S2 (E) (18%), S3 (E) (6%)
	3.52375	5.39E-03	0.2819	0.4319	T4 (A) (24%), S2 (E) (19%), T6 (E) (17%), S3 (E) (7%)
	3.52971	7.26E-04	0.0473	0.4223	T6 (E) (54%), T4 (A) (32%)
	3.56183	2.45E-02	0.6239	0.4413	S3 (E) (56%), T5 (A) (24%)
	3.56358	2.55E-02	0.6305	0.4438	S3 (E) (57%), T5 (A) (22%)
	3.64259	3.94E-03	0.3025	0.3577	T7 (E) (32%), S4 (A) (28%), T8 (A) (14%), T6 (E) (10%)
	3.65109	4.19E-03	0.1613	0.3104	T7 (E) (52%), S5 (E) (7%)
	3.65179	4.20E-03	0.1652	0.3152	T7 (E) (58%), S5 (E) (7%), S2 (E) (6%)
	3.65850	2.67E-03	0.1963	0.3327	T7 (E) (38%), T8 (A) (20%), S4 (A) (15%)
	3.66364	4.90E-04	0.0182	0.2778	T7 (E) (80%), T6 (E) (8%)
	3.66564	6.69E-04	0.0247	0.2811	T7 (E) (76%), T6 (E) (7%)
	3.68044	1.29E-03	0.0856	0.2915	T7 (E) (44%), T8 (A) (27%), S4 (A) (6%)
	3.68204	1.42E-03	0.0772	0.3018	T8 (A) (60%)
	3.68270	1.18E-03	0.0517	0.3036	T8 (A) (70%)
	3.68585	3.75E-03	0.2887	0.3215	T7 (E) (46%), S4 (A) (28%), T8 (A) (16%)
	3.72168	2.42E-02	0.7211	0.4103	S5 (E) (72%), T7 (E) (16%)
	3.72277	2.49E-02	0.7151	0.4089	S5 (E) (66%), T7 (E) (17%)
	3.77207	1.05E-02	0.7928	0.4323	S6 (A) (79%), T8 (A) (12%)
	3.84976	2.04E-04	0.0096	0.3562	T9 (A) (69%), T10 (E) (20%)
	3.85809	6.30E-04	0.0198	0.3637	T9 (A) (80%), T10 (E) (13%)
	3.85845	6.33E-04	0.0195	0.3630	T9 (A) (80%), T10 (E) (13%)
	3.86690	4.32E-04	0.0580	0.3621	T10 (E) (90%)
	3.88732	3.53E-04	0.0118	0.3607	T10 (E) (74%), T9 (A) (20%)
	3.89054	8.84E-05	0.0000	0.3560	T10 (E) (77%), T9 (A) (12%)
	3.89138	1.03E-04	0.0000	0.3540	T10 (E) (77%), T9 (A) (12%)
	3.89412	5.99E-04	0.0197	0.3563	T10 (E) (90%)
	3.89437	5.83E-04	0.0190	0.3563	T10 (E) (92%)
	4.24680	4.38E-03	0.2311	0.2655	T11 (A) (38%), S8 (E) (14%)
	4.24815	4.40E-03	0.2236	0.2675	T11 (A) (38%), S8 (E) (15%)
	4.26215	1.09E-03	0.4619	0.3389	S7 (A) (46%)
	4.32570	9.62E-04	0.0672	0.3140	T11 (A) (72%)
	4.34126	5.23E-04	0.0070	0.2661	T11 (A) (26%), T12 (A) (25%), T13 (E) (10%)
	4.34268	5.39E-04	0.0000	0.2613	T11 (A) (26%), T13 (E) (22%)
	4.35396	6.70E-04	0.0323	0.2805	T13 (E) (45%), T12 (A) (25%), T11 (A) (8%)
	4.36795	3.04E-03	0.1160	0.2696	T13 (E) (44%), T12 (A) (12%), T11 (A) (10%)
	4.36821	2.83E-03	0.0994	0.2714	T13 (E) (29%), T12 (A) (28%)
	4.37243	1.48E-03	0.1859	0.2774	T13 (E) (31%), S7 (A) (18%), T12 (A) (8%)
	4.37638	2.14E-03	0.0324	0.2646	T13 (E) (41%), T12 (A) (28%)
	4.37710	2.28E-03	0.0427	0.2604	T13 (E) (65%)
	4.37787	1.32E-03	0.0762	0.2585	T13 (E) (36%), T12 (A) (8%), S7 (A) (5%)
	4.40585	3.97E-03	0.3961	0.2049	S8 (E) (25%), S9 (E) (8%), T16 (E) (7%), T14 (E) (6%)

	4.40783	3.92E-03	0.3962	0.2097	S8 (E) (24%), S9 (E) (10%), T16 (E) (7%), T14 (E) (7%)
	4.41661	1.67E-03	0.0290	0.2096	T14 (E) (58%)
	4.42433	4.77E-04	0.0201	0.1995	T14 (E) (63%), T12 (A) (9%)
	4.42486	4.84E-04	0.0144	0.1948	T14 (E) (63%)
	4.42632	4.91E-04	0.0186	0.1939	T14 (E) (66%), T13 (E) (7%)
	4.42808	4.91E-04	0.0083	0.1888	T14 (E) (72%)
	4.42848	3.68E-04	0.0056	0.1881	T14 (E) (73%)
	4.44871	2.17E-03	0.0681	0.2172	T15 (E) (58%)
	4.45756	1.07E-03	0.0372	0.2176	T15 (E) (68%)
	4.45915	1.81E-03	0.3417	0.2306	T15 (E) (38%), S9 (E) (19%), S8 (E) (13%)
	4.46082	1.95E-03	0.3184	0.2242	T15 (E) (39%), S9 (E) (16%), S8 (E) (14%)
	4.46686	1.13E-03	0.1630	0.2274	T15 (E) (55%), S8 (E) (9%), T16 (E) (6%), S9 (E) (6%)
	4.46899	5.71E-04	0.0372	0.2207	T15 (E) (67%), T16 (E) (6%)
	4.47427	2.02E-03	0.3598	0.2301	T15 (E) (36%), S9 (E) (23%), S8 (E) (10%)
	4.47636	3.23E-03	0.5647	0.2389	S9 (E) (37%), S8 (E) (15%)
	4.49061	3.32E-03	0.1013	0.2203	T17 (A) (52%), S10 (E) (10%)
	4.49189	3.13E-03	0.0975	0.2187	T17 (A) (52%), S10 (E) (9%)
	4.49797	9.20E-04	0.0402	0.2170	T17 (A) (56%), T16 (E) (30%)
	4.52657	1.68E-03	0.0828	0.2580	T16 (E) (58%), S7 (A) (6%)
	4.53380	1.32E-03	0.0269	0.2185	T16 (E) (43%), T20 (E) (11%)
	4.53549	1.09E-03	0.0164	0.2058	T16 (E) (43%), T20 (E) (7%)
	4.53907	1.41E-03	0.0414	0.2034	T16 (E) (28%), T17 (A) (14%), T20 (E) (10%)
	4.54135	1.88E-03	0.1085	0.2067	T16 (E) (35%), S9 (E) (6%), T15 (E) (5%)
	4.54217	1.62E-03	0.0701	0.2113	T16 (E) (37%), T20 (E) (12%), T17 (A) (9%)
	4.55109	2.06E-03	0.0825	0.1992	T18 (A) (59%), T17 (A) (10%), S10 (E) (6%)
	4.55168	9.83E-04	0.0456	0.1846	T18 (A) (60%)
	4.55283	2.35E-03	0.1044	0.1957	T18 (A) (56%), S10 (E) (5%)
	4.58188	1.74E-02	0.4429	0.2098	S13 (A) (13%), S11 (A) (11%), S15 (A) (9%), S17 (A) (8%), T18 (A) (5%)
	4.58351	1.05E-03	0.7839	0.1235	S11 (A) (74%)
	4.59087	1.58E-02	0.5217	0.2704	S10 (E) (43%), T17 (A) (12%), T18 (A) (12%), S14 (E) (6%)
	4.59148	1.58E-02	0.5470	0.2692	S10 (E) (44%), T17 (A) (12%), T18 (A) (10%), S14 (E) (6%)
	4.61100	5.06E-03	0.8937	0.1093	S12 (A) (85%)
	4.61506	1.06E-02	0.2163	0.2144	T19 (A) (45%), S17 (A) (7%), S11 (A) (6%)
	4.62097	2.42E-03	0.0523	0.1952	T19 (A) (42%), T20 (E) (10%)
	4.62287	1.15E-03	0.0097	0.2059	T19 (A) (40%), T20 (E) (22%)
	4.62431	4.13E-03	0.2061	0.1928	T20 (E) (52%), S14 (E) (6%)
	4.62523	3.77E-03	0.1894	0.1928	T20 (E) (56%)
	4.63135	3.15E-03	0.1146	0.1929	T20 (E) (44%), T19 (A) (11%), T21 (A) (7%)
	4.63300	4.63E-03	0.1284	0.1729	T20 (E) (29%), T19 (A) (14%), S14 (E) (6%)
	4.63413	4.31E-03	0.0991	0.1714	T20 (E) (35%), T19 (A) (12%)
	4.65386	4.09E-03	0.0382	0.1909	T20 (E) (60%), T19 (A) (8%)
	4.66918	2.40E-02	0.6657	0.1594	S14 (E) (56%), S13 (A) (6%)

	4.67086	2.42E-02	0.6516	0.1460	S14 (E) (59%)
	4.68489	8.21E-03	0.2146	0.1960	T23 (A) (20%), S18 (A) (10%), T22 (E) (9%), S14 (E) (6%)
	4.68616	2.07E-02	0.5648	0.2170	S13 (A) (43%)
	4.68702	7.80E-03	0.2113	0.2035	T23 (A) (22%), S19 (E) (11%), T22 (E) (11%)
	4.70128	3.14E-03	0.0347	0.1753	T22 (E) (38%), T23 (A) (13%), T21 (A) (11%)
	4.72456	8.96E-03	0.1591	0.1657	T22 (E) (51%), S16 (E) (9%)
	4.72543	5.91E-03	0.1122	0.1539	T22 (E) (45%), T21 (A) (14%)
	4.73156	7.86E-03	0.1743	0.1779	T22 (E) (28%), T21 (A) (18%), S16 (E) (12%), T24 (E) (5%)
	4.73228	9.52E-03	0.1789	0.1750	T21 (A) (18%), T22 (E) (9%), S16 (E) (7%), T24 (E) (5%)
	4.73548	1.58E-02	0.3249	0.2251	S15 (A) (21%), T22 (E) (16%), T23 (A) (13%), S17 (A) (8%)
	4.74284	2.21E-03	0.0438	0.1631	T21 (A) (38%), T22 (E) (18%)
	4.74507	2.49E-03	0.0382	0.1640	T21 (A) (55%), T22 (E) (14%)
	4.74544	3.15E-03	0.0557	0.1615	T21 (A) (30%), T22 (E) (22%)
	4.74913	1.86E-02	0.4098	0.2798	S15 (A) (29%), T23 (A) (11%), S17 (A) (8%)
	4.75612	1.22E-02	0.2162	0.2030	S16 (E) (18%), T22 (E) (10%), T24 (E) (7%)
	4.75723	1.40E-02	0.2561	0.2030	S16 (E) (21%), T22 (E) (11%)
	4.76637	1.23E-02	0.0947	0.1802	T22 (E) (52%), T23 (A) (12%), S17 (A) (9%)
	4.77284	4.08E-03	0.0796	0.2290	T24 (E) (31%), T22 (E) (16%)
	4.77501	5.07E-03	0.0879	0.2254	T24 (E) (28%), T22 (E) (17%), S16 (E) (6%)
	4.77881	3.93E-03	0.0371	0.2542	T24 (E) (48%), T22 (E) (26%)
	4.78302	1.74E-02	0.3775	0.2582	S16 (E) (32%), T24 (E) (21%)
	4.78342	2.06E-02	0.4183	0.2600	S16 (E) (37%), T24 (E) (28%)
	4.79736	1.23E-02	0.2872	0.2091	S18 (A) (17%), S20 (A) (10%)
	4.79998	2.42E-02	0.3099	0.1943	S19 (E) (30%)
	4.80609	2.72E-02	0.2466	0.2748	T24 (E) (30%), S17 (A) (17%), T26 (E) (10%), T31 (A) (7%)
	4.90288	5.97E-03	0.0489	0.1819	T25 (A) (60%)
	4.90370	4.00E-03	0.0625	0.1764	T25 (A) (66%)
	4.90433	3.65E-03	0.0608	0.1778	T25 (A) (66%)
	4.91269	1.71E-02	0.1830	0.2393	T26 (E) (38%), T25 (A) (15%), S17 (A) (12%)
	4.91510	2.63E-02	0.4746	0.2517	S19 (E) (28%), S21 (E) (11%), T26 (E) (10%)
	4.91571	2.93E-02	0.4515	0.2418	S20 (A) (18%), T26 (E) (12%), S21 (E) (10%), S19 (E) (7%)
	4.92139	6.44E-03	0.0509	0.2198	T26 (E) (54%), T27 (E) (12%), T23 (A) (11%)
	4.92445	1.38E-03	0.0217	0.2053	T26 (E) (42%), T23 (A) (10%), T27 (E) (9%)
	4.92513	1.60E-03	0.0269	0.2022	T26 (E) (42%), T27 (E) (11%)
	4.93123	5.20E-03	0.0376	0.1597	T27 (E) (42%), T28 (A) (19%)
	4.93297	1.58E-02	0.2458	0.2031	T27 (E) (23%), S19 (E) (20%), T28 (A) (12%)
	4.93383	1.73E-02	0.2563	0.2026	S20 (A) (18%), T28 (A) (18%), T27 (E) (13%)
	4.93595	6.83E-03	0.1208	0.1700	T28 (A) (30%), T27 (E) (21%), S19 (E) (6%)
	4.93727	8.73E-03	0.1390	0.1733	T28 (A) (32%), T27 (E) (17%)
	4.94498	4.51E-03	0.0394	0.1626	T27 (E) (52%), T28 (A) (19%), T23 (A) (7%), T30 (A) (6%)

	4.95590	3.03E-03	0.0368	0.1657	T27 (E) (39%), T28 (A) (22%), T26 (E) (7%)
	4.95702	1.32E-03	0.0000	0.1419	T28 (A) (37%), T27 (E) (26%), T23 (A) (6%)
	4.95817	2.69E-03	0.0293	0.1609	T27 (E) (34%), T28 (A) (18%), T26 (E) (7%)
	4.96564	6.97E-03	0.0788	0.1858	T27 (E) (30%), T26 (E) (24%), S19 (E) (6%)
	4.96600	7.14E-03	0.0936	0.2041	T27 (E) (36%), T26 (E) (12%), S20 (A) (6%)
	4.98332	3.18E-02	0.5438	0.2707	S21 (E) (35%), S19 (E) (17%), T28 (A) (10%), T24 (E) (5%)
	4.98388	3.32E-02	0.5543	0.2785	S21 (E) (36%), S18 (A) (14%)
	4.98814	3.53E-02	0.3633	0.2096	T29 (E) (44%), S22 (A) (35%)
	4.99935	1.48E-03	0.0000	0.2082	T29 (E) (53%), T32 (E) (7%)
	4.99972	3.57E-03	0.0189	0.2070	T29 (E) (63%)
	5.00195	8.05E-04	0.0000	0.2339	T29 (E) (49%), T30 (A) (14%), T32 (E) (8%)
	5.00578	1.13E-02	0.1455	0.2275	T29 (E) (50%), S21 (E) (5%)
	5.00675	7.63E-03	0.1076	0.2285	T29 (E) (44%)
	5.01701	5.35E-02	0.5635	0.1933	S22 (A) (55%), T29 (E) (22%)
	5.02810	1.28E-03	0.1439	0.4541	T33 (A) (68%), S34 (E) (10%)
	5.02998	1.39E-03	0.1505	0.4714	T33 (A) (74%), S34 (E) (11%)
	5.04211	6.23E-03	0.0583	0.2476	T30 (A) (32%), T29 (E) (7%), S23 (A) (6%)
	5.05433	1.06E-02	0.1676	0.2755	T30 (A) (28%), T33 (A) (10%), S18 (A) (6%), T34 (A) (5%), S21 (E) (5%)
	5.05862	1.25E-02	0.1900	0.2641	T30 (A) (34%), S21 (E) (7%), T32 (E) (5%)
	5.06396	7.85E-03	0.0736	0.2515	T32 (E) (32%), T34 (A) (12%), T33 (A) (7%), T31 (A) (6%)
	5.06666	4.66E-03	0.0602	0.2291	T32 (E) (51%)
	5.07159	7.74E-03	0.1072	0.3061	T33 (A) (30%), T32 (E) (27%), T31 (A) (7%)
	5.07674	1.65E-02	0.2701	0.3273	T33 (A) (26%), T34 (A) (12%), S24 (A) (8%), S23 (A) (8%), T32 (E) (7%), S25 (E) (7%)
	5.07789	9.04E-03	0.1408	0.2193	T32 (E) (31%), S25 (E) (8%), T33 (A) (6%)
	5.07988	1.08E-02	0.1209	0.1987	T32 (E) (41%)
	5.08195	1.62E-02	0.7916	0.4806	S24 (A) (78%), T33 (A) (12%)
	5.09105	9.94E-03	0.1348	0.2383	T32 (E) (48%), T34 (A) (14%), S26 (A) (5%)
	5.09301	2.26E-02	0.3181	0.2832	T34 (A) (18%), S23 (A) (13%), T31 (A) (10%), T33 (A) (8%), S25 (E) (7%), T32 (E) (6%)
	5.09699	9.44E-03	0.1381	0.2355	T31 (A) (43%), T34 (A) (11%), S25 (E) (5%)
	5.10171	8.08E-03	0.1235	0.2512	T31 (A) (58%), S25 (E) (6%)
	5.11096	1.97E-02	0.3172	0.2268	S25 (E) (18%), T31 (A) (14%), T34 (A) (10%), S23 (A) (5%)
	5.11208	2.79E-02	0.4619	0.2231	S25 (E) (38%), T31 (A) (12%), T32 (E) (8%), S27 (E) (7%)
	5.11526	3.18E-02	0.5134	0.2310	S25 (E) (36%), T32 (E) (16%), T34 (A) (6%), S27 (E) (6%)
	5.12154	9.82E-03	0.1296	0.2735	T34 (A) (51%)
	5.12870	1.59E-02	0.2940	0.2662	T34 (A) (38%), S25 (E) (7%), S26 (A) (6%), S27 (E) (6%), S28 (A) (5%)
	5.13356	2.90E-02	0.3600	0.2751	T34 (A) (30%), S26 (A) (22%), S23 (A) (5%)
	5.15637	4.43E-02	0.7553	0.3127	S27 (E) (30%), S26 (A) (22%), S23 (A) (18%), T30 (A) (6%)
	5.17250	3.25E-02	0.7083	0.3003	S27 (E) (39%), S26 (A) (17%), T34 (A) (14%)

	5.17358	2.08E-02	0.7282	0.3000	S27 (E) (57%), T34 (A) (6%)
	5.18604	2.79E-02	0.7875	0.3394	S28 (A) (65%), T31 (A) (9%), S26 (A) (8%)
	5.20031	7.41E-03	0.9773	0.2173	S29 (E) (94%)
	5.20186	5.43E-03	0.9753	0.2532	S29 (E) (91%), S30 (E) (5%)
	5.21001	5.55E-03	0.9540	0.3692	S30 (E) (88%)
	5.21171	4.07E-03	0.9552	0.4077	S30 (E) (90%)
	5.25208	1.44E-01	0.9555	0.1906	S31 (A) (94%)
	5.28354	8.43E-03	0.9884	0.1265	S32 (E) (98%)
	5.28523	7.53E-03	0.9897	0.1264	S32 (E) (99%)
	5.30347	7.21E-02	0.9889	0.1324	S33 (A) (98%)
	5.34035	1.25E-03	0.8661	0.4822	S34 (E) (85%), T33 (A) (12%)
	5.34178	1.52E-03	0.8673	0.4839	S34 (E) (85%), T33 (A) (12%)

Complex 3

Label	**Energy (eV)**	**f (a.u.)**	**Singlet Amount**	**MLCT Amount**	**Transitions**
1A	2.82287	1.11E-05	0.0000	0.4557	T1 (A) (72%)
2E	2.83420	2.37E-03	0.0537	0.4628	T1 (A) (80%), T3 (E) (6%)
2E’	2.83473	2.37E-03	0.0540	0.4633	T1 (A) (80%), T3 (E) (6%)
3A	2.86673	1.32E-03	0.1305	0.4432	T2 (E) (78%), S1 (A) (11%)
4E	2.88226	8.93E-05	0.0000	0.4267	T2 (E) (72%)
4E’	2.88448	9.69E-05	0.0000	0.4243	T2 (E) (72%)
5A	2.89214	9.89E-04	0.0452	0.4342	T2 (E) (76%), T1 (A) (6%)
6E	2.89410	1.85E-03	0.0484	0.4282	T2 (E) (78%)
6E’	2.89454	1.37E-03	0.0488	0.4253	T2 (E) (72%)
7A	3.01048	3.63E-03	0.3463	0.4491	T3 (E) (38%), S1 (A) (32%)
8E	3.04909	3.84E-03	0.3406	0.4281	S2 (E) (32%), T4 (A) (18%)
8E’	3.05265	3.86E-03	0.3400	0.4259	S2 (E) (32%), T4 (A) (22%)
	3.17430	1.27E-03	0.0319	0.3936	T3 (E) (45%), T4 (A) (14%), T1 (A) (10%)
	3.17582	1.19E-03	0.0298	0.3887	T3 (E) (51%), T4 (A) (14%)
	3.17757	5.18E-04	0.0163	0.4007	T3 (E) (65%), T1 (A) (11%)
	3.18912	1.55E-03	0.0317	0.3987	T3 (E) (53%), T4 (A) (10%), T5 (E) (7%), T2 (E) (6%)
	3.19057	1.62E-03	0.0396	0.4009	T3 (E) (38%), T4 (A) (18%), T5 (E) (8%), T2 (E) (7%)
	3.20109	7.81E-04	0.0813	0.4152	T4 (A) (58%)
	3.26298	4.16E-03	0.3860	0.4510	S1 (A) (37%), T3 (E) (36%), T6 (A) (7%)
	3.27601	7.31E-03	0.2256	0.3887	T5 (E) (39%), S2 (E) (10%)
	3.27849	7.41E-03	0.2366	0.3824	T5 (E) (21%), T6 (A) (14%), S2 (E) (10%)
	3.31383	1.03E-03	0.0985	0.3820	T5 (E) (34%), T6 (A) (23%), S1 (A) (6%)
	3.32348	4.41E-03	0.1536	0.3814	T3 (E) (18%), T6 (A) (12%), S2 (E) (10%), T4 (A) (10%), T5 (E) (8%)
	3.32579	4.35E-03	0.1683	0.3788	T6 (A) (20%), T4 (A) (12%), S2 (E) (10%), T5 (E) (8%), T3 (E) (8%), S3 (E) (5%)
	3.35687	3.11E-03	0.0568	0.3798	T5 (E) (38%), T6 (A) (18%), T4 (A) (10%)

	3.35895	4.18E-03	0.1016	0.3772	T5 (E) (35%), T6 (A) (18%), T4 (A) (10%), S3 (E) (6%)
	3.37511	3.03E-03	0.1838	0.4120	T5 (E) (40%), T4 (A) (15%), S4 (A) (7%)
	3.37749	9.57E-03	0.3499	0.4101	T5 (E) (22%), S2 (E) (16%), S3 (E) (16%)
	3.37932	1.06E-02	0.3665	0.4023	T5 (E) (22%), S2 (E) (17%), S3 (E) (17%), T6 (A) (6%), T3 (E) (6%)
	3.38164	1.01E-03	0.0338	0.3706	T6 (A) (38%), T5 (E) (24%)
	3.43884	2.09E-02	0.5424	0.4401	S3 (E) (43%), T6 (A) (28%), S2 (E) (7%)
	3.44139	2.18E-02	0.5465	0.4362	S3 (E) (44%), T6 (A) (36%), S2 (E) (7%)
	3.48898	3.79E-03	0.5806	0.3855	S4 (A) (56%)
	3.52339	1.04E-02	0.2181	0.2580	T7 (E) (47%), S5 (E) (18%)
	3.52383	1.09E-02	0.2279	0.2599	T7 (E) (57%), S5 (E) (19%)
	3.53035	1.04E-03	0.0777	0.2158	T7 (E) (46%), T8 (A) (28%)
	3.53715	1.26E-04	0.0023	0.1755	T7 (E) (79%), T5 (E) (6%)
	3.53973	1.30E-04	0.0036	0.1792	T7 (E) (70%), T8 (A) (18%), T5 (E) (6%)
	3.54836	1.72E-03	0.1883	0.2076	T7 (E) (66%), S4 (A) (16%), T8 (A) (5%)
	3.55168	2.18E-03	0.0736	0.1992	T8 (A) (60%), T7 (E) (22%)
	3.55262	5.78E-04	0.0214	0.1854	T8 (A) (58%), T7 (E) (18%)
	3.55315	1.12E-03	0.0648	0.1949	T8 (A) (63%), T7 (E) (6%)
	3.57743	3.59E-02	0.6522	0.3511	S5 (E) (65%), T7 (E) (14%)
	3.57871	3.68E-02	0.6411	0.3482	S5 (E) (64%), T7 (E) (15%)
	3.64872	7.00E-03	0.8557	0.4169	S6 (A) (86%), T8 (A) (6%)
	3.95312	1.05E-04	0.0000	0.3735	T9 (A) (73%), T10 (E) (22%)
	3.96378	2.25E-04	0.0159	0.3760	T9 (A) (82%), T10 (E) (12%)
	3.96389	2.34E-04	0.0165	0.3764	T9 (A) (82%), T10 (E) (12%)
	3.97972	1.50E-03	0.0422	0.3630	T10 (E) (92%)
	4.00240	5.00E-04	0.0060	0.3651	T10 (E) (76%), T9 (A) (21%)
	4.00584	2.36E-05	0.0000	0.3626	T10 (E) (72%), T9 (A) (10%)
	4.00641	2.70E-05	0.0000	0.3624	T10 (E) (74%), T9 (A) (10%)
	4.00915	3.32E-04	0.0114	0.3610	T10 (E) (93%)
	4.00942	3.44E-04	0.0113	0.3616	T10 (E) (94%)
	4.29082	1.06E-04	0.0009	0.1330	T12 (E) (57%), T11 (A) (41%)
	4.29205	4.59E-04	0.0131	0.1323	T11 (A) (52%), T12 (E) (39%)
	4.29310	4.32E-04	0.0145	0.1330	T12 (E) (53%), T11 (A) (42%)
	4.29444	3.76E-04	0.0110	0.1328	T12 (E) (73%), T11 (A) (20%)
	4.30453	2.69E-04	0.0055	0.1310	T12 (E) (59%), T11 (A) (38%)
	4.30551	2.18E-04	0.0025	0.1320	T12 (E) (51%), T11 (A) (47%)
	4.30661	2.49E-04	0.0046	0.1337	T12 (E) (61%), T11 (A) (38%)
	4.30730	2.39E-04	0.0052	0.1324	T12 (E) (98%)
	4.30883	1.00E-04	0.0007	0.1332	T12 (E) (81%)
	4.38309	4.15E-03	0.5890	0.3363	S7 (A) (58%)
	4.40238	3.85E-03	0.2325	0.2160	T13 (A) (36%), S8 (E) (7%)
	4.40366	4.43E-03	0.2404	0.2143	T13 (A) (36%), S8 (E) (8%), S11 (A) (7%)
	4.43276	4.28E-04	0.0000	0.3361	T13 (A) (76%)
	4.45037	2.21E-03	0.2862	0.1946	T13 (A) (36%), S8 (E) (24%), T14 (E) (5%)
	4.45166	2.18E-03	0.2516	0.1902	T13 (A) (36%), S8 (E) (20%)

	4.47557	3.94E-03	0.6340	0.0827	S8 (E) (58%), T14 (E) (9%), S11 (A) (5%)
	4.47930	5.67E-03	0.1685	0.1505	T14 (E) (38%), T15 (E) (26%), S8 (E) (11%)
	4.48041	3.94E-03	0.5457	0.0818	S8 (E) (51%), T14 (E) (8%)
	4.49406	1.68E-03	0.0378	0.1394	T14 (E) (46%), T15 (E) (9%)
	4.49630	1.67E-03	0.0367	0.1327	T14 (E) (50%), T15 (E) (9%)
	4.50140	2.62E-03	0.1394	0.1842	T14 (E) (52%), S7 (A) (14%)
	4.51652	2.29E-03	0.0713	0.1148	T14 (E) (60%), S11 (A) (6%)
	4.51813	1.64E-03	0.0807	0.1040	T14 (E) (49%), T17 (A) (10%)
	4.52491	7.30E-04	0.0335	0.1400	T14 (E) (38%), T15 (E) (28%)
	4.52538	7.75E-04	0.0077	0.1523	T14 (E) (45%), T15 (E) (38%)
	4.52850	9.41E-04	0.0642	0.1564	T15 (E) (36%), T14 (E) (27%)
	4.52982	8.40E-04	0.0354	0.1664	T15 (E) (47%), T14 (E) (39%)
	4.53309	1.17E-03	0.0359	0.1647	T15 (E) (51%), T17 (A) (14%), T14 (E) (8%)
	4.53387	1.51E-03	0.0447	0.1641	T15 (E) (48%), T17 (A) (14%)
	4.54084	3.04E-03	0.1839	0.1179	T17 (A) (36%), T16 (A) (26%), S9 (A) (17%)
	4.55192	3.11E-03	0.6430	0.0966	S9 (A) (61%), T16 (A) (8%), T17 (A) (5%)
	4.55764	5.33E-03	0.3581	0.1874	S10 (E) (15%), T17 (A) (14%), T18 (E) (9%), S13 (E) (9%), S12 (E) (7%)
	4.55929	7.03E-03	0.3563	0.1869	S11 (A) (15%), S13 (E) (10%), T18 (E) (9%), S12 (E) (6%)
	4.56135	1.12E-03	0.1130	0.1732	T16 (A) (22%), T18 (E) (12%)
	4.56204	2.21E-04	0.0133	0.1149	T16 (A) (56%), T17 (A) (34%)
	4.56231	2.57E-04	0.0262	0.1044	T16 (A) (61%), T17 (A) (30%)
	4.56263	9.38E-04	0.0988	0.1469	T16 (A) (38%), T17 (A) (22%)
	4.57128	2.26E-03	0.0235	0.2682	T18 (E) (50%), T13 (A) (8%)
	4.57803	1.31E-02	0.9063	0.0929	S10 (E) (89%)
	4.58231	9.14E-04	0.0232	0.2325	T18 (E) (41%), T15 (E) (12%)
	4.58250	9.18E-04	0.0327	0.2307	T18 (E) (40%), T15 (E) (12%)
	4.59002	1.61E-03	0.0399	0.2367	T18 (E) (50%)
	4.59118	1.97E-03	0.0405	0.2301	T18 (E) (48%)
	4.61882	6.58E-03	0.7265	0.1541	S12 (E) (46%), S11 (A) (15%), T19 (A) (14%)
	4.62182	4.43E-03	0.6103	0.1582	S12 (E) (37%), T19 (A) (22%), S10 (E) (14%)
	4.62943	1.54E-03	0.0079	0.1777	T19 (A) (79%)
	4.63052	4.50E-03	0.2406	0.1929	T19 (A) (50%), S13 (E) (16%)
	4.63129	5.44E-03	0.3410	0.1883	T19 (A) (42%), S13 (E) (19%)
	4.65040	3.18E-02	0.2309	0.1253	T20 (E) (60%), S14 (A) (19%)
	4.65584	9.72E-04	0.0438	0.1171	T20 (E) (80%)
	4.65819	1.66E-03	0.1182	0.1108	T20 (E) (68%)
	4.66154	3.42E-03	0.3254	0.1202	T20 (E) (43%), S12 (E) (13%)
	4.66400	3.76E-03	0.1545	0.0988	T20 (E) (64%), S12 (E) (7%)
	4.66429	2.93E-03	0.1922	0.1158	T20 (E) (56%), S12 (E) (12%)
	4.67003	7.93E-03	0.3362	0.1496	T20 (E) (34%), S13 (E) (10%), S12 (E) (8%)
	4.67091	1.24E-02	0.4192	0.1610	T20 (E) (22%), S12 (E) (11%), S13 (E) (9%)
	4.67313	4.79E-02	0.3611	0.1835	S14 (A) (28%), T20 (E) (24%), T22 (E) (12%)
	4.70309	3.41E-03	0.2662	0.2904	S16 (A) (25%), T27 (E) (10%), T21 (A) (7%)
	4.70629	3.68E-04	0.0317	0.1653	T21 (A) (88%)

	4.70657	3.83E-04	0.0280	0.1670	T21 (A) (86%)
	4.71096	2.85E-03	0.0292	0.1650	T21 (A) (81%)
	4.73406	3.50E-03	0.0808	0.2367	T22 (E) (18%), T25 (A) (14%)
	4.73517	3.80E-03	0.1019	0.2264	T22 (E) (14%), T25 (A) (12%), S13 (E) (6%)
	4.74172	2.96E-03	0.1481	0.2528	T22 (E) (43%), S13 (E) (8%), T18 (E) (6%)
	4.74198	2.84E-03	0.1157	0.2542	T22 (E) (40%), S13 (E) (8%), T18 (E) (6%)
	4.75325	2.06E-02	0.1611	0.2356	T25 (A) (23%), S14 (A) (11%)
	4.75560	3.94E-03	0.0344	0.1808	T23 (E) (76%)
	4.75596	1.32E-03	0.0198	0.1850	T23 (E) (67%), T22 (E) (8%)
	4.75843	1.35E-03	0.0235	0.1839	T23 (E) (63%), T22 (E) (9%)
	4.76033	4.08E-03	0.0884	0.1815	T23 (E) (66%)
	4.76141	3.15E-03	0.1113	0.1753	T23 (E) (74%)
	4.76322	6.71E-03	0.0610	0.1838	T23 (E) (68%)
	4.77021	1.83E-02	0.1462	0.2337	T23 (E) (30%), T22 (E) (28%), S14 (A) (10%), T24 (A) (8%)
	4.77403	4.83E-03	0.1135	0.2137	T25 (A) (16%), T23 (E) (16%), S15 (E) (11%), T22 (E) (10%)
	4.77614	4.88E-03	0.1161	0.2230	T25 (A) (16%), T23 (E) (14%), T22 (E) (13%), S15 (E) (11%)
	4.79654	4.87E-03	0.2181	0.2472	T24 (A) (22%), T25 (A) (18%), S15 (E) (14%), S13 (E) (6%)
	4.79855	5.30E-03	0.2246	0.2454	T24 (A) (22%), T25 (A) (16%), S15 (E) (14%), S13 (E) (5%)
	4.80329	6.27E-03	0.0591	0.2844	T24 (A) (31%), T25 (A) (25%)
	4.82697	4.56E-03	0.0467	0.2946	T22 (E) (28%), T24 (A) (22%), T25 (A) (10%)
	4.83491	5.84E-03	0.6517	0.2025	S17 (E) (49%), S15 (E) (14%)
	4.83628	5.71E-03	0.6330	0.2092	S17 (E) (48%), S15 (E) (13%)
	4.84824	3.91E-03	0.3008	0.2465	S17 (E) (17%), T27 (E) (12%), T24 (A) (10%), S15 (E) (5%)
	4.84935	3.79E-03	0.3029	0.2429	T27 (E) (24%), S17 (E) (17%), S15 (E) (6%)
	4.86067	1.13E-02	0.1377	0.2982	T27 (E) (42%), T24 (A) (9%), S18 (A) (8%), T26 (A) (5%)
	4.86281	4.63E-03	0.1313	0.2689	T27 (E) (35%), S15 (E) (6%)
	4.86412	4.33E-03	0.1256	0.2761	T27 (E) (30%), T24 (A) (12%), S15 (E) (9%)
	4.87226	9.75E-03	0.3008	0.2386	T26 (A) (34%), S16 (A) (11%), S19 (A) (10%), S18 (A) (5%)
	4.87532	1.93E-03	0.0516	0.2442	T26 (A) (24%), T27 (E) (19%), S15 (E) (5%)
	4.87780	1.36E-03	0.0495	0.2456	T26 (A) (26%), T27 (E) (23%), T30 (A) (5%)
	4.88731	2.09E-02	0.3907	0.2305	T26 (A) (41%), S18 (A) (30%), S16 (A) (6%)
	4.89893	2.76E-03	0.1577	0.1809	T26 (A) (54%), T27 (E) (7%), S17 (E) (6%)
	4.89953	2.40E-03	0.1565	0.1854	T26 (A) (52%), T27 (E) (9%), S17 (E) (5%)
	4.90216	2.81E-02	0.5895	0.2931	S18 (A) (30%), S19 (A) (19%), T27 (E) (10%), S16 (A) (8%), T26 (A) (7%)
	4.93107	9.23E-03	0.3131	0.1775	T28 (E) (48%), S19 (A) (17%), S21 (A) (13%)
	4.93594	1.28E-02	0.3454	0.2406	S22 (E) (22%), T31 (A) (12%), S20 (E) (8%), S26 (E) (5%)
	4.93883	1.07E-02	0.3390	0.2162	T28 (E) (20%), T29 (A) (18%), S22 (E) (9%), S20 (E) (7%)

	4.93988	1.09E-02	0.3129	0.2032	T30 (A) (26%), T28 (E) (18%), S21 (A) (10%), S19 (A) (8%), S20 (E) (7%)
	4.94479	1.11E-02	0.2355	0.1999	T28 (E) (54%), S20 (E) (16%), T29 (A) (7%)
	4.94629	9.01E-03	0.1931	0.1902	T28 (E) (51%), T30 (A) (7%), S20 (E) (7%)
	4.95546	4.87E-03	0.1432	0.1833	T28 (E) (48%), T30 (A) (7%)
	4.95560	4.58E-03	0.0814	0.1796	T28 (E) (47%), T29 (A) (21%)
	4.95698	3.03E-03	0.0677	0.1879	T28 (E) (49%), T30 (A) (12%), T29 (A) (12%)
	4.97352	1.53E-02	0.3243	0.2354	S20 (E) (23%), T29 (A) (18%), T28 (E) (14%)
	4.97471	1.59E-02	0.2942	0.2409	S20 (E) (28%), T30 (A) (12%), T28 (E) (10%)
	4.97528	1.20E-02	0.3606	0.2223	T30 (A) (14%), S21 (A) (13%), S20 (E) (12%), T25 (A) (7%), S19 (A) (6%), T28 (E) (5%)
	4.98003	5.36E-03	0.2759	0.2271	T28 (E) (34%), S16 (A) (13%), S19 (A) (8%), T31 (A) (5%)
	4.98402	2.98E-03	0.0677	0.2372	T29 (A) (23%), T31 (A) (14%), T27 (E) (13%), T25 (A) (10%), T28 (E) (7%)
	4.98566	3.73E-03	0.0817	0.2455	T30 (A) (26%), T31 (A) (14%), T27 (E) (12%), T25 (A) (10%), S20 (E) (5%)
	4.98706	4.38E-03	0.3570	0.1724	S21 (A) (27%), T31 (A) (10%), S23 (A) (9%)
	4.99779	9.82E-03	0.1469	0.1981	S20 (E) (9%), T29 (A) (6%), S24 (E) (6%), T30 (A) (5%)
	4.99833	1.01E-02	0.1653	0.2051	S20 (E) (9%), S24 (E) (6%)
	5.00140	7.17E-03	0.3523	0.1709	S23 (A) (24%), T31 (A) (12%), T33 (A) (11%), S21 (A) (7%), T25 (A) (5%)
	5.00742	1.36E-02	0.2798	0.2170	T31 (A) (20%), T33 (A) (12%), T32 (E) (11%), S22 (E) (7%), S26 (E) (7%), S24 (E) (6%), S20 (E) (5%)
	5.00981	1.14E-02	0.2456	0.2158	T31 (A) (24%), T33 (A) (22%), T32 (E) (10%), S26 (E) (7%), S22 (E) (6%)
	5.01552	4.24E-03	0.2074	0.1792	T31 (A) (30%), T32 (E) (28%), S23 (A) (18%)
	5.01668	8.40E-03	0.2044	0.1989	T32 (E) (46%), T31 (A) (16%), S24 (E) (6%), S20 (E) (5%)
	5.01964	9.19E-03	0.2601	0.1981	T32 (E) (43%), T31 (A) (12%), S24 (E) (7%), S20 (E) (6%)
	5.02925	2.76E-03	0.0523	0.1653	T32 (E) (50%), T31 (A) (12%)
	5.03185	3.27E-03	0.0863	0.1697	T32 (E) (43%), S24 (E) (5%)
	5.03464	1.30E-02	0.6527	0.1780	S25 (A) (48%), T32 (E) (16%), S23 (A) (7%)
	5.04235	2.11E-02	0.6201	0.2189	S24 (E) (45%), T32 (E) (11%), S22 (E) (6%)
	5.04450	1.61E-02	0.5515	0.2180	S24 (E) (34%), T32 (E) (22%), S22 (E) (11%)
	5.04839	6.00E-03	0.2977	0.1682	T32 (E) (52%), S23 (A) (20%), T33 (A) (6%), T31 (A) (5%)
	5.05122	3.08E-02	0.5979	0.2600	S22 (E) (20%), S26 (E) (15%), S24 (E) (10%), S27 (E) (9%)
	5.05342	2.78E-02	0.5978	0.2363	S24 (E) (17%), S22 (E) (15%), S26 (E) (11%), S27 (E) (10%), T32 (E) (6%)
	5.05768	9.42E-03	0.4666	0.1780	T32 (E) (46%), S25 (A) (34%), S23 (A) (6%)
	5.07242	3.45E-03	0.0466	0.2274	T33 (A) (44%), T31 (A) (5%)
	5.07878	3.67E-02	0.4011	0.2288	T33 (A) (26%), S26 (E) (23%), S27 (E) (14%)
	5.07934	3.80E-02	0.4091	0.2382	T33 (A) (26%), S26 (E) (22%), S27 (E) (15%)
	5.08552	6.14E-02	0.5521	0.2198	S27 (E) (46%), T34 (E) (20%)

	5.08731	5.99E-02	0.5341	0.2147	S27 (E) (46%), T34 (E) (13%)
	5.10333	8.17E-03	0.1651	0.2443	T34 (E) (53%), S28 (E) (5%)
	5.10379	5.89E-03	0.1151	0.2560	T34 (E) (58%)
	5.10826	6.65E-03	0.1010	0.2785	T34 (E) (72%), T33 (A) (7%), S29 (A) (6%)
	5.11297	6.23E-03	0.0776	0.2706	T34 (E) (72%), T33 (A) (7%)
	5.11693	3.31E-02	0.7203	0.1902	S28 (E) (53%), S26 (E) (11%), T34 (E) (10%)
	5.11906	3.05E-02	0.7032	0.1997	S28 (E) (50%), T34 (E) (14%), S26 (E) (11%)
	5.14053	3.57E-02	0.5666	0.2114	S28 (E) (25%), S26 (E) (15%), T34 (E) (12%), S27 (E) (9%)
	5.14165	3.39E-02	0.5890	0.2111	S28 (E) (29%), S26 (E) (13%), T34 (E) (10%), T33 (A) (10%), S27 (E) (9%)
	5.17348	5.44E-02	0.7724	0.3933	S29 (A) (76%)
	5.20373	1.06E-02	0.9920	0.4807	S31 (A) (75%), S30 (E) (22%)
	5.24216	7.81E-03	0.8792	0.4247	S30 (E) (76%), S31 (A) (10%)
	5.24294	7.80E-03	0.8788	0.4274	S30 (E) (77%), S31 (A) (10%)
	5.25589	8.72E-02	0.8906	0.4193	S32 (A) (87%)
	5.31510	2.71E-02	0.9713	0.4405	S33 (A) (96%)
	5.34797	2.44E-01	0.9386	0.3419	S34 (A) (94%)

Complex 4

Label	**Energy (eV)**	**f (a.u.)**	**Singlet Amount**	**MLCT Amount**	**Transitions**
1A	2.99263	1.17E-05	0.0006	0.4102	T1 (A) (80%)
2E	2.99992	1.78E-03	0.0397	0.4158	T1 (A) (86%)
2E’	3.00029	1.79E-03	0.0388	0.4161	T1 (A) (86%)
3A	3.02789	9.45E-04	0.0698	0.3871	T2 (E) (86%)
4E	3.03575	7.15E-05	0.0000	0.3737	T2 (E) (79%)
4E’	3.03777	7.09E-05	0.0000	0.3701	T2 (E) (76%)
5E	3.04324	1.08E-03	0.0293	0.3770	T2 (E) (82%)
5E’	3.04386	1.16E-03	0.0302	0.3759	T2 (E) (82%)
6A	3.04610	3.95E-04	0.0249	0.3786	T2 (E) (84%), T1 (A) (6%)
7A	3.18667	6.49E-03	0.4280	0.4432	S1 (A) (41%), T3 (E) (38%)
8E	3.23329	4.26E-03	0.3606	0.4096	S2 (E) (36%), T4 (A) (14%), T3 (E) (6%)
8E’	3.23692	4.26E-03	0.3596	0.4088	S2 (E) (36%), T4 (A) (18%), T3 (E) (6%)
	3.33143	3.95E-05	0.0000	0.3826	T3 (E) (64%), T5 (A) (16%), T1 (A) (10%)
	3.33577	3.29E-03	0.0929	0.3840	T3 (E) (47%), T4 (A) (14%)
	3.33766	2.57E-03	0.0742	0.3813	T3 (E) (37%), T4 (A) (22%), T6 (E) (5%)
	3.34565	1.42E-03	0.0240	0.3686	T3 (E) (47%), T6 (E) (17%), T2 (E) (5%)
	3.34668	6.69E-04	0.0000	0.3578	T3 (E) (28%), T6 (E) (20%), T4 (A) (18%), T2 (E) (6%)
	3.35003	1.55E-03	0.1188	0.3914	T4 (A) (50%), S4 (A) (7%)
	3.42034	6.06E-03	0.1308	0.3570	T6 (E) (32%), T5 (A) (30%), T7 (E) (11%), S5 (E) (7%)
	3.42299	6.25E-03	0.1310	0.3635	T6 (E) (46%), T5 (A) (18%), T7 (E) (11%), S5 (E) (7%)

	3.43647	7.35E-04	0.0718	0.3745	T6 (E) (52%), T5 (A) (15%), T8 (A) (10%), S6 (A) (7%)
	3.47418	6.33E-03	0.4165	0.4478	T3 (E) (54%), S1 (A) (41%)
	3.50108	2.68E-03	0.2143	0.4001	T3 (E) (46%), S2 (E) (20%), T6 (E) (6%)
	3.50360	2.59E-03	0.2101	0.3984	T3 (E) (45%), S2 (E) (20%), T4 (A) (12%), T6 (E) (8%)
	3.52677	2.27E-03	0.0259	0.3534	T5 (A) (22%), T3 (E) (15%), T6 (E) (14%), T4 (A) (10%)
	3.52760	3.01E-03	0.0506	0.3566	T5 (A) (24%), T3 (E) (17%), T6 (E) (14%)
	3.53433	3.72E-04	0.0223	0.3692	T5 (A) (46%), T6 (E) (12%), T3 (E) (12%)
	3.54790	4.49E-03	0.2224	0.4010	T4 (A) (26%), T6 (E) (20%), S2 (E) (16%), T3 (E) (5%)
	3.54847	5.19E-03	0.2501	0.4001	T6 (E) (28%), T4 (A) (22%), S2 (E) (17%), T3 (E) (7%), S3 (E) (6%)
	3.55186	8.73E-04	0.0569	0.3819	T6 (E) (50%), T4 (A) (30%)
	3.63092	2.89E-02	0.6735	0.4405	S3 (E) (62%), T5 (A) (24%)
	3.63280	2.96E-02	0.6698	0.4385	S3 (E) (62%), T5 (A) (26%)
	3.67525	2.41E-03	0.2263	0.3338	T7 (E) (40%), S4 (A) (18%), T8 (A) (14%)
	3.68403	4.26E-03	0.1407	0.3053	T7 (E) (62%)
	3.68464	3.47E-03	0.1287	0.3048	T7 (E) (62%)
	3.69089	1.21E-03	0.0307	0.2853	T7 (E) (76%), T6 (E) (7%)
	3.69304	1.13E-03	0.0651	0.2897	T7 (E) (68%), T8 (A) (6%)
	3.69354	1.15E-03	0.0381	0.2851	T7 (E) (71%)
	3.70791	5.56E-04	0.0268	0.2953	T8 (A) (40%), T7 (E) (36%)
	3.71003	1.74E-03	0.1003	0.3163	T8 (A) (72%)
	3.71038	1.43E-03	0.0691	0.3074	T8 (A) (72%)
	3.71578	5.00E-03	0.5376	0.3739	S4 (A) (53%), T7 (E) (26%)
	3.76314	3.51E-02	0.7986	0.4241	S5 (E) (77%), T7 (E) (10%)
	3.76437	3.68E-02	0.7955	0.4238	S5 (E) (77%), T7 (E) (10%)
	3.82862	6.94E-03	0.8540	0.4353	S6 (A) (85%), T8 (A) (9%)
	3.94605	7.83E-05	0.0000	0.3737	T9 (A) (75%)
	3.95696	2.60E-04	0.0184	0.3815	T9 (A) (84%), T10 (E) (11%)
	3.95726	2.73E-04	0.0184	0.3819	T9 (A) (82%), T10 (E) (11%)
	3.97532	2.00E-03	0.0500	0.3671	T10 (E) (92%)
	3.99918	3.86E-04	0.0069	0.3690	T10 (E) (78%), T9 (A) (18%)
	4.00162	4.52E-05	0.0000	0.3633	T10 (E) (81%)
	4.00326	7.01E-05	0.0009	0.3663	T10 (E) (84%), T9 (A) (12%)
	4.00593	5.47E-04	0.0112	0.3639	T10 (E) (94%)
	4.00608	5.88E-04	0.0134	0.3647	T10 (E) (92%)
	4.37328	4.46E-03	0.1948	0.1354	T11 (A) (46%), S10 (A) (6%)
	4.37428	3.84E-03	0.1853	0.1267	T11 (A) (44%)
	4.39163	3.72E-03	0.5058	0.2876	S7 (A) (51%)
	4.40811	8.63E-04	0.0084	0.1520	T11 (A) (67%), T12 (E) (14%)
	4.42356	7.81E-04	0.0165	0.0815	T12 (E) (84%)
	4.42517	3.76E-04	0.0056	0.0885	T12 (E) (77%), T11 (A) (12%)
	4.42608	5.52E-04	0.0187	0.0810	T12 (E) (90%)
	4.42688	2.18E-04	0.0031	0.1005	T12 (E) (59%), T11 (A) (26%)

	4.42973	3.03E-04	0.0202	0.0894	T12 (E) (83%), T11 (A) (8%)
	4.43038	1.06E-04	0.0030	0.0831	T12 (E) (83%)
	4.44690	1.85E-03	0.1070	0.1157	T11 (A) (32%), S8 (E) (8%), T13 (E) (6%)
	4.44883	1.89E-03	0.1239	0.1074	T11 (A) (20%), T12 (E) (18%), S8 (E) (10%), T13 (E) (6%)
	4.47745	3.59E-03	0.8238	0.0758	S8 (E) (77%)
	4.48047	3.82E-03	0.0437	0.1758	T13 (E) (56%)
	4.48208	3.50E-03	0.8277	0.0709	S8 (E) (78%), T13 (E) (7%)
	4.49639	1.15E-03	0.0357	0.1579	T13 (E) (33%), T14 (A) (14%)
	4.49743	1.06E-03	0.0245	0.1604	T13 (E) (33%), T14 (A) (14%)
	4.50069	4.67E-03	0.1894	0.2220	T13 (E) (28%), S7 (A) (18%), T14 (A) (16%)
	4.50983	1.14E-03	0.0383	0.1895	T14 (A) (43%), T13 (E) (24%)
	4.51095	1.55E-03	0.0580	0.1849	T14 (A) (46%), T13 (E) (26%)
	4.51243	1.66E-03	0.0677	0.1886	T14 (A) (44%), T13 (E) (25%)
	4.53473	1.29E-03	0.0330	0.1268	T15 (A) (52%), T13 (E) (7%)
	4.53616	1.51E-03	0.0454	0.1308	T15 (A) (52%), T13 (E) (7%)
	4.53916	1.66E-03	0.0700	0.1610	T16 (E) (26%), T13 (E) (18%)
	4.53995	2.30E-03	0.0238	0.1521	T16 (E) (28%), T13 (E) (16%), T15 (A) (14%)
	4.54135	1.25E-03	0.0262	0.1348	T15 (A) (47%), T16 (E) (7%)
	4.54314	1.67E-03	0.1126	0.1449	T16 (E) (24%), T15 (A) (19%), T13 (E) (12%)
	4.54482	1.32E-03	0.0752	0.1592	T16 (E) (28%), T15 (A) (24%), T13 (E) (18%)
	4.54572	1.16E-03	0.0526	0.1701	T16 (E) (52%), T13 (E) (8%)
	4.54839	1.10E-03	0.0641	0.1736	T16 (E) (46%), T13 (E) (11%)
	4.55884	4.30E-03	0.1597	0.1900	T16 (E) (12%), T18 (E) (10%), S10 (A) (8%), S13 (E) (6%)
	4.55905	2.30E-03	0.1298	0.1577	T17 (A) (26%), T16 (E) (26%), T18 (E) (8%), S11 (A) (5%)
	4.56052	9.19E-04	0.0517	0.1679	T17 (A) (46%), T14 (A) (12%)
	4.56177	3.43E-03	0.1563	0.1775	T17 (A) (26%), S10 (A) (7%), T18 (E) (6%), S13 (E) (5%)
	4.56923	2.71E-03	0.2648	0.1358	T17 (A) (57%), S9 (A) (17%), S12 (A) (6%)
	4.57202	7.18E-03	0.7284	0.0991	S9 (A) (53%), T17 (A) (18%), S11 (A) (16%)
	4.57917	7.02E-03	0.6162	0.1371	S12 (A) (42%), S11 (A) (18%)
	4.58808	5.08E-03	0.2417	0.1887	T18 (E) (36%), T16 (E) (22%), S12 (A) (17%), S11 (A) (6%)
	4.59225	3.30E-03	0.0911	0.2351	T18 (E) (62%), T16 (E) (10%)
	4.59384	1.23E-03	0.0238	0.1860	T18 (E) (33%), T16 (E) (7%)
	4.59474	1.74E-03	0.0405	0.1948	T18 (E) (36%), T16 (E) (18%)
	4.59949	2.41E-03	0.0861	0.2026	T18 (E) (44%), T16 (E) (13%), T19 (E) (7%)
	4.60065	2.96E-03	0.0957	0.2059	T18 (E) (47%), T16 (E) (12%), T19 (E) (7%), S10 (A) (5%)
	4.62204	1.40E-02	0.7212	0.2163	S13 (E) (27%), S10 (A) (23%), S14 (E) (16%)
	4.62498	1.22E-02	0.7395	0.1959	S13 (E) (25%), S14 (E) (18%), S11 (A) (14%), S12 (A) (9%)
	4.66299	4.44E-02	0.2968	0.2063	T19 (E) (48%), S15 (A) (22%), S7 (A) (6%)
	4.66887	8.62E-03	0.2874	0.1894	T20 (A) (28%), S14 (E) (20%)
	4.66996	8.86E-03	0.2950	0.1935	T20 (A) (34%), S14 (E) (24%)

	4.67606	2.00E-03	0.0171	0.1808	T19 (E) (44%), T20 (A) (30%)
	4.68491	1.99E-03	0.0701	0.1798	T19 (E) (62%), T21 (E) (7%)
	4.68815	2.96E-03	0.0995	0.1798	T19 (E) (54%), T21 (E) (7%), S14 (E) (7%)
	4.69140	1.71E-03	0.1134	0.1974	T19 (E) (48%), S13 (E) (11%)
	4.69274	3.03E-03	0.1542	0.1901	T19 (E) (42%), S13 (E) (9%)
	4.69648	1.69E-03	0.0174	0.1867	T20 (A) (41%), T19 (E) (24%)
	4.70904	1.28E-02	0.4517	0.1977	T20 (A) (34%), S14 (E) (28%), S13 (E) (5%)
	4.71074	1.29E-02	0.4347	0.1933	T20 (A) (34%), S14 (E) (29%), T19 (E) (5%)
	4.71404	6.65E-02	0.3463	0.2005	T21 (E) (34%), S15 (A) (33%), T19 (E) (12%)
	4.75456	2.71E-03	0.0172	0.1975	T21 (E) (51%), T22 (A) (12%)
	4.75461	9.95E-03	0.0923	0.1976	T21 (E) (51%), S18 (A) (6%)
	4.75666	2.00E-03	0.0116	0.2027	T21 (E) (46%), T22 (A) (14%)
	4.76429	4.97E-03	0.1398	0.2186	T21 (E) (60%)
	4.76565	4.54E-03	0.1471	0.2248	T21 (E) (56%), S13 (E) (6%)
	4.77180	4.77E-02	0.2548	0.2249	T21 (E) (26%), S15 (A) (23%), T22 (A) (22%)
	4.79367	8.38E-03	0.2845	0.2359	S16 (E) (23%), T22 (A) (22%), T21 (E) (11%)
	4.79557	8.21E-03	0.2726	0.2379	T22 (A) (26%), S16 (E) (21%), T21 (E) (10%)
	4.79973	1.08E-02	0.1820	0.2524	T21 (E) (24%), S18 (A) (17%), T22 (A) (15%), T24 (A) (7%)
	4.82395	7.69E-03	0.1465	0.2435	T22 (A) (19%), S18 (A) (15%), T21 (E) (10%)
	4.82761	9.71E-03	0.3095	0.2268	T24 (A) (22%), S16 (E) (20%), T22 (A) (12%), T21 (E) (6%)
	4.82920	9.23E-03	0.2816	0.2218	T24 (A) (24%), S16 (E) (18%), T23 (A) (10%), T21 (E) (6%)
	4.84213	7.95E-03	0.1516	0.2023	T24 (A) (19%), T22 (A) (16%), S16 (E) (14%), T25 (E) (12%)
	4.84329	7.05E-03	0.1408	0.2034	T24 (A) (20%), T22 (A) (14%), T25 (E) (12%), S16 (E) (11%)
	4.84372	9.28E-03	0.0988	0.1981	T24 (A) (21%), T25 (E) (14%), T22 (A) (10%), T23 (A) (7%), S16 (E) (5%)
	4.86096	4.00E-03	0.0257	0.1688	T25 (E) (50%), T23 (A) (17%)
	4.86314	1.85E-03	0.0072	0.1750	T25 (E) (40%), T23 (A) (16%), T24 (A) (12%)
	4.86402	2.33E-03	0.0087	0.1733	T25 (E) (35%), T23 (A) (18%), T24 (A) (14%)
	4.87022	2.41E-02	0.6100	0.3058	S17 (A) (59%)
	4.87592	9.56E-04	0.0133	0.1711	T23 (A) (58%), T25 (E) (15%), T24 (A) (12%)
	4.87705	6.88E-04	0.0074	0.1686	T23 (A) (54%), T25 (E) (22%)
	4.87795	1.56E-03	0.0316	0.1762	T23 (A) (62%), T24 (A) (13%)
	4.88134	5.92E-03	0.1299	0.1817	T25 (E) (56%), S16 (E) (11%)
	4.88393	5.75E-03	0.1332	0.1807	T25 (E) (60%), S16 (E) (10%)
	4.89616	1.02E-02	0.2446	0.2384	T25 (E) (44%), S17 (A) (17%), T24 (A) (10%), S18 (A) (7%)
	4.92805	9.32E-03	0.0914	0.1684	T26 (E) (69%)
	4.92918	9.06E-03	0.0813	0.1646	T26 (E) (66%)
	4.93516	1.60E-03	0.0000	0.1651	T26 (E) (75%)
	4.93593	4.96E-04	0.0000	0.1689	T26 (E) (79%)
	4.93742	1.22E-03	0.0066	0.1657	T26 (E) (73%), T28 (E) (5%)
	4.95053	9.02E-03	0.0898	0.1850	T26 (E) (58%)

	4.95164	1.60E-02	0.1508	0.1775	T26 (E) (29%), T28 (E) (14%), T27 (A) (12%), S19 (E) (10%)
	4.95367	2.21E-02	0.1854	0.1853	T28 (E) (19%), T26 (E) (17%), S19 (E) (16%), T27 (A) (12%)
	4.98189	2.19E-02	0.1881	0.2030	T28 (E) (44%), S19 (E) (17%)
	4.98233	3.42E-03	0.0176	0.1783	T27 (A) (47%)
	4.98306	2.50E-02	0.2140	0.1957	T28 (E) (32%), S19 (E) (18%), T27 (A) (18%)
	4.98773	4.50E-02	0.3788	0.1970	S19 (E) (35%), T27 (A) (16%), T28 (E) (11%)
	4.98833	4.00E-02	0.3351	0.2049	T28 (E) (32%), S19 (E) (32%)
	4.99084	5.22E-03	0.0575	0.2161	T28 (E) (58%)
	5.00167	3.19E-03	0.0475	0.1900	T28 (E) (36%), T27 (A) (20%)
	5.00179	3.42E-03	0.0492	0.1837	T28 (E) (43%), T27 (A) (18%)
	5.00283	4.75E-03	0.0624	0.2002	T28 (E) (58%), T27 (A) (5%)
	5.02718	1.66E-02	0.3507	0.2905	S22 (E) (25%), T29 (E) (10%), S19 (E) (7%), T28 (E) (5%)
	5.02996	1.59E-02	0.3397	0.2849	S22 (E) (24%), T29 (E) (12%), S19 (E) (7%), T28 (E) (6%)
	5.04328	3.34E-02	0.6856	0.2350	S21 (A) (58%), T29 (E) (12%), S18 (A) (10%)
	5.05909	3.37E-02	0.5654	0.2552	S20 (E) (55%), T29 (E) (15%)
	5.06070	3.23E-02	0.5279	0.2509	S20 (E) (46%), T29 (E) (18%)
	5.07168	1.95E-02	0.3026	0.2614	T29 (E) (39%), S20 (E) (22%)
	5.07242	1.99E-02	0.2978	0.2583	T29 (E) (38%), S20 (E) (23%)
	5.07310	3.98E-03	0.0574	0.2616	T29 (E) (58%), T27 (A) (18%)
	5.08904	1.31E-02	0.2942	0.2547	T29 (E) (32%), T30 (A) (25%), S18 (A) (13%), S21 (A) (12%)
	5.10425	7.49E-03	0.1968	0.2954	T29 (E) (52%), S22 (E) (15%)
	5.10564	7.27E-03	0.1953	0.2931	T29 (E) (53%), S22 (E) (15%)
	5.12273	4.48E-03	0.0573	0.1745	T30 (A) (66%)
	5.12343	4.21E-03	0.0496	0.1712	T30 (A) (68%)
	5.12623	1.09E-02	0.2329	0.2038	T30 (A) (41%), S21 (A) (13%), S18 (A) (6%)
	5.13335	3.09E-03	0.2777	0.1685	T33 (E) (42%), S24 (A) (26%), T31 (E) (10%)
	5.14125	4.30E-03	0.0770	0.2164	T31 (E) (57%)
	5.14220	4.07E-03	0.0696	0.2097	T31 (E) (55%)
	5.14690	5.86E-03	0.0620	0.2003	T31 (E) (29%), T33 (E) (19%)
	5.14840	7.39E-03	0.0926	0.2016	T33 (E) (34%), T31 (E) (29%)
	5.15020	3.76E-03	0.0497	0.1826	T33 (E) (58%), T31 (E) (24%)
	5.15581	6.34E-03	0.0695	0.1764	T33 (E) (51%), T32 (A) (11%)
	5.15707	7.31E-03	0.1045	0.1595	T33 (E) (69%), S23 (E) (6%)
	5.15982	2.74E-02	0.1475	0.2235	T31 (E) (42%), S26 (A) (11%), T32 (A) (11%), T33 (E) (9%)
	5.16678	1.00E-02	0.1177	0.1980	T31 (E) (32%), T33 (E) (18%), S24 (A) (7%)
	5.16829	3.74E-03	0.0662	0.1929	T33 (E) (50%), S22 (E) (5%)
	5.17024	9.18E-03	0.1458	0.2014	T31 (E) (28%), T32 (A) (16%), S24 (A) (6%)
	5.18557	4.75E-03	0.5248	0.1540	S24 (A) (49%), T33 (E) (30%), T32 (A) (7%)
	5.19211	3.35E-02	0.7847	0.2292	S25 (E) (57%), S23 (E) (20%)
	5.19256	3.98E-02	0.7122	0.2819	S23 (E) (34%), S25 (E) (31%)
	5.19625	2.80E-02	0.6570	0.2550	S25 (E) (36%), S23 (E) (15%), S22 (E) (12%),

					T31 (E) (6%)
	5.19764	3.65E-02	0.6915	0.2922	S23 (E) (33%), S25 (E) (23%), S22 (E) (13%), T31 (E) (5%)
	5.20661	8.18E-03	0.0698	0.2011	T32 (A) (26%), T31 (E) (22%), T33 (E) (10%), T30 (A) (7%)
	5.22786	2.20E-02	0.5730	0.2505	T32 (A) (24%), S27 (E) (17%), S23 (E) (13%), S22 (E) (12%), S25 (E) (11%)
	5.22897	1.79E-02	0.6174	0.2369	S27 (E) (31%), T32 (A) (22%), S22 (E) (11%), S25 (E) (9%), S23 (E) (5%)
	5.23757	6.85E-02	0.9480	0.2056	S28 (A) (50%), S26 (A) (27%), S27 (E) (15%)
	5.24375	1.44E-02	0.7795	0.1912	S27 (E) (62%)
	5.24474	1.33E-02	0.8755	0.1768	S27 (E) (56%), S28 (A) (22%)
	5.26740	4.88E-02	0.9084	0.1778	S29 (A) (64%), S26 (A) (15%), S28 (A) (9%)
	5.29516	7.35E-02	0.7540	0.2114	S29 (A) (33%), S26 (A) (28%), S28 (A) (10%), T32 (A) (7%)
	5.33432	2.30E-03	0.8953	0.3614	S30 (E) (83%), S33 (E) (5%)
	5.33531	2.34E-03	0.8916	0.3648	S30 (E) (84%)
	5.34950	5.40E-02	0.9257	0.4131	S31 (A) (83%), S32 (A) (8%)
	5.35843	2.29E-03	0.9769	0.1378	S33 (E) (90%)
	5.36043	5.81E-02	0.9540	0.3813	S32 (A) (62%), S35 (A) (18%), S33 (E) (9%), S31 (A) (6%)
	5.36190	6.24E-03	0.9782	0.1338	S33 (E) (85%), S32 (A) (6%)
	5.38279	1.95E-02	0.9570	0.3694	S34 (A) (92%)
	5.38886	1.64E-02	0.9562	0.4459	S35 (A) (77%), S32 (A) (16%)

Appendix D

Supplementary Video Animation to Chapter 6

Neutron Reflectometry Animation

Figure 6.5a

Film 1

Appendix E

Published papers arising from this Thesis

Copyright Acknowledgements

Smith, A. R. G.; Riley, M. J.; Lo, S.-C.; Burn, P. L.; Gentle, I. R.; Powell, B. J., Physical Review B, 83, 041105(R). "Copyright (2011) by the American Physical Society."

License Number	2772890079683
License date	Oct 20, 2011
Licensed content publisher	John Wiley and Sons
Licensed content publication	ChemPhysChem
Licensed content title	Spin–Orbit Coupling in Phosphorescent Iridium(III) Complexes
Licensed content author	Arthur R. G. Smith, Paul L. Burn, Ben J. Powell
Licensed content date	Sep 12, 2011
Start page	2429
End page	2438
Type of use	Dissertation/Thesis
Requestor type	Author of this Wiley article
Format	Print and electronic
Portion	Full article
Will you be translating?	No

Reprinted (adapted) with permission from Smith, A. R. G.; Riley, M. J.; Burn, P. L.; Gentle, I. R.; Lo, S.-C.; Powell, B. J. Effects of Fluorination on Iridium(III) Complex Phosphorescence: Magnetic Circular Dichroism and Relativistic Time-Dependent Density Functional Theory, Inorg. Chem. **2012**, *51*, 2821. Copyright (2012) American Chemical Society.

License Number	2772881073337
License date	Oct 20, 2011
Licensed content publisher	John Wiley and Sons
Licensed content publication	Advanced Functional Materials
Licensed content title	Investigating Morphology and Stability of Fac-tris (2-phenylpyridyl)iridium(III) Films for OLEDs
Licensed content author	Arthur R. G. Smith, Jeremy L. Ruggles, Hamish Cavaye, Paul E. Shaw, Tamim A. Darwish, Michael James, Ian R. Gentle, Paul L. Burn
Licensed content date	Jun 21, 2011
Start page	2225
End page	2231
Type of use	Dissertation/Thesis
Requestor type	Author of this Wiley article
Format	Print and electronic
Portion	Full article
Will you be translating?	No

License Number	2772881320049
License date	Oct 20, 2011
Licensed content publisher	John Wiley and Sons
Licensed content publication	Advanced Functional Materials
Licensed content title	Organic Light-Emitting Diodes: Investigating Morphology and Stability of Fac-tris (2-phenylpyridyl)iridium(III) Films for OLEDs (Adv. Funct. Mater. 12/2011)
Licensed content author	Arthur R. G. Smith, Jeremy L. Ruggles, Hamish Cavaye, Paul E. Shaw, Tamim A. Darwish, Michael James, Ian R. Gentle, Paul L. Burn
Licensed content date	Jun 21, 2011
Start page	2164
End page	2164
Type of use	Dissertation/Thesis
Requestor type	Author of this Wiley article
Format	Print and electronic
Portion	Full article
Will you be translating?	No

License Number	2872781354199
License date	Mar 19, 2012
Licensed content publisher	John Wiley and Sons
Licensed content publication	Advanced Materials
Licensed content title	Diffusion – the Hidden Menace in Organic Optoelectronic Devices
Licensed content author	Arthur R. G. Smith, Kwan H. Lee, Andrew Nelson, Michael James, Paul L. Burn, Ian R. Gentle
Licensed content date	Feb 7, 2012
Start page	822
End page	826
Type of use	Dissertation/Thesis
Requestor type	Author of this Wiley article
Format	Print and electronic
Portion	Full article
Will you be translating?	No

PHYSICAL REVIEW B **83**, 041105(R) (2011)

Relativistic effects in a phosphorescent Ir(III) complex

A. R. G. Smith,[1,2] M. J. Riley,[2] S.-C. Lo,[1,2] P. L. Burn,[1,2] I. R. Gentle,[2] and B. J. Powell[1,3,*]

[1]*Centre for Organic Photonics & Electronics, University of Queensland, Brisbane, Queensland 4072, Australia*

[2]*School of Chemistry & Molecular Biosciences, University of Queensland, Brisbane, Queensland 4072, Australia*

[3]*School of Mathematics & Physics, University of Queensland, Brisbane, Queensland 4072, Australia*

(Received 8 December 2010; published 21 January 2011)

We compare high field magnetic circular dichroism, absorption, and photoluminescence spectra for $Ir(ptz)_3$ with time-dependent density functional theory. By gradually turning on the relativistic effects we identify several distinct relativistic effects in the spectra of this complex. We show that relativistic effects must be included to accurately predict the low-temperature spectra. This leads to new insights into the low-lying excitations responsible for the observed phosphorescence, and suggests new avenues to improve the performance of organic light emitting diodes.

DOI: 10.1103/PhysRevB.83.041105 PACS number(s): 81.05.Lg, 31.15.aj, 33.55.+b, 85.60.Jb

Relativistic effects lead to many important phenomena in heavy metals such as gold's yellow color[1] and lead's face-centered cubic-crystal structure, which causes it to be a metal rather than an insulator.[2] However, to date, little is known about relativistic effects in organometallic complexes. One expects relativistic effects to play an important role on the metal, but to be negligible on the organic ligand. Therefore, relativistic effects need to be properly included to give a thorough description of metal-to-ligand charge transfer (MLCT) excitations, which are often important in organometallic complexes. The phosphorescent decay and fast intersystem crossing[3] observed in organometallic complexes are mediated by spin-orbit coupling (SOC). For closed-shell molecules SOC only appears at second order (in, say, $1/c^2$).[4] Thus, first-order corrections also need to be considered.

Understanding these effects is important because organometallic complexes hold enormous promise as the active components in optoelectronic devices such as organic light emitting diodes (OLEDs) and dye-sensitized solar cells. Since the seminal report[5] of an OLED comprised of a phosphorescent Ir(III) complex there has been a plethora of papers describing new complexes and their use in devices.[6] However, while some general design principles are now known[7] less is understood about why small variations can cause large changes in, for example, the photoluminescence quantum yield (PLQY).[8–11] Understanding the photophysical and electronic properties of these complexes remains a major challenge and the major impediment to the rational design of new, highly emissive materials and complexes used in photovoltaic devices.

Time-dependent density functional theory (TDDFT) has been routinely applied to describe the optical properties of new Ir(III) complexes since Hay[12] first showed that TDDFT could reproduce excitation energies of Ir(III) complexes reasonably accurately.

However, these TDDFT calculations do not, typically, include relativistic effects, such as SOC.[13] They are therefore incapable of describing the fine structure of Ir(III) complexes that low-temperature (LT) spectroscopic measurements reveal.[8,14] This is a major problem as these measurements suggest that the fine structure of the excitations plays an important role in determining optoelectronic properties and hence the performance of OLED's based on these materials.

In this Rapid Communication we report LT absorption, photoluminescence (PL), and magnetic circular dichroism (MCD) spectra of the blue emissive phosphorescent $Ir(ptz)_3$ complex (Fig. 1). We calculate these spectra via three flavors of TDDFT: *nonrelativistic* (NR) calculations based on the Schrödinger equation; *scalar relativistic* (SR)[4] calculations based on the zeroth-order regular approximation (ZORA)[15] to the Dirac equation; and second-order perturbation theory in the SOC[15] about the SR results. We report all electron TDDFT calculations[16] performed in ADF[17] using the Becke, three-parameter, Lee-Yang-Parr (B3LYP) functional with a triple-ζ polarized basis of Slater orbitals.[18,19]

We show that relativistic effects must be taken into account before one can accurately predict the spectra of Ir(III) complexes. Once both the SR and SOC corrections are included we are able to explain the observed LT MCD, absorption and PL spectra. This combination of LT spectroscopy and relativistic theory allows us to resolve a number of fundamental issues about the nature of the excited states in general and the emissive state in particular. $Ir(ptz)_3$ has a solution PLQY of 66% and Commission Internationale de l'Eclairage coordinates of (0.16, 0.20).[9] The addition of electron withdrawing groups to the ligand causes the PL to blue shift, but this comes at the cost of a dramatic decrease in the PLQY.[9] Hence, we were motivated to understand the excitation spectra of this complex as a starting point for developing deeper blue compounds that might form the basis of highly efficient OLED's as well as providing a platform for the design of highly luminescent complexes that emit across the visible spectrum.

We collected the LT (10 K), high field (5 T) MCD spectrum of $Ir(ptz)_3$ in 2-methyltetrahydrofuran (Fig. 2).[16] The LT absorption spectrum (Fig. 2), measured simultaneously, is significantly sharper than that at room temperature[9] and shows extra features throughout the absorption band. A clear MCD A term, indicating a transition to a degenerate excited state,[20] is found around the lowest-energy band at ~2.8 eV. There appears to be at least one shoulder in this peak, suggesting that there is more than one degenerate state in this energy range. The oscillations present at higher energies could be several overlapping A terms, or a combination of A and B terms. A detailed mapping of the low-energy excitations of $Ir(ptz)_3$ is therefore not possible from this experimental data alone.

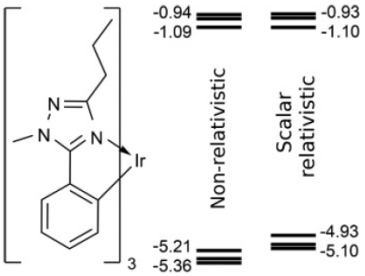

FIG. 1. *Fac*-tris (1-methyl-5-phenyl-3-*n*-propyl-[1,2,4]triazolyl) iridium(III), $Ir(ptz)_3$, (left) and a schematic MO energy level diagram for the NR and SR DFT calculations.

Nonetheless, the MCD clearly demonstrates that there are several states with small oscillator strengths at low energies.

In an effort to understand the photophysical properties of $Ir(ptz)_3$ we used NR-TDDFT to calculate its excitation spectrum. Figure 2(a) shows a level of agreement with the measured absorption spectrum that is typical of the accuracy

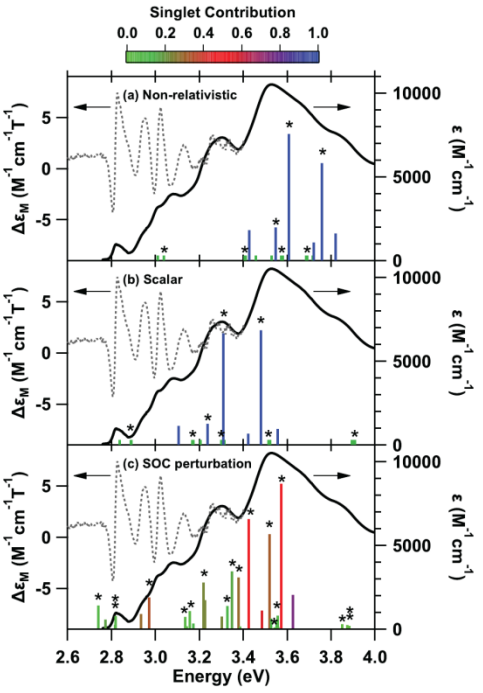

FIG. 2. (Color online) Absorption (solid line) and MCD (dashed line) spectra of $Ir(ptz)_3$ collected at 10 K under an applied field of 5 T compared to the "stick" absorption spectra calculated by (a) NR-TDDFT, (b) SR-TDDFT, and (c) perturbative SOC correction to the SR calculation. Degenerate (E) states are denoted with * (** marks two nearby E states). In the NR and SR calculations the (formally forbidden) triplet excitations are given small arbitrary oscillator strengths for clarity.

of this method for this type of complex. Specifically, there is a large density of states coincident with the strongest peak in the absorption with a smaller number of weaker transitions at longer wavelengths. If the comparison to the experiment were limited to room temperature absorption this may appear to be reasonable agreement. However, the LT spectroscopic data make it clear that there are a large number of states at lower energies not reproduced by NR-TDDFT. Further, NR-TDDFT does not predict sufficient numbers of low-energy states to describe the MCD spectrum even qualitatively. Finally, the lowest-energy triplet state is 0.25 eV above the first peak in the PL spectrum.

We therefore turned to SR-TDDFT [Fig. 2(b)]. Comparing these results to the NR-TDDFT [Fig. 2(a)], one immediately notices dramatic improvements in the correlation between the calculated transitions and measured absorption spectrum. There are singlet states with large oscillator strengths at energies close to each of the three largest peaks in the absorption. Further, the SR calculation also predicts three low-energy triplets with energies comparable to the lowest-energy features in the absorption and, importantly, the highest-energy features in the PL. However, these calculations do not provide sufficient accuracy to explain the MCD; we will show in the following that SOC is vital for understanding the MCD.

Understanding of the physical origin of the differences in the NR and SR excitation spectra is aided by considering the Kohn-Sham molecular orbitals (MO's) of the underlying DFT calculations. Both calculations predict that the highest-occupied MO (HOMO) and lowest-unoccupied MO (LUMO) are nondegenerate A states, whereas the HOMO−1 and LUMO+1 are two-fold degenerate E manifolds (cf., Fig. 1). Plots of the electron densities of these MO's (Fig. 3) show that the occupied orbitals have a significant contribution from the Ir atom whereas the virtual orbitals do not. A Mulliken population analysis[16] shows that the Ir 5*d* orbitals contribute ∼50% of the electron density in both the HOMO and HOMO−1.

To connect the DFT orbitals to the TDDFT spectra we report the MO weights of the transitions.[16] The two strongest singlets, S_3 and S_5, belong to the E representation of C_3. These excitations are dominated (> 92 %) by the HOMO−1 →

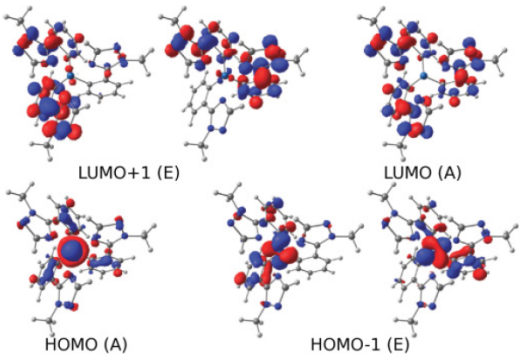

FIG. 3. (Color online) Electron densities in the frontier orbitals of $Ir(ptz)_3$ calculated from SR-DFT.

LUMO and HOMO → LUMO+1 transitions, respectively. Thus these transitions have a significant MLCT character (∼50%, Ref. 16).

It is well known from atomic physics[21] that there are two important relativistic effects on atomic orbitals (AOs). The *direct* relativistic effect arises from the increase in the mass of the electron due to its relativistic velocity, which leads to a decrease in the Bohr radius of the electron and hence a stabilization of the AOs. An *indirect* effect is also observed because the core electrons are closer to the nucleus due to the direct effect. Thus the core electrons screen the valence electrons more effectively, which destabilizes the valence electrons. The direct effect dominates for *s* electrons; for *p* electrons the two effects nearly cancel; but for *d* electrons the indirect effect is larger. SR-DFT calculations for the isolated Ir atom nicely reproduce these trends.[16] In particular, there is a ∼0.28 eV destabilization of the Ir 5*d* AOs at the level of theory used for $Ir(ptz)_3$.[16]

The above discussion leads to a simple explanation of the observed differences between the NR and SR excitation spectra. The indirect relativistic effect destabilizes the Ir 5*d* AOs. This destabilizes the HOMO and HOMO−1 levels, which have a large contribution from the Ir 5*d* orbitals, by 0.27–0.28 eV. However, the LUMO and LUMO+1 do not contain any significant contribution from the Ir AOs. Thus, there are only small SR corrections (<10 meV) to the LUMO and LUMO+1 energies (cf., Fig. 1). This shift in MO energies is the single largest effect responsible for the changes between the NR and SR-TDDFT excitation spectra. Therefore, the relativistic effects in the absorption of $Ir(ptz)_3$ are closely related to the relativistic effects responsible for the yellow color of gold[1] and the metallicity of lead.[2]

The relativistic effects on the low-lying triplet excitations are slightly more complicated. In the NR calculation the HOMO → LUMO transition contributes 53% of the weight of T_1. In the SR calculation this increases to 69%. This lowers the T_1 excitation even more than would be expected from the relativistic destabilization of the Ir 5*d* AOs alone. Similar changes occur in T_2, which arises predominately from the HOMO → LUMO+1 and HOMO−1 → LUMO transitions.[16]

SOC mixes singlets and triplets. Nevertheless, many excitations retain a strong triplet character after the SOC perturbation is included, in particular, the lowest-energy excitations remain predominately triplet. Thus, the description of the emission as phosphorescence remains substantially valid even after SOC is included. An important consequence of the reduced symmetry, once SOC is included, is the zero-field splitting (ZFS) of the triplets, which are degenerate in the scalar calculation. This is responsible for the increased number of lines in Fig. 2(c).

A significant number of low-lying states are important for understanding the MCD spectrum. The lowest two excitations [which we henceforth refer to as 1(A) and 2(E) as the first excitation has A symmetry and the second has E symmetry] result primarily from the ZFS of T_1. 1(A) is predicted to have a very weak oscillator strength because it remains almost a pure triplet even when SOC is included. Indeed the "stick" corresponding to this state is too small to be visible in Fig. 1(c). Hence, we do not believe that 1(A) plays a significant role in any of our measurements.

Higher-lying excited states play an important role in the photophysics, particularly at room temperature (cf., Ref. 14). Therefore it is important to understand and control these states if one wants to tailor the properties of organometallic complexes for optoelectronic applications. The excitations 3(A), 4(E), 5(A), and 6(E) arise predominately from the ZFS of T_2 (E). Excitations 7(A) and 8(E) are rather more complex and have significantly more singlet character than the lower-energy excitations. However, the singlet character of 7(A) and 8(E) arises predominately from S_1 and S_2, whereas most of the singlet character of 2(E)–6(E) comes from S_3. S_3 has significantly more oscillator strength than S_1 and S_2 [Fig. 2(b)]. This explains why 7(A) and 8(E) are not significantly brighter than 2(E)–6(E) despite their greater singlet character.

Thus the inclusion of SOC allows for a natural interpretation of the MCD spectrum. Before giving our assignment, it is important to recall that the states belonging to the E representation of C_3 are only two-fold degenerate under the assumption of time-reversal symmetry. As the application of a magnetic field breaks time reversal symmetry it will always lift this degeneracy, leading to A terms in the MCD spectrum. We assign the A term at low energies to the manifold of triplet states around 2.8 eV, which can be traced back through T_1 and T_2 to HOMO → LUMO, HOMO →LUMO+1, and HOMO−1 → LUMO transitions. Significant contributions to this feature arise from both 2(E) and 6(E) and a B term from 3(A) may also be implicated in the apparent shoulder(s) in this term. There is then a B term arising from excitation 7(A) and a second A term arising from excitation 8(E). Although the natures of these excitations can also be traced back to the MO's, this yields little insight as these higher-energy excitations are complex combinations of many MO transitions.[16] This assignment has been tested by comparison to similar predictions for a series of related compounds, which will be reported elsewhere.

The energy of the lowest excitations, 1(A) and 2(E), correspond, to within the inherent accuracy of the calculation, to the first peak. This suggests that, neglecting ZFS for the moment, T_1 is the phosphorescent state at LT, as one would expect from Kasha's rule. If this is correct one should expect

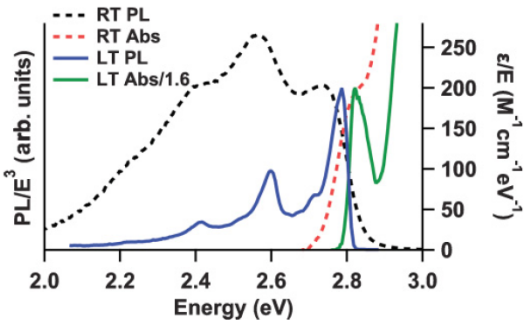

FIG. 4. (Color online) Scaled absorption and PL spectra of $Ir(ptz)_3$ at room temperature (RT) and LT. A clear mirror image rule is observed in the LT data. The Stokes shift is significantly reduced at LT due to the freezing of the solvent.

the mirror image rule to be obeyed. It can be seen from Fig. 4 that this is indeed the case. So far as we are aware, this is the first demonstration of the applicability of the mirror image rule to this type of complex. However, SOC produces very different oscillator strengths in the ZFS states. Excitation 2(E) will have a much shorter radiative lifetime than 1(A). This should be manifest as a strongly temperature dependent lifetime. One should also expect that the coupling of these two states to vibrational excitations is very different because of their different symmetry. Understanding how these effects are modified by chemical substitutions may allow one to increase the efficiency of OLED's based on Ir(III) complexes.

We have therefore seen that both spin-free (scalar) relativistic effects and SOC are vital for understanding the spectra of phosphorescent Ir(III) complexes. SR corrections destabilize the Ir *5d* orbitals and, as the low-lying excitations in phosphorescent Ir(III) complexes involve considerable MLCT character, this significantly alters the spectra. SOC is also important, not only for the phosphorescence and fast intersystem crossing, but also to understand the ZFS and subtle redistribution of spectral weight observed via the MCD.

We thank Anthony Jacko, Tom Stace, and Seth Olsen for helpful conversations. This work was funded by the ARC and calculations were performed on NF-NCI. ARGS thanks AINSE for a PGRA. PLB and BJP are supported by ARC under the Federation (FF0668728) and Queen Elizabeth II (DP0877875) schemes respectively..

*bjpowell@gmail.com

[1] P. Pyykkö, Angew. Chem. **43**, 4412 (2004).
[2] N. E. Christensen, S. Satpathy, and Z. Pawlowska, Phys. Rev. B **34**, 5977 (1986).
[3] M. van Veenendaal, J. Chang, and A. J. Fedro, Phys. Rev. Lett. **104**, 067401 (2010).
[4] K. G. Dyall and K. Fægri, *Introduction to Relativistic Quantum Chemistry* (Oxford University Press, Oxford, 2007).
[5] M. A. Baldo *et al.*, Appl. Phys. Lett. **75**, 4 (1999).
[6] C. Ulbricht *et al.*, Adv. Mater. **21**, 4418 (2009).
[7] Y. You and S. Y. Park, Dalton Trans. 1267 (2009).
[8] H. Yersin and W. J. Finkenzeller, *Highly Efficient OLEDs with Phosphorescent Materials* (Wiley, New York, 2008); A. F. Rausch, M. E. Thompson, and H. Yersin, J. Phys. Chem. A **113**, 5927 (2009).
[9] S.-C. Lo *et al.*, Chem. Mater. **18**, 5119 (2006).
[10] A. C. Jacko, R. H. McKenzie, and B. J. Powell, J. Chem. Phys. **133**, 124314 (2010).
[11] A. C. Jacko, B. J. Powell, and R. H. McKenzie, J. Mat. Chem. **20**, 10301 (2010).
[12] P. J. Hay, J. Phys. Chem. A **106**, 1634 (2002).
[13] For exceptions see, K. Nozaki, J. Chin. Chem. Soc. **53**, 101 (2006); T. Matsushita, T. Asada, and S. Koseki, J. Phys. Chem. C **111**, 6897 (2007).
[14] W. J. Finkenzeller and H. Yersin, Chem. Phys. Lett. **377**, 299 (2003); H. Yersin and D. Donges, Top. Curr. Chem. **214**, 81 (2001); T. Hofbeck and H. Yersin, Inorg. Chem. **49**, 9290 (2010).
[15] C. Chang, M. Pélissier, and P. Durand, Phys. Scr. **34**, 394 (1986); F. Wang and T. Ziegler, J. Chem. Phys. **123**, 154102 (2005).
[16] See supplemental material at [http://link.aps.org/supplemental/10.1103/PhysRevB.83.041105] for additional details of the experimental and computational methods and for tabulations of the calculated quantities indicated in the main text.
[17] C. Fonseca Guerra, J. G. Snijders, G. te Velde, and E. J. Baerends, Theor. Chim. Acta **99**, 391 (1998); G. te Velde *et al.*, J. Comput. Chem. **22**, 931 (2001).
[18] E. V. Lenthe and E. J. Baerends, J. Comput. Chem. **24**, 1142 (2003).
[19] P. J. Stephens, F. J. Devlin, C. F. Chabalowski, and M. J. Frisch, J. Phys. Chem. **98**, 11623 (1994).
[20] W. R. Mason, *A Practical Guide to Magnetic Circular Dichroism Spectroscopy* (John Wiley & Sons, New Jersey, 2007).
[21] J. P. Desclaux and Y.-K. Kim, J. Phys. B **8**, 1177 (1975); S. J. Rose, I. P. Grant, and N. C. Pyper, *ibid.* **11**, 1171 (1978).

DOI: 10.1002/cphc.201100397

Spin–Orbit Coupling in Phosphorescent Iridium(III) Complexes

Arthur R. G. Smith,[b] Paul L. Burn,[b] and Ben J. Powell*[a]

We study the excited states of two iridium(III) complexes with potential applications in organic light-emitting diodes: *fac*-tris(2-phenylpyridyl)iridium(III) [Ir(ppy)$_3$] and *fac*-tris(1-methyl-5-phenyl-3-*n*-propyl-[1,2,4]triazolyl)iridium(III) [Ir(ptz)$_3$]. Herein we report calculations of the excited states of these complexes from time-dependent density functional theory (TDDFT) with the zeroth-order regular approximation (ZORA). We show that results from the one-component formulation of ZORA, with spin–orbit coupling included perturbatively, accurately reproduce both the results of the two-component calculations and previously published experimental absorption spectra of the complexes. We are able to trace the effects of both scalar relativistic correction and spin–orbit coupling on the low-energy excitations and radiative lifetimes of these complexes. In particular, we show that there is an indirect relativistic stabilisation of the metal-to-ligand charge transfer (MLCT) states. This is important because it means that indirect relativistic effects increase the degree to which SOC can hybridise singlet and triplet states and hence plays an important role in determining the optical properties of these complexes. We find that these two compounds are remarkably similar in these respects, despite Ir(ppy)$_3$ and Ir(ptz)$_3$ emitting green and blue light respectively. However, we predict that these two complexes will show marked differences in their magnetic circular dichroism (MCD) spectra.

1. Introduction

Phosphorescent iridium(III) complexes show significant promise as active materials in organic light-emitting diodes (OLEDs). Phosphorescent materials are particularly desirable over fluorescent emitters due to their potential to harvest both singlet and triplet excitations generated in a device.[1,2] However, the development of efficient deep-blue phosphorescent emitters, which are required for full-colour OLED displays,[3–6] has remained a persistent problem since the field was established with the discovery of the green phosphorescent complex *fac*-tris(2-phenylpyridyl)iridium(III) [Ir(ppy)$_3$; Figure 1 and Table 1].[7] *Fac*-tris(1-methyl-5-phenyl-3-*n*-propyl-[1,2,4]triazolyl)iridium(III) [Ir(ptz)$_3$; Figure 1] emits blue light at room temperature,[4] see Table 1. Thus we are motivated to study both complexes to develop a clear understanding of the differences between the optoelectronic properties of these materials. A complete understanding of all the processes responsible for highly efficient phosphorescent organometallic complexes has remained elusive. This significantly hampers the goal of designing new complexes for OLED applications.

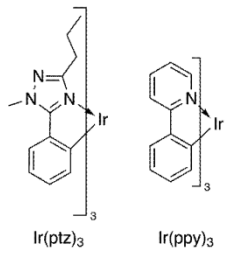

Figure 1. Complexes studied herein: *fac*-tris(1-methyl-5-phenyl-3-*n*-propyl-[1,2,4]triazolyl)iridium(III) [Ir(ptz)$_3$; left] and *fac*-tris(2-phenylpyridyl)iridium(III) [Ir(ppy)$_3$; right].

Table 1. Selected properties of Ir(ptz)$_3$ and Ir(ppy)$_3$ at 300 K; from Lo et al.[4] and Hofbeck and Yersin[36] respectively. Photoluminescence quantum yield (PLQY), emission lifetime, and photoluminescence (PL) Commission Internationale de l'Eclairage (CIE) coordinates are given.

Complex	PLQY [%]	Lifetime [μs]	PL CIE (*x*, *y*)
Ir(ptz)$_3$	66±7	1.08	(0.16, 0.20)
Ir(ppy)$_3$	90±5	1.6	(0.33, 0.61)

There are a number of clear indications that relativistic effects are important for understanding the optical and optoelectronic properties of iridium(III) complexes. Firstly, these materials display signatures of strong spin–orbit coupling (SOC): most notably phosphorescent decay and fast intersystem crossing,[8] which are both mediated by SOC. This has motivated several groups to include SOC in their calculations. Both

[a] *Prof. B. J. Powell*
Centre for Organic Photonics and Electronics
School of Mathematics and Physics
The University of Queensland
QLD 4072 (Australia)
E-mail: bjpowell@gmail.com

[b] *A. R. G. Smith, Prof. P. L. Burn*
Centre for Organic Photonics and Electronics
School of Chemistry and Molecular Biosciences
The University of Queensland
QLD 4072 (Australia)

Supporting information for this article is available on the WWW under http://dx.doi.org/10.1002/cphc.201100397.

Matsushita et al.[9] and Jansson et al.[10] studied $Ir(ppy)_3$ with SOC included via the semi-empirical effective nuclear charge method,[11,12] which includes SOC on top of non-relativistic calculations. Matsushita et al.[9] studied the mixing of singlet and triplet states and the implications of this for phosphorescence and Jansson et al.[10] investigated the nature of the T_1 excitation in some depth. Minaev et al.[13] used quadratic response TDDFT to calculate the radiative rates of several phosphorescent complexes, while De Angelis et al. have presented a qualitative analysis of the SOC matrix elements in iridium(III) complexes[14] and discussed the effects of solvation on these matrix elements.[15] Nozaki et al.[16,17] have also investigated organometallic complexes with the SOC included perturbatively about non-relativistic TDDFT calculations. Nozaki[16] showed that this method provides a reasonable description of the zero-field splittings and oscillator strengths of $Ir(ppy)_3$, and in a further study Nozaki and collaborators investigated the differences in the optical properties in a range of tris(2,2′-bipyridine) transition metal complexes using the same method.[17] However, it has recently been shown that scalar relativistic corrections are also important.[18] In particular, scalar relativistic TDDFT calculations with spin–orbit coupling included perturbatively accurately predict the low-temperature, high-field magnetic circular dichroism and absorption spectra of $Ir(ptz)_3$. The low-lying excited states are believed to have a strong metal-to-ligand charge transfer (MLCT) character. Although DFT has some well-known issues in describing charge transfer transitions,[19,20] the use of hybrid functionals, which include exact exchange can alleviate this problem.[21] As one expects relativistic effects to be important on the metal, but negligible on the ligand, this suggests that a correct description of the relativistic corrections is necessary for the accurate description of these excitations. Therefore, relativistic effects need to be included to correctly describe the excitations that need to be controlled in order to design new active materials for OLED applications.

The field of relativistic quantum chemistry is well established, but outside the experience of many practicing chemists. We therefore give a brief pedagogical introduction in the remainder of this introduction. We also refer readers interested in more details to the monographs by Dyall and Fægri[22] or Dreizler.[23] There are no new results in the discussion and experts may wish to turn directly to the Results and Discussion (Section 2).

The Dirac equation[24,25] provides a Lorentz invariant formulation of quantum mechanics for spin $^1/_2$ particles, such as electrons, and therefore represents the unification of quantum mechanics with special relativity. This is one of the greatest achievements of theoretical physics and led directly to a natural explanation of spin, the prediction of the positron and development of quantum electrodynamics (QED). However, whereas in non-relativistic quantum theory the wavefunction is a complex scalar field, in the relativistic theory the wavefunction for spin $^1/_2$ particles is a complex four-vector field, that is, a four-spinor. For each solution of the Schrödinger equation the Dirac equation has four eigenvalues. These have a simple physical interpretation: two eigenvalues have positive energy and represent matter with spin-α and spin-β; the two negative energy solutions represent antimatter with spin-α and spin-β. This significantly increases the difficulty, and hence the computational cost, of relativistic calculations.

A significant difficulty with relativistic theory is that the Coulomb interaction is retarded, that is, the Coulomb interaction is mediated by photons, which travel at the (finite) speed of light. The correct treatment of this retarded interaction requires a Lorentz invariant interaction, the quantisation of the field and the full machinery of QED. This would render quantum chemical calculations intractable. Therefore, approximations need to be introduced. An important simplification is to work in the Born–Oppenheimer frame. This means that the theory is no longer Lorentz-invariant, but allows the most important relativistic corrections to be kept.

The full relativistic machinery is not necessary for most chemical problems. Therefore, it is natural to consider only the leading relativistic correlations in a perturbation theory in $\frac{1}{mc^2}$, where m is the mass of the electron and c is the speed of light. This leads to the Breit–Pauli Hamiltonian. However, the Breit–Pauli Hamiltonian is not ideal for quantum chemistry because the expansion is only valid for $|V-E|<2mc^2$, where V is the potential and E is the orbital energy. Neither V nor E are bounded from above; in particular, $|V-E|$ is always greater than $2mc^2$ sufficiently close to the nucleus. Therefore it is preferable to perform the expansion in $\frac{1}{2mc^2-V}$, which leads to an analytic expansion, even arbitrarily close to the nucleus. This is known as the regular or Chang–Pélissier–Durand approximation.[26] The regular approximation contains corrections to all orders in $\frac{1}{mc^2}$, even at zeroth order. This can be seen immediately from the Hamiltonian for zeroth-order regular approximation (ZORA) [Eq. (1)]:

$$\begin{aligned} H_{\mathrm{ZORA}} &= V+\left(\vec{\sigma}.\vec{p}\right)\frac{c^2}{2mc^2-V}\left(\vec{\sigma}.\vec{p}\right) \\ &= V+\frac{1}{2m}\left(\vec{\sigma}.\vec{p}\right)\left[1+\frac{V}{2mc^2}+\frac{V^2}{4m^2c^4}+\ldots\right]\left(\vec{\sigma}.\vec{p}\right) \end{aligned} \tag{1}$$

where $\vec{\sigma}$ is the vector of Pauli matrices, and $\vec{p}$ is the momentum three-vector.

The relativistic Hohenberg–Kohn theorem[27–29] proves that the ground-state energy of a covariant system is a unique functional of the ground-state four-current. However, analogously to non-relativistic theory, practical implementations require the solution of the Dirac–Kohn–Sham equations [Eq. (2)]:[22,23]

$$\begin{pmatrix} V & c\vec{\sigma}\cdot\vec{p} \\ c\vec{\sigma}\cdot\vec{p} & V \end{pmatrix}\begin{pmatrix} \psi^{\mathrm{L}} \\ \psi^{\mathrm{S}} \end{pmatrix} = E\begin{pmatrix} \psi^{\mathrm{L}} \\ \psi^{\mathrm{S}} \end{pmatrix} \tag{2}$$

where $V=V_{\mathrm{nuc}}+V_{\mathrm{Hartree}}+V_{\mathrm{xc}}$, V_{Hartree} is the Hartree potential, V_{xc} is the exchange–correlation potential and ψ^{L} and ψ^{S} are two-spinors, known as the large and small components respectively. These names arise because for the matter solutions the large component is larger than the small component (somewhat confusingly, the reverse is true for the antimatter solu-

tions). As we will only be concerned with the matter solutions, we can simplify the Kohn–Sham equations by eliminating the small component, which yields Equation (3):

$$\left[(T+V-E)+\frac{V-E}{2mc^2+E-V}T - \frac{c^2}{(2mc^2+E-V)^2}\left[\left(\vec{p}V\right).\vec{p}+i\vec{\sigma}.\left(\vec{p}V\right)\times\vec{p}\right]\right]\psi^L=0 \quad (3)$$

where T is the non-relativistic kinetic energy operator. This two-component relativistic theory is a dramatic simplification as now one need only deal with a two-spinor. The loss of information about the antimatter solutions is not a significant drawback for chemical applications.

Note that only the last term in Equation (3), the SOC, is spin dependent and that, for closed-shell systems, this term only appears at the second order, whereas there are spin-free (scalar) relativistic corrections even at the first order. This motivates the scalar relativistic approximation, where one neglects the SOC. In this approximation the two components of ψ^L decouple and the problem reduces to a one-component theory. This one-component theory is as computationally tractable as the non-relativistic Schrödinger equation. SOC can then be included perturbatively around the results of the scalar calculation.[30]

2. Results and Discussion

2.1. Optimised Geometries

The optimised geometries of $Ir(ppy)_3$ and $Ir(ptz)_3$ are summarised in Table 2, and full structures can be found in the supporting information. For $Ir(ppy)_3$ we find very good agreement to the optimised geometry reported by Hay,[31] who used a similar methodology to determine the geometry, and also good agreement with recent solid-state and gas-phase structural studies.[32] The optimised geometry of $Ir(ptz)_3$ is also a good match to the reported crystal structure.[4]

2.2. Two-component Calculations

The fifty lowest-energy electronic excitations of $Ir(ptz)_3$ and $Ir(ppy)_3$ were calculated with the self-consistent two-component ZORA method. The excitation energies and oscillator strengths of these transitions are tabulated in the Supporting Information and plotted in Figure 2. In order to facilitate comparison with experiment we also show "spectra" where each transition is broadened by a Lorentzian of width 0.1 eV. We stress that this is not intended as a realistic estimate of the broadening, but rather as a guide to the eye. Indeed comparison with previously published experimental data, reproduced in Figure 2, shows that this somewhat underestimates the broadening at room temperature.

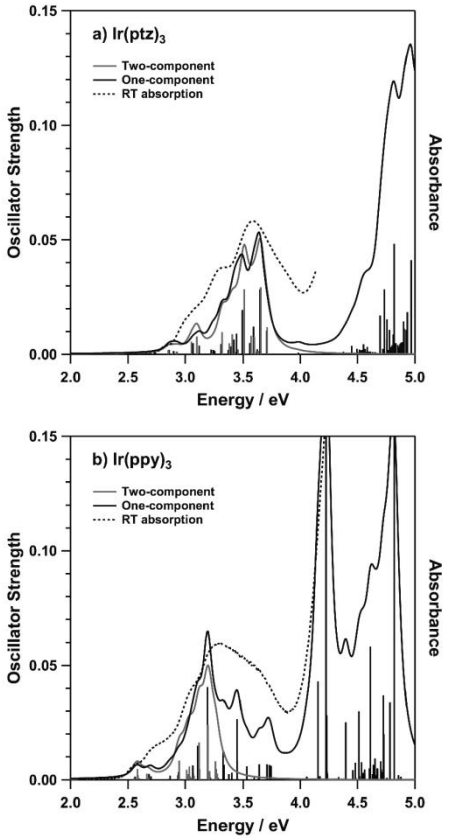

Figure 2. Comparison of the excitation spectra calculated from one- and two-component ZORA-TDDFT with the absorption spectra previously measured by Smith et al.[18] and Hofbeck and Yersin[36] of a) $Ir(ptz)_3$ and b) $Ir(ppy)_3$. Bars indicate transitions with the height indicating the calculated oscillator strengths. Curves represent the calculated excitation spectra broadened by Lorentzians of full width half maximum 0.1 eV; this is intended as a guide to the eye, rather than as a serious simulation of the broadening. Both calculations use the DZP basis with a frozen core electron approximation.

Table 2. Selected bond lengths (in Å) of the optimised molecular geometries of $Ir(ppy)_3$ and $Ir(ptz)_3$. The complete optimised structures are reported in the Supporting Information.

Bond	$Ir(ptz)_3$ this work	$Ir(ptz)_3$ X-ray diffraction[4]	$Ir(ppy)_3$ this work	$Ir(ppy)_3$ gas-phase electron diffraction[32]	$Ir(ppy)_3$ X-ray diffraction[32]
Ir–N	2.151	2.166	2.168	2.158	2.130
Ir–N	2.151	2.151	2.168	2.158	2.130
Ir–N	2.151	2.135	2.168	2.158	2.130
Ir–C	2.046	2.042	2.036	2.033	2.016
Ir–C	2.046	2.022	2.036	2.033	2.016
Ir–C	2.046	2.002	2.036	2.033	2.016

The low-energy excitations in both complexes have previously been assigned as metal-to-ligand charge transfer (MLCT) bands. We will follow this nomenclature. However, a detailed discussion of the degree of MLCT is given in Section 2.4. For $Ir(ptz)_3$ the calculated spectrum is in excellent agreement with the measured spectrum of the MLCT band. However, higher-energy excitations are not included in the calculation and so are not reproduced. This results from the major limitation of the two-component methodology for complexes of this size, namely the large computational cost, which we discuss further below. Interestingly, the density of states is much higher in $Ir(ppy)_3$. This means that only the lowest-energy part of the MLCT band is described by the fifty lowest-energy excitations. Nevertheless, this part of the spectrum is reproduced quite accurately by the two-component theory.

2.3. One-Component Calculations

To calculate a wider range of the spectrum we need to turn to the one-component theory, with SOC included perturbatively. We calculated the lowest 200 excitations at this level of theory. In order to make a fair comparison of these calculations with the two-component theory we began by performing one-component calculations in the same (double-zeta with polarization function, DZP) basis set and with the same frozen core as used for the two-component calculations. The calculated excitation energies and oscillator strengths are tabulated in the Supporting Information and plotted in Figure 2. The calculated spectrum, broadened by Lorentzians with 0.1 eV full width half-maxima is also plotted in Figure 2.

The lowest fifty excitations of both theories are in excellent agreement with one another. This is clearly evident for $Ir(ptz)_3$ where, since the MLCT band is completely described within fifty excitations, the energies, oscillator strengths and symmetry designations of the two-component results are almost perfectly replicated by the one-component perturbation calculation. In the case of $Ir(ppy)_3$ the comparison is a little more difficult because only part of the MLCT band is described by the lowest fifty excitations. From the one-component perturbation calculation we find that ninety excitations are required to describe the MLCT band. Nonetheless there is still good agreement between the low-energy excitations. Figure 3 shows a comparison of the lowest-energy excitations in the two complexes, where the excellent agreement is particularly clear despite the small ranges on both axes.

The most significant deviations between the one- and two-component calculations are that the one-component calculation assigns a small oscillator strength to states that are essentially dark in the two-component calculation. Thus, upon casual inspection of Figure 2 there appears to be a lower density of states in the two-component calculation. We stress that this is not the case, but is due to the presence of a large number of states with very little oscillator strength. For example, for $Ir(ptz)_3$ the transitions around 3.25 eV are almost completely forbidden in the two-component calculation, whereas in the one-component calculation they are given a small oscillator strength (see Figure 2). A closer examination of these states reveals that they are of predominately triplet character. This can be understood because SOC is only included via second-order perturbation theory in the one-component theory. Pure triplet excitations are forbidden and therefore have zero oscillator strength. However, SOC mixes singlet and triplets states.[33] States with small oscillator strengths typically correspond to predominately triplet states with only small singlet admixtures. Thus, for weakly allowed transitions, extremely small changes in the *fraction* of singlet character will lead to large changes in the *absolute* oscillator strength. Hence, one expects these oscillator strengths to show the largest discrepancy between the one- and two-component calculations, as

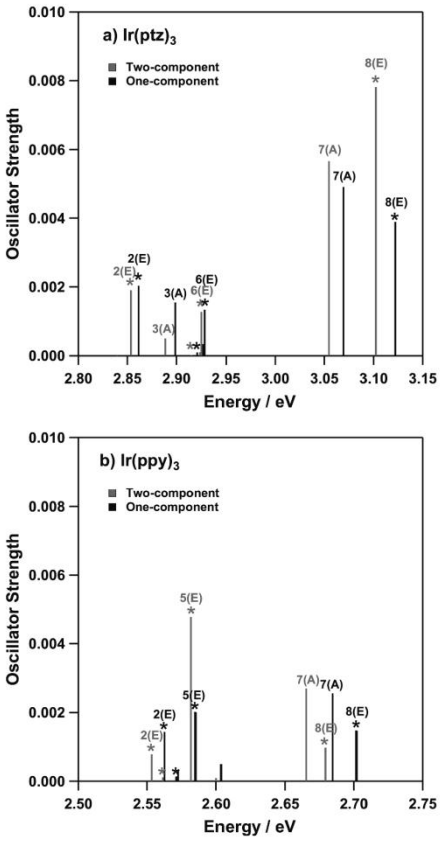

Figure 3. Excitations 1–8 calculated from one- and two-component ZORA-TDDFT with DZP basis and frozen core (note the different energy scales for the different complexes). Asterisks mark two-fold degenerate E states and states with significant oscillator strengths are labelled. Very good agreement between the two methods is found for both complexes. These low-lying excitations dominate the optical properties, and hence the technological applications, of these complexes. The excitation spectra of the two complexes are quite similar in this energy range. However, note that the 7A and 8E excitations have significantly more oscillator strength in $Ir(ptz)_3$ than the equivalent excitations in $Ir(ppy)_3$. These excitations are responsible for strong features in the MCD of $Ir(ptz)_3$ therefore we predict that $Ir(ppy)_3$ will not show such pronounced features in an MCD spectrum.

we observe numerically. In perturbation theory the singlet contribution to the wavefunctions of states that are triplet at zeroth order depends sensitively on $[E_i^{(0)}-E_j^{(0)}]^{-1}$, where $E_i^{(0)}$ is the energy of the triplet state at zeroth order and $E_j^{(0)}$ is the energy of singlet state at zeroth order.[34] Thus, any finite order of perturbation theory will have larger errors when states are nearly degenerate. Generically, one expects that such accidental near-degeneracies will be most important in regions with high densities of states.[35] This is indeed borne out by the calculations reported above where these issues are slightly more prominent in the MLCT band of $Ir(ppy)_3$ than they are in the MLCT band of $Ir(ptz)_3$.

Nevertheless, it should be stressed that the issues above only appear for the transitions that are *least* important spectroscopically. Therefore, the one-component calculations do an excellent job of reproducing spectra predicted by the two-component calculations and hence the experimental absorption spectra. However, it is interesting and surprising that these problems *do not* lead to widespread or significant errors in the calculated spectrum of excitations.

In terms of computational cost, the one-component calculations are, unsurprisingly, significantly faster. On a single node of the VAYU cluster the one-component calculation is an order of magnitude faster per self-consistent TDDFT iteration than the two-component calculation (~2 vs ~16 h/self-consistent field iteration). This is in spite of the fact that we included 200 excitations in the one-component theory, but only 50 excitations in the two-component calculations. Practical limitations, such as the available computational time, prevent us from improving on the DZP basis with a frozen-core approximation for the two-component calculations on our current cluster. However, one-component all-electron calculations in a triple-zeta basis with polarization function (TZP), which we discuss below, still have a significantly lower cost than two-component calculations presented above.

In the Supporting Information we compare the effects of increasing the quality of the basis set and the differences between frozen-core and all-electron calculations. This is limited to the one-component calculations because of the computational expense associated with the two-component formalism. It is interesting to note that the changes from increasing the size of the basis sets are more significant than the differences between the one- and two-component theories. This suggests that, given the current limitations on computer power, all-electron one-component calculations performed in a high-quality basis set will give more reliable answers than frozen core two-component calculations in a small basis set for iridium(III) complexes.

2.4. Analysis of Spin Mixing, Metal-to-Ligand Charge Transfer, Degeneracy, Radiative Lifetime and Magnetic Circular Dichroism

Now that we have established the reliability of the one-component ZORA with spin–orbit coupling included perturbatively, both in relation to the higher level two-component formalism and in reproducing previously measured spectra (see also ref. [18]), we move to discussing issues of real chemical and technological interest. The one-component calculations lend themselves naturally to analyses that allow one to extract important information for understanding the nature of the low-lying excitations in these complexes. In this section we present an analysis for the all-electron calculations in a TZP basis.

In Figure 4 and Tables S5 and S6 of the Supporting Information we report the degree of singlet character for the calculated excitations in both complexes. As one might expect, there is a strong correlation between the strength of the transition and degree of singlet character. In $Ir(ptz)_3$ there are very few transitions in the MLCT band with more than 50% singlet character, but there are several transitions with a very large singlet weight in $Ir(ppy)_3$. This is clearly correlated with the much

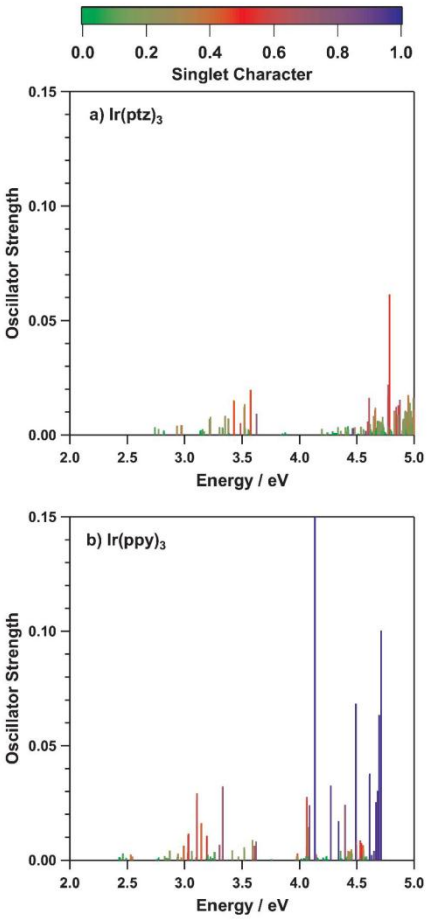

Figure 4. Singlet character of the low-lying excitations in a) $Ir(ptz)_3$ and b) $Ir(ppy)_3$. Both sets of data are from all-electron, one component ZORA-TDDFT calculations in a TZP basis set. There is a clear correspondence between the oscillator strengths and the degree of singlet character, as one would expect. In particular the several states that are nearly pure singlets give rise to the stronger oscillator strengths observed in $Ir(ppy)_3$, while such transitions are absent in $Ir(ptz)_3$.

larger oscillator strengths predicted in $Ir(ppy)_3$, particularly for these predominately singlet transitions. An interesting question for future work will be to understand how these differences relate to the very different colours of the two complexes, and how they affect the energy transfer processes that occur on photo- or electrical excitation.

An important question, which has strongly influenced design strategies for iridium(III) complexes is the degree of MLCT in the low-lying excited states. To investigate this question we performed a Mulliken population analysis and calculated the MLCT character for the low-energy excitations, details of which are given in the Supporting Information. In Figure 5 and the Supporting Information we report the MLCT character of the low-lying excitations of both complexes. It should be noted that even in the lowest-lying band, which is usually assigned as the "MLCT band", none of the excitations have more than ~50% MLCT character. This can be understood by relating the TDDFT excitations to the Kohn–Sham orbitals in the single-component ZORA (time-independent) DFT calculation underlying the TDDFT. Details of the Kohn–Sham molecular orbitals, including a Mulliken population analysis of the contribution from the Ir-5d orbital to each MO is given in the Supporting Information. Both complexes have similar structures in their frontier orbitals, shown in Figures 6 and 7. Recall that both complexes are C_3 symmetric; and under the assumption of time reversal symmetry C_3 has a one-dimensional irreducible representation (A) and a two-dimensional irreducible representation (E). In both complexes the HOMO and LUMO are non-degenerate (A) and the HOMO−1 and LUMO+1 are two-fold degenerate

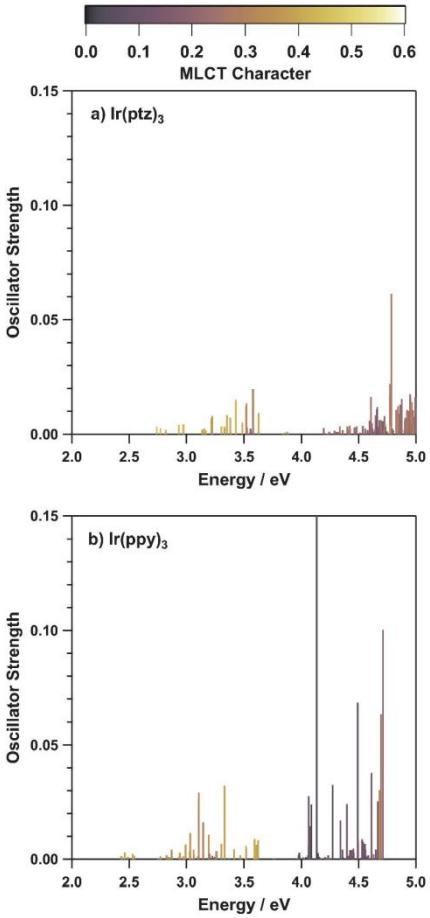

Figure 5. Metal-to-ligand charge transfer character of the low-lying excitations in a) $Ir(ptz)_3$ and b) $Ir(ppy)_3$. Both sets of data are from all-electron, one-component ZORA-TDDFT calculations in a TZP basis set. In neither complex does one observe states with more than ~50% MLCT character. However, given this restriction the characterisation of the lowest bands in both complexes as "MLCT" bands is largely borne out by the observation that these bands do have substantially more MLCT character than the higher lying excited states.

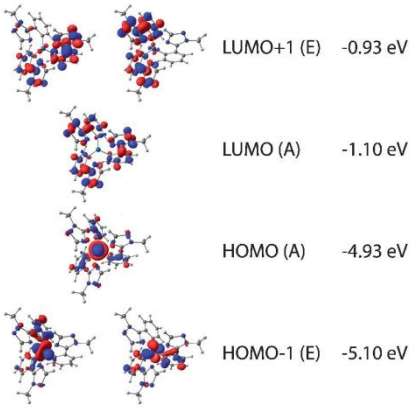

Figure 6. Frontier Kohn–Sham molecular orbitals and their energies in $Ir(ptz)_3$ and the corresponding molecular orbital energies. Calculated from all-electron ZORA-DFT in the TZP basis set.

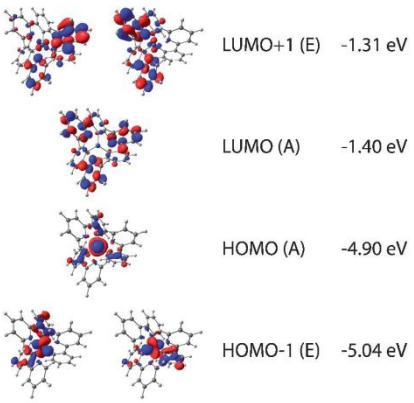

Figure 7. Frontier Kohn–Sham molecular orbitals and their energies in $Ir(ppy)_3$ and the corresponding molecular orbital energies. Calculated from all-electron ZORA-DFT in the TZP basis set.

(E). Further, in both complexes the HOMO is rather similar to the HOMO−1 and the LUMO is similar to the LUMO+1. In particular the HOMO and HOMO−1 have a significant (~50%) contribution weight on the iridium atom, whereas the LUMO and LUMO+1 do not.

Both complexes have approximate octahedral symmetries. If they were truly O_h symmetric the frontier orbitals would have T_{2g} symmetry and form two three-fold degenerate manifolds. The true C_3 symmetry splits the T_{2g} manifold into the observed A and E motifs. Nevertheless the approximate octahedral symmetry is still manifest in the similarities between the HOMO and the HOMO-1 and the similarities between the LUMO and the LUMO+1.

If one writes the scalar TDDFT excitations in terms of transitions between the Kohn–Sham orbitals (see the Supporting Information, Tables S11 and S12) one finds that the low-energy excitations are dominated by transitions between the frontier orbitals (Table 3). In both $Ir(ppy)_3$ and $Ir(ptz)_3$ the singlet transitions S_1 and S_2 are dominated by the HOMO→LUMO and HOMO→LUMO+1 transitions respectively. The situation is slightly more complicated for the triplet excitations, but T_1 and T_2 are still dominated by transitions between the frontier molecular orbitals.

Table 3. Composition of selected excitations in terms of transitions between Kohn–Sham orbital transitions. Details for all studied excitations are given the Supporting Information (Tables S11 and S12).

Excitation	$Ir(ptz)_3$	$Ir(ppy)_3$
S_1(A)	HOMO→LUMO (98%)	HOMO→LUMO (97%)
S_2(E)	HOMO→LUMO+1 (98%)	HOMO→LUMO+1 (97%)
T_1(A)	HOMO→LUMO (69%)	HOMO→LUMO (70%)
	HOMO−1→LUMO+1 (21%)	HOMO−1→LUMO+1 (19%)
T_2(E)	HOMO→LUMO+1 (48%)	HOMO→LUMO+1 (63%)
	HOMO−1→LUMO (25%)	HOMO−1→LUMO (14%)
	HOMO−1→LUMO+1 (5%)	HOMO−1→LUMO+1 (11%)

Thus the ~50% limit on the MLCT character in the "MLCT band" observed in both complexes arises because these states involve transitions from the HOMO and/or HOMO−1 to the LUMO and/or LUMO+1. (The high-lying occupied Kohn–Sham orbitals below the HOMO−1 have smaller contributions from the Ir-5d orbitals.) The low-lying unoccupied Kohn–Sham orbitals above the LUMO+1 also have negligible contributions from the Ir-5d orbitals. Thus, no excitations can have more than ~50% MLCT character.

We can further understand the low-energy excitations of these complexes by examining how the scalar relativistic TDDFT results, obtained prior to the perturbation due to SOC, hybridise to give the excitations found in the SOC perturbation theory (Tables S9 and S10 report the largest contributions to each of the excitations once SOC is included). In both complexes T_1 is a non-degenerate state (A) and T_2 is two-fold degenerate (E). SOC induces a zero-field splitting in these states. In both complexes T_1 is split into a non-degenerate state, which we label 1A, and a two-fold level, 2E, at slightly higher energy. It is interesting to note that in both complexes 1A has a very small oscillator strength. This has previously been found experimentally.[18,36] However, the zero-field splitting of T_2 shows some subtle differences between the two complexes. In $Ir(ptz)_3$ the T_2 manifold has symmetry A, E, A, E (in order of increasing excitation energy) whereas in $Ir(ppy)_3$ the same triplet manifold has symmetry E, A, E, A. Thus the zero-field splitting has different signs in the two T_2 manifolds.

This redistribution of the states has important experimental consequences. In Figure 8 we plot the radiative lifetimes for both complexes at different levels of theory, assuming that excitations are populated according to the Boltzmann distribution [Eq. (4)]:

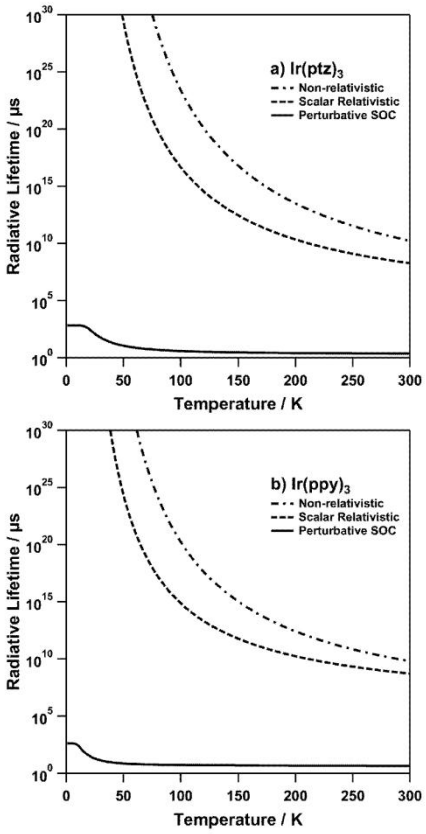

Figure 8. The radiative lifetime of a) $Ir(ptz)_3$ and b) $Ir(ppy)_3$ predicted at various levels of theory in an all-electron TZP basis. The predictions are remarkably similar for both complexes. The calculation including spin–orbit coupling (SOC) perturbatively is directly relevant to experiment and predicts that the radiative lifetime is strongly temperature dependent. This is similar to what is observed experimentally for the total lifetime.[36] However, the differences between the scalar relativistic and non-relativistic calculations also provide important insights to the relativistic effects in these complexes. In particular the difference of several orders of magnitude between these complexes is due to the indirect relativistic stabilisation of metal-to-ligand charge transfer states.

$$\frac{1}{\tau_R(T)} = \frac{\sum_i \left(\frac{e^{-E_i/k_B T}}{\tau_R^{(i)}} \right)}{\sum_i e^{-E_i/k_B T}} \quad (4)$$

where $\tau_R(T)$ is the radiative lifetime of the complex at temperature T, $\tau_R^{(i)}$ is the radiative lifetime of the ith excited state, and E_i is the energy of the ith excitation. It is important to note that the E excitations appear twice in the sums in Equation (4), once for each of the degenerate states. The radiative lifetime (and hence the radiative rate) for each excitation is calculated from the Strickler–Berg relation.[37,38]

A number of interesting effects can be observed from Figure 8. The calculation that includes spin–orbit coupling is most directly relevant to experiment. Here we see a dramatic variation in τ_R in both complexes. This can be understood as follows. At low temperatures only the lowest state (1A) is occupied, and as noted above, this state has a very long radiative lifetime. Hence, the complex has a low radiative rate. As the temperature is raised, higher-lying excitations are (thermally) populated. These excitations have lower radiative lifetimes and therefore as the temperature is raised the total radiative lifetime of the complex decreases. At room temperature six excitations (three A and three E) have a significant thermal population. These states arise from the zero-field split T_1(A) and T_2(E) states, which are basically t_{2g} states. Hofbeck and Yersin[36] have observed a similar temperature dependence in the *total* lifetime of $Ir(ppy)_3$ experimentally. Herzberg–Teller coupling is an important complication that is *not* included in our calculation. Given the long radiative lifetime of the lowest-energy excitation it may be expected that the Herzberg-Teller effect will somewhat decrease the radiative lifetime of this excitation. Therefore, although we expect the overall trend predicted in this calculation to be correct, the prediction for the radiative lifetime at low temperatures may not be quantitatively accurate. Indeed the radiative lifetime can be strongly dependent on small changes in the perturbation calculation (see the Supporting Information, Figure S3).

Some further insights can be gained from looking at the radiative rates at different levels of calculation. Unsurprisingly the scalar relativistic and non-relativistic calculations predict that the complexes have very much longer radiative lifetimes than the above calculation. This is a result of the neglect of spin–orbit coupling in the scalar relativistic and non-relativistic calculations. In the absence of spin–orbit coupling, phosphorescence is strictly forbidden and all radiative decay results from singlet states. As these are at significantly higher energies than the triplets, the radiative lifetime of the complex is exponentially enhanced [see Eq. (4)]. What is more interesting is that the radiative lifetime is predicted to be several orders of magnitude smaller by the scalar relativistic calculation than by the non-relativistic calculation. Remarkably, this has a simple explanation in terms of atomic physics and important consequences for the high photoluminescence quantum yields (PLQY) observed in these two complexes at room temperature.

It has long been understood that there are two important scalar relativistic effects in atomic physics: the "direct effect"—the relativistic mass enhancement of the electron reduces the Bohr radius and means that electrons are more tightly bound to the nucleus—and the "indirect effect" whereby electrons far from the nucleus are more effectively screened because the direct effect on the electrons closer to the nucleus—this means that electrons are more weakly bound.[39,40] The direct effect dominates for s electrons, the two effects roughly cancel for p electrons, but the indirect effect dominates for d electrons. The two lowest-energy singlet states, S_1 and S_2, have ~50% MLCT character in both complexes, as discussed above. Therefore the indirect relativistic effect lowers the energies of S_1 and S_2 because it destabilises the Ir-5d orbital, so less energy is required to cause MLCT. This effect is important because the closer the singlet is in energy to a triplet the more strongly spin–orbit coupling can hybridise the two states.[35] Thus the indirect relativistic effect increases the phosphorescent decay rate and hence increases the PLQY of these complexes.

Low-temperature, high-field magnetic circular dichroism (MCD) experiments have recently been reported for $Ir(ptz)_3$.[18] These show an interesting structure that can be understood on the basis of the type of calculations reported herein. Briefly, one observes an MCD A term at low energies arising from the manifold of triplet states around 2.8 eV, which can be traced back through T_1 and T_2 to HOMO→LUMO, HOMO→LUMO+1 and HOMO−1→LUMO transitions. There is then a B term arising from excitation 7A and a second A term arising from excitation 8E. Although the natures of these excitations can also be traced back to the MOs, this yields less insight as these higher-energy excitations are complex combinations of many molecular orbital transitions, the largest contributions coming from the T_3 and S_1 (7A) and S_2 (8E) excitations. Neither the non-relativistic nor the scalar relativistic calculation predict any excitations at energies comparable to those of 7A and 8E, consistent with the finding that these excitations are of highly mixed character due to the SOC. Thus, neither the non-relativistic nor the scalar relativistic calculations accurately predict the MCD data for $Ir(ptz)_3$.[18]

Excitations 7A and 8E, which give rise to the large MCD signal observed in $Ir(ptz)_3$, have significantly lower oscillator strength in $Ir(ppy)_3$ and are more closely spaced in energy. Our relativistic calculations therefore lead us to predict that the MCD signal from $Ir(ppy)_3$ will be greatly reduced compared to that of $Ir(ptz)_3$. The only MCD experiments we are aware of were carried out on a thin film of $Ir(ppy)_3$ at 15 K under an applied field of 0.84 T.[41] Low-temperature, high-field solution MCD measurements for $Ir(ppy)_3$ would therefore be an interesting test of our predictions.

2.5. Correlation and Solvation Effects

It is worthwhile to ask how reasonable the excellent agreement with experiment found above is. In particular we have only included electronic correlations at the B3LYP level and we entirely neglected any solvent effects. Transition metals are well known to lead to strong electronic correlations, so the success of B3LYP, particularly of excited-state energies is sur-

prising. Further, solvent and solid-state environments are known to have significant effects on the optoelectronic properties of organic electronic materials.[42] It has recently been shown that for a simple (and exactly soluble) model of organometallic complexes, such as those discussed herein, the configuration interaction singles (CIS) approximation gives accurate results.[35] The CIS approximation is closely related to TDDFT, particularly when the time-dependent Kohn–Sham equations are solved by a linear response approximation (the Tamm–Dankoff approximation to the Hartree–Fock equations is precisely equivalent to CIS[43]). This accuracy arises because the low-lying excitations in the simple model are predominately singles (or a linear superposition of singles) and therefore relatively weakly correlated. As one expects TDDFT to outperform CIS for this problem this suggests that TDDFT will be reliable, consistent with the excellent agreement we find between our calculations and experiment. The TDDFT results above show that the excitations are predominately singles or mixtures of singles, which is consistent with the above argument. Therefore it appears that correlations are correctly described even at the B3LYP level of theory.

The absence of a significant solvatochromic effect is more difficult understand,[42] but does seem broadly consistent with what is observed experimentally in these complexes.[36] In materials such as these iridium(III) complexes which exhibit weak MLCT transitions, changing the dipole strength of the surrounding environment does not greatly perturb the system.[44] In cases where strong MLCT transitions occur (e.g. the ruthenium dye N3) significant solvatochromism is observed.[45–47] Nevertheless, explicit calculation of the solvent effects would be an interesting subject to pursue in the future. There are a number of mature methods by which this could be undertaken.[48,49] This could provide useful insights beyond those of De Angelis et al.[15]

3. Conclusions

We have shown that it is possible to trace the genealogy of the excited states of $Ir(ppy)_3$ and $Ir(tpz)_3$ back to atomic physics by considering a series of calculations at different levels of theory. Firstly, we showed that one-component ZORA calculations, with spin–orbit coupling included perturbatively, accurately reproduce the results of two-component calculations. As well as being significantly lower cost, the one-component calculations allow one to systematically "turn off" relativistic effects and thus to understand them better. In this way we have shown that both scalar relativistic and spin–orbit effects lead to important consequences for the photophysics of these complexes. In particular, there is an indirect relativistic stabilisation of the MLCT states. This means that indirect relativistic effects increase the degree to which SOC can hybridise singlet and triplet states[35] and hence plays an important role in determining the optical properties of these complexes. The low-energy spectra of these two complexes share very similar structures and can be qualitatively understood in the same terms. Nevertheless there are important differences between these two complexes beyond their colour. We have predicted that these should be particularly apparent in MCD experiments.

Experimental Section

Closed-shell geometry optimisation of both complexes was performed using GAMESS[50,51] with the B3LYP hybrid functional.[52,53] The LANL2DZ basis[54] set was employed for iridium, while the 6-31G basis set[55,56] was used for nitrogen, carbon and hydrogen. C_3 symmetry was enforced during the optimisation routine. The geometry of $Ir(ptz)_3$ was optimised without the *n*-propyl solubilising groups (substituted by a single hydrogen) as these additional degrees of freedom significantly increase the computational cost of both the geometry optimisation procedure and the higher level calculations to follow, whereas the *n*-propyl groups only have a weak inductive effect and hence will not alter the optical properties of $Ir(ptz)_3$ significantly.

TDDFT calculations were carried out with the Amsterdam Density Functional (ADF) 2009.01 program.[57–59] As with the geometry optimisation, the B3LYP functional was used throughout. Self-consistent two-component spin–orbit TDDFT calculations within the ZORA[60–62] were performed for the fifty lowest spin-polarized excitations. One-component ZORA TDDFT calculations,[30] which included SOC perturbatively, were performed on the fifty lowest scalar relativistic singlet and triplet excitations. This results in a total of 200 spin-mixed excitations.

All calculations use a TZP basis set on the iridium, and henceforth the basis set of a particular calculation refers to that applied to the light elements. Due to their computational cost, the two-component calculations were limited to a DZP basis set on the light elements and a frozen-core approximation encompassing the iridium 4s, 3p, 2d and 1f orbital, the nitrogen 1s orbitals and carbon 1s orbital. Both DZP and TZP basis sets were investigated in the single-component theory. Further, the lower computational cost of the single component calculations allowed us to compare all-electron calculations and the frozen-core approximation.

We have chosen the B3LYP functional and the basis sets described above because of their widespread use. However, further improvement of these calculations may be possible by judicious choice of functional and basis set.[63]

All calculations were performed on the VAYU cluster at the Australian National Computing Infrastructure National Facility (NCI-NF). The cluster is comprised of Infiniband connected nodes of Sun X6275 blade servers each containing two quad-core 2.93 GHz Intel CPUs and 24 Gbytes of accessible memory.

Acknowledgements

We thank Hartmut Yersin and Thomas Hofbeck for providing us with their published data and Anthony Jacko, Seth Olsen and Paul Schwenn for helpful conversations. This work was supported by the Australian Research Council (ARC) and the National Computational Infrastructure (NCI). A.R.G.S. thanks AINSE for a PGRA, P.L.B. was supported by an ARC Federation Fellowship (FF0668728) and B.J.P. was supported by an ARC Queen Elizabeth II Fellowship (DP0877875). All calculations were performed on the NCI National Facility under a grant from the Merit Application Scheme. We would like to thank the staff at the NCI, and particu-

larly David Singleton, for their assistance in performing these calculations.

Keywords: density functional calculations · organic light-emitting diodes · phosphorescence · relativity · spin–orbit coupling

[1] M. Baldo, D. O'Brien, Y. You, A. Shoustikov, S. Sibley, M. Thompson, S. Forrest, *Nature* **1998**, *395*, 151 – 154.
[2] A. C. Jacko, B. J. Powell, R. H. McKenzie, *J. Chem. Phys.* **2010**, *133*, 124314.
[3] Y. You, S. Y. Park, *Dalton Trans.* **2009**, 1267 – 1282.
[4] S. C. Lo, C. P. Shipley, R. N. Bera, R. E. Harding, A. R. Cowley, P. L. Burn, I. D. W. Samuel, *Chem. Mater.* **2006**, *18*, 5119 – 5129.
[5] S. Haneder, E. D. Como, J. Feldmann, J. M. Lupton, C. Lennartz, P. Erk, E. Fuchs, O. Molt, I. Münster, C. Schildknecht, G. Wagenblast, *Adv. Mater.* **2008**, *20*, 3325 – 3330.
[6] C.-F. Chang, Y.-M. Cheng, Y. Chi, Y.-C. Chiu, C.-C. Lin, G.-H. Lee, P.-T. Chou, C.-C. Chen, C.-H. Chang, C.-C. Wu, *Angew. Chem.* **2008**, *120*, 4618 – 4621; *Angew. Chem. Int. Ed.* **2008**, *47*, 4542 – 4545.
[7] M. A. Baldo, S. Lamansky, P. E. Burrows, M. E. Thompson, S. R. Forrest, *Appl. Phys. Lett.* **1999**, *75*, 4 – 6.
[8] M. van Veenendaal, J. Chang, A. J. Fedro, *Phys. Rev. Lett.* **2010**, *104*, 067401.
[9] T. Matsushita, T. Asada, S. Koseki, *J. Phys. Chem. C* **2007**, *111*, 6897 – 6903.
[10] E. Jansson, B. Minaev, S. Schrader, H. Agren, *Chem. Phys.* **2007**, *333*, 157 – 167.
[11] S. Koseki, M. S. Gordon, M. W. Schmidt, N. Matsunaga, *J. Phys. Chem.* **1995**, *99*, 12764 – 12772.
[12] S. Koseki, M. W. Schmidt, M. S. Gordon, *J. Phys. Chem. A* **1998**, *102*, 10430 – 10435.
[13] B. Minaev, H. Agren, F. De Angelis, *Chem. Phys.* **2009**, *358*, 245 – 257.
[14] F. De Angelis, S. Fantacci, N. Evans, C. Klein, S. M. Zakeeruddin, J. E. Moser, K. Kalyanasundaram, H. J. Bolink, M. Gratzel, M. K. Nazeeruddin, *Inorg. Chem.* **2007**, *46*, 5989 – 6001.
[15] F. De Angelis, L. Belpassi, S. Fantacci, *J. Mol. Struct. THEOCHEM* **2009**, *914*, 74 – 86.
[16] K. Nozaki, *J. Chin. Chem. Soc.* **2006**, *53*, 101 – 112.
[17] K. Nozaki, K. Takamori, Y. Nakatsugawa, T. Ohno, *Inorg. Chem.* **2006**, *45*, 6161 – 6178.
[18] A. R. G. Smith, M. J. Riley, S.-C. Lo, P. L. Burn, I. R. Gentle, B. J. Powell, *Phys. Rev. B* **2011**, *83*, 041105(R).
[19] W. T. Yang, A. J. Cohen, P. Mori-Sanchez, *Science* **2008**, *321*, 792 – 794.
[20] A. Dreuw, J. L. Weisman, M. Head-Gordon, *J. Chem. Phys.* **2003**, *119*, 2943 – 2946.
[21] J. A. Vlček, S. Zális, *Coord. Chem. Rev.* **2007**, *251*, 258 – 287.
[22] K. G. Dyall, K. Fægri, *Introduction to Relativistic Quantum Chemistry*, Oxford University Press, New York, **2007**.
[23] R. Dreizler, *Relativistic Density Functional Theory*, Springer, Berlin, **2003**.
[24] W. Greiner, *Relativistic Quantum Mechanics: Wave Equations*, Springer, Berlin, **1994**.
[25] P. Strange, *Relativistic Quantum Mechanics*, Cambridge University Press, Cambridge, **1998**.
[26] C. Chang, M. Pelissier, P. Durand, *Phys. Scr.* **1986**, *34*, 394 – 404.
[27] A. H. MacDonald, S. H. Vosko, *J. Phys. C* **1979**, *12*, 2977 – 2990.
[28] A. K. Rajagopal, *J. Phys. C* **1978**, *11*, L943.
[29] A. K. Rajagopal, J. Callaway, *Phys. Rev. B* **1973**, *7*, 1912 – 1919.
[30] F. Wang, T. Ziegler, *J. Chem. Phys.* **2005**, *123*, 154102 – 154112.
[31] P. J. Hay, *J. Phys. Chem. A* **2002**, *106*, 1634 – 1641.
[32] R. J. F. Berger, H. G. Stammler, B. Neumann, N. W. Mitzel, *Eur. J. Inorg. Chem.* **2010**, 1613 – 1617.
[33] Formally, once SOC is included the energy eigenstates are required to be eigenstates of the total angular momentun, $J = L + S$, rather than of the spin, S, and orbital angular momentum, L, separately.
[34] A. C. Jacko, R. H. McKenzie, B. J. Powell, *J. Mater. Chem.* **2010**, *20*, 10301 – 10307.
[35] A. C. Jacko, B. J. Powell, *Chem. Phys. Lett.* **2011**, *508*, 22 – 28.
[36] T. Hofbeck, H. Yersin, *Inorg. Chem.* **2010**, *49*, 9290 – 9299.
[37] R. S. Knox, *Photochem. Photobiol.* **2003**, *77*, 492 – 496.
[38] J. J. Riesz, J. B. Gilmore, R. H. McKenzie, B. J. Powell, M. R. Pederson, P. Meredith, *Phys. Rev. E* **2007**, *76*, 021915.
[39] J. P. Desclaux, Y.-K. Kim, *J. Phys. B* **1975**, *8*, 1177 – 1182.
[40] S. J. Rose, I. P. Grant, N. C. Pyper, *J. Phys. B* **1978**, *11*, 1171 – 1176.
[41] T. Tsuboi, M. Tanigawa, *Thin Solid Films* **2003**, *438 – 439*, 301 – 307.
[42] P. E. Schwenn, P. L. Burn, B. J. Powell, *Org. Electron.* **2011**, *12*, 394 – 403.
[43] J. B. Foresman, M. Head-Gordon, J. A. Pople, M. J. Frisch, *J. Phys. Chem. A* **1992**, *96*, 135 – 149.
[44] K. Dedeian, J. Shi, E. Forsythe, D. C. Morton, P. Y. Zavalij, *Inorg. Chem.* **2007**, *46*, 1603 – 1611.
[45] S. Fantacci, F. De Angelis, A. Selloni, *J. Am. Chem. Soc.* **2003**, *125*, 4381 – 4387.
[46] F. Cecchet, A. M. Gioacchini, M. Marcaccio, F. Paolucci, S. Roffia, M. Alebbi, C. A. Bignozzi, *J. Phys. Chem. B* **2002**, *106*, 3926 – 3932.
[47] P. Péchy, T. Renouard, S. M. Zakeeruddin, R. Humphry-Baker, P. Comte, P. Liska, L. Cevey, E. Costa, V. Shklover, L. Spiccia, G. B. Deacon, C. A. Bignozzi, M. Grätzel, *J. Am. Chem. Soc.* **2001**, *123*, 1613 – 1624.
[48] C. C. Pye, T. Ziegler, *Theor. Chem. Acc.* **1999**, *101*, 396 – 408.
[49] DALTON, a molecular electronic structure program, Release 2.0, http://daltonprogram.org/, **2005**.
[50] M. W. Schmidt, K. K. Baldridge, J. A. Boatz, S. T. Elbert, M. S. Gordon, J. H. Jensen, S. Koseki, N. Matsunaga, K. A. Nguyen, S. Su, T. L. Windus, M. Dupuis, J. John, A. Montgomery, *J. Comput. Chem.* **1993**, *14*, 1347 – 1363.
[51] "Advances in Electronic Structure Theory: GAMESS a decade later": M. S. Gordon, M. W. Schmidt in *Theory and Applications of Computational Chemistry: the first forty years* (Eds.: C. E. Dykstra, G.Frenking, K. S.Kim, G. E.Scuseria), Elsevier, Amsterdam, **2005**.
[52] A. D. Becke, *J. Chem. Phys.* **1993**, *98*, 5648 – 5652.
[53] P. J. Stephens, F. J. Devlin, C. F. Chabalowski, M. J. Frisch, *J. Phys. Chem.* **1994**, *98*, 11623 – 11627.
[54] P. J. Hay, W. R. Wadt, *J. Chem. Phys.* **1985**, *82*, 299 – 310.
[55] R. Ditchfield, W. J. Hehre, J. A. Pople, *J. Chem. Phys.* **1971**, *54*, 724 – 728.
[56] W. J. Hehre, R. Ditchfield, J. A. Pople, *J. Chem. Phys.* **1972**, *56*, 2257 – 2261.
[57] C. Fonseca Guerra, J. G. Snijders, G. te Velde, E. J. Baerends, *Theor. Chem. Acc.* **1998**, *99*, 391 – 403.
[58] G. te Velde, F. M. Bickelhaupt, E. J. Baerends, C. F. Guerra, S. J. A. van Gisbergen, J. G. Snijders, T. Ziegler, *J. Comput. Chem.* **2001**, *22*, 931 – 967.
[59] ADF2009.01, SCM, Theoretical Chemistry, Vrije Universiteit, Amsterdam, The Netherlands, http://www.scm.com/.
[60] E. van Lenthe, E. J. Baerends, J. G. Snijders, *J. Chem. Phys.* **1993**, *99*, 4597 – 4610.
[61] E. van Lenthe, E. J. Baerends, J. G. Snijders, *J. Chem. Phys.* **1994**, *101*, 9783 – 9792.
[62] E. van Lenthe, J. G. Snijders, E. J. Baerends, *J. Chem. Phys.* **1996**, *105*, 6505 – 6516.
[63] F. Neese, *Coord. Chem. Rev.* **2009**, *253*, 526 – 563.

Received: May 23, 2011
Published online on July 22, 2011

Inorganic Chemistry

Article

pubs.acs.org/IC

Effects of Fluorination on Iridium(III) Complex Phosphorescence: Magnetic Circular Dichroism and Relativistic Time-Dependent Density Functional Theory

A. R. G. Smith,[†,‡] M. J. Riley,[‡] P. L. Burn,*[,†,‡] I. R. Gentle,[†,‡] S.-C. Lo,[†,‡] and B. J. Powell*[,†,§]

[†]Centre for Organic Photonics & Electronics, [‡]School of Chemistry & Molecular Biosciences, and [§]School of Mathematics & Physics, The University of Queensland, Brisbane, Queensland 4072, Australia

Supporting Information

ABSTRACT: We use a combination of low temperature, high field magnetic circular dichroism, absorption, and emission spectroscopy with relativistic time-dependent density functional calculations to reveal a subtle interplay between the effects of chemical substitution and spin−orbit coupling (SOC) in a family of iridium(III) complexes. Fluorination at the *ortho* and *para* positions of the phenyl group of *fac*-tris(1-methyl-5-phenyl-3-*n*-propyl-[1,2,4]triazolyl)iridium(III) cause changes that are independent of whether the other position is fluorinated or protonated. This is demonstrated by a simple linear relationship found for a range of measured and calculated properties of these complexes. Further, we show that the phosphorescent radiative rate, k_r, is determined by the degree to which SOC is able to hybridize T_1 to S_3 and that k_r is proportional to the inverse fourth power of the energy gap between these excitations. We show that fluorination in the *para* position leads to a much larger increase of the energy gap than fluorination at the *ortho* position. Theory is used to trace this back to the fact that fluorination at the *para* position increases the difference in electron density between the phenyl and triazolyl groups, which distorts the complex further from octahedral symmetry, and increases the energy separation between the highest occupied molecular orbital (HOMO) and the HOMO-1. This provides a new design criterion for phosphorescent iridium(III) complexes for organic optoelectronic applications. In contrast, the nonradiative rate is greatly enhanced by fluorination at the *ortho* position. This may be connected to a significant redistribution of spectral weight. We also show that the lowest energy excitation, 1A, has almost no oscillator strength; therefore, the second lowest excitation, 2E, is the dominant emissive state at room temperature. Nevertheless the mirror image rule between absorption and emission is obeyed, as 2E is responsible for both absorption and emission at all but very low (<10 K) temperatures.

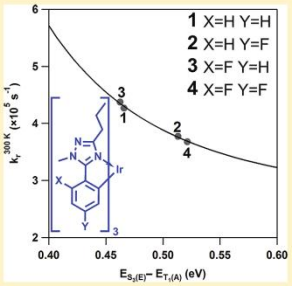

INTRODUCTION

Organic light emitting diodes (OLEDs) based on phosphorescent emitters can efficiently harvest both singlet and triplet excitations.[1−3] From a device point of view this is advantageous, since the internal quantum efficiency can approach 100%,[4] making phosphorescent materials prime candidates for full-color displays[1,5] and solid-state lighting.[6−8]

To date, the best phosphorescent materials for OLEDs are based on iridium(III) complexes.[3,9−11] Ligand modification has been used to tune the emission color,[12] but it is not possible to predict the photoluminescence quantum yields (PLQYs) of the resultant metal complexes.[10,13] The subtle effect played by spin−orbit coupling (SOC), which enables phosphorescence, has been inadequately studied, which makes it difficult to understand the relationship between ligand substitution and the radiative rate of phosphorescence.

For display and lighting applications, the development of highly efficient deep blue OLEDs remains an outstanding problem.[1] Here we focus on *fac*-tris(1-methyl-5-phenyl-3-*n*-propyl-[1,2,4]triazolyl)iridium(III) [Ir(ptz)$_3$; **1**; Figure 1], which displays sky blue phosphorescence with a high PLQY of 66%.[10] Fluorination at the X and/or Y positions (*ortho* and *para* to the triazolyl ring) successfully drives the phosphorescence to a deeper blue (shorter wavelength); however, this also results in a dramatic drop in the PLQY (see Table 1).[10]

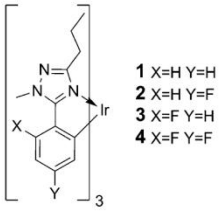

Figure 1. Structures of complexes **1**−**4** investigated in this study based on the parent *fac*-tris(1-methyl-5-phenyl-3-*n*-propyl-[1,2,4]triazolyl)-iridium(III). Fluorination on the ligand phenyl ring blue shifts the emission, but results in a decrease in the PLQY.[10]

Received: August 31, 2011
Published: February 16, 2012

Table 1. Selected Room Temperature Spectroscopic Properties of Iridium(III) Complexes 1−4[a]

	experimental						calculated	
complex	PL λ_{max} (nm)	CIE (x, y)	Φ_{PL}	τ (μs)	k_r ($\times 10^5$ s^{-1})	k_{nr} ($\times 10^5$ s^{-1})	k_r ($\times 10^5$ s^{-1})	ZFS T_1(A) $\Delta E_{1A\text{-}2E}$ (meV)
1	449	0.158, 0.202	0.66 ± 0.07	1.08 ± 0.03	6.1 ± 0.8	3.1 ± 1.0	4.3	11.6
2	428	0.157, 0.127	0.27 ± 0.05	1.25 ± 0.30	2.2 ± 0.9	5.8 ± 2.8	3.8	8.7
3	443	0.155, 0.161	0.06	0.15	4.0	63	4.4	11.3
4	425	0.159, 0.117	0.03 ± 0.01	0.15 ± 0.07	2.0 ± 1.6	65 ± 33	3.7	7.3

[a]Fluorine substitution shifts the emission from sky to deep blue [as evidenced by both the wavelength of the photoluminescence maximim (PL λ_{max}) and the Commission Internationale de l'Eclairage (CIE) coordinates]; however, the PLQY (Φ_{PL}) falls off precipitously. Both the absolute values and the trend in the calculated radiative rates are similar to those determined experimentally. Like the experimental data,[10] complexes **1** and **3** have higher calculated radiative rates than **2** and **4**. Errors have not been reported for complex **3**. Nevertheless it is important to note that the radiative rates of complexes **2** and **4** are the same within experimental error and if there is a difference between the radiative rates of complexes **1** and **3** it has not yet been seen in these experiments. The calculated zero field splitting (ZFS) of the lowest triplet T_1(A) is also given.

We are therefore motivated to understand the changes in PLQY caused by substitutions on the ligand in complexes **1**−**4**. In particular it is important to note that there are two competing contributions to the PLQY: radiative decay and nonradiative decay. In this paper we will focus on understanding the differences in the radiative decay of these four iridium(III) complexes. We will show that these can be understood in terms of the interplay between SOC and the changes in electronic structure caused by chemical substitutions.

There have been few reported attempts to understand the role of SOC in phosphorescent iridium(III) complexes in particular for blue emissive materials. Previous work has focused on the green phosphorescent complex *fac*-tris(2-phenylpyridyl)iridium(III), [Ir(ppy)$_3$]. Hofbeck and Yersin[14] identified three close lying excited states from low temperature spectroscopic measurements as the zero field split sublevels of the lowest triplet excitation, T_1. Ir(ppy)$_3$ has C_3 symmetry, and one expects SOC to split a nonorbitally degenerate triplet state into a nondegenerate (A) state and a 2-fold degenerate (E) state, with the A state having slightly lower energy.[15] It is therefore interesting that Hofbeck and Yersin found three distinct states, none of which were split by a magnetic field, suggesting that they are all nondegenerate. Thus, Hofbeck and Yersin argued that the C_3 symmetry is lifted by solvent effects. Interestingly, a number of in vacuo density functional calculations[16,17] suggest that the symmetry of the iridium(III) complex is lower in the T_1 state than in the ground state, S_0. Since the symmetry lowering can occur in equivalent ways because of the 3-fold symmetry of the S_0 state, this results in the existence of equivalent minima on the T_1 potential energy surface.

The three level substructure observed in the emitting "triplet" manifold of Ir(ppy)$_3$ has similarities to the related d^6 systems Ru(bpy)$_3^{2+}$ and Os(bpy)$_3^{2+}$.[18−20] The existence of three nondegenerate states implies lower symmetry than the ground state (D_3) in these cases. With isotopic substitution in suitable host lattices it is possible to investigate whether the excited emitting states correspond to a localization of the metal-to-ligand charge transfer (MLCT) state onto one ligand using high resolution spectroscopy.[21] The driving force for this low symmetry distortion (vibronic coupling) and the interaction with the environment is beyond the scope of this work. A major difference between the Ru and Os systems and the Ir complexes of the present study is the greater influence of the SOC in mixing singlet character into the lowest T_1 state, because of both the larger SOC constant for Ir and the changes in the energies of the singlet−triplet levels (discussed below).

A number of groups have studied relativistic effects theoretically.[16,17,22−28] Most approaches taken have included SOC perturbatively. We have recently shown[28] that this approximation accurately reproduces the results of calculations in the two-component formalism, which includes SOC to all orders, in these complexes. We have also shown that scalar relativistic effects are sizable in these iridium(III) complexes, and play a key role in determining the degree of MLCT character and hence their optical properties.[27] Both Matsushita et al.[23] and Jansson et al.[17] studied Ir(ppy)$_3$ with SOC included via the semiempirical effective nuclear charge method, which includes SOC on top of nonrelativistic calculations. Matsushita et al.[23] studied the mixing of singlet and triplet states and the implications of this for phosphorescence, and Jansson et al.[17] investigated the nature of the T_1 excitation in some depth. Nozaki et al.[16,29] have also investigated organometallic complexes with the SOC included perturbatively about nonrelativistic TDDFT calculations. It was shown[16] that this method provides a reasonable description of the zero-field splittings and oscillator strengths of Ir(ppy)$_3$, and in a further study Nozaki and collaborators investigated the differences in the optical properties in a range of tris(2,2′-bipyridine) transition metal complexes using the same method.[29]

Trends across related molecules can also provide important insights into the role of SOC in iridium(III) complexes. Li et al.[30] pointed out that, to leading order in perturbation theory, the radiative rate from T_1 is proportional to the inverse square of the energy gap between T_1 and S_1. Haneder et al.[31] also discussed this effect but found poor agreement with experiment. However, Jacko et al.[32−34] have recently found that an additional dependence on the energy gap between T_1 and S_1, which is also inverse square to leading order, arises from the details of the hybridization between ligand-centered (LC) and MLCT excitations required to form T_1. Thus Jacko et al.'s[33] work predicts that the radiative rate of T_1 varies as the fourth power of the inverse of the energy gap between T_1 and S_1.

EXPERIMENTAL SECTION

Synthesis and Characterization. The synthesis and characterization of complexes **1**, **2**, and **4** has been previously reported by Lo et al.[10] **3** was prepared by a similar synthetic method, details of which are given in the Supporting Information. Oxidation potentials were determined by cyclic voltammetry in dichloromethane and referenced against the ferricenium/ferrocene couple (Supporting Information).[10]

Experimental Method. Magnetic circular dichroism (MCD) experiments were performed at 10 K and an applied 5 T magnetic field. The iridium(III) complexes were dissolved in 2-methyltetrahydrofuran, which was chosen for its capacity to form high quality glasses suitable for low temperature MCD measurements. The total and differential circularly polarized light intensities were measured simultaneously using a single beam instrument consisting of a xenon arc lamp dispersed by a Jobin/Yvon 750 S monochromator. The beam

was linearly polarized by a calcite crystal (extinction <10^{-6}), mechanically chopped at 500 Hz (New Focus 3501), circularly polarized by a photoelastic modulator at a frequency of 42 kHz (Hinds PEM II/IS42), and passed through the sample held in an Oxford Instruments Spectromag 7 T superconducting magnet. Light was detected with either an S-5 photomultiplier (Hamamatsu R7459) or a Si avalanche photodiode detector. All instrument control and data collection was achieved with GPIB protocols and LABVIEW software. Emission spectra were collected using the 350.7 nm line of a Kr^+ laser and a SPEX1704 monochromator.

MCD is the differential absorption of left and right circularly polarized light in the presence of a magnetic field.[35] MCD spectra can be analyzed in terms of the so-called A, B, and C-terms. A and C-terms arise from degeneracy in the excited or ground states respectively, while B-terms are from mixing between electronic states or changes in the total angular momentum. MCD A-terms appear as a derivative line shape in the spectra, owing to spectral overlap between degeneracies lifted by the magnetic field (see Supporting Information, Figure S1). C-terms appear as a single band, but because of their ground state degeneracy, C-terms are temperature sensitive. B-terms also appear as single bands, but show no temperature dependence as the line shape is not determined by degenerate states.

Computational Method. The measured[10] crystal structure of **1** was used as the initial input for the geometry optimization. The *n*-propyl groups were removed from the ligands since they have only a weak inductive effect and are unlikely to affect the electronic structure significantly and will complicate the potential energy surface. The structures of **1**−**4** were relaxed via density functional theory (DFT) using the B3LYP hybrid functional[36−38] in the GAMESS suite of programs.[39,40] These calculations used a LANL2DZ basis[41] for the iridium and 6-31G basis for hydrogen, carbon, nitrogen, and fluorine.[42,43] Motivated by our MCD results, see Results and Discussion, care was taken to conserve the C_3 symmetry of these *facial* complexes throughout the geometry optimization procedure. The converged molecular structures changed little from measured crystal geometries (see Supporting Information).

Time-dependent DFT (TDDFT) property calculations were carried out with the Amsterdam Density Functional (ADF2009.01) program.[44−46] As with the geometry optimization, the B3LYP hybrid functional was used. On the basis of the one-component zeroth order regular approximation (ZORA),[47,48] the 50 lowest scalar relativistic singlet and triplet excitations were calculated. SOC was included perturbatively around the one-component TDDFT calculations,[49] leading to a total of 200 spin-mixed excitations. The calculations were performed with a Slater type TZP basis set[50,51] and a frozen core approximating the iridium [1s 2s 2p 3s 3p 3d 4s 4p 4d 4f], fluorine [1s], nitrogen [1s] and carbon [1s] shells. Nonrelativistic calculations were also carried out for comparison.

Extensive benchmarking calculations have shown that the choice of basis set has a large effect on the calculated energies and that the TZP basis is the minimum required to get good agreement with experiment.[28] Treating the core electrons on the iridium atom within the frozen core approximation has little effect on the calculated excitations. Including SOC as a perturbation to the scalar ZORA, TDDFT gives essentially the same results as those obtained from more expensive two-component methods, and is more easily related to the underlying molecular orbital excitations.[28]

C_3 molecular symmetry could not be utilized in the ADF TDDFT calculations because the C_3 point group contains complex irreducible representations. As a result small splittings between formally degenerate excitations can occur (cf. Supporting Information) despite the C_3 symmetry of the input geometry. These small splittings are artifacts of the calculation and have no physical significance. Symmetry labels were determined manually by examining the full range of properties of the excitations.

To investigate the total redistribution of charge after successive fluorination, the molecule was divided into three fragments comprising the iridium, phenyl, and triazolyl moieties. A Hirshfeld population analysis was performed according to these divisions.[52]

SOC mixes singlet and triplet states. It is well-known that TDDFT favors low-spin states over high-spin states because of the approximate treatment of the exchange interaction.[53−55] Thus, triplet excitations will tend to be destabilized relative to singlets. This may have two important consequences for our results: in the scalar relativistic DFT this will shift the energies of the excitations as described above; further this will lead to an overestimation of the degree of hybridization between singlets and triplets because of SOC. Quantifying these errors is beyond the scope of this work; however, a rough estimate might be made by comparing to Dirac−Hartree−Fock calculations as the Hartree−Fock approximation displays the opposite bias.[53]

■ RESULTS AND DISCUSSION

Degeneracy and Symmetry. The absorption and MCD of complexes **1**−**4** share many similarities (Figure 2). Only low temperature measurements will be discussed below; however, many of the features are still present at room temperature but are, as might be expected, considerably broadened and therefore poorly resolved.

In the MCD spectra between 2.7−3.2 eV a number of features can be clearly identified. The MCD spectra continue above 3.2 eV but because of the strong optical absorption the spectra become noisy and unreliable. It is clear that the higher energy absorptions beyond 3.2 eV are the result of a complex ensemble of excitations, so it is not clear that MCD data in this region provides significant insight into the electronic structure. Further, these higher lying states (>0.5 eV above the absorption onset) are of little significance to the emission mechanism at room temperature.

The first feature to note in the MCD is the strong A-term localized just after the absorption onset. The peak energy of the corresponding absorption band is reported in Table 2. In all the complexes the A-term feature has similar intensity.

It is interesting to compare this result with Hofbeck and Yersin's spectroscopic studies of $Ir(ppy)_3$, which shares many similarities with complexes **1**−**4**.[28] On the basis of these measurements Hofbeck and Yersin argued that in $Ir(ppy)_3$ the lowest triplet excitation, T_1, is split into three substates. This led them to postulate that the symmetry of $Ir(ppy)_3$ is lowered from C_3 by distortions induced from a host material, whether a solvent or a solid matrix.[14,56] Indeed this group has argued that spectroscopic measurements reveal three distinct substates of T_1 in many iridium(III) complexes.[56−59]

Therefore, the clear resolution of MCD A-terms in all four complexes is an interesting result. While an A-term is due to an excited state degeneracy, the degree of degeneracy is only established within the line width of the feature. These linewidths are comparable with the observed splitting in $Ir(ppy)_3$,[14] but the clear equal and opposite signed peaks observed in Figure 2 indicates that the "pseudo A-term" must arise from the 2E state at C_3 symmetry. That is, any symmetry lowering does not split the E levels of the lowest T_1 manifold enough to destroy the derivative shaped $\Delta\varepsilon$ expected for an A-term from a degenerate E state. The symmetric shape of this MCD feature is maintained at all field strengths and so is not a result of (B-term) magnetic field mixing. Therefore, the observed MCD A-term must be due to excitation into the (degenerate) E electronic substate of the first triplet state in C_3 (or to excitation into two close lying levels that originate from an E state, but that cannot be resolved in these experiments.) Further, a clear mirror image symmetry is observed between the lowest energy observed feature in absorption and the highest energy observed feature in emission (Figure 3). The relatively small Stokes shift (~220 cm^{-1}) is consistent with the observed lowest energy absorption feature also being responsible for the emission. At temperatures $\gtrsim$10 K most of the emission is coming from the E manifold, the same state which

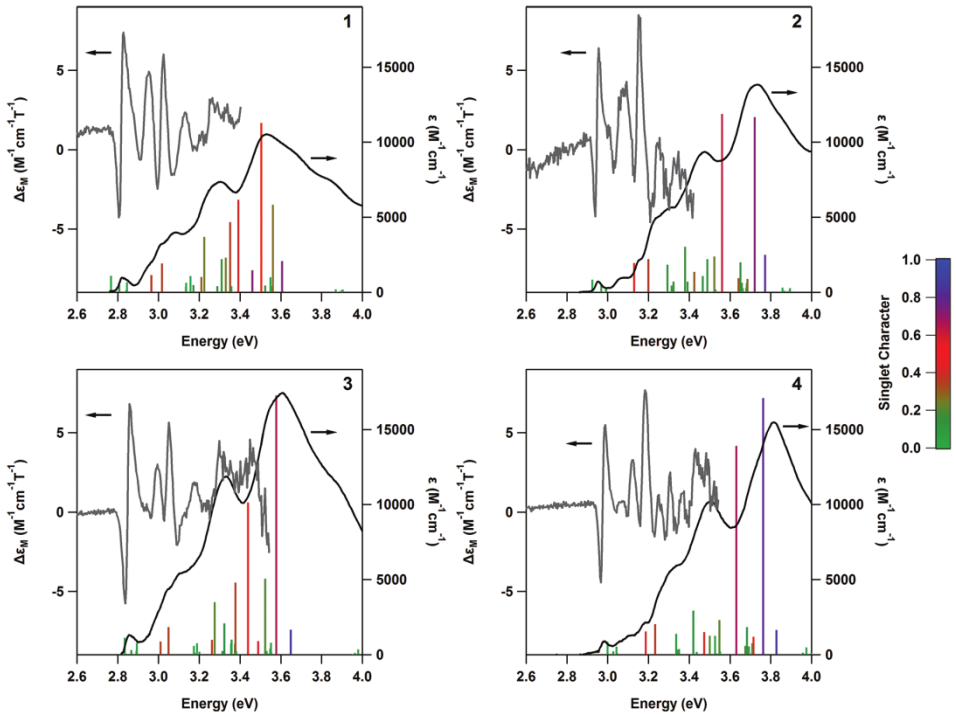

Figure 2. Low temperature absorption, MCD, and calculated relativistic TDDFT excitations (which include SOC perturbatively) for iridium(III) complexes **1**−**4**. ε is the usual molar extinction coefficient while $\Delta\varepsilon_M$ is the MCD extinction coefficient scaled to the magnetic field strength. The calculated excitations are color-coded according to the degree of singlet character. In all the complexes, a strong MCD A-term occurs around the first absorption band.

Table 2. Measured Optical Energy Gaps from Low Temperature Absorption Spectroscopy, Oxidation Potentials from Cyclic Voltammetry,[10] and the Orbital Energies from Scalar Relativistic DFT Calculations[a]

	experimental		calculated energy (eV)						
complex	E_{opt} (eV)	$E_{1/2}$ (ox) (V)	HOMO-1	HOMO	LUMO	LUMO+1	$\Delta E_{HOMO-HOMO-1}$	$\Delta E_{LUMO-HOMO}$	$\Delta E_{LUMO+1-LUMO}$
1	2.82	0.28	−5.154	−4.980	−1.166	−0.989	0.174	3.814	0.177
2	2.95	0.50	−5.583	−5.393	−1.405	−1.229	0.190	3.988	0.176
3	2.85	0.50	−5.544	−5.382	−1.489	−1.335	0.162	3.893	0.154
4	2.98	0.72	−5.969	−5.781	−1.701	−1.557	0.188	4.080	0.144
(**1** + **4**) − (**2** + **3**)	0.00	0.00	0.004	0.014	0.027	0.018	0.010	0.013	−0.009

[a]The row labelled (**1**+**4**)−(**2**+**3**) is a test of eq 6, formally, $(\Pi_1 + \Pi_4) - (\Pi_2 + \Pi_3)$. Hence, an entry of 0 indicates perfect agreement between experiment/DFT and the predictions of that equation. The observation that entries of this row are all zero to a very high accuracy indicates that the changes to the excitation energies caused by fluorination at the X and Y positions act independently of one another.

carries the absorption intensity. At low temperature (2 K) the emission changes dramatically as the upper levels are depopulated. Similar to that described for $Ir(ppy)_3$,[14] a Herzberg−Teller vibronically allowed emission is observed and this, together with the magnetic circular photoluminescence, will be the subject of a future publication.[60]

At energies above the first A-term two positive bands can be identified in the MCD spectra (cf. Figure 2). It is not possible to definitively label these features as arising from particular MCD terms using the experimental data alone, although it is clear that a number of B and A-terms are clearly required to describe the spectrum.

Relativistic Electronic Structure Calculations: Comparison with Spectroscopy. To further understand the MCD spectra we carried out relativistic TDDFT calculations. These calculations give us information at three levels of theory: (i) scalar relativistic DFT, these are the simplest calculations to understand and interpret as they fit most closely with chemical intuition about molecular orbitals; (ii) scalar relativistic TDDFT, these calculations give us access to what the excited states of the complexes would be in the absence of SOC and can allow us to understand the excitations in terms of transitions between the orbitals in the scalar relativistic DFT calculations; and (iii) perturbation theory with SOC about the scalar relativistic TDDFT.

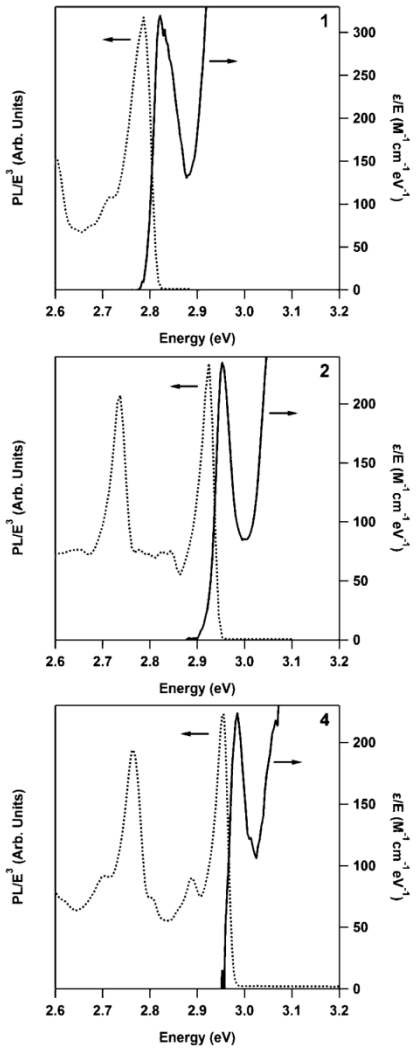

Figure 3. Plots of the absorption and emission of complexes **1**, **2**, and **4** at 10 K. The absorption and emission axes have been rescaled according to the energy and energy cubed, respectively. Similar spectra are obtained at temperatures above 10 K, but are significantly broader and poorly resolved.[10,27] All three complexes show clear mirror image symmetry, indicating that the state responsible for the observed lowest energy absorption is also responsible for the emission at this temperature.

The latter calculations are the most accurate and are directly comparable to experiment, and also allow an understanding of these transitions in terms of the scalar relativistic TDDFT. Full results of all three levels of theory are tabulated in the Supporting Information.

We will focus initially on the calculations that include SOC and a comparison of these with experiment. We have previously shown that this level of theory gives good agreement with full two-component ZORA calculations for iridium(III) complexes, despite its much lower computational cost[28] and therefore we expect good agreement with experiment.

The vertical lines in Figure 2 show the calculated excitation spectrum: the heights of the lines indicate the calculated oscillator strengths and the colors indicate the degree of singlet character of the excitations (because of the mixing of singlets and triplets by SOC). The calculations accurately reproduce the experimentally measured absorption spectrum. In the Supporting Information, Figure S2 we compare calculated spectra that have been convoluted with bandshapes of finite width, making the agreement with experiment even more clear. In particular, the absorption onset and peak energies are very closely reproduced. Further, the relativistic TDDFT calculations provide an accurate prediction of the energy at which light is emitted.

SOC splits the first triplet state $T_1(A)$ (we include the label A to stress that there is no orbital degeneracy as the orbital part of this state transforms according to the A irreducible representation of C_3) into a nondegenerate A and 2-fold degenerate E spin−orbit states (which we will henceforth refer to as 1A and 2E). The calculated zero field splitting (ZFS) of $T_1(A)$ is presented in Table 1. The lowest energy state, 1A, is predicted to have a very small oscillator strength ($<10^{-5}$ au) in all four complexes. Four higher energy excitations (two A and two E; numbered 3−6) lie above the $T_1(A)$ manifold because of the ZFS of the second triplet state $T_2(E)$ (Figure 4).

In light of the calculated excitations we may begin to assign the MCD spectrum. The lowest energy MCD A-term feature can be assigned as originating from the transitions to the 2E levels. If there is a symmetry lowering perturbation as occurs in $Ir(ppy)_3$ and similar systems as discussed above the levels are split by less than the line width of the spectral features. The calculated oscillator strength of the transition to the 2E state is similar across all four complexes as is the observed MCD signal. It is also the strongest excitation in the entire manifold of $T_1(A)$ and $T_2(E)$ excitations (Figure 4). The negligible oscillator strength predicted for 1A in all complexes is consistent with this first A-term being the lowest energy observable feature in the MCD and with the energy of this feature coinciding with the absorption onset.

Higher energy excitations 7A and 8E coincide with the strong MCD features between 2.9 and 3.2 eV, which allows their assignment to an MCD B-term followed by an A-term (Figure 2). This pair of excitations arises from a complex mix of scalar excitations with no one singlet or triplet excitation dominating. Above ~3.2 eV the density of states becomes much greater and unambiguous identification of MCD features is difficult. However, as noted above, these states are not important for the emissive properties of the complexes at room temperature.

Temperature Dependence of Radiative Rates. Note that the above assignments predict that 1A does not play a significant role in the absorption of light by these complexes. It is clearly interesting, given the potential optoelectronic applications of these complexes, to ask what role excitation 2E, and more generally all of the excited states, play in the emission of light. To examine this question we will assume that the vibration relaxation from the initially excited state achieves thermal equilibrium. The fractional Boltzmann probability, $p_i(T)$, of an

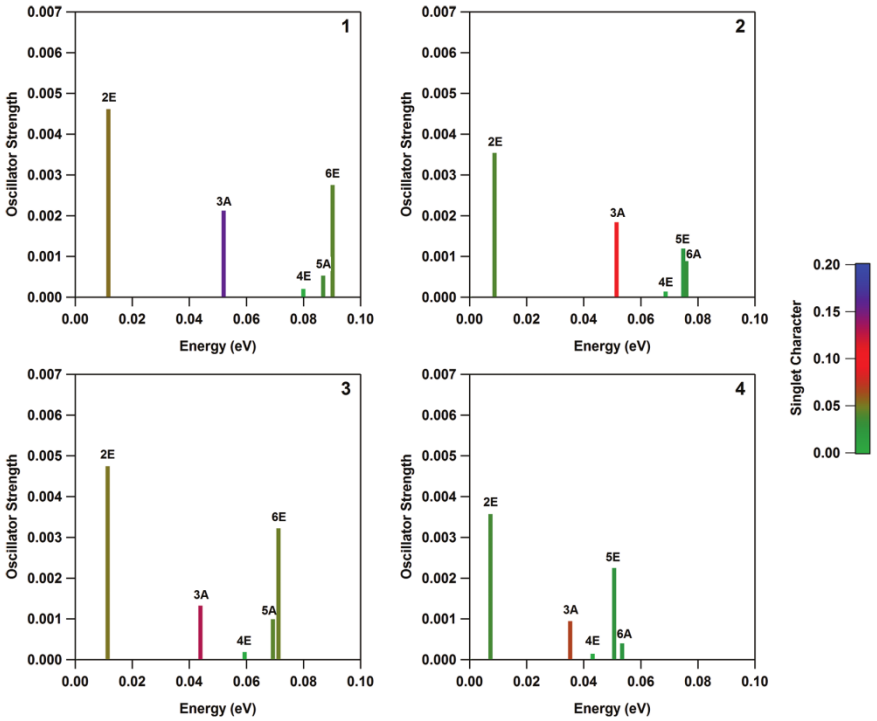

Figure 4. Lowest six excitations of iridium(III) complexes **1**–**4** calculated from SOC perturbation TDDFT with the complexes constrained to C_3 symmetry. Plotted with respect to the energy of the first excitation 1A [which has an extremely small ($f < 10^{-5}$ au) oscillator strength], the energy range between excitations 1 and 6 decreases with fluorine substitution. The ZFS of the T_2 manifold (excitations 3–6) is also reduced by fluorination. Note that the color coding indicating the singlet character has been rescaled, compared to Figure 2, to emphasize the small differences in singlet character.

excited complex being in the ith excited state at temperature T is given by

$$p_i(T) = \frac{g_i e^{-(E_i - E_{1A})/k_B T}}{\sum_j g_j e^{-(E_j - E_{1A})/k_B T}} \quad (1)$$

where g_i is the degeneracy, E_i is the energy, k_B is Boltzmann's constant, and E_{1A} is the energy of the lowest energy excitation, 1A. Thence, the probability $P_i(T)$ that a detected photon was emitted from excitation i is given by

$$P_i(T) = \frac{p_i(T)k_i^R}{\sum_j p_j(T)k_j^R\left(\frac{k_i^R + k_i^{NR}}{k_j^R + k_j^{NR}}\right)} \approx \frac{p_i(T)k_i^R}{\sum_j p_j(T)k_j^R} \quad (2)$$

where k_j^R and k_j^{NR} are, respectively, the radiative and nonradiative rates from the jth level, and the final approximation holds if there is sufficiently little variation in the total decay rates across all states with a significant thermal population, $p_i(T)$, at a given temperature, which we expect not to induce large errors because the measured total radiative rates are the same magnitude as the measured radiative rate.[10] Radiative rates and lifetimes were calculated from the TDDFT results via the Stickler–Berg relation.[61,62] The predictions of eq 2 for

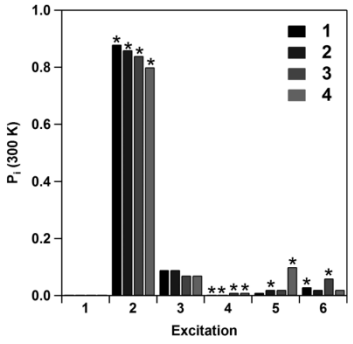

Figure 5. Zeroth order probability, P_i(300 K), of observing emission from iridium(III) complexes **1**–**4** for the lowest six excitations calculated from SOC perturbation TDDFT. At room temperature the probability of observing emission from 1A is close to zero. Degenerate, E, excitations are denoted by an *.

all four complexes at 300 K are reported in Figure 5. In particular we find that to leading order, at 300 K, ≥80% of the emission comes from 2E in all four complexes. The vanishingly small probability of emission from 1A suggests that the bulk of the

emission does not occur from the lowest excited state level in these complexes at temperatures ≥10 K; this result is highly robust to higher order corrections in $(k_i^R + k_i^{NR})/(k_j^R + k_j^{NR})$.

The calculations also predict that the lowest state with significant absorption (2E) is also responsible for the bulk of the emission at temperatures where this state has a significant thermal population (specifically above about 10 K). This is responsible for the mirror image symmetry between absorption and emission spectra as neither the absorption nor the emission processes involve the lowest energy excited state. Therefore, theory predicts that these complexes will display mirror image symmetry at $T \geq 10$ K. The mirror image rule is indeed obeyed experimentally as shown by the results shown in Figure 3. This is strong experimental evidence that the excitation responsible for the MCD A-term and the absorption onset (2E) also dominates the emission process at temperatures greater than ∼10 K.

The calculated radiative lifetime of all four complexes reveals very similar temperature dependent profiles (Figure 6), which

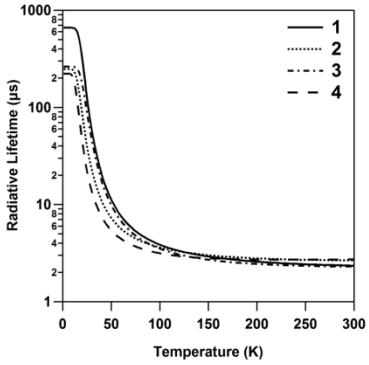

Figure 6. Temperature dependence of the radiative lifetimes of iridium(III) complexes **1**−**4** predicted from SOC perturbation TDDFT excitations. Below 10 K only the lowest state 1A has significant population and so the radiative lifetime is long and plateaus. At 300 K complexes **1** and **3**, which have protons at the Y position, have similar lifetimes, as do complexes **2** and **4**, which have fluorines at the Y position.

closely resembles the measured total lifetime of many similar iridium(III) complexes.[14,58,63] Below ∼10 K the radiative lifetime plateaus, as the lowest energy state, 1A, is essentially fully populated. As the lowest state has such weak oscillator strength even a slight change in the calculated oscillator strength for this state will have a dramatic effect on the final lifetime at low temperature.[28] The true radiative rate at low temperature is likely to be enhanced by Herzberg−Teller (HT) coupling, which is not included in our calculations but may well give rise to a radiative rate larger than, or of a similar magnitude to, the calculated direct radiative rate. Nevertheless we expect the qualitative shape of the curves in Figure 6 to be correct although the intercepts may be somewhat lower.

Although most of the light is emitted from 2E, a substate of T_1(A), the occupation of the T_2(E) states may still have important consequences for the optoelectronic properties of these complexes. Figure 4 shows that fluorination leads to important changes in properties of the T_2(E) manifold:

First, relative to the energy of the first excitation, 1A, the T_2(E) manifold of excitations (3−6) shifts down in energy following fluorine substitution (Figure 4). This can be understood by considering the scalar relativistic TDDFT calculations where the energy separation between the T_1(A) and T_2(E) excitations is also reduced with fluorine substitution (see Supporting Information). These low energy excitations are formed almost exclusively from transitions between the frontier orbitals. In all complexes T_1(A) is primarily composed of HOMO→LUMO (>62%) and HOMO-1→LUMO+1 (>15%) transitions, whereas T_2(E) is made up of HOMO→LUMO+1 (>47%) and HOMO-1→LUMO (>11%) transitions (see Supporting Information). The changes in excitation energy can be traced back to the effects that fluorination has on these orbital energies. Specifically, if we examine the orbital transitions with the greatest contribution in the T_1(A) and T_2(E) excitations (HOMO→LUMO and HOMO→LUMO+1, respectively), the energy separation between the T_1(A) and T_2(E) excitations is dependent on the LUMO−LUMO+1 energy gap. In order of complexes **1**−**4** the LUMO−LUMO+1 energy separation decreases (Table 2) consistent with the calculated decrease in the T_1(A)−T_2(E) separation (Table 1).

Second, the predicted overall splitting of the T_2(E) excitation manifold (excitations 3−6) decreases with fluorination, from a maximum of 38 meV for **1** to 18 meV for **4** (Figure 4).

These two effects have important consequences for the occupation of the T_2 manifold. In the parent complex, **1**, an excitation only has a Boltzmann probability of 12% of being in the T_2 manifold at room temperature (Supporting Information, Figure S3). This probability rises to 15% in **2**, 20% in **3**, and 29% in **4**. Excitations 3−6 all have weaker oscillator strengths (and therefore slow radiative rates) compared to 2E, so this is our first clue to why fluorination lowers the radiative rate of the complexes at room temperature.

Moreover, this redistribution of spectral weight may also be important for the nonradiative rate. The increase in the population of the T_2 manifold is much larger for fluorination at the X position (which takes **1**→**3** and **2**→**4** and increases the occupation of the T_2 states by a factor of 2) than for fluorination at the Y position (which takes **1**→**2** and **3**→**4**). Although we have not calculated or measured the nonradiative decay rates for individual excitations, it is reasonable to expect that, because they are embedded in the vibrational bands based on the lower T_1 state, the T_2 states may have much higher nonradiative decay rates than the T_1 states. This would then give a natural explanation of why fluorination at the X position increases the nonradiative decay rate much more dramatically than fluorination at the Y position does.

It is interesting to note that the redistribution of spectral weight is not simply an effect of the blue shift. **2** is shifted further to the blue than **3** (Figure 2) yet the population of the T_2 manifold is only 15% in **2**, compared to 20% in **3**.

Linear Response to Fluorination. We will now demonstrate that fluorination at the X and Y positions act independently. To do this we compare a wide range of measured and calculated properties of complexes **1**−**4**. Let us assume initially that fluorination causes a *small* shift in some property, Π, of the complex. The assumption of the small shift allows us to develop a linear response theory[64] for chemical substitution. If we denote the change in Π caused by fluorination at the X position by $\delta\Pi_X$ and the change in Π caused by fluorination at

the Y position by $\delta\Pi_Y$, then the assumption of linearity leads directly to the prediction that

$$\Pi_2 = \Pi_1 + \delta\Pi_Y \quad (3)$$

$$\Pi_3 = \Pi_1 + \delta\Pi_X \quad (4)$$

$$\Pi_4 = \Pi_1 + \delta\Pi_X + \delta\Pi_Y \quad (5)$$

where Π_n is the value of the property Π for the nth complex. Note that **1** is unfluorinated, **2** is fluorinated only at the Y position, **3** is fluorinated only at the X position, and **4** is fluorinated at both the X and Y positions. Thus, we have

$$\Pi_1 + \Pi_4 = \Pi_2 + \Pi_3 \quad (6)$$

Where the property Π is clear from context, it will be useful to introduce the shorthand $(\mathbf{1} + \mathbf{4}) - (\mathbf{2} + \mathbf{3}) = 0$ to summarize eq 6.

The eq 6 is potentially quite general for different families of molecules and where substitutions cause sufficiently subtle effects in some measured property. We will show below that a range of important properties in complexes **1**−**4** display this behavior. Therefore, it may be possible to use this as a design principle for tailoring the properties of organometallic complexes to specific applications.

In Table 2 we report the experimentally measured optical excitation and oxidation potentials (reversible reduction potentials could not be determined for comparison) of complexes **1**−**4**. The gap between the highest occupied molecular orbital (HOMO) and the lowest unoccupied molecular orbital (LUMO) calculated from scalar relativistic DFT calculations (upon which the TDDFT and SOC perturbation calculations are based) follows the trend observed spectroscopically, although, unsurprisingly, it vastly overestimates the measured optical gap (Table 2). Nevertheless, for all three of these properties, we find that eq 6 holds to a very high accuracy.

Analysis of the fragment charge distribution (Table 3) shows the effect of fluorination more clearly. The successive addition of fluorine promotes the redistribution of charge from the triazolyl ring toward the phenyl ring. Here one sees that the relationship $(\mathbf{1} + \mathbf{4}) - (\mathbf{2} + \mathbf{3}) = 0$ with fluorination very clearly. This indicates that redistributions of charge caused by fluorination at the X and Y positions are uncorrelated.

Table 3. Partial Charge Per Fragment Based on Hirshfeld Population Analysis from Scalar Relativistic DFT[a]

fragment	1	2	3	4	(1 + 4) − (2 + 3)
iridium	0.4383	0.4417	0.4086	0.4130	0.0010
triazolyl	0.0368	0.0360	0.1391	0.1392	0.0009
phenyl	−0.4705	−0.4731	−0.5461	−0.5482	0.0005

[a]The total charge distribution changes with fluorination as electron density is redistributed from the triazolyl to the phenyl ring. The column labelled $(\mathbf{1} + \mathbf{4}) - (\mathbf{2} + \mathbf{3})$ is a test of the sum rule for fluorination, eq 6, where an entry of 0 indicates perfect agreement between the Hirshfeld population analysis and the predictions of that equation. The observation that entries of this row are all zero to a very high accuracy indicates that redistributions of charge caused by fluorination at the X and Y positions are independent of one another.

One can also observe the $(\mathbf{1} + \mathbf{4}) - (\mathbf{2} + \mathbf{3}) = 0$ rule in relativistic effects. In all complexes, states arising from the $T_2(E)$ manifold remain predominantly triplet in character (>95%), apart from the 3A state, which has a significant component of singlet character because of the $S_1(A)$ manifold. In complex **1** the singlet character of 3A reaches 16%, but fluorination reduces the singlet component to 10% and 13% for **2** and **3**, respectively (see Supporting Information). The difluorinated complex **4** has the lowest singlet component in 3A with only a 7% contribution. Again the same linear response to fluorination is observed.

At 300 K the radiative rates of complexes **1**−**4** are calculated to be 4.3×10^5, 3.8×10^5, 4.4×10^5, and 3.7×10^5 s^{-1}, respectively, which is the same order of magnitude as measured experimentally (Table 1).[10] Complexes **1** and **3** have similar radiative rates as do complexes **2** and **4**. This suggests that the important difference, in terms of radiative rates, is whether the Y position is protonated (as in complexes **1** and **3**) or fluorinated (as in complexes **2** and **4**). The same trend is observed in the experimentally measure radiative rates (Table 1). Conversely, the experimental data shows that fluorination at the X position increases the nonradiative rate by more than an order of magnitude, whereas fluorination at the Y position has a much smaller effect on the k_{nr}.

Mechanism of Changes in the Radiative Rate Due to Fluorination. Phosphorescence occurs because SOC mixes singlets and triplets. This mixing is reduced as the energy gap between the relevant singlets and triplets is increased. In a related series of complexes one expects the radiative rate to depend on the energy gap between a triplet and the singlet with which it mixes.[30,32,38,42] Li et al.[30] pointed out that the rate depends on the inverse square of this gap at the lowest order in perturbation theory. However, recently Jacko et al.[32−34] have shown that a second inverse square relationship arises because of the hybridization between metal and ligand orbitals. Thus overall the radiative rate should exhibit a quadratic dependence on the inverse of the energy gap between a triplet and the singlet with which it mixes.[33]

As discussed earlier, the complexes studied here predominately emit from the 2E level at room temperature. If we compare the TDDFT results with and without the effects of spin−orbit perturbation (see Supporting Information for full tabulation) we find that in all of the complexes the 2E state is basically a substate of $T_1(A)$ with small but significant contribution from $S_3(E)$ of 5.2%, 4.1%, 5.1%, and 3.7% for complexes **1**−**4**, respectively. It is worth noting that $S_3(E)$ and $S_5(E)$ are the strongest singlet excitations in the MLCT manifold, so it is interesting that a strong excitation like $S_3(E)$ should couple into the lowest triplet more strongly than the closer lying $S_1(A)$ and $S_2(E)$ excitations. This is clearly important for the large radiative rate and hence the high PLQY of, at least, the parent complex (**1**).

The calculated energy gap $S_3(E)$-$T_1(A)$ is strongly dependent on fluorination at the Y position: this gap is ∼10% larger in complexes **2** and **4** (where Y = F) than in complexes **1** and **3** (where Y = H). However, fluorination at the X position has little effect on the $S_3(E)$-$T_1(A)$ gap. In Figure 7 we compare the calculated $S_3(E)$-$T_1(A)$ gap with the calculated radiative rates. The data is consistent with the prediction of Jacko and Powell[33] that the radiative rate decreases as the fourth power of the $S_3(E)$-$T_1(A)$ energy gap (Figure 7).

Therefore, the question becomes why does fluorination increase the $S_3(E)$-$T_1(A)$ gap? To understand this, it is helpful to compare the scalar relativistic DFT and TDDFT calculations. In the Supporting Information we tabulate the largest contributions to each TDDFT excitation in terms of transitions between DFT molecular orbitals. We find that, in all four complexes, $T_1(A)$ is predominately a HOMO→LUMO

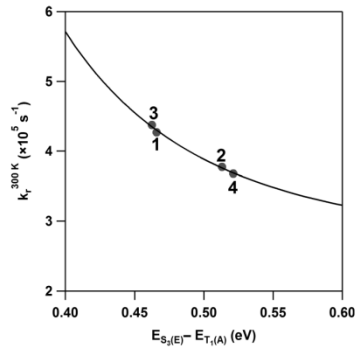

Figure 7. Calculated total radiative rate at 300 K for iridium(III) complexes **1**−**4**, plotted against the calculated energy gap between the scalar TDDFT excitations $S_3(E)$ and $T_1(A)$. The $S_3(E)$-$T_1(A)$ energy gap is found to be strongly dependent on the fluorination at the Y position, whereas fluorination at X does not change the relative energy separation significantly. The line is a best fit for the predicted dependence between the inverse fourth power of the radiative rate and the singlet−triplet energy gap.[33] The calculated radiative rate is the same order of magnitude as the experimentally measured rate.[10]

transition (with weights of 72%, 66%, 69%, and 62% in complexes **1**−**4**, respectively) and $S_3(E)$ is dominated by the HOMO-1→LUMO transition (with weights of 94%, 96%, 94%, and 97% in complexes **1**−**4**, respectively). Note that both of these weights obey the (**1** + **4**) − (**2** + **3**) = 0 rule and that in both cases fluorination at the Y position has a greater effect than that at the X position.

On the basis of the above analysis one expects that, to leading order, the main effect of fluorination on the $S_3(E)$-$T_1(A)$ energy gap, and hence on the radiative rate, is therefore to increase the energy gap between the HOMO and HOMO-1. (One might also ask if there is an effect on the strength of the exchange interaction, but we will not consider this here.) In Table 2 we have listed the energies of the frontier orbitals. The energy gap between the HOMO and HOMO-1 clearly obeys the (**1** + **4**) − (**2** + **3**) = 0 rule. Although these complexes have C_3 symmetry, the iridium(III) atom sits in an approximately octahedral environment formed by the covalent bonds to the carbon atoms and the dative bonds to the nitrogen atoms. If this octahedral symmetry were exact the HOMO (A) and HOMO-1 (E) would form a triply degenerate T_{2g} manifold. This is responsible for the marked similarities between the HOMOs and (HOMO-1)s of homoleptic iridium(III) complexes.[27,28]

Fluorination at the Y position (**1**→**2**, **3**→**4**) has an important effect on increasing the HOMO−HOMO-1 gap (∼0.2 eV), whereas fluorination at the X position (**1**→**3**, **2**→**4**) has a much smaller effect on the HOMO−HOMO-1 gap. Therefore fluorination at the Y position changes the radiative rate by increasing the degree to which octahedral symmetry is broken, whereas fluorination at the X position only weakly affects this asymmetry. This simple molecular orbital analysis overestimates the magnitude of the increase in the $S_3(E)$-$T_1(A)$ gap because it neglects the other molecular orbital transitions that contribute to $S_3(E)$ and, particularly $T_1(A)$. Nevertheless, this simple molecular orbital picture does correctly reproduce the trend seen in both the relativistic TDDFT calculation with spin orbit coupling and experiment.

Finally, we note that this analysis does not just apply to 2E. For example, the character of 3A is dominated by the combination of the $T_2(E)$ and $S_1(A)$ states. The singlet character of 3A can be directly related to the energy difference between the $T_2(E)$ and $S_1(A)$ states, which in order of the complexes **1**−**4** is 0.20, 0.24, 0.21, and 0.26 eV; these values again satisfy eq 6. As the energy difference between the two states increases, less of the $S_1(A)$ excitation is coupled into 3A.

■ CONCLUSIONS

The combination of low temperature, high field MCD, absorption and emission spectroscopy with relativistic time-dependent density functional calculations has allowed a rather complete mapping of the low-energy excited states of a family of iridium(III) complexes. This has allowed us to understand the subtle changes induced by fluorination on the experimental spectra and to accurately describe the molecular properties. This has revealed a subtle interplay between the effects of chemical substitutions and SOC and thus photoluminescence efficiency.

The current experiments can be interpreted in terms of C_3 symmetry complexes. No symmetry lowering effects (possible in some excited states because of vibronic coupling and interaction with the environment that would result in localization) are resolved in our measurements. The lowest energy excitation 1A has an extremely small oscillator strength, and as a result transitions to and from the second lowest excitation 2E dominate both the absorption and the emission spectra, respectively, at room temperature (Figure 5). Therefore, a mirror image between absorption and emission is still observed (Figure 3). 2E is a 2-fold degenerate excitation and, as such, is responsible for the distinct MCD A-term found in all complexes (Figure 2).

We have demonstrated that the properties of a family of fluorinated phosphorescent iridium(III) complexes are determined by the independent action of each fluorine substitution (Tables 2 and 3). This independence is demonstrated by the (**1** + **4**) − (**2** + **3**) = 0 rule, eq 6, which one should expect to hold provided the changes due to a substitution are sufficiently small for a linear response theory to be valid. Therefore, this may represent a general rule to aid the design of new phosphorescent complexes. In this context it is interesting to note (cf. Table 1) that fluorination of the Y position (which takes **1**→**2** and **3**→**4**) reduces the radiative rate by a factor of 2−3; whereas fluorination of the X position (**1**→**3** and **2**→**4**) leads to an order of magnitude increase in the nonradiative rate, but has a much smaller change in the radiative rate.

The calculated radiative lifetime in this family of complexes is found to be dependent on the $S_3(E)$-$T_1(A)$ energy gap, and is consistent with the predicted quadratic dependence on the inverse of the singlet−triplet energy gap. Fluorination at the Y position lowers this gap (Figure 7) and is responsible for suppression of the radiative rate between complexes **1** and **2**, and complexes **3** and **4**. On the other hand, fluorination at the X position does not significantly alter the gap (Figure 7), which explains the similar radiative rates observed in complexes **1** and **3**, and in complexes **2** and **4**. As we have not considered the nonradiative decay mechanisms, we cannot give a full explanation of why fluorinations at the X and Y positions have such different effects on the nonradiative decay rates. However, the fluorination at the X position causes more significant redistribution of the low energy spectral weight: decreasing the T_1-T_2 energy difference by reducing the (LUMO+1)-LUMO gap and decreasing the ZFS of T_2. This reduces the probability

of excitations equilibrating into the main emissive state, 2E, which, it is tempting to speculate, may be related to the dramatic increase in the nonradiative rate.

■ ASSOCIATED CONTENT

Supporting Information

Further details are given in Figures S1−S3 and in tables containing the geometry of optimized structures and transition energies. This material is available free of charge via the Internet at http://pubs.acs.org.

■ AUTHOR INFORMATION

Corresponding Author

*E-mail: p.burn2@uq.edu.au (P.L.B.), bjpowell@gmail.com (B.J.P.).

Notes

The authors declare no competing financial interest.

■ ACKNOWLEDGMENTS

We thank Anthony Jacko and Seth Olsen for helpful conversations. This work was funded by the Australian Research Council (ARC). All calculations were performed on NF-NCI. A.R.G.S. thanks AINSE for a PGRA. P.L.B. and B.J.P. are supported by an ARC Federation Fellowship (FF0668728) and an ARC Queen Elizabeth II Fellowship (DP0877875), respectively.

■ REFERENCES

(1) Xiao, L.; Chen, Z.; Qu, B.; Luo, J.; Kong, S.; Gong, Q.; Kido, J. *Adv. Mater.* **2011**, *23*, 926.
(2) Baldo, M. A.; Lamansky, S.; Burrows, P. E.; Thompson, M. E.; Forrest, S. R. *Appl. Phys. Lett.* **1999**, *75*, 4.
(3) Chou, P. T.; Chi, Y. *Chem.—Eur. J.* **2007**, *13*, 380.
(4) Adachi, C.; Baldo, M. A.; Thompson, M. E.; Forrest, S. R. *J. Appl. Phys.* **2001**, *90*, 5048.
(5) Holder, E.; Langeveld, B.; Schubert, U. *Adv. Mater.* **2005**, *17*, 1109.
(6) Gather, M. C.; Köhnen, A.; Meerholz, K. *Adv. Mater.* **2011**, *23*, 233.
(7) Sasabe, H.; Kido, J. *Chem. Mater.* **2011**, *23*, 621.
(8) Reineke, S.; Lindner, F.; Schwartz, G.; Seidler, N.; Walzer, K.; Lussem, B.; Leo, K. *Nature* **2009**, *459*, 234.
(9) Lo, S.-C.; Harding, R. E.; Shipley, C. P.; Stevenson, S. G.; Burn, P. L.; Samuel, I. D. W. *J. Am. Chem. Soc.* **2009**, *131*, 16681.
(10) Lo, S.-C.; Shipley, C. P.; Bera, R. N.; Harding, R. E.; Cowley, A. R.; Burn, P. L.; Samuel, I. D. W. *Chem. Mater.* **2006**, *18*, 5119.
(11) Lamansky, S.; Djurovich, P.; Murphy, D.; Abdel-Razzaq, F.; Lee, H.-E.; Adachi, C.; Burrows, P. E.; Forrest, S. R.; Thompson, M. E. *J. Am. Chem. Soc.* **2001**, *123*, 4304.
(12) You, Y.; Park, S. Y. *Dalton Trans.* **2009**, 1267.
(13) Baranoff, E.; Fantacci, S.; De Angelis, F.; Zhang, X.; Scopelliti, R.; Grätzel, M.; Nazeeruddin, M. K. *Inorg. Chem.* **2011**, *50*, 451.
(14) Hofbeck, T.; Yersin, H. *Inorg. Chem.* **2010**, *49*, 9290.
(15) Orgel, L. E. *J. Chem. Soc.* **1961**, 3683.
(16) Nozaki, K. *J. Chin. Chem. Soc.* **2006**, *53*, 101.
(17) Jansson, E.; Minaev, B.; Schrader, S.; Agren, H. *Chem. Phys.* **2007**, *333*, 157.
(18) Harrigan, R. W.; Crosby, G. A. *J. Chem. Phys.* **1973**, *59*, 3468.
(19) Kober, E. M.; Meyer, T. J. *Inorg. Chem.* **1984**, *23*, 3877.
(20) Krausz, E.; Riesen, H. *Coord. Chem. Rev.* **1997**, *159*, 9.
(21) Riesen, H.; Wallace, L.; Krausz, E. *Mol. Phys.* **1996**, *87*, 1299.
(22) Obara, S.; Itabashi, M.; Okuda, F.; Tamaki, S.; Tanabe, Y.; Ishii, Y.; Nozaki, K.; Haga, M. A. *Inorg. Chem.* **2006**, *45*, 8907.
(23) Matsushita, T.; Asada, T.; Koseki, S. *J. Phys. Chem. C* **2007**, *111*, 6897.
(24) Tong, G. S. M.; Che, C. M. *Chem.—Eur. J.* **2009**, *15*, 7225.
(25) Minaev, B.; Agren, H.; De Angelis, F. *Chem. Phys.* **2009**, *358*, 245.
(26) De Angelis, F.; Belpassi, L.; Fantacci, S. *J. Mol. Struct.: THEOCHEM* **2009**, *914*, 74.
(27) Smith, A. R. G.; Riley, M. J.; Lo, S.-C.; Burn, P. L.; Gentle, I. R.; Powell, B. J. *Phys. Rev. B* **2011**, *83*, 041105(R).
(28) Smith, A. R. G.; Burn, P. L.; Powell, B. J. *ChemPhysChem* **2011**, *12*, 2429.
(29) Nozaki, K.; Takamori, K.; Nakatsugawa, Y.; Ohno, T. *Inorg. Chem.* **2006**, *45*, 6161.
(30) Li, J.; Djurovich, P. I.; Alleyne, B. D.; Yousufuddin, M.; Ho, N. N.; Thomas, J. C.; Peters, J. C.; Bau, R.; Thompson, M. E. *Inorg. Chem.* **2005**, *44*, 1713.
(31) Haneder, S.; Como, E. D.; Feldmann, J.; Lupton, J. M.; Lennartz, C.; Erk, P.; Fuchs, E.; Molt, O.; Münster, I.; Schildknecht, C.; Wagenblast, G. *Adv. Mater.* **2008**, *20*, 3325.
(32) Jacko, A. C.; McKenzie, R. H.; Powell, B. J. *J. Mater. Chem.* **2010**, *20*, 10301.
(33) Jacko, A. C.; Powell, B. J. *Chem. Phys. Lett.* **2011**, *508*, 22.
(34) Jacko, A. C.; Powell, B. J.; McKenzie, R. H. *J. Chem. Phys.* **2010**, *133*, 124314.
(35) Mason, W. R. *A Practical Guide to Magnetic Circular Dichroism Spectroscopy*; Wiley-Interscience: Hoboken, NJ, 2007.
(36) Stephens, P. J.; Devlin, F. J.; Chabalowski, C. F.; Frisch, M. J. *J. Phys. Chem.* **1994**, *98*, 11623.
(37) Becke, A. D. *J. Chem. Phys.* **1993**, *98*, 5648.
(38) Lee, C.; Yang, W.; Parr, R. G. *Phys. Rev. B* **1988**, *37*, 785.
(39) Schmidt, M. W.; Baldridge, K. K.; Boatz, J. A.; Elbert, S. T.; Gordon, M. S.; Jensen, J. H.; Koseki, S.; Matsunaga, N.; Nguyen, K. A.; Su, S.; Windus, T. L.; Dupuis, M.; John A. Montgomery, J. *J. Comput. Chem.* **1993**, *14*, 1347.
(40) Gordon, M. S.; Schmidt, M. W. In *Theory and Applications of Computational Chemistry: the first forty years*; Dykstra, C. E., Frenking, G., Kim, K. S., Scuseria, G. E., Eds.; Elsevier: Amsterdam, The Netherlands, 2005.
(41) Hay, P. J.; Wadt, W. R. *J. Chem. Phys.* **1985**, *82*, 299.
(42) Hehre, W. J.; Ditchfield, R.; Pople, J. A. *J. Chem. Phys.* **1972**, *56*, 2257.
(43) Ditchfield, R.; Hehre, W. J.; Pople, J. A. *J. Chem. Phys.* **1971**, *54*, 724.
(44) te Velde, G.; Bickelhaupt, F. M.; Baerends, E. J.; Guerra, C. F.; van Gisbergen, S. J. A.; Snijders, J. G.; Ziegler, T. *J. Comput. Chem.* **2001**, *22*, 931.
(45) Fonseca Guerra, C.; Snijders, J. G.; te Velde, G.; Baerends, E. J. *Theor. Chim. Acta* **1998**, *99*, 391.
(46) *ADF2009.01*; SCM, Theoretical Chemistry, Vrije Universiteit: Amsterdam, The Netherlands; http://www.scm.com/.
(47) van Lenthe, E.; Baerends, E. J.; Snijders, J. G. *J. Chem. Phys.* **1993**, *99*, 4597.
(48) van Lenthe, E.; Baerends, E. J.; Snijders, J. G. *J. Chem. Phys.* **1994**, *101*, 9783.
(49) Wang, F.; Ziegler, T. *J. Chem. Phys.* **2005**, *123*, 154102.
(50) Chong, D. P. *Mol. Phys.* **2005**, *103*, 749.
(51) Lenthe, E. V.; Baerends, E. J. *J. Comput. Chem.* **2003**, *24*, 1142.
(52) Hirshfeld, F. L. *Theor. Chim. Acta* **1977**, *44*, 129.
(53) Neese, F.; Petrenko, T.; Ganyushin, D.; Olbrich, G. *Coord. Chem. Rev.* **2007**, *251*, 288.
(54) Fouqueau, A.; Casida, M. E.; Daku, L. M. L.; Hauser, A.; Neese, F. *J. Chem. Phys.* **2005**, *122*, 044110.
(55) Fouqueau, A.; Mer, S.; Casida, M. E.; Daku, L. M. L.; Hauser, A.; Mineva, T.; Neese, F. *J. Chem. Phys.* **2004**, *120*, 9473.
(56) Finkenzeller, W. J.; Yersin, H. *Chem. Phys. Lett.* **2003**, *377*, 299.
(57) Finkenzeller, W. J.; Hofbeck, T.; Thompson, M. E.; Yersin, H. *Inorg. Chem.* **2007**, *46*, 5076.
(58) Rausch, A. F.; Thompson, M. E.; Yersin, H. *Inorg. Chem.* **2009**, *48*, 1928.
(59) Finkenzeller, W. J.; Thompson, M. E.; Yersin, H. *Chem. Phys. Lett.* **2007**, *444*, 273.

(60) Smith, A. R. G.; Riley, M. J.; Burn, P. L.; Gentle, I. R.; Powell, B. J.; Krausz, E.; Hall, J. (to be published).
(61) Knox, R. S. *Photochem. Photobiol.* **2003**, *77*, 492.
(62) Riesz, J. J.; Gilmore, J. B.; McKenzie, R. H.; Powell, B. J.; Pederson, M. R.; Meredith, P. *Phys. Rev. E* **2007**, *76*, 021915.
(63) Sajoto, T.; Djurovich, P. I.; Tamayo, A. B.; Oxgaard, J.; Goddard, W. A.; Thompson, M. E. *J. Am. Chem. Soc.* **2009**, *131*, 9813.
(64) Plischke, M.; Bergersen, B. *Equilibrium Statistical Physics*; World Scientific: Singapore, 2006.

ADVANCED FUNCTIONAL MATERIALS
www.afm-journal.de

Investigating Morphology and Stability of *Fac*-tris (2-phenylpyridyl)iridium(III) Films for OLEDs

Arthur R. G. Smith, Jeremy L. Ruggles, Hamish Cavaye, Paul E. Shaw, Tamim A. Darwish, Michael James, Ian R. Gentle, and Paul L. Burn**

Stable film morphology is critical for long-term high performance organic light-emitting diodes (OLEDs). Neutron reflectometry (NR) is used to study the out-of-plane structure of blended thin films and multilayer structures comprising evaporated small molecules. It is found that as-prepared blended films of *fac*-tris(2-phenylpyridyl)iridium(III) [Ir(ppy)$_3$] in 4,4′-bis(*N*-carbazolyl) biphenyl (CBP) are uniformly mixed, but the occurrence of phase separation upon thermal annealing is dependent on the blend ratio. Films comprised of the ratio of 6 wt% of Ir(ppy)$_3$ in CBP typically used in OLEDs are found to phase separate with moderate heating while a higher weight percent mixture (12 wt%) is found to be stable. Furthermore, it is found that thermal annealing of a multilayer film comprised of typical layers found in efficient devices ([tris(4-carbazoyl-9-ylphenyl)amine (TCTA)/Ir(ppy)$_3$:CBP/bathocuproine (BCP)]) causes the BCP layer to become mixed with the emissive blend layer, whereas the TCTA interface remains unchanged. This significant structural change causes no appreciable difference in the photoluminescence of the stack although such a change would have a dramatic effect on the charge transport through the device, leading to changes in performance. These results demonstrate the effect of thermal stress on the delicate interplay between the chemical composition and morphology of OLED films.

1. Introduction

Organic light-emitting diode (OLED) materials fall into three main classes; small molecules,[1,2] conjugated polymers,[3] and dendrimers,[4,5] with small molecules being generally processed by evaporation under high vacuum while polymers and dendrimers are solution processed. While the early work on OLEDs focused on fluorescent materials, the discovery that phosphorescent materials could be used in the light-emitting layer led to a step change in device performance.[1,2,6,7] At the vangaurd of this revolution has been the development of iridium(III) complexes, with materials that emit from saturated blue through to red being reported.[8] Since the first results, much effort has gone into improving the performance in terms of efficiency and lifetime of phosphorescent OLEDs. The most efficient OLEDs based on small molecule phosphorescent iridium(III) complexes are now reported to have essentially 100% internal quantum efficiencies.[7,9] The reason why such high efficiencies are achievable is that both the singlet and triplet excitons that are formed in the device can be captured for emission. These highly efficient devices tend to have complicated architectures with numerous layers and an emissive layer comprised of a phosphorescent iridium(III) complex blended with a host material which is generally the major component. For example, blends of *fac*-tris(2-phenylpyridyl)iridium(III) [Ir(ppy)$_3$] in 4,4′-bis(*N*-carbazolyl) biphenyl (CBP) (**Figure 1**) typically comprise between 6–8 weight percent (wt%) of the complex in the most efficient devices.[6] While efficiencies of OLEDs have risen quickly, the task of preparing OLEDs with lifetimes suitable for displays and lighting has proved challenging. Intrinsic factors such as photochemical, electrochemical, and thermal degradation of the active layers,[10–13] and extrinsic factors including encapsulation and layer adhesion all affect the lifetime of OLEDs.[14] However, in addition to the intrinsic and extrinsic factors, the morphological stability of the layers in the device can also affect device efficiency and lifetime. This latter factor is particularly important for OLEDs based on small molecule phosphorescent iridium(III) complexes due to the differing thermal properties of the materials in the different layers, and the fact that the complex is blended in a host. In fact, with blends, it is difficult to elucidate whether the guest is evenly distributed throughout the film or whether there are concentration variations in parts of the film.

The ability to relate the physical structure to the optoelectronic properties of a film is a challenge. One recently reported method uses a combination of grazing incidence wide angle X-ray scattering and optical reflectance to probe the structure of pentacene

A. R. G. Smith, H. Cavaye, Dr. P. E. Shaw, Prof. P. L. Burn
Centre for Organic Photonics and Electronics
The University of Queensland
Brisbane, QLD 4072, Australia
E-mail: p.burn2@uq.edu.au
Dr. J. L. Ruggles, Prof. I. R. Gentle
School of Chemistry and Molecular Biosciences
The University of Queensland, Brisbane, QLD 4072, Australia
E-mail: i.gentle@uq.edu.au
Dr. T. A. Darwish, Prof. M. James
Bragg Institute
Australian Nuclear Science and Technology Organisation
Locked Bag 2001, Kirrawee DC, NSW 2232, Australia
Prof. M. James
School of Chemistry
University of New South Wales
Sydney, NSW 2052, Australia

DOI: 10.1002/adfm.201002365

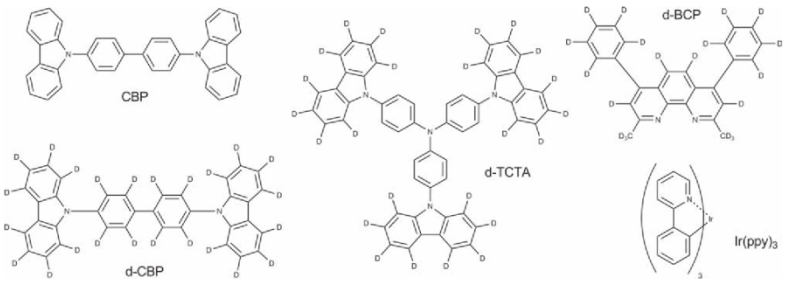

Figure 1. Structures of the materials used in this study. D represents deuterium and shows the positions that are at least partially deuterated.

films.[15] However, X-ray reflectometry is not the ideal technique for studying the structure of multilayers or blends where the electron density is similar in each of the materials. A more powerful technique for probing such structures is neutron reflectometry. NR (neutron reflectometry) is an excellent method for investigating the internal structure of thin (typically <1000 Å) films perpendicular to the substrate. In blended films, where there may be out-of-plane phase separation of the components within the blend, judicious deuteration enables differentiation of the components in the blend and any separation to be observed. In the case of multilayer structures, a combination of deuterated and protonated layers can give excellent contrast in the NR experiment. In this context, NR has been used to study the physical structure of films of conjugated materials on silicon wafers[16–18] and indium tin oxide.[19–21] We have also developed a combined in situ NR/photoluminescence (PL) measurement that allows the simultaneous collection of the neutron reflectivity data and emission spectrum.[20] An additional feature of the experiment is that the sample can be heated in situ thus enabling the direct determination of the effect of annealing on the physical and photophysical properties.

In this manuscript we use our combined NR/PL technique to study blends of $Ir(ppy)_3$ in CBP and the effect of thermal annealing. We show that the morphological stability of the film is dependent on the wt% of the $Ir(ppy)_3$ in the CBP. In addition, we report the effects of thermal annealing on a three layer structure typical of those found in multilayer phosphorescent OLEDs, [tris(4-carbazoyl-9-ylphenyl)amine (TCTA)/$Ir(ppy)_3$:CBP/bathocuproine (BCP)], and show that the BCP diffuses into the blended $Ir(ppy)_3$:CBP layer even at modest temperatures. In contrast, the TCTA was found to give a well-defined interface with the $Ir(ppy)_3$:CBP layer with no diffusion occurring at elevated temperatures. The thermal annealing temperatures are those which the devices might encounter during their lifetime.

2. Results and Discussion

2.1. $Ir(ppy)_3$:CBP Blend Films

An integral part of the study was determining the effect of thermal annealing on the blended and multilayer films. Previous accelerated degradation tests on OLEDs have been done in the temperature range from room temperature to 100 °C[22] and hence we limited our thermal annealing to less than or equal to 100 °C. It is important to note that OLEDs could realistically encounter temperatures of this magnitude. For example, temperatures in multilayer OLEDs have been measured to be above ambient[23] and as high as 86 °C.[24] In addition, it is not just the temperature of the device that is important but the environment in which the device is being used or stored. For example, the ambient cabin temperature of a car in summer can easily exceed 80 °C.[25,26]

In the first part of this study we investigated the composition of $Ir(ppy)_3$:CBP blended films. Three film combinations were prepared; neat d-CBP and d-CBP:$Ir(ppy)_3$ blends (where the prefix d- denotes the molecules where at least a portion of the protons are replaced by deuterons) with nominal composition of 6 wt% and 10 wt% of $Ir(ppy)_3$ based on relative evaporation rates. The PL spectra of the films on quartz are shown in **Figure 2**. The films were excited at 340 nm, thus enabling excitation of both the CBP and the $Ir(ppy)_3$. The neat CBP film was found to have an emission maximum at 393 nm. In contrast, the emission from both blend concentrations was entirely from the $Ir(ppy)_3$ indicating that the $Ir(ppy)_3$ was distributed such that it was within the diffusion length of an exciton formed on the CBP.

2.1.1. Neat d-CBP

The NR and PL of the films were measured on the SURF reflectometer. The films were measured under vacuum at 25 °C, 50 °C, and 80 °C before being allowed to cool to room temperature. The films were held at each elevated temperature for around ten minutes

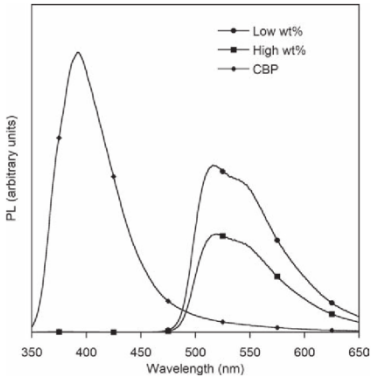

Figure 2. PL spectra of films of neat d-CBP and nominally 6 wt% (low) and 10 wt% (high) blends of $Ir(ppy)_3$ in d-CBP.

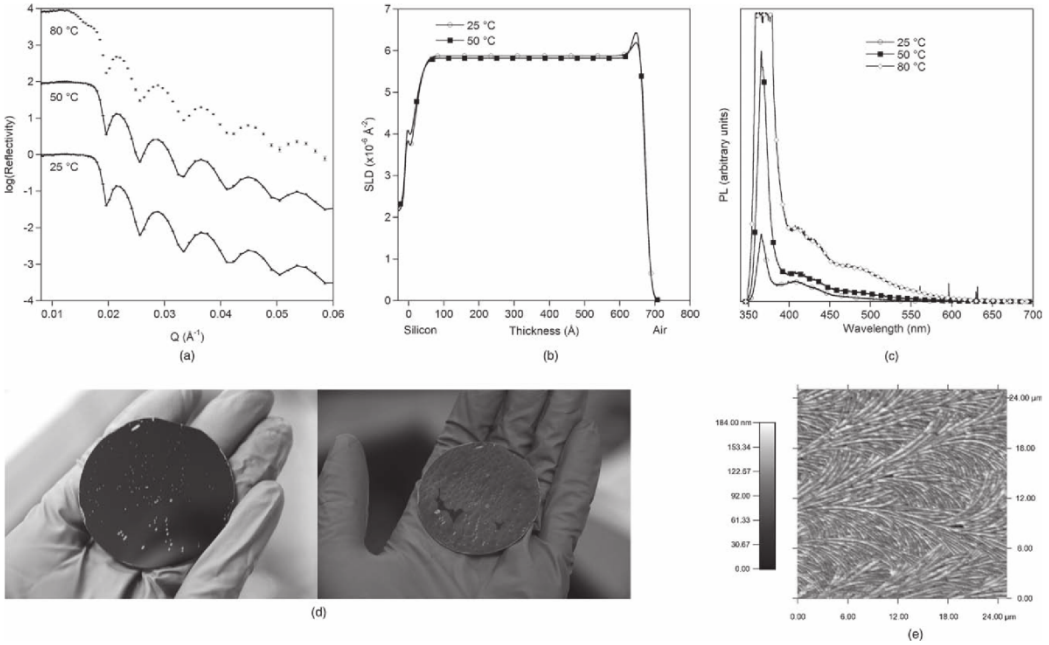

Figure 3. a) NR profiles collected for the d-CBP film. The points are the NR data and the solid lines the fit to the profile. b) SLD versus thickness for the d-CBP film. c) In situ PL measurements for the d-CBP film. d) Neat d-CBP film before and after annealing to 80 °C. e) AFM image of the neat d-CBP film after annealing and cooling to room temperature. Fiber-like structures spread across the film surface radiating outwards to form disc structures on the macro scale.

before the NR profile was collected. The reflectivity profiles, scattering length density (SLD) versus thickness, and PL spectra of the neat d-CBP film after annealing at different temperatures are shown in **Figure 3**. At 25 °C, the NR profile could be modeled with the bulk of the film having a thickness of 638 ± 7 Å and an SLD of $5.9 \pm 0.1 \times 10^{-6}$ Å^{-2}. In addition, the best fit to the NR profile included a low density layer with a thickness of ~15 Å and an SLD of $2.5 \pm 1.1 \times 10^{-6}$ Å^{-2} at the d-CBP/silicon interface, and a thin (typically less than 20 Å) dense layer (SLD of $7.0 \pm 0.5 \times 10^{-6}$ Å^{-2}) at the d-CBP/air interface (see Figure 3b). Low-density layers have previously been observed at conjugated polymer/substrate interfaces.[19] We attribute the dense layer at the CBP/air interface to the presence of a highly structured, possibly crystalline layer, which forms at the surface after film preparation. On heating to 50 °C, the NR profile only changed a small amount, with the neutron fit being consistent with the film having expanded slightly and becoming a little less dense. However, between 50 and 80 °C there was a substantial change to the NR profile with a significant shift of the critical edge from 0.018 to 0.013 Å^{-1} and it was no longer possible to fit the NR profile with a simple model. The in situ PL measurements gave important insight to the changes that had occurred in the film (Figure 3c). In the experimental set up the UV excitation source is incident on the sample at an angle of 45° with a detector placed normal to the substrate. This arrangement is designed to minimize detection of the excitation light, which occurs due to scattering. Nevertheless, in the case where the film is completely smooth (Figure 3d), a small level of scattered or reflected excitation light is always detected and, hence, the PL spectrum has two components; one peak at 365 nm, corresponding to reflected excitation light, and the second due to the luminescence of the film under interrogation. For the neat film of CBP at 25 °C. the ratio of the reflected light to the PL of CBP is relatively small (Figure 3c). However, on heating to 50 °C and then 80 °C the reflected excitation beam dominates the emission from the CBP, and this is consistent with the surface of the film becoming significantly rougher. Therefore, even at these relatively low temperatures there are significant changes in the surface morphology of the film. On cooling to room temperature, the amount of reflected excitation beam becomes even larger. Microscopy measurements on the film (Figure 3e) reveal that fiber-like structures which propagate radially outward forming disc-like structures (Figure 3d) formed during the thermal anneal, indicating that crystallization has at least occurred on the surface.

2.1.2. Low Weight Percentage Blend

The blend films were investigated under the same conditions as the neat d-CBP film. Apart from a small low density region at the interface between film and substrate (~25 Å, SLD $2.3 \pm 2.4 \times 10^{-6}$ Å^{-2}), the profile for the 6 wt% blend (**Figure 4**a) could be fitted as a single layer. Figure 4b shows the SLD versus film thickness at the different temperatures. This is an important result as it provides physical evidence for the first time that homogeneous co-evaporated films can be prepared. That is, there is no localisation of either component within a specific layer in the film. Up to 80 °C there was little change in the NR profile suggesting that the

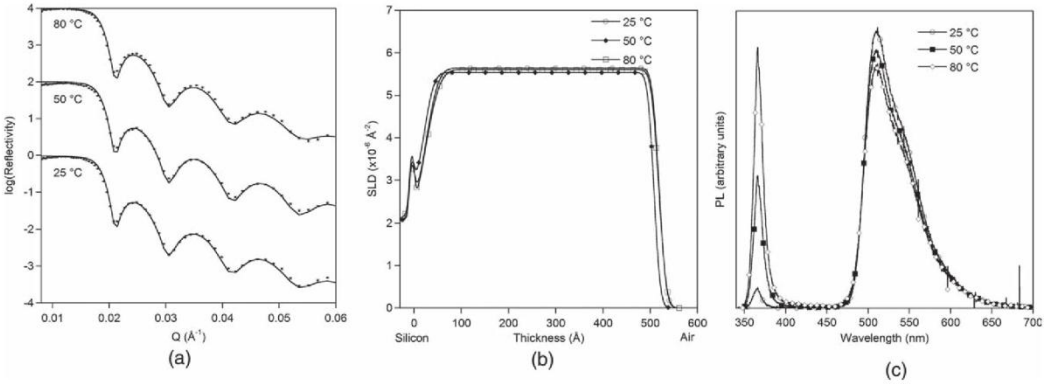

Figure 4. a) NR profiles collected for the 6 wt% blend of $Ir(ppy)_3$ in d-CBP. The points are the NR data and the solid lines the fit to the profile. b) SLD versus film thickness for the 6 wt% blend of $Ir(ppy)_3$ in d-CBP. c) In situ PL measurements for the 6 wt% blend of $Ir(ppy)_3$ in d-CBP.

film structure was quite stable. The SLD of the film was measured as $5.6 \pm 0.1 \times 10^{-6}$ Å^{-2}. Given the SLD of d-CBP is $5.9 \pm 0.1 \times 10^{-6}$ Å^{-2} and that of $Ir(ppy)_3$ being $2.0 \pm 0.1 \times 10^{-6}$ Å^{-2} (Supporting Information) we calculate the weight percent of $Ir(ppy)_3$ in CBP to be 6.4 ± 3.6 wt%, which is essentially the same as that expected from the evaporation rates. The PL spectra of the film under the different conditions gave important insight into changes that had occurred in the film during the annealing process (Figure 4c). The scattered excitation beam (365 nm) was found to increase relative to the luminescence of the film with each temperature step. The increase in reflected excitation light indicates that the surface roughness has increased in a similar manner as the neat CBP film. There was also weak emission at 400 nm arising from CBP, which shows that during the annealing process phase separation was occurring. That is, there is no longer complete energy transfer from the CBP to the $Ir(ppy)_3$. After annealing and cooling to room temperature crystalline regions (discs) could be clearly seen (**Figure 5**a) and luminescence microscopy (Figure 5b and Supporting Information) revealed that fiber-like phase separation between CBP and $Ir(ppy)_3$ rich regions had occurred.

2.1.3. High Weight Percentage Blend

The higher concentration (nominally 10 wt%) film of $Ir(ppy)_3$ blended with d-CBP was measured while going through the same annealing cycle. At room temperature, the NR profile (**Figure 6**a) could be modeled as a single uniform layer showing that, even at this higher concentration, the $Ir(ppy)_3$ is evenly distributed throughout the film and there was little change at the higher temperatures (Figure 6b). From the SLD of the film the blend ratio was calculated to be 12.2 ± 3.2 wt%. The lack of change in the NR profile was mirrored in the PL spectra (Figure 6c). After cooling there were no obvious crystalline domains (Figure 6d), and, unlike the low wt% blend, the reflected light component of the PL spectra did not increase dramatically during the thermal annealing process and in addition, no CBP emission was observed. When viewed by luminescence microscopy the entire field of view was saturated green emission, indicating no phase separation between $Ir(ppy)_3$ and CBP. This is an important result as, while films with blend ratios of 6–8 wt% are usually considered the best in terms of device efficiency, higher blend ratios may confer greater operational stability. The effect of the $Ir(ppy)_3$ is straightfoward to understand and is similar to the effect of impurities seen in the crystallisation of organic compounds–impurities can hinder the crystal packing. CBP has a strong propensity to crystallise[27] and in the doped film the $Ir(ppy)_3$ is acting as an impurity, which depresses the ability of the CBP to order in the solid state, thus keeping the film amorphous.

2.2. (d-TCTA)/$Ir(ppy)_3$:CBP/(d-BCP) Multilayer Film

The final part of the study was to investigate the effect of thermal annealing on a multilayer stack comprised of d-tris(4-carbazoyl-9-ylphenyl)amine (d-TCTA)/$Ir(ppy)_3$:CBP/

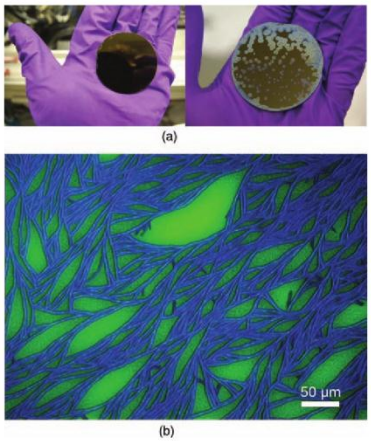

Figure 5. a) 6 wt% (low) blend film before and after annealing to 80 °C. b) Luminescence microscopy of the 6 wt% blend film, after heating to 80 °C and then cooling. The figure is a composite of two images taken at different excitation and emission wavelengths (blue–340 nm excitation, 370–400 nm capture; green–390 nm excitation, 495–550 nm capture) to discriminate between CBP (blue) and $Ir(ppy)_3$ (green) emission.

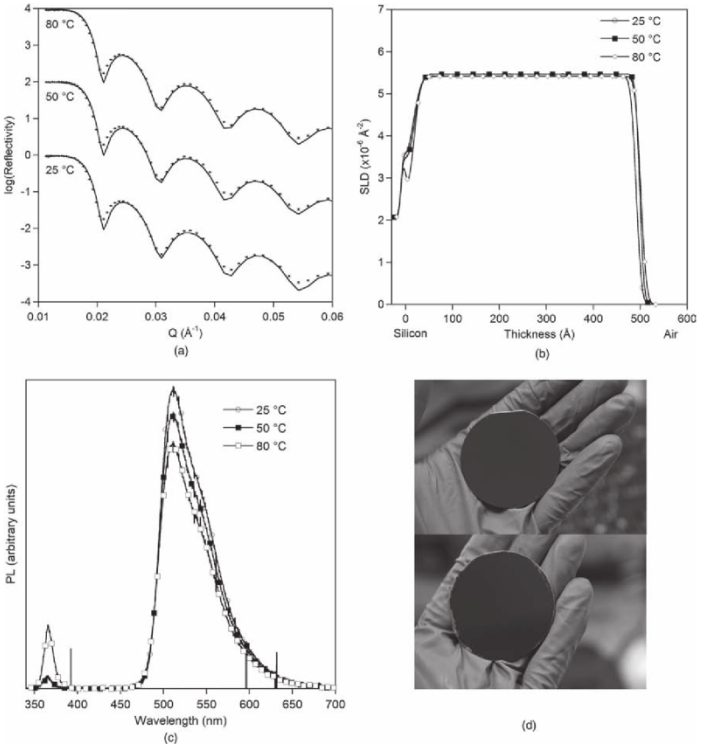

Figure 6. a) NR profiles collected for the 12 wt% blend of $Ir(ppy)_3$ in d-CBP. The points are the NR data and the solid lines the fit to the profile. b) Scattering length density versus film thickness for the 12 wt% blend of $Ir(ppy)_3$ in d-CBP. c) In situ PL measurements for the 12 wt% blend of $Ir(ppy)_3$ in d-CBP. d) 12 wt% (high) blend film before and after annealing to 80 °C. Note the film has not degraded like that of the 6 wt% blend.

d-bathocuproine (d-BCP), with the NR measurements being undertaken using the Platypus reflectometer. When the TCTA and BCP are deuterated and the CBP and $Ir(ppy)_3$ protonated, there is substantial scattering contrast, which allows each of the layers to be identified as the TCTA and BCP have significantly higher SLDs. The $Ir(ppy)_3$:CBP blend layer was prepared under the same conditions for the low wt% film and, hence, the concentration was ~6 wt%. The observed and fitted NR profiles from this multilayer film before, during, and after annealing are shown in **Figure 7**a. It can be clearly seen that the reflectivity profiles are more complicated than for a single uniform film. Figure 7b shows the SLD profiles for this multilayer film and it can be seen that at room temperature, the as-formed film has sharp interfaces between each of the layers. The film structure is stable to 60 °C, but at 100 °C there is a dramatic change in the profile of the multilayer film. At this modest temperature, the model of the NR profile shows that the d-BCP has substantially diffused into the $Ir(ppy)_3$:CBP blend layer. In contrast, the interface between the d-TCTA remains unchanged, showing that it does not diffuse into the "emissive layer". Comparison between the 100 °C data and that for the cooled film indicate that, during cooling to room temperature, the d-BCP continues to migrate into the emissive $Ir(ppy)_3$:CBP layer such that there is only a small amount of 'pristine' $Ir(ppy)_3$:CBP left. The diffusion of the d-BCP into the emissive layer caused little change in either the amount of reflected light or indeed the luminescence from the stacked layers (see Figure 7c). The fact that the luminescence does not change is easily understood. In the emissive layer, the $Ir(ppy)_3$ is diluted in the CBP to avoid intermolecular interactions that lead to quenching. The diffusion of BCP effectively dilutes the $Ir(ppy)_3$ in the layer further and, hence, there is no change in the photoluminescence spectra. This is an important result because it shows that photophysical measurements on their own may not be an effective probe to changes in these types of films. However, while diffusion of BCP in the $Ir(ppy)_3$:CBP layer does not affect the luminescence spectrum, it will affect charge transport in the stack. For example, it could lead to charge trapping or an imbalance of charge injection and transport leading to a change in device performance. Indeed, it is interesting to note that the instability of BCP film morphology has been directly attributed to degradation in device performance.[28]

3. Conclusions

The combination of NR and in situ PL measurements provide a powerful tool to study the relationship between film morphology and photophysical properties. In applying this for the first time to small molecule evaporated layers of materials used in highly efficient OLEDs, we have found that the morphological stability of $Ir(ppy)_3$ blends is dependent on the concentration of the $Ir(ppy)_3$ in the CBP. The higher weight percent blend did not phase separate, suggesting that, in terms of long-term device behavior, there could be a trade-off between efficiency and durability. It was also found that the structure of multilayer stacks could change significantly under relatively mild annealing conditions. In this work, BCP was found to diffuse readily into an emissive $Ir(ppy)_3$:CBP blend in contrast to TCTA, which was found to form a stable layer. These results have important implications for materials and device design, not only for OLEDs but also for stacked organic photovoltaic devices.

4. Experimental Section

Film Preparation: The structures of the materials used in this study are shown in Figure 1 with the d-CBP, d-TCTA, and d-BCP having deuteration levels of ≈96%, ≈63%, and ≈70% respectively. Films were prepared by thermal evaporation under high vacuum (10^{-6} mbar) onto silicon wafers and quartz substrates. Silicon

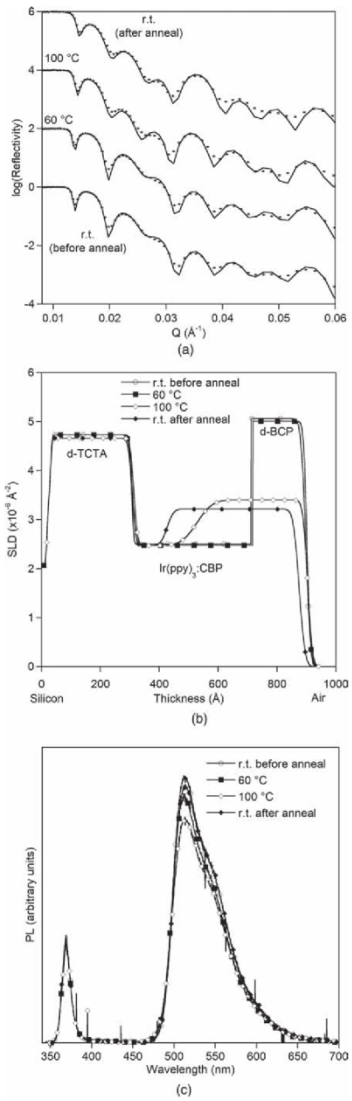

Figure 7. a) NR profiles collected for the d-TCTA/Ir(ppy)$_3$:CBP/d-BCP multilayer structure. The points are the NR data and the solid lines the fit to the profile. b) SLD versus film thickness for the d-TCTA/Ir(ppy)$_3$:CBP/d-BCP multilayer structure. c) In situ PL measurements for the d-TCTA/Ir(ppy)$_3$:CBP/d-BCP multilayer structure.

wafers (Si-Mat, Germany) of 50 mm diameter and quartz slides (H. A. Groiss & Co., Australia) were cleaned with piranha solution (a 2:1 mixture of sulfuric acid and 30% hydrogen peroxide). The silicon wafers had a native oxide layer, which was not removed. Prior to film deposition, the substrates were sonicated in acetone for 5 min, rinsed with 2-propanol and then dried under a stream of clean nitrogen. Film thicknesses were measured with a Veeco Dektak 150 surface profilometer. Atomic force microscope (AFM) images were obtained using an Asylum Research MFP-3D atomic force microscope operated in AC mode, placed on a Herzan anti-vibration table within a TCM acoustic isolation enclosure (Herzan, CA, USA). TAP 300 cantilevers (Budget Sensors, Bulgaria) driven close to their resonant frequency, 300 kHz, at scanning rates between 0.4 to 0.6 Hz were used for all the samples. Luminescence spectra were recorded on a Horiba Jobin-Yvon Fluorolog-3 Tau or FluoroMax-4. Excitation and emission slit widths were 2 nm. Absorption spectra were measured on a Varian Cary 5000 UV–vis–NIR spectrophotometer.

Neutron Reflectometry: Neutron reflectometry experiments were made on the "white beam" reflectometer SURF at the Rutherford-Appleton Laboratory, United Kingdom. The wavelength of the neutrons used ranged from 0.55 Å < λ < 6.8 Å. Blank silicon wafer measurements were performed for substrate characterization. A flat background, determined by extrapolation to high values of momentum transfer Q (Q = (4π sin θ)/λ, where θ is the glancing angle of incidence and λ the wavelength) was subtracted. Reflectivity profiles were measured at incident angles 0.25°, 0.5°, and 0.8° or 0.35° and 0.8° taking ~3 h with the data reduced to yield a single reflectivity profile for fitting. NR measurements were also recorded using the Platypus time-of-flight neutron reflectometer and a cold neutron spectrum (2.8 Å < λ < 18.0 Å) at the OPAL 20 MW research reactor [Australian Nuclear Science and Technology Organisation (ANSTO), Sydney, Australia].[29,30] 20 Hz neutron pulses were generated using a disc chopper system (EADS Astrium GmbH) in the medium resolution mode ($\Delta\lambda/\lambda$ = 4%) and recorded on a two-dimensional helium-3 neutron detector (Denex GmbH). Reflected beam spectra were collected at 0.5° for 1 h (0.2 mm slits) and 2.0° for 2 h (0.8 mm slits). Direct beam measurements were collected under the same collimation conditions. It is important to note that the covered Q range was 0.15 Å^{-1}, although data to a Q value of 0.06 Å^{-1} are shown in the figures. A custom built experimental cell was used for simultaneous NR and PL measurements, with in situ annealing capabilities. The luminescence of the films was monitored with an Ocean Optics USB2000 spectrometer using a Nichia UV-LED 365 nm excitation source. An aluminium block heating stage, isolated from the neutron cell by a ceramic stand, was heated (10 °C min^{-1} during ramp) with two cartridge heaters and the temperature controlled by a Watlow series 988 temperature controller. The cell was under vacuum (~1 mbar) during all experiments. Analysis of the reflectivity profiles was performed using the Motofit reflectometry analysis program.[31] All the NR fits included a ~10 Å oxide layer on the surface of the substrate.

Microscopy: Luminescence microscopy images were obtained on a Nikon Eclipse TE2000-E microscope with a Cairn 150 W xenon arc lamp and an Olympus IX70 microscope with a mercury lamp UV excitation source.

Supporting Information

Supporting Information is available from the Wiley Online Library or from the author.

Acknowledgements

We are grateful for the use of Australian National Fabrication Facility – Queensland Node resources, especially for the help of Dr. Indu Mahadevan (CBP deuteration) and Dr. Muhsen Aljada (film evaporations). We thank Dr. Bronwyn Battersby for the use of the fluorescence microscopes. We also wish to acknowledge the Australian National Deuteration Facility for providing deuterated TCTA and BCP. A.R.G.S. would like to thank the Australian Institute of Nuclear Science and Engineering for a postgraduate research award. H.C. is the recipient of an Endeavour International Postgraduate Research Scholarship. The authors acknowledge funding for the ISIS experiments from the Access to Major Research Facilities Program, which is supported by the Commonwealth of Australia under the International Science Linkages program.

Received: November 10, 2010
Published online: March 25, 2011

[1] C. W. Tang, S. A. VanSlyke, *Appl. Phys. Lett.* **1987**, *51*, 913.
[2] C. W. Tang, S. A. VanSlyke, C. H. Chen, *J. Appl. Phys.* **1989**, *65*, 3610.
[3] A. C. Grimsdale, K. L. Chan, R. E. Martin, P. G. Jokisz, A. B. Holmes, *Chem. Rev.* **2009**, *109*, 897.
[4] P. L. Burn, S.-C. Lo, I. D. W. Samuel, *Adv. Mater.* **2007**, *19*, 1675.
[5] S.-C. Lo, P. L. Burn, *Chem. Rev.* **2007**, *107*, 1097.
[6] M. A. Baldo, S. Lamansky, P. E. Burrows, M. E. Thompson, S. R. Forrest, *Appl. Phys. Lett.* **1999**, *75*, 4.
[7] C. Adachi, M. A. Baldo, M. E. Thompson, S. R. Forrest, *J. Appl. Phys.* **2001**, *90*, 5048.
[8] L. Xiao, Z. Chen, B. Qu, J. Luo, S. Kong, Q. Gong, J. Kido, *Adv. Mater.* **2011**, *23*, 926.
[9] M. Ikai, S. Tokito, Y. Sakamoto, T. Suzuki, Y. Taga, *Appl. Phys. Lett.* **2001**, *79*, 156.
[10] N. C. Giebink, B. W. D'Andrade, M. S. Weaver, J. J. Brown, S. R. Forrest, *J. Appl. Phys.* **2009**, *105*, 124514.
[11] V. Sivasubramaniam, F. Brodkorb, S. Hanning, O. Buttler, H. P. Loebl, V. van Elsbergen, H. Boerner, U. Scherf, M. Kreyenschmidt, *Solid State Sci.* **2009**, *11*, 1933.
[12] J. Chang, Y.-J. Yu, J. H. Na, J. An, C. Im, D.-H. Choi, J.-I. Jin, S. H. Lee, Y. K. Kim, *J. Polym. Sci., Part B: Polym. Phys.* **2008**, *46*, 2395.
[13] N. C. Giebink, B. W. D'Andrade, M. S. Weaver, P. B. Mackenzie, J. J. Brown, M. E. Thompson, S. R. Forrest, *J. Appl. Phys.* **2008**, *103*, 044509.
[14] F. So, D. Kondakov, *Adv. Mater.* **2010**, *22*, 3762.
[15] A. Amassian, V. A. Pozdin, R. Li, D.-M. Smilgies, G. G. Malliaras, *J. Mater. Chem.* **2010**, *20*, 2623.
[16] G. R. Webster, W. J. Mitchell, P. L. Burn, R. K. Thomas, G. Fragneto, J. P. J. Markham, I. D. W. Samuel, *J. Appl. Phys.* **2002**, *91*, 9066.
[17] P. C. Jukes, S. J. Martin, A. M. Higgins, M. Geoghegan, R. A. L. Jones, S. Langridge, A. Wehrum, S. Kirchmeyer, *Adv. Mater.* **2004**, *16*, 807.
[18] A. J. Parnell, A. D. F. Dunbar, A. J. Pearson, P. A. Staniec, A. J. C. Dennison, H. Hamamatsu, M. W. A. Skoda, D. G. Lidzey, R. A. L. Jones, *Adv. Mater.* **2010**, *22*, 2444.
[19] W. J. Mitchell, P. L. Burn, R. K. Thomas, G. Fragneto, *Appl. Phys. Lett.* **2003**, *82*, 2724.
[20] W. J. Mitchell, P. L. Burn, R. K. Thomas, G. Fragneto, J. P. J. Markham, I. D. W. Samuel, *J. Appl. Phys.* **2004**, *95*, 2391.
[21] S. V. Vickers, H. Barcena, K. A. Knights, R. K. Thomas, J. C. Ribierre, S. Gambino, I. D. W. Samuel, P. L. Burn, G. Fragneto, *Appl. Phys. Lett.* **2010**, *96*, 263302.
[22] H. Aziz, Z. D. Popovic, N.-X. Hu, *Appl. Phys. Lett.* **2002**, *81*, 370.
[23] S. Chung, J.-H. Lee, J. Jeong, J.-J. Kim, Y. Hong, *Appl. Phys. Lett.* **2009**, *94*, 253302.
[24] X. Zhou, J. He, L. S. Liao, M. Lu, X. M. Ding, X. Y. Hou, X. M. Zhang, X. Q. He, S. T. Lee, *Adv. Mater.* **2000**, *12*, 265.
[25] A. Grundstein, V. Meentemeyer, J. Dowd, *Int. J. Biometeorol.* **2009**, *53*, 255.
[26] W. Marty, T. Sigrist, D. Wyler, *Am. J. Forensic. Med. Pathol.* **2001**, *22*, 215.
[27] J. H. Kwon, T. J. Park, W. S. Jeon, J. J. Park, *Proc. SPIE* **2007**, *6828*, 682802.
[28] B. W. D'Andrade, S. R. Forrest, A. B. Chwang, *Appl. Phys. Lett.* **2003**, *83*, 3858.
[29] M. James, A. Nelson, A. Brule, J. C. Schulz, *J. Neutron Res.* **2006**, *14*, 91.
[30] M. James, A. Nelson, S. A. Holt, T. Saerbeck, W. A. Hamilton, F. Klose, *Nucl. Instr. Meth. Phys. Res. A* **2011**, *632*, 112.
[31] A. Nelson, *J. Appl. Crystallogr.* **2006**, *39*, 273.

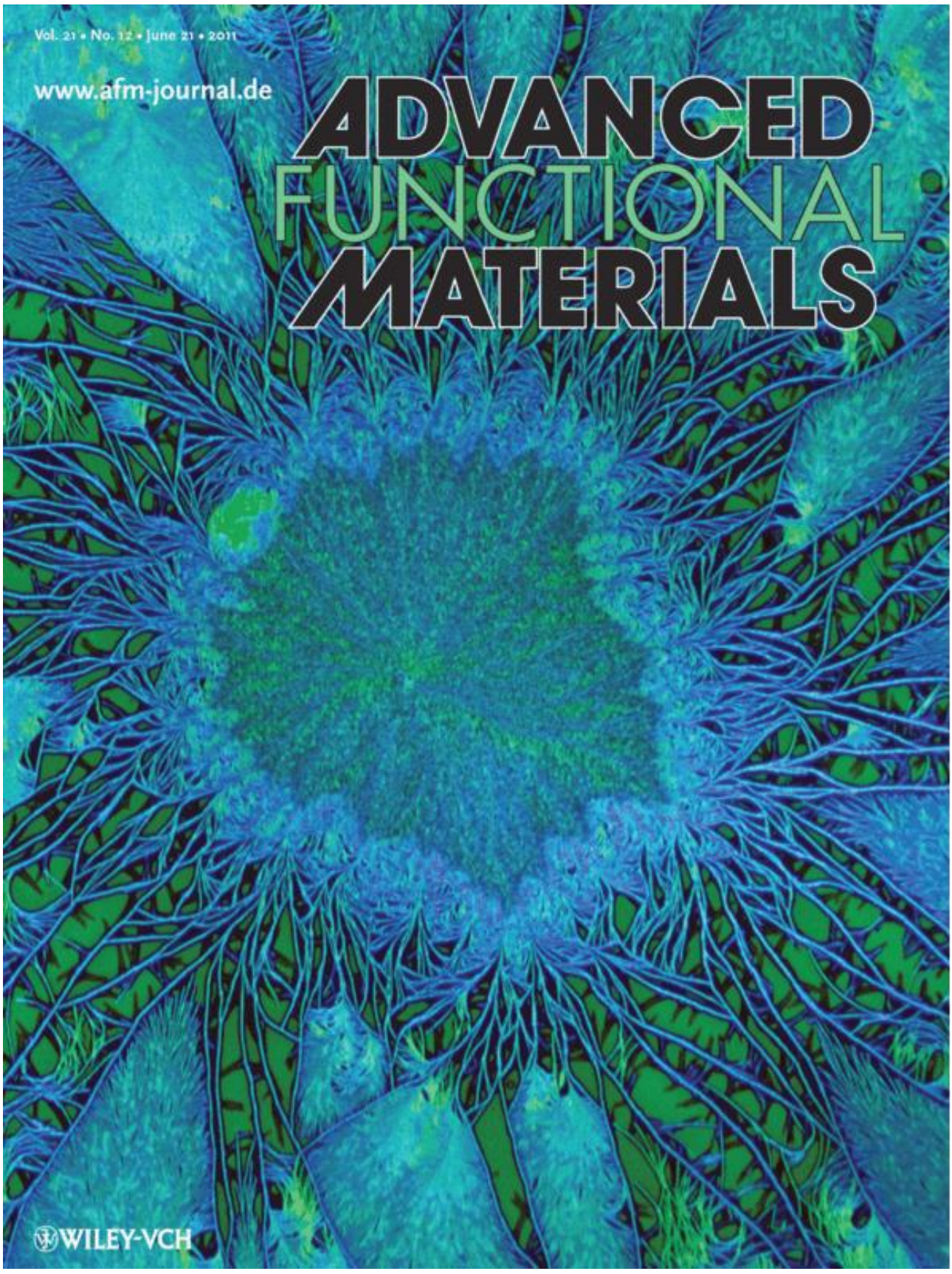
Vol. 21 • No. 12 • June 21 • 2011
www.afm-journal.de
ADVANCED
FUNCTIONAL
MATERIALS
WILEY-VCH

ADVANCED MATERIALS
www.advmat.de

Materials Views
www.MaterialsViews.com

Diffusion – the Hidden Menace in Organic Optoelectronic Devices

Arthur R. G. Smith, Kwan H. Lee, Andrew Nelson, Michael James, Paul L. Burn, and Ian R. Gentle**

Multilayer and/or blended organic films are found in organic semiconductor devices such as organic light-emitting diodes (OLEDs) and organic solar cells (OSCs) comprised of small molecules, polymers, or dendrimers. The design principles for maximizing efficiency are now well understood, and in the case of OLEDs have enabled an increasing market penetration. However, there are still significant gaps in our knowledge. For example, it is often assumed that the deposited layers and blends are in their thermodynamically most stable state but little is known about what happens under the thermal stress encountered during their operation. The reason for this is that the changes are difficult to probe directly in a non-destructive manner due to the fact that the thickness of the layers is of order 100 nanometers and the chemical and physical contrast between the organic layers are generally small. As a consequence what happens at buried interfaces in multilayer films and the effects of subtle changes in morphology of organic films are often inferred from electrical or photophysical properties.[1–4] A powerful technique for investigating organic multilayer structures is neutron reflectometry (NR). By enhancing the scattering contrast with selective deuteration, NR can reveal the precise structure and morphological features of multilayer organic films, with essentially atomic resolution.

In this work we apply NR with in situ photoluminescence (PL) measurements to probe the effect of thermal stress on the layers and materials typically found in highly efficient phosphorescent OLEDs. Such OLEDs consist of a blended light-emitting layer sandwiched between hole and electron transport layers, supported on a transparent electrode, although more complicated designs are sometimes employed.[5–11] A top contact, such as a metallic layer, completes the device. Careful selection of hole and electron transport materials allows excitons to be generated and confined within the light-emitting layer. Internal efficiencies approaching 100% have been common for several years,[12] yet the degradation processes that occur over time, particularly under thermal stress, are not well understood.[13,14] That is, the efficiency of a device will degrade over time as a result of extended operation or external stresses,[15–17] but the color of the emission may not change. It is therefore ambiguous as to whether the decrease in efficiency occurs due to material degradation or changes at the layer interfaces and/or film morphology. These device design features are not unique to OLEDs. For example, OSCs are also comprised of a blended layer to achieve exciton separation and further layers to enhance charge extraction.

Films were prepared on silicon (Si) wafers with layer thicknesses typical of those used in OLEDs (**Figure 1**) and OSCs. The emissive guest:host layer comprised *fac*-tris(2-phenylpyridyl)iridium(III) [Ir(ppy)$_3$] and 4,4′-bis(*N*-carbazolyl)biphenyl (CBP) which were deposited simultaneously across the films to ensure that the thickness and 6 wt% Ir(ppy)$_3$:CBP blend ratio (based on evaporation rates) were consistent.[18] Bathocuproine (BCP) and 4,4′,4″-tris(*N*-carbazolyl)triphenylamine (TCTA) (both deuterated in order to enhance contrast) were used as the electron and hole transport layers as along with CBP both materials have been used in OLEDs and OSCs.[8,19–24]

The first film stack studied (**Film 1**, Figure 1) was composed of the three organic layers plus an aluminium electrode with the NR profiles shown in **Figure 2**. Prior to thermally stressing, the layer thicknesses were modeled as d-TCTA/(Ir(ppy)$_3$:CBP/d-BCP/Al being 277.5 ± 0.2 Å, 335.0 ± 0.2 Å, 156.2 ± 0.3 Å, and 94.4 ± 0.3 Å, respectively. All interface roughness values between the organic layers were low (<10 Å) showing that vacuum deposition can form sharp interfaces. In contrast the d-BCP/Al interface was not as uniform and had a roughness of 20.8 ± 0.3 Å. Under thermal stress the NR profile began to change at 90 °C, which is above the reported bulk glass transition temperatures of CBP[25–27] and BCP,[28–30] but below that of TCTA.[31,32] Modeling showed that the change was consistent with the d-BCP layer beginning to diffuse into the emissive guest:host layer (Figure 2). After stressing the film at 100 °C the d-BCP was found to have diffused throughout the Ir(ppy)$_3$:CBP layer but not into the d-TCTA. In contrast, the d-TCTA layer was morphologically stable. The NR profile showed that the thickness of the 'pure' Al layer appeared to decrease from 94.4 ± 0.3 Å to 66.2 ± 1.2 Å. However, the difference in scattering length density (SLD) of Al and the underlying organic layer is small and hence it is difficult to accurately model the exact thickness despite the small statistical errors reported. In order to elucidate what was happening at the Al/organic interface we used X-ray reflectometry (XRR) (Figure 2). The advantage of XRR in

A. R. G. Smith, Dr. K. H. Lee, Prof. P. L. Burn, Prof. I. R. Gentle
Centre for Organic Photonics & Electronics
School of Chemistry and Molecular Biosciences
The University of Queensland
Brisbane, QLD 4072, Australia
E-mail: p.burn2@uq.edu.au; i.gentle@uq.edu.au
Dr. A. Nelson, Prof. M. James
Bragg Institute
Australian Nuclear Science and Technology Organisation
Locked Bag 2001, Kirrawee DC, NSW 2232, Australia

DOI: 10.1002/adma.201104029

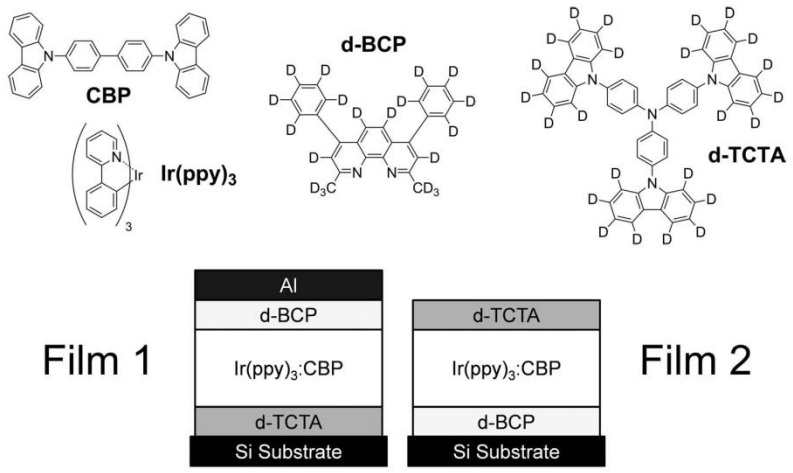

Figure 1. Compounds used in this study: $Ir(ppy)_3$, CBP, d-TCTA, and d-BCP. Schematic layouts of film stacks **1** and **2**.

this case is that Al has a much higher electron density than the organic materials and so its distribution can be easily seen. The XRR data showed that following cooling the Al layer thickness was 97.4 ± 1.0 Å but with a broad interface with the underlying organic layer showing that the Al and underlying organic layer had partially mixed.

Finally, we found that throughout the thermal stress cycle the emission continued to be from the $Ir(ppy)_3$ (λ_{max} = 510 nm) in spite of the complete mixing of the blend layer with the BCP. However, the integrated PL decreased by 33% on thermal annealing showing that simple mixing of layers can have a dramatic effect on the photophysical properties. CBP[8] and BCP[33] are both used as efficient hosts for $Ir(ppy)_3$ and therefore the decrease in the PL signal is most likely due to phase separation and aggregation of $Ir(ppy)_3$,[18] which leads to excited state quenching via triplet-triplet annihilation.[34]

Given that the BCP diffused into the light-emitting layer we were interested to understand the process by which this was occurring. We did not want to include the aluminium electrode in the study because of the extra level of complication in the modeling. However, if the aluminium was not present we found the d-BCP sublimed from the top of the film upon heating to 100 °C. As a consequence we prepared a second film with the stack reversed (**Film 2**), that is, with the BCP near the Si. The NR of the Si/d-BCP/($Ir(ppy)_3$:CBP)/d-TCTA film measured at room temperature gave thicknesses of 150.3 ± 0.3 Å, 346.7 ± 0.3 Å and 267.2 ± 0.2 Å respectively. There was very low roughness (<10 Å) at all the interfaces. On heating to 100 °C the NR profile again showed distinct changes and the refined model indicates that the d-BCP and $Ir(ppy)_3$:CBP layers had almost completely blended together (**Figure 3**). A small residual section of the $Ir(ppy)_3$:CBP layer remained (87.0 ± 1.2 Å). There was also a high interfacial roughness of 32.0 ± 1.3 Å between the new d-BCP:$Ir(ppy)_3$:CBP layer and the remaining $Ir(ppy)_3$:CBP layer. After cooling, the NR was essentially the same [film thickness of 780.6 ± 1.2 Å] as that measured at 100 °C and XRR (764.0 ± 0.2 Å) confirmed the thickness of the film (Figure 3b).

To follow the structural evolution of the film during thermal annealing at 100 °C we used time dependent NR. After heating from 90 to 100 °C at 10 °C/min, data at a fixed angle (0.7°) were collected in event mode and rebinned to 5 min intervals for analysis. A selection of the measured NR and calculated models is presented in **Figure 4**. There is a significant difference between the measured structure at 90 °C and the first measurement taken at 100 °C (which encompasses a time window of 15–20 min after first heating to 100 °C). The reflectivity features in Figure 4a change subtly (see Movie S1 in the Supporting Information) but in each case very good fits with low χ^2 using a 3-layer slab model and with the 90 °C parameters as a starting point was achieved. All roughness parameters, and the SLD and thickness of the d-TCTA layer were fixed with the thickness and SLD of the d-BCP layer, and the thickness of the $Ir(ppy)_3$:CBP layer allowed to vary. The SLD of the $Ir(ppy)_3$:CBP layer was partly restrained ($\geq 2.5 \times 10^{-6}$ Å^{-2}).

The modeling showed that the total film thickness did not change significantly during annealing but the thickness and SLD of the layer that was originally the d-BCP layer did change with time, reaching an equilibrium structure ~2.5 hours after the film was first heated from 90 to 100 °C (Figure 4b). The propagation of interfaces in diffusion couples (in this case the d-BCP/$Ir(ppy)_3$:CBP couple) occurs when the two diffusing species have different intrinsic diffusion coefficients. Diffusion is described as Fickian when the time dependence of the position of the interface follows $x \propto t^n$ with $n = 0.5$, while so-called Case II diffusion occurs for $n = 1$.[35–37] For the d-BCP/$Ir(ppy)_3$:CBP couple the moving interface displays time dependence with an exponent of $n = 0.34$, and is defined as anomalous Fickian interdiffusion.[38–40] Such behavior indicates diffusion asymmetry with the diffusion coefficients strongly dependent on layer composition. Behavior like this has been reported for diffusion between Si/Ge layers.[38,40] Si diffuses rapidly through

ADVANCED MATERIALS
www.advmat.de

Materials Views
www.MaterialsViews.com

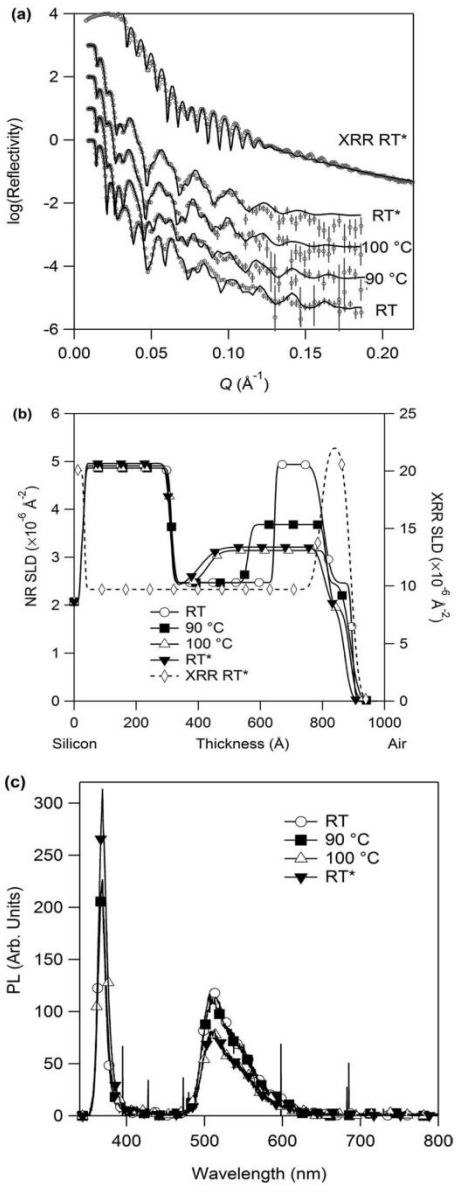

Figure 2. Si/d-TCTA/(Ir(ppy)$_3$:CBP)/d-BCP/Al **Film 1**. (a) Neutron and X-ray reflectivity data (points) and refined models (lines) at different stages of the annealing cycle. (b) The NR and XRR SLD profiles corresponding to the reflectivity models. The film thickness after annealing determined by XRR is essentially the same as that found by NR. (c) PL spectra collected in situ with the neutron experiments reveal a decrease in the PL intensity of the Ir(ppy)$_3$ after annealing at 100 °C. The scattered excitation intensity increases after annealing at 100 °C indicating a higher surface roughness than before annealing. RT* indicates measurements taken after the annealing process, and once the film had cooled below 30 °C.

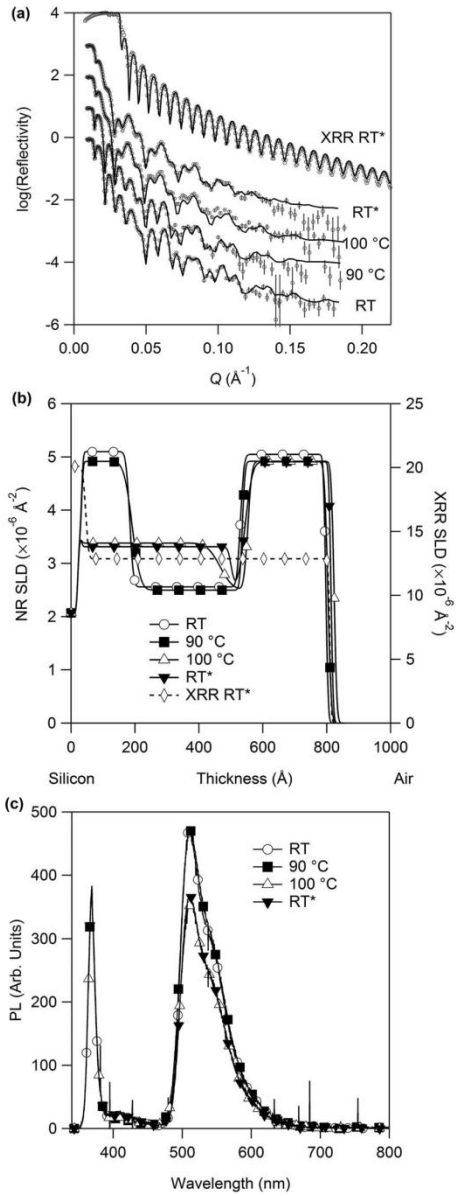

Figure 3. Si/d-BCP/(Ir(ppy)$_3$:CBP)/d-TCTA **Film 2**. (a) Neutron and X-ray reflectivity data (points) and refined models (lines) at different stages of the annealing cycle. (b) The corresponding NR and XRR SLD profiles to the reflectivity models. The film thickness after annealing determined by XRR is essentially the same as that found by NR. (c) PL spectra collected in situ with the neutron experiments reveal a decrease in the PL intensity of the Ir(ppy)$_3$ after annealing at 100 °C. The scattered excitation intensity does not change indicating a constant surface roughness. RT* indicates measurements taken after the annealing process, and once the film had cooled below 30 °C.

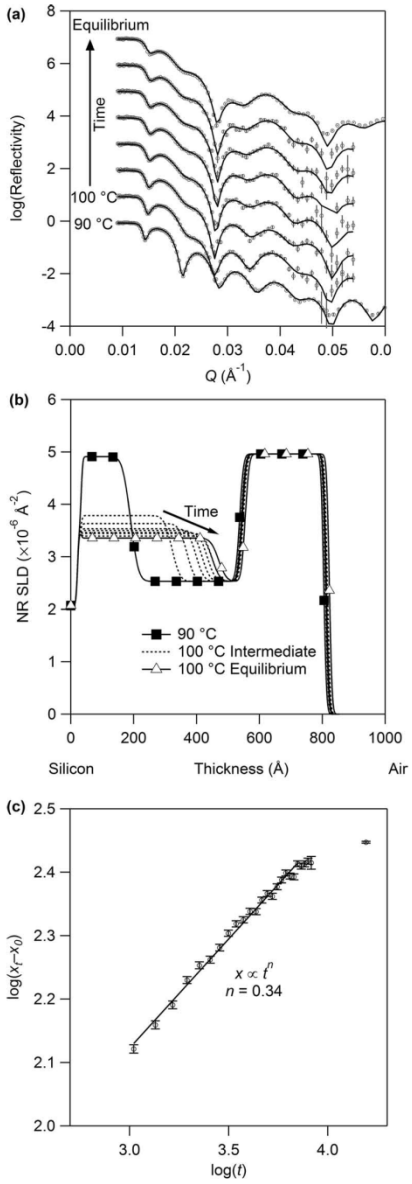

Figure 4. Monitoring the diffusion between the d-BCP and Ir(ppy)$_3$:CBP guest:host layers in **Film 2**. (a) NR profiles collected in 5 min time bins for the first angle until equilibrium was reached (only a selection of the NR profiles is shown for clarity). Sequential modeling (b) of the intermediate and equilibrium measurements was performed with only three free parameters: d-BCP layer thickness, Ir(ppy)$_3$:CBP layer thickness and d-BCP layer SLD. (c) The position of the interface between the d-BCP rich and Ir(ppy)$_3$:CBP layers is described by $x \propto t^n$ with $n = 0.34$. The absolute interface position, x_t, with respect to the initial thickness of the d-BCP layer, x_0, is plotted according to the midpoint of each time window.

Ge, while diffusion of Ge into Si is poor, and the interface propagates into the Si. Therefore, by analogy the Ir(ppy)$_3$:CBP diffuses very quickly in d-BCP, whereas diffusion of d-BCP in Ir(ppy)$_3$:CBP is limited.[37,38,40] To our knowledge this is the first direct measurement of diffusion between organic semiconductor layers comprised of distinctly different materials in real time, highlighting a critical issue for the durability and longevity of organic devices.

In conclusion, multilayer films formed by evaporation of small molecules can form sharp interfaces. However, interdiffusion between layers can occur rapidly under thermal stress at temperatures similar to those reported for accelerated testing,[41] and measured in environments, for example, car cabins,[42,43] in which the devices could be located. It is also important to note that the inefficiencies of OLEDs means that they operate at temperatures above ambient,[44] with one report stating that the internal temperature can be as high as 86 °C.[45] The diffusion is strongly dependent on the structure of the materials, and the fact that it occurs has important ramifications for all multilayer organic optoelectronic devices. In this study the mixing of d-BCP into Ir(ppy)$_3$:CBP reduced the PL intensity, disrupted the aluminium cathode deposited on the d-BCP layer, and would change the charge mobility of the stack. These results clearly show that the choice of materials and order of deposition is critical for the provision of stable layers and interfaces.

Experimental Section

Film Preparation: Films were prepared by thermal evaporation under high vacuum (10^{-6} mbar) onto silicon substrates. Silicon wafers (Si-Mat, Germany) of 50 mm diameter were cleaned with piranha solution (a 2:1 mixture of sulfuric acid and 30% hydrogen peroxide). The native oxide layer was not removed. Prior to film deposition the substrates were sonicated in acetone for 5 min, rinsed with 2-propanol and then dried under a stream of clean nitrogen.

X-ray Reflectometry: X-ray reflectivity profiles were measured using a Panalytical Ltd X'Pert Pro Reflectometer using Cu Kα X-ray radiation. The X-ray beam was collimated using a Göbel mirror, a 0.1 mm slit and a post-sample parallel collimator. Reflectivity data were collected over the angular range $0.05° \leq \theta \leq 4.00°$, with a step size of 0.005° and counting times of 1 s per step. Least squares analysis of the reflectivity profiles were performed using the Motofit reflectometry analysis program,[46] with error estimates on fitted parameters reported as ±1 standard deviation.

Neutron Reflectometry: NR measurements were recorded using the Platypus time-of-flight neutron reflectometer and a cold neutron spectrum (2.8 Å < λ < 18.0 Å) at the OPAL 20 MW research reactor [Australian Nuclear Science and Technology Organisation (ANSTO), Sydney, Australia].[47,48] 20 Hz Neutron pulses were generated using a disk chopper system (EADS Astrium GmbH) in the medium resolution mode ($\Delta\lambda/\lambda$ = 4%) and recorded on a 2-dimensional helium-3 neutron detector (Denex GmbH). Reflected beam spectra were collected at 0.7° for 20 min (0.27 mm slits) and 2.5° for 110 min (0.95 mm slits). Direct beam measurements were collected under the same collimation conditions. Time dependent NR measurements were acquired in event mode (Time of flight, x and y position and frame number time are recorded for each neutron), and rebinned to 5 min time windows for analysis.

A custom built experimental cell was used for simultaneous NR and PL measurements, with in situ annealing capabilities. The luminescence of the films was monitored with an Ocean Optics USB2000 spectrometer using a Nichia UV-LED 365 nm excitation source. An aluminium block heating stage, isolated from the neutron cell by a ceramic stand, was heated (10 °C min^{-1} during ramp) with two cartridge heaters and the

temperature controlled by a Watlow series 988 temperature controller. Measurements were taken at room temperature (RT, 22 °C) and at 10 °C steps from 60 to 100 °C. The film was then cooled (RT*, <30 °C) under a stream of clean nitrogen when a final measurement was taken. The cell was under vacuum (~1 mbar) during all experiments. NR measurements were performed at each temperature until such a time as the film had reached thermal equilibrium. Least squares analysis of the reflectivity profiles were performed using the Motofit reflectometry analysis program,[46,49] with error estimates on fitted parameters reported as ±1 standard deviation.

Supporting Information

Supporting Information is available from the Wiley Online Library or from the author.

Acknowledgements

ARGS would like to thank the Australian Institute of Nuclear Science and Engineering for a Postgraduate Research Award. KHL is a University of Queensland Postdoctoral Research Fellow. PLB is a recipient of an Australian Research Council Federation Fellowship (Project FF0668728). Deuterated materials were generously supplied by the Australian National Deuteration Facility.

Received: October 20, 2011
Published online: December 29, 2011

[1] S. A. Van Slyke, C. H. Chen, C. W. Tang, *Appl. Phys. Lett.* **1996**, *69*, 2160.
[2] C. Adachi, K. Nagai, N. Tamoto, *Appl. Phys. Lett.* **1995**, *66*, 2679.
[3] M. Thomschke, S. Hofmann, S. Olthof, M. Anderson, H. Kleemann, M. Schober, B. Lussem, K. Leo, *Appl. Phys. Lett.* **2011**, *98*, 083304.
[4] R. C. Kwong, M. R. Nugent, L. Michalski, T. Ngo, K. Rajan, Y.-J. Tung, M. S. Weaver, T. X. Zhou, M. Hack, M. E. Thompson, S. R. Forrest, J. J. Brown, *Appl. Phys. Lett.* **2002**, *81*, 162.
[5] C. W. Tang, S. A. Van Slyke, *Appl. Phys. Lett.* **1987**, *51*, 913.
[6] J. Kido, M. Kimura, K. Nagai, *Science* **1995**, *267*, 1332.
[7] Z. Shen, P. E. Burrows, V. Bulović, S. R. Forrest, M. E. Thompson, *Science* **1997**, *276*, 2009.
[8] M. A. Baldo, S. Lamansky, P. E. Burrows, M. E. Thompson, S. R. Forrest, *Appl. Phys. Lett.* **1999**, *75*, 4.
[9] M. Ikai, S. Tokito, Y. Sakamoto, T. Suzuki, Y. Taga, *Appl. Phys. Lett.* **2001**, *79*, 156.
[10] L. S. Liao, K. P. Klubek, C. W. Tang, *Appl. Phys. Lett.* **2004**, *84*, 167.
[11] S. Reineke, F. Lindner, G. Schwartz, N. Seidler, K. Walzer, B. Lussem, K. Leo, *Nature* **2009**, *459*, 234.
[12] C. Adachi, M. A. Baldo, M. E. Thompson, S. R. Forrest, *J. Appl. Phys.* **2001**, *90*, 5048.
[13] X. Zhou, J. He, L. S. Liao, M. Lu, X. M. Ding, X. Y. Hou, X. M. Zhang, X. Q. He, S. T. Lee, *Adv. Mater.* **2000**, *12*, 265.
[14] Y. J. Lee, S.-S. Park, J. Kim, H. Kim, *Appl. Phys. Lett.* **2009**, *94*, 223305.
[15] P. E. Burrows, V. Bulović, S. R. Forrest, L. S. Sapochak, D. M. McCarty, M. E. Thompson, *Appl. Phys. Lett.* **1994**, *65*, 2922.
[16] H. Aziz, Z. D. Popovic, *Chem. Mater.* **2004**, *16*, 4522.
[17] F. So, D. Kondakov, *Adv. Mater.* **2010**, *22*, 3762.
[18] A. R. G. Smith, J. L. Ruggles, H. Cavaye, P. E. Shaw, T. A. Darwish, M. James, I. R. Gentle, P. L. Burn, *Adv. Funct. Mater.* **2011**, *21*, 2225.
[19] H. Gommans, B. Verreet, B. P. Rand, R. Muller, J. Poortmans, P. Heremans, J. Genoe, *Adv. Funct. Mater.* **2008**, *18*, 3686.
[20] M. Vogel, S. Doka, C. Breyer, M. C. Lux-Steiner, K. Fostiropoulos, *Appl. Phys. Lett.* **2006**, *89*, 163501.
[21] M. Zhang, H. Wang, C. W. Tang, *Appl. Phys. Lett.* **2010**, *97*, 143503.
[22] Y. Sun, N. C. Giebink, H. Kanno, B. Ma, M. E. Thompson, S. R. Forrest, *Nature* **2006**, *440*, 908.
[23] Y. Tao, C. Yang, J. Qin, *Chem. Soc. Rev.* **2011**, *40*, 2943.
[24] B. W. D'Andrade, R. J. Holmes, S. R. Forrest, *Adv. Mater.* **2004**, *16*, 624.
[25] B. E. Koene, D. E. Loy, M. E. Thompson, *Chem. Mater.* **1998**, *10*, 2235.
[26] M.-H. Tsai, Y.-H. Hong, C.-H. Chang, H.-C. Su, C.-C. Wu, A. Matoliukstyte, J. Simokaitiene, S. Grigalevicius, J. V. Grazulevicius, C.-P. Hsu, *Adv. Mater.* **2007**, *19*, 862.
[27] M.-H. Ho, B. Balaganesan, T.-Y. Chu, T.-M. Chen, C. H. Chen, *Thin Solid Films* **2008**, *517*, 943.
[28] H. Tsuji, K. Sato, Y. Sato, E. Nakamura, *Chem. Asian J.* **2010**, *5*, 1294.
[29] B. W. D'Andrade, S. R. Forrest, A. B. Chwang, *Appl. Phys. Lett.* **2003**, *83*, 3858.
[30] M.-H. Wu, J.-H. Lee, M.-K. Leung, C.-C. Liao, Y. Chang, *Proc. SPIE - Int. Soc. Opt. Eng.* **2004**, *5519*, 263.
[31] Y. Kuwabara, H. Ogawa, H. Inada, N. Noma, Y. Shirota, *Adv. Mater.* **1994**, *6*, 677.
[32] J. Ding, Q. Wang, L. Zhao, D. Ma, L. Wang, X. Jing, F. Wang, *J. Mater. Chem.* **2010**, *20*, 8126.
[33] C. Adachi, M. A. Baldo, S. R. Forrest, M. E. Thompson, *Appl. Phys. Lett.* **2000**, *77*, 904.
[34] S. Reineke, G. Schwartz, K. Walzer, M. Falke, K. Leo, *Appl. Phys. Lett.* **2009**, *94*, 163305.
[35] J. Crank, *The Mathematics of Diffusion*, Oxford **1979**.
[36] H. Mehrer, *Diffusion in Solids*, Springer, Berlin **2007**.
[37] Z. Erdélyi, D. Beke, *J. Mater. Sci.* **2011**, *46*, 6465.
[38] A. Csik, G. A. Langer, D. L. Beke, Z. Erdelyi, M. Menyhard, A. Sulyok, *J. Appl. Phys.* **2001**, *89*, 804.
[39] Z. Erdélyi, G. L. Katona, D. L. Beke, *Phys. Rev. B* **2004**, *69*, 113407.
[40] B. S. Cao, M. K. Lei, *Thin Solid Films* **2008**, *516*, 1843.
[41] H. Aziz, Z. D. Popovic, N.-X. Hu, *Appl. Phys. Lett.* **2002**, *81*, 370.
[42] A. Grundstein, V. Meentemeyer, J. Dowd, *J. Int. J. Biometeorol.* **2009**, *53*, 255.
[43] W. Marty, T. Sigrist, D. Wyler, *Am. J. Forensic. Med. Pathol.* **2001**, *22*, 215.
[44] S. Chung, J.-H. Lee, J. Jeong, J.-J. Kim, Y. Hong, *Appl. Phys. Lett.* **2009**, *94*, 253302.
[45] X. Zhou, J. He, L. S. Liao, M. Lu, X. M. Ding, X. Y. Hou, X. M. Zhang, X. Q. He, S. T. Lee, *Adv. Mater.* **2000**, *12*, 265.
[46] A. Nelson, *J. Appl. Crystallogr.* **2006**, *39*, 273.
[47] M. James, A. Nelson, S. A. Holt, T. Saerbeck, W. A. Hamilton, F. Klose, *Nucl. Instrum. Methods Phys. Res., Sect. A* **2011**, *632*, 112.
[48] M. James, A. Nelson, A. Brule, J. C. Schulz, *J. Neutron Res.* **2006**, *14*, 91.
[49] A. Nelson, *J. Phys.: Conf. Ser.* **2010**, *251*, 012094.

References

1. Forrest, S. R. The Path to Ubiquitous and Low-Cost Organic Electronic Appliances on Plastic, *Nature* **2004**, *428*, 911.
2. Bernanose, A.; Comte, M.; Vouaux, P. Sur Un Nouveau Mode Demission Lumineuse Chez Certains Composes Organiques, *J. Chim. Phys. Phys.-Chim. Biol.* **1953**, *50*, 64.
3. Tang, C. W.; Van Slyke, S. A. Organic Electroluminescent Diodes, *Appl. Phys. Lett.* **1987**, *51*, 913.
4. Xiao, L.; Chen, Z.; Qu, B.; Luo, J.; Kong, S.; Gong, Q.; Kido, J. Recent Progresses on Materials for Electrophosphorescent Organic Light-Emitting Devices, *Adv. Mater.* **2011**, *23*, 926.
5. *Xel-1 | Organic El Tv | Sony*, Retrieved 20 March, 2011, http://www.sony.jp/oel/products/XEL-1/
6. *Sony Xel-1 Oled Tv*, Retrieved 21 March, 2011, http://www.oled-info.com/sony-xel-1
7. *News Samsung*, Retrieved 20 March, 2011, http://www.samsung.com/us/news/newsRead.do?news_seq=19806
8. Kido, J.; Kimura, M.; Nagai, K. Multilayer White Light-Emitting Organic Electroluminescent Device, *Science* **1995**, *267*, 1332.
9. Reineke, S.; Lindner, F.; Schwartz, G.; Seidler, N.; Walzer, K.; Lussem, B.; Leo, K. White Organic Light-Emitting Diodes with Fluorescent Tube Efficiency, *Nature* **2009**, *459*, 234.
10. Gather, M. C.; Köhnen, A.; Meerholz, K. White Organic Light-Emitting Diodes, *Adv. Mater.* **2011**, *23*, 233.
11. Matsushita, T.; Asada, T.; Koseki, S. Relativistic Study on Emission Mechanism in Tris(2-Phenylpyridine)Iridium, *J. Phys. Chem. C* **2007**, *111*, 6897.
12. De Angelis, F.; Fantacci, S.; Evans, N.; Klein, C.; Zakeeruddin, S. M.; Moser, J. E.; Kalyanasundaram, K.; Bolink, H. J.; Gratzel, M.; Nazeeruddin, M. K. Controlling Phosphorescence Color and Quantum Yields in Cationic Iridium Complexes: A Combined Experimental and Theoretical Study, *Inorg. Chem.* **2007**, *46*, 5989.
13. Nozaki, K. Theoretical Studies on Photophysical Properties and Mechanism of Phosphorescence in [Fac-Ir(2-Phenylpyridine)$_3$], *J. Chin. Chem. Soc.* **2006**, *53*, 101.
14. Nozaki, K.; Takamori, K.; Nakatsugawa, Y.; Ohno, T. Theoretical Studies of Phosphorescence Spectra of Tris(2,2'-Bipyridine) Transition Metal Compounds, *Inorg. Chem.* **2006**, *45*, 6161.
15. Obara, S.; Itabashi, M.; Okuda, F.; Tamaki, S.; Tanabe, Y.; Ishii, Y.; Nozaki, K.; Haga, M. A. Highly Phosphorescent Iridium Complexes Containing Both Tridentate Bis(Benzimidazolyl)-Benzene or -Pyridine and Bidentate Phenylpyridine: Synthesis, Photophysical Properties, and Theoretical Study of Ir-Bis(Benzimidazolyl)Benzene Complex, *Inorg. Chem.* **2006**, *45*, 8907.
16. Yutaka, T.; Obara, S.; Ogawa, S.; Nozaki, K.; Ikeda, N.; Ohno, T.; Ishii, Y.; Sakai, K.; Haga, M. a. Syntheses and Properties of Emissive Iridium(III) Complexes with Tridentate Benzimidazole Derivatives, *Inorg. Chem.* **2005**, *44*, 4737.
17. Anthopoulos, T. D.; Frampton, M. J.; Namdas, E. B.; Burn, P. L.; Samuel, I. D. W. Solution-Processable Red Phosphorescent Dendrimers for Light-Emitting Device Applications, *Adv. Mater.* **2004**, *16*, 557.
18. Lo, S. C.; Namdas, E. B.; Burn, P. L.; Samuel, I. D. W. Synthesis and Properties of Highly Efficient Electroluminescent Green Phosphorescent Iridium Cored Dendrimers, *Macromolecules* **2003**, *36*, 9721.
19. Lo, S.-C.; Shipley, C. P.; Bera, R. N.; Harding, R. E.; Cowley, A. R.; Burn, P. L.; Samuel, I. D. W. Blue Phosphorescence from Iridium(III) Complexes at Room Temperature, *Chem. Mater.* **2006**, *18*, 5119.
20. Ho, P. K. H.; Kim, J.-S.; Burroughes, J. H.; Becker, H.; Li, S. F. Y.; Brown, T. M.; Cacialli, F.; Friend, R. H. Molecular-Scale Interface Engineering for Polymer Light-Emitting Diodes, *Nature* **2000**, *404*, 481.

21. Baldo, M. A.; Lamansky, S.; Burrows, P. E.; Thompson, M. E.; Forrest, S. R. Very High-Efficiency Green Organic Light-Emitting Devices Based on Electrophosphorescence, *Appl. Phys. Lett.* **1999**, *75*, 4.
22. Bulovic, V.; Deshpande, R.; Thompson, M. E.; Forrest, S. R. Tuning the Color Emission of Thin Film Molecular Organic Light Emitting Devices by the Solid State Solvation Effect, *Chem. Phys. Lett.* **1999**, *308*, 317.
23. Shi, J.; Tang, C. W. Doped Organic Electroluminescent Devices with Improved Stability, *Appl. Phys. Lett.* **1997**, *70*, 1665.
24. Tang, C. W.; Van Slyke, S. A.; Chen, C. H. Electroluminescence of Doped Organic Thin Films, *J. Appl. Phys.* **1989**, *65*, 3610.
25. Tao, Y.; Yang, C.; Qin, J. Organic Host Materials for Phosphorescent Organic Light-Emitting Diodes, *Chem. Soc. Rev.* **2011**, *40*, 2943.
26. Sasabe, H.; Kido, J. Multifunctional Materials in High-Performance Oleds: Challenges for Solid-State Lighting, *Chem. Mater.* **2011**, *23*, 621.
27. So, F.; Kondakov, D. Degradation Mechanisms in Small-Molecule and Polymer Organic Light-Emitting Diodes, *Adv. Mater.* **2010**, *22*, 3762.
28. Kulkarni, A. P.; Tonzola, C. J.; Babel, A.; Jenekhe, S. A. Electron Transport Materials for Organic Light-Emitting Diodes, *Chem. Mater.* **2004**, *16*, 4556.
29. D'Andrade, B. W.; Thompson, M. E.; Forrest, S. R. Controlling Exciton Diffusion in Multilayer White Phosphorescent Organic Light Emitting Devices, *Adv. Mater.* **2002**, *14*, 147.
30. Hughes, G.; Bryce, M. R. Electron-Transporting Materials for Organic Electroluminescent and Electrophosphorescent Devices, *J. Mater. Chem.* **2005**, *15*, 94.
31. Shirota, Y.; Kageyama, H. Charge Carrier Transporting Molecular Materials and Their Applications in Devices, *Chem. Rev.* **2007**, *107*, 953.
32. Yersin, H. In *Top. Curr. Chem.*; Spinger-Verlag: Berlin, 2004; Vol. 241, p 1.
33. Burroughes, J. H.; Bradley, D. D. C.; Brown, A. R.; Marks, R. N.; Mackay, K.; Friend, R. H.; Burns, P. L.; Holmes, A. B. Light-Emitting Diodes Based on Conjugated Polymers, *Nature* **1990**, *347*, 539.
34. Adachi, C.; Tokito, S.; Tsutsui, T.; Saito, S. Electroluminescence in Organic Films with 3-Layer Structure, *Jpn. J. Appl. Phys. Part 2 - Lett.* **1988**, *27*, L269.
35. Baldo, M. A.; O'Brien, D. F.; Thompson, M. E.; Forrest, S. R. Excitonic Singlet-Triplet Ratio in a Semiconducting Organic Thin Film, *Phys. Rev. B* **1999**, *60*, 14422.
36. Friend, R. H.; Gymer, R. W.; Holmes, A. B.; Burroughes, J. H.; Marks, R. N.; Taliani, C.; Bradley, D. D. C.; Santos, D. A. D.; Bredas, J. L.; Logdlund, M.; Salaneck, W. R. Electroluminescence in Conjugated Polymers, *Nature* **1999**, *397*, 121.
37. Baldo, M.; O'Brien, D.; You, Y.; Shoustikov, A.; Sibley, S.; Thompson, M.; Forrest, S. Highly Efficient Phosphorescent Emission from Organic Electroluminescent Devices, *Nature* **1998**, *395*, 151.
38. King, S. M.; Cass, M.; Pintani, M.; Coward, C.; Dias, F. B.; Monkman, A. P.; Roberts, M. The Contribution of Triplet-Triplet Annihilation to the Lifetime and Efficiency of Fluorescent Polymer Organic Light Emitting Diodes, *J. Appl. Phys.* **2011**, *109*, 074502.
39. Kondakov, D. Y.; Pawlik, T. D.; Hatwar, T. K.; Spindler, J. P. Triplet Annihilation Exceeding Spin Statistical Limit in Highly Efficient Fluorescent Organic Light-Emitting Diodes, *J. Appl. Phys.* **2009**, *106*, 124510.
40. Jacko, A. C.; McKenzie, R. H.; Powell, B. J. Models of Organometallic Complexes for Optoelectronic Applications, *J. Mater. Chem.* **2010**, *20*, 10301.
41. Adachi, C.; Baldo, M. A.; Thompson, M. E.; Forrest, S. R. Nearly 100% Internal Phosphorescence Efficiency in an Organic Light-Emitting Device, *J. Appl. Phys.* **2001**, *90*, 5048.

42. Thomson, A. J.; Skarda, V.; Cook, M. J.; Robbins, D. J. Magnetic Circular-Dichroism Spectra of Tris-Chelate Complexes of 2,2'-Bipyridyl and 1,10-Phenanthroline with Iron(II), Ruthenium(II), and Osmium(II) at 4.2 K, *J. Chem. Soc.-Dalton Trans.* **1985**, 1781.
43. Kober, E. M.; Meyer, T. J. Concerning the Electronic Structure of the Ions $M(Bpy)_3^{3+}$ (M = Fe, Ru, Os; Bpy = 2,2'-Bipyridine), *Inorg. Chem.* **1983**, *22*, 1614.
44. Kober, E. M.; Meyer, T. J. Concerning the Absorption Spectra of the Ions $M(Bpy)_3^{2+}$ (M = Fe, Ru, Os; Bpy = 2,2'-Bipyridine), *Inorg. Chem.* **1982**, *21*, 3967.
45. Kober, E. M.; Meyer, T. J. An Electronic Structural Model for the Emitting Mlct Excited States of $Ru(Bpy)_3^{2+}$ and $Os(Bpy)_3^{2+}$, *Inorg. Chem.* **1984**, *23*, 3877.
46. Ferguson, J.; Krausz, E. The Excitation Dependence of the Luminescence and Mcpl of Ru(Bpy)2+3 in Rigid Solutions, *J. Lumin.* **1986**, *36*, 129.
47. Yoon, S.; Kukura, P.; Stuart, C. M.; Mathies, R. A. Direct Observation of the Ultrafast Intersystem Crossing in Tris(2,2 '-Bipyridine) Ruthenium(II) Using Femtosecond Stimulated Raman Spectroscopy, *Mol. Phys.* **2006**, *104*, 1275.
48. Gawelda, W.; Johnson, M.; deGroot, F. M. F.; Abela, R.; Bressler, C.; Chergui, M. Electronic and Molecular Structure of Photoexcited $[Ru(II)(Bpy)_3]^{2+}$ Probed by Picosecond X-Ray Absorption Spectroscopy, *J. Am. Chem. Soc.* **2006**, *128*, 5001.
49. O'Regan, B.; Gratzel, M. A Low-Cost, High-Efficiency Solar Cell Based on Dye-Sensitized Colloidal Tio2 Films, *Nature* **1991**, *353*, 737.
50. Fantacci, S.; De Angelis, F.; Selloni, A. Absorption Spectrum and Solvatochromism of the $[Ru(4,4'\text{-}Cooh\text{-}2,2'\text{-}Bpy)_2(Ncs)_2]$ Molecular Dye by Time Dependent Density Functional Theory, *J. Am. Chem. Soc.* **2003**, *125*, 4381.
51. You, Y.; Park, S. Y. Phosphorescent Iridium(III) Complexes: Toward High Phosphorescence Quantum Efficiency through Ligand Control, *Dalton Trans.* **2009**, 1267.
52. Yu, J.-K.; Hu, Y.-H.; Cheng, Y.-M.; Chou, P.-T.; Peng, S.-M.; Lee, G.-H.; Carty, A. J.; Tung, Y.-L.; Lee, S.-W.; Chi, Y.; Liu, C.-S. A Remarkable Ligand Orientational Effect in Osmium-Atom-Induced Blue Phosphorescence, *Chemistry - A European Journal* **2004**, *10*, 6255.
53. Chou, P. T.; Chi, Y. Phosphorescent Dyes for Organic Light-Emitting Diodes, *Chem.-Eur. J.* **2007**, *13*, 380.
54. Holder, E.; Langeveld, B.; Schubert, U. New Trends in the Use of Transition Metal–Ligand Complexes for Applications in Electroluminescent Devices, *Adv. Mater.* **2005**, *17*, 1109.
55. Ulbricht, C.; Beyer, B.; Friebe, C.; Winter, A.; Schubert, U. S. Recent Developments in the Application of Phosphorescent Iridium(III) Complex Systems, *Adv. Mater.* **2009**, *21*, 4418.
56. Yersin, H.; Strasser, J. Triplets in Metal-Organic Compounds. Chemical Tunability of Relaxation Dynamics, *Coord. Chem. Rev.* **2000**, *208*, 331.
57. Greenham, N. C.; Samuel, I. D. W.; Hayes, G. R.; Phillips, R. T.; Kessener, Y. A. R. R.; Moratti, S. C.; Holmes, A. B.; Friend, R. H. Measurement of Absolute Photoluminescence Quantum Efficiencies in Conjugated Polymers, *Chem. Phys. Lett.* **1995**, *241*, 89.
58. Reineke, S.; Schwartz, G.; Walzer, K.; Falke, M.; Leo, K. Highly Phosphorescent Organic Mixed Films: The Effect of Aggregation on Triplet-Triplet Annihilation, *Appl. Phys. Lett.* **2009**, *94*, 163305.
59. Baldo, M. A.; Adachi, C.; Forrest, S. R. Transient Analysis of Organic Electrophosphorescence. II. Transient Analysis of Triplet-Triplet Annihilation, *Phys. Rev. B* **2000**, *62*, 10967.
60. Kawamura, Y.; Brooks, J.; Brown, J. J.; Sasabe, H.; Adachi, C. Intermolecular Interaction and a Concentration-Quenching Mechanism of Phosphorescent Ir(III) Complexes in a Solid Film, *Phys. Rev. Lett.* **2006**, *96*, 017404.
61. Giebink, N. C.; D'Andrade, B. W.; Weaver, M. S.; Mackenzie, P. B.; Brown, J. J.; Thompson, M. E.; Forrest, S. R. Intrinsic Luminance Loss in Phosphorescent Small-Molecule Organic Light Emitting Devices Due to Bimolecular Annihilation Reactions, *J. Appl. Phys.* **2008**, *103*, 044509.

62. Sprouse, S.; King, K. A.; Spellane, P. J.; Watts, R. J. Photophysical Effects of Metal-Carbon .Sigma. Bonds in Ortho-Metalated Complexes of Iridium(III) and Rhodium(III), *J. Am. Chem. Soc.* **1984**, *106*, 6647.
63. King, K. A.; Finlayson, M. F.; Spellane, P. J.; Watts, R. J. Luminescence Spectroscopy and Oxidative Quenching of Orthometallated Complexes of Iridium(III), *Sci. Papers I.P.C.R.* **1984**, *78*, 97.
64. King, K. A.; Spellane, P. J.; Watts, R. J. Excited-State Properties of a Triply Ortho-Metalated Iridium(III) Complex, *J. Am. Chem. Soc.* **1985**, *107*, 1431.
65. Frampton, M. J.; Namdas, E. B.; Lo, S.-C.; Burn, P. L.; Samuel, I. D. W. The Synthesis and Properties of Solution Processable Red-Emitting Phosphorescent Dendrimers, *J. Mater. Chem.* **2004**, *14*, 2881.
66. Tsuboyama, A.; Iwawaki, H.; Furugori, M.; Mukaide, T.; Kamatani, J.; Igawa, S.; Moriyama, T.; Miura, S.; Takiguchi, T.; Okada, S.; Hoshino, M.; Ueno, K. Homoleptic Cyclometalated Iridium Complexes with Highly Efficient Red Phosphorescence and Application to Organic Light-Emitting Diode, *J. Am. Chem. Soc.* **2003**, *125*, 12971.
67. Lamansky, S.; Djurovich, P.; Murphy, D.; Abdel-Razzaq, F.; Kwong, R.; Tsyba, I.; Bortz, M.; Mui, B.; Bau, R.; Thompson, M. E. Synthesis and Characterization of Phosphorescent Cyclometalated Iridium Complexes, *Inorg. Chem.* **2001**, *40*, 1704.
68. Lo, S.-C.; Male, N. A. H.; Markham, J. P. J.; Magennis, S. W.; Burn, P. L.; Salata, O. V.; Samuel, I. D. W. Green Phosphorescent Dendrimer for Light-Emitting Diodes, *Adv. Mater.* **2002**, *14*, 975.
69. Nazeeruddin, M. K.; Humphry-Baker, R.; Berner, D.; Rivier, S.; Zuppiroli, L.; Graetzel, M. Highly Phosphorescence Iridium Complexes and Their Application in Organic Light-Emitting Devices, *J. Am. Chem. Soc.* **2003**, *125*, 8790.
70. Lo, S.-C.; Harding, R. E.; Shipley, C. P.; Stevenson, S. G.; Burn, P. L.; Samuel, I. D. W. High-Triplet-Energy Dendrons: Enhancing the Luminescence of Deep Blue Phosphorescent Iridium(III) Complexes, *J. Am. Chem. Soc.* **2009**, *131*, 16681.
71. Sasabe, H.; Takamatsu, J. i.; Motoyama, T.; Watanabe, S.; Wagenblast, G.; Langer, N.; Molt, O.; Fuchs, E.; Lennartz, C.; Kido, J. High-Efficiency Blue and White Organic Light-Emitting Devices Incorporating a Blue Iridium Carbene Complex, *Adv. Mater.* **2010**, *22*, 5003.
72. Rausch, A. F.; Thompson, M. E.; Yersin, H. Blue Light Emitting Ir(III) Compounds for Oleds - New Insights into Ancillary Ligand Effects on the Emitting Triplet State, *J. Phys. Chem. A* **2009**, *113*, 5927.
73. Chang, C.-F.; Cheng, Y.-M.; Chi, Y.; Chiu, Y.-C.; Lin, C.-C.; Lee, G.-H.; Chou, P.-T.; Chen, C.-C.; Chang, C.-H.; Wu, C.-C. Highly Efficient Blue-Emitting Iridium(III) Carbene Complexes and Phosphorescent Oleds, *Angew. Chem., Int. Ed.* **2008**, *47*, 4542.
74. Dedeian, K.; Shi, J.; Forsythe, E.; Morton, D. C.; Zavalij, P. Y. Blue Phosphorescence from Mixed Cyano-Isocyanide Cyclometalated Iridium(III) Complexes, *Inorg. Chem.* **2007**, *46*, 1603.
75. Dedeian, K.; Djurovich, P. I.; Garces, F. O.; Carlson, G.; Watts, R. J. A New Synthetic Route to the Preparation of a Series of Strong Photoreducing Agents: Fac-Tris-Ortho-Metalated Complexes of Iridium(III) with Substituted 2-Phenylpyridines, *Inorg. Chem.* **1991**, *30*, 1685.
76. Colombo, M. G.; Brunold, T. C.; Riedener, T.; Guedel, H. U.; Fortsch, M.; Buergi, H.-B. Facial Tris Cyclometalated Rhodium(3+) and Iridium(3+) Complexes: Their Synthesis, Structure, and Optical Spectroscopic Properties, *Inorg. Chem.* **1994**, *33*, 545.
77. Tamayo, A. B.; Alleyne, B. D.; Djurovich, P. I.; Lamansky, S.; Tsyba, I.; Ho, N. N.; Bau, R.; Thompson, M. E. Synthesis and Characterization of Facial and Meridional Tris-Cyclometalated Iridium(III) Complexes, *J. Am. Chem. Soc.* **2003**, *125*, 7377.

78. Ragni, R.; Plummer, E. A.; Brunner, K.; Hofstraat, J. W.; Babudri, F.; Farinola, G. M.; Naso, F.; De Cola, L. Blue Emitting Iridium Complexes: Synthesis, Photophysics and Phosphorescent Devices, *J. Mater. Chem.* **2006**, *16*, 1161.
79. Yang, C.-H.; Fang, K.-H.; Chen, C.-H.; Sun, I. W. High Efficiency Mer-Iridium Complexes for Organic Light-Emitting Diodes, *Chem. Comm.* **2004**, 2232.
80. Colombo, M. G.; Hauser, A.; Gudel, H. U. In *Top. Curr. Chem.*; Springer-Verlag: Berlin, 1994; Vol. 171, p 143.
81. Dedeian, K.; Shi, J.; Shepherd, N.; Forsythe, E.; Morton, D. C. Photophysical and Electrochemical Properties of Heteroleptic Tris-Cyclometalated Iridium(III) Complexes, *Inorg. Chem.* **2005**, *44*, 4445.
82. Endo, A.; Suzuki, K.; Yoshihara, T.; Tobita, S.; Yahiro, M.; Adachi, C. Measurement of Photoluminescence Efficiency of Ir(III) Phenylpyridine Derivatives in Solution and Solid-State Films, *Chem. Phys. Lett.* **2008**, *460*, 155.
83. Sajoto, T.; Djurovich, P. I.; Tamayo, A. B.; Oxgaard, J.; Goddard, W. A.; Thompson, M. E. Temperature Dependence of Blue Phosphorescent Cyclometalated Ir(III) Complexes, *J. Am. Chem. Soc.* **2009**, *131*, 9813.
84. Hofbeck, T.; Yersin, H. The Triplet State of Fac-Ir(Ppy)$_3$, *Inorg. Chem.* **2010**, *49*, 9290.
85. Hay, P. J. Theoretical Studies of the Ground and Excited Electronic States in Cyclometalated Phenylpyridine Ir(III) Complexes Using Density Functional Theory, *J. Phys. Chem. A* **2002**, *106*, 1634.
86. Smith, A. R. G.; Burn, P. L.; Powell, B. J. Spin-Orbit Coupling in Phosphorescent Iridium(III) Complexes, *ChemPhysChem* **2011**, *12*, 2429.
87. Forrest, S. R.; Bradley, D. D. C.; Thompson, M. E. Measuring the Efficiency of Organic Light-Emitting Devices, *Adv. Mater.* **2003**, *15*, 1043.
88. Adachi, C.; Kwong, R. C.; Djurovich, P.; Adamovich, V.; Baldo, M. A.; Thompson, M. E.; Forrest, S. R. Endothermic Energy Transfer: A Mechanism for Generating Very Efficient High-Energy Phosphorescent Emission in Organic Materials, *Appl. Phys. Lett.* **2001**, *79*, 2082.
89. Nam, E. J.; Kim, J. H.; Kim, B.-O.; Kim, S. M.; Park, N. G.; Kim, Y. S.; Kim, Y. K.; Ha, Y. A Synthesis and Luminescence Study of Ir(Ppz)$_3$ for Organic Light-Emitting Devices, *Bull. Chem. Soc. Jpn.* **2004**, *77*, 751.
90. Lee, S. J.; Park, K.-M.; Yang, K.; Kang, Y. Blue Phosphorescent Ir(III) Complex with High Color Purity: *Fac*-Tris(2′,6′-Difluoro-2,3′-Bipyridinato-N,C4′)Iridium(III), *Inorg. Chem.* **2009**, *48*, 1030.
91. Harding, R. E.; Lo, S.-C.; Burn, P. L.; Samuel, I. D. W. Non-Radiative Decay Mechanisms in Blue Phosphorescent Iridium(III) Complexes, *Organic Electronics* **2008**, *9*, 377.
92. Rausch, A. F.; Thompson, M. E.; Yersin, H. Matrix Effects on the Triplet State of the Oled Emitter Ir(4,6-Dfppy)$_2$(Pic) (Firpic): Investigations by High-Resolution Optical Spectroscopy, *Inorg. Chem.* **2009**, *48*, 1928.
93. Finkenzeller, W. J.; Thompson, M. E.; Yersin, H. Phosphorescence Dynamics and Spin-Lattice Relaxation of the Oled Emitter Ir(Btp)$_2$(Acac), *Chem. Phys. Lett.* **2007**, *444*, 273.
94. Finkenzeller, W. J.; Hofbeck, T.; Thompson, M. E.; Yersin, H. Triplet State Properties of the Oled Emitter Ir(Btp)$_2$(Acac): Characterization by Site-Selective Spectroscopy and Application of High Magnetic Fields, *Inorg. Chem.* **2007**, *46*, 5076.
95. Breu, J.; Stossel, P.; Schrader, S.; Starukhin, A.; Finkenzeller, W. J.; Yersin, H. Crystal Structure of *Fac*-Ir(Ppy)$_3$ and Emission Properties under Ambient Conditions and at High Pressure, *Chem. Mater.* **2005**, *17*, 1745.
96. Finkenzeller, W. J.; Yersin, H. Emission of Ir(Ppy)$_3$. Temperature Dependence, Decay Dynamics, and Magnetic Field Properties, *Chem. Phys. Lett.* **2003**, *377*, 299.
97. Hedley, G. J.; Ruseckas, A.; Samuel, I. D. W. Ultrafast Intersystem Crossing in a Red Phosphorescent Iridium Complex, *J. Phys. Chem. A* **2009**, *113*, 2.

98. Hedley, G. J.; Ruseckas, A.; Samuel, I. D. W. Ultrafast Luminescence in $Ir(Ppy)_3$, *Chem. Phys. Lett.* **2008**, *450*, 292.
99. Baranoff, E.; Fantacci, S.; De Angelis, F.; Zhang, X.; Scopelliti, R.; Grätzel, M.; Nazeeruddin, M. K. Cyclometalated Iridium(III) Complexes Based on Phenyl-Imidazole Ligand, *Inorg. Chem.* **2011**, *50*, 451.
100. Yang, L.; Okuda, F.; Kobayashi, K.; Nozaki, K.; Tanabe, Y.; Ishii, Y.; Haga, M.-a. Syntheses and Phosphorescent Properties of Blue Emissive Iridium Complexes with Tridentate Pyrazolyl Ligands, *Inorg. Chem.* **2008**, *47*, 7154.
101. Li, J.; Djurovich, P. I.; Alleyne, B. D.; Yousufuddin, M.; Ho, N. N.; Thomas, J. C.; Peters, J. C.; Bau, R.; Thompson, M. E. Synthetic Control of Excited-State Properties in Cyclometalated Ir(III) Complexes Using Ancillary Ligands, *Inorg. Chem.* **2005**, *44*, 1713.
102. Perdew, J. P.; Ruzsinszky, A.; Constantin, L. A.; Sun, J.; Csonka, G. b. I. Some Fundamental Issues in Ground-State Density Functional Theory: A Guide for the Perplexed, *J. Chem. Theory Comput.* **2009**, *5*, 902.
103. Neese, F. Prediction of Molecular Properties and Molecular Spectroscopy with Density Functional Theory: From Fundamental Theory to Exchange-Coupling, *Coord. Chem. Rev.* **2009**, *253*, 526.
104. Vlcek, J. A.; Zális, S. Modeling of Charge-Transfer Transitions and Excited States in D^6 Transition Metal Complexes by Dft Techniques, *Coord. Chem. Rev.* **2007**, *251*, 258.
105. Dyall, K. G.; Fægri, K. *Introduction to Relativistic Quantum Chemistry*; Oxford University Press: New York, 2007.
106. van Lenthe, E.; Baerends, E. J.; Snijders, J. G. Relativistic Regular Two-Component Hamiltonians, *J. Chem. Phys.* **1993**, *99*, 4597.
107. van Lenthe, E.; Baerends, E. J.; Snijders, J. G. Relativistic Total Energy Using Regular Approximations, *J. Chem. Phys.* **1994**, *101*, 9783.
108. Chang, C.; Pelissier, M.; Durand, P. Regular Two-Component Pauli-Like Effective Hamiltonians in Dirac Theory, *Phys. Scr.* **1986**, *34*, 394.
109. van Lenthe, E.; Snijders, J. G.; Baerends, E. J. The Zero-Order Regular Approximation for Relativistic Effects: The Effect of Spin--Orbit Coupling in Closed Shell Molecules, *J. Chem. Phys.* **1996**, *105*, 6505.
110. van Lenthe, E.; Ehlers, A.; Baerends, E.-J. Geometry Optimizations in the Zero Order Regular Approximation for Relativistic Effects, *J. Chem. Phys.* **1999**, *110*, 8943.
111. Wang, F.; Ziegler, T. A Simplified Relativistic Time-Dependent Density-Functional Theory Formalism for the Calculations of Excitation Energies Including Spin-Orbit Coupling Effect, *J. Chem. Phys.* **2005**, *123*, 154102.
112. Pyykko, P. Relativistic Effects in Structural Chemistry, *Chem. Rev.* **1988**, *88*, 563.
113. Jansson, E.; Minaev, B.; Schrader, S.; Agren, H. Time-Dependent Density Functional Calculations of Phosphorescence Parameters for *Fac*-Tris(2-Phenylpyridine) Iridium, *Chem. Phys.* **2007**, *333*, 157.
114. Berger, R. J. F.; Stammler, H. G.; Neumann, B.; Mitzel, N. W. Fac-$Ir(Ppy)_3$: Structures in the Gas-Phase and of a New Solid Modification, *Eur. J. Inorg. Chem.* **2010**, 1613.
115. Hay, P. J.; Wadt, W. R. Ab Initio Effective Core Potentials for Molecular Calculations. Potentials for K to Au Including the Outermost Core Orbitals, *J. Chem. Phys.* **1985**, *82*, 299.
116. Aziz, H.; Popovic, Z. D. Degradation Phenomena in Small-Molecule Organic Light-Emitting Devices, *Chem. Mater.* **2004**, *16*, 4522.
117. Sheats, J. R.; Antoniadis, H.; Hueschen, M.; Leonard, W.; Miller, J.; Ron, M.; Roitman, D.; Stocking, A. Organic Electroluminescent Devices, *Science* **1996**, *273*, 884.
118. Fujihira, M.; Do, L.-M.; Koike, A.; Han, E.-M. Growth of Dark Spots by Interdiffusion across Organic Layers in Organic Electroluminescent Devices, *Appl. Phys. Lett.* **1996**, *68*, 1787.
119. Liew, Y.-F.; Aziz, H.; Hu, N.-X.; Chan, H. S.-O.; Xu, G.; Popovic, Z. Investigation of the Sites of Dark Spots in Organic Light-Emitting Devices, *Appl. Phys. Lett.* **2000**, *77*, 2650.

120. Burrows, P. E.; Bulovic, V.; Forrest, S. R.; Sapochak, L. S.; McCarty, D. M.; Thompson, M. E. Reliability and Degradation of Organic Light Emitting Devices, *Appl. Phys. Lett.* **1994**, *65*, 2922.
121. Scott, J. C.; Kaufman, J. H.; Brock, P. J.; DiPietro, R.; Salem, J.; Goitia, J. A. Degradation and Failure of Meh-Ppv Light-Emitting Diodes, *J. Appl. Phys.* **1996**, *79*, 2745.
122. Lo, S. C.; Burn, P. L. Development of Dendrimers: Macromolecules for Use in Organic Light-Emitting Diodes and Solar Cells, *Chem. Rev.* **2007**, *107*, 1097.
123. Adamovich, V.; Brooks, J.; Tamayo, A.; Alexander, A. M.; Djurovich, P. I.; D'Andrade, B. W.; Adachi, C.; Forrest, S. R.; Thompson, M. E. High Efficiency Single Dopant White Electrophosphorescent Light Emitting Diodes, *New J. Chem.* **2002**, *26*, 1171.
124. Liu, Z. W.; Guan, M.; Bian, Z. Q.; Nie, D. B.; Gong, Z. L.; Li, Z. B.; Huang, C. H. Red Phosphorescent Iridium Complex Containing Carbazole-Functionalized B-Diketonate for Highly Efficient Nondoped Organic Light-Emitting Diodes, *Adv. Funct. Mater.* **2006**, *16*, 1441.
125. Bera, R. N.; Cumpstey, N.; Burn, P. L.; Samuel, I. D. W. Highly Branched Phosphorescent Dendrimers for Efficient Solution-Processed Organic Light-Emitting Diodes, *Adv. Funct. Mater.* **2007**, *17*, 1149.
126. Lo, S.-C.; Anthopoulos, T. D.; Namdas, E. B.; Burn, P. L.; Samuel, I. D. W. Encapsulated Cores: Host-Free Organic Light-Emitting Diodes Based on Solution-Processible Electrophosphorescent Dendrimers, *Adv. Mater.* **2005**, *17*, 1945.
127. Shirota, Y.; Kuwabara, Y.; Okuda, D.; Okuda, R.; Ogawa, H.; Inada, H.; Wakimoto, T.; Nakada, H.; Yonemoto, Y.; Kawami, S.; Imai, K. Starburst Molecules Based on [Pi]-Electron Systems as Materials for Organic Electroluminescent Devices, *J. Lumin.* **1997**, *72-74*, 985.
128. Adachi, C.; Kwong, R.; Forrest, S. R. Efficient Electrophosphorescence Using a Doped Ambipolar Conductive Molecular Organic Thin Film, *Organic Electronics* **2001**, *2*, 37.
129. Matsusue, N.; Ikame, S.; Suzuki, Y.; Naito, H. Charge Carrier Transport in an Emissive Layer of Green Electrophosphorescent Devices, *Appl. Phys. Lett.* **2004**, *85*, 4046.
130. Koene, B. E.; Loy, D. E.; Thompson, M. E. Asymmetric Triaryldiamines as Thermally Stable Hole Transporting Layers for Organic Light-Emitting Devices, *Chem. Mater.* **1998**, *10*, 2235.
131. Tsai, M.-H.; Hong, Y.-H.; Chang, C.-H.; Su, H.-C.; Wu, C.-C.; Matoliukstyte, A.; Simokaitiene, J.; Grigalevicius, S.; Grazulevicius, J. V.; Hsu, C.-P. 3-(9-Carbazolyl)Carbazoles and 3,6-Di(9-Carbazolyl)Carbazoles as Effective Host Materials for Efficient Blue Organic Electrophosphorescence, *Adv. Mater.* **2007**, *19*, 862.
132. Adachi, C.; Baldo, M. A.; Forrest, S. R.; Thompson, M. E. High-Efficiency Organic Electrophosphorescent Devices with Tris(2-Phenylpyridine)Iridium Doped into Electron-Transporting Materials, *Appl. Phys. Lett.* **2000**, *77*, 904.
133. Strohriegl, P.; Grazulevicius, J. V. Charge-Transporting Molecular Glasses, *Adv. Mater.* **2002**, *14*, 1439.
134. Tsutsui, T.; Yang, M.-J.; Yahiro, M.; Nakamura, K.; Watanabe, T.; Tsuji, T.; Fukuda, Y.; Wakimoto, T.; Miyaguchi, S. High Quantum Efficiency in Organic Light-Emitting Devices with Iridium-Complex as a Triplet Emissive Center, *Jpn. J. Appl. Phys.* **1999**, *38*, L1502.
135. Garditz, C.; Winnacker, A.; Schindler, F.; Paetzold, R. Impact of Joule Heating on the Brightness Homogeneity of Organic Light Emitting Devices, *Appl. Phys. Lett.* **2007**, *90*, 103506.
136. Gong, J.-R.; Wan, L.-J.; Lei, S.-B.; Bai, C.-L.; Zhang, X.-H.; Lee, S.-T. Direct Evidence of Molecular Aggregation and Degradation Mechanism of Organic Light-Emitting Diodes under Joule Heating: An Stm and Photoluminescence Study, *J. Phys. Chem. B* **2005**, *109*, 1675.
137. Aziz, H.; Popovic, Z. D.; Hu, N.-X. Organic Light Emitting Devices with Enhanced Operational Stability at Elevated Temperatures, *Appl. Phys. Lett.* **2002**, *81*, 370.

138. Ishii, M.; Taga, Y. Influence of Temperature and Drive Current on Degradation Mechanisms in Organic Light-Emitting Diodes, *Appl. Phys. Lett.* **2002**, *80*, 3430.
139. Vamvounis, G.; Aziz, H.; Hu, N.-X.; Popovic, Z. D. Temperature Dependence of Operational Stability of Organic Light Emitting Diodes Based on Mixed Emitter Layers, *Synthetic Metals* **2004**, *143*, 69.
140. Sivasubramaniam, V.; Brodkorb, F.; Hanning, S.; Buttler, O.; Loebl, H. P.; van Elsbergen, V.; Boerner, H.; Scherf, U.; Kreyenschmidt, M. Degradation of Htl Layers During Device Operation in Pholeds, *Solid State Sci.* **2009**, *11*, 1933.
141. Kondakov, D. Y.; Lenhart, W. C.; Nichols, W. F. Operational Degradation of Organic Light-Emitting Diodes: Mechanism and Identification of Chemical Products, *J. Appl. Phys.* **2007**, *101*, 024512.
142. Zhou, X.; He, J.; Liao, L. S.; Lu, M.; Ding, X. M.; Hou, X. Y.; Zhang, X. M.; He, X. Q.; Lee, S. T. Real-Time Observation of Temperature Rise and Thermal Breakdown Processes in Organic Leds Using an Ir Imaging and Analysis System, *Adv. Mater.* **2000**, *12*, 265.
143. Chung, S.; Lee, J.-H.; Jeong, J.; Kim, J.-J.; Hong, Y. Substrate Thermal Conductivity Effect on Heat Dissipation and Lifetime Improvement of Organic Light-Emitting Diodes, *Appl. Phys. Lett.* **2009**, *94*, 253302.
144. Marty, W.; Sigrist, T.; Wyler, D. Temperature Variations in Automobiles in Various Weather Conditions. An Experimental Contribution to the Determination of Time of Death, *Am. J. Forensic. Med. Pathol.* **2001**, *22*, 215.
145. Grundstein, A.; Meentemeyer, V.; Dowd, J. Maximum Vehicle Cabin Temperatures under Different Meteorological Conditions, *Int. J. Biometeorol.* **2009**, *53*, 255.
146. Adachi, C.; Nagai, K.; Tamoto, N. Molecular Design of Hole Transport Materials for Obtaining High Durability in Organic Electroluminescent Diodes, *Appl. Phys. Lett.* **1995**, *66*, 2679.
147. Gommans, H.; Verreet, B.; Rand, B. P.; Muller, R.; Poortmans, J.; Heremans, P.; Genoe, J. On the Role of Bathocuproine in Organic Photovoltaic Cells, *Adv. Funct. Mater.* **2008**, *18*, 3686.
148. Vogel, M.; Doka, S.; Breyer, C.; Lux-Steiner, M. C.; Fostiropoulos, K. On the Function of a Bathocuproine Buffer Layer in Organic Photovoltaic Cells, *Appl. Phys. Lett.* **2006**, *89*, 163501.
149. Zhang, M.; Wang, H.; Tang, C. W. Effect of the Highest Occupied Molecular Orbital Energy Level Offset on Organic Heterojunction Photovoltaic Cells, *Appl. Phys. Lett.* **2010**, *97*, 143503.
150. Sun, Y.; Giebink, N. C.; Kanno, H.; Ma, B.; Thompson, M. E.; Forrest, S. R. Management of Singlet and Triplet Excitons for Efficient White Organic Light-Emitting Devices, *Nature* **2006**, *440*, 908.
151. D'Andrade, B. W.; Holmes, R. J.; Forrest, S. R. Efficient Organic Electrophosphorescent White-Light-Emitting Device with a Triple Doped Emissive Layer, *Adv. Mater.* **2004**, *16*, 624.
152. Thomschke, M.; Hofmann, S.; Olthof, S.; Anderson, M.; Kleemann, H.; Schober, M.; Lussem, B.; Leo, K. Improvement of Voltage and Charge Balance in Inverted Top-Emitting Organic Electroluminescent Diodes Comprising Doped Transport Layers by Thermal Annealing, *Appl. Phys. Lett.* **2011**, *98*, 083304.
153. Campoy-Quiles, M.; Ferenczi, T.; Agostinelli, T.; Etchegoin, P. G.; Kim, Y.; Anthopoulos, T. D.; Stavrinou, P. N.; Bradley, D. D. C.; Nelson, J. Morphology Evolution Via Self-Organization and Lateral and Vertical Diffusion in Polymer:Fullerene Solar Cell Blends, *Nat. Mater.* **2008**, *7*, 158.
154. van Bavel, S.; Sourty, E.; de With, G.; Frolic, K.; Loos, J. Relation between Photoactive Layer Thickness, 3d Morphology, and Device Performance in P3ht/Pcbm Bulk-Heterojunction Solar Cells, *Macromolecules* **2009**, *42*, 7396.

155. Noh, Y.-Y.; Lee, C.-L.; Kim, J.-J.; Yase, K. Energy Transfer and Device Performance in Phosphorescent Dye Doped Polymer Light Emitting Diodes, *J. Chem. Phys.* **2003**, *118*, 2853.
156. You, Y.; Kim, S. H.; Jung, H. K.; Park, S. Y. Blue Electrophosphorescence from Iridium Complex Covalently Bonded to the Poly(9-Dodecyl-3-Vinylcarbazole): Suppressed Phase Segregation and Enhanced Energy Transfer, *Macromolecules* **2006**, *39*, 349.
157. Kang, J.; Shin, N.; Jang, D. Y.; Prabhu, V. M.; Yoon, D. Y. Structure and Properties of Small Molecule−Polymer Blend Semiconductors for Organic Thin Film Transistors, *J. Am. Chem. Soc.* **2008**, *130*, 12273.
158. Mitchell, W. J.; Burn, P. L.; Thomas, R. K.; Fragneto, G.; Markham, J. P. J.; Samuel, I. D. W. Relating the Physical Structure and Optical Properties of Conjugated Polymers Using Neutron Reflectivity in Combination with Photoluminescence Spectroscopy, *J. Appl. Phys.* **2004**, *95*, 2391.
159. Mitchell, W. J.; Burn, P. L.; Thomas, R. K.; Fragneto, G. Probing the Polymer-Electrode Interface Using Neutron Reflection, *Appl. Phys. Lett.* **2003**, *82*, 2724.
160. Han, E.-M.; Do, L.-M.; Yamamoto, N.; Fujihira, M. Study of Interfacial Degradation and Morphological Change of the Vapor-Deposited Bilayer of Alq_3/Tpd for Organic Electroluminescent Devices by Afm and Pl Technique, *Mol. Cryst. Liq. Cryst.* **1995**, *267*, 411.
161. Han, E.-M.; Do, L.-M.; Yamamoto, N.; Fujihira, M. Study of Interfacial Degradation of the Vapor-Deposited Bilayer of Alq_3/Tpd for Organic Electroluminescent (El) Devices by Photoluminescence, *Chem. Lett.* **1995**, *24*, 57.
162. Fenter, P.; Schreiber, F.; Bulovic, V.; Forrest, S. R. Thermally Induced Failure Mechanisms of Organic Light Emitting Device Structures Probed by X-Ray Specular Reflectivity, *Chem. Phys. Lett.* **1997**, *277*, 521.
163. Wu, C.-C.; Chen, C.-W.; Cho, T.-Y. Three-Color Reconfigurable Organic Light-Emitting Devices, *Appl. Phys. Lett.* **2003**, *83*, 611.
164. Chen, C.-W.; Cho, T.-Y.; Wu, C.-C.; Yu, H.-L.; Luh, T.-Y. Fuzzy-Junction Organic Light-Emitting Devices, *Appl. Phys. Lett.* **2002**, *81*, 1570.
165. Wu, C.-C.; Chen, C.-W.; Lin, Y.-T.; Yu, H.-L.; Hsu, J.-H.; Luh, T.-Y. Programmable Organic Light-Emitting Devices, *Appl. Phys. Lett.* **2001**, *79*, 3023.
166. Naka, S.; Okada, H.; Onnagawa, H.; Tsutsui, T. High Electron Mobility in Bathophenanthroline, *Appl. Phys. Lett.* **2000**, *76*, 197.
167. Lin, W.-C.; Wang, W.-B.; Lin, Y.-C.; Yu, B.-Y.; Chen, Y.-Y.; Hsu, M.-F.; Jou, J.-H.; Shyue, J.-J. Migration of Small Molecules During the Degradation of Organic Light-Emitting Diodes, *Organic Electronics* **2009**, *10*, 581.
168. Liu, C.-P.; Wang, W.-B.; Lin, C.-W.; Lin, W.-C.; Liu, C.-Y.; Kuo, C.-H.; Lee, S.-H.; Kao, W.-L.; Yen, G.-J.; You, Y.-W.; Chang, H.-Y.; Jou, J.-H.; Shyue, J.-J. Molecular Migration Behaviors in Organic Light-Emitting Diodes with Different Host Structures, *Organic Electronics* **2011**, *12*, 376.
169. Pyykkö, P. Theoretical Chemistry of Gold, *Angew. Chem., Int. Ed.* **2004**, *43*, 4412.
170. Christensen, N. E.; Satpathy, S.; Pawlowska, Z. First-Principles Theory of Tetrahedral Bonding and Crystal Structure of Lead, *Phys. Rev. B* **1986**, *34*, 5977.
171. van Veenendaal, M.; Chang, J.; Fedro, A. J. Model of Ultrafast Intersystem Crossing in Photoexcited Transition-Metal Organic Compounds, *Phys. Rev. Lett.* **2010**, *104*, 067401.
172. *Highly Efficient Oleds with Phosphorescent Materials*; Yersin, H., Ed.; Wiley-VCH Verlag GmbH & Co. KGaA: Weinheim, Germany, 2008.
173. Jacko, A. C.; Powell, B. J.; McKenzie, R. H. Sensitivity of the Photophysical Properties of Organometallic Complexes to Small Chemical Changes, *J. Chem. Phys.* **2010**, *133*, 124314.
174. Yersin, H.; Donges, D. In *Top. Curr. Chem.*; Springer-Verlag: Berlin, 2001; Vol. 214, p 81.
175. Fonseca Guerra, C.; Snijders, J. G.; te Velde, G.; Baerends, E. J. Towards an Order-N Dft Method, *Theor. Chim. Acta* **1998**, *99*, 391.

176. Velde, G. t.; Bickelhaupt, F. M.; Baerends, E. J.; Guerra, C. F.; Gisbergen, S. J. A. v.; Snijders, J. G.; Ziegler, T. Chemistry with Adf, *J. Comput. Chem.* **2001**, *22*, 931.
177. ADF2009.01, SCM, Theoretical Chemistry, Vrije Universiteit, Amsterdam, The Netherlands, http://www.scm.com/.
178. Lenthe, E. V.; Baerends, E. J. Optimized Slater-Type Basis Sets for the Elements 1-118, *J. Comput. Chem.* **2003**, *24*, 1142.
179. Chong, D. P. Augmenting Basis Set for Time-Dependent Density Functional Theory Calculation of Excitation Energies: Slater-Type Orbitals for Hydrogen to Krypton, *Mol. Phys.* **2005**, *103*, 749.
180. Becke, A. D. Density-Functional Thermochemistry. III. The Role of Exact Exchange, *J. Chem. Phys.* **1993**, *98*, 5648.
181. Stephens, P. J.; Devlin, F. J.; Chabalowski, C. F.; Frisch, M. J. Ab Initio Calculation of Vibrational Absorption and Circular Dichroism Spectra Using Density Functional Force Fields, *J. Phys. Chem.* **1994**, *98*, 11623.
182. Gordon, M. S.; Schmidt, M. W. In *Theory and Applications of Computational Chemistry: The First Forty Years*; Dykstra, C. E., G.Frenking, K.S.Kim, G.E.Scuseria, Eds.; Elsevier: Amsterdam, 2005.
183. Schmidt, M. W.; Baldridge, K. K.; Boatz, J. A.; Elbert, S. T.; Gordon, M. S.; Jensen, J. H.; Koseki, S.; Matsunaga, N.; Nguyen, K. A.; Su, S.; Windus, T. L.; Dupuis, M.; John A. Montgomery, J. General Atomic and Molecular Electronic Structure System, *J. Comput. Chem.* **1993**, *14*, 1347.
184. Ditchfield, R.; Hehre, W. J.; Pople, J. A. Self-Consistent Molecular-Orbital Methods. Ix. An Extended Gaussian-Type Basis for Molecular-Orbital Studies of Organic Molecules, *J. Chem. Phys.* **1971**, *54*, 724.
185. Hehre, W. J.; Ditchfield, R.; Pople, J. A. Self-Consistent Molecular Orbital Methods. XII. Further Extensions of Gaussian-Type Basis Sets for Use in Molecular Orbital Studies of Organic Molecules, *J. Chem. Phys.* **1972**, *56*, 2257.
186. Mulliken, R. S. Electronic Population Analysis on Lcao[Single Bond]Mo Molecular Wave Functions. I, *J. Chem. Phys.* **1955**, *23*, 1833.
187. Mason, W. R. *A Practical Guide to Magnetic Circular Dichroism Spectroscopy*; John Wiley & Sons, Inc.: New Jersey, 2007.
188. Desclaux, J. P.; Yong-Ki, K. Relativistic Effects in Outer Shells of Heavy Atoms, *J. Phys. B: At. Mol. Phys.* **1975**, *8*, 1177.
189. Rose, S. J.; Grant, I. P.; Pyper, N. C. The Direct and Indirect Effects in the Relativistic Modification of Atomic Valence Orbitals, *J. Phys. B: At. Mol. Phys.* **1978**, *11*, 1171.
190. Kasha, M. Characterization of Electronic Transitions in Complex Molecules, *Discussions of the Faraday Society* **1950**, *9*, 14.
191. Haneder, S.; Como, E. D.; Feldmann, J.; Lupton, J. M.; Lennartz, C.; Erk, P.; Fuchs, E.; Molt, O.; Münster, I.; Schildknecht, C.; Wagenblast, G. Controlling the Radiative Rate of Deep-Blue Electrophosphorescent Organometallic Complexes by Singlet-Triplet Gap Engineering, *Adv. Mater.* **2008**, *20*, 3325.
192. Koseki, S.; Gordon, M. S.; Schmidt, M. W.; Matsunaga, N. Main Group Effective Nuclear Charges for Spin-Orbit Calculations, *J. Phys. Chem.* **1995**, *99*, 12764.
193. Koseki, S.; Schmidt, M. W.; Gordon, M. S. Effective Nuclear Charges for the First- through Third-Row Transition Metal Elements in Spin-Orbit Calculations, *J. Chem. Phys. A* **1998**, *102*, 10430.
194. Minaev, B.; Agren, H.; De Angelis, F. Theoretical Design of Phosphorescence Parameters for Organic Electro-Luminescence Devices Based on Iridium Complexes, *Chem. Phys.* **2009**, *358*, 245.
195. De Angelis, F.; Belpassi, L.; Fantacci, S. Spectroscopic Properties of Cyclometallated Iridium Complexes by Tddft, *J. Mol. Struct.: THEOCHEM* **2009**, *914*, 74.

196. Smith, A. R. G.; Riley, M. J.; Lo, S.-C.; Burn, P. L.; Gentle, I. R.; Powell, B. J. Relativistic Effects in a Phosphorescent Ir(III) Complex, *Phys. Rev. B* **2011**, *83*, 041105(R).
197. Yang, W. T.; Cohen, A. J.; Mori-Sanchez, P. Insights into Current Limitations of Density Functional Theory, *Science* **2008**, *321*, 792.
198. Dreuw, A.; Weisman, J. L.; Head-Gordon, M. Long-Range Charge-Transfer Excited States in Time-Dependent Density Functional Theory Require Non-Local Exchange, *J. Chem. Phys.* **2003**, *119*, 2943.
199. Dreizler, R. *Relativistic Density Functional Theory*; Springer: Berlin, 2003.
200. Greiner, W. *Relativistic Quantum Mechanics: Wave Equations*; Springer: Berlin, 1994.
201. Strange, P. *Relativistic Quantum Mechanics*; Cambridge University Press: Cambridge, 1998.
202. MacDonald, A. H.; Vosko, S. H. A Relativistic Density Functional Formalism, *J. Phys. C: Solid State Phys.* **1979**, *12*, 2977.
203. Rajagopal, A. K. Inhomogeneous Relativistic Electron Gas, *J. Phys. C: Solid State Phys.* **1978**, *11*, L943.
204. Rajagopal, A. K.; Callaway, J. Inhomogeneous Electron Gas, *Phys. Rev. B* **1973**, *7*, 1912.
205. Jacko, A. C.; Powell, B. J. Electronic Correlations in Organometallic Complexes, *Chem. Phys. Lett.* **2011**, *508*, 22.
206. Knox, R. S. Dipole and Oscillator Strengths of Chromophores in Solution, *Photochem. Photobiol.* **2003**, *77*, 492.
207. Riesz, J. J.; Gilmore, J. B.; McKenzie, R. H.; Powell, B. J.; Pederson, M. R.; Meredith, P. Transition Dipole Strength of Eumelanin, *Phys. Rev. E* **2007**, *76*, 021915.
208. Tsuboi, T.; Tanigawa, M. Optical Characteristics of Ptoep and $Ir(Ppy)_3$ Triplet-Exciton Materials for Organic Electroluminescence Devices, *Thin Solid Films* **2003**, *438-439*, 301.
209. Schwenn, P. E.; Burn, P. L.; Powell, B. J. Calculation of Solid State Molecular Ionisation Energies and Electron Affinities for Organic Semiconductors, *Org. Elec.* **2011**, *12*, 394.
210. Foresman, J. B.; Head-Gordon, M.; Pople, J. A.; Frisch, M. J. Toward a Systematic Molecular Orbital Theory for Excited States, *J. Phys. Chem. A* **1992**, *96*, 135.
211. Cecchet, F.; Gioacchini, A. M.; Marcaccio, M.; Paolucci, F.; Roffia, S.; Alebbi, M.; Bignozzi, C. A. Solvent Effects on the Oxidative Electrochemical Behavior of Cis-Bis(Isothiocyanato)Ruthenium(II)-Bis-2,2‘-Bipyridine-4,4‘-Dicarboxylic Acid, *J. Phys. Chem. B* **2002**, *106*, 3926.
212. Péchy, P.; Renouard, T.; Zakeeruddin, S. M.; Humphry-Baker, R.; Comte, P.; Liska, P.; Cevey, L.; Costa, E.; Shklover, V.; Spiccia, L.; Deacon, G. B.; Bignozzi, C. A.; Grätzel, M. Engineering of Efficient Panchromatic Sensitizers for Nanocrystalline Tio_2-Based Solar Cells, *J. Am. Chem. Soc.* **2001**, *123*, 1613.
213. Pye, C. C.; Ziegler, T. An Implementation of the Conductor-Like Screening Model of Solvation within the Amsterdam Density Functional Package, *Theor. Chem. Acc.* **1999**, *101*, 396.
214. *Dalton, a Molecular Electronic Structure Program, Release 2.0* http://daltonprogram.org/, 2005.
215. Lamansky, S.; Djurovich, P.; Murphy, D.; Abdel-Razzaq, F.; Lee, H.-E.; Adachi, C.; Burrows, P. E.; Forrest, S. R.; Thompson, M. E. Highly Phosphorescent Bis-Cyclometalated Iridium Complexes: Synthesis, Photophysical Characterization, and Use in Organic Light Emitting Diodes, *J. Am. Chem. Soc.* **2001**, *123*, 4304.
216. Orgel, L. E. Double Bonding in Chelated Metal Complexes, *J. Chem. Soc.* **1961**, 3683.
217. Harrigan, R. W.; Crosby, G. A. Symmetry Assignments of the Lowest Ct Excited States of Ruthenium (II) Complexes Via a Proposed Electronic Coupling Model, *J. Chem. Phys.* **1973**, *59*, 3468.
218. Krausz, E.; Riesen, H. Developments in Laser Selective Spectroscopy and Photophysics of D6 Metal-(Di-Imine) Complexes, *Coord. Chem. Rev.* **1997**, *159*, 9.

219. Riesen, H.; Wallace, L.; Krausz, E. Intramolecular Mini-Excitons in the Series [Os(Bpy)3-X (Bpy-D 8) X]2+ (X = 0-3 in [Zn(Bpy)3](Clo4)2 and [Ru(Bpy)3](Clo4)2 (Bpy = 2,2′-Bipyridine), *Mol. Phys.* **1996**, *87*, 1299.
220. Tong, G. S. M.; Che, C. M. Emissive or Nonemissive? A Theoretical Analysis of the Phosphorescence Efficiencies of Cyclometalated Platinum(II) Complexes, *Chem.-Eur. J.* **2009**, *15*, 7225.
221. Smith, A. R. G.; Riley, M. J.; Burn, P. L.; Gentle, I. R.; Lo, S.-C.; Powell, B. J. Effects of Fluorination on Iridium(III) Complex Phosphorescence: Magnetic Circular Dichroism and Relativistic Time-Dependent Density Functional Theory, *Inorg. Chem.* **2012**, *51*, 2821.
222. Lee, C.; Yang, W.; Parr, R. G. Development of the Colle-Salvetti Correlation-Energy Formula into a Functional of the Electron Density, *Phys. Rev. B* **1988**, *37*, 785.
223. Hirshfeld, F. L. Bonded-Atom Fragments for Describing Molecular Charge Densities, *Theor. Chim. Acta* **1977**, *44*, 129.
224. Bickelhaupt, F. M.; van Eikema Hommes, N. J. R.; Fonseca Guerra, C.; Baerends, E. J. The Carbon−Lithium Electron Pair Bond in $(Ch_3li)_N$ (N = 1, 2, 4), *Organometallics* **1996**, *15*, 2923.
225. Smith, A. R. G.; Riley, M. J.; Burn, P. L.; Gentle, I. R.; Powell, B. J.; Krausz, E.; Hall, J., *(to be published).*
226. Plischke, M.; Bergersen, B. *Equilibrium Statistical Physics*; World Scientific: Singapore, 2006.
227. Grimsdale, A. C.; Leok Chan, K.; Martin, R. E.; Jokisz, P. G.; Holmes, A. B. Synthesis of Light-Emitting Conjugated Polymers for Applications in Electroluminescent Devices, *Chem. Rev.* **2009**, *109*, 897.
228. Burn, P. L.; Lo, S. C.; Samuel, I. D. W. The Development of Light-Emitting Dendrimers for Displays, *Adv. Mater.* **2007**, *19*, 1675.
229. Ikai, M.; Tokito, S.; Sakamoto, Y.; Suzuki, T.; Taga, Y. Highly Efficient Phosphorescence from Organic Light-Emitting Devices with an Exciton-Block Layer, *Appl. Phys. Lett.* **2001**, *79*, 156.
230. Giebink, N. C.; D'Andrade, B. W.; Weaver, M. S.; Brown, J. J.; Forrest, S. R. Direct Evidence for Degradation of Polaron Excited States in Organic Light Emitting Diodes, *J. Appl. Phys.* **2009**, *105*, 124514.
231. Chang, J.; Yu, Y.-J.; Na, J. H.; An, J.; Im, C.; Choi, D.-H.; Jin, J.-I.; Lee, S. H.; Kim, Y. K. Photodegradation-Induced Photoluminescence Behaviors of Π-Conjugated Polymers Upon the Doping of Organometallic Triplet Emitters, *J. Polym. Sci., Part B: Polym. Phys.* **2008**, *46*, 2395.
232. Amassian, A.; Pozdin, V. A.; Li, R.; Smilgies, D.-M.; Malliaras, G. G. Solvent Vapor Annealing of an Insoluble Molecular Semiconductor, *J. Mater. Chem.* **2010**, *20*, 2623.
233. Webster, G. R.; Mitchell, W. J.; Burn, P. L.; Thomas, R. K.; Fragneto, G.; Markham, J. P. J.; Samuel, I. D. W. Neutron Reflection Study on Soluble and Insoluble Poly[2-(2'-Ethylhexyloxy)-5-Methoxy-1,4-Phenylenevinylene) Films, *J. Appl. Phys.* **2002**, *91*, 9066.
234. Jukes, P. C.; Martin, S. J.; Higgins, A. M.; Geoghegan, M.; Jones, R. A. L.; Langridge, S.; Wehrum, A.; Kirchmeyer, S. Controlling the Surface Composition of Poly(3,4-Ethylene Dioxythiophene)–Poly(Styrene Sulfonate) Blends by Heat Treatment, *Adv. Mater.* **2004**, *16*, 807.
235. Parnell, A. J.; Dunbar, A. D. F.; Pearson, A. J.; Staniec, P. A.; Dennison, A. J. C.; Hamamatsu, H.; Skoda, M. W. A.; Lidzey, D. G.; Jones, R. A. L. Depletion of Pcbm at the Cathode Interface in P3ht/Pcbm Thin Films as Quantified Via Neutron Reflectivity Measurements, *Adv. Mater.* **2010**, *22*, 2444.
236. Lee, K. H.; Schwenn, P. E.; Smith, A. R. G.; Cavaye, H.; Shaw, P. E.; James, M.; Krueger, K. B.; Gentle, I. R.; Meredith, P.; Burn, P. L. Morphology of All-Solution-Processed "Bilayer" Organic Solar Cells, *Adv. Mater.* **2011**, *23*, 766.

237. Vickers, S. V.; Barcena, H.; Knights, K. A.; Thomas, R. K.; Ribierre, J. C.; Gambino, S.; Samuel, I. D. W.; Burn, P. L.; Fragneto, G. Light-Emitting Dendrimer Film Morphology: A Neutron Reflectivity Study, *Appl. Phys. Lett.* **2010**, *96*, 263302.
238. Penfold, J.; Thomas, R. K. The Application of the Specular Reflection of Neutrons to the Study of Surfaces and Interfaces, *J. Phys.: Condens. Matter* **1990**, *2*, 1369.
239. Thomas, R. K.; Penfold, J. Neutron and X-Ray Reflectometry of Interfacial Systems in Colloid and Polymer Chemistry, *Curr. Opin. Colloid Interface Sci.* **1996**, *1*, 23.
240. Zhou, X.-L.; Chen, S.-H. Theoretical Foundation of X-Ray and Neutron Reflectometry, *Phys. Rep.* **1995**, *257*, 223.
241. Dianoux, A. J.; Lander, G. H.; Institut Laue-Langevin. *Neutron Data Booklet*; 2nd ed.; Old City: Philadelphia, PA, 2003.
242. Swallen, S. F.; Kearns, K. L.; Mapes, M. K.; Kim, Y. S.; McMahon, R. J.; Ediger, M. D.; Wu, T.; Yu, L.; Satija, S. Organic Glasses with Exceptional Thermodynamic and Kinetic Stability, *Science* **2007**, *315*, 353.
243. Nelson, A. Co-Refinement of Multiple-Contrast Neutron/X-Ray Reflectivity Data Using Motofit, *J. Appl. Crystallogr.* **2006**, *39*, 273.
244. Tian, N.; Lenkeit, D.; Pelz, S.; Fischer, L. H.; Escudero, D.; Schiewek, R.; Klink, D.; Schmitz, O. J.; González, L.; Schäferling, M.; Holder, E. Structure–Property Relationship of Red- and Green-Emitting Iridium(III) Complexes with Respect to Their Temperature and Oxygen Sensitivity, *Eur. J. Inorg. Chem.* **2010**, *2010*, 4875.
245. Atzrodt, J.; Derdau, V.; Fey, T.; Zimmermann, J. The Renaissance of H/D Exchange, *Angew. Chem., Int. Ed.* **2007**, *46*, 7744.
246. Ito, N.; Esaki, H.; Maesawa, T.; Imamiya, E.; Maegawa, T.; Sajiki, H. Efficient and Selective Pt/C-Catalyzed H-D Exchange Reaction of Aromatic Rings, *Bull. Chem. Soc. Jpn.* **2008**, *81*, 278.
247. Yamamoto, M.; Oshima, K.; Matsubara, S. Platinum Catalyzed H-D Exchange Reaction of Various Aromatic Compounds under Hydrothermal Condition, *Heterocycles* **2006**, *67*, 353.
248. Low, P. J.; Paterson, M. A. J.; Yufit, D. S.; Howard, J. A. K.; Cherryman, J. C.; Tackley, D. R.; Brook, R.; Brown, B. Towards an Understanding of Structure-Property Relationships in Hole-Transport Materials: The Influence of Molecular Conformation on Oxidation Potential in Poly(Aryl)Amines, *J. Mater. Chem.* **2005**, *15*, 2304.
249. Koyuncu, S.; Gultekin, B.; Zafer, C.; Bilgili, H.; Can, M.; Demic, S.; Kaya, I.; Icli, S. Electrochemical and Optical Properties of Biphenyl Bridged-Dicarbazole Oligomer Films: Electropolymerization and Electrochromism, *Electrochim. Acta* **2009**, *54*, 5694.
250. Jeon, J. Y.; Park, T. J.; Jeon, W. S.; Park, J. J.; Jang, J.; Kwon, J. H.; Lee, J. Y. Bipolar Host Materials for Green Triplet Emitter in Organic Light-Emitting Diodes, *Chem. Lett.* **2007**, *36*, 1156.
251. James, M.; Nelson, A.; Brule, A.; Schulz, J. C. Platypus: A Time-of-Flight Neutron Reflectometer at Australia's New Research Reactor, *J. Neutron Res.* **2006**, *14*, 91.
252. James, M.; Nelson, A.; Holt, S. A.; Saerbeck, T.; Hamilton, W. A.; Klose, F. The Multipurpose Time-of-Flight Neutron Reflectometer "Platypus" at Australia's Opal Reactor, *Nucl. Instrum. Methods Phys. Res., Sect. A* **2011**, *632*, 112.
253. Nelson, A. Motofit – Integrating Neutron Reflectometry Acquisition, Reduction and Analysis into One, Easy to Use, Package, *J. Phys.: Conf. Ser.* **2010**, *251*, 012094.
254. Kwon, J. H.; Park, T. J.; Jeon, W. S.; Park, J. J. Bipolar Host Materials for Red and Green Phosphorescent Oled, *Proc. SPIE* **2007**, *6828*, 682802.
255. D'Andrade, B. W.; Forrest, S. R.; Chwang, A. B. Operational Stability of Electrophosphorescent Devices Containing P and N Doped Transport Layers, *Appl. Phys. Lett.* **2003**, *83*, 3858.
256. Shen, Z.; Burrows, P. E.; Bulović, V.; Forrest, S. R.; Thompson, M. E. Three-Color, Tunable, Organic Light-Emitting Devices, *Science* **1997**, *276*, 2009.

257. Liao, L. S.; Klubek, K. P.; Tang, C. W. High-Efficiency Tandem Organic Light-Emitting Diodes, *Appl. Phys. Lett.* **2004**, *84*, 167.
258. Lee, Y. J.; Park, S.-S.; Kim, J.; Kim, H. Interface Morphologies and Interlayer Diffusions in Organic Light Emitting Device by X-Ray Scattering, *Appl. Phys. Lett.* **2009**, *94*, 223305.
259. Van Slyke, S. A.; Chen, C. H.; Tang, C. W. Organic Electroluminescent Devices with Improved Stability, *Appl. Phys. Lett.* **1996**, *69*, 2160.
260. Kwong, R. C.; Nugent, M. R.; Michalski, L.; Ngo, T.; Rajan, K.; Tung, Y.-J.; Weaver, M. S.; Zhou, T. X.; Hack, M.; Thompson, M. E.; Forrest, S. R.; Brown, J. J. High Operational Stability of Electrophosphorescent Devices, *Appl. Phys. Lett.* **2002**, *81*, 162.
261. Lee, Y.-J.; Lee, H.; Byun, Y.; Song, S.; Kim, J.-E.; Eom, D.; Cha, W.; Park, S.-S.; Kim, J.; Kim, H. Study of Thermal Degradation of Organic Light Emitting Device Structures by X-Ray Scattering, *Thin Solid Films* **2007**, *515*, 5674.
262. Smith, A. R. G.; Ruggles, J. L.; Cavaye, H.; Shaw, P. E.; Darwish, T. A.; James, M.; Gentle, I. R.; Burn, P. L. Investigating Morphology and Stability of *Fac*-Tris (2-Phenylpyridyl)Iridium(III) Films for Oleds, *Adv. Funct. Mater.* **2011**, *21*, 2225.
263. Ho, M.-H.; Balaganesan, B.; Chu, T.-Y.; Chen, T.-M.; Chen, C. H. A Morphologically Stable Host Material for Efficient Phosphorescent Green and Red Organic Light Emitting Devices, *Thin Solid Films* **2008**, *517*, 943.
264. Tsuji, H.; Sato, K.; Sato, Y.; Nakamura, E. Benzophosphole Oxide and Sulfide for Thermally Stable Cathode Buffer Layers in Organic Thin-Film Photovoltaic Devices, *Chem.-Asian J.* **2010**, *5*, 1294.
265. Wu, M.-H.; Lee, J.-H.; Leung, M.-K.; Liao, C.-C.; Chang, Y. Low-Power-Consumption and Long-Lifetime Oled with a High T_g N-Type Organic Transport Material, *Proc. SPIE-Int. Soc. Opt. Eng.* **2004**, *5519*, 263.
266. Kuwabara, Y.; Ogawa, H.; Inada, H.; Noma, N.; Shirota, Y. Thermally Stable Multilared Organic Electroluminescent Devices Using Novel Starburst Molecules, 4,4′,4″-Tri(N-Carbazolyl)Triphenylamine (Tcta) and 4,4′,4″-Tris(3-Methylphenylphenylamino)Triphenylamine (M-Mtdata), as Hole-Transport Materials, *Adv. Mater.* **1994**, *6*, 677.
267. Ding, J.; Wang, Q.; Zhao, L.; Ma, D.; Wang, L.; Jing, X.; Wang, F. Design of Star-Shaped Molecular Architectures Based on Carbazole and Phosphine Oxide Moieties: Towards Amorphous Bipolar Hosts with High Triplet Energy for Efficient Blue Electrophosphorescent Devices, *J. Mater. Chem.* **2010**, *20*, 8126.
268. Fullagar, W. K.; Aberdeen, K. A.; Bucknall, D. G.; Kroon, P. A.; Gentle, I. R. Conformational Changes in Sp-B as a Function of Surface Pressure, *Biophys. J.* **2003**, *85*, 2624.
269. Cavaye, H.; Smith, A. R. G.; James, M.; Nelson, A.; Burn, P. L.; Gentle, I. R.; Lo, S. C.; Meredith, P. Solid-State Dendrimer Sensors: Probing the Diffusion of an Explosive Analogue Using Neutron Reflectometry, *Langmuir* **2009**, *25*, 12800.
270. Crank, J. *The Mathematics of Diffusion*; Oxford, 1979.
271. Mehrer, H. *Diffusion in Solids*; Springer: Berlin, 2007.
272. Erdélyi, Z.; Beke, D. Nanoscale Volume Diffusion, *J. Mater. Sci.* **2011**, *46*, 6465.
273. Csik, A.; Langer, G. A.; Beke, D. L.; Erdelyi, Z.; Menyhard, M.; Sulyok, A. Interdiffusion in Amorphous Si/Ge Multilayers by Auger Depth Profiling Technique, *J. Appl. Phys.* **2001**, *89*, 804.
274. Erdélyi, Z.; Katona, G. L.; Beke, D. L. Nonparabolic Nanoscale Shift of Phase Boundaries in Binary Systems with Restricted Solubility, *Phys. Rev. B* **2004**, *69*, 113407.
275. Cao, B. S.; Lei, M. K. Nonlinear Interdiffusion in Binary Nanometer-Scale Multilayers Submitted to Thermal Annealing, *Thin Solid Films* **2008**, *516*, 1843.
276. Lin, X. C. Taking Snapshots of Photoexcited Molecules in Disordered Media by Using Pulsed Synchrotron X-Rays, *Angew. Chem., Int. Ed.* **2004**, *43*, 2886.